UNIVERSIDADE FEDERAL DO RIO GRANDE DO SUL
INSTITUTO DE GEOCIÊNCIAS
PROGRAMA DE PÓS-GRADUAÇÃO EM GEOCIÊNCIAS

LITOFÁCIES, FÁBRICA MAGNÉTICA E GEOQUÍMICA DE CONDUTOS ALIMENTADORES E LAVAS ÁCIDAS DO GRUPO SERRA GERAL NO NORDESTE DO RIO GRANDE DO SUL

MATHEUS SILVA SIMÕES

ORIENTADOR – Prof. Dr. Evandro Fernandes de Lima
CO-ORIENTADOR – Prof. Dr. Carlos Augusto Sommer

Volume único

Porto Alegre – 2018

UNIVERSIDADE FEDERAL DO RIO GRANDE DO SUL
INSTITUTO DE GEOCIÊNCIAS
PROGRAMA DE PÓS-GRADUAÇÃO EM GEOCIÊNCIAS

LITOFÁCIES, FÁBRICA MAGNÉTICA E GEOQUÍMICA DE CONDUTOS ALIMENTADORES E LAVAS ÁCIDAS DO GRUPO SERRA GERAL NO NORDESTE DO RIO GRANDE DO SUL

MATHEUS SILVA SIMÕES

ORIENTADOR – Prof. Dr. Evandro Fernandes de Lima
CO-ORIENTADOR – Prof. Dr. Carlos Augusto Sommer

BANCA EXAMINADORA

Prof. Dr. Valdecir de Assis Janasi – Instituto de Geociências, Universidade de São Paulo

Profa. Dra. Eleonora Maria Gouvea Vasconcellos – Departamento de Geologia, Universidade Federal do Paraná

Prof. Dr. Jairo Francisco Savian – Instituto de Geociências, Universidade Federal do Rio Grande do Sul

Tese de Doutorado apresentada como requisito parcial para a obtenção do Título de Doutor em Ciências.

Porto Alegre – 2018

Simões, Matheus Silva

Litofácies, fábrica magnética e geoquímica de condutos alimentadores e lavas ácidas do Grupo Serra Geral no Nordeste do Rio Grande do Sul. / Matheus Silva Simões. - Porto Alegre: IGEO/UFRGS, 2018.

[255 f.] il.

Tese (Doutorado).- Universidade Federal do Rio Grande do Sul. Programa de Pós-Graduação em Geocências. Instituto de Geociências. Porto Alegre, RS - BR, 2018.

Orientador: Evandro Fernandes de Lima

Co-Orientador – Prof. Dr. Carlos Augusto Sommer

1. Geoquímica. 2. Estratigrafia de sequencias. 3. Vulcanismo. 4. Nordeste do Rio Grande do Sul. I. Título.

CDU 551.21

Catalogação na Publicação

Biblioteca Instituto de Geociências - UFRGS

Renata Cristina Grun CRB 10/1113

Universidade Federal do Rio Grande do Sul - Campus do Vale Av. Bento Gonçalves, 9500 - Porto Alegre - RS - Brasil

CEP: 91501-970 / Caixa Postal: 15001.

Fone: +55 51 3308-6569

E-mail: bibgeo@ufrgs.br

AGRADECIMENTOS

Primeiramente gostaria de agradecer aos meus pais, Maria Cristina Vital Silva e Jorge Luiz Simões, minha irmã Amanda Baraldo e à minha avó Ligia Vital Silva pelo carinho, pela educação que me deram, pela amizade, apoio, compreensão, além dos momentos de diversão e descontração, que hoje são multiplicados pela presença do meu afilhado Pietro Baraldo. /À Daniela Bessa, pelo carinho, amizade, momentos maravilhosos, risadas gostosas, além de estar sempre disposta a ouvir meu papo geológico./Ao Prof. Dr. Evandro Fernandes de Lima, meu orientador. Há dez anos me tornei bolsista da sala 102-B do DEMIPE-UFRGS. Eu, que quando cheguei não sabia nem fazer a minha agenda de horários no excel, sou muito grato pelas oportunidades, instigações, broncas, moderações e pelos seus ensinamentos, sendo o principal deles: "questione a todos, inclusive a mim". Caro amigo, me formaste não apenas como geólogo, mas como pessoa, mostrando a ética no trabalho e principalmente dando valor profissional aos que se dedicam às suas carreiras./Ao Prof. Dr Carlos Augusto Sommer, meu co-orientador e professor desde o primeiro ano de geologia. Obrigado por também auxiliar na minha formação e por participar do nosso trabalho com a sua excelência em geologia, contribuindo com ideias importantes e decisivas./Aos colegas de curso desde o primeiro semestre, Lucas M. M. Rossetti, que participou ativamente em etapas de campo e na contribuição intelectual para o trabalho da tese e Eduardo Bortolin pela amizade, risadas, churrascos e cervejas compartilhadas./À Profa. Dra. Maria Irene B. Raposo por ter sido tão aplicada nos trabalhos de campo, no laboratório, nas discussões, e por ter me ensinado muitas coisas sobre a técnica de anisotropia de susceptibilidade magnética, engrandecendo esta parte da tese./À CPRM (Companhia de Pesquisa de Recursos Minerais/Serviço Geológico do Brasil) pelos treinamentos, experiências, trabalhos de campo e pela oportunidade de desenvolver trabalhos em geologia. Em especial também agradeço os ensinamentos do ex-superintendente regional de Porto Alegre, Geól. Eduardo Camozzato (*in memoriam*), que auxiliou na minha formação profissional, e aos laminadores e auxiliares de campo da SUREG-Manaus, Oscar Brito e Wianey Assunção, pela confecção e polimento das lâminas./Ao Prof Dr. Ruy Paulo Philipp, orientador do meu mestrado, que também me forneceu um vasto conhecimento em geologia regional e estrutural./ À turma de bolsistas das vulcânicas: Marcos Rossetti, Fernando da Luz, Roberto Noll Filho, Natália Gauer, e Jonas Weschenfelder pela ajuda no campo, no laboratório, na organização, e como companhia para discutir geologia./Aos meus amigos e colegas da CPRM-Manaus, Gilmar Honorato, Paulo Benevides Filho, Raul Meloni, Sérgio Almada, Lucas Balsini, Tomas Lisboa, Renê Luzardo, Leonardo Aguiar, Lila Queiroz e Luna Gripp por compartilharem felicidades, angústias, mapeamentos, artigos e convivência./Aos professores Dr. Edinei Koester, Dra. Márcia B. Gomes e Dr. Jairo F. Savian pelas correções, sugestões e colaborações na minha qualificação, o último também por emprestar a sua perfuratriz./À Profa. Dra. Maria de Fátima Saraiva Bitencourt por emprestar a máquina perfuratriz reserva em uma das campanhas de campo./ Ao Dr. Marcelo Vasquez e ao técnico Paulo Mileo pela orientação e execução nas análises de MEV na superintendência da CPRM em Belém./ À Isabela Sousa e Íris Dias pelo auxílio e ensinamentos durante a etapa de microssonda eletrônica na UnB.

Por fim, agradeço a todos pela paciência!

Num meio dia de fim de primavera
eu tive um sonho como uma fotografia.
Eu vi Jesus Cristo descer à Terra,
Ele veio pela encosta de um monte
tornado outra vez menino,
a correr e a rolar-se pela erva,
e a arrancar flores para as deitar fora
e a rir de modo a ouvir-se de longe!

Ele tinha fugido do céu,
era nosso demais para fingir
de segunda pessoa da Trindade.
No céu era tudo falso, tudo em desacordo
com flores e árvores e pedras,
No céu Ele tinha que estar sempre sério,
e de vez em quando de se tornar outra vez homem,
e subir para a cruz, e estar sempre a morrer
com uma coroa toda à roda de espinhos
e os pés espetados por um prego com cabeça,
e até com um trapo à roda da cintura,
como os pretos nas ilustrações.

[...]

Um dia que Deus estava a dormir
e o Espírito Santo andava a voar,
Ele foi à caixa dos milagres e roubou três:
Com o **primeiro**
fez que ninguém soubesse que ele tinha fugido,
com o **segundo**
criou-se eternamente humano e menino,
com o **terceiro**
criou um Cristo eternamente na cruz
e deixou-o pregado na cruz que há no céu
e serve de modelo às outras.

Depois fugiu para o sol
e desceu pelo primeiro raio que apanhou.
Hoje, vive na minha aldeia comigo.
É uma criança bonita de riso e natural.
Ele limpa o nariz no braço direito,
Ele chapinha nas poças de água,
Ele colhe as flores e gosta delas.
Esquece-as.
Atira pedras nos burros,
rouba as frutas dos pomares
e foge a chorar e a gritar dos cães.
E, porque sabe que elas não gostam,
e que toda a gente acha graça,
Ele corre atrás das raparigas
que vão em ranchos pelas estradas
com aquelas bilhas nas cabeças,
e levanta-lhes as saias!

A mim, **ensinou-me tudo**.
Ensinou-me a olhar para as coisas,
aponta-me todas as coisas que há nas flores,
mostra-me como as pedras são engraçadas
quando a gente as tem na mão
e olha devagar para elas.

[...]

Depois, cansado,
o menino Jesus adormece nos meus braços
e eu levo-o ao colo para casa.

Ele mora comigo na minha casa,
a meio do outeiro.
Ele é a Eterna Criança.
O deus que faltava.
Ele é o humano que é natural.
Ele é o divino que sorri e que brinca.
E por isso é que eu sei com toda a certeza
que Ele é o Menino Jesus verdadeiro.
Damo-nos tão bem um com o outro,
na companhia de tudo,
que nunca pensamos um no outro,
mas vivemos juntos os dois.
Com um acordo íntimo,
como a mão direita e a esquerda.

[...]

Depois eu conto-lhe histórias das coisas só dos homens
e ele sorri, porque tudo é incrível.
Ele ri dos reis
e dos que não são reis,
E tem pena de ouvir falar das guerras,
dos comércios, da violência,
dos navios que ficam fumo no ar dos altos-mares.
Porque ele sabe que a tudo isso falta àquela verdade
que uma flor tem ao florescer
e que anda com a luz do sol
a variar os montes e os vales,
e fazem doer aos olhos, os muros caiados.
Depois ele adormece e eu deito-o.
Levo-o ao colo para dentro de casa
e deito-o, despindo-o lentamente.
E como seguindo um ritual muito limpo
e todo materno até ele estar nu.
Ele adormece dentro da minha alma
e às vezes acorda de noite
e brinca com os meus sonhos,
vira uns de pernas para o ar,
põe uns em cima dos outros
e bate as palmas sozinho
Sorrindo para o meu sono.

Quando eu morrer,
conta-me histórias
caso eu acorde,
para eu tornar a adormecer.
E dai-me sonhos teus para eu brincar
até que nasça,
qualquer dia que tu sabes qual é.

[...]

Esta é a história do meu Menino Jesus.
Por que razão que se perceba
não há de ser ela mais verdadeira
que tudo quanto os filósofos pensam
e tudo quanto as religiões ensinam?

Alberto Caeiro (Fernando Pessoa)

RESUMO

Na região nordeste do Rio Grande do Sul aflora uma sucessão vulcânica com mais de 800m. Na porção superior desta sequência encontram-se as vulcânicas ácidas (~200m) da LIP Paraná-Etendeka. Três áreas desta região foram escolhidas para investigação: Mato Perso (MP), São Marcos (SM) e Jaquirana-Cambará do Sul (JC). Nestas áreas foi reconhecida uma arquitetura de litofácies de condutos alimentadores e de lavas. Os condutos possuem ~15-25 m de largura, exibindo, no seu núcleo, litofácies coerentes e pouco vesiculadas de cor preta, bandadas e dobradas. Nas bordas ocorrem litofácies coerentes vesiculadas oxidadas, vitrófiros esferulíticos e brechas. As lavas são compostas por vitrófiros maciços ou com foliação horizontal, localmente bandados, ou microfraturados. Em Mato Perso, lavas oxidadas ocorrem na base da sequência estratigráfica. Estruturas regionais de direção NE-SW, como o Lineamento Antas, limitam estruturas de menor escala de direção NW-SE, onde os condutos afloram. As estruturas verticais no núcleo dos condutos estão orientadas nas direções NE-SW e NW-SE, e sua fábrica magnética possui K_{max} horizontal a localmente vertical, sugerindo fluxo horizontal. No entanto, a alta dispersão dos dados em alguns sítios deve-se a obstrução do fluxo por fragmentos e pelos padrões de dobramento complexos. As lavas possuem planos de foliação magnética horizontais, com lineação magnética mergulhando para NE, NW, SE e SW. O baixo conteúdo de vesículas no interior dos condutos e nas lavas manteve as direções de fluxo e baixos parâmetros de capilaridade, sendo potenciais zonas de preservação da trama magnética original. Na borda dos condutos, as altas taxas de cisalhamento, além do alto conteúdo de fragmentos e bolhas induziram a instabilidade do fluxo, favorecendo a distribuição aleatória da trama. As feições distintivas das áreas estudadas são o conteúdo e tamanho dos fenocristais e microfenocristais de plagioclásio+clinopiroxênio+titanomagnetita±sanidina, que diminuem de MP para SM e JC. Diferenças também são conferidas na química mineral: em MP e SM os plagioclásios são cálcicos e os piroxênios levemente menos férricos que JC, onde os plagioclásios são sódicos. Modelos de assimilação e cristalização fracionada (AFC) e balanço de massa forneceram bons resultados para o fracionamento de andesitos basálticos, sotopostos na pilha vulcânica, gerando proporções de assembleia fracionada muito próximas das observadas em lâmina. Os padrões de elementos-traço e terras raras, normalizados pelo manto primitivo, são muito parecidos com os dos andesitos basálticos, sendo apenas levemente mais enriquecidos. Diferenças em razões de elementos incompatíveis, são atribuídas a variações da fonte e da crosta assimilada. Altas temperaturas (>1000°C), conteúdos de água em torno de 0,5-1,3% e viscosidades entre 10^6-10^3 Pa s mantiveram o carácter efusivo das erupções. Paleopressões calculadas (~4-9 kbar) são compatíveis com modelos onde o reservatório estacionou no limite manto-crosta. A variação de temperatura no manto superior ocorreu em resposta à tectônica de placas nas margens do Gondwana. Movimentos constritivos progressivos, antes da quebra do Supercontinente, diminuíram a distância entre o reservatório e a superfície, possibilitando maiores taxas de efusão e ascensão dos magmas ácidos. O magma ascendeu por falhas e os condutos serviram de fonte proximal para as lavas.

ABSTRACT

The northeastern portion of Rio Grande do Sul exposes a ~800m volcanic succession. In upper part of the sequence there are silicic volcanics (~200m) of the Paraná-Etendeka LIP. Three areas from this portion were chosen for investigation: Mato Perso (MP), São Marcos (SM) and Jaquirana-Cambará do Sul (JC). Conduit-related and lava-related lithofacies architecture were recognized in these areas. The conduits are ~15-25m in width, and display coherent, banded and folded poorly vesicular lithofacies at their core. In the boarders there are oxidized vesicle-rich lithofacies together with spherulitic vitrophyres and breccias. Lavas are composed of massive or flat-lying foliated vitrophyres, locally banded or microfractured. At Mato Perso, oxidized lavas were described in the base of the silicic stratigraphic sequence. Regional structures trending NE-, like the Antas lineament, control smaller-scale structures trending NW-, where conduits outcrop. Vertical structures in the core of the conduits are trending NE- and NW-, and magnetic fabric has horizontal, locally vertical, K_{max}, suggesting horizontal flow. Although, high dispersion of data in some sites is explained by obstruction of the flow by fragments and by complex folding patterns. Lavas have flat-lying magnetic foliation planes and magnetic lineation plunging to NE, NW, SE and SW. Low vesicle content in conduit cores and lavas maintained the flow directions and low capillarity parameters, being potential zones for preservation of original magnetic fabric. At conduit boarders, the high shear rates besides high fragment and bubble contents induced flow unsteadiness, favoring the random distribution of the magnetic fabric. Distinctive features between study areas are the plagioclase+clinopyroxene+titanomagnetite±sanidine phenocryst/microphenocryst size and content. They decrease from MP to SM and JC. Differences are observed in mineral chemistry too: MP and SM plagioclases are more calcic and the pyroxenes less ferric than JC, where plagioclases are sodic. Assimilation and fractional crystallization (AFC) and mass balance models yielded good results for underlying basaltic andesite fractioning, generating mineral assembly in proportions similar to those observed in thin-section. Primitive mantle normalized trace-element and rare earth patterns resemble those of basaltic andesites, being slightly more enriched. Difference on incompatible trace element ratios is ascribed to variations within the source and the assimilated crust. High temperatures (>1000°C), water contents between 0.5-1.3 wt.% and viscosities between 10^6-10^3 Pa s kept the effusive behavior of eruptions. Calculated paleopressures (~4-9 kbar) are compatible with models where the reservoir was ponded in the mantle-crust boundary. The temperature variation in the upper mantle has occurred in response to Gondwana plate tectonics at active margins. Progressive constrictive movements, before the Supercontinent break-up, decreased the distance between the reservoir and the surface, enabling higher effusion rates and ascent of silicic magmas. The magma ascended through faults and the conduits were the lavas proximal sources.

Lista de Figuras

Lista de Quadros

GLOSSÁRIO

Afinidade toleítica – afinidade geoquímica de rochas que mostram o trend de Fenner, de correlação positiva seguida de correlação negativa entre FeO e MgO.

Anisotropia de susceptibilidade magnética (ASM) – técnica geofísica que mede os parâmetros de forma e a orientação da trama magnética, geralmente representados por elipsoides e estereogramas, respectivamente.

Aparente coerente – textura gerada em rochas piroclásticas por alto grau de soldagem, gerando um aspecto coerente, como em depósitos de ignimbritos reomórficos ou *lava-like*.

Aparente vulcanoclástico – textura gerada por processos de alteração que ocorrem geralmente em fraturas, fazendo com que a rocha coerente pareça um tufo soldado ou uma brecha lítica. Texturas microesferulíticas também podem lembrar feições psamíticas.

Associação de fácies – conjunto de fácies que não é dividido por discordâncias. A interpretação desta associação é uma ferramenta utilizada para a caracterização de paleoambiente vulcânico ou sedimentar.

Autobrecha – brecha autoclástica formada por fragmentos da própria rocha que sofreu cominuição.

Autoclástico – material gerado durante processos onde a lava resfria e se fragmenta, sendo típica de derrames entre o espectro *'a'a* e rubbly pahoehoe em lavas basálticas ou no topo e base de lavas ácidas.

Chron – unidade magnetoestratigráfica que possui uma direção da polaridade magnética remanente característica em uma sequência estratigráfica.

Coeficiente de partição – razão entre as concentrações de um dado elemento químico em um mineral (sólido) e um magma (líquido).

Coerente – textura gerada por resfriamento da lava, podendo ser porfirítica, afanítica, afírica ou totalmente vítrea. Foliações, bandamento, esferulitos, vesículas e litofises são comuns, mas não são os principais elementos texturais.

Conduto alimentador – porção do sistema vulcânico que transporta magma da sua região de armazenamento até a sua chaminé (tradução para o português de *vent*), a partir da qual entra em erupção.

Corrente de densidade piroclástica – mistura de gás e sólidos em suspensão ejetada durante uma erupção explosiva sustentada que forma um fluido denso, movendo-se em altas velocidades próximo ao chão.

Couleé – derrame de lava intermediária ou ácida com forma alongada que entra em erupção geralmente a partir de um flanco de vulcão. As margens do couleé podem ser blocadas e em alto ângulo (levees).

Dique – fratura preenchida por material vulcânico, que corta as rochas encaixantes.

Domo de lava – fluxo de lava relativamente pequeno e curto.

Equação VFT – equação de Volgel-Fulcher-Tammann, que descreve a dependência não-Arrheniana de viscosidade em relação à temperatura.

Erupção pliniana – descarga explosiva sustentada composta por gás vulcânico e piroclastos, formando uma grande coluna eruptiva na atmosfera.

Esferulito - agregado radial, concêntrico ou alongado composto geralmente por quartzo e feldspato formados pela devitrificação de magmas ácidos.

Fenocristal – cristal de grandes proporções imerso em uma matriz fina.

Fiamme – lentes de material vítreo pumíceo que sofreu baixo a médio grau de soldagem.

Fire fountaining – erupções de conduto central que ejetam material vulcânico na forma de jatos incandescentes que ascendem centenas de metros.

Fissura – fratura na rocha que forma uma superfície alongada pela qual o magma entra em erupção.

Fluxo de lava – depósito individual de uma fase discreta de uma erupção efusiva.

Fluxo de lava canalizado – fluxo de lava no qual a lava líquida move-se em uma porção central e é bordejada por bancos laterais (levées) ou uma fluxo de lava estacionário.

Geobarometria – parte da ciência geológica que desenvolve ou aplica métodos geoquímicos experimentais para estimativas de paleopressões de formação de minerais/rochas.

Geotermometria - parte da ciência geológica que desenvolve ou aplica métodos geoquímicos experimentais para estimativas de paleotemperaturas a partir da formação de minerais e equilíbrio com o magma hospedeiro.

Grau de anisotropia – parâmetro de magnitude da ASM, baseado na razão das susceptilidade máxima e mínima, segundo a equação $P=K_1/K_3$.

Ignimbrito – unidade formada a partir da deposição de porções pouco diluídas de correntes de densidade piroclásticas.

Ignimbrito *lava-like* – unidade de ignimbrito ou parte de unidade que sofreu alto grau de soldagem (reomorfismo), fazendo com que a fina amálgama de partículas vulcânicas oblitere muitas texturas piroclásticas, dando um aspecto coerente aparente ao produto final.

Inflação – 1: aumento da câmara magmática devido a adição de magma a partir do manto. 2: processo pelo qual um fluxo de lava adquire maior espessura, como um resultado de adição de magma no seu interior.

K_{int} ou K_2 – eixo intermediário de anisotropia de susceptibilidade magnética

K_{max} ou K_1 – maior eixo de anisotropia de susceptibilidade magnética

K_{min} ou K_3 - menor eixo de anisotropia de susceptibilidade magnética

Large Igneous Province (LIP) – Depósitos contínuos com grande volume de rochas magmáticas extrusivas e/ou intrusivas ocorrendo em margens passivas vulcânicas, platôs oceânicos, cadeias submarinas, grupos de montes submarinos e basaltos de bacias oceânicas. São resultados de atividades magmáticas contínuas de grande área e volume durante um curto período de tempo (~1 – 5 Ma).

Liquidus – temperatura sobre a qual o magma está completamente fundido.

Litofácies – corpo ou intervalo de rocha com características descritivas únicas definíveis que o distinguem de outras litofácies.

Litofises – cavidades concêntricas ou alongadas geradas pela expansão de gases em rochas vulcânicas ácidas.

Microfenocristal – cristais que, mesmo identificados em microscópio, são maiores que os cristais da matriz.

Micrólito – cristal muito pequeno que compõe a matriz da rocha e é visível apenas ao microscópio.

Não-newtoniano – fluido no qual a taxa de deformação não é diretamente proporcional à taxa de estresse aplicado.

Newtoniano – Fluido no qual qualquer mudança no estresse aplicado produz uma mudança diretamente proporcional na taxa de deformação

Obsidiana – também é um nome para rocha vulcânica porfirítica vítrea, neste trabalho mantida apenas para as rochas não devitrificadas.

Ogiva – porção interna da lava ácida que é pressionada e ascende para a superfície, formando uma crista.

Pahoehoe – morfologia de derrame basáltico com topo liso ou em cordas, mostrando padrões de vesiculação em sistema fechado.

Pahoehoe composto – morfologia de derrame basáltico formada pela sobreposição de vários lobos de pequena dimensão (poucos metros) com topo liso ou em cordas e com padrões de vesiculação em sistema fechado.

Pahoehoe simples (sheet) – morfologia derrame tipo pahoehoe de grande extensão e espessura.

Perlito – fratura conchoidal gerada a partir da hidratação de vidro vulcânico.

Piroclástico - material gerado após um evento magmático explosivo, onde são ejetadas partículas quentes juvenis, cristais e fragmentos de rochas encaixantes cognatas ou não cognatas.

Pluma mantélica – parte do manto onde a flutuação (diferença de densidade) causa a ascensão das rochas quentes do manto até a crosta.

Ponded pahoehoe – derrame de lava basáltica confinado por obstáculos.

Primeiro ponto de ebulição – formação de bolhas a partir da exsolução de água solubilizada no magma.

Púmice – material vulcânico altamente vesiculado ejetado durante erupções explosivas. O termo também pode ser usado como adjetivo para materiais vulcânicos vesiculados (ex.: fragmentos pumíceos).

Reoignimbrito – ignimbrito cujas textura piroclástica foram drasticamente obliteradas, podendo apresentar foliações e dobras de fluxo.

Ressedimentado – depósito piroclástico ou autoclástico que sofreu pequeno transporte e deposição após a erupção.

Rubbly pahoehoe – morfologia de derrame do tipo pahoehoe no qual a porção de topo da lava se rompe, gerando brechas autoclásticas.

Sedimentar vulcanogênico – depósito sedimentar com mais de 50% de partículas vulcanoclásticas e que já passou por processos de transporte e deposição bem estabelecidos.

Segundo ponto de ebulição – exsolução de água a partir da cristalização de fases anidras e supersaturação relativa de água no magma.

Shard – fragmento vítreo (tradução do inglês – caco), com diversas formas, sendo sua origem comum durante a explosão de materiais pumíceos, gerando shards na forma de contramoldes de bolhas de gás.

SLIP – Acumulações de rochas vulcânicas com grande extensão e grande volume dominadas por termos ácidos (>65% SiO_2) com assinaturas geoquímicas transicionais entre intra-placa e cálcio-alcalino ou de margem convergente. Magmas de baixo-Ti podem estar presentes juntamente com os de alto-Ti.

Soldagem – desenvolvimento de força mecânica entre dois piroclastos em contato causando com que um fique grudado ao outro.

Surge piroclástico – depósito associado as porções mais diluídas de correntes de densidade piroclásticas, cujas partículas são transportadas por saltação e rolamento.

Susceptibilidade média – valor médio da susceptibilidade direcional sobre um espécime como um todo. Fornecida pela equação $K_{médio} = K_1 + K_2 + K_3/3$

Textura micropoiquilítica – Agregados de cristais muito pequenos que se formam a partir da devitrificação de fragmentos ou de rocha hialina.

Vitrófiro – rocha vulcânica com fenocristais imersos em matriz vítrea.

Vulcanoclástico – termo meramente descritivo aplicado a depósitos ricos em partículas de origem vulcânica. Não implica nenhum processo formador de partículas, de transporte ou de deposição.

Vulcanologia física – ciência que considera os processos físicos de erupção magmática, começando pela sua fonte e seguindo até sua colocação em superfície.

SUMÁRIO

APRESENTAÇÃO

A presente tese de doutoramento, com início em março de 2014, foi realizada por meio do Programa de Pós-graduação em Geociências (PPGGeo) da Universidade Federal do Rio Grande do Sul (UFRGS) na área de concentração de geoquímica. Foi desenvolvida com o financiamento de projetos de pesquisa dos orientadores, Prof. Dr. Evandro Fernandes de Lima e Prof. Dr. Carlos Augusto Sommer via Conselho Nacional de Desenvolvimento Científico e Tecnológico (CNPq) e Fundação de Amparo à Pesquisa do Estado de São Paulo (FAPESP).

ESTRUTURA DA TESE

A estrutura da tese está organizada a partir de um capítulo de introdução com a localização, acesso e fisiografia das áreas, objetivos e justificativas, além de uma revisão em forma de estado da arte sobre temas e áreas relacionadas com a pesquisa, além da apresentação de estudos de caso. A revisão geral e aprofundamento na teoria das técnicas analíticas estão presentes no volume da monografia de qualificação no ano de 2015, disponível na biblioteca do Instituto de Geociências-UFRGS. Após estes primeiros capítulos, são apresentados 04 artigos científicos na língua inglesa, todos relacionados ao tema central da tese, que foram submetidos ou publicados em revistas nos estratos qualis da CAPES A1, A2, B1, B2, B3, de acordo com a Norma 103 do PPGGeo-UFRGS.

O primeiro artigo, intitulado "*Structures and lithofacies of inferred silicic conduits in the Paraná-Etendeka LIP, southernmost Brazil*" foi publicado na edição especial sobre a província Paraná-Etendeka do *Journal of Volcanology and Geothermal Research*, e apresenta uma primeira percepção em escala regional do reconhecimento da geologia da área. Neste trabalho as relações de campo e a petrografia são detalhadas, discutindo-se também a sua composição química, com foco em uma arquitetura de litofácies comum aos grupos de afloramentos estudados.

O segundo artigo, intitulado "*The Mato Perso Conduit System: evidence of silicic magma transport in the southern Paraná-Etendeka LIP*" e aceito para publicação na edição especial sobre a província Paraná-Etendeka do *Brazilian Journal of Geology*, é composto por um mapeamento de detalhe em uma das áreas da tese, e tem como objetivo mostrar as relações espaciais entre os tipos de rochas vulcânicas identificadas, além de relações estratigráficas que servem de suporte para o modelo geral.

O terceiro artigo, intitulado "*Magmatic flow patterns in silicic feeder conduits and lava flows from Paraná-Etendeka LIP, Southern Brazil: AMS fabric, magma transport properties and implications for emplacement*" foi submetido ao *Bulletin of Volcanology*, e apresenta um estudo com os dados de anisotropia de susceptibilidade magnética e a caracterização de diferentes propriedades físicas que influenciam no fluxo magmático.

O quarto artigo, intitulado "*Storage and emplacement of low-Ti silicic volcanics in the southern Paraná-Etendeka LIP: extensional tectonics controlling the ~134 Ma silicic volcanism in the early stages of Gondwana break-up*", submetido ao periódico International Geology Review, contém uma caracterização de química mineral e geoquímica de rocha-total. A partir destes dados foram testados modelos de balanço de massa e cristalização fracionada, a fim de comparar possíveis fontes magmáticas. Parâmetros como temperatura, conteúdo de água, viscosidade e paleopressões foram calculados e um modelo de evolução tectônica para o magmatismo é apresentado.

Capítulo 1 - INTRODUÇÃO

O magmatismo é um fenômeno geológico que ocorre quando as frações sólidas do manto ou da crosta perdem sua estabilidade termodinâmica e passam a fundir parcialmente. Aumento de temperatura, diminuição de pressão, variação no conteúdo de água do magma e a interação com outros corpos magmáticos são as variáveis mais discutidas para descrever as condições de formação de magmas. Existem quatro tipos principais de ambientes tectônicos onde magmas podem ser gerados (Wilson, 1989):

- Margens de placa construtivas: limites de placa divergentes que incluem o sistema de dorsais meso-oceânicas e centros de espalhamento em *back-arcs*;

- Margens de placa destrutivas: limites de placa convergentes que incluem arcos de ilha e margens ativas continentais;

- Ambientes intraplaca oceânicos: ilhas e platôs oceânicos;

- Ambientes intraplaca continentais: províncias basálticas continentais (PBCs), zonas de rifte continental e ocorrências de magmatismo potássico e ultrapotássico não relacionado a zonas de rifte.

Os ambientes intraplaca, oceânicos e continentais, são os locais mais frequentes de ocorrência de Large Igneous Provinces (LIPs, **figura 1**). LIPs são depósitos contínuos com grande volume de rochas magmáticas, incluindo PBCs, e rochas intrusivas associadas, ocorrendo em margens vulcânicas passivas, platôs oceânicos, cadeias submarinas, grupos de montes submarinos e basaltos de bacias oceânicas (Coffin & Eldholm, 1994). Seus depósitos, com extensões areais maiores que 0,1 Mkm^2, volumes ígneos maiores que 0,1 Mkm^3 são gerados por atividades magmáticas contínuas, de grande área e volume, durante um curto período de tempo (1-5 Ma, Bryan & Ernst, 2008). Adicionalmente, deve-se considerar que 'existem LIPs e LIPs' (Saunders, 2005), no sentido de que tipos, composições e modos de ocorrência de rochas vulcânicas podem variar, sendo cada caso um caso.

Os produtos vulcânicos que dominam a arquitetura de LIPs são extensos campos de lavas basálticas (e.g. Self *et al.*, 1997; Jerram, 2002; White *et al.*, 2009; Bryan, 2010), sendo também seus constituintes as intrusões de sills e diques (Jerram, 2002; Raposo et al., 2011). Algumas províncias, como a LIP Siberiana podem exibir extensos depósitos vulcanoclásticos máficos (Ross *et al.*, 2005). Piroclásticas e efusivas ácidas também são registradas em LIPs como Atlântico Norte e Central, Columbia River, Deccan, Emeishan, Ethiopian, Karoo, Ferrar e Paraná-Etendeka (Leeman, 1982; Xu *et al.*, 2010; Natali *et al.*, 2011; Milner *et al.*, 1992, 1995; Bryan, 2002). Embora constituam menos de 5% do volume total da LIP associada, o magmatismo ácido pode construir volumes de até 10^6 km^3 (Bryan, 2002).

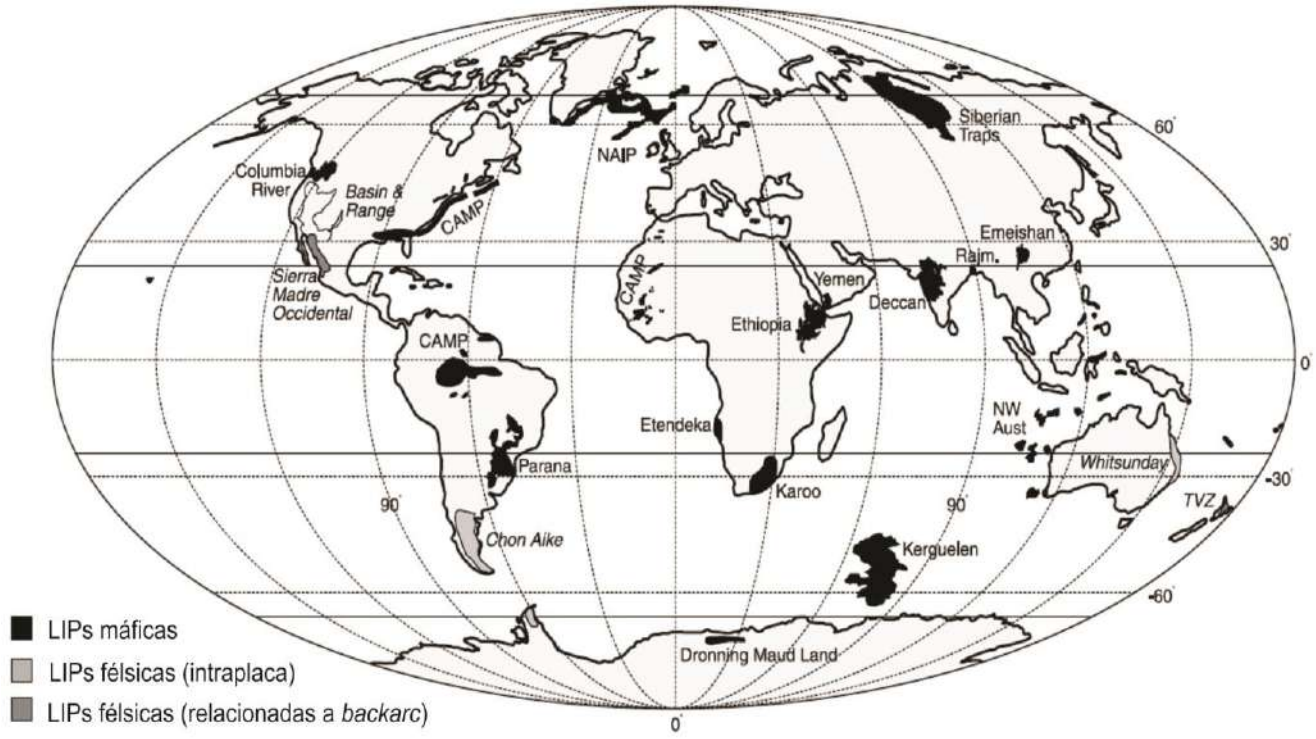

Figura 1 – Distribuição das principais ocorrências de Large Igneous Provinces. NAIP = *North Atlantic igneous province*, CAMP = *Central Atlantic magmatic province,* Rajm = *Rajmahal basalts*, TVZ = *Taupo volcanic zone*, NW Aust = *Northwest Australian oceanic plateaus*. Modificado de Bryan (2002).

Na LIP Paraná-Etendeka, os maiores volumes de vulcânicas ácidas ocorrem no sul do Brasil, ocupando uma área superior a 70 km² e repousando na parte superior de uma sequência com mais de 800 m de lavas basálticas. No presente trabalho será apresentado um detalhamento geológico de três áreas de ocorrência de vulcânicas ácidas que foram escolhidas como objeto de estudo na porção nordeste do Rio Grande do Sul. Para isso, foram utilizadas técnicas de mapeamento geológico básico, análises petrográficas, geoquímicas e de fábrica magnética, detalhadas nos capítulos seguintes da tese.

1.1 Fisiografia, localização e acesso às áreas de estudo

Se tomarmos a fisiografia do Estado como referência, as áreas escolhidas ocorrem nas porções mais elevadas, onde as altitudes variam entre ~400 e ~1200 m acima do nível do mar (**Fig. 2**). Nesta região, a maior bacia hidrográfica é atribuída ao rio das Antas, com jusante no extremo nordeste do Estado e montante no rio Taquari, formando sua rede de drenagem principal com uma forma curva, alongada na direção NE-SW.

Estas áreas pertencem aos municípios de São Marcos, Jaquirana, Cambará do Sul e Flores da Cunha, onde está localizado o distrito de Mato Perso. O acesso pode ser realizado a partir de Porto Alegre pela BR-116 ou alternativamente pela BR-290 até o seu encontro com a BR-453 ou ERS-486 (Rota do Sol), com duração de aproximadamente 2-3h de viagem de carro (**Fig. 3**).

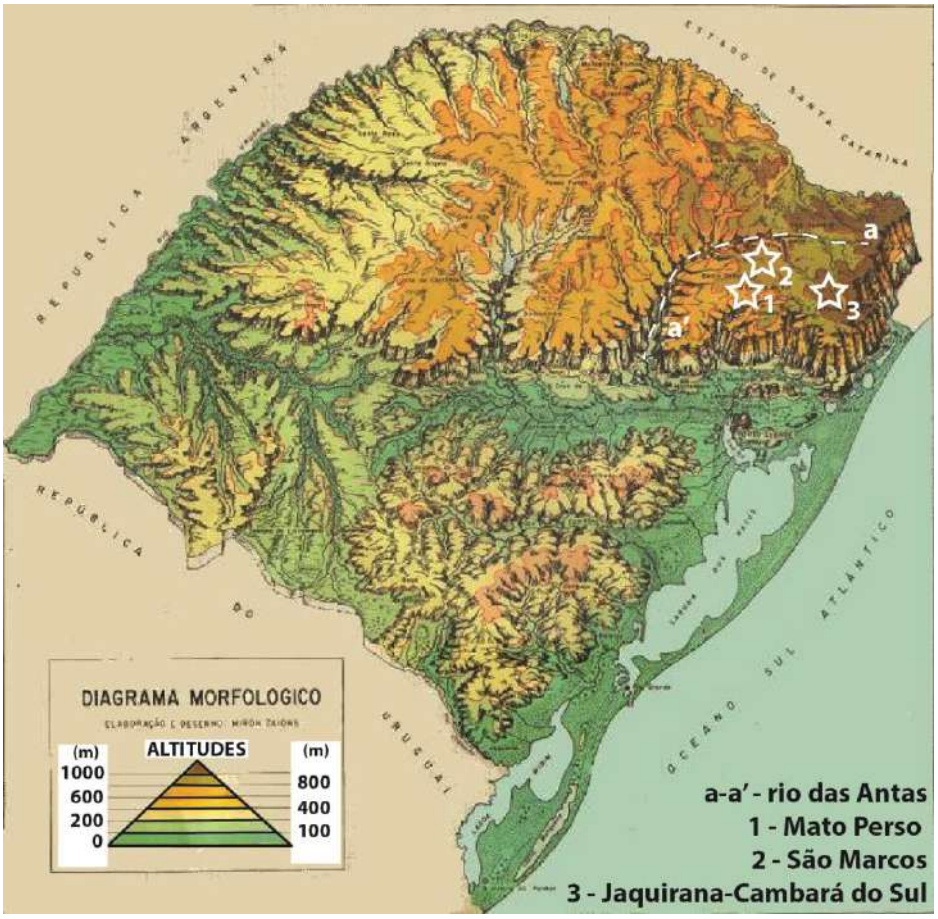

Figura 2 – Mapa geomorfológico do Rio Grande do Sul modificado de Zaions (1989).

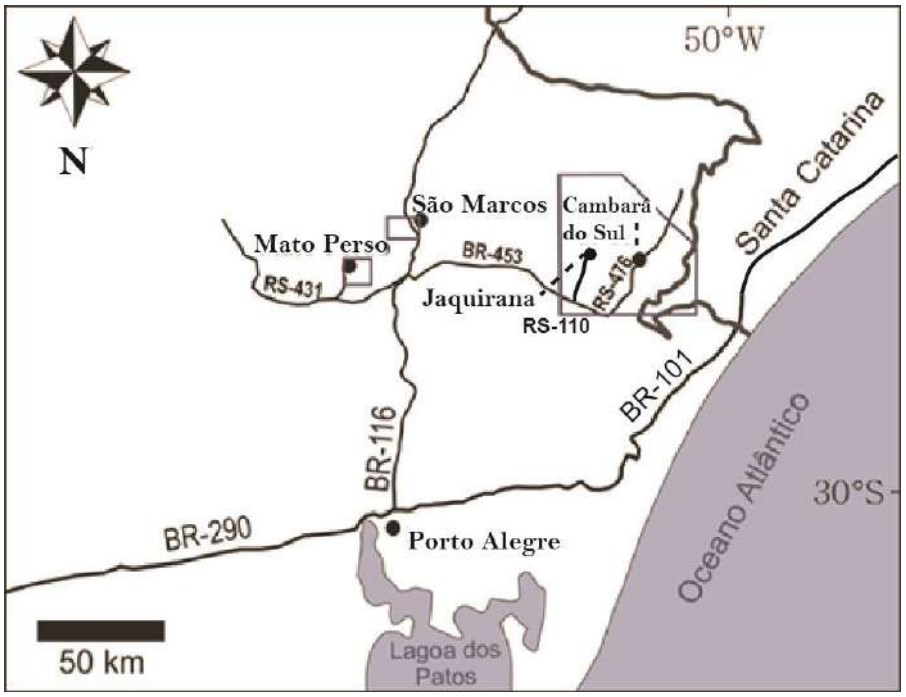

Figura 3 – Mapa de localização das áreas de estudo.

1.2 Justificativa

As rochas ácidas do Grupo Serra Geral (GSG, *sensu* Rossetti *et al.*, 2017) foram extensivamente estudadas nos anos 1980 e 1990, resultando em trabalhos que envolveram caracterizações geoquímicas e paleomagnéticas (e.g. Bellieni *et al.*, 1983, 1984, 1986, 1988; Peate *et al.*, 1992; Peate, 1997; Garland *et al.*, 1995; Janasi *et al.*, 2007; Nardy et al., 2008), estratigrafia com base em dados geoquímicos (e.g. Melfi *et al.*, 1988, Milner *et al.*, 1995), petrografia (e.g. Comin-Chiaramonti *et al.*, 1988, Roisenberg, 1989; Milner *et al.*, 1992), geocronologia (e.g. Piccirilo *et al.*, 1987; Renne *et al.*, 1992; Turner *et al.*, 1994; Pinto *et al.*, 2010; Janasi *et al.*, 2011) e geoquímica isotópica (e.g. Mantovani *et al.*, 1985; Cordani *et al.*, 1988; Garland *et al.* 1995).

O avanço no reconhecimento regional de diferentes unidades com afinidades geoquímicas próprias, além do arcabouço estratigráfico já estabelecido serviram de base para estudos de vulcanologia física e associação de litofácies (e.g. Umann *et al.*, 2001; Lima *et al.*, 2012; Waichel *et al.*, 2012; Polo & Janasi, 2014; Simões *et al.*, 2014; Lima *et al.*, 2018).

As justificativas de investigação do presente trabalho são a identificação prévia de litofácies e estruturas indicativas de diferentes tipos de sistemas e depósitos vulcânicos de composição ácida na porção sul da LIP Paraná-Etendeka, topo do GSG (e.g. Lima *et al.*, 2012; Waichel *et al*, 2012; Polo & Janasi 2014; Simões *et al.*, 2014). Outro aspecto fomentador da investigação foi o reconhecimento de estruturas e texturas, ainda muito pouco discutidas na literatura sobre a área, em rochas expostas nas pedreiras de corte e extração para rocha ornamental no município de São Marcos. Os trabalhos de

Rizzon (2010) e Lima *et al.* (2012) sugeriram que as feições observadas são indicativas de sistemas associados a condutos vulcânicos alimentadores. A repetição destas associações de estruturas como foliações sub-verticais, dobras e fragmentos em uma distribuição regional tornou-se uma justificativa para descrever as demais ocorrências. Para isso foi necessário tentar identificar as principais semelhanças e diferenças entre depósitos interpretados como lavas ou como condutos, e estabelecer comparações entre as diferentes áreas de estudo.

1.3 Objetivos

A presente tese tem como objetivo geral a caracterização das rochas vulcânicas ácidas do GSG nas três áreas de estudo propostas. Esta investigação é conduzida com enfoque na descrição de litofácies, petrologia e determinação de direções de fluxo magmático por estudos de anisotropia de susceptibilidade magnética. O acervo de dados adquirido serve para fornecer uma discussão adequada aos aspectos de vulcanologia física, ou seja, na aplicação de princípios físicos básicos para descobrir como vulcões funcionam (Parfitt and Wilson, 2008), ou funcionaram.

Os objetivos específicos são: (1) Mapeamento geológico para a espacialização dos tipos de rochas e de estruturas, aquisição de dados estruturais, coleta de amostras e verificação de estruturas previamente identificadas em imagens de satélite. Realizado a partir de levantamento em escalas de trabalho de semi-detalhe (1:100.000, 1:25.000) para a confecção de mapas e de detalhe (1:10.000, escala de afloramento) para a confecção de seções locais e croquis esquemáticos; (2) Análise petrográfica para identificação dos minerais constituintes, texturas e microestruturas presentes nas rochas estudadas; (3) Utilização de dados de geoquímica de rocha total a fim de uma investigação sobre diferentes tipos químicos, correspondência composicional entre diferentes porções do ambiente vulcânico e a identificação de *trends* de diferenciação; (4) Caracterização da orientação da trama magnética mineral das amostras com o uso do método de anisotropia de susceptibilidade magnética (ASM) para investigar as principais direções e os principais fatores que influenciam o fluxo magmático nas rochas estudadas; (5) Investigação por meio de Microscópio Eletrônico de Varredura – *Energy Dispersive X-ray Spectroscopy* (EDS) e microssonda eletrônica para a verificação semi-quantitativa e quantitativa da composição química dos minerais e da distribuição de elementos químicos ao longo dos cristais, além do estabelecimento de temperaturas e pressões de formação.

Capítulo 2 - MÉTODOS

2.1 Revisão Bibliográfica

A literatura acerca das áreas investigadas está conectada às publicações que abordam as rochas vulcânicas da Bacia do Paraná em geral, com algumas delas já existentes sobre as áreas de São Marcos e Cambará do Sul (e.g. Umann et al., 2001; Rizzon, 2010; Lima et al., 2012; Lima et al., 2018). Contínuas investigações e a realização do projeto temático sobre a província Paraná-Etendeka na FAPESP resultaram na publicação de um considerável número de trabalhos científicos nos anos de 2017 e 2018, por meio da edição especial do *Journal of Volcanology and Geothermal Research*. Além da geologia regional e local, os trabalhos que detalham os depósitos vulcânicos ácidos, sua caracterização geoquímica e isotópica, e aplicações diretas da técnica de anisotropia de susceptibilidade magnética em depósitos de lavas e diques foram constantemente consultados.

2.2 Mapeamento Geológico

As três áreas de estudo foram selecionadas em função da frequência de afloramentos de rochas com bandamento sub-vertical, brechas e dobras de fluxo na porção nordeste do Rio Grande do Sul. No conjunto de afloramentos estudados também foram identificadas unidades de vulcânicas ácidas com foliações horizontais. A base de planimetria e altimetria usada é calcada nas cartas da Diretoria de Serviço Geográfico do Exército em escala 1:50.000 e a base cartográfica vertorial contínua do Rio Grande do Sul, na mesma escala, de Hasenack & Weber (2010). Para o traçado dos lineamentos de cristas e de vales utilizou-se imagens de radar SRTM (*Shuttle Radar Topography Mission*) 1 *arc-second global* e imagens de satélite *Google Earth* e *Bing Maps*. A separação de litofácies ocorreu, principalmente, nas etapas de campo. Os critérios utilizados foram a delimitação de unidades com semelhança entre as aspectos como cor, vesiculação, cristalinidade e estruturas, além do tamanho e forma dos minerais. A coleta de amostras para as etapas posteriores teve foco em amostras representativas para cada litofácies.

2.3 Petrografia

A confecção de cerca de 30 lâminas petrográficas foi realizada, em maior parte, pela *Spectrum Petrographics Inc.*, e em menor parte pelo Laboratório de Análises Minerais – CPRM, adicionando-se a um acervo confeccionado pelo laboratório de preparação de amostras da UFRGS. As fotomicrografias foram adquiridas por meio de um microscópio da marca Meiji acoplado a um *software* de imagens

.

2.4 Mapas de elementos químicos por MEV-EDS

As análises por microscopia eletrônica de varredura (MEV) foram feitas em um microscópio modelo LS15 da Zeiss no laboratório da Superintentência Regional de Belém da CPRM-Serviço Geológico do Brasil. Foi utilizado o modo de Alto Vácuo (3,0-1,5 10^{-5} mPa) e filamento de tungstênio. As lâminas polidas foram cobertas por uma película de ouro de 10 μm de espessura. As imagens de elétron retroespalhado (*Backscattered Eletron*-BSE) dos minerais e texturas foram obtidas com 20 kV, corrente de chegada entre 70 e 90 pA, distâncias de trabalho de 8,5 mm e ampliação entre 100 e 500 vezes. As análises da composição química dos minerais foram por espectrometria por dispersão de energia (*Energy Dispersive Spectrometry*-EDS) de raios X em um detector X-Act SSD 10 mm^2 da Oxford Instruments. Os resultados analíticos foram adquiridos a uma distância de trabalho foi de 8,5 mm, com voltagem de 20 kV, corrente de chegada de 170 a 400 pA para manter uma taxa de contagem de saída de cerca de 2000 cps, tanto nas análises pontuais quanto nos mapas de elementos.

2.5 Química mineral por microssonda eletrônica

Um total de 13 lâminas foi analisado em microssonda eletrônica (Electron Probe MicroAnalyzer, EPMA) para quantificar os teores de óxidos maiores como SiO_2, Al_2O_3, K_2O, Na_2O, CaO, MgO, Fe_2O_3 (total), MnO, TiO_2 e Cr_2O_3 em cristais de plagioclásio, sanidina, piroxênios, óxidos de Fe-Ti e também na matriz vítrea. As análises de EPMA foram realizadas na Universidade de Brasília (UnB) em um equipamento da marca JEOL JXA-8230, com cinco espectrômetros WDS (Wavelenght-Dispersive Spectroscopy) com cristais analisadores STE/TAP, TAP/PET, PET/LIF, PET/LIF e PET/LF, além de um detector de silício EDS. As análises foram feitas sob condições de 15 kV de corrente, 20 nA de aceleração e tamanhos dos spots entre 5 e 10 micrômetros em cristais de piroxênio e óxidos de Fe-Ti . Nas análises de matriz vítrea e plagioclásios, para evitar a difusão de elementos como Na e K, as correntes foram reduzidas para 10 nA e o raio foi descocado para 15 a 20 micrômetros de diâmetro.

2.6 Geoquímica de rocha-total

Análises de geoquímica de rocha total foram realizadas em 34 amostras, 09 de Mato Perso, 13 de Jaquirana-Cambará do Sul e 12 de São Marcos, estas últimas compiladas de Lima et al. (2012). Os procedimentos analíticos foram desenvolvidos no Acme Analytical Laboratories Ltd., in Vancouver, Canada, usando as rotinas 4A e 4B. Na primeira, a abundância total dos principais óxidos e diversos elementos menores for obtida com 0,2 g de amostra pulverizada por espectroscopia de emissão com plasma induzido acoplado (ICP-ES, Inductively Coupled Plasma — Emission Spectrometry) com limite de detecção de 0,01% para SiO_2, Al_2O_3, Fe_2O3, CaO, MgO, Na_2O, K_2O, MnO, TiO_2 and P_2O_5. Na segunda, os resultados para elementos refratários e terras raras foram obtidos utilizando a mesma

quantidade de amostra por espectrometria de massa (ICP-MS, mass spectrometry) com limites de detecção de 1 ppm para Ba, Be e Sn, 0.1 ppm para Ce, Cs, Hf, La, Nb, Rb, Ta, U, Y e Zr, 0.2 ppm para Co e Th, 0.3 para Nd, e entre 0.01 e 0.05 ppm para Dy, Er, Eu, Gd, Ho, Lu, Pr, Sm, Tb, Tm, e Yb.

2.7 Anisotropia de Susceptibilidade Magnética (ASM)

A aquisição de testemunhos orientados de rocha foi realizada em duas etapas de campo, onde foram priorizados afloramentos com boa descrição do arcabouço estrutural em etapas anteriores. Foi utilizada uma máquina perfuratriz da marca Stihl e brocas com ponta diamantada, confeccionadas pela empresa Person Bouquet.

As medidas envolvendo ASM foram obtidas no laboratório de anisotropias e magnetismo de rochas do Instituto de Geociências da Universidade de São Paulo (USP). Cada testemunho, com cerca de 8 cm, foi fatiado em espécimes de aproximadamente 2,2 cm, usadas para as medidas de anisotropia em um instrumento MFK1-FA da AGICO. As medidas consistiram na aplicação de um campo magnético baixo (425 A/m) na amostra ao longo da sua rotação em três eixos ortogonais. A orientação de cada espécime é representada em estereogramas equi-área de hemisfério inferior. As orientações médias dos principais eixos magnéticos é representada por símbolos maiores nos diagramas e foram calculadas pelo software ANISOFT 4.2 (Chadima and Jelinek, 2009) utilizando a estatística de Hext-Jelinek (Hext, 1963; Jelinek, 1978). As variáveis calculadas são divididas em parâmetros de forma e magnitude. Os de magnitude são o tensor médio de susceptibilidade ($k_m=k_{max}+k_{int}+k_{min}/3$), que representa a média da susceptibilidade total de cada espécime e o grau de anisotropia corrigido (Pj), que é uma medida da anisotropia total. O parâmetro de forma T define a excentricidade do elipsoide de strain, onde $0<T\leq1$ é referido a formas oblatas, $-1\leq T<0$ a formas oblatas e T=1 a formas triaxiais. Esta relação também pode ser observada plotando os parâmetros T versus Pj (Jelinek, 1981; Hrouda 1982).

2.8 Geotermometria

2.8.1 *Saturação em apatita*

O modelo de saturação em apatita de Harrison & Watson (1984) foi elaborado experimentalmente, a partir da dissolução de cristais de apatita em fusões com 0-10% de H_2O. A solubilidade da apatita nestes experimentos pode ser descrita em função da temperatura, de acordo com a equação:

$$\text{Ln } D_P^{\text{apatita/fusão}} = [(8400 + ((SiO_2 - 0{,}5)\ 2{,}64 \times 10^4))/T] - [3.1 + (12.4\ (SiO_2 - 0{,}5))] \quad (1)$$

Este modelo foi utilizado para adquirir temperaturas próximas à *liquidus*, tendo em vista que a apatita é o principal mineral acessório, na forma de micrólitos. Por definição, foi assumido um coeficiente de partição 42 para o fósforo, de acordo com Watson & Green (1981) e Prowwatke & Klemme (2006), e os resultados de análises de geoquímica de rocha total para P_2O_5 foram utilizados como partição da apatita no magma, considerando o fósforo um constituinte estrutural essencial (e.g. Sun & Hanson, 1975).

2.8.2 *Equilíbrio plagioclásio-líquido*

Outra abordagem de geotermometria é fornecida por Putirka (2005), onde o autor calibra um geotermômetro baseado no equilíbrio entre o plagioclásio, uma das principais fases presentes nas amostras estudadas, e o líquido, a partir de um valor de pressão assumido:

$$10^4/T(K) = 6{,}12 + 0{,}257 \ln([An^{pl}]/[Ca^{liq}(Al^{liq})^2(Si^{liq})^2]) - 3.166[Ca^{liq}] + 0.2166[H_2O^{liq}] \quad (2)$$

$$-3.137[Al^{liq}/Al^{liq}+Si^{liq}] + 1{,}216[Ab^{pl}]^2 - 2.475 \times 10^{-2}\,[P(kbar)],\ R=0{,}99;\ \text{erro padrão: } 23\ K$$

Neste modelo, a temperatura é inserida em Kelvins e pressão em kbar. An^{pl} e Ab^{pl} são as frações de anortita e albita em plagioclásio, calculadas como frações catiônicas: $An=CaO/(CaO+Na_2O+K_2O)$ e $Ab=Na_2O/(CaO+Na_2O+K_2O)$. Termos como Al^{liq} referem-se à fração catiônica anidra de Al no líquido.

2.9 Higrômetro (plagioclásio-líquido)

Higrômetros baseados no equilíbrio entre o plagioclásio e o líquido, assim como os geotermômetros, são baseados na reação de troca da anortita ($CaAl_2Si_2O_8$) e da albita ($NaAlSi_3O_8$) entre o plagioclásio cristalino e o líquido magmático: $CaAl_2Si_2O_8^{cristal} + NaAlSi_3O_8^{líquido} = CaAl_2Si_2O_8\ ^{líquido} + NaAlSi_3O_8^{cristal}$. De acordo com o modelo de Waters & Lange (2015), a quantidade de água no sistema também depende de parâmetros experimentais de calibração do equilíbrio (a,b, d_i) e da água dissolvida d_{H2O}:

$$wt\%H_2O = mx + a' + b'/T + \Sigma\, X_i d_i', \quad (3)$$

$$\text{onde: } m = 1/d_{H2O},\ a' = a/\text{-}d_{H2O},\ b' = b/\text{-}d_{H2O},\ d_i' = d_i/\text{-}d_{H2O}$$

2.10 Geobarômetro (piroxênio)

As proporções de distribuição das frações de Mg, Na, diopsídio-hedenbergita (DiHd), Al (no sítio VI) e enstatita-ferrosilita (EnFs) são utilizadas, juntamente com a temperatura, como variáveis para a definição da pressão de formação dos piroxênios. A equação 32a de Putirka (2008) depende apenas da composição do clinopiroxênio, não exigindo condições de equilíbrio com o líquido e fornecendo erros sistemáticos apenas para experimentos com alta quantidade de água:

$$P(kbar) = 3205+0{,}384T(K) - 518\ln T(K) - 5{,}62\,(X^{cpx}_{Mg}) + 83{,}2\,(X^{cpx}_{Na}) + 68{,}2\,(X^{cpx}_{DiHd}) + 2{,}52\ln(X^{cpx}_{Al(VI)}) - 51{,}1\,(X^{cpx}_{DiHd})2 + 34{,}8(X^{cpx}_{EnFs})^2 \quad (4)$$

2.11 Viscômetro

O modelo usado para estimativa de viscosidades, de Giordano et al. (2008), é calibrado em mais de 1770 amostras em análises experimentais com um amplo espectro de temperaturas e composições magmáticas. A partir das composições químicas de rocha total, ele fornece uma dependência Newtoniana não-Arrheniana aos líquidos silicáticos, a partir da equação VFT:

$$\log\eta = A + B/T(K) - C \quad (5)$$

O parâmetro A é o valor de logη (Pa s) à temperatura infinita ($10^{-4.6}$ Pa s), representando o limite superior de temperatura para a viscosidade de um magma silicático. Já os parâmetros B e C são composicionais e dependem da combinação linear dos valores de óxidos maiores e um número subordinado de termos cruzados multiplicativos de óxidos:

$$B = \Sigma^{7}_{i=1}[b_i M_i] + \Sigma^{3}_{j=1}[b_{ij}(M1_{1j}.M2_{1j})]; \quad (6)$$

$$C = \Sigma^{6}_{i=1}[c_i N_i] + [c1_1\,(N1_{11}.N2_{11})] \quad (7)$$

Sendo:

$b_1=SiO_2+TiO_2$, $b_2=Al_2O_3$, $b_3=FeO(T)+MnO+P_2O_5$, $b_4=MgO$, $b_5=Na_2O+V$, $b_7=V+\ln(1+H_2O)$, $b_{11}=(SiO_2+TiO_2)*FM$, $b_{12}=SiO_2+TA+P_2O_5*NK+H_2O$, $b_{13}=Al_2O_3*NK$.

$c_1=SiO_2$, $c_2=TA$, $c_3=FM$, $c_4=CaO$, $c_5=NK$, $c_6=\ln(1+V)$, $c_{11}=(Al_2O_3+FM+CaO-P_2O_5)*NK+V$, $V=H_2O+F_2O^{-1}$, $TA=TiO_2+Al_2O_3$, $FM= FeO(T)+MnO+MgO$, $NK=Na_2O+K_2O$.

Capítulo 3 - ESTADO DA ARTE

3.1 *Large Igneous Provinces* (LIPs), Províncias Basálticas Continentais (PBCs) e *Silicic Large Igneous Provinces* (SLIPs)

O conceito de LIP - postulado na introdução - já foi desmembrado em uma série de sub-tipos de províncias, como no trabalho de Sheth (2007), que propôs uma subdivisão em *Large Volcanic Provinces* (LVPs), constituídas por províncias de rochas vulcânicas e em *Large Plutonic Provinces* (LPPs), constituídas por termos intrusivos (complexos máfico-ultramáficos, enxames de diques e batólitos graníticos). A partir dessa subdivisão, foram criadas divisões em termos de composição, como *Large Basaltic Provinces*, *Large Rhyolitic Provinces*, *Large Andesitic Provinces*, *Large Basaltic-Rhyolitic Provinces* e *Large Granitic Provinces*. Restritivamente, existem condicionantes para que o postulado inicial de Coffin and Eldholm (1992, 1994) sobre LIPs se mantenha. Devem-se considerar duas escalas de tempo: a duração total da atividade na província e a duração provável de eventos individuais, balizada pela estratigrafia (Cañón-Tapia, 2010).

Dentro das subdivisões das LIPs, as PBCs são construções vulcânicas lateralmente extensas (vários milhares de km^2) e espessas (cerca de 1 km em média), representando a erupção de grandes volumes de magmas derivados do manto em períodos de tempo relativamente curtos (poucos milhões de anos) e geralmente de composição toleítica (Coffin & Eldholm, 1992; Sheth, 2007). São comumente associadas com anomalias de fusão localizadas no manto superior e constituem um subconjunto das LIPs, que podem incluir corpos eruptivos e intrusivos de diferentes composições químicas (Jerram & Widdowson, 2005).

Províncias magmáticas com predomínio de rochas ácidas, extensões areais maiores que 0,1 Mkm^2, volumes de extrusivas e subvulcânicas associadas maior que 0,25 Mkm^3 e que extrudiram em um curto período de tempo são definidas como Silicic Large Igneous Provinces (SLIPs). De acordo com Bryan (2007), as composições ígneas são volumetricamente dominadas por termos ácidos (> 65% SiO_2), mas geralmente mostram uma variação de basaltos a riolitos alta-sílica. Os riolitos mostram assinaturas geoquímicas transicionais entre intra-placa e cálcio-alcalino ou de margem convergente, e ambos os magmas com baixo- e alto-Ti estão presentes. O papel das adições crustais hidratadas durante episódios anteriores a subducção é considerado crucial para desencadear ampla fusão crustal e prevenindo um domínio de rochas máficas em superfície (Bryan, 2007). Tanto no conceito de LIP, como no de SLIP, também é válido que o reconhecimento e detalhamento estratigráfico são fundamentais, tendo em vista que apenas um conjunto de idades de rochas cuja relação espacial não é bem definida não caracteriza uma província.

Todas as PBCs de idade jurássica a cretácea, e associadas à quebra do Supercontinente Gondwana, têm diversas quantidades de rochas ígneas ácidas intercaladas ou sobrepostas, tal como é

na província do Deccan na Índia, Karoo no sul da África, no terciário do Atlântico Norte, na Yemen-Etiópia, Emeishan na China e Columbia River nos EUA, além do platô oceânico Kerguelen. Juntamente com os pulsos principais do magmatismo basáltico, o vulcanismo ácido pode ocorrer tanto em fases iniciais quanto nas partes tardias, no topo da pilha vulcânica (Bryan, 2002). Exemplos quaternários de erupções ácidas em LIPs possuem produtos de grande volume (>10 a 1000 km³), relacionados a correntes de densidade piroclásticas, fluxos de lavas e domos (Bryan *et al.*, 2010), embora produtos de queda, comuns em erupções ácidas sejam mais raras (Wilson, 2008). Depósitos de lavas em LIPs, e principalmente na LIP Paraná-Etendeka, foram subestimados pelas definições de Bryan (2002) e Bryan *et al.* (2010), tidos como mais comuns em SLIPs como a Gawler Range na Austrália (e.g. McPhie *et al.*, 2008; Agangi *et al.*, 2011). No entanto, trabalhos recentes, inclusive os que estão contidos na presente tese, ratificam que as lavas são os principais componentes das unidades ácidas no sul da LIP Paraná-Etendeka, considerando a porção Sul-americana (e.g. Umann *et al.*, 2001; Lima *et al.*, 2012; Luchetti et al., 2014; Guimarães *et al.*, 2017; Polo & Janasi, 2014; Polo *et al.*, 2017a,b).

3.2 A LIP/PBC Paraná-Etendeka

A LIP/PBC Paraná-Etendeka ocupa, aproximadamente, um volume de pelo menos 1.700.000 km³ (Frank *et al.*, 2009), do qual 90% está localizado na América do Sul, sobre os depósitos sedimentares eólicos da Formação Botucatu na Bacia do Paraná e ocupando uma área de 917.000 km² (±15.000). Sobre a Bacia do Paraná, a sequência vulcânica atinge até ~1.500 m e na área de estudo a espessura da pilha é de aproximadamente 800 m (**Fig. 4**). Na placa africana, as lavas de Etendeka estão espalhadas por uma área de ~ 80.000 km², dominantemente no norte da Namíbia, mas também em algumas regiões da Angola (Erlank et al., 1984).

A referência estratigráfica para esta LIP no sul Brasil é definida como Formação Serra Geral ou Grupo Serra Geral (GSG), que é uma associação de rochas de afinidade toleítica com cerca de 1.700 m e com uma grande proporção (97,5%) de lavas de composição básica a intermediária com um volume menos representativo (2,5%) de rochas de composição ácida (Melfi *et al.*, 1988). A idade das rochas da província, antes estabelecida por um largo espaço de tempo (138 – 128 Ma, método Ar-Ar em plagioclásio, Turner et al., 1994; Stewart et al., 1996) foi recalculado por Thiede e Vasconcelos (2010) e restrito a um período em torno de 134 Ma. Idades em torno de 134 Ma também foram adquiridas para rochas básicas e ácidas da porção central da província (U-Pb SHRIMP em zircão – 01 basalto, 03 ácidas, Pinto et al., 2010; U-Pb em badeleíta – 01 ácida, Janasi et al., 2011).

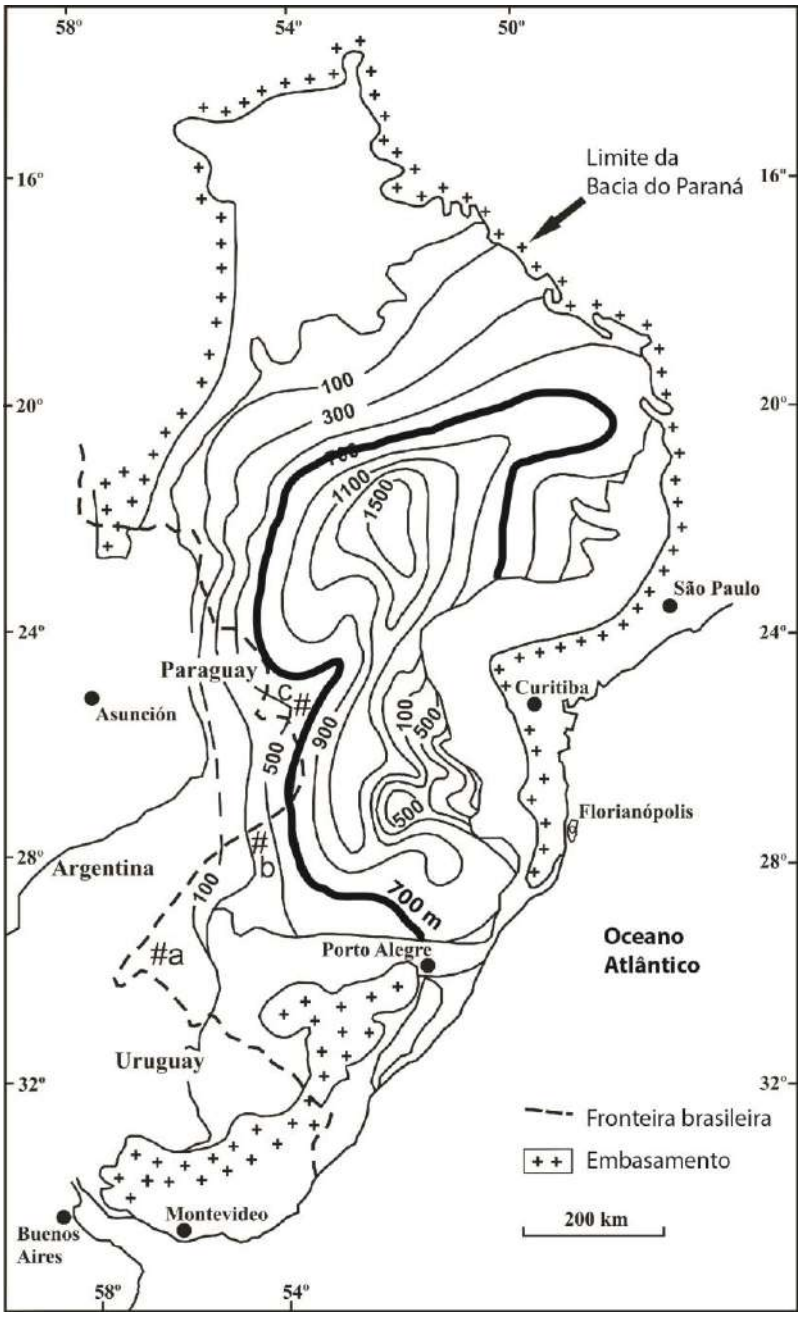

Figura 4 – Mapa de isópacas das rochas extrusivas do GSG (modificado de Frank *et al.*, 2009 e Zalán *et al.*, 1986) com ênfase na isópaca de 700 m, acima da qual encontram-se as áreas de estudo.

Esta província também é composta por exposições de enxames de diques nas porções costeiras do Brasil e da África, onde cortam o embasamento Proterozoico, além da porção leste do Paraguai (Peate, 1997). Os três principais enxames de diques no Brasil, Ponta Grossa, Florianópolis e Santos-Rio de Janeiro possuem áreas de 0,05 a 0,1 Mkm², cada um (Piccirillo et al., 1990; Raposo et al., 1998; Valente et al., 2007; Florisbal et al., 2017). No nordeste do Rio Grande do Sul a ocorrência de diques de diabásio também é comum, cortando as rochas sedimentares da bacia do Paraná e as próprias rochas da pilha vulcânica (Sarmento et al., 2017).

Uma exposição de rochas vulcânicas no município de Jaguarão, próximo a divisa com o Uruguai, e com cerca de 3 km² apresentou idades pelos métodos K-Ar e Rb-Sr entre 143 – 139 Ma (Horbach et al., 1986; Bossi and Umpierre, 1975; Comin-Chiaramonti, 2000). As rochas dacíticas, contendo cordierita, ortopiroxênio, plagioclásio e ilmenita como fases *liquidus*, possuem xenólitos do embasamento e sua gênese é atribuída a reações de fusão parcial, envolvendo a quebra da biotita em um terreno de fonte quartzo-feldspática. As unidades básicas do GSG do sul do Brasil estendem-se para sul, ocupando a porção noroeste do Uruguai. Na porção sudoeste deste país, ocorrem rochas vulcânicas básicas e ácidas em uma área de aproximadamente 8.000 km², alongada na direção NE. Estas unidades, localizadas entre os lineamentos Cebollatí-Merín e Aiguá-Chuy, possuem idades entre 132 Ma e 124 Ma ($^{40}Ar/^{39}Ar$, Stewart et al., 1996; Kirstein et al., 2001; Lustrino et al., 2005) e podem ser consideradas um *outlier* em relação à Bacia do Paraná.

As vulcânicas da LIP constituem a seção pré-rifte da Bacia de Pelotas na porção Sul-americana (Stica *et al.*, 2014) sendo o ambiente tectônico onde a província se desenvolveu caracterizado pelo início da separação do oceano Atlântico Sul no início do Cretáceo (Peate, 1997). Estudos de paleomagnetismo mostraram que idades de 134 Ma (chron M13 de Channell *et al.*, 1995 ou M10r de Collier *et al.*, 2017) são correlatas a anomalias lineares na crosta oceânica do Atlântico Sul e a LIP Paraná-Etendeka (Chron 12 r/n de Dodd *et al.*, 2015), sugerindo a formação do vulcanismo durante a quebra do continente e formação de assoalho oceânico (Collier *et al.*, 2017).

3.2.1 Correlações da Supersequência Gondwana III com o Grupo Etendeka e arcabouço estratigráfico do Grupo Serra Geral

A LIP Paraná-Etendeka desenvolveu-se conjuntamente com os sedimentos mais tardios da Bacia do Paraná. O arcabouço estratigráfico desta bacia compreende seis supersequências do Ordoviciano ao Neocretáceo: Rio Ivaí, Paraná, Gondwana I, Gondwana II, Gondwana III e Bauru. No Rio Grande do Sul afloram as supersequências Gondwana I (grupos Itararé, Guatá, Passa Dois), Gondwana II (Formação Santa Maria) e Gondwana III (Formação Botucatu e GSG). As supersequências Gondwana I e II compreendem uma seção do Permiano ao Meso-Jurássico. São compostas predominantemente por sedimentos de ambientes glaciais, fluviais, lacustres e marinhos, sendo sucedidas estratigraficamente no Eocretáceo pelos sedimentos eólicos da Formação Botucatu e pelas rochas vulcânicas do GSG, estes últimos representando a Supersequência Gondwana III (Milani *et al.* 2007).

Para a correlação estratigráfica com as rochas juro-cretáceas da Bacia Huab, a Formação Guará - neojurássica, que é composta por arenitos grossos a conglomeráticos fluviais que se interdigitam com arenitos finos a médios eólicos e são sobrepostos pela Formação Botucatu (Scherer & Lavina 2006) é

considerada correlata com o Membro Krone (flúvio-eólica), que precede os depósitos eólicos da Formação Etjo na contraparte africana. O Membro Krone é composto por conglomerados fluviais clasto-suportados que gradam para arenitos fluviais intercalados com depósitos de dunas eólicas na "seção mista" (Jerram *et al.* 1999).

As Formações Botucatu e Etjo são sucessões de até 150 m de arenitos finos a médios com estratificação cruzada de grande porte que representam formas de leito de *draa* migratórias que rapidamente preencheram o espaço de acomodação da bacia (Jerram *et al.* 1999, Scherer 2000). A transição do predomínio de sedimentação eólica para o predomínio do vulcanismo se dá pela colocação de fluxos do tipo *compound* e *ponded pahoehoe* (Jerram & Widdowson 2005, Rossetti *et al.*, 2014; Rossetti et al., 2017) que cobrem parte dos *ergs* formando estruturas de deformação, diápiros de areia e brechas peperíticas (Waichel *et al.* 2007, Luchetti et al., 2014; Rossetti *et al.*, 2014). O sistema de erg ativo é progressivamente engolfado pelos basaltos, resultando em uma boa preservação de partes do sistema de dunas (Jerram *et al.* 1999, Waichel *et al.* 2007).

Na porção africana, as rochas vulcânicas do Grupo Etendeka são divididas formalmente em duas formações: Awahab e Tafelberg (Milner *et al.* 1994). A Formação Awahab possui três tipos principais: (1) basaltos com olivina e sedimentos intercalados com associação de fácies de *pahoehoe* composto, lobado ou tabular; (2) basaltos e andesitos basálticos e textura fina com base e núcleo maciços e topo brechado e vesicular; e (3) quartzo latitos (classificação petrográfica). Os basaltos com olivina possuem teores mais elevados de MgO, TiO_2, FeO_T e são geoquimicamente classificados como basaltos do tipo-Tafelkop (Milner *et al.*, 1994, Milner & Ewart, 1989) ou basaltos LTZ.H (Ewart *et al.*, 1998a). O Membro Tafelkop, que se intercala com lavas do tipo-Tafelberg, foi definido 50 km a sul da seção-tipo da Formação Awahab. Essas rochas correlacionam-se com o Evento Vulcânico Básico I (EVA I, Waichel *et al.* 2012), Unidade I (Rossetti *et al.* 2014) ou Formação Torres do Grupo Serra Geral (Rossetti et al., 2017).

Os basaltos e andesitos basálticos são geoquimicamente equivalentes aos basaltos tipo LTZ.L (Ewart *et al.* 1998a) ou tipo-Tafelberg (Milner *et al.* 1994). No entanto, essas rochas estão encobertas por basaltos de outras sequências e por uma desconformidade que separa a estratigrafia da Fm. Awahab da Fm. Tafelberg. Além do mais, não são estratigraficamente correlatos aos basaltos Tafelberg da seção-tipo, mas possuem assinatura geoquímica tipo-Tafelberg. Jerram *et al.* (1999) utilizaram o nome Membro Tsuhasis para estas rochas, que são correlatas ao Evento Vulcânico Básico II (EVA II, Waichel *et al.* 2012), Unidade II (Rossetti *et al.* 2014) ou Formação Vale do Sol (Rossetti et al., 2017). A porção superior da Formação Awahab contém a primeira ocorrência de um grande volume de rochas vulcânicas ácidas, os quartzo latitos Gobobseb (I e II) e o quartzo latito Sprinkbok. A Formação Tafelberg é separada da Formação Awahab por uma desconformidade regional entre duas unidades principais: (1) basaltos e andesitos basálticos (abaixo) e (2) quartzo latitos (acima). A desconformidade

regional é estendida para a porção brasileira da província, entre andesitos basálticos e as rochas ácidas do tipo-Palmas (Whittingham 1989, Milner *et al.* 1995, Jerram *et al.* 1999) ou Formação Palmas (Rossetti et al., 2017).

O detalhamento litoestratigráfico de Rossetti *et al.* (2017) propõe que a Formação Torres, que sucede a Formação Botucatu, representa o início do vulcanismo e é caracterizada por campos de derrames *pahoehoe* compostos de composição basáltica mais primitiva (> 5% MgO). A Formação Vale do Sol é composta por volumosos derrames do tipo *rubbly pahoehoe* e é recoberta pelas lavas e domos de composição dacítica a riolítica da Formação Palmas. A Formação Esmeralda é a unidade superior do GSG no sul do Brasil, sendo formada por campos de derrames basálticos do tipo pahoehoe e depositada durante a fase minguante do vulcanismo (**Fig. 5**). As intercalações sedimentares são abundantes ao longo da pilha vulcânica, representando períodos de quiescência na atividade vulcânica, e representam importantes marcadores estratigráficos (ex.: arenitos no contato entre as formações Torres e Vale do Sol).

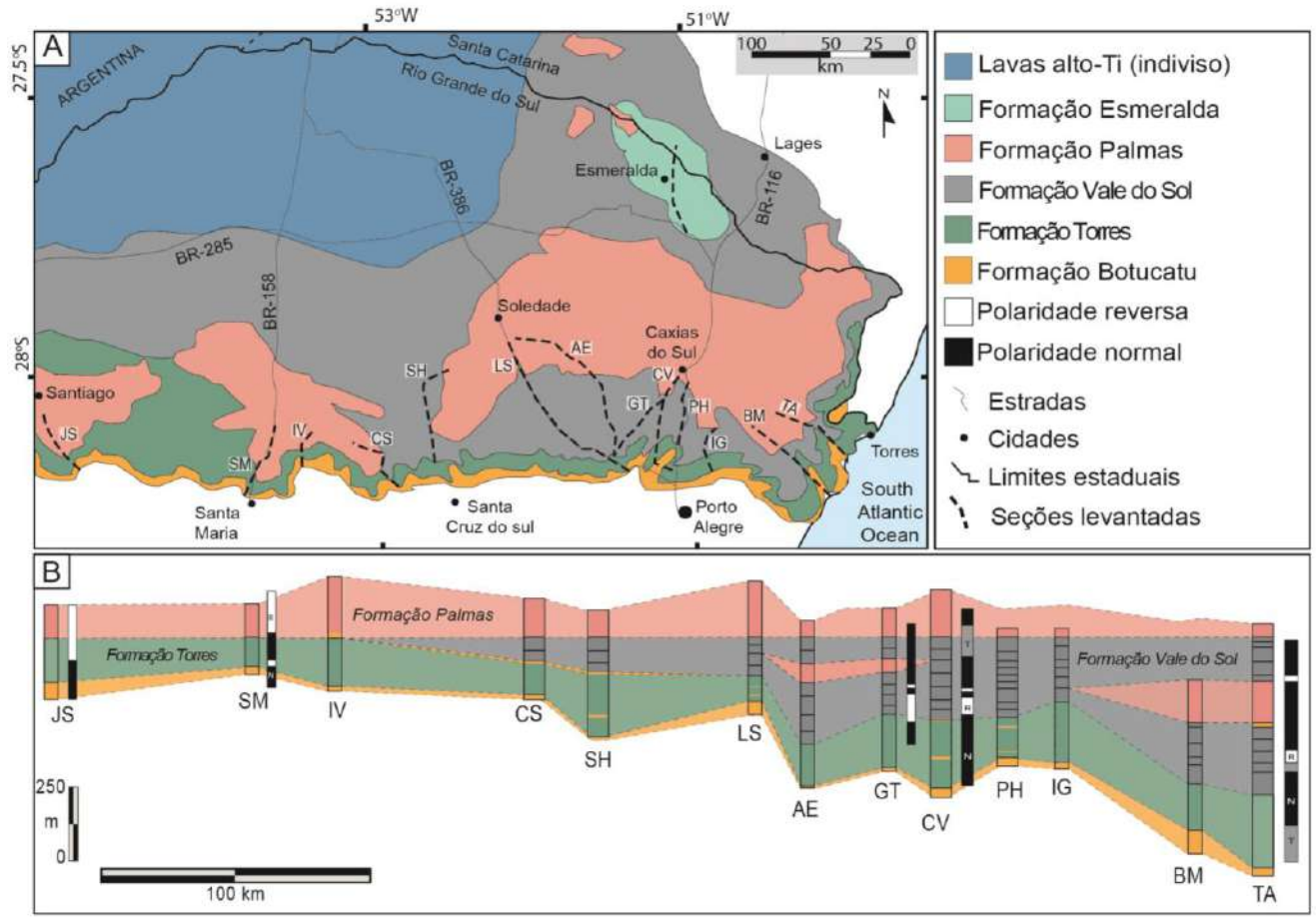

Figura 5 – A) Mapa da distribuição de unidades litoestratigráficas na porção sul da LIP Paraná Etendeka. B) Distribuição estratigráfica das formações, seções e correlação com dados paleomagnéticos (de Ernesto & Pacca, 1988). JS=Jaguari-Santiago; SM=SantaMaria; IV=Ivorá; CS=Candelária-Sobradinho; SH=Santa Cruz do Sul-Herveiras; LS=Lajeado-Soledade; AE=Arvorizinha-Encantado; GT

= Garibaldi-Teotônia; CV=São Sebastião do Caí-Caxias do Sul; PH=Picada Café-Nova Petrópolis; IG= Igrejinha-Gramado; BM=Barra do Ouro-Morrinhos; TA=Terra de Areia-Aratinga (modificado de Rossetti *et al.*, 2017).

3.2.2 *Magmas-tipo e geoquímica das vulcânicas do GSG*

O magmatismo da PBC Paraná-Etendeka é historicamente descrito a partir de uma estratigrafia definida por parâmetros químicos obtidos, principalmente, em análises químicas de rocha total (Belieni *et al.* 1986, Peate *et al.* 1992, Peate 1997, Nardy *et al.* 2008). O primeiro e mais utilizado esquema de classificação elaborado por Peate *et al.* (1992) a partir de Bellieni *et al.* (1986) e reforçado por Peate (1997) está sumarizado na **figura 6**. O esquema de classificação é inicialmente simples, à medida que separa as rochas com alto conteúdo de TiO_2 (> 2%) das rochas com baixo conteúdo de TiO_2 (< 2%). As rochas de alto-Ti, cujos subgrupos são Esmeralda, Gramado e Ribeira, ocorrem mais comumente na porção norte da Bacia do Paraná e as rochas baixo-Ti, divididas em Urubici, Pitanga e Paranapanema estariam mais restritas a porção sul. Em relação às fontes dos magmas parentais, o magma-tipo Ribeira (baixo-Ti) possui as razões de Rb/Ba e Ti/Y assemelhadas às razões dos magma-tipo de alto-Ti.

Para as rochas vulcânicas ácidas do GSG a divisão foi efetuada a partir de dois grandes grupos, de acordo com aspectos petrográficos e geoquímicos (**Fig. 7**): magma-tipos Palmas e Chapecó (Bellieni *et al.* 1986; Peate, 1997). As rochas do tipo Palmas ocorrem preferencialmente nas porções centro-sul e sul da Bacia do Paraná e são dacitos e riolitos afíricos de baixo-Ti com altas razões $^{86}Sr/^{87}Sr_{(i)}$ e alto δO^{18}. Os dacitos são subdivididos nos subtipos Caxias do Sul, Anita Garibaldi, e Jacuí (Nardy *et al.*, 2008). Os riolitos são subdivididos nos subtipos Santa Maria e Clevelândia (Peate *et al.*, 1992, Nardy *et al.*, 2008). As rochas do tipo Chapecó ocorrem preferencialmente nas porções centro-norte e norte da Bacia do Paraná e são traquitos porfiríticos de alto-Ti com menores valores para $^{86}Sr/^{87}Sr_{(i)}$ e δO^{18}, maiores teores relativos de Ba, Nb, La, Ce, Zr, P, Nd, Y, Yb, Lu e K e menores teores de Rb, Th e U que o tipo Palmas. Este magma-tipo também é subdividido nos subtipos Ourinhos, Guarapuava (Peate 1997) e Tamarana (Nardy *et al.* 2008).

Na contraparte africana da LIP também foram descritas séries de magmas-tipo. No entanto, é importante ressaltar que o sistema de classificação das rochas ácidas utilizado nos trabalhos efetuados no continente africano é petrográfico. De acordo com a sistemática recomendada pela IUGS (*International Union of Geological Sciences*) as mesmas rochas chamadas de quartzo latitos ocupam campos de traquitos, traquidacitos e riolitos no diagrama TAS e campos de dacitos e riolitos alto-K no diagrama SiO_2 *versus* K_2O (Milner *et al.* 1992), ambos diagramas sugeridos por LeMaitre *et al.* (1989).

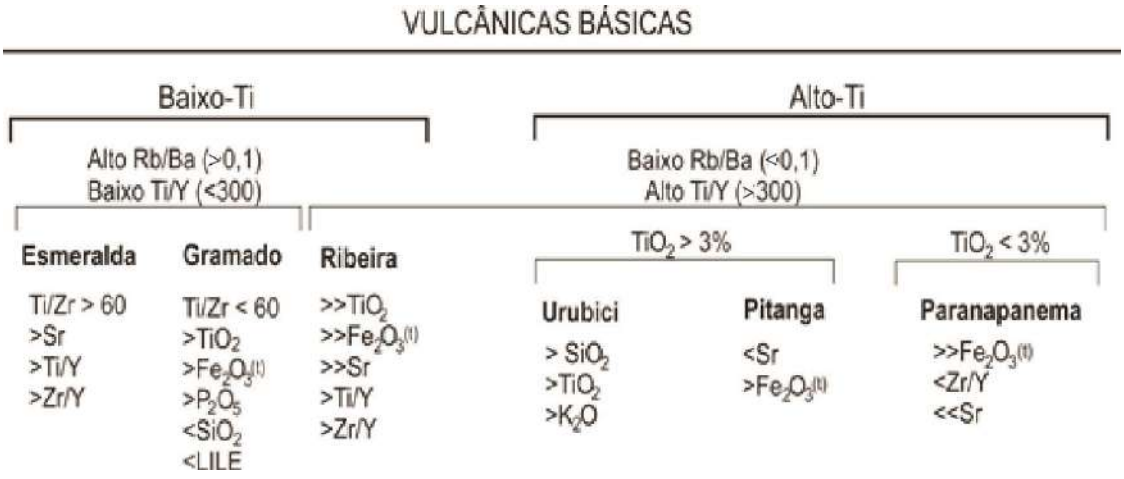

Figura 6 – Esquema de classificação de magmas-tipo para as rochas vulcânicas básicas da Formação Serra Geral a partir de Peate *et al.* (1992).

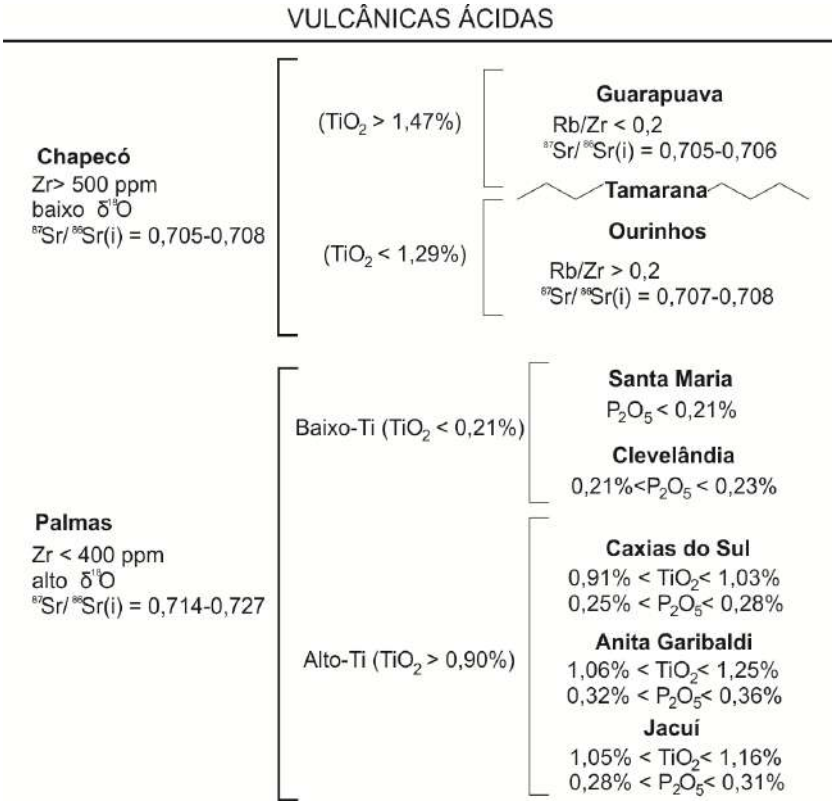

Figura 7 – Esquema de classificação das rochas vulcânicas ácidas da Formação Serra Geral a partir de Peate *et al.* (1992), Garland *et al.* (1995) e Nardy *et al.* (2008).

Os quartzo latitos de baixo-Ti são representados pelos tipos *Goboboseb*, *Springbok*, *Wereldsend*, *Grootberg*, *Beacon*, *Hoas* e *Fria*. Os magma-tipos de alto-Ti são representados pelos latitos *Nil Despeandum*, *Nadas*, *Sechomib* e *Hoarusib* e, também, pelos quartzo latitos *Sarusas*, *Ventura*, *Khoraseb*, *Naudé* e *Elliot* (Marsh *et al.*, 2001). As correlações regionais e equivalências geoquímicas dos teores de elementos maiores e traço entre as duas contrapartes da PBC Paraná-

Etendeka foram reconhecidas como Santa Maria→*Fria*, Ourinhos→*Khoraseb* e Guarapuava→*Sarusas* (Marsh *et al.*, 2001) ou Guarapuava→*Ventura* e Tamarana→*Sarusas* (Bryan *et al.*, 2010).

3.2.3 *Modelos prévios de fonte eruptiva das vulcânicas de baixo-Ti*

A correlação entre as rochas vulcânicas ácidas da contraparte africana com as rochas da parte sul-americana foi realizada por Milner et al. (1995) e é baseada nas comparações geoquímicas entre unidades. A partir deste estudo, os autores sugeriram que o subgrupo mais inferior do tipo Palmas teria sua origem vinculada ao complexo Messum (**Fig. 8**), um complexo intrusivo que abriga rochas como granitos e gabros com afinidade geoquímica similar às vulcânicas. Adicionalmente, as correntes de densidade piroclásticas geradas na caldera Messum teriam percorrido cerca de 340 km até depositarem-se onde hoje é a porção Sul-americana da província (Milner et al., 1995; Bryan et al., 2010). A descrição de zonas interpretadas como condutos na região de São Marcos, onde as lavas são do tipo Palmas, reabriram a discussão sobre as fontes eruptivas (e.g. Lima et al., 2012; Lima et al., 2018).

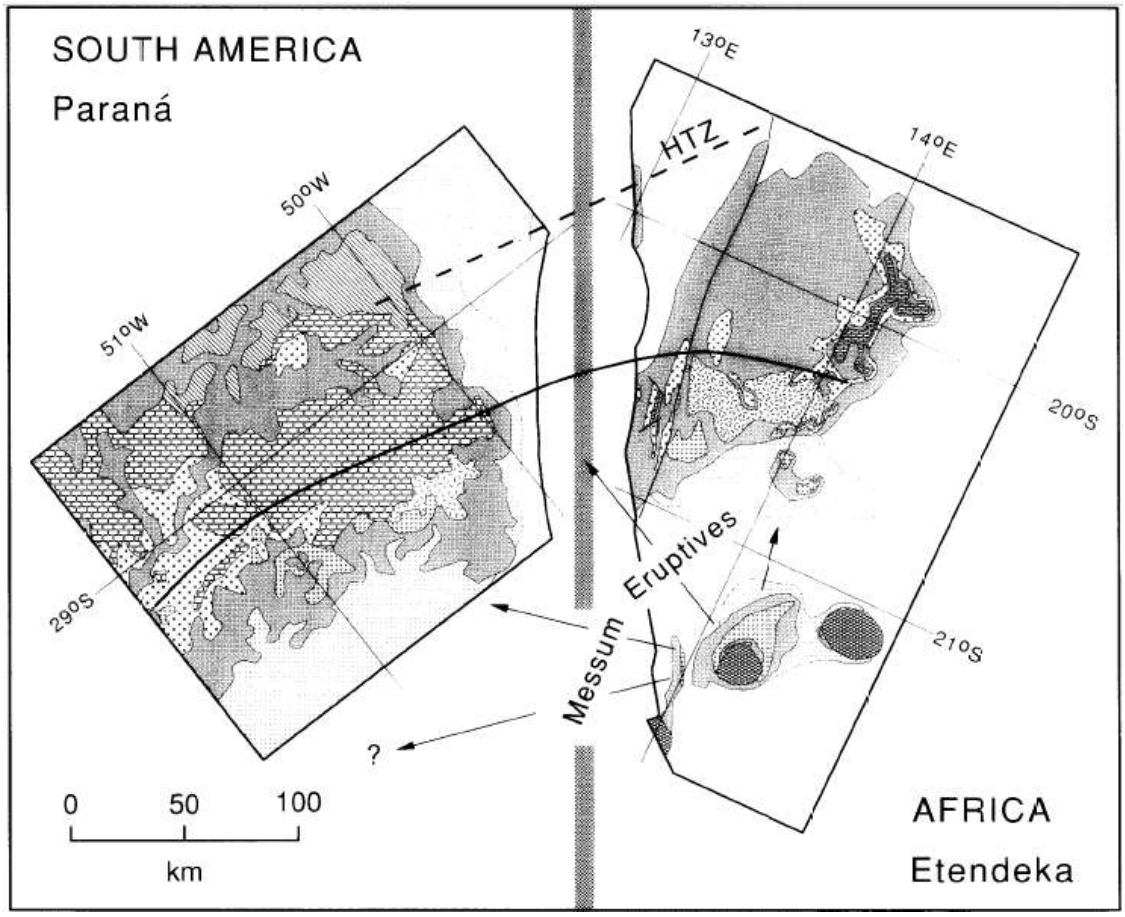

Figura 8 – Correlação transcontinental das rochas ácidas da província Paraná-Etendeka com indicação e fonte eruptiva no complexo Messum, na Namíbia (extraído de Milner et al., 1995).

3.3 Litofácies e vulcanismo de alta temperatura

3.3.1 Litofácies em lavas ácidas

Uma fácies é um corpo ou um intervalo de rocha ou sedimento que possui um caráter único definível que o distingue de outras fácies ou de intervalos de rocha ou sedimento. O caráter definitivo de uma fácies pode ser associado a aspectos composicionais, texturais e estruturais. O grau de detalhe usado para subdividir uma sucessão estratigráfica em fácies é controlado pelos propósitos do estudo, da informação disponível e do nível de entendimento possível (Cas & Wright, 1988). As características descritivas e não-interpretativas de uma fácies são definidas como uma litofácies (Miall, 2000).

Os principais elementos descritivos de uma fácies (**Quadro 1**) são: (i) geometria, (ii) litologia, (iii) estruturas sedimentares, (iv) paleocorrentes ou padrões de movimento dos sedimentos e (v) fósseis (Selley, 1978). Na aplicação em sistemas vulcânicos, as estruturas podem ser vulcânicas piroclásticas, vulcânicas magmáticas, estruturas de ressedimentação ou estruturas sedimentares em rochas vulcanogênicas. A rara presença de fósseis em rochas vulcânicas pode caracterizar uma fácies, mesmo não sendo de comum ocorrência como nas rochas sedimentares.

Fácies associadas entre si podem ser diferentes e podem ser geneticamente correlacionadas como parte de um mesmo evento deposicional ou eruptivo, por exemplo, um único ignimbrito (Cas & Wright, 1988). O conjunto de fácies é chamado de associação de fácies e a interpretação das associações de fácies caracterizam um ambiente deposicional ou vulcânico, permitindo uma conclusão genética baseada em análises em várias dimensões e escalas. A análise de fácies em rochas vulcânicas deve ser complementada por estudos petrográficos, que auxiliam na caracterização de rochas afaníticas, porfiríticas de matriz afanítica ou com granulação muito fina.

Estas etapas permitem a avaliação e classificação dos processos eruptivos para depósitos vulcânicos e vulcanoclásticos, além da sua subsequente redeposição, erosão, transporte e deposição na forma de depósitos ressedimentados ou sedimentares vulcanogênicos (McPhie *et al,*. 1993).

As duas principais categorias texturais que envolvem a análise de litofácies de rochas vulcânicas são a vulcanoclástica e a coerente. O termo “vulcanoclástico” é meramente descritivo e se aplica a depósitos compostos predominantemente de partículas vulcânicas (Fisher, 1966). Esse conceito não implica nenhum processo formador de partículas, processos de transporte ou deposição. As quatro principais categorias genéticas para depósitos vulcanoclásticos são: autoclástico, piroclástico, ressedimentado ou sedimentar vulcanogênico (McPhie *et al.*, 1993). O termo “coerente” é aplicado quando são identificadas texturas geradas por resfriamento de lava ou magma. As texturas mais comuns são porfirítica, afírica, afanítica ou totalmente vítrea. Vesículas, foliações de fluxo, esferulitos e litofises também são comuns, mas não são diagnósticas apenas de depósitos coerentes. Devem-se considerar, além das duas categorias citadas, mais duas categorias adicionais que abrigam padrões

texturais “falsos” ou “aparentes”: aparente vulcanoclástica, gerada por processos de alteração que ocorrem geralmente em fraturas, fazendo com que a rocha coerente pareça um ignimbrito soldado ou uma brecha lítica, bem como por texturas microesferulíticas, fazendo com que a rocha coerente pareça um arenito maciço bem selecionado e aparente coerente, gerada por alto grau de soldagem, dando aspecto de depósitos de lava a reoignimbritos ou ignimbritos *lava-like* (McPhie *et al.*, 1993).

Quadro 1 – Elementos descritivos de fácies (Cas & Wright, 1988).

ELEMENTOS DESCRITIVOS DE FÁCIES	
Geometria	- paleorelevo - volume de material depositado - acomodação do depósito - agente deposicional - propriedades físicas do transporte - erosão pós-deposicional - deformação subsequente
Litologia	- constituintes físicos - composição - textura
Estruturas	- feições erosionais - estruturas geradas por corrente - deformação por fluidização
Paleocorrentes	- *ripples* - dunas - indicatores de fluxo - lineações de partição
Fósseis	- condições paleoambientais

Os processos de cristalização e exsolução de voláteis, bem como a devitrificação e o desenvolvimento de texturas se dá a partir do decréscimo de temperatura desde a pré-erupção até a pós-erupção. O primeiro ponto de ebulição induz a vesiculação e a formação de micrólitos, já o segundo ponto de ebulição ocorre devido a cristalização de fases anidras. Devido à instabilidade termodinâmica dos materiais vítreos, processos de devitrificação em alta temperatura darão origem a texturas tais como esferulitos (matrizes radiais a alongadas de fibras cristalinas), litofises (esferulitos com uma cavidade central) e textura micropoiquilíticas (manchas de cristais <1 mm que englobam demais cristais) que se desenvolve geralmente em quartzo e feldspato (McPhie *et al.*, 1993). O desenvolvimento de autobrechação, juntas de resfriamento, hidratação do vidro e geração de perlitos (rachaduras curviplanares associadas à hidratação) são processos de mais baixa temperatura (**Fig. 9**).

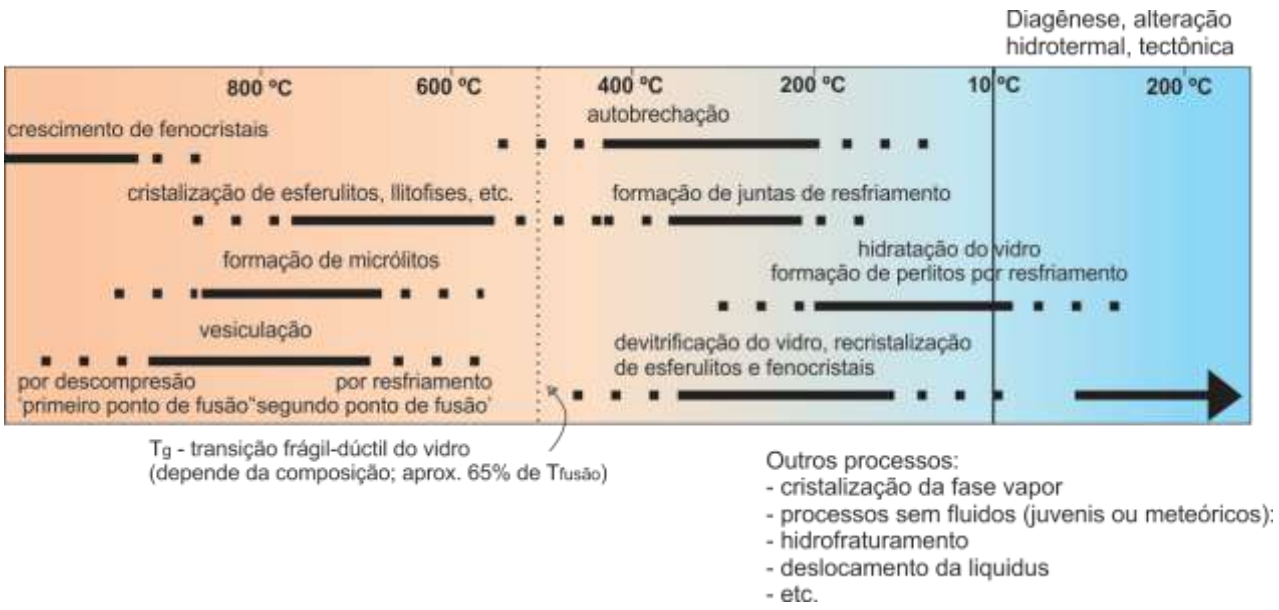

Figura 9 –Texturas desenvolvidas em rochas ácidas a partir do decréscimo de temperatura (modificado de Breitkreuz, 2001). Ponto de fusão=ponto de ebulição.

3.3.2 *Depósitos de lavas e intrusões sin-vulcânicas x depósitos piroclásticos*

Quando o magma atinge níveis rasos antes da erupção, ele tende a tornar-se saturado em voláteis, como resultado da descompressão ou pela cristalização de fases anidras (Sparks, 1978; Burnham, 1983). Em sistemas fechados, o tamponamento dos condutos e a rápida devolatilização geram altas explosividades em erupções de magmas ácidos, dando origem a erupções explosivas plinianas. Já em sistemas abertos, o escape da fase gasosa permite a colocação passiva de fluxos e domos de lava (Cashman, 2004). As texturas e fácies mais comuns em depósitos de lavas e intrusões sin-vulcânicas e em depósitos piroclásticos estão presentes nos **quadros 2 e 3**. A distribuição de fácies coerentes e autoclásticas em lavas ácidas depende da taxa de *strain*, da temperatura e do conteúdo de voláteis (Fink, 1983). O fluxo ocorre quando o estresse de cisalhamento aplicado excede o limite de elasticidade. Já a ruptura frágil da rocha ocorre quando o estresse de cisalhamento aplicado excede o limite de resistência à tração. Os dois limites tendem a diminuir com o aumento da temperatura (Fink & Manley, 1987). A parte interna quente do fluxo de lava é capaz de deformar e fluir entre camadas mais frias, rígidas e não deformáveis nas porções de base e de topo (McPhie *et al.*, 1993).

Os três principais tipos de erupção explosiva – explosiva magmática, hidrovulcânica e freática – diferem na fonte do gás e na proporção de envolvimento direto do magma. Erupções hidrovulcânicas e freáticas são mecanismos que envolvem participação de vapor gerado por fonte de água externa, já a erupção explosiva magmática envolve apenas os gases magmáticos. Todos os três tipos de erupção explosiva são capazes de gerar piroclastos de tamanho cinza fina a bloco. Os piroclastos são dispersos por: (i) Injeção na atmosfera seguida por queda em suspensão. (ii) correntes de alta concentração de

partículas – fluxos piroclásticos e (iii) saltação e rolamento de partículas em baixa concentração – *surges* piroclásticos (Cas & White, 1988).

Quadro 2 – Fácies características de lavas e intrusões sin-vulcânicas (modificado de McPhie *et al.*, 1993).

LAVAS E INTRUSÕES SIN-VULCÂNICAS	
Fácies coerente	- estrutura interna maciça ou com foliação de fluxo - textura porfirítica ou afanítica - texturas de devitrificação em alta temperatura (esferulitos, litofises, textura micropoquilítica) - não vesicular ou vesicular
Fácies autoclástica	-monomítica - clastos com textura porfirítica ou afanítica - textura *jigsaw-fit* em abundância
Autobrecha	- clastos em placa ou foliados com terminações dentadas - clastos irregulares ou blocados maciços - margem dos clastos sem texturas de rápido resfriamento - presença comum de clastos vesiculados - baixa proporção de clastos menores que 2 mm - raramente com cristaloclastos separados
Brecha hialoclastítica	- clastos blocados com contornos curviplanares - margem dos clastos com matriz vítrea - interior dos clastos vítreo ou recristalizado - pequenas juntas normais ao longo das bordas do clasto - matriz da brecha com tamanho entre 1 e4 mm - cristaloclastos separados podem ser abundantes - podem ocorrer clastos vesiculados

As rochas vulcânicas ácidas efusivas podem ser classificadas de acordo com a sua forma em três grupos distintos (Cas & Wright, 1988): (i) domos - circulares em planta e com pouca extensão de área, (ii) mesa lavas – aproximadamente circulares em planta formando corpos achatados e (iii) *couleés* – lavas que se formam quando o fluxo é assimétrico e concentrado em um dos lados do conduto produzindo uma forma alongada em planta. De acordo com os mesmo autores, as litologias mais comuns nesse tipo de rocha são obsidianas, camadas com esferulitos, camadas com lava vesiculada, horizontes líticos (cristalizados e com granulometria muito fina), perlitos e fragmentos fluidais a não-fluidais de rochas de composição mais básica (**Fig. 10**). As obsidianas podem apresentar foliação de fluxo que, por vezes, ocorre dobrada.

Quadro 3 – Fácies características de depósitos piroclásticos.

DEPÓSITOS PIROCLÁSTICOS	
depósitos de erupções explosivas magmáticas e freatomagmáticas	- fragmentos de cristais, púmice ou escória, clastos juvenis, fragmentos líticos - clastos de púmice, escória ou juvenis com textura porfirítica/afanítica - fragmentos de cristais em abundância na matriz - fragmentos líticos esparsos a abundantes
explosiva magmática	- presença abundante de *glass shards* na matriz - clastos de púmice e escória com margens irregulares delgadas e forma lenticular, em placa ou em bloco - ocorrência de lápili acrescionário - soldado ou não-soldado
hidromagmática	- presença abundante de *shards* na forma de lascas ou blocos - clastos juvenis tipicamente blocados - presença comum de lápili acrescionário - geralmente não-soldados - predominância da fração cinza e lápili fino
freática	- composto por piroclastos líticos, com presença comum de clastos com alteração hidrotermal - presença comum de lápili acrescionário - pequenos volumes de depósito (< 1 km³) - principalmente depósitos de queda e *surge* - não-soldado

As feições de topo de fluxos ácidos (geralmente *couleés*) são tipicamente blocadas e irregulares formadas por cristas curvas chamadas de ogivas (Fink & Fletcher, 1978; Cas & Wright, 1988). Estas cristas curvas são geralmente côncavas na direção do fluxo, possuem espaçamento de dezenas de metros e são separadas por sinclinais cúspides apertadas geralmente preenchidas por blocos de lava vesiculada (Fink, 1980a). A sua origem é atribuída a estruturas de rampa (MacDonald, 1972), dobras nas superfícies das lavas (Loney, 1968; Fink, 1980a) ou também como "extrusões por espremedura" (*squeeze-ups*) durante a extensão da superfície externa do fluxo. Outras feições de topo de fluxos ácidos são diápiros de púmice oriundos das camadas vesiculadas basais devido à instabilidade gravitacional induzida pela inversão de densidade de dentro do fluxo (Fink, 1980b).

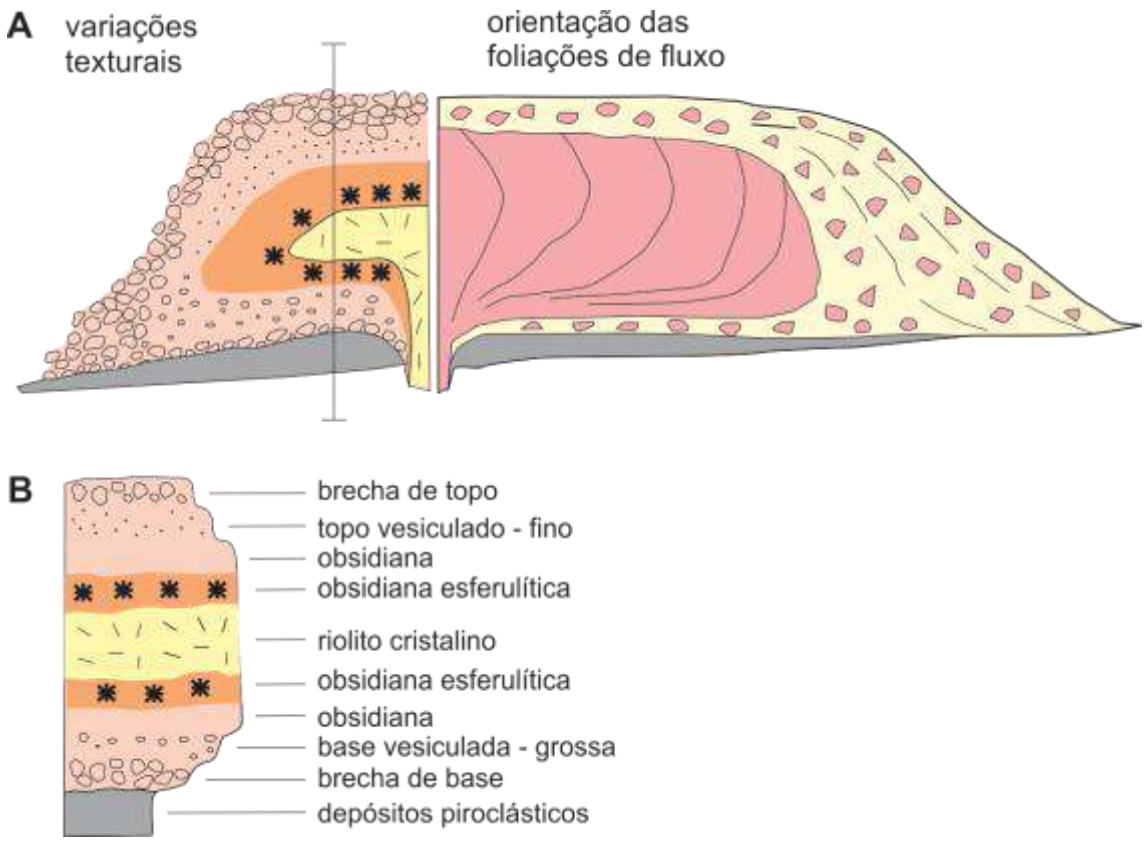

Figura 10 - (A) Seção esquemática de um fluxo de lava subaéreo. O lado esquerdo mostra as variações texturais internas originadas por vesiculação, devitrificação e fragmentação de fluxo. O lado direito mostra a orientação das foliações de fluxo internas e do acamamento em brecha de talus da margem do fluxo. (B) Seção vertical do fluxo indicado na figura A. (modificado de McPhie *et al.*, 1993).

As porções frontais íngremes dos fluxos de lava ácida são geralmente compostas por depósitos de tálus e blocos de lava vesiculada. Esses depósitos são atribuídos tanto à autobrechação das lavas, quanto ao efeito "*caterpillar*", no qual a lava se movimenta sob e sobre porções brechadas, em um movimento semelhante ao de um trator. Em relação ao crescimento e as estruturas internas, Cas & Wright (1988) descrevem a foliação de fluxo de lavas ácidas como camadas com diferentes cristalinidades (obsidiana *versus* riolito cristalizado), diferentes conteúdos de esferulitos e diferentes vesicularidades. Essas foliações são acentuadas por processos de distensão e cisalhamento causados pelo *stress* do fluxo magmático. As direções de fluxo de lavas podem ser determinadas pela análise estrutural da orientação de foliações, dobras, vesículas, cristais tabulares e achatados, e vidro vulcânico distendido. Movimentos tardios de lava resfriada foram verificados por meio da identificação de *slickensides* (espelhos de falha) e *tension gashes* (fraturas de cisalhamento escalonadas) (Christiansen & Lipman, 1966; Loney, 1968; Fink, 1980).

A geometria da foliação de fluxo em lavas tende a ser concêntrica nas margens quando vista em planta, mas em corte é vertical ou muito inclinada na porção de núcleo e mergulha com baixos ângulos na porção de margem, formando uma estrutura em rampa. Quando a lava já está resfriada ou parcialmente resfriada, nas superfícies das estruturas em rampa é possível identificar *slickensides* (espelhos de falha) que indicam a direção do movimento. A frente autobrechada dos fluxos ácidos tende a retardar o avanço da lava e tornar o regime interno de fluxo compressivo. Os planos de cisalhamento serão inclinados em direção ao conduto (Hall, 1978). Em regiões onde a inclinação do terreno é acentuada, o regime de fluxo tende a ser distensivo e os mergulhos dos planos de cisalhamento mergulham em direção oposta ao conduto (**Fig. 11**).

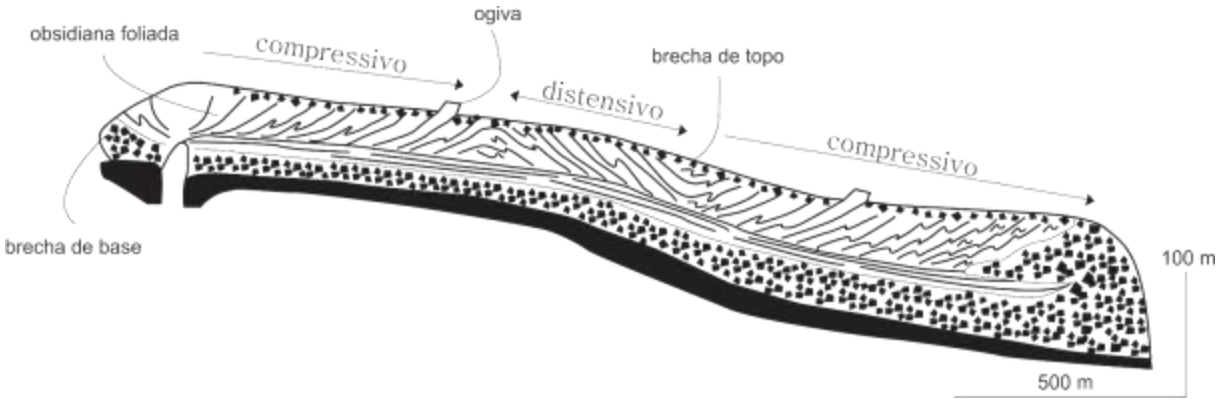

Figura 11 - Seção paralela ao comprimento de um *coulée* de obsidiana, com padrões de foliação (Cas & Wright, 1987; depois de Hall, 1978).

Nos modelos clássicos de colocação de fluxos ácidos em ambiente subaéreo, têm-se descrito morfologias que são mais comuns descritas para fluxos de natureza básica a intermediária, devido a sua baixa viscosidade. Essas morfologias incluem formas lobadas que podem ser descritas com diversas extensões em área (Manley, 1996; Pankhurst et al., 2011; Tuffen *et al.*, 2013). Morfologias do tipo *ponded* também são descritas quando lobos de lava ácida são bloqueados por algum obstáculo e ficam represados em um determinado local (Manley, 1996).

Recentemente, a utilização de técnicas de imageamento de alta resolução como a foto-reconstrução automatizada e imagens de satélite sequenciais realizada por Tuffen *et al.* (2013), nas rochas ácidas riolíticas do Complexo Vulcânico *Puyehue-Cordón Caulle* no Chile, identificou morfologias de frente de lava com predomínio de fácies do tipo *rubbly pahoehoe* com depósitos de tálus associada a lobos de lava com porção superior lisa a dobrada geralmente cortadas por estruturas do tipo *crease* e fraturas distensivas escalonadas (*en échelon*) perpendiculares às margens do canal (*breakout lobes*). A alta mobilidade desses fluxos (por mais de 3,5 km) e geometria de lobos compostos

foi atribuída à eficiência do isolamento termal por uma carapaça externa e os autores exaltam a similaridade de colocação desses fluxos com os campos de lava basáltica compostos.

3.3.3 *Riolitos tipo SR (Snake River)*

Uma categoria de vulcanismo de ampla exposição, intitulada vulcanismo tipo-SR, foi definida por Branney *et al.* (2008) para descrever uma associação de fácies distinta que aflora na seção miocênica do *central Snake River Plain*, porção oeste dos EUA. A associação de fácies inclui: (1) ignimbritos de grande volume pobres em fragmentos líticos e púmice na fração lápili; (2) depósitos de queda extensos, com laminação paralela e granulometria média a grossa com shards cúspides, cristais e escassez de púmice na fração lápili; (3) lavas riolíticas extraordinariamente extensas de grande volume; (4) soldagem intensa, reomorfismo e desenvolvimento amplamente difundido de fácies de *lava-like* em ignimbritos; (5) extensivos depósitos de cinza fina com agregados de cinza em abundância (*pellets* e lápili acrescionário); (6) os depósitos de queda e ignimbritos contêm clastos de obsidiana e vitrófiro abundantes; (7) associação bimodal entre rochas riolíticas e escudos de lava basáltica; e (8) persistentes evidências de *emplacement* em ambientes flúvio-lacustres.

Muitas das erupções riolíticas tiveram grande volume e envolveram magmas metaluminosos, pobres em H_2O, com baixo $\delta^{18}O$ e com viscosidades extremamente baixas devido a temperaturas entre 900ºC e 1050 ºC. As lavas do *central Snake River Plain* são consideravelmente mais extensas (dezenas de km) e mais volumosas (>10 km^3) que domos riolíticos e couleés riolíticos associados a vulcões de rochas ácidas explosivas em caldeiras. As razões de forma dos riolitos tipo-SR são muito baixas, e coincidem com as de lavas basálticas. As dimensões incomuns já serviram como base para interpretações dessas lavas como ignimbritos (Ekren et al., 1984). A presença comum de brechas basais, terminações lobadas abruptas e espessas associadas a depósitos de tálus serviram de critérios para a interpretação desses depósitos como lavas. As lavas são blocadas, com carapaças de autobrecha espessas (> 5 m) e texturas vitroclásticas que lembram texturas piroclásticas em porções onde a autobrechação ocorreu durante o fluxo. As porções centrais dos fluxos são litoidais (microcristalinas), maciças ou com bandamento de fluxo, e dominadas por disjunções colunares, além de disjunções tabulares de baixo ângulo (Fig. 7) que, em lugares onde forma *sets* de interseção, produz disjunções "tipo-lápis". Esferulitos e litofises são comuns quando próximo à base da porção litoidal. Algumas das lavas aflorantes na porção oeste do *central Snake River Plain* exibem texturas aglutinadas, com pedaços de *spatter*, indicando uma origem clastogênica, por meio de *fire fountaining* riolítico (Branney *et al.*, 2008).

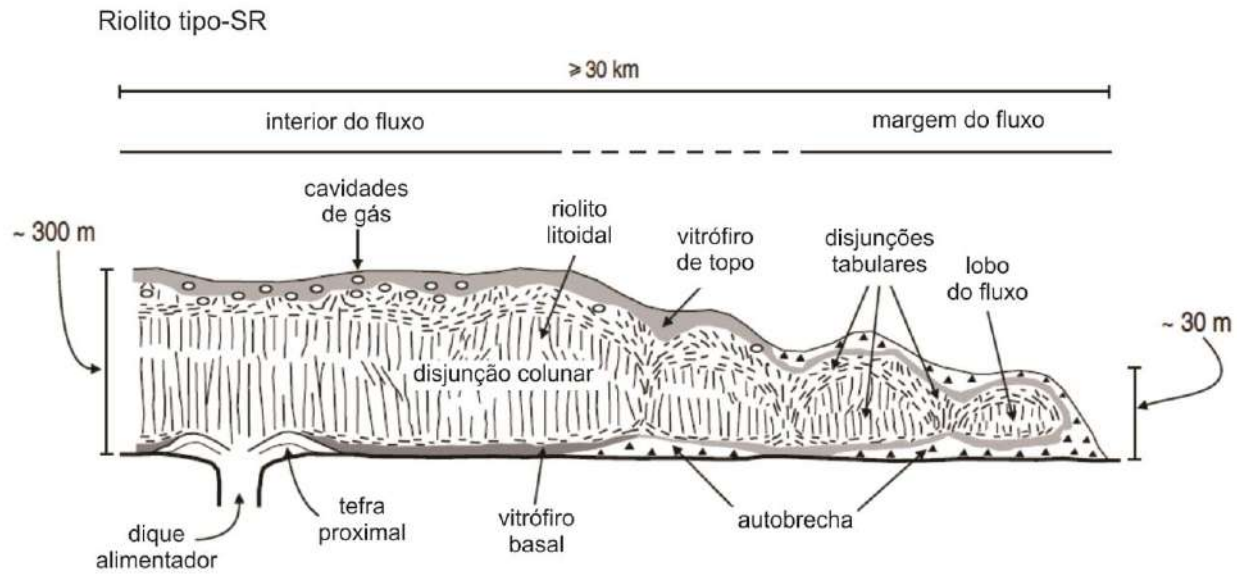

Figura 12 – Principais características e estruturas dos riolitos tipo-SR com extensões maiores que 30 km e espessuras em torno de 300 m com litofácies de autobrecha desenvolvidas nas porções mais distais dos fluxos.

3.3.4 Vulcanismo ácido de alta temperatura – soldagem e reomorfismo

A soldagem é a amálgama e a deformação plástica de piroclastos juvenis (principalmente púmice ou escória e *shards* de vidro) quentes e de baixa viscosidade (Smith, 1960). A deformação plástica das partículas vítreas gera a eliminação do espaço poroso por compactação e o depósito piroclástico original é transformado em uma rocha relativamente densa. A compactação resulta no desenvolvimento de foliações aproximadamente paralelas ao acamamento definidas por clastos de púmice ou escória e *shards* alinhados e achatados (geração de *fiamme* e textura eutaxítica). O reomorfismo é a deformação dútcil de material piroclástico quente e soldado, que precisa de alta temperatura para que haja aderência das partículas durante e após a sua deposição. Este processo depende da viscosidade do piroclasto e da carga litostática, bem como da temperatura, da composição e da espessura do depósito (Ragan & Sheridan, 1972; Riehle, 1973).

O comportamento do material vítreo depende da viscosidade do vidro e consequentemente da temperatura. A temperatura de transição do vidro (T_g) é um limite cinético, dado um *stress* aplicado, entre respostas mecânicas viscosas e elásticas. Acima da T_g, as partículas vítreas deformam de forma viscosa, permitindo a soldagem. Abaixo da T_g, o vidro responde ao stress de maneira elástica, impossibilitando a soldagem (Dingwell & Webb, 1990; Giordano *et al.*, 2005). A T_g possui um papel tão importante quanto a temperatura de *emplacement*, a temperatura de cristalização e a temperatura mínima de soldagem. Se, por exemplo, um material vulcânico tem sua colocação a altas temperaturas,

muito acima da temperatura mínima para a soldagem, e perto da sua temperatura de cristalização, a cristalização sin- e pós-*emplacement* pode ocorrer, possivelmente impedindo a soldagem (Giordano *et al.*, 2005).

A maioria dos estudos sobre soldagem na literatura trata de ignimbritos ácidos, no entanto, feições de soldagem são descritas em diversos depósitos, incluindo fluxos piroclásticos (Smith, 1960; Boyd, 1961), depósitos de queda (e.g. Sparks & Wright, 1979), lavas alimentadas por *spatter* (e.g. Wolff & Sumner, 2000, Gottsman & Dingwell, 2001), bases e margens de fluxos de lava (Naranjo *et al.*, 1992; Sparks *et al.*, 1993) e condutos vulcânicos (Kano *et al.*, 1997; Tuffen *et al.*, 2003). A soldagem é especialmente prevalente em depósitos de composição peralcalina, onde também exibe comumente sinais de fluxo reomórfico (e.g. Schimincke & Swanson, 1967; Wolff & Wright, 1981; Kobberger & Schmincke, 1999).

3.3.5 Vulcanismo ácido de alta temperatura – lavas versus reoignimbritos

Rochas ácidas de alta temperatura, incluindo tufos fortemente soldados e lavas ácidas de grande extensão são abundantes no registro geológico e descritas em diversas províncias mesozoicas e cenozoicas, incluindo as províncias Trans-Pecos Texas, Snake River Plain, Idaho, sul da África e Paraná-Etendeka (Henry & Wolff, 1992; Green & Fitz III, 1993). No entanto, seus mecanismos de erupção e colocação são controversos e critérios tradicionais usados para distinguir ignimbritos de lavas geralmente falham na tentativa de distinguir os depósitos de alta temperatura (Henry & Wolff, 1992).

No trabalho de Henry & Wolff (1992), ambas as características diagnósticas ou não diagnósticas para depósitos de alta temperatura são relatadas. Dentre elas, os autores afirmam para depósitos de lava que:

(1) É comum a presença de brechas basais compostas por uma variedade de tipos texturais do próprio fluxo em uma matriz clástica;
(2) Bases maciças ou com bandamento de fluxo são mais comuns para origem efusiva do que piroclástica;
(3) Lavas são espessas para as margens e possuem frentes abruptas, sendo paradas por obstáculos, quando não são mais espessas que o mesmo;
(4) Lavas entram em erupção dominantemente por fissuras e mantêm espessuras uniformes ao longo da sua extensão.

Já para depósitos de ignimbritos de alta temperatura, as principais características atribuídas são:

(i) Ignimbritos afinam a não mais de poucos metros nas suas bordas, onde geralmente não apresentam feições de fluxo secundárias;
(ii) Em velocidades relativamente baixas, os fluxos piroclásticos podem superar obstáculos muito maiores que o depósito resultante.
(iii) Ignimbritos geralmente entram em erupção a partir de calderas e podem acumular espessuras muito maiores do que as do depósito vulcânico relacionado ao colapso de erupções.

Bandamento e dobras de fluxo, rampas, vesículas alongadas e brechas de topo podem ocorrer nos dois tipos de depósito, portanto não são características diagnósticas. Púmices e *shards* também ocorrem em lavas (e.g. Manley & Fink, 1987) e ignimbritos de alta temperatura, apesar de ocorrerem ao longo de uma unidade de ignimbrito e geralmente nas partes marginais de brechas de lavas (Henry & Wolff, 1992). Texturas que lembram *shards* soldados, comuns em depósitos piroclásticos de alta temperatura, também foram descritas em fluxos de lava ácida (e.g. Manley, 1995; 1996). O autor explica a origem dessas texturas - que são localizadas – por meio de descompressão e inflação da superfície vesiculada do fluxo. A superfície vesiculada é cominuída subsequentemente, produzindo *shards*, púmice, pedaços de vidro denso e fragmentos de fenocristais. Esse depósito é introduzido entre blocos maiores, por meio de fraturas abertas, onde pode ser reaquecido e comprimido em vários graus, gerando uma camada de vitrófiro que pode ser texturalmente homogênea, em áreas próximas da lava bandada, lembrando um ignimbrito soldado com púmices achatados (Manley, 1996).

3.4 Estudos de caso – modelos eruptivos de lavas ácidas

Nesta seção foram escolhidos três estudos de caso para colocação de lavas ácidas. As áreas escolhidas possuem exposições contínuas e estudos detalhados em ambientes tectônicos que envolvem a erupção de magmas básicos e ácidos, ao passo que o enfoque é nos modelos de *emplacement* de domos e lavas de composição dacítica a riolítica.

3.4..1 Estudo de caso 1 – lavas ácidas do oeste dos Estados Unidos

O vulcanismo Holoceno registrado na porção oeste dos Estados Unidos da América (EUA), estados do Arizona, Califórnia e Oregon principalmente, é caracterizado pela erupção de fluxos e domos de lavas de composição dacítica a riolítica, inclusive com a preservação das litofácies de obsidianas (e.g. Skinner, 1983).

Nestas regiões é possível reconhecer estruturas morfológicas na escala de imagens de satélites, mostrando feições lobadas, similares às descritas na erupção de 2011-13 do vulcão Puyehue-Cordón Caulle, no Chile (**Fig. 13a,b**). A seção principal das lavas ácidas segue uma estrutura que possui, da base para o topo: tefra basal, brecha basal, zona vesiculada grossa, obsidiana, zona vesiculada fina e brecha de topo (e.g. Fink, 1983; Fink and Manley, 1987). A temperatura é maior no núcleo de obsidiana do derrame, juntamente com a menor viscosidade e maior densidade. À medida que se afasta do núcleo, as camadas mais porosas dissipam a energia térmica e resfriam, tal como os processos descritos para derrames escoriáceos de composição basáltica (e.g. MacDonald, 1953; Tuffen et al., 2013; Harris et al., 2017).

A descrição dos condutos na cadeia vulcânica de Inyo indicam que a ascensão do magma foi acompanhada por fraturas que se propagaram para baixo, e novas fraturas com foliações em alto ângulo, transportando o magma lateralmente para fora do conduto. As foliações sub-verticais refletem parcialmente a geometria destas fraturas, que por sua vez correspondem às orientações dos condutos alimentadores (Fink, 1983; Sampson, 1987). A geometria dos diques pode ser em uma forma segmentada escalonada (**Fig. 13c**) com propagação lateral. No Oligoceno do estado do Colorado, Poland et al. (2004) mapearam um trend de diques, juntamente com medidas de ASM e concluíram que o magma ascendeu verticalmente até atingir um nível neutro de flutuabilidade, e depois fluiu lateralmente e só voltou a fluir verticalmente na ponta das falhas, até interceptar os flancos do vulcão, onde entrou em erupção como lava (**Fig. 13d**).

Diques escalonados, como na **figura 13c**, se conectam em profundidade com diques de maior porte (**Fig. 14**, Fink, 1985; Blake & Fink, 1987), ou também na forma tubular (Sampson, 1987) e de calderas (Fink & Anderson., 2017). As principais estruturas associadas às áreas de condutos são zonas

de fraturas alinhadas e escalonadas em escala quilométrica, onde o fluxo de magma é vertical apenas nas pontas das falhas (**Fig. 15**). Estes tipos condutos podem alimentar campos de lavas com derrames mostrando até 0,1 km³ em volume, como os depósitos do vulcão Summer Coon e o Big Obsidian Flow (Gardner *et al.*, 1998).

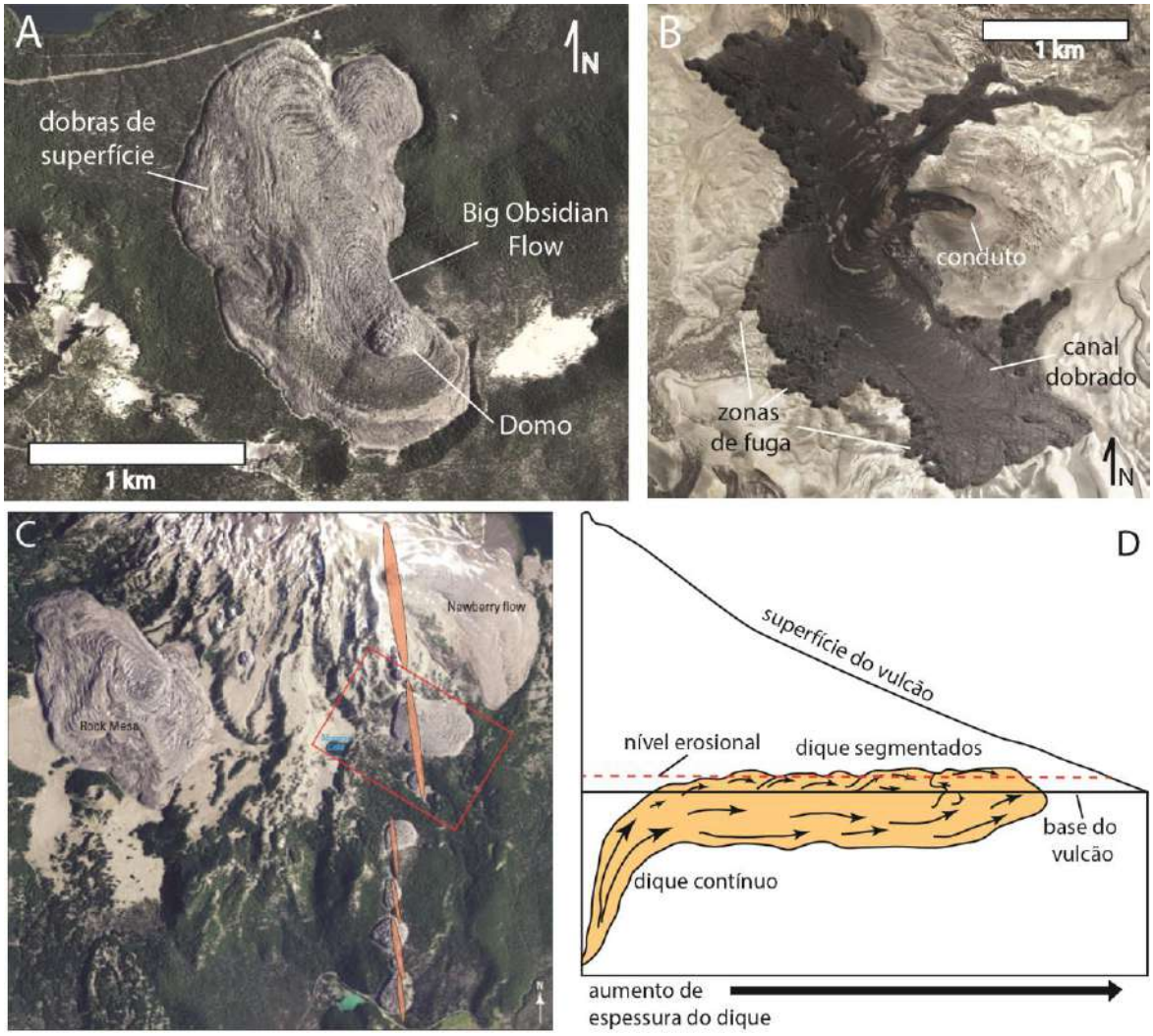

Figura 13 – Feições geológicas das lavas ácidas e modelo de condutos (extraídas de Fink & Anderson, 2017). A) Imagem de satélite do Big Obsidian Flow, Oregon. (B) Imagem do Google Earth do riodacito da erupção de 2011-13 do vulcão Córdon Caulle. (C) Flanco sul do vulcão South Sister mostrando os condutos escalonados representados por elipses de cor laranja. (D) Modelo de emplacement do vulcão Summer-Coon, centro-sul do Colorado. As setas mostram o fluxo lateral para a parede do vulcão.

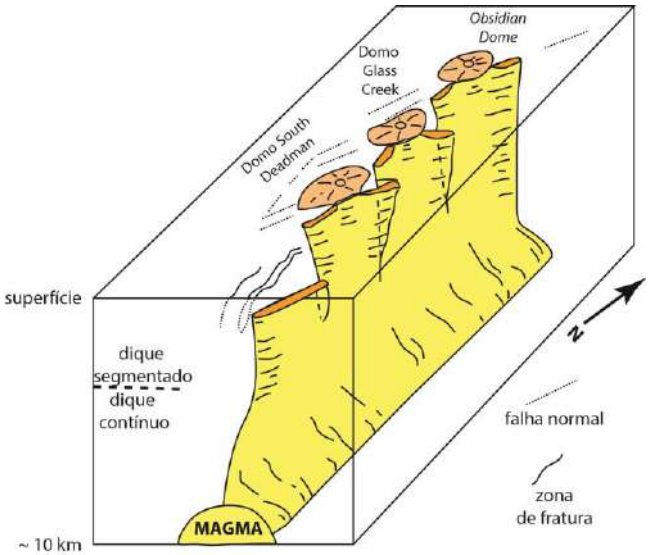

Figura 14 – Diques escalonados no modelo de condutos de Blake & Fink (1987) para três domos de lava alinhados no estado do Oregon (EUA).

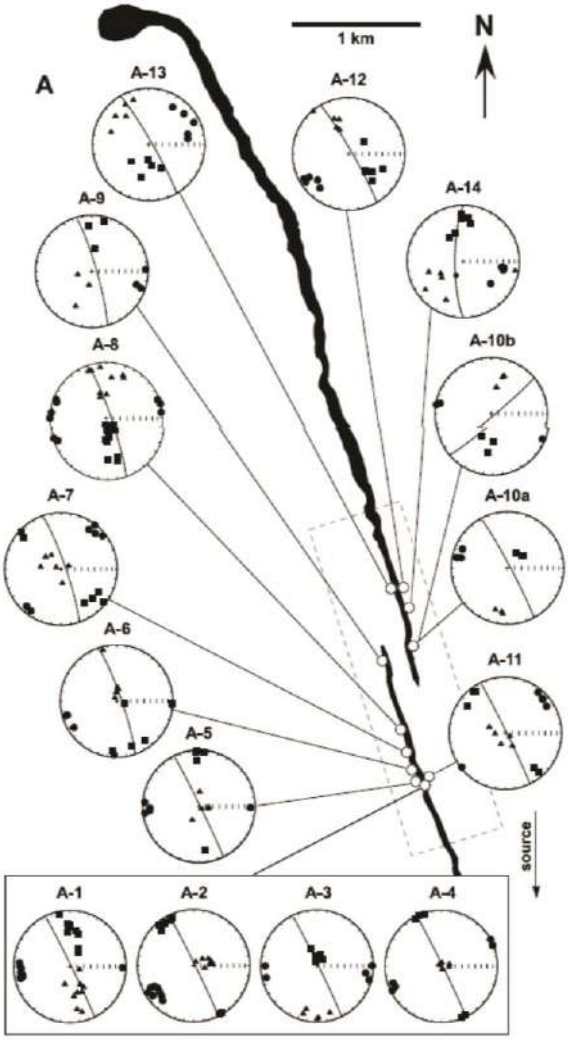

Figura 15 – Dados de anisotropia de susceptibilidade magnética para diques de lavas ácidas no vulcão Summer Coon, Colorado. Notar os eixos de K_{max} (quadrados) verticais geralmente nas pontas das falhas, onde o fluxo magmático é inferido como vertical. Nas demais porções, K_{max} é horizontal.

3.4.2 Estudo de caso 2 – vulcanismo extensional na Islândia

Na Islândia, o vulcanismo é extremamente diverso, havendo ocorrências de todos os tipos de vulcões e estilos de erupção conhecidos na Terra (Thorarinsson and Saemundsson, 1979; Thoratinsson, 1981). O platô vulcânico se estende por mais de 3 km acima do assoalho oceânico e cobre cerca de 350.000 km² (e.g. Gudmundsson, 2000). Sua gênese é atribuída a uma pluma mantélica ativa há pelo menos 65 Ma que formou a Província Ígnea do Atlântico Norte, com 2000 km de comprimento, incluindo a Islândia, a única parte onde o magmatismo ainda é ativo (e.g. Saunders et al., 1997).

O sistema vulcânico é a principal feição geológica na Islândia, sendo caracterizado por conspícuas feições de arquitetura vulcanotectônica como enxames de fissuras preenchidos por diques ou vulcões centrais. Os enxames de fissuras consistem em estruturas alongadas que normalmente alinham-se de forma sub-paralela ao eixo da zona vulcânica hospedeira. O vulcão central, quando presente, é o ponto focal da atividade eruptiva e, tipicamente, o maior edifício vulcânico de cada sistema (Thordarson and Larsen, 2007; **fig. 15**).

De acordo com a revisão de Thordarson and Larsen (2007), dois modelos contrastantes predominam para explicar a origem dos episódios vulcânicos na Islândia, considerando-se as estruturas em sub-superfície e o comportamento do sistema de armazenamento magmático durante os episódios de rifte: (a) onde o mecanismo de rifteamento no sistema vulcânico é consequência da reposição e pressurização de magma de uma câmara crustal rasa e subsequente injeção lateral de diques dentro de um enxame de fissuras; e (b) onde os episódios de rifteamento nos sistemas vulcânicos são consequência da pressurização de magma em reservatórios amplos e alongados na base da crosta (>20 km de profundidade) e subsequente injeção de diques subverticais na crosta superior.

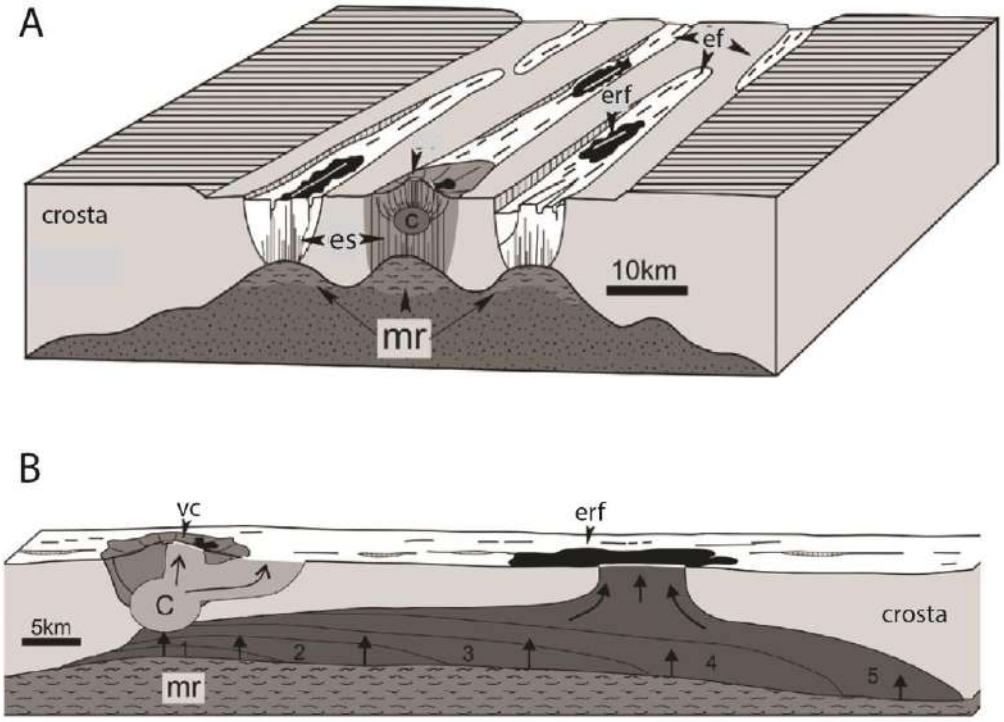

Figura 16 – Estruturas-chave dos sistemas vulcânicos na Islândia (modificado de Thordarson and Larsen, 2007). C - câmara magmátca, Mr – reservatório de magma, es – enxame de diques, ef – enxame de fissuras, erf – erupção fissural, vc – vulcão central.

As erupções efusivas dacíticas a riolíticas são significantes, mas relativamente raras, gerando produtos de pequeno volume (<0,2 km³) na forma de lavas em bloco, couleés e domos, bem como domos e montanhas tabulares subglaciais. A razão de forma das lavas na Islândia é geralmente menor do que aquele obtido em outras regiões (e.g. Walker, 1973). Esta baixa razão de forma é atribuída à altas temperaturas eruptivas (~1000°C) e baixas viscosidades (10^5 a 10^6 Pa s) para os magmas ácidos (Thordarson and Larsen, 2007).

Condutos de obsidianas como Thumall e Skriöugi alimentaram lavas riolíticas que formam um complexo com cerca de 6 km³ no vulcão central de Torfajökull, com estruturas de fluxo verticais (**Fig. 16**), cujas orientações de fluxo magmático são paralelas às fissuras principais da região (Tuffen and Dingwell, 2005). Na ilha de Krafla, uma erupção por meio de um dique riolítico de ~2,5 km formou uma crista de 80 m acima das rochas encaixantes, com volume total <0,05 km³. As litofácies intrusivas incluem um dique alimentador, com cerca de 2 m de espessura cujos contatos com a encaixante não são observáveis, e lava perlítica. As litofácies de fragmentos são compostas por tufos pumíceos e brechas hialoclastíticas perlíticas. Já as lavas subaéreas são compostas por obsidiana fraturada, obsidiana bandada, zonas vesiculadas ricas em litofises e uma zona interna esferulítica, além de texturas de interação lava e gelo (Tuffen and Castro, 2009).

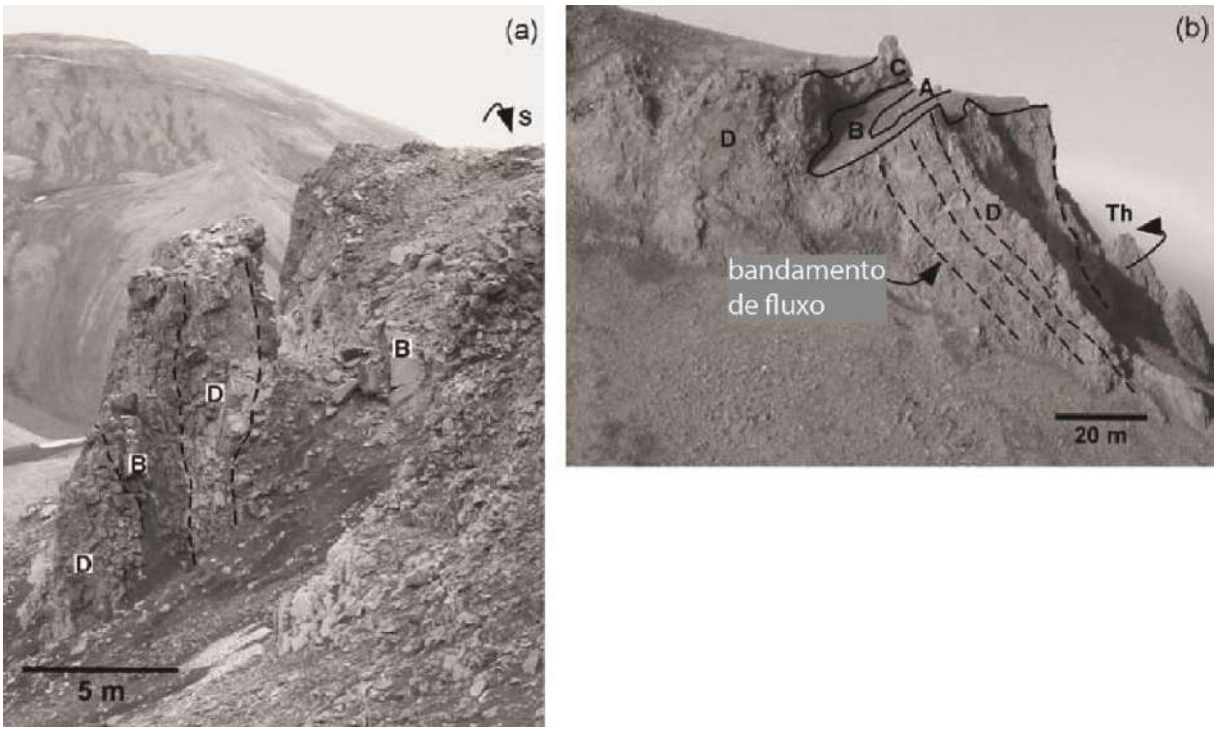

Figura 17 – Visão geral dos condutos descritos por Tuffen and Dingwell (2005). (a) Conduto Thumall. As zonas texturais são: A – obsidiana vesicular, B – obsidiana sem vesículas, C – brecha de obsidiana esferulítica, D – riolito esferulítico. (b) Conduto Skriöugil (s) com as zonas texturais e a referência geográfica do conduto Thumall (Th).

O sistema vulcânico Bardarbunga, localizado na zona vulcânica leste da Islândia, é um ambiente sob um regime tectônico extensional onde a intrusão de magma foi controlada por rifteamento (Sigmundsson et al., 2014). O desenvolvimento da erupção se deu por injeção vertical de magma em um conduto central, a partir do qual a intrusão do magma foi lateral (Sigmundsson et al., 2014; Geiger et al., 2016). A análise estrutural apresentada por Müller et al. (2017) durante a erupção Holuhraun, de 2014/2015, através de modelos 2D e 3D a partir imagens de alta resolução (satélite, UAVs[1] e laser scanning) mostrou que o deslocamento ao longo de falhas normais, deslocamento transtrativo e a formação de um gráben foram os mecanismos principais para a ascensão do magma e erupção (**Fig. 17**).

[1] Unmanned Aerial Vehicles

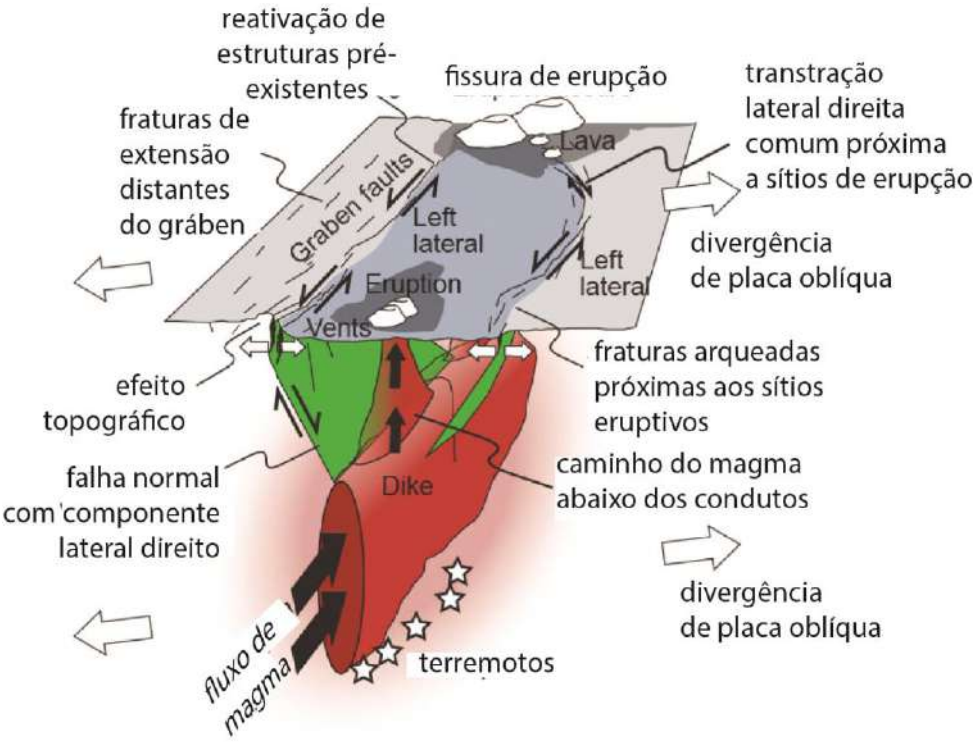

Figura 18 – Esquema das relações estruturais nos locais da erupção Holuhraun. A subsidência do gráben é identificada sobre o dique alimentador, e delimitada pelas falhas do gráben e menores fraturas à distância. Em superfície, as falhas do gráben mostram deslocamentos transtrativos. Próximo à superfície, as falhas aparentam um mergulho sub-vertical. Modificado de Müller et al. (2017).

3.4.3 Estudo de caso 3 – lavas ácidas da Província Gawler Range (Austrália)

A Província Gawler Range é composta pelas vulcânicas Gawler Range e a Suíte Hiltaba, constituindo uma SLIP mesoproterozoica que aflora em uma vasta área do cráton Gawler, no sul da Austrália. O volume estimado da província é da ordem de 100.000 km³ (McPhie et al., 2008) e o volume total das vulcânicas Gawler Range em torno de >30.000 km³ (Pankhurst et al., 2011). Esta província representa um remanescente de um dos mais volumosos eventos magmáticos félsicos preservados na Terra, além de abrigar depósitos metalogenéticos correlatos aos que formaram os depósitos de Au-U de Olympic Dam. Uma hipótese sobre sua origem atribui este magmatismo a uma atividade de hot-spot que também afetou a porção central da Austrália (Betts et al., 2009).

Segundo Agangi et al. (2012), a colocação das vulcânicas durou cerca de 2 Ma e pode ser separada em duas fases. A primeira fase contém por sequências espessas (de até 3 km) formadas por erupções localizadas em centros distintos, incluindo um volume de até 150 km³ de lavas félsicas, ignimbritos e uma porção menor de lavas máficas a intermediárias. A segunda fase inclui lavas de grande extensão com mais de 1000 km³ em volume e 200 km de comprimento. As unidades

individuais de lavas possuem volumes que variam de 1 a 168 km³, texturas dominantemente coerentes, camadas de brechas autoclásticas, bandamento e lineações de fluxo.

As lavas félsicas possuem afinidade geoquímica do tipo-A, com altas razões Ga/Al e alto conteúdo de halógenos como F^- e Cl^-. As altas temperaturas de 950-1100°C e excesso de halógenos geram viscosidades calculadas menores que $10^{3,5}$ Pa s, considerando um conteúdo de água de 2% (**Fig. 18**). A baixa viscosidade destes magmas produziu um sistema magmático único, em uma escala inigualável no planeta (Pankhurst et al., 2011; Agangi et al., 2012).

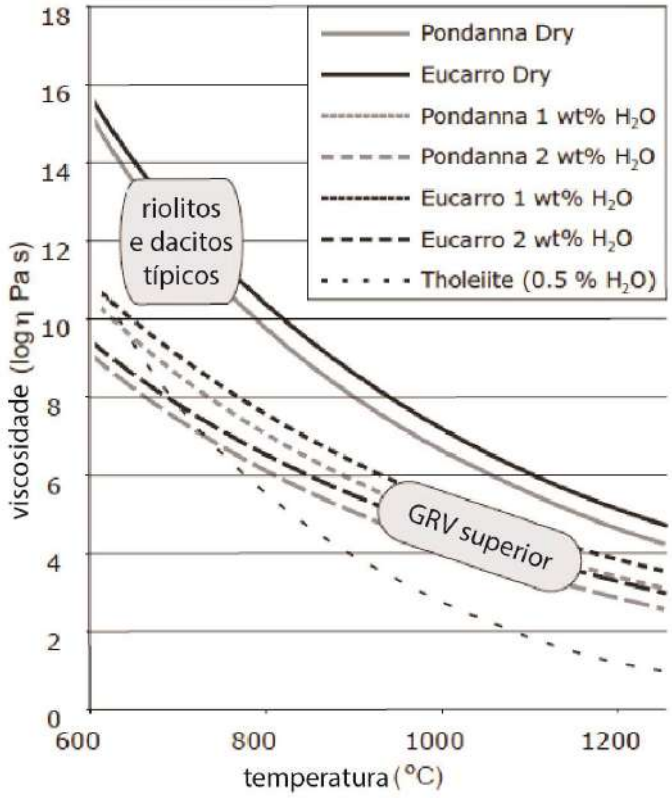

Figura 19 –Diagrama de viscosidade vs. temperatura ilustrando as paleoviscosidades para o Dacito Pondanna e o Riolito Eucarro, com alto F^- e 0,02, 1 e 2% de H_2O. GRV = Vulcânicas Gawler Range.

REFERÊNCIAS

Agangi, A., Kamenetsky, V.S., McPhie, J. **2012**. Evolution and emplacement of high fluorine rhyolites in the Mesoproterozoic Gawler silicic large igneous province, South Australia. Precambrian Research, 208-211, 124-144.

Bellieni G., Brotzu P., Morbidelli L., Piccirillo E.M., Traversa G. **1986**. Petrology and mineralogy of miocene fissural volcanism of the East Kenya plateau. Neues Jahrbuch fur Mineralogie Abhandlungen, 154, 153-178.

Bellieni, G., Brotzu, P., Comin-Chiaramonti, P., Ernesto, M., Melfi, A.J., Pacca, I.G., Piccirillo, E.M., Stolfa, D. **1983**. Petrological and paleomagnetic data on the plateau basalt to rhyolite sequences of the Southern Paraná Basin (Brazil). Anais da Academia Brasileira de Ciências, 55, 355-383.

Bellieni, G., Brotzu, P., Comin-Chiaramonti, P., Ernesto, M., Melfi, A.J., Pacca, I.G., Piccirillo, E.M. **1984**. Flood basalt to rhyolite suites in the southern Paraná plateau (Brazil): paleomagnetism, petrogenesis and geodynamic implications. Journal of Petrology, 25, 579-618.

Bellieni, G., Comin-Chiaramonti, P., Marques, L.S., Melfi, A.J., Nardy, A.J.R., Papatrechas, C., Piccirillo, E.M., Roisenberg, A., Stolfa, D. **1986**. Petrogenetic aspects of acid and basaltic lavas from the Paraná plateau (Brazil): geological, mineralogical and petrochemical relationships. Journal of Petrology, 27, 915-944.

Bellieni, G., Piccirillo, E.M., Comin-Chiaramonti, P., Melfi, A.J., Da Roit, P. **1988**. Mineral chemistry of continental stratoid volcanics and related intrusives from the Paraná Basin (Brazil). In: Piccirilo, E.M. & Melfi, A.J. (eds) The Mesozoic Flood Volcanism of the Paraná Basin. São Paulo: IAG-USP Press.

Betts, P.G., Giles, D., Foden, J., Schaefer, B.F., Mark, G., Pankhurst, M.J., Forbes, C.J., Williams, H.A., Chalmers, N.C., Hills, Q. **2009**. Mesoproterozoic plume-modified orogenesis in eastern Precambrian Australia. Tectonics, 28, TC3006.

Blake, S., Fink, J.H. **1987**. The dynamics of magma withdrawal from a density stratified dyke. Earth and Planetary Science Letters, 85, 516-524.

Bossi, J., Umpierre, M. **1975**. Magmatismo mesozoico del Uruguay y Rio Grande del Sur: sus recursos minerals asociados y potenciales. Anais 2 Congreso Iberoamericano de Geologia Economica, Buenos Aires, pp. 119–142.

Boyd, F.R. **1961**. Welded tuffs and flows in the rhyolite plateau of Yellowstone Park, Wyoming. Geological Society of America Bulletin, 72, 387– 426.

Branney , M.J., Bonnichsen B., Andrews G.D.M., Ellis B., Barry T.L., McCurry M. **2008**. “Snake River (SR)-type” volcanism at the Yellowstone hotspot track: distinctive products from unusual, high-temperature silicic super-eruptions. Bulletin of Volcanology: 70(3), 293-314.

Breitkreuz C. **2001**. Introduction to physical volcanology and volcanic textures. Short course notes.

Bryan, S. **2007**. Silicic large igneous provinces. Episodes, 30(1), 1-12.

Bryan, S. E., Peate, I. U., Peate, D. W., Self, S., Jerram, D. A., Mawby, M. R., Marsh, J. S., Miller, J.A. **2010**. The largest volcanic eruptions on Earth. Earth-Science Reviews, 102(3-4), 207-229.

Bryan, S.E., Ernst, R.E. **2008**. Revised definition of Large Igneous Provinces (LIPs). Earth Science Reviews, 86, 175–202.

Bryan, S.E., Riley, T.R., Jerram, D.A., Stephens, C.J., Leat, P.T. **2002**. Silicic volcanism: an undervalued component of large igneous provinces and volcanic rifted margins. Special Papers-Geological Society of America, 97-118.

Burnham, C. W. **1983**. Deep submarine pyroclastic eruptions. In: Ohmoto and Skinner, 142-8.

Cañón-Tapia, E. **2010**, Origin of Large Igneous Provinces: The importance of a definition, in Cañón-Tapia, E., and Szakács, A., eds., What Is a Volcano?: Geological Society of America Special Paper 470, 77–101.

Cas, R.A.F., Wright, J.V. **1988**. Volcanic succession, modern and ancient: a geological approach to processes, products and successions, Chapman & Hall, London

Cashman, K.V. **2004**. Volatile controls on magma ascent and eruption. Geophysical Monograph, 150 (19), 109–124.

Chadima, M., Jelinek, V. **2009**. AniSoft 42 Software, Anisotropy Data Browser for Windows. Brno, Czech Republic.

Channell, J.E.T., Cecca, F., and Erba, E. **1995**. Correlations of Hauterivian and Barremian (Early Cretaceous) stage boundaries to polarity chrons. Earth and Planetary Science Letters, 134, 237–252.

Christiansen, R. L. and P. W. Lipman. **1966**. Emplacement and thermal history of a rhyolite lava flow near Fortymile Canyon, southern Nevada. Geological Society of America Bulletin, 77, 671-84.

Coffin, M.F., Eldholm O. **1994**. Large Igneous Provinces: crustal structure, dimensions and external consequences. Reviews of Geophysics, 32, 1-36.

Coffin, M.F., Eldholm, O. **1992**. Volcanism and continental break-up: a global compilation of large igneous provinces. In: B.C Storey, T. Alabaster, R.J. Pankhurst (eds.), Magmatism and the Causes of Continental Breakup. Special Publication of the Geological Society of London, 17-30.

Collier, J.S., McDermott, C., Warner, G., Gyori, N., Schnabel, M., McDermott, K., Horn, B.W. **2017**. New constraints on the age and style of continental breakup in the South Atlantic from magnetic anomaly data. Earth and Planetary Science Letters, 477, 27–40.

Comin-Chiaramonti P., Bellieni G., Piccirillo E.M., Melfi A.J. **1988**. Classification and petrography of continental stratoid volcanic and related intrusive from the Paraná Basin (Brasil). In: Piccirilo, E.M. & Melfi, A.J. (eds) The Mesozoic Flood Volcanism of the Paraná Basin. São Paulo: IAG-USP Press.

Comin-Chiaramonti, P. **2000**. Peraluminous lavas from Jaguarão (Rio Grande Do Sul, Brazil). DICAMP: Quaderni di Mineralogia, Petrografia e Geochimica Applicate, Trieste University 17, 1–15.

Cordani, U.G., Civetta, L., Mantovani, M.S.M., Petrini, R., Kawashita, K., Hawkesworth, C.J., Taylor, P., Longinelli, A., Cavazzini, G., Piccirillo, E.M. **1988**. Isotope geochemistry of flood volcanics from the Paraná Basin (Brazil). In: Piccirilo, E.M. & Melfi, A.J. (eds) The Mesozoic Flood Volcanism of the Paraná Basin. São Paulo: IAG-USP Press.

Dingwell, D.B., Webb, S.L. **1990**. Relaxations in silicate melts. European Journal of Mineralogy, 2, 427–449.

Dodd, S.C., Niocaill, C.M., Muxworthy, A.R. **2015**. Long duration (>4 Ma) and steady-state volcanic activity in the early Cretaceous Paraná-Etendeka Large Igneous Province: New paleomagnetic data from Namibia. Earth and Planetary Science Letters, 414, 16-29.

Ekren, E.B., McIntyre, D.H., Bennett, E.H. **1984**. High-temperature, largevolume, lava like ash-flow tuffs without calderas in southwestern Idaho. US Geolological Survey Professional, 1272.

Ernesto, M., Pacca, I.G. **1988**. Paleomagnetism of the Paraná Basin flood volcanics, southern Brazil. In: Piccirilo, E.M. & Melfi, A.J. (eds) The Mesozoic Flood Volcanism of the Paraná Basin. São Paulo: IAG-USP Press.

Ewart, A., Milner, S.C., Armstrong, R.A., Duncan, A.R. **1998**. Etendeka volcanism of the Goboboset Mountains and Messum Igneous Complex, Namibia. Part I: Geochemical evidence of Early Cretaceous Tristan plume melts and the role of crustal contamination in the Paraná-Etendeka CFB. Journal of Petrology, 39, 191-225.

Fink J. H. **1983**. Structure and emplacement of a rhyolitic obsidian flow; Little Glass Mountain, Medicine Lake Highland, northern California. Geological Society of America Bulletin, 94(3), 362-380.

Fink J. H., Manley C. R. **1987**. Origin of pumiceous and glassy textures in rhyolite flows and domes. Special Paper Geological Society of America, 212, 77-88.

Fink, J. H. **1980a**. Surface folding and viscosity of rhyolite flows. Geology, 8, 250-4.

Fink, J. H. **1980b**. Gravity instability in the Holocene Big and Little Glass Mountain rhyolitic obsidian flows, northern California. Tectonophysics, 66, 147-66.

Fink, J. H., R. C. Fletcher. **1978**. Ropy pahoehoe: surface folding of a viscous fluid. Journal of Volcanology and Geothermal Research: 4, 151-70.

Fink, J.H. **1985**. Geometry of Silicic Dikes Beneath the Inyo Domes, California. Journal of Geophysical Research, 90, 127-133.

Fink, J.H., Anderson, S. **2017**. Emplacement of Holocene Silicic Lava Flows and Domes at Newberry, South Sister and Medicine Lake Volcanoes, California and Oregon. USGS, Scientific Investigations Report 2017-5022-I.

Fisher, R. V. **1966**. Rocks composed of volcanic fragments and their classification. Earth-Sciences Reviews: 1, 287-98.

Florisbal, L.M., Janasi, V.A., Bitencourt, M.F., Nardi, L.V.S., Marteleto, N.S. **2017**. Geological, geochemical and isotope diversity of ~134 Ma dykes from the Florianópolis Dyke Swarm, Paraná Magmatic Province: Geodynamic controls on petrogenesis. Journal of Volcanology and Geothermal Research, in press.

Frank, H.T., Gomes, M.E.B., Formoso, M.L.L. **2009**. Review of the areal extent and volume of the Serra Geral Formation, Paraná Basin, South America. Pesquisas em Geociências, 36(1), 49-57.

Gardner, J.E., Carey, S., and Sigurdsson, H. **1998**, Plinian eruptions at Glacier Peak and Newberry volcanoes, United States—Implications for volcanic hazards in the Cascade Range. Geological Society of America Bulletin, 110, 173–187.

Garland, F.E., Hawkesworth, C.J., Mantovani, M.S.M. **1995**. Description and petrogenesis of the Paraná rhyolites. Journal of Petrology, 36, 1193–1227.

Geiger, H., Mattsson, T., Deegan, F.M., et al. **2016**. Magma plumbing for the 2014-2015 Holuhraun eruption, Iceland. Geochemistry, Geophysics, Geosystems, 17, 1-16.

Giordano, D., Nichols, A.R.L., Dingwell, D.B. **2005**. Glass transition temperatures of natural hydrous melts: a relationship with shear viscosity and implications for the welding process. Journal of Volcanology and Geothermal Research, 142, 105-118.

Giordano, D., Russell, J.K., Dingwell, D.B. **2008**. Viscosity of magmatic liquids: A model. Earth and Planetary Science Letters, 271, 123-134.

Gottsmann, J., Dingwell, D.B. **2001**. Cooling dynamics of spatterfed phonolite obsidian flows on Tenerife, Canary Islands. Journal of Volcanology and Geothermal Research, 105, 323–342.

Green, J.C., Fitz III, T.J. **1993**. Extensive felsic lavas and rheoignimbrites in the Keweenawan Midcontinent Rift plateau volcanics, Minnesota: petrographic and field recognition: Journal of Volcanology and Geothermal Research, 54, 177-196.

Gudmundsson, A. **2000**. Dynamics of volcanic systems in Iceland: example of tectonism and volcanism at juxtaposed hot spot and mid-ocean ridge systems. Ann. Rev. Earth Planet. Sci. 28, 107–140.

Hall, S. H. **1978**. The stratigraphy of northern Lipari and the structure of the Rocche Rosse rhyolite flow and its implications. Thesis, University of Leeds.

Harris, A.J.L.M., Rowland, S.K., Villeneuve, N., Thordarson, T. **2017**. Pahoehoe, 'a'a, and block lava: an illustrated history of the nomenclature. Bulletin of Volcanology, 79, 7.

Harrison, T.M., Watson, E.B. **1984**. The behaviour of apatite during crustal anatexis: equilibrium and kinetic considerations. Geochimica et Cosmochimica Acta, 48(7), 1467-1477.

Hasenack, H., Weber, E. **2010**. Base cartográfica vetorial contínua do Rio Grande do Sul - escala 1:50.000. Porto Alegre, UFRGS, IB - Centro de Ecologia. DVD-ROM (Série Geoprocessamento, 3).

Henry, C. D., Wolff, J. A. **1992**. Distinguishing strongly rheomorphic tuffs from extensive silicic lavas. Bulletin of Volcanology, 54, 171-186.

Hext, G.R. **1963**. The estimation of second-order tensors, with related tests and designs. Biometrika, 50, 353–373.

Horbach, R., Kuck, L., Marimom, R.G., Moreira, H.L., Fuck, G.F., et al. **1986**. Geologia. In: Projeto Radambrasil, Folha SH.22 Porto Alegre a parte das folhas SH.21 Uruguaiana e SI.22 Lagoa Mirim. Rio de Janeiro, IBGE, Levantamento de Recursos Naturais, 33, 29–312.

Hrouda, F. **1982**. Magnetic anisotropy of rocks and its application in geology and geophysics. Surveys in Geophysics, 5, 37–82

Janasi, V.A., de Freitas, V.A., Heaman, L.H. **2011**. The onset of flood basalt volcanism, Northern Paraná Basin, Brazil: a precise U–Pb baddeleyite/zircon age for a Chapecó type dacite. Earth and Planetary Science Letters, 302 (1–2), 147–153.

Janasi, V.A., Montanheiro, T.J., Freitas, V.A., Reis, P.M., Negri, F.A., Dantas, F.A. **2007**. Geology, petrography and geochemistry of the acid volcanism of the Paraná Magmatic Province in the Piraju–Ourinhos region, SE Brazil. Revista Brasileira de Geociências, 37, 745–759.

Jelinek, V. **1978**. Statistical processing of anisotropy of magnetic susceptibility measured on groups of specimens and its applications, Studia Geophysica et Geodaetica, 22, 50 – 62.

Jelinek, V. **1981**. Characterization of the magnetic fabric of rocks. Tectonophysics, 79, 63– 67.

Jerram, D.A. **2002**. Volcanology and facies architecture of flood basalts, in Menzies, M.A., Klemperer, S.L., Ebinger, C.J., Baker, J. (eds.) Volcanic Rifted Margins: Geological Society of America Special Paper 362, 119-132.

Jerram, D.A., Mountney, N., Holzförster, F., Stollhofen, H. **1999**. Internal stratigraphic relationships in the Etendeka Group in the Huab Basin, NW Namibia. Journal of Geodynamics, 28, 393–418.

Jerram, D.A., Widdowson, M. **2005**. The anatomy of Continental Flood Basalt Provinces: geological constraints on the processes and products of flood volcanism. Lithos, 79(3), 385-405.

Kano, K., Matsuura, H., Yamauchi, S. **1997**. Miocene rhyolitic welded tuff infilling a funnel-shaped eruption conduit Shiotani, southeast of Matsue, SW Japan. Bulletin of Volcanology, 59, 125– 135.

Kirstein, L.A., Hawkesworth, C.J, Gargland, F.G. **2001**. Felsic lavas or rheomorphic ignimbrites: is there a chemical distinction? Contributions to Mineralogy and Petrology, 142, 309-322.

Kobberger, G., Schmincke, H.U. **1999**. Deposition of rheomorphic ignimbrite D (Mogan Formation) Gran Canaria, Canary Islands, Spain. Bulletin of Volcanology, 60, 465– 485.

Leeman, W.P. **1982**. Development of the Snake River Plain – Yellowstone Plateau province, Idaho and Wyoming: An overview and petrologic model. In: Bonnischsen, B., Breckenridge, R.M.(eds) Cenozoic Geology of Idaho: Idaho Bureau of Mines and Geology Bulletin, 26, 155-177.

LeMaitre, R.W. **1989**. A Classification of Igneous Rocks and Glossary of Terms, Blackwell, Oxford

Lima E.F., Philipp R.P., Rizzon G.C., Waichel B.L., Rossetti L.M.M. **2012**. Sucessões Vulcânicas e Modelo de Alimentação e Geração de Domos de Lava Ácidos da Formação Serra Geral na Região de São Marcos-Antonio Prado (RS). Geologia USP Série Científica, 12, 49-64.

Lima, E.F., Waichel, B.L., Rossetti, L.M.M., Sommer, C.A., Simões, M.S. **2018**. Feeder systems of acidic lava flows from the Paraná-Etendeka Igneous Province in Southern Brazil and their implications for eruption style. Journal of South American Earth Sciences, 81, 1-9.

Loney, R. A. **1968**. Flow structure and composition of the Southern Coulee, Mono craters, California – a pumiceous rhyolite flow. In: Coats et al., 153-210.

Luchetti, A.C.F., Nardy, A.J.R., Machado, F.B., Madeira, J.E.O., Arnosio, J.M. **2014**. New insights on the occurrence of peperites and sedimentary deposits within the silicic volcanics sequences of the Paraná Magmatic Province, Brazil. Solid Earth, 5, 121-130.

Lustrino, M., L. Melluso, P. Brotzu, C.B. Gomes, L. Morbidelli, R. Muzio, E. Ruberti and C. Tassinari. **2005**. Petrogenesis of the Early Cretaceous Valle Chico igneous complex (SE Uruguay): relationships with Paraná - Etendeka magmatism. Lithos 82, 407-434.

Macdonald, G. A. **1972**. Volcanoes. Englewood Cliffs, New Jersey: Prentice-Hall.

MacDonald, G.A. **1953**. Pahoehoe, aa and block lava. American Journal of Science, 251(3), 169-191.

Manley, C.R., Fink J. H. **1987**. Internal textures of rhyolite flows as revealed by research drilling. Geology, 15(6), 549-552.

Manley, C.R. **1995**. How voluminous rhyolite lavas mimic rheomorphic ignimbrites: Eruptive style, emplacement conditions, and formation of tuff-like textures. Geology, 23(4), 349-352.

Manley, C.R. **1996**. Physical volcanology of a voluminous rhyolite lava flow: The Badlands lava, Owyhee Plateau, southwestern Idaho. Journal of Volcanology and Geothermal Research, 71, 129-153.

Mantovani, M.S.M., Cordani, U.G., Roisenberg, A. **1985**. Geoquímica isotópica em vulcânicas ácidas da Bacia do Paraná e implicações genéticas associadas. Revista Brasileira de Geociências, 15 (1), 61-65.

Marsh, J.S., Ewart, A., Milner, S.C., Duncan, A.R., Miller, R. **2001**. The Etendeka Igneous Province: magma types and their stratigraphic distribution with implications for the evolution of the Paraná-Etendeka flood basalt province. Bulletin of Volcanology, 62, 464-486.

McPhie, J., DellaPasqua, F., Allen, S.R., Lackie, M.A. **2008**. Extreme effusive eruptions: Paleoflow data on an extensive felsic lava in the Mesoproterozoic Gawler Range Volcanics. Journal of Volcanology and Geothermal Research, 172, 148 – 161.

McPhie, J., Doyle, M., Allen, R. **1993**. Volcanic Textures: A guide to the interpretation of textures in volcanic rocks. Tasmania

Melfi A.J., Nardy A.J.R., Piccirillo E.M. **1988**. Geological and magmatic aspects of the Paraná Basin: An introduction. In: Piccirillo E.M. & Melfi A.J. (eds.) The Mesozoic flood volcanism of the Paraná Basin: Petrogenetic and geophysical aspects. São Paulo: IAG-USP Press

Miall, A.D. **2000**. Principles of Sedimentary Basin Analysis. 3rd edition. Springer-Verlag Inc., New York

Milani, E.J., Melo, J.H.G., Souza, P.A., Fernandes, L.A., França, A.B. **2007**. Bacia do Paraná. In: Boletim de Geociências da PETROBRAS, 15(2), 265-287.

Milner, S.C., Duncan, A. R., Whittingham, A. M., Ewart, A. **1995**. Trans-Atlantic correlation of eruptive sequences and individual silic volcanic units within Paraná- Etendeka Igneous Province. Journal of Volcanology and Geothermal Research, 69, 137-157.

Milner, S.C., Duncan, A.R., Ewart, A. **1992**. Quartz latite rheoignimbrite flow of the Etendeka Formation, North-Western Namibia. Bulletin of Volcanology, 54, 200-219.

Milner, S.C., Duncan, A.R., Ewart, A., Marsh, J.S. **1994**. Promotion of the Etendeka Formation to Group status: A new integrated stratigraphy. Communications of the Geological Survey of Namibia, 9, 5-11.

Milner, S.C., Ewart, A. **1989**. The geology of the Goboboseb Mountain volcanics and their relationship to the Messum Complex. Communications of the Geological Survey of Namibia, 5, 31-40.

Müller, D., Walter, T.R., Schöpa, A., Witt, T. et al. **2017**. High-Resolution Digital Elevation Modeling from TLS and UAV Campaign Reveals Structural Complexity at the 2014/2015 Holuhraun Eruption Site, Iceland. Frontiers in Earth Science, 5, 59.

Naranjo, J.A., Sparks, R.S.J., Stasiuk, M.V., Moreno, H., Ablay, G.J. **1992**. Morphological, textural and structural variations in the 1988–1990 andesite lava of Lonquimay. Geological Magazine: 129, 657–678.

Nardy A.J.R., Machado F.B., Oliveira M.A.F. **2008**. As rochas vulcânicas mesozoicas ácidas da Bacia do Paraná: litoestratigrafia e considerações geoquímicas-estratigráficas. Revista Brasileira de Geociências, 38(1), 178-195.

Natali, C., Beccaluva, L., Bianchini, G., Siena, F. **2011**. Rhyolites associated to Ethiopian CFB: Clues for initial rifting at the Afar plume axis. Earth and Planetary Science Letters, 312, 59-68.

Pankhurst M.J., Schaefer B.F., Betts P.G., Phillips N., Hand M. **2011**. A Mesoproterozoic continental flood rhyolite province, the Gawler Ranges, Australia: the end member example of the Large Igneous Province clan. Solid Earth, 2, 25-33.

Parfitt, E.A., Wilson, L. **2008**. Fundamentals of Physical Volcanology. Blackwell Publishing.

Peate, D.W. **1997**. The Paraná-Etendeka province. In: Mahoney, J.J., Coffin, M.R. (eds.) Large Igneous Provinces: Continental, Oceanic and Planetary Flood Volcanism: Geophysical Monograph, 100, 217-245.

Peate, D.W., Hawkesworth, C.J., Mantovani, M.S.M. **1992**. Chemical stratigraphy of the Paraná lavas (S. America): classification of magma types and their spatial distribution. Bulletin of Volcanology, 55, 119-139.

Piccirillo, E.M., Bellieni, G., Cavazzini, G. et al. **1990**. Lower Cretaceous tholeiitic dyke swarms from the Ponta Grossa Arch (southeast Brazil): Petrology, Sr-Nd isotopes and genetic relationships with the Paraná flood volcanics. Chemical Geology, 89, 19-48.

Piccirillo, E.M., Raposo, M.I.B., Melfi, A.J., Comin-Chiaramonti, P., Bellieni, G., Cordani, U.G., Kawashita, K. **1987**. Bimodal fissural volcanic suites from the Paraná basin (Brazil): K-Ar age, Sr-isotopes and geochemistry. Geochimica Brasiliensis, 1, 53-69.

Pinto, V.M., Hartmann, L.A., Santos, J.O.S., McNaughton, N.J., Wildner, W. **2011**. Zircon U-Pb geochronolgy from the Paraná bimodal volcanics province support a brief eruptive cycle at ~ 135 Ma. Chemical Geology, 1-2, 93-102.

.Poland, M.P., Fink, J.H., Tauxe, L. **2004**. Patterns of magma flow in segmented silicic dikes at Summer Coon volcano, Colorado—AMS and thin section analysis. Earth and Planetary Science Letters, 219(1), 155–169.

Polo, L.A., Janasi, V.A., Giordano, D., Cañón-Tapia, E., Lima, E.F., Roverato, M. **2017**. Effusive silicic volcanism in the Paraná Magmatic Province, South Brazil: evidence for locallyfed lava flows and domes from detailed field work. Journal of Volcanology and Geothermal Research (in press).

Polo, L.A. & Janasi V.A. **2014**. Volcanic stratigraphy of intermediate to acidic rocks in Southern Paraná Magmatic Province, Brazil. Geologia USP Série Científica, 14, 83-100.

Polo, L.A., Giordano, D., Janasi, V.A., Guimarães, L.F. **2017**. Effusive volcanism in the Paraná Magmatic Province, South Brazil: Physico-chemical conditions of storage and eruption and consideration on the rheological behavior during emplacement. Journal of Volcanology and Geothermal research (in press).

Prowatke, S., Klemme, S. **2006**. Trace element partitioning between apatite and silicate melts. Geochimica et Cosmochimica Acta, 70, 4513-4527.

Ragan, D. H. and M. F. Sheridan. **1972**. Compaction of the Bishop Tuff, California. Geological Society of America Bulletin, 83, 95-106.

Raposo, M.I.B., Ernesto, M., Renne, P.R. **1998**. Paleomagnetism and dating of the early Cretaceous Florianópolis dike swarm (Santa Catarina Island), Southern Brazil. Physics of the Earth Solid Interior, 108 (4), 275–290.

Raposo, M.I.B. **2011**. Magnetic fabric of the Brazilian dike swarms. A review. In: Petrovský, E., Herrero-Bervera, E., Harinarayana T., Ivers, D. (eds.) The Earth's Magnetic Interior. IAGA Special Sopron Book Series 1, 247–262.

Renne, P.R., Ernesto, M., Pacca, I.G., Coe, R.S., Glen, J., Prevot, M., Perrin, M. **1992**. The age of Parana flood volcanism, rifting of Gondwanaland, and the Jurassic-Cretaceous boundary. Science, 258, 975-979.

Riehle, J.R. **1973**. Calculated compaction profiles of rhyolitic ash-flow tuffs: computational model. Bulletin of Volcanology, 57, 319–336.

Rizzon, G.C. **2010**. Caracterização petrográfica e tecnológica dos riodacitos da raiz de um domo na região de Frei Caneca, São Marcos, RS. Monografia de conclusão de curso, Universidade Federal do Rio Grande do Sul.

Roisenberg, A. **1989**. Petrologia e geoquímica do vulcanismo ácido mesozoico da Província Meridional da Bacia do Paraná. PhD Thesis, Instituto de Geociências, Universidade Federal do Rio Grande do Sul, Porto Alegre.

Ross, P.-S., Peate, I.U., McClintock, M.K. et al. **2005**. Mafic volcaniclastic deposits in flood basalt provinces: A review. Journal of Volcanology and Geothermal Research, 145, 281-314.

Rossetti, L., Lima, E.F., Waichel, B.L. Hole, M.J., Simões, M.S., Scherer, C.M.S. **2017**. Lithostratigraphy and volcanology of the Serra Geral Group, Paraná-Etendeka Igneous Province in Southern Brazil:

Towards a formal stratigraphical framework. Journal of Volcanology and Geothermal Research (in press).

Rossetti L.M.M., Lima E.F., Waichel B.L., Scherer C.M.S., Barreto C.J. **2014**. Stratigraphical framework of basaltic lavas in Torres Syncline main valley, Southern Paraná-Etendeka Volcanic Province. Journal of South American Earth Sciences, 56, 409-421.

Sampson, D.E. **1987**. Textural heterogeneities and vent area structures in the 600 year old lavas of the Inyo volcanic chain, eastern California. Geological Society of America Special Paper, 212, 89-102.

Saunders, A.D., Fitton, J.G., Kerr, A.C., Norry, M.J., Kent, R.W. **1997**. The North Atlantic Igneous Province. In: Mahoney, J.J., Coffin, M.F. (Eds.), Large Igneous Provinces: Continental, Oceanic, and Planetary Flood Volcanism. Geophysical Monograph 100, 45–93.

Saunders, A.D. **2005**. Large Igneous Provinces: Origin and environmental consequences. Elements, 1, 259–297.

Scherer, C.M.S. **2000**. Eolian dunes of the Botucatu Formation (Cretaceous) in Southernmost Brazil: morphology and origin. Sedimentary Geology, 137, 63–84.

Scherer, C.M.S., Lavina, E.L.C. **2006**. Stratigraphic evolution of a fluvial-eolian succession: The example of the Upper Jurassic-Lower Cretaceous Guará and Botucatu formations, Paraná Basin, Southernmost Brazil. Gondwana Research, 9, 475-484.

Schmincke, H.U., Swanson, D.A. **1967**. Laminar viscous flowage structures in ash-flow tuffs from Gran Canaria, Canary islands. The Journal of Geology, 75, 641– 664.

Self, S., Thordarson, T., Keszthelyi, L. **1997**. Emplacement of continental flood basalt lava flows. In: Mahoney, J.J., Coffin, M.F. (eds.) Large Igneous Provinces. AGU Geophysical Monograph, 100, 381-410.

Selley, R.C. **1978**. Ancient sedimentary environments. London, Chapman & Hall.

Sheth, H. **2007**. Large Igneous Provinces (LIPs): definition, recommended terminology, and a hierarchical classification. Earth Science Reviews, 85, 117-124.

Sigmundsson, F., Hooper, A., Hreinsdóttir, S., Vogfjörd, K., Ófeigsson, B.G., et al. **2016**. Segmented lateral dyke in rifting event at Bardarbunda volcanic system, Iceland. Nature, 517, pages191–195.

Simões, M.S., Rossetti, L.M.M., Lima, E.F., Ribeiro, B.P. **2014**. The role of viscosity in the emplacement of high-temperature acidic flows of Serra Geral Formation in Torres Syncline (Rio Grande do Sul State, Brazil). Brazilian Journal of Geology, 44(4), 669-679.

Skinner, C. **1983**. Obsidian studies in Oregon. Dissertation. University fo Oregon.

Smith, J.V., Houston, E.C. **1994**. Folds produced by gravity spreading of a banded rhyolite lava flow. Journal of Volcanology and Geothermal Research, 63, 89-94.

Smith, R. L. **1960**. Zones and zonal variations in welded ash-flows, 149-59. US Geological Survey Professional Paper, 354.

Sparks, R. S. J. **1978**. The dynamics of bubble formation and growth in magmas: a review and analysis. Journal of Volcanology and Geothermal Research, 3, 1-37.

Sparks, R. S. J., Sigurdsson, H., Wilson, L. **1977**. Magma mixing: a mechanism for triggering acid explosive eruptions. Nature, 267, 315-8.

Sparks, R.S.J., Stasiuk, M.V., Gardeweg, M., Swanson, D.A. **1993**. Welded breccias in andesite lavas. Journal of the Geological Society (London), 150, 897– 902.

Sparks, R.S.J., Wright, J.V. **1979**. Welded air-fall tuffs. In: Chapin, C.E., Elston, W.E. (eds.) Ash-Flow Tuffs. Special Paper Geological Society of America, 180, 155–166.

Stewart, K., S.P. Turner, S. Kelley, C. Hawkesworth, L. Kirstein and M.S.M. Mantovani, **1996**. 3-D $^{40}Ar/^{39}Ar$ geochronology in the Paraná continental flood basalt province. Earth and Planetary Science Letters, 143, 95-109.

Stica, J.M., Zalán, P.V., Ferrari, A.L. **2014**. The evolution of rifting on the volcanic margin of the Pelotas Basin and the contextualization of the Paraná-Etendeka LIP in the separation of Gondwana in the South Atlantic. Marine and Petroleum Geology, 50, 1-21.

Sun, S.S., Hanson, G.N. **1975**. Origin of Ross Island Basanitoids and limitations upon the heterogeneity of mantle sources for alkali basalts and nephelinites. Contributions to Mineralogy and Petrology, 52, 77-106.

Thiede, D.S., Vasconcelos, P.M. **2010**. Parana flood basalts: rapid extrusion hypothesis confirmed by new $^{40}Ar/^{39}Ar$ results. Geology, 38 (8), 747–750.

Thorarinsson, S. **1981**. Jardeldasvædi á nútíma (Volcanic areas of the Holocene). In: Náttúra Íslands, Almenna bókafélagid, Reykjavík, 81–119.

Thorarinsson, S., Sæmundsson, K. **1979**. Volcanic activity in historical time. Jökull, 29, 29–32.

Thordarson, T., Larsen, G. **2007**. Volcanism in Iceland in historical time: Volcano types, eruption styles and eruptive history. Journal of Geodynamics, 43, 118-152.

Tuffen, H., Castro, J.M. **2009**. The emplacement of an obsidian dyke through thin ice: Hrafntinnuhryggur, Krafla Iceland. Journal of Volcanology and Geothermal Research, 185, 352–366

Tuffen, H., Dingwell, D.B., Pinkerton, H. **2003**. Repeated fracture and healing of silicic magma generate flow banding and earthquakes? Geology, 31, 1089–1092.

Tuffen, H., James, M. R., Castro, J. M., Schipper, C. I. **2013**. Exceptional mobility of an advancing rhyolitic obsidian flow at Cordón Caulle volcano in Chile. Nature Communnications, 4, 1-7.

Turner, S., Regelous,M., Kelley, S., Hawkesworth, C.,Mantovani,M. **1994**.Magmatism and continental break-up in the South Atlantic: high precision ^{40}Ar-^{39}Ar geochronology. Earth and Planetary Science Letters, 121, 333–348.

Umann L.V., Lima E.F., Sommer C.A., De Liz J.D. **2001**. Vulcanismo ácido da região de Cambará do Sul-RS: litoquímica e discussão sobre a origem dos depósitos. Revista Brasileira de Geociências, 31(3), 357-364.

Valente, S.d.C., Corval, A., Duarte, B.P., Ellam, R.M., Fallick, A.E., Meighan, I.G., Dutra, T. **2007**. Tectonic boundaries, crustal weakness zones and plume-subcontinental lithospheric mantle interactions in the Serra do Mar dyke swarm, SE Brazil. Revista Brasileira de Geociências, 37 (1), 194–201.

Waichel B.L., Lima E.F., Viana A.R., Scherer M.S., Bueno G.V., Dutra G.T. **2012**. Stratigraphy and volcanic facies architecture of the Torres Syncline, Southern Brazil, and its role in understanding the Paraná-Etendeka Continental Flood Basalt Province. Journal of Volcanology and Geothermal Research, 215, 74-82.

Waichel, B.L., Lima, E.F., Sommer, C.A., Lubachesky, R. **2007**. Peperite formed by lava flows over sediments: an example from the central Paraná Continental Flood Basalts, Brazil. Journal of Volcanology and Geothermal Research 159(4), 343-354.

Walker, G.P.L. **1973**. Lengths of lava flows. Philosophy Transactions of the Royal Society, 274, 107–118.

Watson, E.B., Green, T.H. **1981**. Apatite/liquid partition coefficients for rare earth elements and strontium. Earth and Planetary Science Letters, 56, 405-421.

White, J.D.L., Bryan, S.E., Ross, P.-S., Self, S., Thordarson, T. **2009**. Physical volcanology of continental large igneous provinces: update and review. In: Thordarson, T., Self, S., Larsen, G., Rowland, S.K., Hoskuldsson, A. (eds.), Studies in Volcanology: The Legacy of George Walker. Special Publications of IAVCEI, 2. Geological Society, London, 291–321.

Whittingham, A. M. **1989**. Geological features and geochemistry of the acid units of the Serra Geral Formation, south Brazil. In: Continental Magmatism, IAVCEI Abstracts: Santa Fé, New Mexico.

Wilson, C.J.N. **2008**. Supereruptions and supervolcanoes: Processes and products. Elements 4, 29–34.

Wilson, M. **1989**. Igneous Petrogenesis: A global tectonic approach. Ed. Dordrecht, Springer.

Wolff, J. A., Wright, J.V. **1981**. Rheomorphism of welded tuffs Journal of Volcanology and Geothermal Research, 10, 13-34.

Wolff, J.A., Sumner, J.M. **2000**. Lava fountains and their products. In: Sigurdson, H. (ed.) Encyclopedia of Volcanoes. Academic Press, 321– 329.

Xu, Y., Chung, S., Shao, H., He, B. **2010**. Silicic magmas from the Emeishan large igneous province, Southwest China: Petrogenesis and their link with the end-Guadalupian biological crisis. Lithos, 199, 47-60.

Zaions, M. **1989**. Mapa Morfológico. Porto Alegre, Secretaria da Agricultura e Abastecimento, 1:900.000.

Zalán, P.V., Conceição, J.C.J., Wolff, S., Astolfi, M.A.M., Vieira, I.S., et al. **1986**. Análise da Bacia do Paraná. Relatório Interno da Petrobrás. Depex/Cenpes 1035-5765, Rio de Janeiro.

Journal of Volcanology and Geothermal Research xxx (2017) xxx–xxx

Contents lists available at ScienceDirect

Journal of Volcanology and Geothermal Research

journal homepage: www.elsevier.com/locate/jvolgeores

Structures and lithofacies of inferred silicic conduits in the Paraná-Etendeka LIP, southernmost Brazil

M.S. Simões [a,b,*], E.F. Lima [a], C.A. Sommer [a], L.M.M. Rossetti [a,c]

[a] Instituto de Geociências, Universidade Federal do Rio Grande do Sul, Av. Bento Gonçalves, 9500, Prédio 43136, Caixa Postal 15001, Agronomia, CEP: 91501-970 Porto Alegre, RS, Brazil
[b] CPRM – Serviço Geológico do Brasil (Geological Survey of Brazil) – Manaus, Av. André Araújo, 2160, CEP 69060-000 AM, Brazil
[c] Department of Geology and Petroleum Geology, University of Aberdeen, Aberdeen AB24 3UE, UK

ARTICLE INFO

Article history:
Received 7 August 2016
Received in revised form 2 December 2017
Accepted 17 December 2017
Available online xxxx

Keywords:
Paraná-Etendeka LIP
Silicic conduit
Lava flows
Lithofacies

ABSTRACT

Extensive silicic units in the Paraná-Etendeka LIP have been long interpreted as pyroclastic density currents (rheomorphic ignimbrites) derived from the Messum Complex in Namibia. In recent literature, however, they have been characterized as effusive lava flows and domes. In this paper we describe structures and lithofacies related to postulated silicic lava feeder conduits at Mato Perso, São Marcos and Jaquirana-Cambará do Sul areas in southern Brazil. Inferred conduits are at least 15–25 m in width and the lithofacies include variably vesicular monomictic welded and non-welded breccias in the margins to poorly vesicular, banded, spherulitic and microfractured vitrophyres in the central parts. Flat-lying coherent vitrophyres and massive obsidian are considered to be the subaerial equivalents of the conduits. Large-scale, regional tectonic structures in southern Brazil include the NE-SW aligned Porto Alegre Suture, Leão and Açotea faults besides the Antas Lineament, a curved tectonic feature accompanying the bed of Antas river. South of the Antas Lineament smaller-scale, NW-SE lineaments limit the exposure areas of the inferred conduits. NE-SW and subordinate NW-SE structures within this smaller-scale lineaments are represented by the main postulated conduit outcrops and are parallel to the dominant sub-vertical banding in the widespread banded vitrophyre lithofacies. Upper lava flows display flat-lying foliation, pipe-like and spherical vesicles and have better developed microlites. Petrographic characteristics of the silicic vitrophyres indicate that crystal-poor magmas underwent distinct cooling paths for each inferred conduit area. The vitrophyre chemical composition is defined by the evolution of trachydacitic/dacitic vitrophyres with 62–65 wt% SiO_2 to rhyodacite and rhyolite with 66–68 wt% SiO_2. The more evolved rocks are assigned to the latest intrusive grey vitrophyre outcropping in the center of the conduits. Degassing pathways formed during fragmentation and fracturing episodes within the conduits may have helped to inhibit the explosivity of the eruptions. Based on the documented lithofacies architecture, we attribute the source of the silicic lava flows in the studied localities to tectonic-controlled, local conduits, rather than pyroclastic density currents from distant vent areas.

1. Introduction

Silicic conduits have been described for relatively dry (<1% of volatiles) obsidian flows (Fink, 1983), phreatic vents (Eichelberger et al., 1988), lava domes (Heiken et al., 1988; Stasiuk et al., 1996), eroded maar volcanoes (Sillitoe et al., 1984), polygenetic intermediate to silicic volcanoes (Goto et al., 2008) and caldera environments (Kurozumi and Doi, 2003). Well-exposed silicic dykes and conduits have also been documented in Iceland, where they feed both rhyolitic lava flows (Tuffen and Dingwell, 2005) and small-volume domes (Tuffen and Castro, 2009). In the Paraná-Etendeka Large Igneous Province (LIP), the transport of silicic magma is still a poorly known subject. Initial approaches as recognition of field features, spatial distribution of lithofacies and the observation of microscopic textures in silicic intrusive rocks – indispensable for the study of aphanitic or fine-grained volcanic and subvolcanic rocks – are still improving along the province.

LIPs are large-area and large-volume igneous sequences including Continental Flood Basalts (CFBs) and associated intrusive rocks, which occur in volcanic passive margins, oceanic plateaus, submarine chains, submarine mount groups and ocean basin basalts (Coffin and Eldholm, 1994). These deposits are the result of magmatic activities that are common in the geological record and are produced by similar processes (Cañón-Tapia, 2010) during a geologically brief period of time (1–5 Ma, Bryan and Ernst, 2008).

* Corresponding author at: CPRM – Serviço Geológico do Brasil (Geological Survey of Brazil) – Manaus, Av. André Araújo, 2160, CEP 69060-000 AM, Brazil.
E-mail address: matheus.simoes@ufrgs.br (M.S. Simões).

https://doi.org/10.1016/j.jvolgeores.2017.12.013
0377-0273/

The Paraná-Etendeka LIP occupies an area of 917,000 ± 15,000 km^2 (Frank et al., 2009) of which 90% is located in South America and 10% is in Africa, above the aeolian sedimentary rocks of Botucatu and Etjo formations. In South America the Paraná-Etendeka LIP comprises a 1700 m-thick association of tholeiitic magmas (Melfi et al., 1988), with basaltic to intermediate lavas, dykes and sills prevalent (97.5% of total volume) over silicic units (2.5%). The large-volume volcanism of the Paraná-Etendeka LIP has been described from whole-rock chemostratigraphy, supported by mineral chemistry, paleomagnetic data and isotopic studies (e.g. Bellieni et al., 1983, 1984, 1986; Peate et al., 1992; Peate, 1997; Garland et al., 1995; Nardy et al., 2008). Stratigraphic reconstruction, based on lithofacies architecture, recognized a sequence of ponded, compound, sheet and rubbly pahoehoe for the mafic units (Waichel et al., 2012; Barreto et al., 2014; Rossetti et al., 2014), which are covered by silicic volcanic rocks.

The silicic volcanics described in the South-American counterpart of Paraná-Etendeka LIP are classified, based on their SiO_2 and $Na_2O + K_2O$ contents (LeMaitre, 1989), as aphyric low-Ti dacites and rhyolites (Palmas magma-type) and porphyritic high-Ti trachytes (Chapecó magma-type; e.g. Peate et al., 1992). In the African counterpart, these rocks are classified as quartz latites (e.g. Milner et al., 1992). Apatite saturation and pyroxene-liquid geothermometry data indicate that silicic magma from Paraná-Etendeka LIP had very high pre- and syn-eruptive temperatures, in the order of 1000–1100 °C, giving abnormally low viscosities for rhyodacite-rhyolite magmatic systems (e.g. Milner et al., 1992; Bellieni et al., 1984; Bellieni et al., 1986; Garland et al., 1995; Kirstein et al., 2001; Janasi et al., 2007; Simões et al., 2014; Polo et al., this issue).

These silicic volcanics were first described as volatile-poor and high-temperature rheomorphic ignimbrites. Arguments used include their laterally persistent sheet-like nature and the absence of typical ignimbrite textures even near the top and base of each unit, which was attributed to obliteration by intense welding (Bellieni et al., 1986; Melfi et al., 1988; Petrini et al., 1989; Roisenberg, 1989; Garland et al., 1995; Milner et al., 1995; Bryan et al., 2010). Milner et al. (1995) proposed the

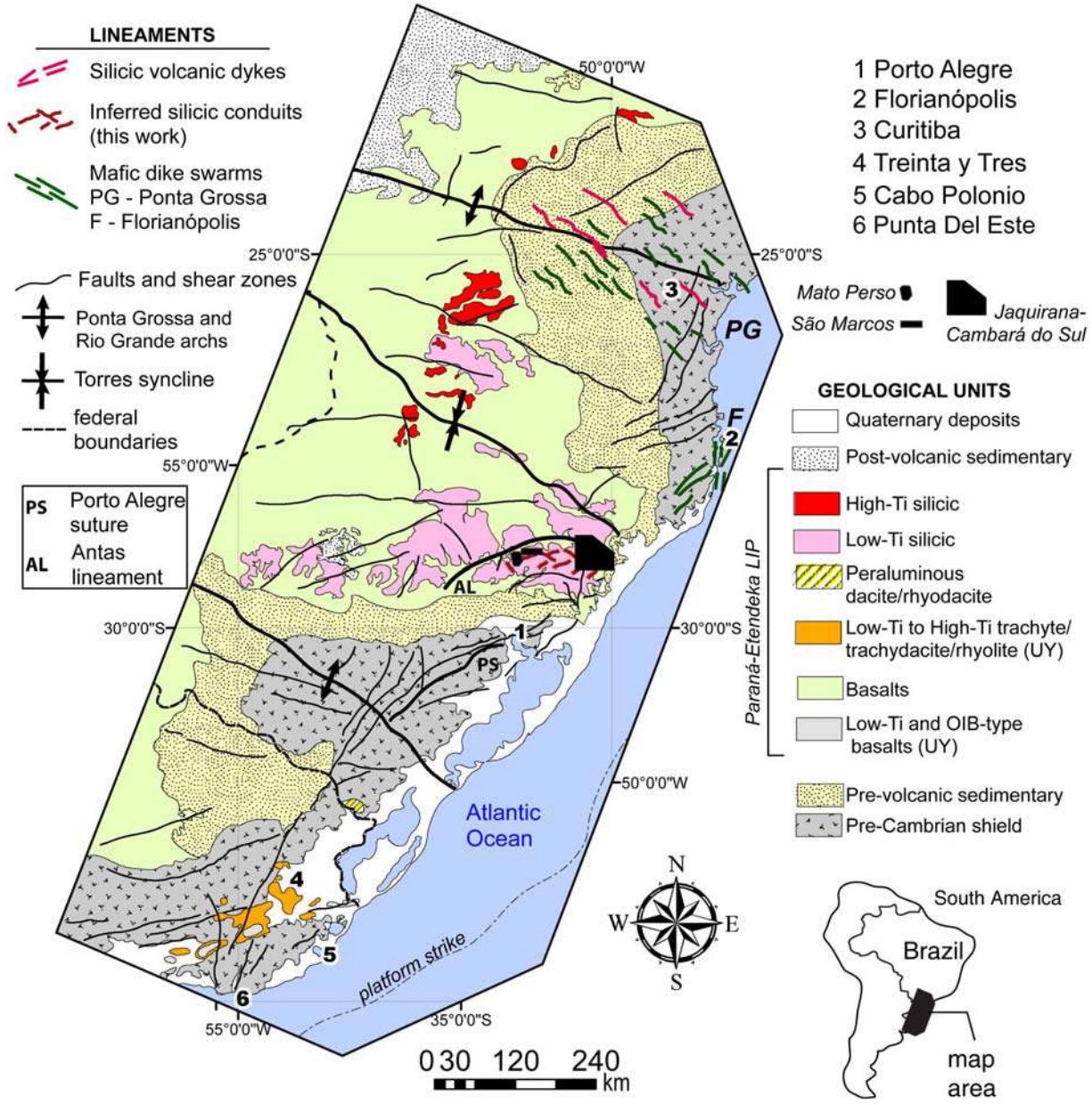

Fig. 1. Distribution of Paraná-Etendeka LIP volcanic units in southeastern Brazil. The geological nomenclature and structure compilation map is based in Fernandes et al. (1995), Kirstein et al. (2000), Nardy et al. (2008), Florisbal et al. (2014). Individual study areas (Mato Perso, São Marcos and Jaquirana-Cambará do Sul) are indicated with black polygons and detailed in Fig. 2. The Antas lineament, proposed in this study, is a NE-trending curved structure accompanying the Antas river bed.

Please cite this article as: Simões, M.S., et al., Structures and lithofacies of inferred silicic conduits in the Paraná-Etendeka LIP, southernmost Brazil, J. Volcanol. Geotherm. Res. (2017), https://doi.org/10.1016/j.jvolgeores.2017.12.013

correlation of some subgroups of Palmas magma-type with the Namibian quartz latites. The intrusive, circular Messum Complex, was identified as a potential emission center (Milner and Duncan, 1987; Milner et al., 1992; Ewart et al., 1998; Ewart et al., 2002), even though the thickness of the silicic volcanic sequence is inferior in the African counterpart. In this models, the silicic deposits in South America would need to have traveled >300 km from their source and been deposited as extensive pyroclastic density currents (e.g. Milner et al., 1995; Bryan et al., 2010).

The paucity of pyroclastic lithofacies, with recognition of only local pyroclastic textures in extensive petrographic studies (Comin-Chiaramonti et al., 1988), together with the regional description of coherent and autoclastic lithofacies in a variety of lava bodies (lobes, domes and flows) led other authors to suggest that the silicic deposits are predominantly effusive (Henry and Wolff, 1992; Umann et al., 2001; Lima et al., 2012; Polo and Janasi, 2014; Simões et al., 2014; Guimarães et al., this issue; Polo et al., this issue). Silicic lava feeder conduits were described showing compound magmatic foliation revealed by bands of contrasting crystallinity and oxidation (Lima et al., 2012, 2018).

In this study we propose that silicic feeder conduits are widespread within the Paraná-Etendeka LIP in the northeastern portion of the Rio Grande do Sul state. Evidence presented includes geometrical relations with regional-scale structures, detailed investigation of field relationships through lithofacies description, structural analysis and petrographic characterization, together with reconnaissance of whole-rock geochemical data.

1.1. Geological setting, stratigraphy and structural framework

In South America, the Ordovician to Cretaceous deposits of the Paraná Basin are divided in six super-sequences: Rio Ivaí, Paraná, Gondwana I, Gondwana II, Gondwana III and Bauru (Milani et al., 2007). The Gondwana III Super-sequence consists of Cretaceous aeolian sedimentary rocks of the Botucatu Formation and the volcanic rocks of the Serra Geral Group (SGG), which correlate with the Etjo Formation and the Etendeka Volcanics, respectively, in Africa (Jerram et al., 1999).

Waichel et al. (2012) and Rossetti et al. (this issue) described the facies architecture of SGG in the Torres Syncline, a large NW-SE tectonic valley located between the Ponta Grossa and the Rio Grande archs, identifying distinct volcanic episodes. The more chemically primitive lavas are dominated by simple pahoehoe basaltic flows in the base, and are assigned to the Torres Formation. Vertically stacked sheet-like rubbly pahoehoe basaltic flows of the Vale do Sol Formation cover the compound flows and represent the more voluminous basaltic lava unit. The silicic volcanics overlying these basalt flows are included in the Palmas Formation. The last volcanic manifestations in the area are the compound and simple oxidized mafic flows of the Esmeralda Formation.

In the study area, also exposed along the Torres Syncline, the structural framework is characterized by Neoproterozoic basement structures (trending 295–315° and 30–70°) and younger E-W structures related to the separation of Gondwana in the Phanerozoic (Fig. 1). The large-scale NE-trending structures within the basin are the Leão and Açotea faults (Zalán et al., 1991) in addition to the Antas Lineament (present work), a curved tectonic structure accompanying the Antas River bed. North of the Antas Lineament the silicic volcanic units tend to occur at lower elevations (290–330 m above sea level) than to the south of the lineament (530–860 m). The basement structures are transcurrent sinistral shear zones (Passo dos Marinheiros and Dorsal de Canguçú shear zones) besides the Porto Alegre Suture, a large magnetic alignment trending 30–70° (Fig. 1; e.g. Fernandes et al., 1995).

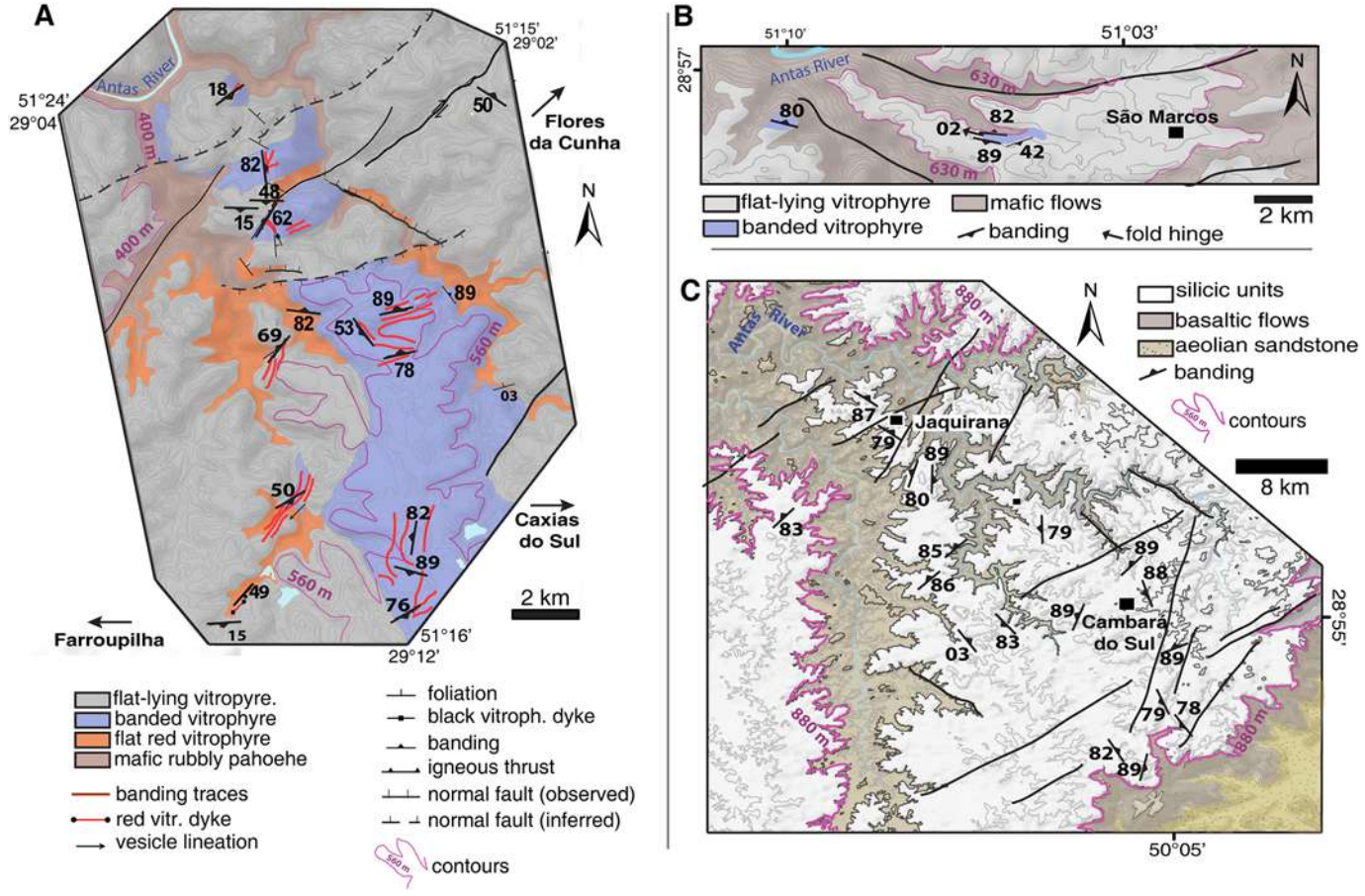

Fig. 2. Geological map of the studied areas. (A) Mato Perso. (B) São Marcos. (C) Jaquirana-Cambará do Sul. Banded vitrophyre units in A and B are a simplification of the conduit outcrops, which involve the occurrence of another lithofacies as breccias and other types of vitrophyre.

Please cite this article as: Simões, M.S., et al., Structures and lithofacies of inferred silicic conduits in the Paraná-Etendeka LIP, southernmost Brazil, J. Volcanol. Geotherm. Res. (2017), https://doi.org/10.1016/j.jvolgeores.2017.12.013

2. Field and petrographic features of inferred conduits and subaerial-related lavas

The present study was carried out in three areas located south of the Antas River (Fig. 1), northeastern portion of Rio Grande do Sul State: Mato Perso (a district of Flores da Cunha city), São Marcos, Jaquirana and Cambará do Sul (Fig. 2). In each location we describe lithofacies, structures and petrographic features. Lithofacies descriptions and their use in this paper are based on the definitions of Cas and Wright (1988) and Miall (2000), in which facies have unique and definitive characters related to their compositional, textural and structural features, and lithofacies are their descriptive and non-interpretative features (Miall, 2000). The hierarchy of the nomenclature used is based on features as color (red, grey), texture (coherent, massive), structure (microfractured, banded), vesicularity (vesicular, poorly-vesicular) written in lower case and are followed by upper case letters with the lithology description (vitrophyre, obsidian, breccia). Obsidian is distinguished from vitrophyres from its vitreous aspect and black color. In Table 1, lithofacies code, name, spatial distribution and description are synthetized.

2.1. Mato Perso area

The proposed Mato Perso area (MP) outcrops occur at high elevations in Farroupilha, Flores da Cunha and Caxias do Sul cities, being overlain by flat-lying vitrophyres. The highlands (>650 m) of Farroupilha and Caxias do Sul expose the silicic conduits that are downthrown to ~400–550 m elevations by NE-trending normal faults through the Antas river, where flat-lying vitrophyres are again in direct contact with basaltic pahoehoe flows (Fig. 2A). The inferred conduits were not observed cross-cutting the mafic units, and only faulted contacts were verified in the field or inferred by stratigraphic relations.

The lithologies of MP comprise four distinct types of vitrophyre: red, vesicular (rvV); red, poorly-vesicular (rpV); grey, poorly-vesicular (gpV), and banded (bV). These are associated with monomictic breccia lithofacies (mB) and flat-lying coherent vitrophyres (fcV). Intact rvV and rpV lithofacies occur either as individual outcrops with up to 25 m of lateral extent exhibiting at least 4 m thick flat-lying lava flows or as tabular dykes with 0.5–1.5 m in width (Simões et al., in press). They also occur as clasts that range from metric to centimetric in scale, are either sub-rounded or elongate with irregular edges, and contain vesicles 2–5 mm in length. Vesicle contents vary from <1% in rpV to 50–60% in rvV. rpV also locally displays folding structures, with several discrete hues of red lava, and is locally boudinaged between gpV layers in pinch-and-swell structures. The gpV lithofacies is a grey microporphyritic poorly vesicular vitrophyre that cross-cuts rvV, containing its centimeter-scale fragments.

Banded bV outcrops as 2–15 m in width inclined exposures (Fig. 3A, B) being found in the valleys or in the highlands of the mapped area (Fig. 2A) and is constituted by vitrophyres with dominant subvertical (>60°), thick (7–10 cm) banding (Fig. 3C) that grades laterally into thin (0.2–2 cm) flat-lying (<40°) banding and is marked by intercalation of

Table 1
The lithofacies code, name, description and spatial distribution of silicic units and lithofacies types.

Code	Lithofacies	Spatial distribution	Appearance
rvV	Red vesicular vitrophyre	5–100 cm sized fragments embedded by rpV and bV	cm-scale sub-rounded to stretched aphanitic oxidized vitrophyre fragments with irregular edges
rpV	Red poorly-vesicular vitrophyre	2–5 m expositions where bV grades to rpV. rpV than grades laterally to mB	Red to orange microporphyritic oxidized poorly vesiculated vitrophyre which occurs
gpV	Grey poorly-vesicular vitrophyre	1–3 m thick dykes cross-cutting bV and rpV	Grey microporphyritic poorly vesiculated vitrophyre containing rpV and rvV cm-scale fragments
bV	Banded vitrophyre	15–30 m long expositions. Grades laterally to rpV, sV and mV	Intercalation of 2- to 7-cm thick oxidized red colored bands and grey colored bands
wB	Welded breccias	Welded breccias occur as 0.2–1 m thick steeply inclined layers within bV	mm- to cm-scale stretched vesiculated oxidized fragments, sometimes with undeformed shards
mB	Monomitic breccia	1–2 m thick breccia layers	–mm to –cm scale angular vesiculated oxidized red to brown fragments with sharp edges in seriate arrangement cemented by calcite and silica
fcV	Flay-lying coherent vitrophyre	~5–20 m thick flat-lying units with at least 10 km^2 area	Coherent microporphyritic vitrophyres sparsely vesiculated
sV	Spherulitic vitrophyre	2–3 m thick layers grading laterally to bV	Light-grey vitrophyres composed of equigranular spherulites with 0.5 cm to 1 cm in size
mO	Massive obsidian	~10–20 m thick obsidian units	Aphanitic, dark grey to black obsidian with oxidized layers
mV	Microfractured vitrophyre	2–10 m thick units laterally grading or in fault contacts with bVs	Light grey vitrophyre with apparent flat-lying banding

Code	Structures	Vesicles	Microtexture
rvV	Oriented stretched vesicles.	mm–cm-scale, rounded or stretched	Vesiculated, hematite-rich, microporphyritic, with well to poorly developed microlites
rpV	Steeply-inclined mm-scale banding, folds and mixing textures with gpV, boudinaged between gpV layers.	2–5 mm, stretched to rounded	Hematite-rich microporphyritic vitrophyres with well to poorly developed microlites
gpV	Steeply-inclined mm-scale banding.	mm-scale, stretched	Microporphyritic vitrophyre with poorly-developed microlites within glassy matrix
bV	Steeply-inclined to flay lying cm- to mm-scale banding.	mm–cm-scale, stretched	Microporphyritic vitrophyres with poorly-developed microlites within a devitrified matrix
wB	Orientation of stretched fragments.	mm-scale stretched	Low- to medium-grade welding of vitreous fragments sometimes preserving bubble shapes
mB	Randomly oriented angular clasts.	Stretched within the fragments	Angular fragments cemented by quartz with tridymite inclusions
fcV	10–20 cm flat-lying tabular foliation.	Pipe-like in the base, spheroidal towards the top	Microporphyritic vitrophyre with well-developed microlites and glassy groundmass
sV	mm-scale inclined banding (locally).	mm-scale rounded	Massive spherulitic
mO	cm-scale banding (locally).	mm-scale rounded and cm-scale ellipsoidal in the top	Massive microporphyritic with glassy groundmass
mV	mm- to cm-scale flat-lying apparent banding marked by dark-grey alteration halos.	mm-scale rounded to stretched	5–10 mm spaced microfractures filled with quartz, microporphyritic texture

Please cite this article as: Simões, M.S., et al., Structures and lithofacies of inferred silicic conduits in the Paraná-Etendeka LIP, southernmost Brazil, J. Volcanol. Geotherm. Res. (2017), https://doi.org/10.1016/j.jvolgeores.2017.12.013

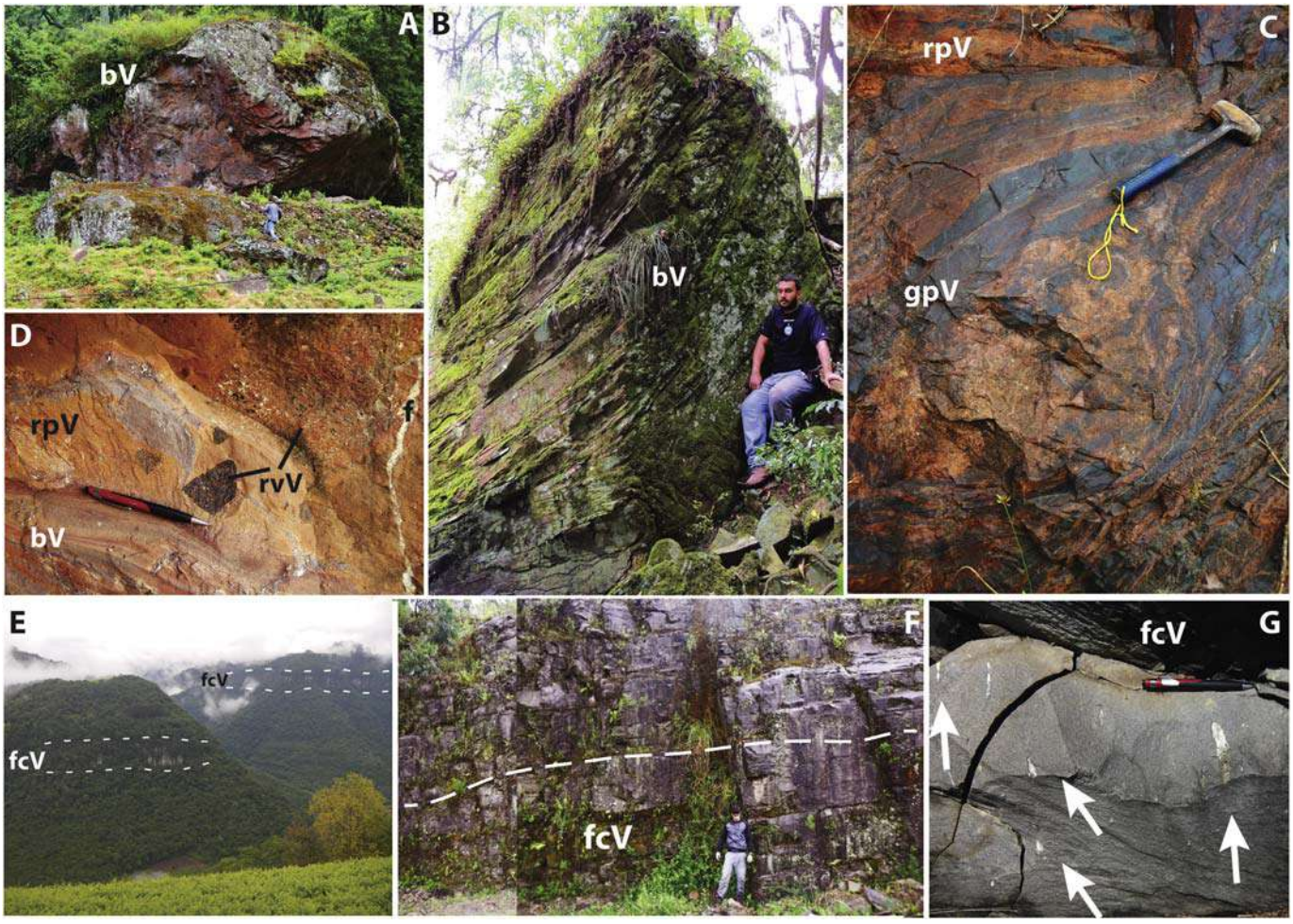

Fig. 3. Field macroscopic features of Mato Perso area lithologies. (A) Inclined tabular dike-like outcrop composed of banded vitrophyres (bV) in the elevation of 550 m. The geometry is parallel to the dominant banding (dipping 58° to NNE). The country rock bed was eroded. (B) Steeply inclined outcrop of bV displaying sub-vertical banding dipping 50° to 85° to SE. (C) Banded vitrophyre showing 5–20 cm thick bands composed poorly-vesicular grey (gpV) and red (rpV) vitrophyres. (D) Fragments of red vesicular vitrophyre lithofacies (rvV) into the red poorly-vesicular vitrophyre lithofacies (rpV) grading to banded vitrophyres (bV). Note the vertical extensional fracture (f) filled with quartz. (E) 20–30 m flat-lying vitrophyre lava flows highlighted by flat zones absent of vegetation. (F) Horizontal tabular foliation marked by cm-spaced fractures in the vitrophyre. (G) Centimeter-size pipe-like vesicles near the base of a flat-lying vitrophyre (lava flow). (For interpretation of the references to color in this figure legend, the reader is referred to the web version of this article.)

oxidized red colored bands and grey colored bands. This banding is folded in two major types of folds: (i) 0.2- to 1 m-wavelength open to close folds plunging upright with hinge gently plunging to NE and (ii) mm- to cm-scale wavelength disharmonic, polyclinal folds that are asymmetric to symmetric and horizontal to reclined, with axial surface parallel to the banding. Banding in rpV generally dissipates within 5–10 m of outcrop margins, where instead cm-size rvV fragments are observed, together with a high density of quartz-filled extensional fractures (Fig. 3D). The outcrop of monomictic breccia lithofacies (mB) at conduit margins occurs parallel to banding in the conduit center, and is composed of angular, mm- to cm-scale vesicular fragments of oxidized red to brown glassy lava, with sharp edges in seriate arrangement cemented by calcite and silica. Flat-lying coherent vitrophyres (Fcv) are ~5–20 m thick flat units (Fig. 3E) with inferred areas of at least 10 km^2 based on the extent of exposures. They show flat-lying tabular foliation (Fig. 3F), pipe-like vesicles close to their bases (Fig. 3G), and spheroidal vesicles towards the top of flow units. Basal breccia is locally present (Simões et al., in press), and these units are interpreted as subaerial lava flows, also on the basis of their sheet-like nature and greater vesicularity towards flow tops. Flow thickness is less than that of most documented rhyolitic flows (~35–40 m, e.g. Fink, 1983; Tuffen et al., 2013), potentially due to the higher eruptive temperature.

The main petrographic feature found throughout MP vitrophyres is their microporphyritic texture, with 2–11 vol% of plagioclase, pyroxene and Ti-magnetite microphenocrysts occurring in respective proportions of 6:3:1. The same mineral assemblage is present in the groundmass as microlites, with respective proportions of 4:2:4, together with minor apatite ± quartz.

The banded bV lithofacies displays mm-scale folded red to grey bands. Phenocrysts in red and grey bands are: (i) plagioclase, with weak banding-parallel preferred orientation; (ii) clinopyroxene, with stronger banding-parallel preferred orientation, and alteration to clay minerals (Fig. 4A); (iii) globular to rhombohedral Ti-magnetite in crescent-shaped aggregates (Fig. 4B) and (iv) globular quartz. The red groundmass shows alternating mm- to sub-mm-scale bands of darker and paler material (Fig. 4C). It contains acicular plagioclase and globular pyroxene microlites (<0.1 mm) scattered in a vitric oxidized groundmass with very fine hematite lamellae. In the grey bands the groundmass is uniform, with hematite contents increasing towards the red bands. The microlites of plagioclase, clinopyroxene, apatite and Ti-magnetite are scattered in a quartz-rich groundmass displaying quartz amoeboid crystals and a minor content of fine hematite. Grains of mono- to polycrystalline quartz with concentric zoning are common in banding-parallel quartz rich zones (Fig. 4D). In the bV lithofacies the banding is characterized by abrupt to gradational contacts between

Please cite this article as: Simões, M.S., et al., Structures and lithofacies of inferred silicic conduits in the Paraná-Etendeka LIP, southernmost Brazil, J. Volcanol. Geotherm. Res. (2017), https://doi.org/10.1016/j.jvolgeores.2017.12.013

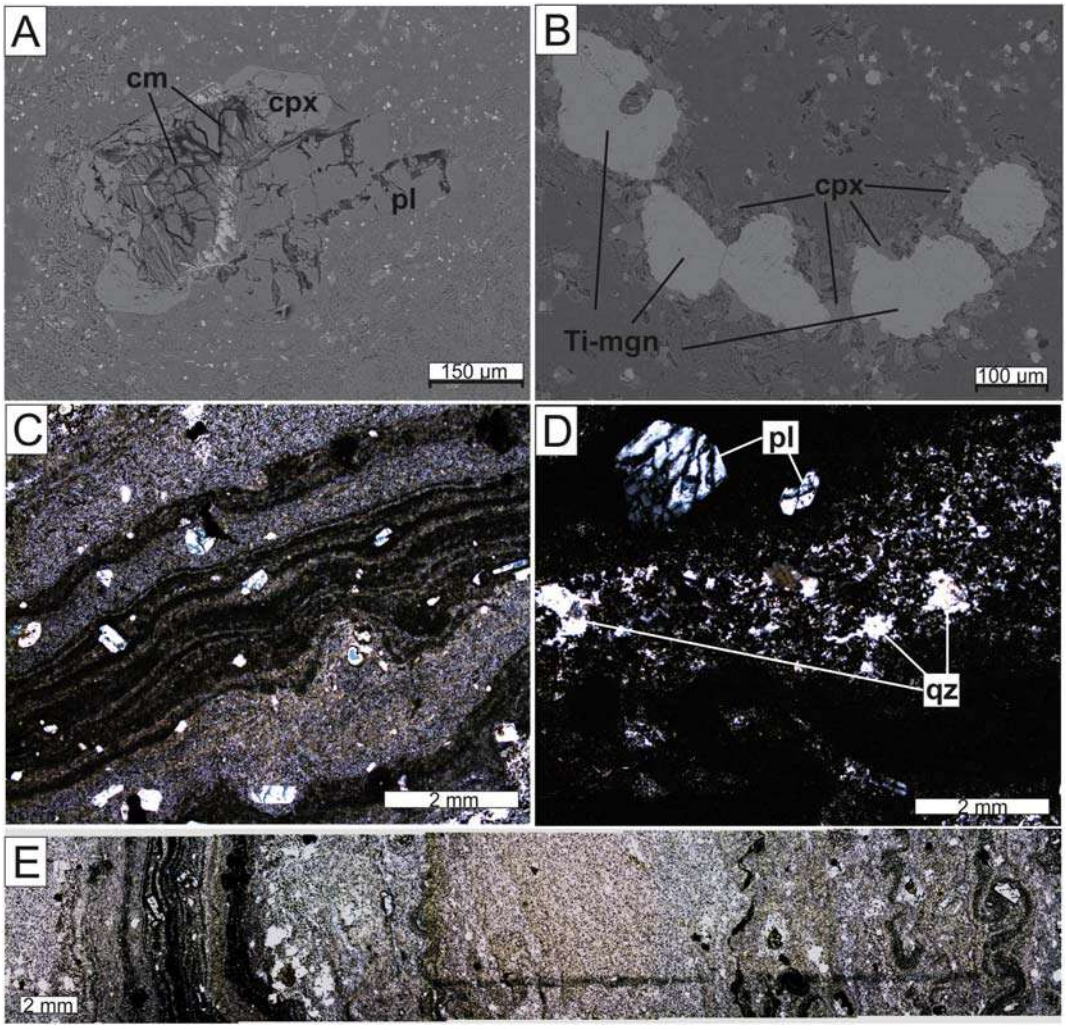

Fig. 4. Microscopic features of Mato Perso area vitrophyres – A–B are back-scattered electron images, C–E are transmitted light microscope images. (A) Clinopyroxene (cpx) and plagioclase (pl) microphenocrysts. Clinopyroxene is altered to clay minerals (cm) in the center of the crystals. (B) Ti-magnetite (Ti-mgn) microphenocrysts in crescent-shaped texture surrounded by clinopyroxene microlites and cristalites. (C) Compound banding of banded vitrophyre (bV) with microporphyritic texture (plane-polarized light). (D) Band-parallel zone enriched in polycrystalline quartz (qz) (crossed polarizers). (E) Panoramic photomicrography of bV with ptygmatic and polyclinal folds (plane-polarized light).

pale and dark bands, and forms polyclinal, ptygmatic and buckled folds (Fig. 4E).

2.2. São Marcos area

The São Marcos area outcrops are geomorphological highs between two WNW-oriented valleys south of Antas River (Fig. 2B). An intrusive contact of the conduits is not observed, and transition between the silicic lava flows and underlying rubbly basaltic pahoehoe flows (at 630 m elevation) is flat-lying, abrupt and irregular (Fig. 5A, B; Fig. 6A). The rubbly pahoehoe flow top is at least 1.5 m thick and comprises cm-scale vesicular blocks suspended within a zeolitized, sand-grade matrix (Fig. 6B). However, there is no continuous layer of sandstone observed between the rubbly basalt and overlying silicic unit. In the base of the silicic unit dense fracturing creates monomictic breccia textures, like the ones described by Smith (1996). Towards the top of the unit, the lava develops a cm-scale near-horizontal foliation with isoclinal folds and WNW-trending intersection lineation between the foliation planes. The dip of banding markedly increases from this exposure to the postulated conduit outcrop (Fig. 5B).

The main part of the inferred conduit outcrops at 670 m elevation, ~40 m above the flat-lying contact of the underlying silicic flows with the basalts, but ~25 m below a fcV silicic lava unit (Fig. 5B). The conduit exposure zone is <500 m in width, as demonstrated in the distribution of the banded vitrophyre unit in Fig. 2B and is oriented according to a WNW-ESE, near E-W structure. Besides, individual conduit outcrops do not exceed 50 m in width. It consists of the full variety of vitrophyre lithofacies, associated with monomictic breccias (mB) and welded breccias (wB).

The field relationships are indicative of gpV cross-cutting and mixing with rpV to form bV (Figs. 5C, 6C, D, E). Red vesicular vitrophyres occur as xenoliths within rpV and gpV (Fig. 6C). Monomictic breccias occur in the contacts between red vesicular vitrophyres and rpV, gpV or bV (Fig. 6D). Zones of steeply-oriented poorly-sorted welded breccias 20–50 cm in width occur parallel to the bV orientation (Fig. 6E) and are composed of vesicular, mostly elongate, oxidized fragments with irregular shapes, containing stretched vesicles (Fig. 6F). All lithofacies are cross-cut by extensional fractures, with mm- to cm-scale aperture, filled with diaphanous quartz (Fig. 6C) that is banding-parallel to oblique and locally form monomictic breccias with highly angular fragments. A distinctive feature in the postulated conduit is a meter-scale structure with steeply inclined divergent banding (Fig. 5C) composed of banded vitrophyre lithofacies with rotated rvV meter-scale fragments. A brecciated red vesicular vitrophyre occurs at 711 m elevation, with quartz vein fill, and a massive, grey, vesicular vitrophyre (fcV) >2 m thick exposure crops out at 715 m elevation (Fig. 5D).

Please cite this article as: Simões, M.S., et al., Structures and lithofacies of inferred silicic conduits in the Paraná-Etendeka LIP, southernmost Brazil, J. Volcanol. Geotherm. Res. (2017), https://doi.org/10.1016/j.jvolgeores.2017.12.013

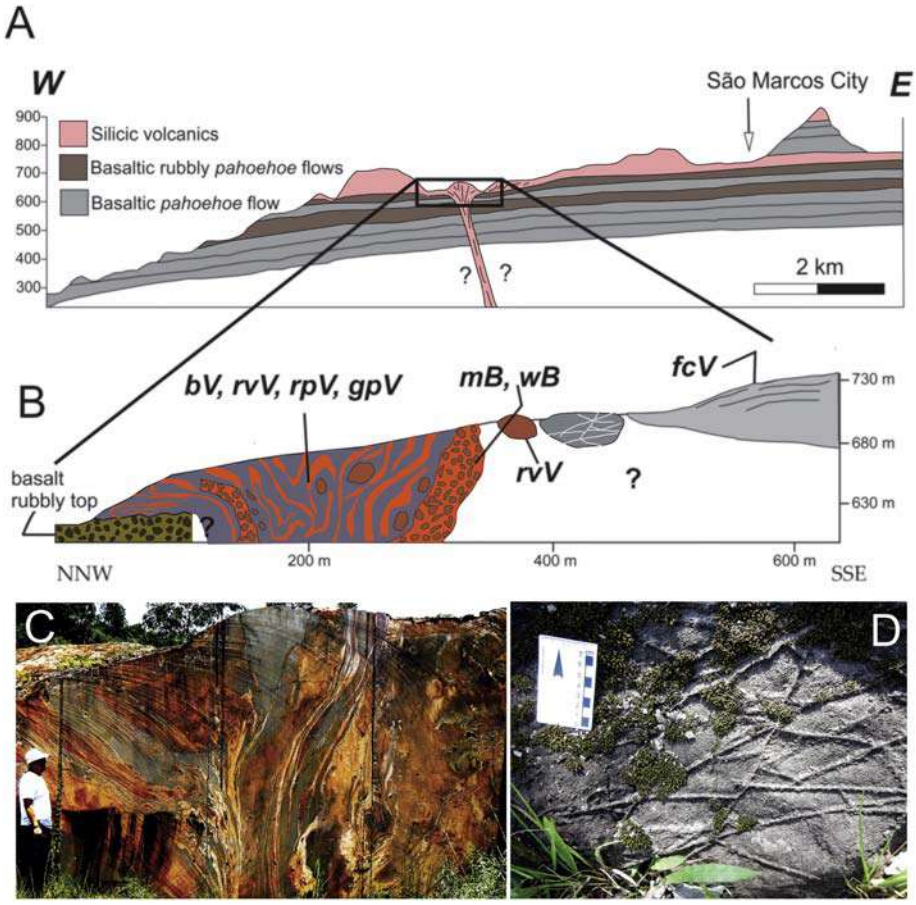

Fig. 5. Stratigraphic-structural sketches and field features of São Marcos area. (A) Regional stratigraphy of volcanic units in São Marcos area (modified from Lima et al., 2012). (B) Geological profile of São Marcos area showing field relationships and contact with lower mafic flows. Brown breccias are the top of a rubbly pahoehoe flow. Banded vitrophyre, red fragments and red breccias are part of the conduit. (C) Steeply inclined divergent structure in the banded vitrophyres. Note gpV is mixed with rpV and cross-cuts older rvV. (E) Quartz-filled fractures in coherent vitrophyre. (For interpretation of the references to color in this figure legend, the reader is referred to the web version of this article.)

Microscopically, the banded vitrophyre contains cm-scale bands with different grey and red colors. Sparse plagioclase, opaque and clinopyroxene microphenocrysts are present, with locally trachytic texture. The groundmass in red bands has plagioclase microlites in a glassy oxidized matrix, whereas the glassy matrix of the grey bands is devitrified but not oxidized (Fig. 7A, B). The contact between the bands is abrupt (Fig. 7B) to gradational and contacts between variably oxidized material are intercepted by elongated veins filled by epitaxial to diaphanous quartz.

The flat-lying massive grey vitrophyre is microporphyritic with swallow-tail plagioclase, skeletal forms and empty crystals (Fig. 7C), clinopyroxene and Fe-Ti oxides. The groundmass contains plagioclase, Fe-Ti oxide and clinopyroxene microlites immersed in a vitreous matrix. Other expositions of flat-lying vitrophyres in the area also display glomeroporphyritic textures with plagioclase, oxide and clinopyroxene crystals engulfed in a microlite-rich groundmass (Fig. 7D).

2.3. Jaquirana-Cambará area

The Jaquirana-Cambará area outcrops in the extreme northeastern of the Rio Grande do Sul state. Even though individual lithofacies have not been mapped in Fig. 2C, there is a semi-continuous outcrop extent of the lithofacies described below. The contact where silicic lavas overlie rubbly pahoehoe mafic flows occurs between 860 and 890 m elevations (Fig. 2C). Above these elevations there are ~10–40 m-thick stacked obsidian flows with elongated geometries, some recognized exhibiting 150 m in width and at least 500 m in length. Stratigraphically between obsidian flows there are 15–30 m in width outcrops displaying microfractured vitrophyre (mV) and spherulitic vitrophyre (sV), together with mB, wB, and bV. The nature of the outcrops is similar to those found in Mato Perso, with banded vitrophyre grading laterally into breccias.

The bV is characterized by NNW-, NW- and NE-trends of grey and red colored cm-scale bands with subvertical dip orientation in 1–2 m zones that are contorted into plunging upright folds over wavelengths of centimeters to 1.5 m (Fig. 8A, B). The mixing degree between grey and red bands increases towards the boarders of outcrops and generates mm-scale bands with a wide spectrum of red and grey colors and more complex folding patterns (Fig. 8C). The occurrence of rvV and rpV between gpV layers is common as well as the lateral gradation to a ≥1–2 m dominantly steep, only locally flat, thick autobrecciated zone, containing mB and wB with angular non-welded to incipiently welded vitrophyre clasts (Fig. 8D). Vesicles are elongated parallel to the banding or to the axial surfaces of cm-scale folds (Fig. 8E). A vertical variation observed in road profiles indicate intrusive and faulted contacts with massive obsidian lithofacies (mO). The mO is aphanitic, dark grey to black in color (Fig. 8F) with bimodal distribution of vesicles and amygdales (0.5–1 cm round vesicles and ~7 cm oblate amygdales). Towards the top of the flow, the obsidian turn to an altered material with only amygdales preserved. The upper part of obsidian flows exhibit an autobreccia, containing centimetric angular vesicular clasts with irregular edges (Fig. 11C). The mO is overlain by microfractured vitrophyres and is cross-cut by the bV. The microfractured vitrophyre lithofacies (mV) have near-horizontal apparent banding characterized by cm-scale irregular,

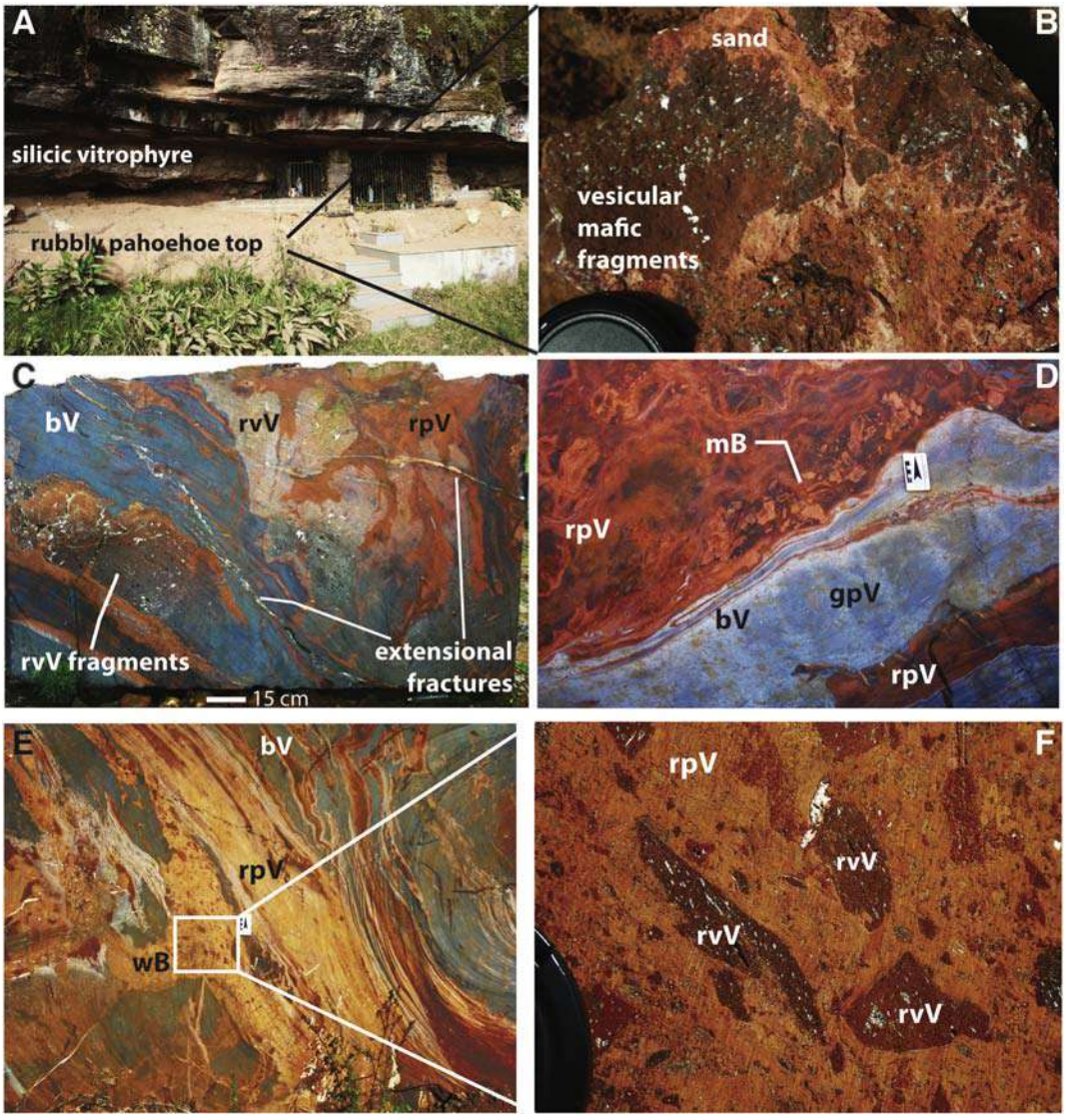

Fig. 6. Field features of the São Marcos area. (A) Contact between rubbly pahoehoe mafic flow and silicic vitrophyre with flat-lying banding. (B) Detail in the rubbly top of the basaltic flow with angular vesicular fragments cemented by sand. (C) 50–80 cm rvV fragments immersed in the banded vitrophyres. (D) gpV and rpV layers generating bV and showing monomictic breccia in the margin of the rpV layer. (E) bV and rpV vitrophyres with 15–30 cm banding-parallel breccia with stretched vesicular fragments. (F) Detail on the angular stretched vesicular fragments.

discontinuous dark-grey alteration halos in a light-grey vitrophyre (Fig. 8G). Alteration halos appear to originate from predominantly horizontal microfracture networks.

Spherulitic vitrophyre lithofacies (sV) occur in some outcrops, with light-grey vitrophyres containing equigranular 0.5–1 cm spherulites (Fig. 8H). Contacts between bV and mV lithofacies occur either as faults or as a gradual reduction in banding as bV gives way to a single unit of massive, grey vitrophyre.

In microscopic scale, the bV lithofacies show < 1% of microphenocrysts and is characterized by centimeter to millimeter-size banding with tight re-folded asymmetrical "Z" to "S" shape folds. Oxidized red bands and grey bands are microporphyritic with sparse plagioclase, opaque and clinopyroxene crystals. The contact with less oxidized grey bands is abrupt (forming hematite-rich irregular surfaces) or gradational (forming diffuse contact surfaces Fig. 9A). Banding-parallel quartz-filled fractures (aperture ~ 0.1 mm) commonly occur, including series of tension gashes (Fig. 9B).

mB autobreccias laterally associated to bV and rvV at postulated conduit outcrops display mm-sized angular fragments of non-vesicular oxidized vitrophyre (Fig. 9C) containing plagioclase microlites. These non-welded breccias are highly porous, and show some of the pore space filled by polycrystalline quartz/tridymite. Differently, wB breccias contain stretched oxidized vitrophyre clasts, perlitically fractured oxidized vitrophyre clasts, and pumiceous fragments. Pumiceous fragments display variable welding, viscous strain as defined by elongated clasts, and truncated vesicles (Fig. 9D), indicating mixed brittle-ductile deformation.

The mV lithofacies show sparse microphenocrysts of plagioclase, clinopyroxene, Fe-Ti oxide and apatite microlites in the groundmass. The glassy fraction of the groundmass is oxidized with perlitic fractures and contains spherulitic to amoeboid cryptocrystalline quartz. The apparent banding is formed by oxidation intensity variation in fracture-related halos (Fig. 9E).

The sV lithofacies is composed of isotropic microporphyritic vitrophyres with resorbed plagioclase, opaques with melt inclusions and scant clinopyroxene. The groundmass contains plagioclase, clinopyroxene, opaque and apatite microlites and crystallites. Spherulites are 2–5 mm across and globular to slightly elliptic in

Please cite this article as: Simões, M.S., et al., Structures and lithofacies of inferred silicic conduits in the Paraná-Etendeka LIP, southernmost Brazil, J. Volcanol. Geotherm. Res. (2017), https://doi.org/10.1016/j.jvolgeores.2017.12.013

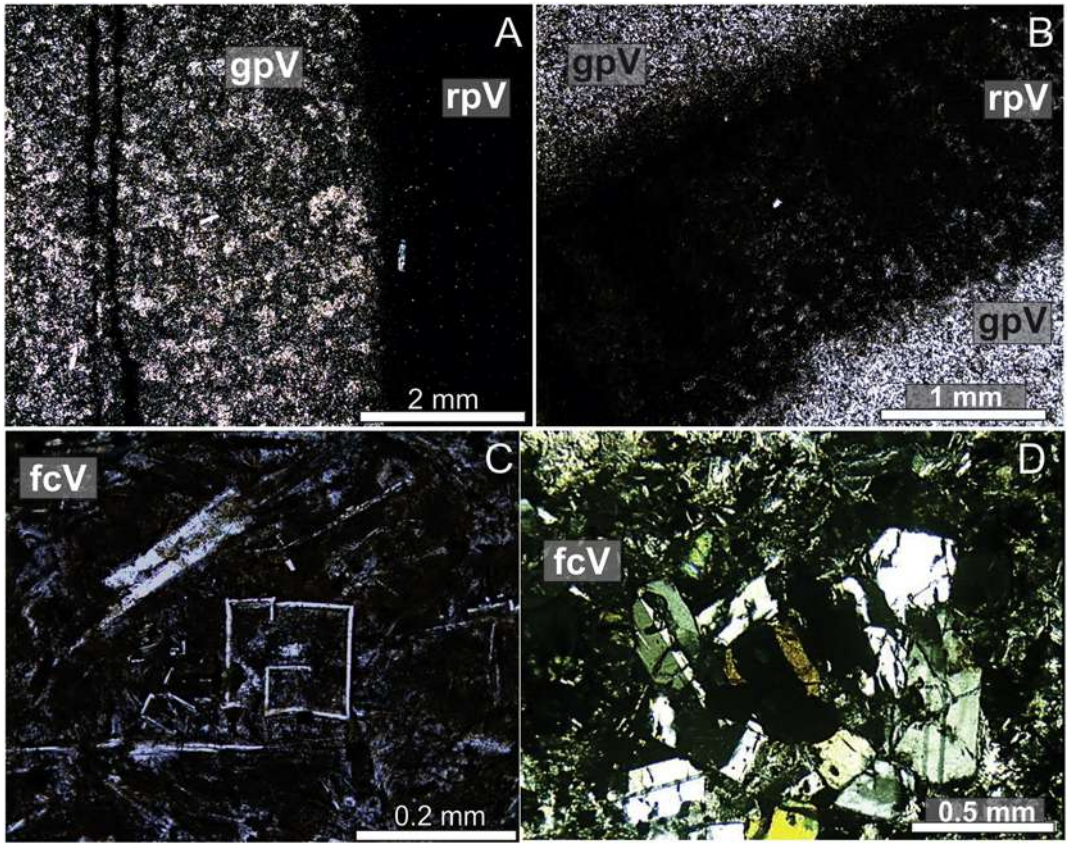

Fig. 7. Microscopic features of São Marcos area vitrophyres. (A) Different oxidation patterns in bV are due to the presence of millimeter-size rpV and gpV bands (crossed polarizers). (B) Detail in the contact between gpV and rpV bands. (C) Empty plagioclase prisms (center) with skeletal plagioclase fragments (scattered) and swallow-tail termination (upper left corner) present in flat-lying coherent vitrophyres (fcV). (E) Microporphyritic texture in fcV marked by plagioclase, Fe-Ti oxide and clinopyroxene glomeroporphyritic aggregates engulfed by hemi-crystalline groundmass composed dominantly by plagioclase microlites.

form (Fig. 9F), with either amoeboid quartz or vesicles at their centers.

3. Whole-rock chemical composition

The whole-rock composition of 28 samples was determined for comparison between sites and lithofacies and is presented in Table 2. Analyses were conducted at Acme Analytical Laboratories Ltd., in Vancouver, Canada. Major oxides and several minor elements were analyzed using Inductively Coupled Plasma—Emission Spectrometry (ICP-ES) on a 0.2 g powdered sample, with detection limits of 0.01% for SiO_2, Al_2O_3, Fe_2O3, CaO, MgO, Na_2O, K_2O, MnO, TiO_2 and P_2O_5. Rare earth and refractory elements were analyzed by ICP–MS (Mass Spectrometry), with 0.2 g of powdered sample and detection limit of 0.1 ppm for Zr.

The bulk of analyzed samples gave SiO_2 contents of 62.6–68.96 wt%. Total $Na_2O + K_2O$ values were 6.3–7.9 wt% in all considered localities. There is no systematic difference between lithofacies, with ranges for banded, grey and red vitrophyres largely overlapping. However, banded vitrophyres gave the broadest range of SiO_2 contents (62.60–68.88 wt%, 6 samples), whereas grey vitrophyres (gpV) display a more restricted range (67.23–68.18 wt%, 3 samples). In the R_1 vs. R_2 plot (Fig. 10A) of De La Roche et al. (1980) the samples lie predominantly in the rhyodacite field with two exceptions in the rhyolite field (MS-22, red vitrophyre) and in the dacite field (GA-03v, banded vitrophyre). In the SiO_2 vs. $Na_2O + K_2O$ diagram (Le Bas et al., 1986) the samples plot in the dacite field, whereas one sample (GA-03v) plots in the trachydacite/trachyte field (Fig. 10B). The value of $Q > 20$, being Q = normative $100 * Q / Q + or + ab + an$ (Q = quartz, or = orthoclase, ab = albite, an = anorthite), allows classification as trachydacite.

The low zirconium content of Palmas magma types and Caxias do Sul subtypes (Peate et al., 1992) under 400 ppm is demonstrated in the Zr vs. SiO_2 plot (Fig. 10C). The lower SiO_2 contents differentiate Palmas and Caxias do Sul subtypes from the Santa Maria subtype. Comparison of P_2O_5 vs. TiO_2 contents (following Nardy et al., 2008) indicates the predominance of the Caxias do Sul subtype in the analyzed samples, although two samples (GA-03v and GA-34) have higher P and Ti contents plot in the Jacuí subtype (Fig. 10D).

4. Structural elements

Structural elements were observed over multiple scales via satellite imagery, field data and petrographic analysis. Over the widest scale, there is a preferential NW-SE and WNW-ESE orientation of valley alignment to the south of the Antas lineament. Between these structures there are outcrops of the inferred feeder conduits in the Mato Perso and São Marcos areas, as shown in the mapped banded vitrophyre units in Fig. 2. Away from the area limited by these lineaments, most of the outcrops of silicic lava flows display near-horizontal flow foliations and conduit-related lithofacies are nearly absent. Outcrops of massive obsidian also occur aligned to NE-SW and NW-SE directions. In the Jaquirana-Cambará do Sul area satellite images reveal ENE-WNW, NW-SE and near N-S ridge alignments (Fig. 11A). The alignments are coincident with the main banding directions in outcrops of banded vitrophyres, are 10–20 m wide and ≥1 km in length, and are cut by

Please cite this article as: Simões, M.S., et al., Structures and lithofacies of inferred silicic conduits in the Paraná-Etendeka LIP, southernmost Brazil, J. Volcanol. Geotherm. Res. (2017), https://doi.org/10.1016/j.jvolgeores.2017.12.013

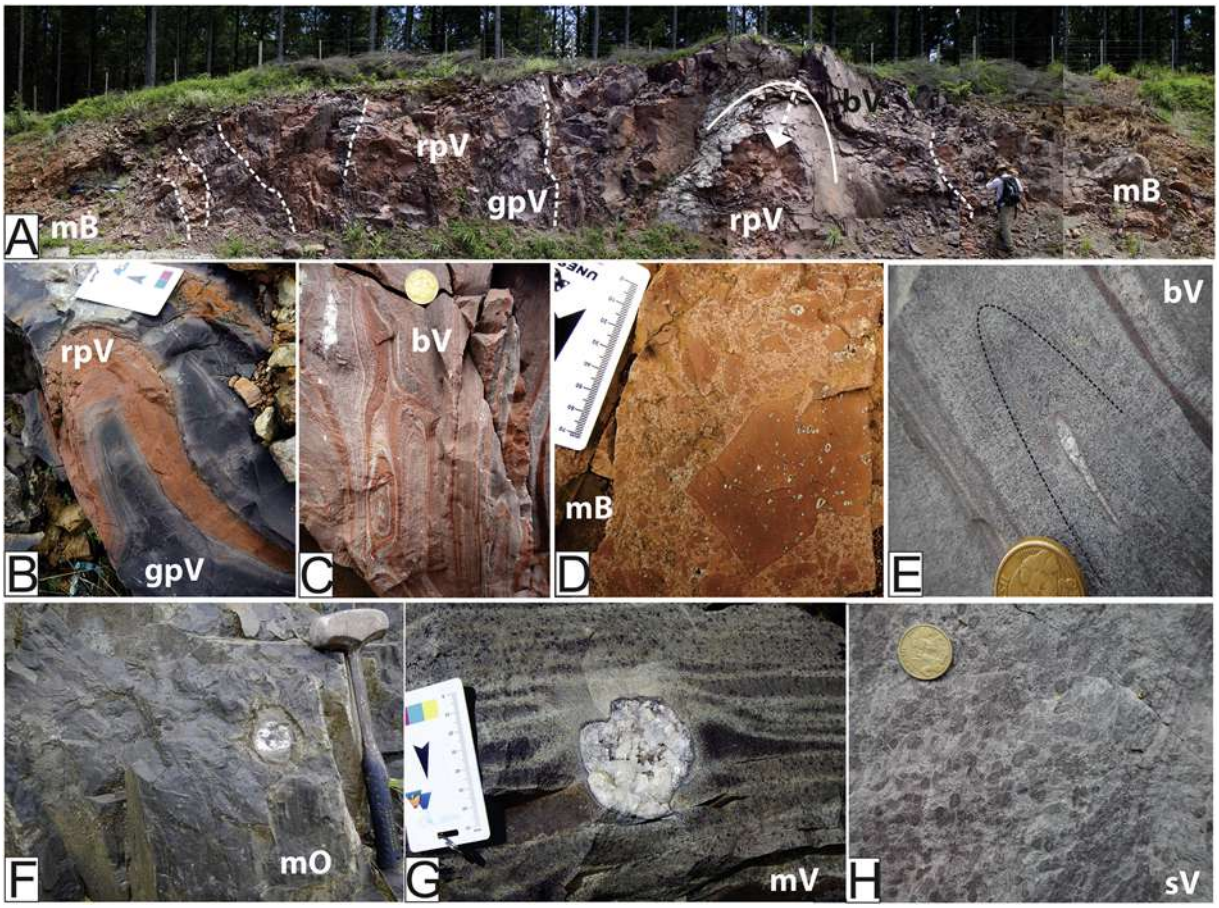

Fig. 8. Field and macroscopic features of Jaquirana-Cambará area. (A) Approximately 15 m-long outcrop with alternate rpV, gpV and bV with vertical banding and monomictic breccias (mB) in the outcrop margins. The arrow points to the hinge of an open fold surrounding a red vitrophyre pod. (B) Stretched fold of rpV between gpV layer. (C) bV with thin layers folded in sheath fold (left). (D) Autobreccia with angular red vitrophyre fragments. (E) Stretched fold in bV showing an elongated vesicle reaching the fold hinge. (F) mO with pitchstone aspect and cm-scale amygdale filled with quartz. (G) mV with flat-lying microfracturing-related halos and cm-size amygdale filled by calcite and quartz. (H) Grey spherulitic massive vitrophyre (sV). (For interpretation of the references to color in this figure legend, the reader is referred to the web version of this article.)

younger E-W, NE-SW, NW-SE and N-S valley lineaments verified in the field as normal to oblique faults.

At Mato Perso bV show sub-vertical banding orientation (Fig. 11B, left stereonets) and oblique to reverse fault planes (Fig. 11B, right stereonet), which were not observed in the upper lavas. Banding orientation is dominantly sub-vertical and commonly folded (Fig. 11C, top left stereonet). Apparent banding in microfractured vitrophyres (mV) is near-horizontal where the vitrophyre is not affected by younger faults (Fig. 11C, top right stereonet). Fault surfaces in some outcrops show oblique, reverse and transcurrent relative movements (Fig. 11C, bottom stereonet).

At outcrop scale, flow bands in lava are predominantly aligned NE-SW, with minor NW-SE trends, in addition to subordinate E-W and N-S orientations, based on a total of 142 field measurements. The banding dips are variable, from 01° to 89°, with predominance of sub-vertical dips of 68° to 89° (Fig. 11D). The hinge plunges are sub-horizontally oriented along NE-SW and NW-SE directions. Where bands are thinner and the lithofacies mixing degree is stronger the folds are multiple hinged (polyclinal) with mm-scale wavelength showing generally more than two phases of folding. A late-stage type of structure associated with the conduits is characterized by non-polished fault surfaces with oblique to subvertical dip geometries. The surfaces are generally parallel to the main banding and have vertical dipping slickensides and striations (Fig. 11E), which are indicative of reverse to oblique reverse relative movement.

5. Discussion

5.1. Structure of inferred conduits, lithofacies relative chronology and crystal contents

The proposal that lava-feeder conduits occur in the studied area is based on the systematic occurrence of outcrops with 15–25 m lateral extent (and minor ~2 m vitrophyre dykes; Simões et al., in press) with lateral variation from banded vitrophyres in the center grading to oxidized vesicular vitrophyres and then to massive and welded breccias at the outcrop margins (Fig. 12). Some features of the described lithologies are shared with silicic magma conduits in extensional settings (e.g. Stasiuk et al., 1996; Thordarson and Larsen, 2007; Tuffen and Castro, 2009). Another model for obsidian emplacement in agreement with conduit and lava described lithofacies is proposed by Fink (1983) for the Little Glass Mountain (west USA), where subvertical flow banding in vent areas indicates that fracturing accompanies the emergence of lava. The structure of the domes that form over vent areas may reflect the orientation of dike-like conduits as well as the local state of stress during extrusion. Beyond, the absence of flow base/top features such as domains of flow-top pumice found in subaerial lava flows (e.g. Hall, 1978; Fink, 1980; Fink, 1983; Cas and Wright, 1988; Tuffen et al., 2003), the carrying of large vesicular vitrophyre fragments and the identification of the base of subaerial flows in higher elevations are evidence to support the interpretation of these structures as feeder conduits.

Please cite this article as: Simões, M.S., et al., Structures and lithofacies of inferred silicic conduits in the Paraná-Etendeka LIP, southernmost Brazil, J. Volcanol. Geotherm. Res. (2017), https://doi.org/10.1016/j.jvolgeores.2017.12.013

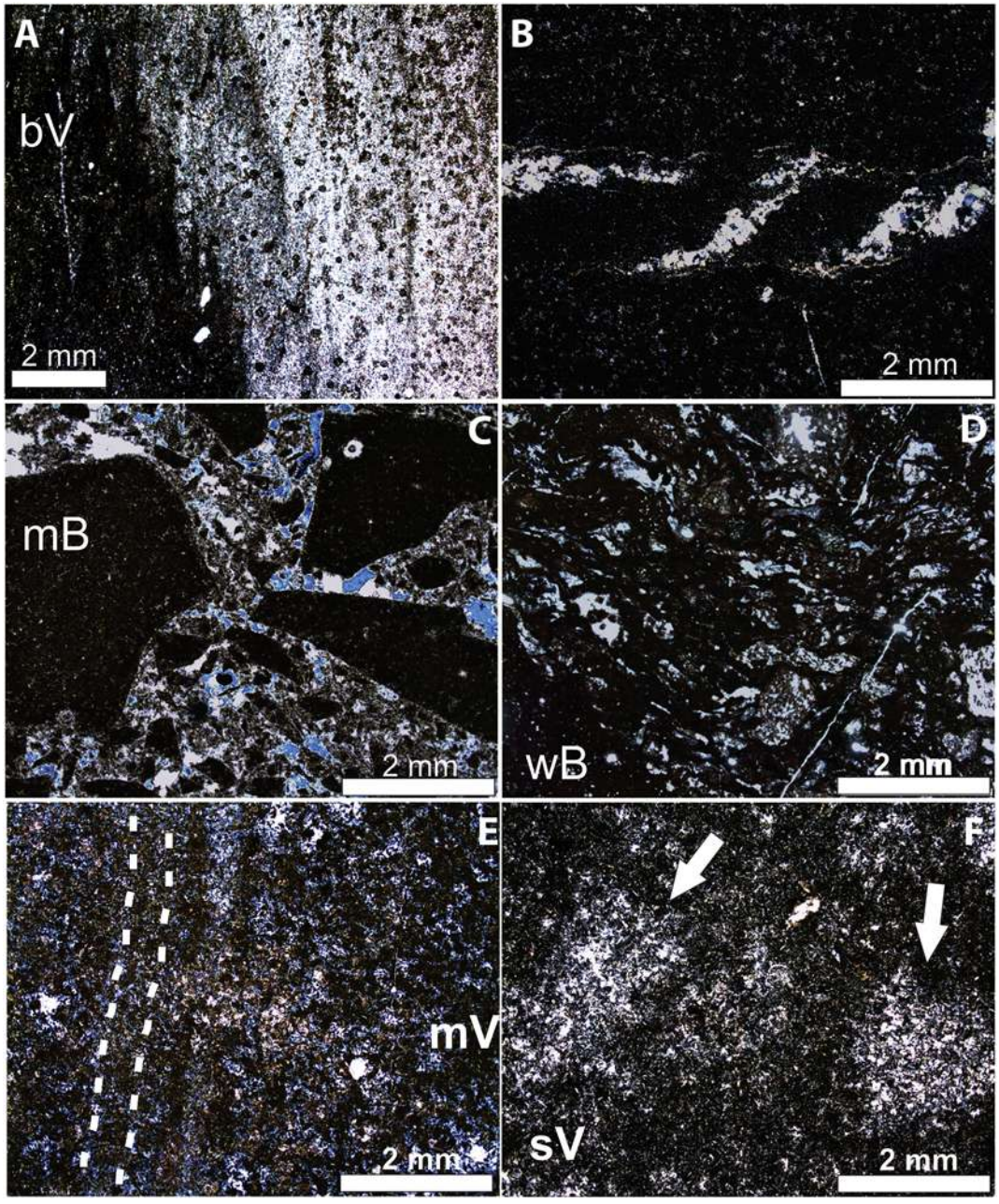

Fig. 9. Microscopic features of Jaquirana-Cambará area lithologies. A, C, D, E and F with plane-polarized light, B with crossed polarizers. (A) Gradational contact between more oxidized (rpV) and less oxidized vitrophyre (gpV). (B) Tension gashes filled with polycrystalline quartz. (C) Poorly sorted angular red vitrophyre fragments in porous autobreccia. (D) Welded breccias (wB) with elongated pumiceous fragments. (E) microfractured vitrophyre (mV) showing fracture-parallel oxidation halos. (F) Spherulitic vitrophyre with arrows indicating the spherules. (For interpretation of the references to color in this figure legend, the reader is referred to the web version of this article.)

In São Marcos area the divergence of banding orientation from vertical in the inferred conduit to horizontal in the contact of the silicic flow with basaltic flows is clearly exposed such as intrusive relations between grey and red vitrophyres (Lima et al., 2012, 2018; Cañón-Tapia and Raposo, this issue; Figs. 5, 6A, this study). The stratigraphic position, above the basaltic and some of the silicic units, is suggestive of a shallow level for the inferred conduits that fed the upper silicic flows.

The postulated conduits are characterized by multi-step textural evolution during silicic lava emplacement. The earliest-emplaced lithofacies are the red vesicular vitrophyres, which occur as xenoliths in the red poorly-vesicular, grey and banded vitrophyres. The rpV intercalates and is also cross-cut by the grey poorly vesicular vitrophyre, the youngest conduit-associated lithofacies. The early solidification of the rvV combined with late intrusion of rpV and gpV suggest the separation of different textural types occurred during prolonged magma ascent in the conduit.

Another important property observed in different inferred conduit areas is the crystal content. In Mato Perso region (Fig. 2A) the silicic units from conduits and lava flows have microphenocryst content of 2–11%, while São Marcos and Jaquirana-Cambará vitrophyres have < 2%.The subaerial lavas that we propose to be correlated with the conduits show the same proportion of microphenocrysts as their intrusive equivalents, although presenting bigger and better formed microlites then conduit lithofacies. Different crystallization pathways for the microphenocryst formation in each conduit system indicate they were independent systems with their own histories of magma ascent, undercooling, and possibly had sources with different pressure and temperature conditions.

Please cite this article as: Simões, M.S., et al., Structures and lithofacies of inferred silicic conduits in the Paraná-Etendeka LIP, southernmost Brazil, J. Volcanol. Geotherm. Res. (2017), https://doi.org/10.1016/j.jvolgeores.2017.12.013

Table 2
Whole-rock compositional data. Major oxides are in wt% and Zr is in ppm. MP = Mato Perso, J = Jaquirana, C = Cambará do Sul, SM = São Marcos. Lithofacies codes are given in Table 1.

Sample	MS-01	MS-03A	MS-04	MS-05B	MS-19A	MS-22	MS-22E	MS-22D	MS-24A	MS-24B	PSJ-006	MS-29A	MS-32C	MS-38
Local	MP	MP	MP	MP	J	J	J	J	J	J	J	C	C	C
Lithofacies	fcV	bV	fcV	gpV	sV	rpV	rpV	gpV	gpV	rpV	bV	fcV	sV	sV
SiO_2	67.32	65.30	67.18	67.23	65.80	64.78	65.47	67.80	68.18	67.35	66.00	66.32	67.38	66.04
Al_2O_3	12.66	13.11	12.88	12.74	12.72	13.75	12.95	12.53	12.05	12.37	12.63	12.90	12.55	12.85
Fe_2O_3	6.23	6.30	6.02	6.12	6.68	6.83	6.41	6.06	6.05	6.04	5.87	6.18	6.37	6.35
MgO	1.33	1.29	1.27	1.26	1.65	0.91	1.52	1.37	1.31	1.32	1.24	1.60	1.41	1.59
CaO	3.28	2.96	3.12	3.23	3.14	1.02	3.41	2.90	2.83	2.85	3.28	2.99	3.07	3.02
Na_2O	2.95	2.90	2.77	2.96	2.80	2.09	2.90	2.89	2.89	2.87	3.27	2.76	2.83	2.77
K_2O	3.78	3.94	4.00	3.80	3.95	4.86	4.00	3.98	3.80	4.13	3.10	4.06	4.04	4.14
TiO_2	0.92	0.95	0.89	0.93	0.95	1.01	0.95	0.92	0.89	0.92	0.88	0.95	0.96	0.94
P_2O_5	0.27	0.28	0.26	0.27	0.29	0.25	0.27	0.25	0.26	0.26	0.25	0.27	0.27	0.29
Zr	243.8	247.1	245.3	236.1	250.4	269.7	245.7	234.3	239.2	246.6	242.2	250.8	255.1	251.2

5.2. Banding origin

The origin of banding in silicic lavas may be ascribed to viscous magma mixing, repeated fragmentation and welding during flow towards the surface, rheomorphism of pyroclastic fragments, or vapor-phase crystallization in stretched vesicles (e.g. Seaman, 1995, Tuffen et al., 2003; Castro et al., 2005; Gonnermann and Manga, 2005; Tuffen and Dingwell, 2005).

Field and petrographic observations of the studied areas show that vesiculation patterns are parallel to the banding but not penetrative and the variation of sub-millimeter microlite concentration between bands can be masked by intense oxidation. The repetition of different color bands (e.g. Fink, 1983; Seaman, 1995) is thought to be characterized by different hematite contents. Compositional analyses of different color vitrophyres in banded lithofacies show that grey vitrophyres have slightly higher silica content than red vitrophyres, and the compositional differences may be enhanced by different degrees of porosity, vapor-phase precipitation, hydration and oxidation. Shearing of homogeneous melt can lead to localized heating (Nelson, 1981) and thus spatial variations in oxidation and degassing. Other plausible contributors to banding formation include magma mixing (Seaman, 1995), and hypersolidus heterogeneity of water concentration in the magma (Seaman et al., 2009) due to divergent vesiculation and degassing histories of bands, which can also lead to heterogeneous late-stage spherulite growth (Seaman, 2013).

5.3. Fragmentation: breccias, pyroclastic textures and fracturing

The first fragmentation episode is registered into the conduits and is represented by the presence of large (cm- to m-scale) red vesicular vitrophyres as large sub-rounded to angular xenoliths embedded in younger red and grey vitrophyres. Then, the brecciation of red vesicular and red poorly-vesicular vitrophyres in the intrusion margins generated fine to coarse-grained angular vitrophyre fragments cemented by a porous quartz matrix. Welded monomictic breccias also occur as steeply oriented bodies (Figs. 6E, 12) and represent fragmentation at temperatures above the glass transition field (Dingwell, 2006). Breccia formation involved variably vesicular magma, demonstrated by the wide range of clast vesicularities. This episode records the brittle fragmentation of vitrophyres and pumiceous fragments.

Pyroclastic textures in the inferred conduits occur as elongated vitrophyre clasts and pumiceous fragments between non-pyroclastic vitrophyre layers. They suggest a local fragmentation and welding event, which play an important role in reducing the likelihood of explosive behavior, by facilitating magma degassing (Gonnermann and Manga, 2003). Highly porous lithofacies within obsidian flows can comprise well-connected cavities that act as efficient degassing pathways to the lava surface (Furukawa et al., 2010; Shields et al., 2016), playing a role in providing volcanic gasses to void spaces created in surface fold hinges (Furukawa and Uno, 2015). Formation of autobreccias, fragmentation, annealing and magma fracturing in the edges of intrusion outcrops can be interpreted as shearing and fragmentation near the conduit walls (Tuffen et al., 2003; Cashman, 2004; Castro et al., 2005). Shear localized along the conduit edges creates a locally permeable zone, leaving less-sheared and less-outgassed magma at its center (Okomura et al., 2013).

A late fracturing event is represented by the extensional fracturing phase which cross-cuts all lithofacies and generated extensional breccias filled by angular vitrophyre clasts and quartz (Fig. 12). Some extensional fractures are delimited between vitrophyre layers or breccias and do not appear in subaerial flows, suggesting the late lava movement during syn- to shortly post-eruptive stages.

5.4. Conduit-related subaerial lava flows

The subaerial lithofacies include features such pipe-like vesicles near the flow unit base, local basal breccias and absence or very restricted occurrence of lithic fragments. Lava flow-related breccias are recognized in base and top portions of lavas (Fink, 1983; Tuffen et al., 2013), including those from Paraná-Etendeka LIP outcropping at the southern portion of the province, where they constitute the base, margins and fronts of lava lobes and domes (Waichel et al., 2012; Polo and Janasi, 2014; Rossetti et al., this issue; Simões et al., in press). Pumiceous textures are lacking and there are no preserved pyroclastic textures in the quenched margins, where rapid quenching ought to prevent their obliteration through prolonged dense welding. Although we recognize that the upper surfaces of subaerial silicic flows can include domains of steeply inclined flow banding and welded breccias, in the studied area the subaerial flows are dominated by near-horizontal banding with very local steep dips.

Additionally, massive obsidian and flat-lying coherent vitrophyres have well-developed microlites engulfed in a glassy matrix, contrasting with microlite-poor textures in inferred conduit zones. The units are thus interpreted as lava flows rather than extensive lava-like or high-grade ignimbrites (c.f. Manley, 1995; Henry et al., 1990; Henry and Wolff, 1992). Another important aspect is the high emplacement temperatures of the lavas (Milner et al., 1992; Garland et al., 1995; Simões et al., 2014), which gives low viscosity, suppressing fragmentation and increasing flow mobility (Hausback, 1987; Henry and Wolff, 1992; Green and Fitz III, 1993; Pankhurst et al., 2011). Permeability development during brecciation within conduits is widely assumed to aid the degassing and ascent of magma (Eichelberger et al., 1986; Jaupart and Allegre, 1991; Rust et al., 2004) and may have assisted the outgassing that permitted the effusion of extensive lava units.

5.5. Importance of the regional structures

Documented intrusive systems related to the Paraná-Etendeka LIP include three extensive dyke swarms: Santos-Rio de Janeiro, Ponta Grossa and Florianópolis (Piccirillo et al., 1990; Raposo et al., 1998;

Please cite this article as: Simões, M.S., et al., Structures and lithofacies of inferred silicic conduits in the Paraná-Etendeka LIP, southernmost Brazil, J. Volcanol. Geotherm. Res. (2017), https://doi.org/10.1016/j.jvolgeores.2017.12.013

MS-50	MS-67	GA-03V	GA-03P	GA-04	GA-07	GA-10	GA-11	GA-12	GA-13	GA-16	GA-34	GA-35	GA-37
C	C	SM	SM	SM	SM	SM	SM	SM	SM	SM	SM	SM	SM
bV	fcV	bV	bV	rV	fcV	fcV	fcV	fcV	fcV	bV	fcV	rpV	mO
66.30	65.64	62.60	68.88	66.91	68.96	66.51	66.88	67.07	67.01	67.24	64.99	67.66	65.25
13.04	13.40	14.53	12.13	13.10	11.95	12.87	12.74	13.05	12.76	12.74	13.14	12.92	12.87
6.50	6.16	6.71	5.99	5.87	6.00	5.93	5.84	5.90	5.84	6.24	7.24	6.03	6.32
1.22	1.50	1.48	1.21	0.92	1.13	1.22	1.31	0.95	1.31	1.00	1.52	1.15	1.36
2.63	2.09	3.31	2.96	2.14	2.76	3.10	2.94	2.50	3.03	2.50	3.48	3.02	3.48
2.84	2.56	3.34	2.72	2.54	2.59	2.86	2.84	2.80	2.87	2.63	3.15	3.05	3.55
4.26	3.91	4.58	3.99	4.19	4.46	4.30	4.02	4.09	4.14	4.54	3.57	3.68	2.94
0.94	0.94	1.00	0.87	0.90	0.85	0.89	0.91	0.92	0.90	0.92	1.06	0.96	0.95
0.27	0.26	0.29	0.26	0.26	0.25	0.27	0.28	0.27	0.28	0.27	0.29	0.26	0.27
255.4	261.6	259.6	224.2	248.00	218.6	233.5	233.6	242.9	240.9	238.4	234.3	225.1	222.00

Valente et al., 2007). It has been proposed that the large extent of this magmatism represents the preserved plumbing system of the Paraná-Etendeka LIP in Brazil (Florisbal et al., 2014). For the mafic magmatism of this LIP, regional structures are important controllers of the dyke emplacement, and this relation is also observed in the occurrence of inferred silicic conduits (Fig. 1).

In the study areas, the main regional structures with NE-SW orientations cutting the Paraná Basin and the basement are the Lancinha-Cubatão Fault Zone, Blumenau-Soledade Fault Zone and Leão-Açotea faults (Zalán et al., 1991). The NE-SW structures are coincident with and have branches parallel to Neoproterozoic fault and shear zones, mainly the Dorsal de Canguçu shear zone and the Porto Alegre Suture (Fernandes et al., 1995). Those structures were vulnerable to reactivation in the early stages of the Gondwana breakup. The Antas Lineament, NE-trending, is parallel to the Porto Alegre Suture but does not cut the basement (Fig. 1). The major NW-SE structure is the Torres Syncline – not a significant discontinuity, but instead an ancient tectonic valley that was a locus of deposition for the sediments and volcanic deposits

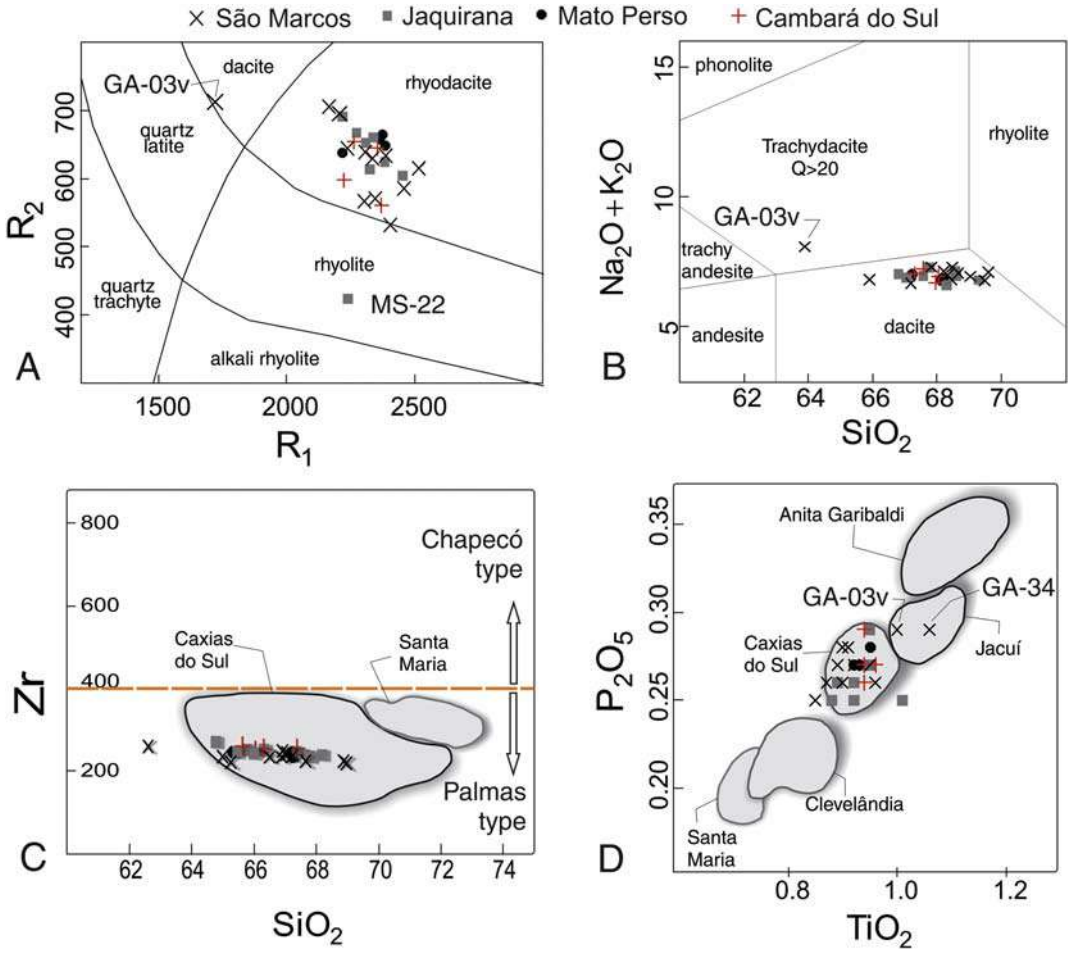

Fig. 10. Classification plots for vitrophyres of the inferred silicic conduits. (A) R_1-R_2 plot of De La Roche et al. (1980) showing the dominantly rhyodacitic composition for studied samples, except for samples GA-03v (dacite) and MS-22 (rhyolite). (B) TAS plot of Le Bas et al. (1986). $Q = Q_{(n)} * 100 / Q_{(n)} + or_{(n)} + ab_{(n)} + an_{(n)}$. (C) Zr vs. SiO_2 diagram (Peate et al., 1992) for classification of magma types (Chapecó and Palmas) and magma subtypes (Caxias do Sul and Santa Maria). (D) P_2O_5 vs. TiO_2 diagram of Nardy et al. (2008) for separation of magma subtypes (Santa Maria, Clevelândia, Caxias do Sul, Jacuí and Anita Garibaldi).

Please cite this article as: Simões, M.S., et al., Structures and lithofacies of inferred silicic conduits in the Paraná-Etendeka LIP, southernmost Brazil, J. Volcanol. Geotherm. Res. (2017), https://doi.org/10.1016/j.jvolgeores.2017.12.013

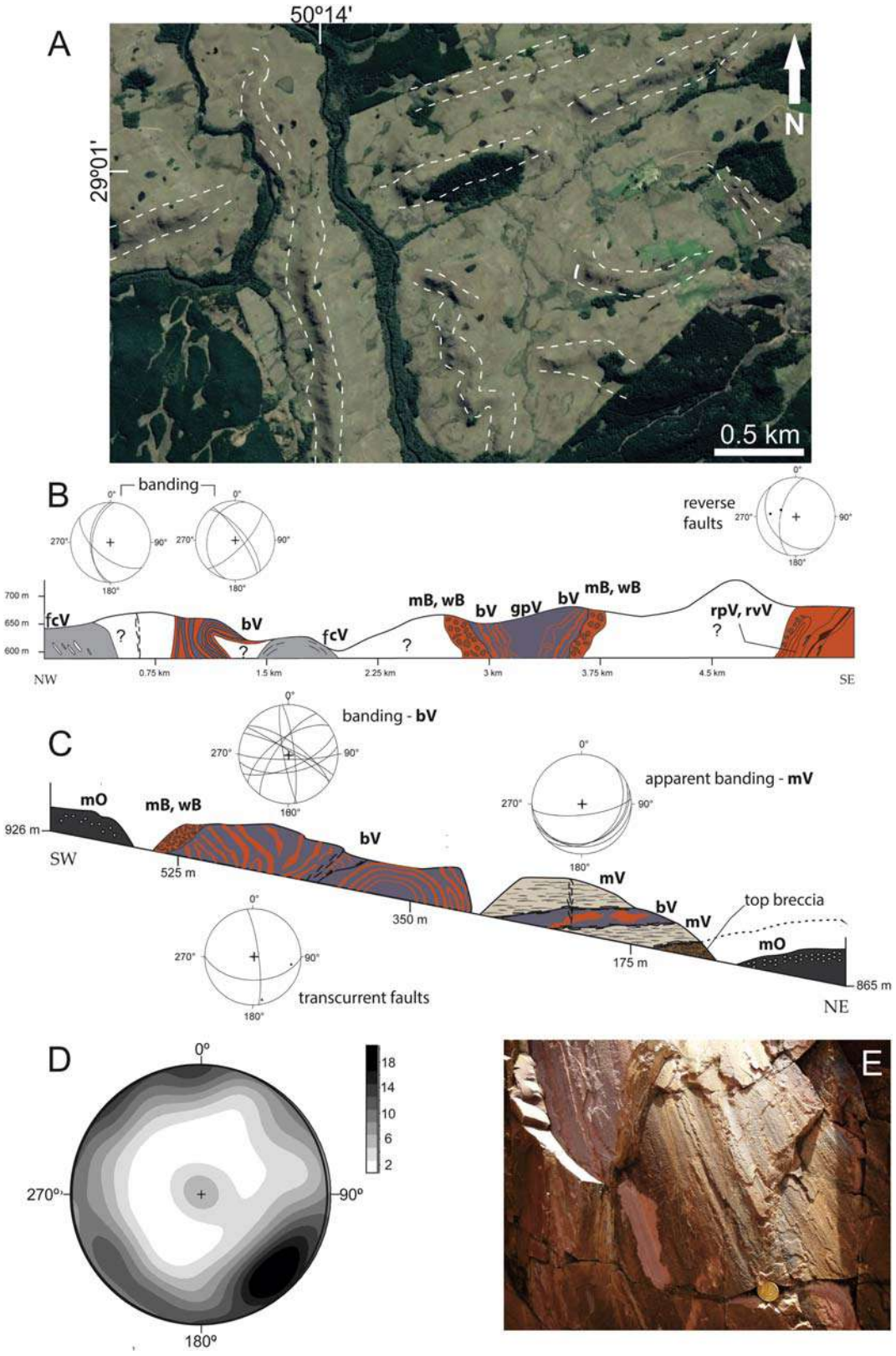

Fig. 11. Structural elements of the studied areas. (A) Satellite imagery in part of the Jaquirana-Cambará area showing aligned ridges (ridge lineaments) indicated by arrows. (B) Geological and structural profile of the inferred Mato Perso area with great outcrop exaggeration. Stereonets show the banding disposition in the indicated outcrops. (C) Geological and structural profile in a section of the Jaquirana-Cambará area. Stereonets show the disposition of the banding. The top right stereonet show the disposition of the apparent-banding in mV. (D) Contour diagram of the banding orientation in all studied areas (Mato Perso, Jaquirana-Cambará and São Marcos) showing a preferential NE trend and a subordinate NW trend (N = 142, maximum density = 20.6, mean density = 6.76, contour intervals = 10). (E) Slickenside with striations indicating reverse oblique relative movement on sliding surfaces.

Please cite this article as: Simões, M.S., et al., Structures and lithofacies of inferred silicic conduits in the Paraná-Etendeka LIP, southernmost Brazil, J. Volcanol. Geotherm. Res. (2017), https://doi.org/10.1016/j.jvolgeores.2017.12.013

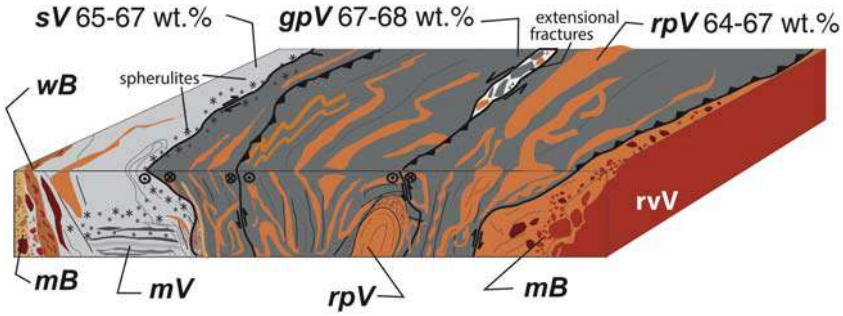

Fig. 12. Model of Jaquirana-Cambará type conduit system lithofacies. Values in wt% represent SiO_2 content. mB = monomictic breccia, sV = spherulitic vitrophyre, mV = microfractured vitrophyre, gpV = grey poorly-vesicular vitrophyre, rpV = red poorly-vesicular vitrophyre, rvV = red vesicular vitrophyre. (For interpretation of the references to color in this figure legend, the reader is referred to the web version of this article.)

of the Paraná Basin. These orientations match the NE-SW and subordinate NW-SE orientation of mafic dikes in the Florianópolis Dike Swarm (FDS). The FDS is interpreted as the feeder system of Urubici-type magmas (high Ti basaltic and trachyandesitic; Florisbal et al., 2014). Anisotropy of Magnetic Susceptibility (AMS) studies of Raposo (1997) and Raposo et al. (1998) showed vertical or sub-vertical dip in FDS dikes, trending mainly NE, although NW-trending dikes are also found. The NE-trending dikes are recognized as corresponding to structural trends of the basement and are occasionally crosscut by NW-trending dikes.

In the three case studies (Mato Perso, São Marcos and Jaquirana-Cambará) the inferred conduits crop out between NW-SE valley lineaments and have smaller-scale NE-SW structures, concordant with the dominant NE-SW direction of the flow banding. These structures were probably potential pathways for magma transport, since the evolution of Paraná Basin was controlled, from the beginning, by transtensional reactivation of crustal discontinuities triggered during Cretaceous orogenies (Milani, 2004).

5.6. Whole rock composition

Compositional data shows that the silicic magma was dominated by rhyodacites. The evolution of vitrophyres with 62–65 wt% SiO_2 to more evolved compositions with 66–68 wt% SiO_2 is encountered in the three study case areas and in the distinguished lithofacies, except for grey vitrophyres (gpV). The gpV vitrophyres tend to form thick stretched and folded bands that frequently crosscut the red vitrophyres (rpV), and so may represent late-stage, more evolved magma. Alternatively, SiO_2 enrichment could relate to localized late-stage precipitation of cristobalite, tridymite or quartz.

The flat-lying subaerial lava flows have similar major (and some trace) element composition. They are correlated to Palmas-type magmas - aphyric to microporphyritic low-Ti magmas - and Caxias do Sul magma sub-types, which have low Zr and intermediate P_2O_5 and TiO_2. As the whole-rock chemistry of inferred local conduits corresponds to the subaerial lava flows, the two can be considered to be cogenetic and the lavas are therefore not necessarily extensive rheomorphic ignimbrites from the Messum Complex in southern Namibia (Milner et al., 1995; Marsh et al., 2001; Bryan et al., 2010). Lateral variation of phenocryst content and phenocryst-compatible elements within the subaerial silicic units was suggested to be generated during density segregation of crystals from the pyroclastic density current during flow, which required a run-out distance of >300 km (Bryan et al., 2010). We propose that this is not the case, and that instead the studied subaerial vitrophyres are lava flows similar to those exposed in adjacent areas in southern Paraná-Etendeka LIP in South America (e.g. Henry and Wolff, 1992; Umann et al., 2001; Garland et al., 1995; Lima et al., 2012, 2018; Polo and Janasi, 2014; Simões et al., 2014; Rossetti et al., this issue; Polo et al., this issue; Guimarães et al., this issue; Cañón-Tapia and Raposo, this issue).

5.7. Evaluation of alternative models for the described areas

5.7.1. Internal portion of silicic lava flows

Banding and folding are common features in internal portions of individual units of silicic lava flows and domes (e.g. Fink, 1985; Seaman, 1995; Manley, 1996; Manley and Fink, 1987; Castro and Cashman, 1999; Morrow and McPhie, 2000; Simões et al., 2014; Polo and Janasi, 2014). Near-vertical structures are not only common adjacent to the vents and they can develop in the upper carapace of silicic lava flows far from the conduit/vent, e.g. due to ramping associated with the compressive folding of the surface crust into ogives or due to rotation associated with the ascent of pumice diapirs from deeper in the lava flow (Hall, 1978; Fink, 1980, 1983; Cas and Wright, 1988; McPhie et al., 1993; Castro and Cashman, 1999). However the vertical variation showing basal and top breccias, foliated obsidian/vitrophyre and horizontal layers of coarse and fine pumice, typical of silicic flow units (e.g. Fink, 1983; McPhie et al., 1993), was not observed in the exposed outcrops. Instead, brecciated lithofacies are generally restricted to the outer portions of the outcrops or as transitional layers in red oxidized vitrophyres and tend to be oblique to vertical (Figs. 6E, 8A).

Comparing the ridges identified in satellite imagery with structures of similar dimensions described as flow ridges on the upper surface of silicic lava flows (e.g. Fink, 1980, 1983; Manley, 1996; Tuffen et al., 2013), they are not characterized by penetrative parallelism or to contain open anticlinal folds (e.g. Fink, 1980), tephra deposits (Manley, 1996) or ogives indicating folding of ~10 m thick surface crusts (Tuffen et al., 2013). In the described areas, ridges are parallel to the sub-vertical banding trends of bV, postulated as the main part of the conduits. Aligned ridges in northeast Rio Grande do Sul reflect also the alignment of obsidian flows.

5.7.2. Thermal erosion of underlying silicic lava flows

Another distinct interpretation concerning the quarry exposure at São Marcos area (Fig. 5C) is given by Cañón-Tapia and Raposo (this issue). Based on the AMS data, the authors assume that features characteristic of dimension stone quarries at São Marcos are ascribed to thermal erosion of underlying flows and are restricted with a very specific region. For this, they interpreted the direction of k_{max}, the longest of the three magnetic susceptibility axes (k_{max}, k_{int}, k_{min}), being parallel to the magma flow.

In dykes, the most common fabric display magnetic foliation (k_{max}-k_{min} plane) approximately parallel to the dyke plane and the magnetic lineation (k_{max}) also parallel do the dyke plane, being vertical, horizontal or even oblique (Rochette et al., 1991; Geoffroy et al., 2002; Callot and Guichet, 2003; Callot and Geoffroy, 2004; Plenier et al., 2005; Philpotts and Philpots, 2007; Hrouda et al., 2016). Magnetic lineation

Please cite this article as: Simões, M.S., et al., Structures and lithofacies of inferred silicic conduits in the Paraná-Etendeka LIP, southernmost Brazil, J. Volcanol. Geotherm. Res. (2017), https://doi.org/10.1016/j.jvolgeores.2017.12.013

is not always parallel to the magmatic flow in rhyolite dykes (Auborg et al., 2002) and random orientations of the magnetic fabric may also be result of very complex magmatic flow patterns or because of severe post-magmatic changes in magnetic minerals (Hrouda, 1985). Experimental work using lavas re-melted in laboratory presented by Cañón-Tapia and Pinkerton (2000) concludes that k_{max} is preferentially parallel to the flow but k_{int} may also be parallel to it. And the work of Závada et al. (2009), in trachyte lava, describe complex magnetic fabrics controlled by chevron folds with a particular type of asymmetric fabric associated to the vertical collapse in the conduit.

In São Marcos, k_{max} is generally oblique to flat-lying (locally vertical) in the divergent structures (Cañón-Tapia and Raposo, this issue) of the banded vitrophyres, like in Fig. 5C, but, unlike the outcrops interpreted as lava flows, they do not present horizontal magnetic foliation (k_{max}-k_{min}). The scatter of k_{max} orientations in banded vitrophyres, varying from oblique to flat or vertical can be a result of several folding phases in macro- and microscale, changing the main direction of magma flow, and so we should not expect k_{max} axes directions to behave like in tabular dykes and sills. Moreover, as cited above, the magnetic fabric in a dyke does not necessarily have vertical k_{max} axes and the horizontal flow of the grey band in the outcrop shown in Fig. 5C does not exclude this as an intrusive feature. The interpretation of downflow in an outcrop by the referred authors may be a common backflow (e.g. Varga et al., 1998; Johnson et al., 1999) or melt-back (e.g. Fialko and Rubin, 1999) feature present in feeder systems and ascribed to be common in magmatic chambers too (Lowman and Hoefer, 2013). Obstacles, like the fragments described by Cañón-Tapia and Raposo (this issue) and the ones described in the present work (see Figs. 3, 5, 6, 8 and 12) are also important features causing the modification of the original flow directions. Thus, the direct interpretation of k_{max} orientation as the dominant flow directions should be taken more carefully.

Thermal erosion, as described by Kerr (2009), should not be a discarded process during the emplacement of basaltic and silicic Paraná-Etendeka lavas and conduits, principally where mafic flows are overlying silicic lavas (see Rossetti et al., this issue), giving more accented temperature contrast. But it is unfavorable that this phenomenon would form tabular dike-like structures containing banded vitrophyres with very similar lithofacies seen in São Marcos as in Fig. 3A or B.

6. Concluding remarks

In the present work we described structures, lithofacies and major regional structural trends of vitrophyres and breccias that we postulate as conduits of silicic lava flows. The occurrence of structurally-controlled variably vesicular lithofacies displaying systematic variation at conduit exposures and outcropping coherently with the regional distribution of faults is recognized. Microscopically, vitrophyres interpreted as conduit-related have glassy groundmass with poorly developed microlites, contrasting with the lava flows, exhibiting well-developed microlites, revealing the contrast of undercooling paths. Aligned ridges match with banded vitrophyre outcrop trends and do not resemble lava-flow related ridges. The conduit-related subaerial lava share textural and structural features with extensive lava flows rather than lava-like or rheomorphic ignimbrites. Degassing pathways formed during fragmentation and fracturing episodes within the inferred conduits may have helped to inhibit the explosivity of the related silicic eruptions. Palmas-type magmas are compositionally equivalent to some magma-types in Namibia (Milner et al., 1995), but the origin of the extensive silicic lava flows in southern Brazil can also be explained by fault-related conduit systems such as those described in the present study.

Acknowledgements

We are grateful to Dr. Heidy Mader for the editorial handling and Dr. Hugh Tuffen for the careful review and thoughtful suggestions that have enormously improved the manuscript. We also thank Conselho Nacional de Desenvolvimento Científico e Tecnológico (CNPq) for funding (Projects CNPQ 9784; FAPERGS 2311-2551/14-1 and FAPESP 2012/06082-6).

References

Auborg, C., Giordano, G., Mattei, M., Speranza, F., 2002. Magma flow in sub-aqueous rhyolitic dikes inferred from magnetic fabric analysis (Ponza Island, W. Italy). Phys. Chem. Earth 27:1263–1272. https://doi.org/10.1016/S1474-7065(02)00113-4.

Barreto, C.J.S., Lima, E.F., Scherer, C.M.S., Rossetti, L.M.M., 2014. Lithofacies analysis of basic lava flows of the Paraná igneous province in the south hinge of Torres Syncline, Southern Brazil. J. Volcanol. Geotherm. Res. 285:81–99. https://doi.org/10.1016/j.jvolgeores.2014.08.008.

Bellieni, G., Brotzu, P., Comin-Chiaramonti, P., Ernesto, M., Melfi, A.J., Pacca, I.G., Piccirillo, E.M., Stolfa, D., 1983. Petrological and paleomagnetic data on the plateau basalt to rhyolite sequences of the Southern Paraná Basin (Brazil). An. Acad. Bras. Cienc. 55, 355–383.

Bellieni, G., Brotzu, P., Comin-Chiaramonti, P., Ernesto, M., Melfi, A.J., Pacca, I.G., Piccirillo, E.M., Stolfa, D., 1984. Flood basalt to rhyolite suites in the southern Paraná plateau (Brazil): paleomagnetism, petrogenesis and geodynamic implications. J. Petrol. 25: 579–618. https://doi.org/10.1093/petrology/25.3.579.

Bellieni, G., Comin-Chiaramonti, P., Marques, L.S., Melfi, A.J., Nardy, A.J.R., Papatrechas, C., Piccirilo, E.M., Roisenberg, A., 1986. Petrogenetic aspects of acid and basaltic lavas from Paraná Basin (Brazil): geological, mineralogical and petrochemical relationships. J. Petrol. 27:915–944. https://doi.org/10.1093/petrology/27.4.915.

Bryan, S.E., Ernst, R.E., 2008. Revised definition of Large Igneous Provinces (LIPs). Earth Sci. Rev. 86:175–202. https://doi.org/10.1016/j.earscirev.2007.08.008.

Bryan, S.E., Peate, I.U., Peate, D.W., Self, S., Jerram, D.A., Mawby, M.R., Marsh, J.S., Miller, J.A., 2010. The largest volcanic eruptions on Earth. Earth Sci. Rev. 102 (3–4): 207–229. https://doi.org/10.1016/j.earscirev.2010.07.001.

Callot, J., Geoffroy, L., 2004. Magma flow in the East Greenland dyke swarm inferred from study of anisotropy of magnetic susceptibility: magmatic growth of a volcanic margin. Geophys. J. Int. 159, 2.

Callot, J.P., Guichet, X., 2003. Rock texture and magnetic lineation in dykes: a simple analytical model. Tectonophysics 366, 207–222.

Cañón-Tapia, E., 2010. Origin of Large Igneous Provinces: the importance of a definition. In: Cañón-Tapia, E., Szakács, A. (Eds.), What Is a Volcano? Geol. S. Am. S.: pp. 77–101 https://doi.org/10.1130/2010.2470(06).

Cañón-Tapia, E., Pinkerton, H., 2000. The anisotropy of magnetic susceptibility of lava flows: an experimental approach. J. Volcanol. Geotherm. Res. 98, 219–233.

Cañón-Tapia, E., Raposo, M.I.B., 2017. Anisotropy of magnetic susceptibility of silicic rocks from quarries in the vicinity of São Marcos, Rio Grande do Sul, South Brazil: implications for emplacement mechanisms. J. Volcanol. Geotherm. Res. (this issue).

Cas, R.A.F., Wright, J.V., 1988. Volcanic Succession, Modern and Ancient: A Geological Approach to Processes, Products and Successions. Chapman and Hall, London, p. 528.

Cashman, K.V., 2004. Volatile controls on magma ascent and eruption. Geophys. Monogr. 150 (19):109–124. https://doi.org/10.1029/150GM10.

Castro, J.M., Cashman, K.V., 1999. Constraints on rheology of obsidian and pumice based on folds in obsidian lavas. J. Struct. Geol. 21:807–819. https://doi.org/10.1016/S0191-8141(99)00070-X.

Castro, J.M., Dingwell, B.D., Nichols, A.R.L., Gardner, J.E., 2005. New insights on the origin of flow bands in obsidian. Geol. So. Am. S. 396:55–65. https://doi.org/10.1130/0-8137-2396-5.55.

Coffin, M.F., Eldholm, O., 1994. Large Igneous Provinces: crustal structure, dimensions and external consequences. Rev. Geophys. 32:1–36. https://doi.org/10.1029/93RG02508.

Comin-Chiaramonti, P., Bellieni, G., Piccirillo, E.M., Melfi, A.J., 1988. Classification and petrography of continental stratoid volcanic and related intrusive from the Paraná Basin (Brasil). In: Piccirillo, E.M., Melfi, A.J. (Eds.), The Mesozoic Flood Volcanism of the Paraná Basin: Petrogenetic and Geophysical Aspects. Instituto Astronômico e Geofísico, São Paulo.

De La Roche, H., Leterrier, J., Grandclaude, P., Marchal, M., 1980. A classification of volcanic and plutonic rocks using R1R2-diagram and major element analyses – its relationships with current nomenclature. Chem. Geol. 29:183–210. https://doi.org/10.1016/0009-2541(80)90020-0.

Dingwell, 2006. Transport properties of magmas: diffusion and rheology. Elements 2: 281–286. https://doi.org/10.2113/gselements.2.5.281.

Eichelberger, J.C., Carrigan, H.R., Westrich, H.R., Price, R.H., 1986. Non-explosive silicic volcanism. Nature 323:598–602. https://doi.org/10.1038/323598a0.

Eichelberger, J.C., Vogel, T.A., Younker, L.W., Miller, C.D., Heiken, G.H., Wohletz, K.H., 1988. Structure and stratigraphy beneath a young phreatic vent: South Inyo Crater, Long Valley Caldera, California. J. Geophys. Res. 93:13208–13220. https://doi.org/10.1029/JB093iB11p13208.

Ewart, A., Milner, S.C., Armstrong, R.A., Duncan, A.R., 1998. Etendeka volcanism of the Goboboseb Mountains and Messum Igneous Complex, Namibia. Part II: voluminous quartz latite volcanism of the Awahab magma system. J. Petrol. 39:227–253. https://doi.org/10.1093/petroj/39.2.227.

Ewart, A., Milner, S.C., Duncan, A.R., Bailey, M., 2002. The Cretaceous Messum igneous complex, S.W. Etendeka, Namibia: reinterpretation in terms of a downsag-cauldron subsidence model. J. Volcanol. Geotherm. Res. 114:251–273. https://doi.org/10.1016/S0377-0273(01)00266-9.

Fernandes, L.A.D., Menegat, R., Costa, A.F.U., Koester, E., Porcher, C.C., Tommasi, A., Kraemer, G., Ramgrab, G.E., Camozzato, E., 1995. Evolução tectônica do Cinturão

Please cite this article as: Simões, M.S., et al., Structures and lithofacies of inferred silicic conduits in the Paraná-Etendeka LIP, southernmost Brazil, J. Volcanol. Geotherm. Res. (2017), https://doi.org/10.1016/j.jvolgeores.2017.12.013

Dom Feliciano no Escudo Sul-Rio-Grandense: Parte II – uma contribuição a partir das assinaturas geofísicas. Rev. Bras. Geosci. 25 (4), 375–384.
Fialko, Y.A., Rubin, A.M., 1999. Thermal and mechanical aspects of magma emplacement in giant dyke swarms. J. Geophys. Res. 104, 23033–23049.
Fink, J.H., 1980. Surface folding and viscosity of rhyolite flows. Geology 8, 250–254.
Fink, J.H., 1983. Structure and emplacement of a rhyolitic obsidian flow; Little Glass Mountain, Medicine Lake Highland, northern California. Geol. Soc. Am. Bull. 94 (3): 362–380. https://doi.org/10.1130/0016-7606(1983)94<362:SAEOAR>2.0.CO;2.
Fink, J.H., 1985. The geometry of silicic dikes beneath the Inyo Domes, California. J. Geophys. Res. 90:1127–1133. https://doi.org/10.1029/JB090iB13p11127.
Florisbal, L.M., Heaman, L.M., Janasi, V.A., Bitencourt, M.F., 2014. Tectonic significance of the Florianópolis Dyke Swarm, Paraná-Etendeka Magmatic Province: a reappraisal based on precise U-Pb dating. J. Volcanol. Geotherm. Res. 289:140–150. https://doi.org/10.1016/j.jvolgeores.2014.11.007.
Frank, H.T., Gomes, M.E.B., Formoso, M.L.L., 2009. Review of the areal extent and volume of the Serra Geral Formation, Paraná Basin, South America. Pesquisas em Geociências 36 (1), 49–57.
Furukawa, K., Uno, K., 2015. Origin and deformation of high porosity bands in the Takanoobane Rhyolite of Aso volcano, Japan. 305:76–83. https://doi.org/10.1016/j.jvolgeores.2015.09.021.
Furukawa, K., Uno, K., Miyagi, I., 2010. Mechanisms of oxidation and degassing in the Takanoobane rhyolite lava of Aso Volcano, Japan. J. Volcanol. Geotherm. Res. 198: 348–354. https://doi.org/10.1016/j.jvolgeores.2010.09.015.
Garland, F.E., Hawkesworth, C.J., Mantovani, M.S.M., 1995. Description and petrogenesis of the Paraná rhyolites. J. Petrol. 36:1193–1227. https://doi.org/10.1093/petrology/36.5.1193.
Geoffroy, L., Callot, J.P., Auborg, C., Moreira, M., 2002. Divergence between magnetic and plagioclases linear fabrics in dykes: a new approach for defining the flow vector using magnetic foliation. TerraNova 14, 183–190.
Gonnermann, H.M., Manga, M., 2003. Explosive volcanism may not be an inevitable consequence of magma fragmentation. Nature 426, 432–435.
Gonnermann, H.M., Manga, M., 2005. Flow banding in obsidian: a record of evolving textural heterogeneity during magma deformation. Earth Planet. Sci. Lett. 236:135–147. https://doi.org/10.1016/j.epsl.2005.04.031.
Goto, Y., Nakada, S., Kurokawa, M., Shimano, T., Sugimoto, T., Sakuma, S., Hoshizumi, H., Yoshimoto, M., Uto, K., 2008. Character and origin of lithofacies in the conduit of Unzen volcano, Japan. J. Volcanol. Geotherm. Res. 175 (1):45–59. https://doi.org/10.1016/j.jvolgeores.2008.03.041.
Green, J.C., Fitz III, T.L., 1993. Extensive felsic lavas and rheoignimbrites in the Keweenawan Midcontinent Rift plateau volcanics, Minnesota: petrographic and field recognition. J. Volcanol. Geotherm. Res. 54:177–196. https://doi.org/10.1016/0377-0273(93)90063-W.
Guimarães, L.F., Raposo, M.I.B., Janasi, V.A., Cañón-Tapia, E., Polo, L.A., 2017. An AMS study of different silicic units from the southern Paraná-Etendeka Magmatic Province in Brazil: implications for the identification of flow directions and local feeding. J. Volcanol. Geotherm. Res. (this issue).
Hall, S.H., 1978. The Stratigraphy of Northern Lipari and the Structure of the Rocche Rosse Rhyolite Flow and Its Implications. University of Leeds (Unpublished. B. Sc. Thesis).
Hausback, B.P., 1987. An extensive, hot, vapor-charged rhyodacite flow, Baja California, Mexico. GSA Special Papers vol. 212:pp. 111–118. https://doi.org/10.1130/SPE212-p111.
Heiken, G., Wohletz, K., Eichelberger, J., 1988. Fracture fillings and intrusive pyroclasts, Inyo domes, California. J. Geophys. Res. 93:4335–4350. https://doi.org/10.1029/JB093iB05p04335.
Henry, C.D., Wolff, J.A., 1992. Distinguishing strongly rheomorphic tuffs from extensive silicic lavas. Bull. Volcanol. 54:171–186. https://doi.org/10.1007/BF00278387.
Henry, C.D., Price, J.G., Rubin, J.N., Laubach, S.E., 1990. Case study of and extensive silicic lava: the Bracks Rhyolite, Trans-Pecos Texas. J. Volcanol. Geotherm. Res. 43: 113–132. https://doi.org/10.1016/0377-0273(90)90048-K.
Hrouda, F., 1985. The magnetic fabric in the Brno Massif. Sbor. Geol. Ved. Uz Geol. 19, 89–112.
Hrouda, F., Verner, K., Sárka, K., Buriánek, D., Faryad, S.W., Chlupácová, M., Holub, V.F., 2016. Magnetic fabric and emplacement of dykes of lamprophyres and related rocks of the Central Bohemian Dyke Swarm (Central European Variscides). J. Geosci. 61, 335–354.
Janasi, V.A., Montanheiro, T.J., Freitas, V.A., Reis, P.M., Negri, F.A., Dantas, F.A., 2007. Geology, petrography and geochemistry of the acid volcanism of the Paraná Magmatic Province in the Piraju-Ourinhos region, SE Brazil. Rev. Bras. Geosci. 37, 745–759.
Jaupart, C., Allegre, C.J., 1991. Gas content, eruption rate and instabilities of eruption regime in silicic volcanoes. Earth Planet. Sci. Lett. 102:413–429. https://doi.org/10.1016/0012-821X(91)90032-D.
Jerram, D., Mountney, N., Holzforster, F., Stollhofen, H., 1999. Internal stratigraphic relationships in the Etendeka group in the Huab Basin, NW Namibia: understanding the onset of flood volcanism. J. Geodyn. 28 (4–5):393–418. https://doi.org/10.1016/S0264-3707(99)00018-6.
Johnson, S.E., Paterson, S.R., Tate, M.C., 1999. Structure and emplacement history of a multiple-center, cone-sheet-bearing ring complex: the Zarza Intrusive Complex, Baja California, Mexico. Geol. Soc. Am. Bull. 111 (4), 607–619.
Kerr, R.C., 2009. Thermal erosion of felsic ground by the laminar flow of a basaltic lava, with application to the Cave Basalt, Mount St. Helens, Washington. J. Geophys. Res. 114 (B9).
Kirstein, L.A., Peate, D., Hawkesworth, C., Turner, S., Harris, C., Mantovani, M., 2000. Early Cretaceous basaltic and rhyolitic magmatism in southern Uruguay associated with the opening of the South Atlantic. J. Petrol. 41, 1413–1438.
Kirstein, L.A., Hawkesworth, C.J., Garland, F.G., 2001. Felsic lavas or rheomorphic ignimbrites: is there a chemical distinction? Contrib. Mineral. Petrol. 142:309–322. https://doi.org/10.1007/s004100100291.
Kurozumi, H., Doi, N., 2003. Inner structure of the Nigorikawa Caldera, Hokkaido, Japan. Bull. Volcano. Soc. Jap. 48 (3), 259–274.
Le Bas, M.J., Le Maitre, R.W., Zanettin, B., 1986. A chemical classification of volcanic rocks based on the total alkali-silica diagram. J. Pet. 27, 745–750.
LeMaitre, R.W., 1989. A Classification of Igneous Rocks and Glossary of Terms. Blackwell, Oxford.
Lima, E.F., Philipp, R.P., Rizzon, G.C., Waichel, B.L., Rossetti, L.M.M., 2012. Sucessões Vulcânicas e Modelo de Alimentação e Geração de Domos de Lava Ácidos da Formação Serra Geral na Região de São Marcos-Antonio Prado (RS). Geol. USP Ser. Cient. 12:49–64. https://doi.org/10.5327/Z1519-874X2012000200004.
Lima, E.F., Waichel, B.L., Rossetti, L.M.M., Sommer, C.A., Simões, M.S., 2018. Feeder systems of acidic lava flows from the Paraná-Etendeka Igneous Province in Southern Brazil and their implications for eruption style. J. S. Am. Earth Sci. 81, 1–9.
Lowman, N.K., Hoefer, M.A., 2013. Dispersive shock waves in viscously deformable media. J. Fluid Mech. 718, 524.
Manley, C.R., 1995. How voluminous rhyolite lavas mimic rheomorphic ignimbrites: eruptive style, emplacement conditions, and formation of tuff-like textures. Geology 23 (4):349–352. https://doi.org/10.1130/0091-7613(1995)023<0349:HVRLMR>2.3.CO;2.
Manley, C.R., 1996. Physical volcanology of a voluminous rhyolite lava flow: the Badlands lava, Owyhee Plateau, southwestern Idaho. J. Volcanol. Geotherm. Res. 71:129–153. https://doi.org/10.1016/0377-0273(95)00066-6.
Manley, C.R., Fink, J.H., 1987. Internal textures of rhyolite flows as revealed by research drilling. Geology 15 (6):549–552. https://doi.org/10.1130/0091-7613(1987)15<549:ITORFA>2.0.CO;2.
Marsh, J.S., Ewart, A., Milner, S.C., Duncan, A.R., Miller, R., 2001. The Etendeka Igneous Province: magma types and their stratigraphic distribution with implications for the evolution of the Paraná-Etendeka flood basalt province. Bull. Volcanol. 62, 464–486.
McPhie, J., Doyle, M., Allen, R., 1993. Volcanic Textures: a Guide to the Interpretation of Textures in Volcanic Rocks. University of Tasmania Centre for Ore Deposit and Exploration Studies, Hobart 198 pp.
Melfi, A.J., Nardy, A.J.R., Piccirillo, E.M., 1988. Geological and magmatic aspects of the Paraná Basin: an introduction. In: Piccirillo, E.M., Melfi, A.J. (Eds.), The Mesozoic Flood Volcanism of the Paraná Basin: Petrogenetic and Geophysical Aspects. Instituto Astronômico e Geofísico, São Paulo.
Miall, A.D., 2000. Principles of Sedimentary Basin Analysis. 3rd edition. Springer-Verlag Inc., New York (616 pp).
Milani, E.J., 2004. Comentários sobre a origem e evolução tectônica da Bacia Do Paraná. In: Mantesso Neto, V., Bartorelli, A., Carneiro, C.D.R., Brito Neves, B.B. (Eds.), Geologia Do Continente Sul-Americano: Evolução da obra de Fernando Flávio Marques de Almeida, São Paulo, Beca, pp. 265–279 (São Paulo).
Milani, E.J., Melo, J.H.G., Souza, P.A., Fernandes, L.A., França, A.B., 2007. Bacia do Paraná. Boletim de Geociências da PETROBRAS vol. 15(2), pp. 265–287.
Milner, S.C., Duncan, A.R., 1987. Geochemical characterization of quartz latite units in the Etendeka Formation. Communications of the Geological Survey of Namibia 3:83–90. https://doi.org/10.1007/BF00278389.
Milner, S.C., Duncan, A.R., Ewart, A., 1992. Quartz latite rheoignimbrite flow of the Etendeka Formation, North-Western Namibia. Bull. Volcanol. 54:200–219. https://doi.org/10.1007/BF00278389.
Milner, S.C., Duncan, A.R., Whittingham, A.M., Ewart, A., 1995. Trans-Atlantic correlation of eruptive sequences and individual silicic volcanic units within Paraná-Etendeka Igneous Province. J. Volcanol. Geotherm. Res. 69:137–157. https://doi.org/10.1016/0377-0273(95)00040-2.
Morrow, N., McPhie, J., 2000. Mingled silicic lavas in the Mesoproterozoic Gawler Range Volcanics, South Australia. J. Volcanol. Geotherm. Res. 96:1–13. https://doi.org/10.1016/S0377-0273(99)00143-2.
Nardy, A.J.R., Machado, F.B., Oliveira, M.A.F., 2008. As rochas vulcânicas mesozoicas ácidas da Bacia do Paraná: litoestratigrafia e considerações geoquímicas-estratigráficas. Rev. Bras. Geosci. 38 (1), 178–195.
Nelson, S.A., 1981. The possible role of thermal feedback in the eruption of siliceous magmas. J. Volcanol. Geotherm. Res. 11:127–137. https://doi.org/10.1016/0377-0273(81)90019-6.
Okomura, S., Nakamura, M., Uesugi, K., Nakano, T., Fujioka, T., 2013. Coupled effect of magma degassing and rheology on silicic volcanism. Earth Planet. Sci. Lett. 362: 163–170. https://doi.org/10.1016/j.epsl.2012.11.0560.
Pankhurst, M.J., Schaefer, B.F., Betts, P.G., Phillips, N., Hand, M., 2011. A Mesoproterozoic continental flood rhyolite province, the Gawler Ranges, Australia: the end member example of the Large Igneous Province clan. Solid Earth 2:25–33. https://doi.org/10.5194/se-2-25-2011.
Peate, D.W., 1997. The Paraná-Etendeka province. In: Mahoney, J.J., Coffin, M.R. (Eds.), Large Igneous Proovinces: Continental, Oceanic and Planetary Flood Volcanism. Geoph. Monog. 100, pp. 217–245.
Peate, D.W., Hawkesworth, C.J., Mantovani, M.S.M., 1992. Chemical stratigraphy of the Paraná lavas (S. America): classification of magma types and their spatial distribution. Bull. Volcanol. 55:119–139. https://doi.org/10.1007/BF00301125.
Petrini, R., Civetta, L., Iacumin, P., Longinelli, A., Bellieni, G., Comin-Chiaramonti, P., Ernesto, M., Marques, L.S., Melfi, A., Pacca, I., Piccirillo, E.M., 1989. High temperature flood silicic lavas (?) from the Paraná Basin (Brasil). Bull. New Mex. Bur. Min. Mineral Resour. 131, 213.
Philpotts, A.R., Philpots, D.E., 2007. Upward and downward flow in a camptonite dike as recorded by deformed vesicles and the anisotropy of magnetic susceptibility (AMS). J. Volcanol. Geotherm. Res. 161, 81–94.

Please cite this article as: Simões, M.S., et al., Structures and lithofacies of inferred silicic conduits in the Paraná-Etendeka LIP, southernmost Brazil, J. Volcanol. Geotherm. Res. (2017), https://doi.org/10.1016/j.jvolgeores.2017.12.013

Piccirillo, E.M., Bellieni, G., Cavazzini, G., Comin-Chiaramonti, P., Petrini, R., Melfi, A.J., Pinese, J.P.P., Zantadeschi, P., DeMin, A., 1990. Lower Cretaceous tholeiitic dyke swarms from the Ponta Grossa Arch (southeast Brazil): petrology, Sr–Nd isotopes and genetic relationships with the Paraná flood volcanics. Chem. Geol. 89 (1–2): 19–48. https://doi.org/10.1016/0009-2541(90)90058-F.

Plenier, G., Camps, P., Henry, B., Ildefonse, B., 2005. Determination of flow directions by combining AMS and thin-section analyses: implications for Oligocene volcanism in the Kerguelen Archipelago (southern Indian Ocean). Geophys. J. Int. 160 (1), 63–78.

Polo, L.A., Janasi, V.A., 2014. Volcanic stratigraphy of intermediate to silicic rocks in Southern Paraná Magmatic Province, Brazil. Geol. USP Ser. Cient 14:83–100. https://doi.org/10.5327/Z1519-874X201400020005.

Polo, L.A., Giordano, D., Janasi, V.A., Guimarães, L.F., 2017. Effusive silicic volcanism in the Paraná Magmatic Province, South Brazil: physico-chemical conditions of storage and eruption and considerations on the rheological behaviour during emplacement. J. Volcanol. Geotherm. Res. (this issue).

Raposo, M.I.B., 1997. Magnetic fabric and its significance in the Florianópolis dyke swarm, southern Brazil. Geophys. J. Int. 131:159–170. https://doi.org/10.1111/j.1365-246X.1997.tb00602.x.

Raposo, M.I.B., Ernesto, M., Renne, P.R., 1998. Paleomagnetism and dating of the early Cretaceous Florianópolis dike swarm (Santa Catarina Island), Southern Brazil. Phys. Earth Planet. Inter. 108 (4):275–290. https://doi.org/10.1016/S0031-9201(98)00102-2.

Rochette, P., Jenatton, L., Dupuy, C., Boudier, F., Reuber, I., 1991. Emplacement modes of basaltic dykes in the Oman ophiolite: evidence from magnetic anisotropy with reference to geochemical studies. In: Peters, T.J., Nicolas, A., Coleman, R.J., Dordrecht, K. (Eds.), Ophiolite Genesis and the Evolution of the Oceanic Lithosphere, pp. 55–82.

Roisenberg, A., 1989. Petrologia e geoquímica do vulcanismo ácido mesozoico da Província Meridional da Bacia do Paraná. Instituto de Geociências, Universidade Federal do Rio Grande do Sul, Porto Alegre (PhD Thesis).

Rossetti, L.M.M., Lima, E.F., Waichel, B.L., Scherer, C.M.S., Barreto, C.J., 2014. Stratigraphical framework of basaltic lavas in Torres Syncline main valley, Southern Paraná-Etendeka Volcanic Province. J. S. Am. Earth Sci. 56:409–421. https://doi.org/10.1016/j.jsames.2014.09.025.

Rossetti, L., Lima, E.F., Waichel, B.L., Hole, M.J., Simões, M.S., Scherer, C.M.S., 2017. Lithostratigraphy and volcanology of the Serra Geral Group, Paraná-Etendeka Igneous Province in Southern Brazil: towards a formal stratigraphical framework. J. Volcanol. Geotherm. Res. (this issue).

Rust, A.C., Cashman, K.V., Wallace, P.J., 2004. Magma degassing buffered by vapor flow through brecciated conduit margins. Geology 32:349–352. https://doi.org/10.1130/G20388.2.

Seaman, S.J., 1995. Multi-stage magma mixing and mingling and the origin of flow banding in the Aliso Lava Dome, Tumacacori Mountains, southern Arizona. J. Geophys. Res. 100:8381–8398. https://doi.org/10.1029/94JB03260.

Seaman, S.J., 2013. Microtexture development during rapid cooling in three rhyolitic lava flows. Am. Mineral. 98:304–318. https://doi.org/10.2138/am.2013.4313.

Seaman, S.J., Dyar, M.D., Marinkovic, N., 2009. The effects of hererogeneity in magma water concentration on the development flow banding and spherulites in rhyolitic lava. J. Volcanol. Geotherm. Res. 183:157–169. https://doi.org/10.1016/j.jvolgeores.2009.03.001.

Shields, J.K., Mader, H.M., Caricchi, L., Tuffen, H., Mueller, S., Pistone, M., Baumgartner, L., 2016. Unravelling textural heterogeneity in obsidian: shear-induced outgassing in the Rocche Rosse flow. J. Volcanol. Geotherm. Res. 310:137–158. https://doi.org/10.1016/j.jvolgeores.2015.12.003.

Sillitoe, R.H., Baker, E.M., Brook, W.A., 1984. Gold deposits and hydrothermal eruption breccias associated with a maar volcano at Wau, Papua New Guinea. Econ. Geol. 79:638–655. https://doi.org/10.2113/gsecongeo.79.4.638.

Simões, M.S., Rossetti, L.M.M., Lima, E.F., Ribeiro, B.P., 2014. The role of viscosity in the emplacement of high-temperature silicic flows of Serra Geral Formation in Torres Syncline (Rio Grande do Sul State, Brazil). Braz. J. Geol. 44 (4):669–679. https://doi.org/10.5327/Z2317488920140040010.

Simões, M.S., Lima, E.F., Sommer, C.A., Rossetti, L.M.M., 2017. The Mato Perso Conduit System: evidence of silicic magma transport in the Paraná-Etendeka LIP. Braz. J. Geol. (accepted manuscript).

Smith, J.V., 1996. Ductile-brittle transition structures in the basal shear zone of a rhyolite lava flow, eastern Australia. J. Volcanol. Geotherm. Res. 72, 217–223.

Stasiuk, M.V., Barclay, J., Carroll, M.R., Jaupart, C., Ratté, J.C., Sparks, R.S.J., Tait, S.R., 1996. Degassing during magma ascent in the Mule Creek vent (USA). Bull. Volcanol. 58: 117–130. https://doi.org/10.1007/s004450050130.

Thordarson, T., Larsen, G., 2007. Volcanism in Iceland in historical time: volcano types, eruption styles and eruptive history. J. Geodyn. 43:118–152. https://doi.org/10.1016/j.jog.2006. 09.005.

Tuffen, H., Castro, J.M., 2009. The emplacement of an obsidian dyke through thin ice: Hrafntinnuhryggur, Krafla Iceland. J. Volcanol. Geotherm. Res. 185:352–366. https://doi.org/10.1016/j.jvolgeores.2008.10.021.

Tuffen, H., Dingwell, D.B., 2005. Fault textures in volcanic conduits: evidence for seismic trigger mechanisms during silicic eruptions. Bull. Volcanol. 67:370–387. https://doi.org/10.1007/s00445-004-0383-5.

Tuffen, H., Dingwell, D.B., Pinkerton, H., 2003. Repeated fracture and healing of silicic magma generate flow banding and earthquakes? Geology 31:1089–1092. https://doi.org/10.1130/G19777.1.

Tuffen, H., James, M.R., Castro, J.M., Pyle, D.M., Mather, T.A., Geraki, T., 2013. Exceptional mobility of a rhyolitic obsidian flow: observations from Cordón Caulle, Chile, 2011–2013. Nat. Commun. 4:2709. https://doi.org/10.1038/ncomms3709.

Umann, L.V., Lima, E.F., Sommer, C.A., De Liz, J.D., 2001. Vulcanismo ácido da região de Cambará do Sul-RS: litoquímica e discussão sobre a origem dos depósitos. Rev. Bras. Geosci. 31 (3):357–364. https://doi.org/10.5327/rbg.v31i3.950.

Valente, S.d.C., Corval, A., Duarte, B.P., Ellam, R.M., Fallick, A.E., Meighan, I.G., Dutra, T., 2007. Tectonic boundaries, crustal weakness zones and plume-subcontinental lithospheric mantle interactions in the Serra do Mar dyke swarm, SE Brazil. Rev. Bras. Geosci. 37 (1), 194–201.

Varga, J.V., Gee, J.S., Staudigel, H., Tauxe, L., 1998. Dike surface lineations as magma flow indicatiors within the sheeted dike complex of the Troodos ophiolite, Cyprys. J. Geophys. Res. 103, 5241–5256.

Waichel, B.L., Lima, E.F., Viana, A.R., Scherer, C.M.S., Bueno, G.V., Dutra, G.T., 2012. Stratigraphy and volcanic facies architecture of the Torres Syncline, Southern Brazil, and its role in understanding the Paraná-Etendeka Continental Flood Basalt Province. J. Volcanol. Geotherm. Res. 215:74–82. https://doi.org/10.1016/j.jvolgeores.2011.12.004.

Zalán, P.V., Wolff, S., Conceição, J.C.J., Astolfi, M.A.M., Vieira, I.S., Appi, V.T., Zanotto, A.O., Marques, A., 1991. Tectonics and sedimentation of the Paraná Basin. Gondwana Symposium, 7: São Paulo, Brazil.

Závada, P., Schulmann, K., Lexa, O., Hrouda, F., Haloda, J., Týcová, P., 2009. The mechanism of flow and fabric development in mechanically anisotropic trachytes lava. J. Struct. Geol. 31, 1295–1307.

Please cite this article as: Simões, M.S., et al., Structures and lithofacies of inferred silicic conduits in the Paraná-Etendeka LIP, southernmost Brazil, J. Volcanol. Geotherm. Res. (2017), https://doi.org/10.1016/j.jvolgeores.2017.12.013

DOI: 10.1590/2317-4889201820170080

ARTICLE

The Mato Perso Conduit System: evidence of silicic magma transport in the southern portion of the Paraná-Etendeka LIP, Brazil

Matheus Silva Simões[1,2]*, Evandro Fernandes de Lima[1], Carlos Augusto Sommer[1], Lucas de Magalhães May Rossetti[1,3]

ABSTRACT: *The Mato Perso Conduit System is described from a ~ 120 km² area in south Brazil exposing silicic volcanics of the Paraná-Etendeka LIP. A volcanic succession is defined by basaltic flows covered by flat-lying oxidized vitrophyres, banded vitrophyres cutting the lower lavas and grey flat-lying vitrophyres covering all the units. Flow morphologies determined by the recognition of structures, textures, and vesicle distribution were observed. Oxidized vitrophyres display massive flat-lying banded cores and flow tops from vesicular to frothy. Grey flat-lying vitrophyres have sharp contacts in the top of both basalt flows and oxidized vitrophyres, locally exhibit basal breccia and have a flat-lying foliation. Conduits are represented by banded vitrophyres and breccias, which outcrop in a 6 km wide, NW-SE oriented segment downthrown by normal faults towards the Antas River. The interpretation of the units on the geological map scale indicates intrusive contact relations. Recognition of dike-like structures in banded vitrophyres and dykes of oxidized vitrophyre are evidence of felsic magma transport. Based on field observations, we propose the emplacement of subaerial oxidized and grey vitrophyres fed by a fault-related conduit system. Sustained high temperature magmatic systems ensure the silicic lavas have a low viscosity and travel great distances.*

KEYWORDS: *Large Igneous Province; magma transport; conduit system; Paraná-Etendeka LIP; Paraná Basin.*

INTRODUCTION

The Paraná-Etendeka Large Igneous Province (LIP) is exposed primarily in South America (~90 outcrop area%), with a minor portion in the African continent (~10 outcrop area%). It erupted at ~134–131 Ma (Ernesto *et al.* 1999, Thiede & Vasconcelos 2010, Janasi *et al.* 2011, Florisbal *et al.* 2014) in an intraplate setting, after a long period of marine and continental sedimentation in the Paraná Basin (for the South American counterpart). This basin is considered a large intracratonic syneclise developed in western Gondwana (Allen & Armitage 2012). In the Cretaceous, the Andean chain uplifting started in the west of this supercontinent, while continental extension accompanied by voluminous volcanism were dominant within the continent (Milani & Ramos 1998). Those episodes were followed by rifting and seafloor spreading, leading to the opening of the South Atlantic Ocean. In South America, this LIP occupies approximately, 917,000±15,000 km² (Frank *et al.* 2009) of a 1,700 m-thick tholeiitic rock association (Melfi *et al.* 1988) with basic to intermediate volcanics dominating (97.5% in volume) over silicic volcanics (2.5% in volume).

The plumbing system which transported magma and fed the volcanic pile on the surface is represented by Ponta Grossa (NW-SE), Santos-Rio de Janeiro (ENE-SSW) and Florianópolis (NNE-SSW) dyke swarms. These intrusive systems are the main exposures of diabase dykes and sills throughout the Paraná Basin (Melfi *et al.* 1988, Raposo & Ernesto 1995, Peate 1997, Raposo *et al.* 1998, Florisbal *et al.* 2014) and are located north of Torres Valley (Fig. 1). In the southern part of the basin, the mafic dykes cutting the sedimentary rocks have NE-SW preferred orientation.

[1]Programa de Pós-Graduação, Instituto de Geociências, Universidade Federal do Rio Grande do Sul – UFRGS, Porto Alegre (RS), Brazil. *E-mails: matheus.simoes@ufrgs.br, evandro.lima@ufrgs.br, casommer@sinos.net, lucasross@hotmail.com*

[2]Serviço Geológico do Brasil – CPRM, Manaus (AM), Brazil.

[3]Department of Geology and Petroleum Geology, University of Aberdeen – Aberdeen, United Kingdom.

*Corresponding author.

Manuscript ID: 20170080. **Received on:** 06/16/2017. **Approved on:** 01/11/2018.

These dykes trend NNW-SSE when cutting the volcanic pile (Sarmento *et al.* 2017).

Silicic dykes are less common among the intrusive units. An example is the Florianópolis dyke swarm, where they are described as ~70–80 m thick porphyritic vitrophyre dykes trending NNE-SSW and NNW-SSE (Marteleto *et al.* 2016). Composite dykes with basaltic andesite mingled with rhyodacite also occur (Tomazzoli & Lima 2006). The intrusive felsic magmatism in the south of this basin is represented by one ~1 m thick occurrence of rhyodacite dyke in the Praia Grande — Cambará do Sul profile (Piccirillo *et al.* 1988). Assuming an average thickness of 120 m for felsic units in southern Brazil (maximum of 400 m, e.g. Rossetti *et al.* 2017) and an estimated volume of 12,000 km^3, one should expect a larger volume of silicic intrusive in the LIP.

The purpose of this work was to present a mapped area of the northeast of the state of Rio Grande do Sul, which exposes different silicic vitrophyre units previously recognized only as fragments within the conduits (e.g. Lima *et al.* 2012, 2017, Simões *et al.* 2017). Field relationships, internal

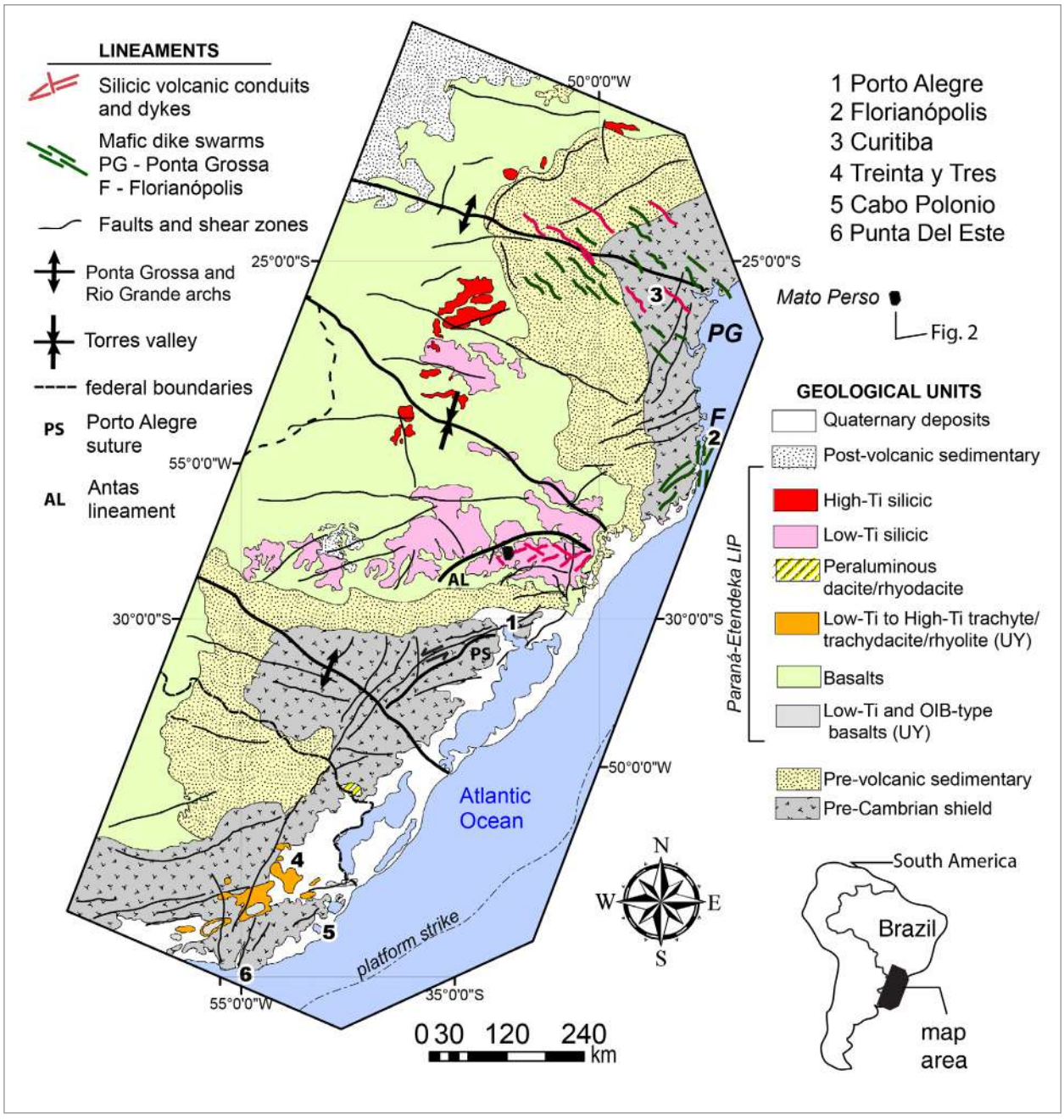

Figure 1. Distribution of Paraná-Etendeka volcanic units in eastern Brazil (UY corresponds to volcanics in Uruguay). The compilation of units and the main structures are from Fernandes *et al.* (1995), Kirstein *et al.* (2000), Nardy *et al.* (2008) and Florisbal *et al.* (2014).

morphologies of the lava flows, structural patterns and vitrophyre texture are shown in order to discuss the magma transport and emplacement, considering their implications for effusive volcanic episodes in the south of the Paraná Basin.

GEOLOGICAL BACKGROUND

In southern Brazil, the volcanic units of Paraná-Etendeka LIP are represented by the Serra Geral Group (Rossetti *et al.* 2017). This association is chemically more primitive and is dominated by simple pahoehoe basaltic flows in the base, assigned to the Torres Formation. The Vertically stacked, sheet-like, rubbly pahoehoe basaltic flows of the Vale do Sol Formation cover the compound flows and represent the more voluminous basaltic lava unit. The silicic volcanics overlying these basalt flows are assigned to the Palmas Formation. The last volcanic manifestations in the area are the compound and simple oxidized mafic flows of Esmeralda Formation.

The chemical classification of the volcanics is based primarily on the TiO_2 content of basic and silicic terms (e.g., Bellieni *et al.* 1984; Peate *et al.* 1992). High-Ti (TiO_2 > 2 wt.%) volcanics are called Chapecó-type magmas (Peate *et al.* 1992). They are exposed in the northern portion of the basin and scarce in the south of Torres Valley (Fig. 1), a NW-SE oriented depositional locus between the Ponta Grossa and Rio Grande arches. In the southern portion of the basin, both mafic and felsic magmas have low-Ti (TiO_2 < 2 wt.%) content. Palmas-type volcanics are dacites and rhyolites presenting no more than ~10 vol.% of phenocrysts. Chapecó-type volcanics are porphyritic, chemically classified as trachytes, with phenocryst content up to ~25 vol.%. Trachytes have higher Ba, Nb, La, Ce, Zr, P, Nd, Y, Yb, Lu and K, being depleted in Rb, Th and U in relation to low-Ti volcanics of the Palmas-type (Peate *et al.* 1992, Peate 1997, Nardy *et al.* 2008).

Further south in the LIP, a small area (3.2 km^3) of peraluminous dacitic lavas with cordierite, orthopyroxene, plagioclase and ilmenite as liquidus phases (Vieira Jr. 1985, Vieira Jr. & Roisemberg 1985) is present in the Jaguarão region, and is related to major shear zones from the Neoproterozoic age that may have been reactivated during the Early Cretaceous (Comin-Chiaramonti *et al.* 2010). In Uruguay, the volcanics are NE-trending oriented and the rocks are also bimodal. The basaltic Santa Lucía magma type has Oceanic Island Basalt (OIB) geochemical signatures with high Nb/La and Treinta Y Trés is broadly similar to the low-Ti Gramado lavas (Kirstein *et al.* 2000). Silicic rocks are dacites to rhyolites from Lavalleja Series (high Ti/Zr, low Nb/Y, higher Sr and Nd isotope ratios) and Aigua Series (high Rb/Sr, high Rb/Ba, high Th).

Figure 1 shows the spatial distribution of different silicic volcanic chemical types in the Paraná-Etendeka LIP. Precambrian structures are highlighted and differentiated from younger faults also cross-cutting the basin. The Ponta Grossa and Santa Catarina dyke swarms as well as postulated conduit systems in Rio Grande do Sul are represented by traces with directions compiled from the literature (Raposo 1997, Florisbal *et al.* 2014, Simões *et al.* 2017; this study).

EMPLACEMENT OF SILICIC UNITS IN PARANÁ-ETENDEKA LIP

The silicic volcanics of the Serra Geral Group generally outcrop with a laterally wide sheet-like form. Bellieni *et al.* (1986) observed this geometry and suggested an explosive origin for the deposits. It was admitted that Palmas-type flows could be traced over 60 km, but typical ignimbrite textures were not usually found. These silicic volcanics were first described as volatile-poor and high-temperature rheomorphic ignimbrites. Arguments used include their laterally persistent sheet-like nature and the absence of typical ignimbrite textures even near the top and base of each unit, which was attributed to obliteration by intense welding (Bellieni *et al.* 1986, Melfi *et al.* 1988, Petrini *et al.* 1989, Roisenberg 1989, Garland *et al.* 1995, Milner *et al.* 1995, Bryan *et al.* 2010). Milner *et al.* (1995) proposed the correlation of some subgroups of Palmas magma-type with the Namibian quartz latites. The intrusive, circular Messum Complex was identified as a potential emission center (Milner & Duncan 1987, Milner *et al.* 1992, Ewart *et al.* 1998, 2002), even though the thickness of the silicic volcanic sequence is inferior in the African counterpart. In these models, the silicic deposits in South America would need to have traveled > 300 km from their source and been deposited as extensive pyroclastic density currents (e.g., Milner *et al.* 1995, Bryan *et al.* 2010).

The paucity of pyroclastic lithofacies, with recognition of only local pyroclastic textures in extensive petrographic studies (Comin-Chiaramonti *et al.* 1988), together with the regional description of coherent and autoclastic lithofacies in a variety of lava bodies (lobes, domes and flows) led other authors to suggest that the silicic deposits are predominantly effusive (Henry & Wolff 1992, Umann *et al.* 2001, Lima *et al.* 2012, Polo & Janasi 2014, Simões *et al.* 2014, Guimarães *et al.* 2015; Polo *et al.* 2017). Silicic lava feeder conduits were described showing compound magmatic foliation revealed by bands of contrasting crystallinity and oxidation (Lima *et al.* 2012, 2017).

Typical pyroclastic deposits are found in the Mesozoic (132–124 Ma) Arequita Formation (AF), Uruguay, and

described by Muzio *et al*. (2009). The AF contains high SiO_2 (> 72 wt.%) lava flows with quartz, K-feldspar and sodic plagioclase phenocrysts. The deposits are confined to the east of the India Muerta Lineament and are consisted of pyroclastic breccias, lapilli tuffs and monomictic breccias. The composition of the pyroclastic rocks is very similar to the lava flows and both are chemically more evolved than the counterpart Brazilian silicic units (with SiO_2 contents of 63–73%, Garland *et al*. 1995).

Conduit feeder systems were first proposed and described in quarries at the city of São Marcos, Rio Grande do Sul (e.g., Lima *et al*. 2012, De Campos *et al*. 2016, Lima *et al*. 2017). This region is characterized by the exposure of vitrophyres with a compound magmatic foliation with alternating layers of different crystallinity and oxidation (Lima *et al*. 2012). Fragmentation episodes involving rheomorphic and re-melting events were described by De Campos *et al*. (2016) and the authors suggested parallel oscillations in a very efficient magma ascent system together with high heat flux for conduit evolution.

The ubiquitous NE-SW or NW-SE orientations of dominantly sub-vertical banding in banded vitrophyres in northeastern Rio Grande do Sul is consistent with the orientation of the main pre-existing Precambrian structures. Some felsic vitrophyre and obsidian flows are aligned according to the regional faulting structural patterns (Simões *et al*. 2015, 2017). The observation of other expositions sharing very similar structural and stratigraphic arrangement at Caxias do Sul, São Marcos, Jaquirana and Cambará do Sul cities indicate that it is widespread along the Antas River adjacencies (Simões *et al*. 2015). The recognition of these systems is an important key to understanding how magma ascended through the crust to the surface as hot voluminous pyroclastic density currents or as structurally-controlled effusive lava flows.

MATO PERSO CONDUIT SYSTEM (MPCS)

The Mato Perso Conduit System (MPCS) is located at the south hinge of Torres Valley, in a district of the city of Farroupilha.. It outcrops in the highest elevations of Farroupilha and Caxias do Sul cities, being covered by dominantly flat-lying grey vitrophyres.

One characteristic feature of MPCS vitrophyres is their microporphyritic texture, with 2–11 vol.% of plagioclase, pyroxene and Ti-magnetite microphenocrysts. This characteristic is found in oxidized, banded and upper grey vitrophyres. Oxidized red vesicular vitrophyres occur as fragments inside red and black poorly-vesicular vitrophyres. Black vitrophyres cross-cut red vitrophyres, but also have very localized oxidized bands. The mixing patterns between these units generate banded lithofacies with dominant sub-vertical (> 60º) to subordinate flat-lying (< 30º) banding. Both banded and coherent vitrophyres have plagioclase (6/10) + clinopyroxene (3/10) + Fe-Ti oxides (1/10) as microphenocrysts. The same mineral assemblage is present in the groundmass as microlites (pl. 4/10, Fe-Ti ox. 4/10, cpx. 2/10) together with apatite (early magmatic) ± quartz (late-magmatic).

Mapping and identification of volcanic units

The geological mapping of the investigated area was made on a scale of 1:50,000, allowing the recognition of different vitrophyre units formerly recognized as fragments in the conduits (Lima *et al*. 2012, Simões *et al*. 2015, De Campos *et al*. 2016). The geological map (Fig. 2) and the interpreted cross-sections (Fig. 3) demonstrate that banded vitrophyres are distributed in a NW-SE trending region and the relationship with the subaerial silicic volcanics is detailed in section 2.2.5. Other details and features of mapped units are discussed in the following sections.

LITHOLOGICAL UNITS

Basaltic rubbly pahoehoe flows (Vale do Sol Formation)

Mafic volcanics are at the base of the volcanic succession in Mato Perso and outcrop in elevations of 290 m (Fig. 3), where they are under grey flat-lying vitrophyre flows on road RS-448 (Fig. 4A). The tops of the basalt flows tend to be covered by vegetation, but in the exposures below them, a vesicular carapace with cm-scale spherical and stretched vesicles filled with calcite crystals (Fig. 4B) can be found. In faulted regions, the basalt flows outcrop at elevations of 470 to 495 m. The tops of the flows also contain rubble (Fig. 4C) and the basaltic units were strongly affected by normal faults, registered in fault slickensides with vertical steps and crystallization of fibrous minerals (Fig. 4D). Regional correlation and the presence of rubble in the top of the flows of the area suggest that the mafic unit belongs to the Vale do Sol Formation, composed of rubbly pahoehoe basaltic and basaltic-andesite flows.

Oxidized vitrophyres (Ov)

The oxidized vitrophyres (Ov) are the lowest silicic unit in the succession. They occur as flat-lying units occupying the valleys in elevations between 350 and 600 m (Figs. 2 and 3). Ov are aphanitic to microporphyritic, showing sparse plagioclase and pyroxene microphenocrysts in a vitreous matrix. A large spectrum of vesiculation degree in Ov varies throughout the parts of the flows. Thus, the vitrophyres can be divided into poorly and highly vesiculated.

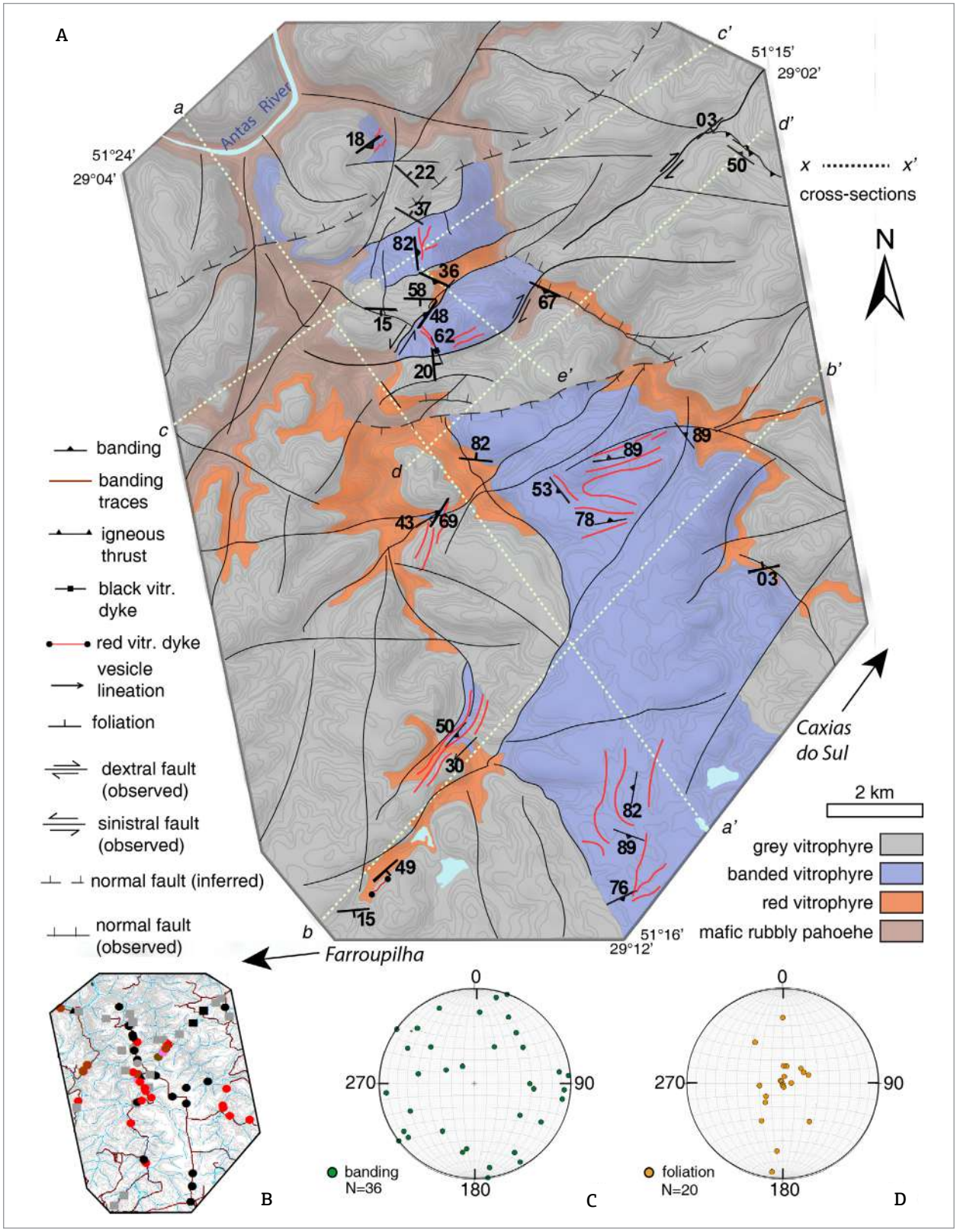

Figure 2. (A) Geological map of Mato Perso area, between cities of Caxias do Sul and Farroupilha indicating the cross-sections of Figure 3 and with (B) geological station map showing the distribution of mapped units (dots: red-oxidized vitrophyre, black-banded vitrophyre, grey- grey flat-lying vitrophyre, brown-basalt rubbly pahoehoe) and roads (brown lines); (C) stereonet showing the variable dipping distribution of poles of banding planes in banded vitrophyres (N = 36); (D) poles of magmatic foliation planes in grey vitrophyres with dominant flat-lying planes (N = 20).

Poorly vesiculated vitrophyre lithofacies are 2–3 m thick units (Fig. 5A) with flat-lying banding marked by cm-spaced continuous planes of more or less oxidized rock (Fig. 5B). The banding is reinforced by regular foliation spaced at approximately 7 cm. The presence of only sparse mm-size spheroid vesicles gives the vitrophyre a vesicle-absent appearance (Fig. 5B).

Vesiculated lithofacies are characterized by globular or stretched vesicles and quartz/calcite-filled amygdales ranging from few millimeters to 5–8 cm (Fig. 5C). Some of the cavities are cm-sized pockets filled with quartz-cemented autobreccias. The breccias are composed of very angular vitrophyre fragments with several mm- to cm-scale sizes (Fig. 5D). The upper parts of the Ov display a frothy (highly vesiculated) aspect with vesicles of up to 1 cm. In this part of the flow, vesicles have a less dispersed size range (Fig. 5E). The vesicles acquire stretched patterns and develop another type of autobreccia with cm-size angular vitrophyre fragments embedded in diaphanous quartz cement (Fig. 5F).

Banded vitrophyres (Bv)

Banded vitrophyres (Bv) occupy an approximately 15-km long NW-SE oriented area from the high elevations of Caxias do Sul city (~760 m) to the valleys at 550 m and 405 m elevations in Mato Perso where their occurrence is more restricted. This unit is characterized by a conspicuous colored banding marked by alternating bands of red to black vitrophyre.

In the valleys, Bv's occur in isolated outcrops where the banding is dominantly sub-vertical (dipping 82 to SW — Fig. 6A). Other exposures display tabular shapes resembling a dike-like structure (Fig. 6B). In this case, the banding parallel to the structure dips 69º–58º to NE and NW. The complex magmatic flow generated a broad range of fold geometries which modify the direction and dip of the bands. Stretched or open types are generally common (Fig. 6C). The presence of boudinated vitrophyre layers parallel to the banding with quartz venules filling the void spaces is another common feature (Fig. 6D).

In the highlands, at elevations of approximately 750 m, the Bv.s are well exposed and exhibit a wide range of magmatic structures which passes from ductile to fragile fields. A common feature of Bv, in the center of the conduits, is the divergent opening geometry formed by the sub-vertical bands with stretched to isoclinal parasitic folds (Fig. 7A). To the boards, Bv gets more oxidized and engulfs cm-sized black vitrophyre angular fragments (Figs. 7B and 7C); the occurrence of boxwork-like fracturing filled with quartz and the intense mixing of oxidized to less-oxidized layers is frequent. Banded vitrophyres register several folding

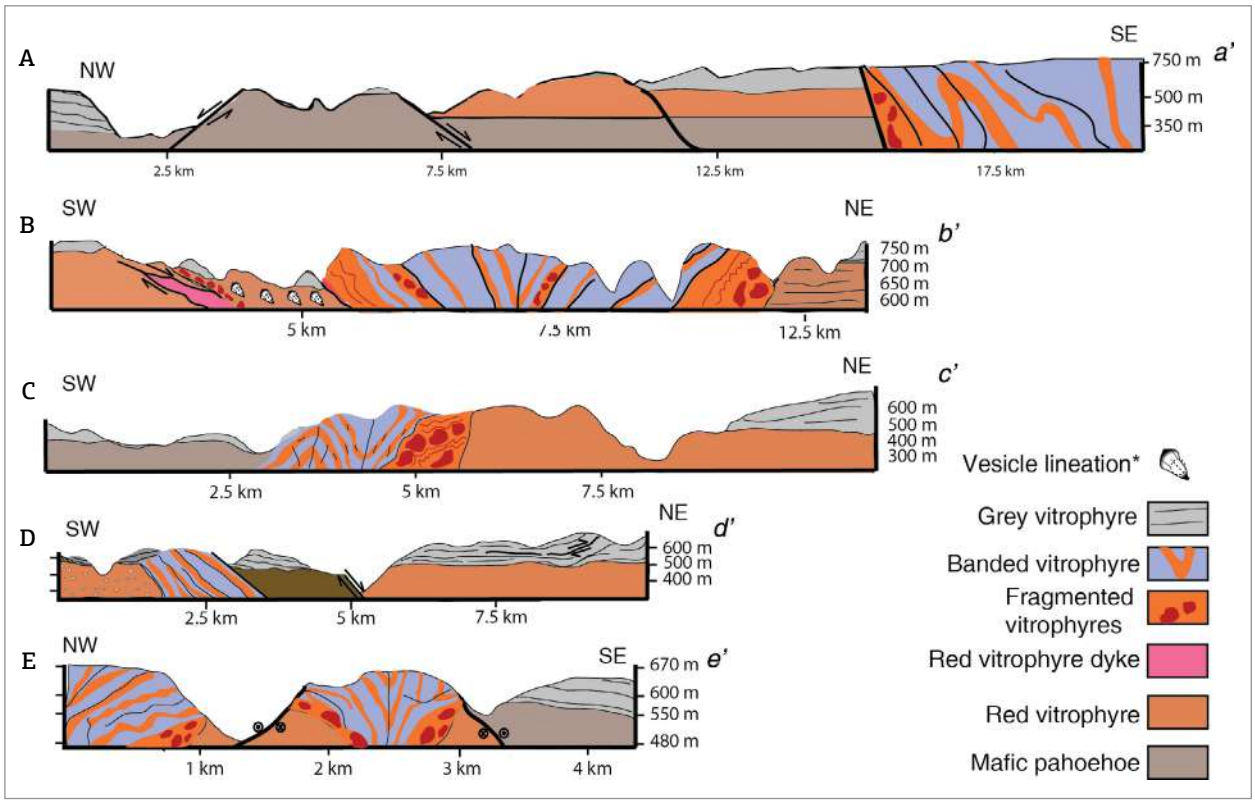

Figure 3. Geological cross-sections showing the field relations between the vitrophyre units. The position of the sections is present in Figure 2. Vesicle lineation* symbol cuts the plane of the paper, plunging to SE.

phases with quartz-filled fractures parallel to the axial surface of F4-phase folds (Fig. 7D). Localized outcrops show the banding of Bv thrusting over a more competent vitrophyre layer (Fig. 7E). Structures reveal that fractions of the magma banding are stretched by backflow movement (Fig. 7F).

A banded vitrophyre exposure laterally associated with breccia outcrops is present in the central part of cross-section 'e' in Figure 3. If we look at this outcrop in detail (Fig. 8A), banded vitrophyres carry and contour large oxidized fragments (Fig. 8B) besides presenting F3-phase folds with flat-lying limbs (Fig. 8C). To board of the system, cm-sized oxidized vitrophyre fragments with high vesicle content are embedded in the banded vitrophyre (Fig. 8D).

Grey flat-lying vitrophyres (Gv)

Grey flat-lying vitrophyres (Gv) are widespread in the area and outcrop in the highest elevations near the city of Caxias do Sul (~803 m) down to 610 m in the São Vitor region, toward northwest. This unit is generally composed of overlying red oxidized vitrophyres and has microporphyritic texture. In the proximities of the Antas River, the Gv occur covering basaltic rubbly pahoehoe flows at an elevation of ~300 m (see section 4). The main feature of Gv is its flat shape, highlighted in the relief by the absence of intense vegetation. This shape is sustained by a penetrative foliation which is flat-lying (< 20º) in most outcrops but can dip to ~40º to 80º (Fig. 9A).

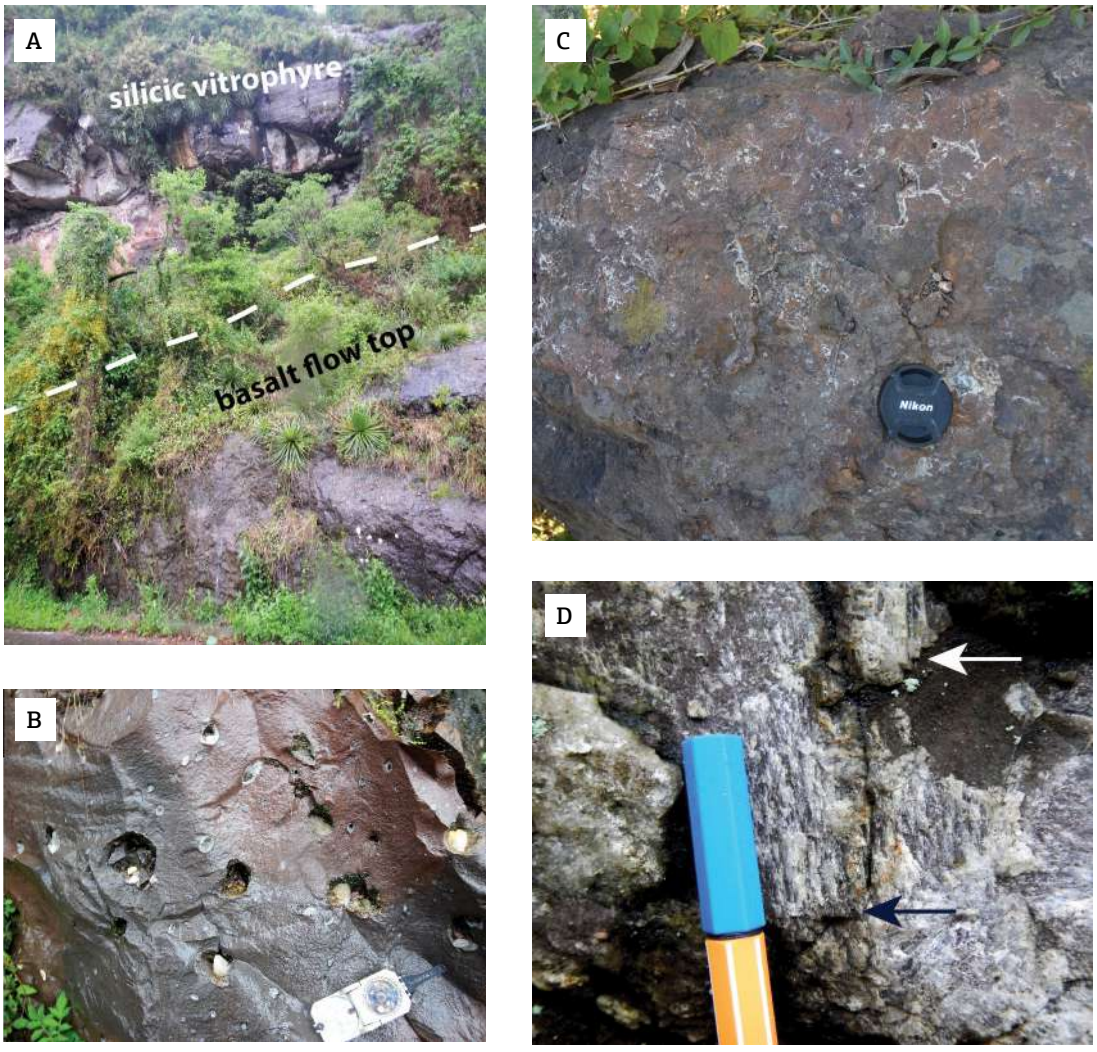

Figure 4. Field features of basaltic flows in the base of the volcanic succession (Vale do Sol Formation). (A) Top of a rubbly pahoehoe flow covered by vegetation in the contact with silicic grey vitrophyres; (B) vesicular crust near the rubbly top of the flow (detail of Fig. 4A); (C) rubbles of mafic vesiculated volcanic in an exposition of the basalt flows near faulted regions; (D) slickenside with vertical steps indicating gravitational movement (following the criteria of Petit 1987).

At the base of these flows are cm-spaced oxidized bands concordant with the main foliation (Fig. 9B). Where the lower oxidized vitrophyres have irregular tops, with more than 1 m of level difference, the Gv develop a poorly sorted autobreccia (Fig. 9C) with angular cm-sized fragments embedded in a mm-sized fragment matrix (Fig. 9D). Another feature of the base of these flows is the arrangement of stretched vesicles with vertical disposition (pipe-like vesicles) having no more than 2 cm in length (Fig. 9E).

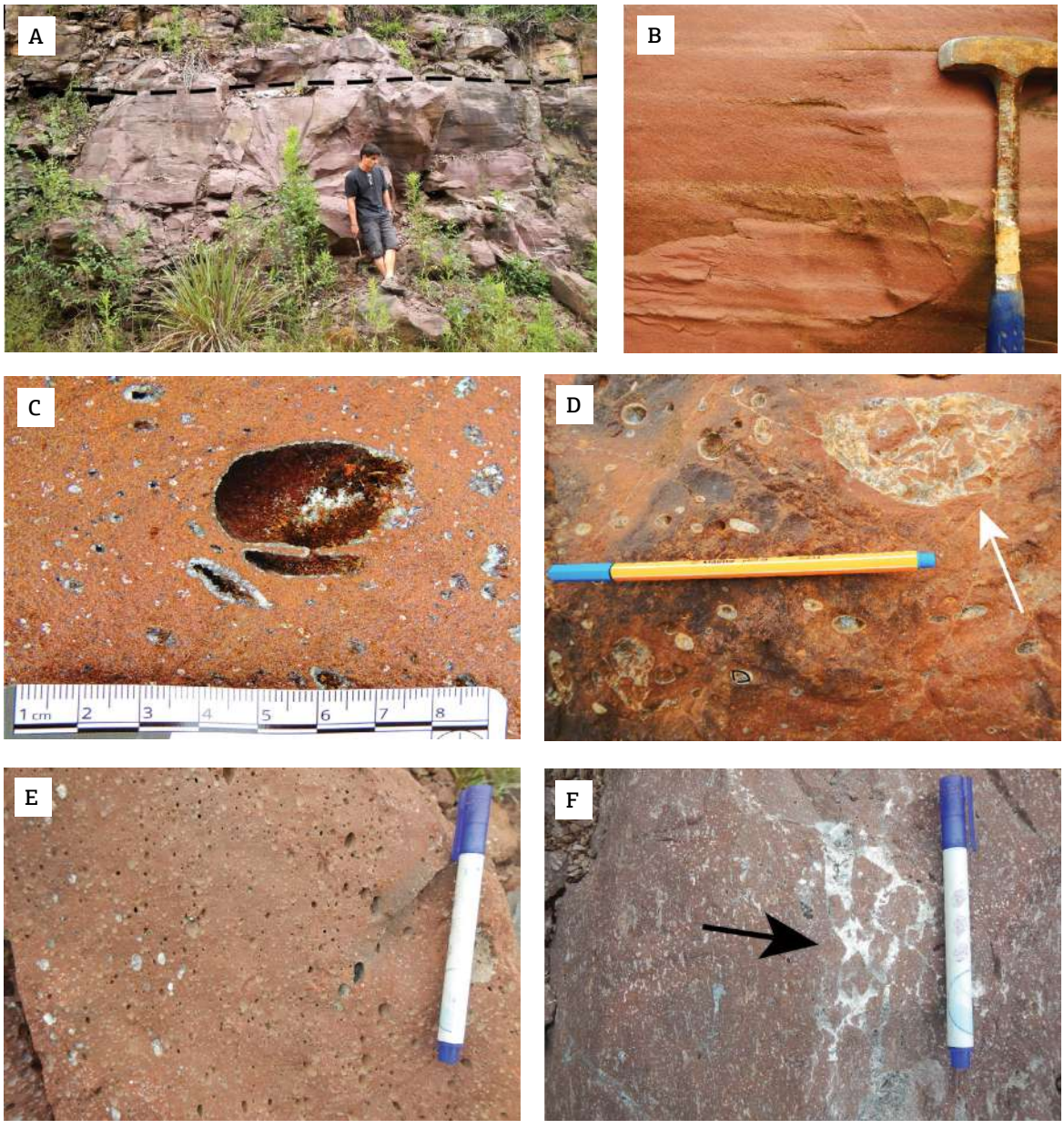

Figure 5. Oxidized vitrophyres in the Mato Perso region. (A) Flat-lying magmatic banding in red poorly vesiculated vitrophyre (elevation 600 m); (B) fresh poorly-vesiculated aphanitic vitrophyre with sparse mm-scale vesicles and horizontal magmatic foliation; (C) highly-vesiculated oxidized vitrophyre with mm- to cm-scale amygdales filled with quartz and calcite; (D) red vesicular vitrophyre with stretched vesicles and amygdales. The arrow points to a pocket with angular fragments cemented by quartz; (E) frothy top of an oxidized vitrophyre flow. The vesicles and amygdales show a narrower distribution of sizes; (F) sheared vesicles and autobreccia with cm-size vitrophyre fragments, near the flow top.

The sheet-like form (Fig. 10A) related to the flat-lying foliation of Gv dips 1º to 23º in general and is highlighted when alteration surfaces are well developed (Fig. 10B). Toward the core of the flows the amount and size of vesicles are in a broader range and present elongated and spherical shapes (Fig. 10C). Rarely, fresh outcrops reveal that Gv are grey colored and the foliation is generated by alteration halos through quartz-filled microfractures (Figs. 10D and 10E).

Geological contacts

As described in section 2.2.1, in RS-448 (290 m of elevation) grey vitrophyres are in direct contact with the top of basaltic rubbly pahoehoe flows at a minimum thickness of 20 m (Fig. 11A). Grey flat-lying vitrophyres cover the vesiculated flow-topping oxidized units with sharp contacts (Fig. 11B). The contacts can be direct (Fig. 11B) or indirect, with cm-size (~30 cm) well-sorted sandstone layers between the two volcanic units (Fig. 11C). Some contacts between the silicic rocks are more complex. For example, in Figure 12A the older unit is composed of large, angular to sub-rounded fragments of a highly vesiculated vitrophyre. The fragments are cm- to meter sized, contain large amygdales (~2–10 cm) filled by quartz and have borders with different degrees of oxidation. The groundmass between the fragments is a vesiculated altered oxidized vitrophyre (Fig. 12B). This vitrophyre has minor vesicles (mm- to cm-size) and is cross-cut by a poorly-vesiculated vitrophyre dyke. The dyke is 1 m thick and is associated with quartz venules associated, indicating normal displacement with a southeast top with slightly oblique components (Fig. 12C). The oxidized vitrophyres are covered by a porphyritic grey vitrophyre with foliation also dipping southeast (Fig. 12D).

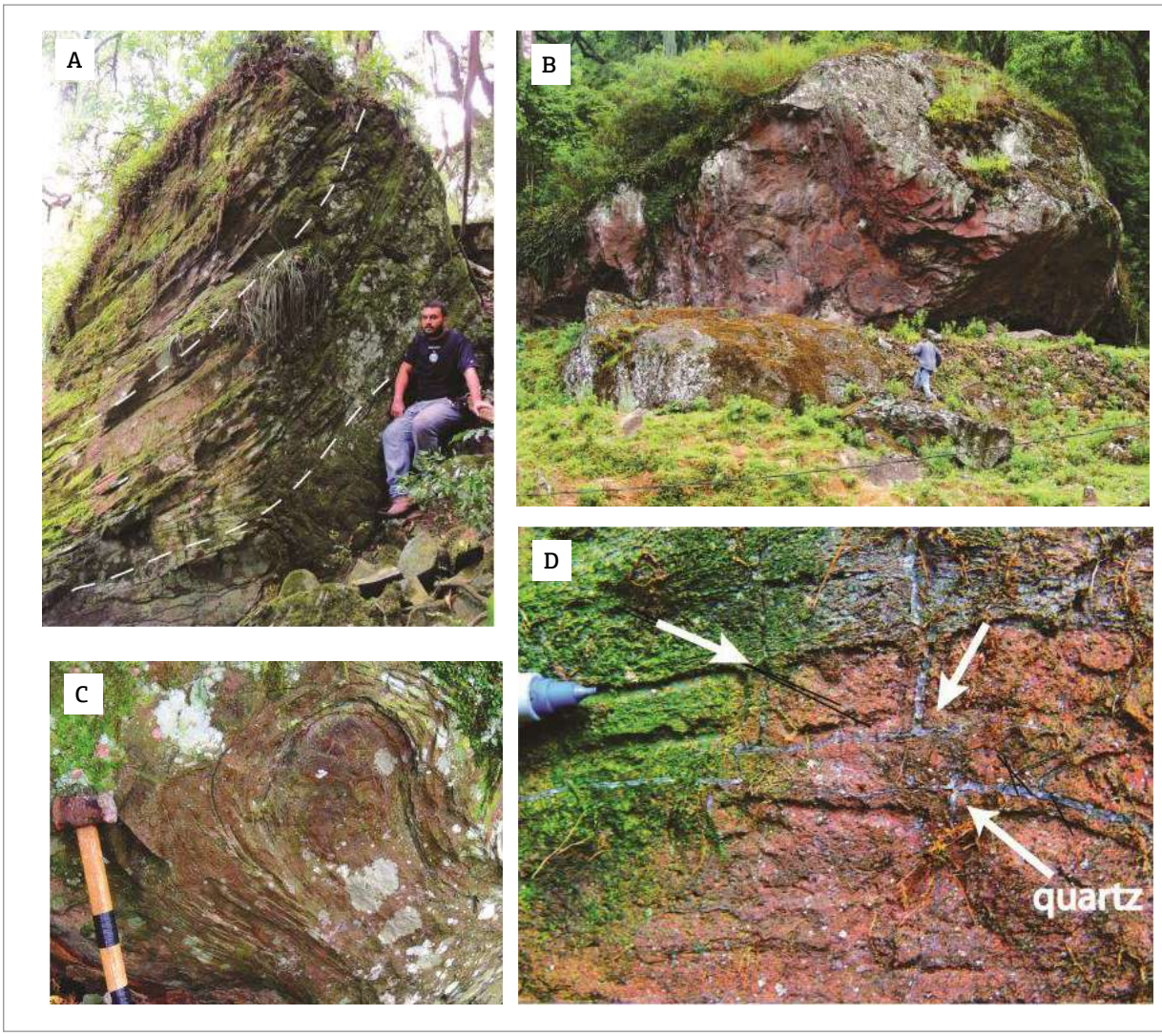

Figure 6. Banded vitrophyres mapped in lower elevations of the area. (A) Magmatic banding dipping 50º to 82º to NW and NE (29º10′44.28″S/51º19′22.28W, altitude of 590 m). (B) Tabular "dike-like" structure (29º8′13.12″S/51º19′38.39″W, elevation of 537 m); (C) fan fold in banded vitrophyre, contorting the magmatic banding; (D) banded vitrophyre showing exsolved diaphanous quartz between boudinated vitrophyre layers.

DISCUSSION

Stratigraphy

The local stratigraphy we propose here is based on the recognition that thick rubbly pahoehoe basaltic flows of Vale do Sol Formation are older volcanics. The relationship between basaltic flows and oxidized vitrophyres remains unclear if we consider that no outcrop of silicic dyke cutting the underlain mafic units was found. In the northwest portion of the area, near the Antas River, the basalts are directly

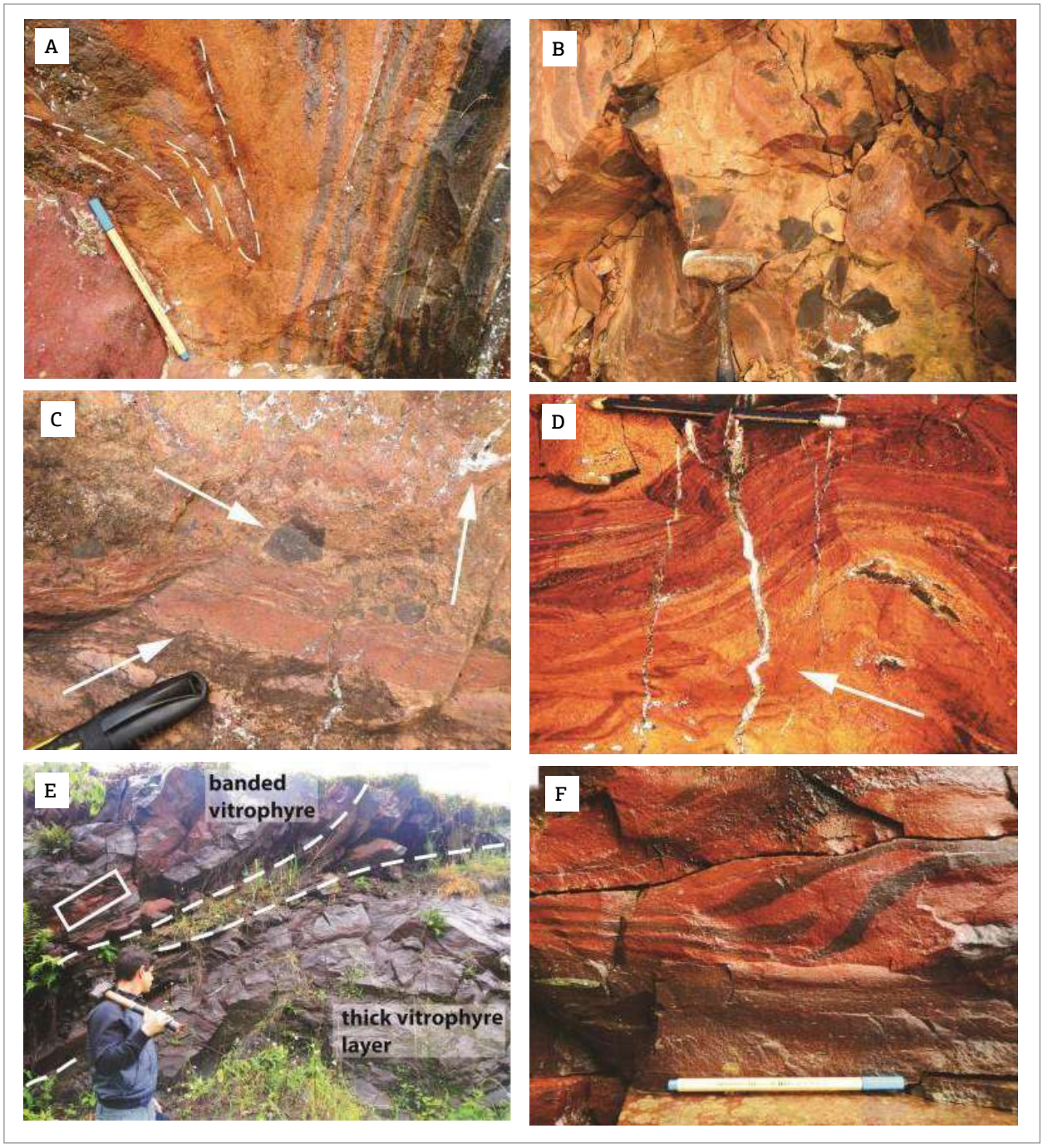

Figure 7. Banded vitrophyres mapped in higher elevations of the area. (A) Vertical banding between black and oxidized vitrophyres (29°11'20.91"S/51°17'8.02"W, elevation of 746 m); (B) boarder of the conduit with black angular vitrophyre fragments within a banded oxidized matrix; (C) boarder of the conduit system with oxidized bands, variable sized black vitrophyre fragments and boxwork-like disposal of fractures filled by quartz; (D) quartz-filled fractures with mm-scale spacing cutting the axial surfaces of F4-related folds; (E) banded vitrophyre layers thrusting a thicker more competent black vitrophyre layer (29°4'4.52"S/51°15'38.31"W, elevation of 680 m); (F) detail of Figure 7D showing the normal relative movement of the magma backflow.

covered by silicic grey vitrophyres. This sharp contact between upper basalt-andesite flows with the grey flat-lying flows of Palmas Formation is very frequently recognized throughout the southern Paraná Basin in elevations between ~350-880 m (Umann *et al.* 2001, Lima *et al.* 2012, Waichel *et al.* 2012, Rossetti *et al.* 2014, Barreto *et al.* 2014, Polo & Janasi 2014, Rossetti *et al.* 2017, Simões *et al.*, 2017).

Even though no contact between oxidized vitrophyres over basaltic flows were observed, the field relations illustrated in Figures 2 and 3 are our support to assume that the former unit is younger than the second. Thus, oxidized vitrophyres are the basal silicic unit, lying over the mafic units and are covered by grey flat-lying silicic vitrophyres.

Banded vitrophyres are regionally exposed along an ~6 km width, NW-trending structure (Fig. 2). According to the distribution of structures in contours, they occur either below or above oxidized vitrophyres and always have a grey vitrophyre unit above them, the contact between the units, however, is frequently absent. Outcrops showing these vitrophyres as dike-like structures, along with the presence of oxidized vitrophyres and breccias toward the borders of the expositions and the association of the inferred intrusive units with regional tectonic structures are arguments for interpreting them as conduits.

Flow morphologies

Flow morphologies and physical characteristics of the subaerial silicic vitrophyres are divided between oxidized and grey units. Both share incomplete characterization because the total area calculation of the flows is difficult due to fault occurrence and cannot be estimated by using conventional remote sensing tools. However, it is inferred from field observations and outcrop elevation correlation that grey flat-lying vitrophyres (Gv) must reach an extent area greater than 30 km^2.

In the oxidized vitrophyres (Fig. 13A), typical base structures such as autobreccias, pipe vesicles and vesicular crusts were not found. By outcrop correlation and comparison with other types of subaerial flows, the poorly-vesiculated vitrophyre with flat-lying foliation (Figs. 5A and 5B) represents the core of the flow unit. Toward the top of the flow, the vesiculation degree rises, the size of the vesicles variate more (Figs. 5C and 5D) and in the upper crust, which is observed in contact with upper grey flows, the vesicles have uniform and smaller sizes (Figs. 5E and 5F).

Oxidized flows (Ov) are estimated to be at least 10 to 30 m thick, and the core-related flat-lying foliations (Fig. 13) are interpreted as flat movement of magma in the flow core. The top of the core with larger vesicles and

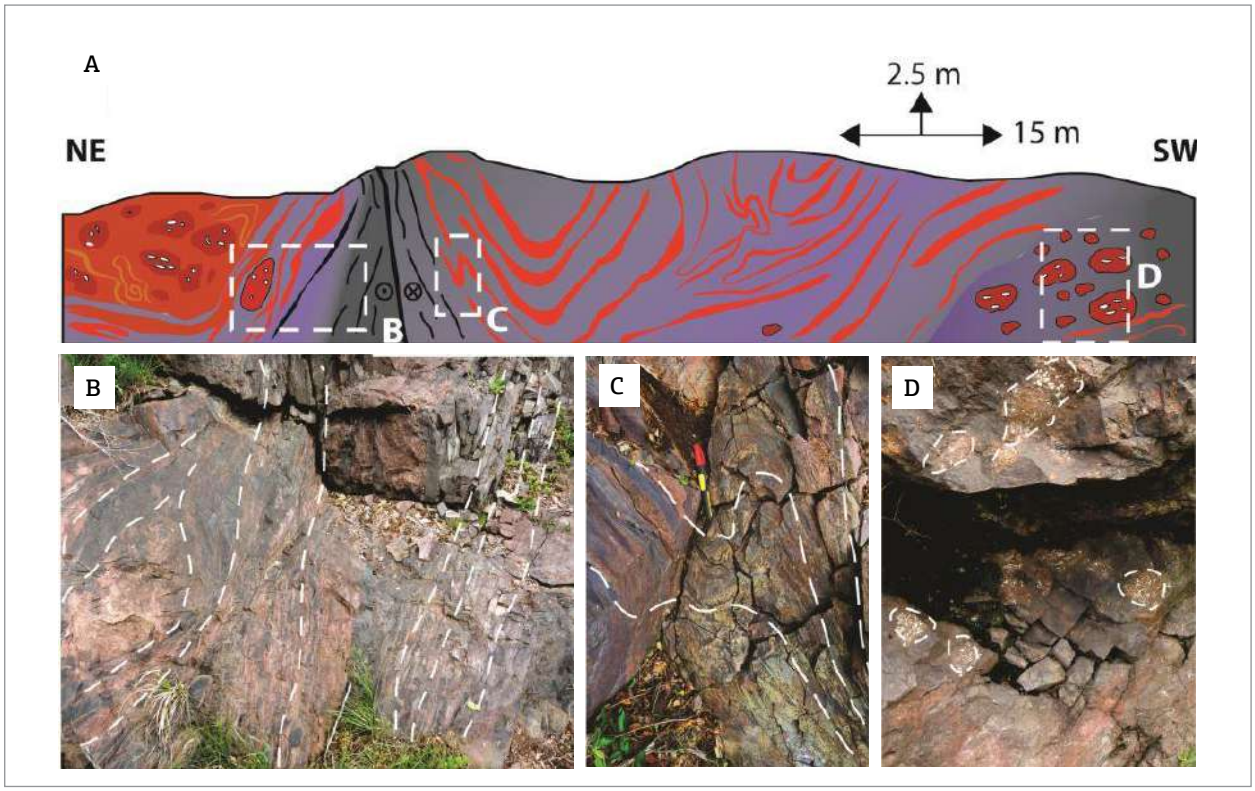

Figure 8. Geological cross section an outcrop of conduit system in highlands (29°6'22.68"S/51°19'38.31"W, elevation 654 m). (A) Schematic sketch showing the field relations between oxidized, brecciated and banded vitrophyres; (B) sub-vertical banding (dipping 72° to NW) in banded vitrophyre; (C) F3-phase fold of banded vitrophyre with sub-horizontal plunge (10° to SE); (D) vesiculated oxidized vitrophyre fragments embedded in banded vitrophyre.

the crust in the top of the flow with abundant smaller vesicles seem like closed-system patterns observed in pahoehoe basaltic flows (e.g., Aubele 1988, Thordarson & Self 1998, Harris *et al*. 2017).

The base of grey vitrophyre flows is characterized by the presence of autobreccias, but only where the paleorelief had dip slopes. The breccias are absent and the contact is sharp where the paleorelief slope is steep. The bases of

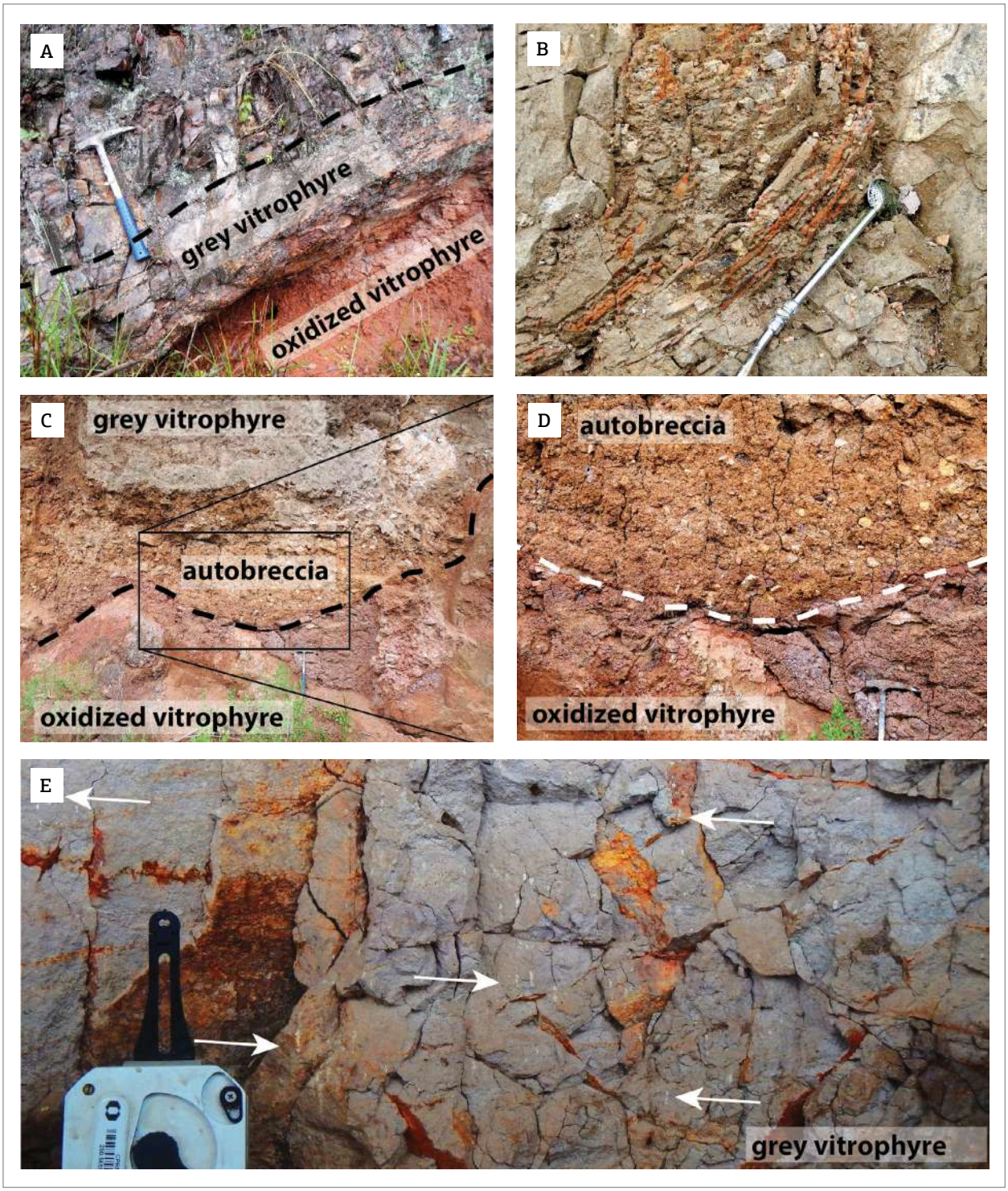

Figure 9. Grey flat-lying lithofacies. (A) Intermediate-angle contact between grey vitrophyre base and an oxidized vitrophyre altered top; (B) oxidized bands in the base of a grey vitrophyre flow; (C) autobreccia in the contact between Ov and Gv. Note the inclination of the paleorelief; (D) detail in the fragment in the altered autobreccia on the top of the oxidized vitrophyre; (E) altered grey vitrophyre with flat foliation and mm-sized pipe vesicles.

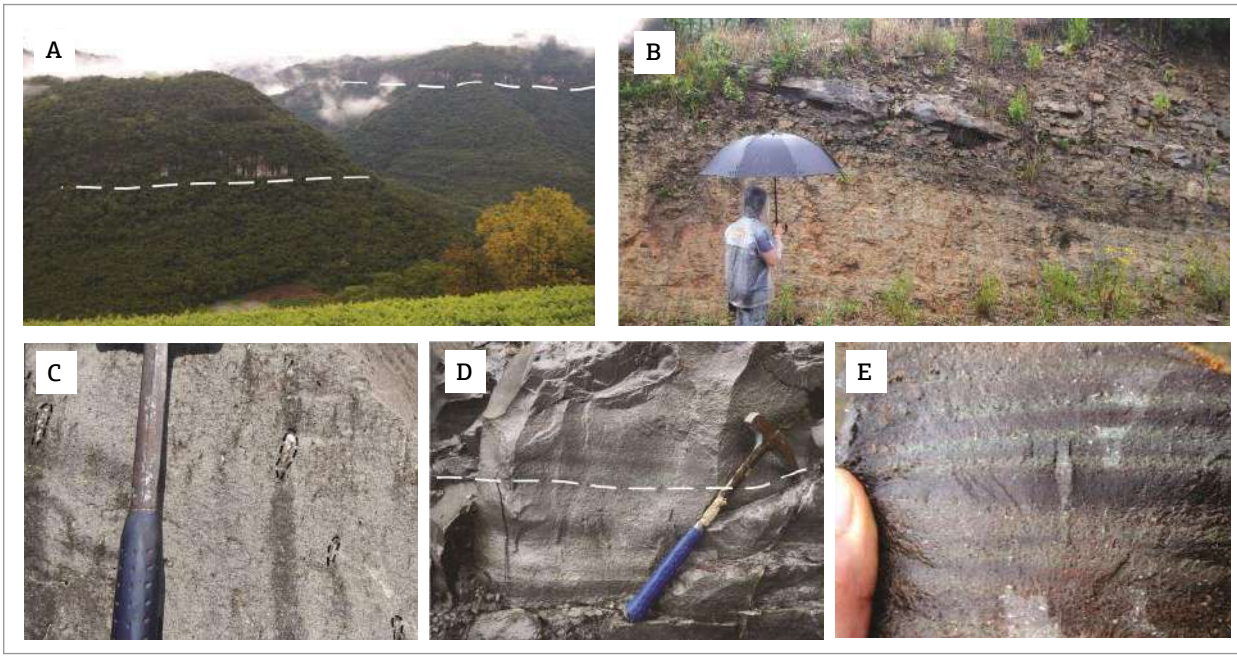

Figure 10. Grey flat-lying vitrophyres field features. (A) Sheet-like form of the expositions, generally absent of vegetation; (B) inclined foliation highlighted by alteration surfaces in grey vitrophyre; (C) grey vitrophyre with mm-size round to stretched vesicles; (D, E) fresh expositions of grey vitrophyre with flat alteration halos.

Figure 11. Contacts between volcanic units in the area. (A) Grey flat-lying felsic vitrophyre covering a basaltic rubbly pahoehoe flow; (B) vesiculated top of a red oxidized flow covered by grey silicic vitrophyre; (C) contact between vesiculated top of oxidized vitrophyre and grey vitrophyre with a ~30 cm sandstone layer in the middle (29°2'3.15"S/51°11'47.48"W, elevation of 790 m).

the flows also have smaller pipe vesicles that grow in size toward the core of the flow, which also displays spherical vesicles. The top of grey vitrophyres was probably eroded, once it is the uppermost geological unit in the area (Fig. 13B). In other expositions through the south of the Paraná Basin, the top of these grey flows were characterized by upper vesicular crust or autobreccia (Waichel *et al*. 2012, Rossetti *et al*. 2017).

Gv flows tend to remain uniform and at least 20 m thick in the area covering the oxidized unit and following the irregular paleorelief. No margins of the flow were observed, but field evidence of lateral autobreccias in similar silicic flows in adjacent areas (e.g., Waichel *et al*. 2012, Polo & Janasi 2014, Simões *et al*. 2014) show hat flow margins of conventional silicic types in Palmas Formation remain thick for long areas, are massive and can be laterally brecciated.

EMPLACEMENT OF THE VOLCANIC UNITS

Rheology

Both oxidized and grey vitrophyres have distinguishing features more compatible with extensive lava flows (e.g., Henry & Wolff 1992). Other similar silicic units in the south of the province have also been recognized as lavas (Umann *et al*. 2001, Polo & Janasi 2014, Simões *et al*. 2014, Guimarães *et al*. 2015). The extension and uniformity of these types of flow are observed in dacite flows with well insulated crusts, allowing even high viscosity magma to attain great distances (Harris & Rowland 2009). A system sustained at high effusion rates is also important to form long simple lava flows (Walker 1971; Walker 1973).

A significant rheological property of the Paraná-Etendeka LIP silicic volcanics is the very high pre- and syn-eruptive temperatures, obtained by apatite saturation and pyroxene-liquid geothermometry data, in the order of 1,000–1,100ºC as well as low relative viscosities for rhyodacite-rhyolite magmas (Milner *et al*. 1992, Bellieni *et al*. 1984, 1986, Garland *et al*. 1995, Janasi *et al*. 2007, Simões *et al*. 2014). Low viscosity is a favorable property for efficient magma flow, emplaced at long distances.

The viscosity of the magma is related to gas loss during eruption; the magma ascent rate is also sensitive to this loss. As the volume proportion of gas affects magma density, compressibility and rheology, it results in both horizontal and vertical pressure gradients in the magma column to allow gas to escape (Sparks 2003).

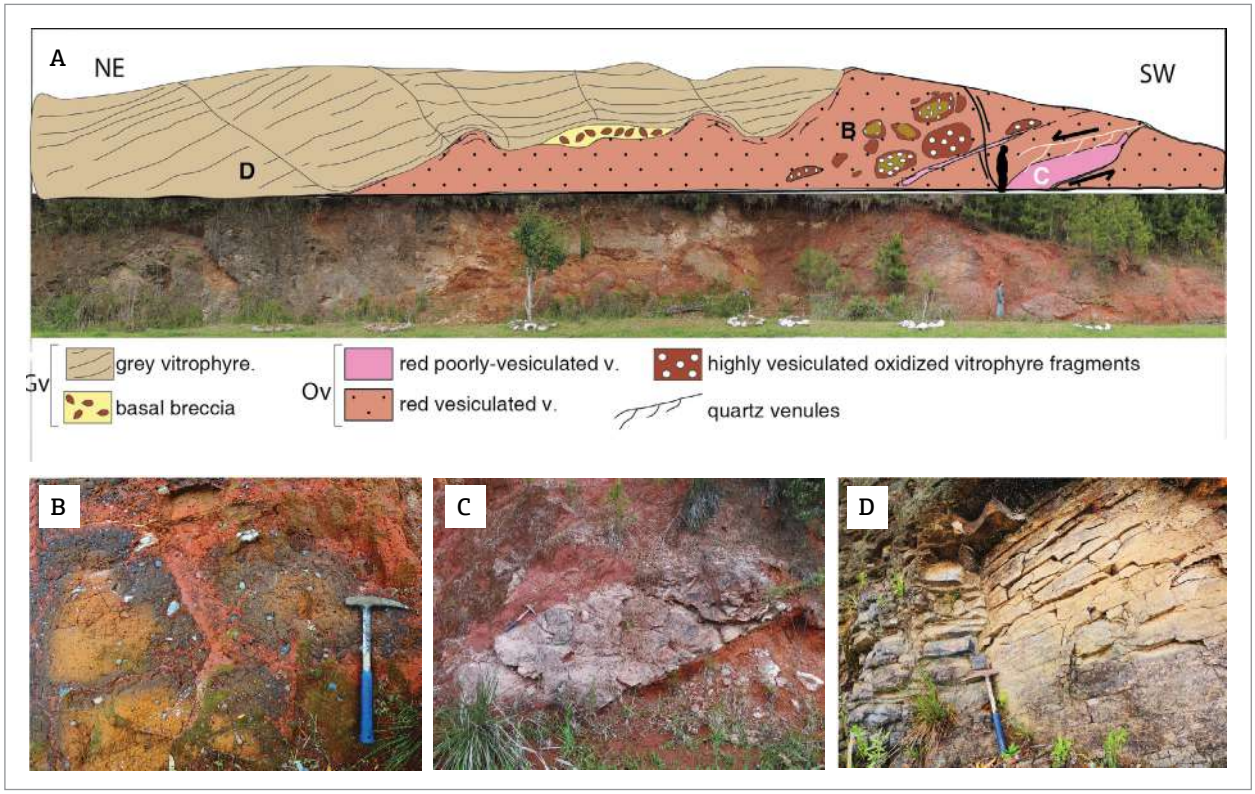

Figure 12. Contacts between volcanic units in the area. (A) Geologic cross-section of approximately 30 m showing field relations (29º12'17.92"S/51º20'16.83"W, elevation of 675 m); (B) large oxidized vitrophyre fragments with cm-sized amygdales; (C) oxidized poorly-vesiculated vitrophyre dyke cutting the sequence with NE-SW direction and dipping 52º to SE; (D) upper grey vitrophyre with variable foliation dips. The main foliation dips 49º to SE.

According to the Massol & Jaupart model (1999), if bubbles are interconnected gases can escape to the conduit walls. In rhyolite lavas, high porosity bands are often developed. Therefore, they potentially act as pathways for gas movement to the lava surface (Sparks 2003, Houghton *et al.* 2010, Furukawa & Uno 2015). A volatile-rich magma is less dense than a degassed magma, both because of reduced dissolved volatiles within the melt (Richet *et al.* 2000) and (at low pressure) because of the presence of an exsolved fluid phase (Witham 2011). When we analyze the mapped units as a whole, the banding, shearing and fragmentation of magma described in variable parts of the conduit outcrops, more commonly in their borders can be interpreted as favorable paths to degassing. Sustained high temperatures and consequently low viscosity could be held by a competent heat flux.

Conditioning structures for the conduit system

A plausible explanation of why the conduit-related rocks were not observed cutting the lower basaltic units is because their outcrops are controlled by tectonic structures. The conduits are regionally exposed, mostly in the south, near the Antas river bed (Fig. 1). This river forms a curved NE-SW structure comprising a set of normal and transcurrent faults (Fig. 2). In the south of the river, the NW-trending structures contain the conduit expositions. It resembles the São Marcos (Lima *et al.* 2012, 2017, Simões *et al.* 2017) and

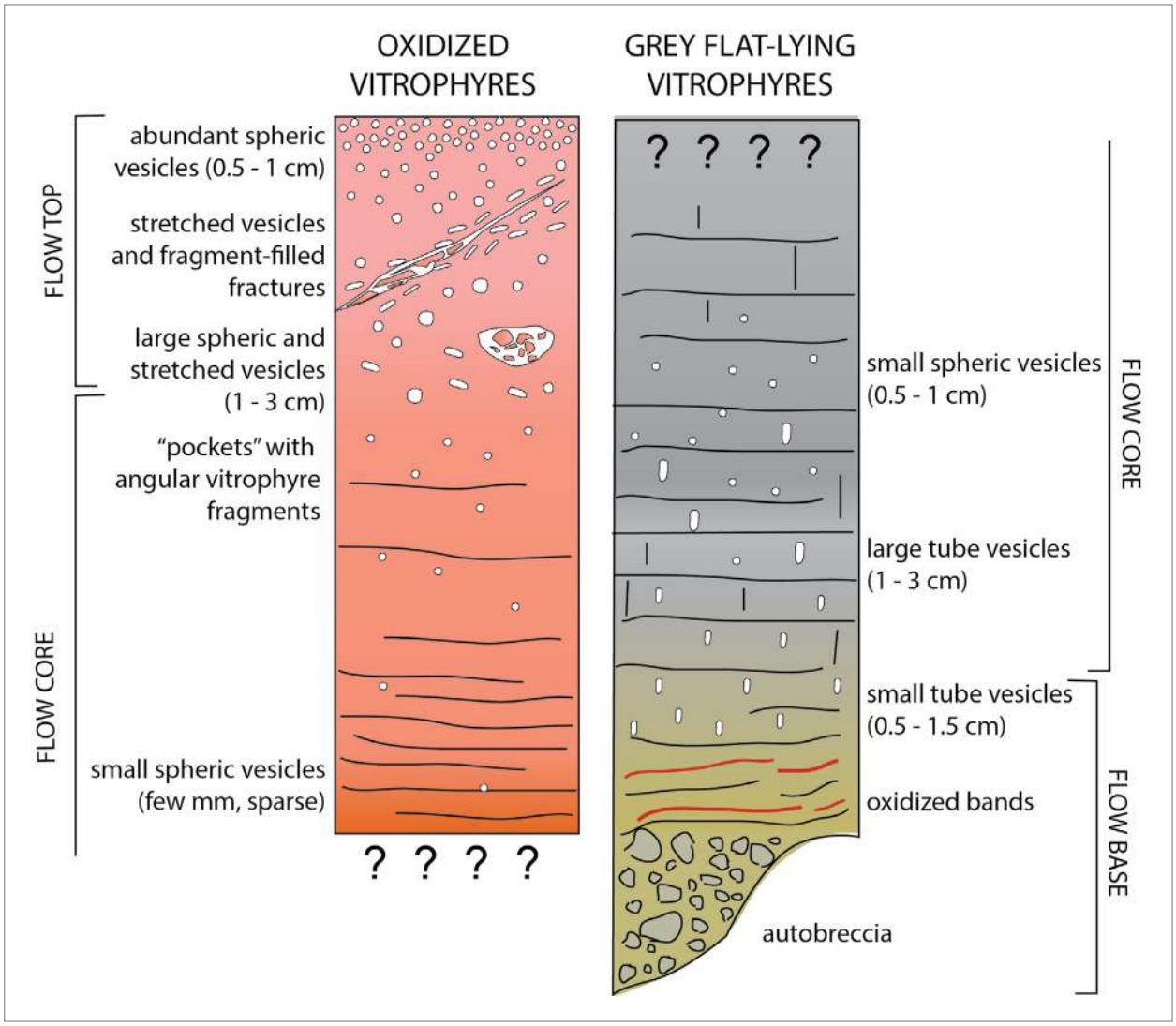

Figure 13. Flow morphologies for oxidized and grey flat-lying vitrophyres. (A) Oxidized vitrophyres have flat-lying banding and sparse spherical vesicles in the flow core. Discrete breccias, elongated and larger vesicles are on the top of the core and abundant spherical vesicles make up the frothy vesicular upper crust; (B) grey vitrophyres display, in the base, autobreccias, where the paleorelief slope is high (> 45º) and sharp contacts at flat paleorelief. Small tube vesicles grow to the core of the flow, where spherical vesicles are also common.

Jaquirana-Cambará do Sul areas (Simões *et al.* 2015, 2017), both also south of this NE-SW structure. The observed banding is folded several times (Figs. 6C, 7A, 7B, 7D, 8). F1- and F2-phase folds are generally present in the center of the conduits, with sub-vertical disposal of the axial surfaces. Toward the margins, a variety of fold phases is generated (at least four) mainly by mixing between more and less oxidized bands (Fig. 7D). Thus, a complex arrangement of flow directions within the conduits is recognized.

One regional scale, the geometrical and kinematical interpretation of transcurrent faults made by Nummer *et al.* (2011), shows that the NW-SE faults with sinistral strike-slip movement are older (Eocretaceous) than NE-SW faults with dextral and NW-SE faults with sinistral relative movements in the northeast of Rio Grande do Sul. The fault reactivation in NE-SW direction coincides with Precambrian structures like the Porto Alegre suture and Dorsal de Canguçu shear zone (Fernandes *et al.* 1995). Additionally, the NE-trending Antas Lineament can be correlated to the NE-SW orientation of Huab, Ugab and several other rivers in Namibia. We interpret that the role of major NE-SW structural reactivation is fundamental to open spaces at NW-SE faults, the dominant trend of conduit area outcrops in this study.

Considering the tectonic setting for the Paraná Basin, the thermomechanical study of Quintas *et al.* (1999) concludes that the major extension of the basin occurred in the Permo-Carboniferous. In the Juro-Cretaceous, during volcanism, the subsidence was associated to reactivation of older structures allied with a thermal component. The thermal component, considered to be plume-related (Hawkesworth *et al.* 1992, Peate 1997, Gibson *et al.* 2006), was connected to the surface through a feeder system that is proposed to reach the mantle at ~35 km, at least in the northern portion of the basin (Molina *et al.* 1988). This indicates that emplacement of the conduits in the shallow crust must be a reflection of a deeper feeder system.

The injection of magma through dykes during gravitational displacement of blocks is evidenced in Figure 12A and may have played an important role in magma transport. In the places where the dykes intruded on more friable rocks, at the valleys of the mapped area, the main intrusive structure remain preserved (see Figs. 6A and 6B). The evolution from the syneclise phase to pre-rift in the Paraná Basin, increasing the regional extension, is an appropriate scenario fostering the propagation of normal fault sets and the reactivation of older structures.

Crustal extension is generally followed by basin cooling (McKenzie 1978, Latin & White 1993), but this does not appear to be the case for the Paraná Basin, where the thermal component remained active. We believe that in the Paraná-Etendeka LIP the movements in regional faults triggered the silicic magma ascent through regional-scale conduit systems.

Geological model for Mato Perso Conduit System

The vitrophyre relative chronology observed in the field favors the hypothesis that oxidized vitrophyres are cut by the conduits. These contain oxidized vitrophyre fragments with variable vesiculation patterns. Transition frombreccias,-most oftenly, and more oxidized vitrophyre in the borders to grey/black vitrophyre intruding them on the center of the conduits, presence of oxidized bands only in the base of the grey vitrophyres and mixing features between vitrophyres lead us to infer that the described conduits fed at least the upper grey vitrophyre units (Fig. 14).

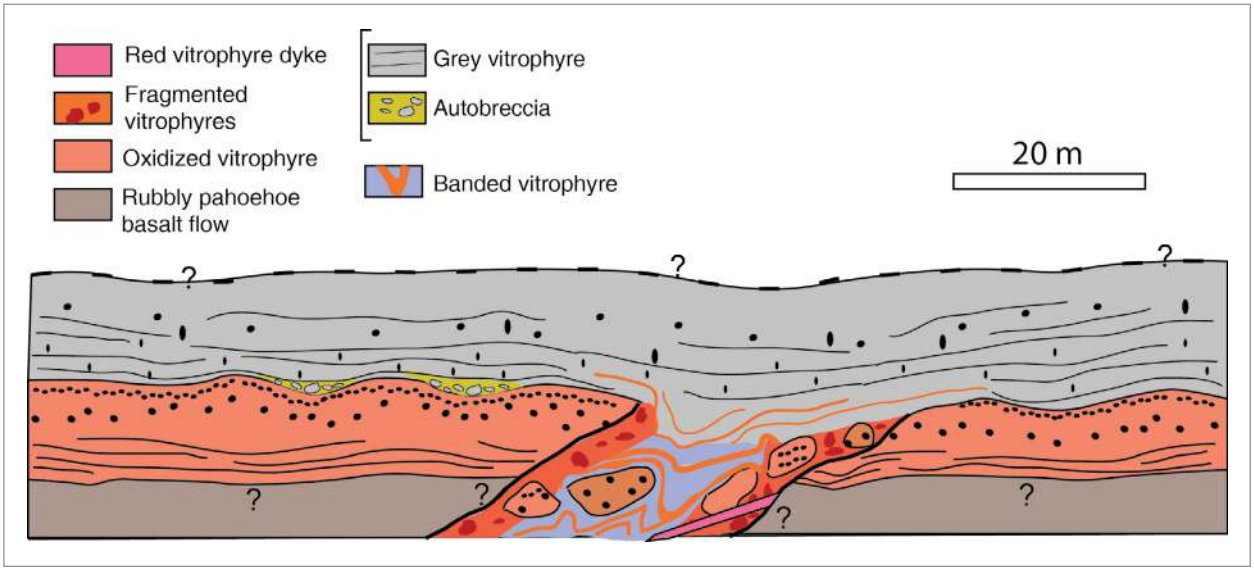

Figure 14. Simplified model for the emplacement of volcanic units in the Mato Perso Conduit System.

CONCLUSIONS

In conclusion, in the Mato Perso area, the silicic volcanic succession overlying the basaltic units of the Vale do Sol Formation, Serra Geral Group, comprises oxidized vitrophyres at the base which are cut and locally incorporated by banded vitrophyres. The conduit system fed the upper grey flat-lying vitrophyres. Subaerial flows are similar to extensive lava flows described in literature, suggesting large emplacement areas. The conduit paths in the crust were conditioned by the normal and oblique faults developed during extensional stages combined with a thermal component in the Paraná Basin. A system sustained at high temperatures ensured that the silicic magma remained in low viscosity during ascent and the emplacement of the upper grey vitrophyre units was driven by effusion rates sufficient for enabling the lava to run at long distances.

ACKNOWLEDGEMENTS

The authors thank *Conselho Nacional de Desenvolvimento Científico e Tecnológico* (CNPq, projects 9784, 441766/2014-5, 303015/2015-2 and 400724/2014-6), FAPESP (project 2012/06082-6) and FAPERGS (project 2311-2551/14-8) for funding. We also thank Fernando da Luz and Natalia G. Pasqualon for helping in the field work.

REFERENCES

Allen P.A. & Armitage J.J. 2012. Cratonic basins. *In*: Busby C., Azor A. (Eds.). *Tectonics of Sedimentary Basins:* Recent Advances. New Jersey, Blackwell Publishing.

Aubele J.C., Crumpler L.S., Elstion W.E. 1988. Vesicle zonation and vertical structure of basalt flows. *Journal of Volcanology and Geothermal Research*, **35**:349-374. https://doi.org/10.1016/0377-0273(88)90028-5

Barreto C.J.S., Lima E.F., Scherer C.M.S., Rossetti L.M.M. 2014. Lithofacies analysis of basic lava flows of the Paraná igneous province in the south hinge of Torres Syncline, Southern Brazil. *Journal of Volcanology and Geothermal Research*, **285**:81-99. DOI: 10.1016/j.jvolgeores.2014.08.008

Bellieni G., Brotzu P., Comin-Chiaramonti P., Ernesto M., Melfi A.J., Pacca I.G., Piccirillo E.M., Stolfa D. 1984. Flood basalt to rhyolite suites in the southern Paraná plateau (Brazil): paleomagnetism, petrogenesis and geodynamic implications. *Journal of Petrology,* **25**:579-618.

Bellieni G., Comin-Chiaramonti P., Marques L.S., Melfi A.J., Nardy A.J.R., Papatrechas C., Piccirilo E.M., Roisenberg A., Stolfa D. 1986. Petrogenetic aspects of acid and basaltic lavas from Paraná Basin (Brazil): geological, mineralogical and petrochemical relationships. *Journal of Petrology*, **27**:915-944. https://doi.org/10.1093/petrology/27.4.915

Bryan S.E., Peate I.U., Peate D.W., Self S., Jerram D.A., Mawby M.R., Marsh J.S., Miller J.A. 2010. The largest volcanic eruptions on Earth. *Earth and Science Reviews*, **102**(3-4):207-229. DOI: 10.1016/j.earscirev.2010.07.001

Comin-Chiaramonti P., Bellieni G., Piccirillo E.M., Melfi A.J. 1988. Classification and petrography of continental stratoid volcanic and related intrusive from the Paraná Basin (Brasil). *In*: Piccirillo E.M., Melfi A.J. (Eds.). *The Mesozoic flood volcanism of the Paraná Basin:* petrogenetic and geophysical aspects. São Paulo, Instituto Astronômico e Geofísico, 600 p.

Comin-Chiaramonti P., Riccomini C., Slejko F., De Min A., Ruberti E., Gomes C.B. 2010. Cordierite-bearing lavas from Jaguarão, Southern Brazil: Petrological evidence for crustal melts during early rifting of Gondwana. *Gondwana Research*, **18**:514-527.

De Campos C.P., Guimarães L.F., Lima E.F., Janasi V.A., Giordano D., Dingwell D.B. 2016. Chaotic flow and fragmentation patterns in the acidic feeder system from the Paraná-Etendeka Large Igneous Province. *Goldschmidt Conference Abstracts*, 2413.

Ernesto M., Raposo M.I.B., Marques L.S., Renne P.R., Diogo L.A., de Min A. 1999. Paleomagnetism, geochemistry and $^{40}Ar/^{39}Ar$ dating of the North-eastern Paraná Magmatic Province: tectonic implications. *Journal of Geodynamics*, **28**(4):321-340. DOI: 10.1016/S0264-3707(99)00013-7

Ewart A., Milner S.C., Armstrong R.A., Duncan A.R. 1998. Etendeka volcanism of the Goboboseb Mountains and Messum Igneous Complex, Namibia. Part II: voluminous quartz latite volcanism of the Awahab magma system. *Journal of Petrology*, **39**:227-253. DOI: 10.1093/petroj/39.2.227

Ewart A., Milner S.C., Duncan A.R., Bailey M. 2002. The Cretaceous Messum igneous complex, S.W. Etendeka, Namibia: reinterpretation in terms of a downsag-cauldron subsidence model. *Journal of Volcanology and Geothermal Research*, **114**:251-273. DOI: 10.1016/S0377-0273(01)00266-9

Fernandes L.A.D., Menegat R., Costa A.F.U., Koester E., Porcher C.C., Tommasi A., Kraemer G., Ramgrab G.E., Camozzato E. 1995. Evolução tectônica do Cinturão Dom Feliciano no Escudo Sul-Rio-Grandense: Parte II – uma contribuição a partir das assinaturas geofísicas. *Revista Brasileira de Geociências*, **25**(4):375-384.

Florisbal L.M., Heaman L.M., Janasi V.A., Bitencourt M.F. 2014. Tectonic significance of the Florianópolis Dyke Swarm, Paraná-Etendeka Magmatic Province: A reappraisal based on precise U-Pb dating. *Journal of Volcanology and Geothermal Research*, **289**:140-150. DOI: 10.1016/j.jvolgeores.2014.11.007

Frank H.T., Gomes M.E.B., Formoso M.L.L. 2009. Review of the areal extent and volume of the Serra Geral Formation, Paraná Basin, South America. *Pesquisas em Geociências*, **36**(1):49-57.

Furukawa K. & Uno K. 2015. Origin and deformation of high porosity bands in the Takanoobane Rhyolite of Aso volcano, Japan. *Journal of Volcanology and Geothermal Research*, **305**:76-83. DOI: 10.1016/j.jvolgeores.2015.09.021

Garland F.E., Hawkesworth C.J., Mantovani M.S.M. 1995. Description and petrogenesis of the Paraná rhyolites. *Journal of Petrology*, **36**:1193-1227. DOI: 10.1093/petrology/36.5.1193

Gibson S.A., Thompson R.N., Day J.A. 2006. Timescales and mechanisms of plume-lithosfere interactions: $^{40}Ar/^{39}Ar$ geochronology and geochemistry of alkaline igneous rocks from the Paraná-Etendeka large igneous province. *Earth and Planetary Science Letters*, **251**:1-17. DOI: 10.1016/j.epsl.2006.08.004

Guimarães L.F., Raposo M.I.B., Janasi V.A., Cañón-Tapia E., Polo L.A. 2015. Petrofabric of the acid volcanic rocks from the Southern Paraná Magmatic Province obtained via AMS: a contribution to the understanding of their emplacement. *In*: Simpósio de Vulcanismo e Ambientes Associados, 6., São Paulo. *Anais*... São Paulo.

Harris A., Rowland S. 2009. Effusion rate controls on lava flowlength and the role of heat loss: a review. *In*: Thordarson T., Self S., Larsen G., Rowland S.K., Hoskuldsson A. (Eds.). *Studies in Volcanology:* The Legacy of George Walker. Special Publications of IAVCEI, p. 33-51.

Harris A.J.L.M, Rowland S.K., Villeneuve N., Thordarson T. 2017. Pahoehoe, 'a'a, and block lava: an illustrated history of the nomenclature. *Bulletin of Volcanology*, **79**:7. DOI: 10.1007/s00445-016-1075-7

Hawkesworth C.J., Gallagher K., Kelley S., Mantovani M., Peate D.W., Regelous M., Rogers N.W. 1992. Parana magmatism and the opening of the South Atlantic. *Geological Society of London*, Spec. Publ., **68**(1):221-240. https://doi.org/10.1144/GSL.SP.1992.068.01.14

Henry C.D., Wolff J. A. 1992. Distinguishing strongly rheomorphic tuffs from extensive silicic lavas. *Bulletin of Volcanology*, **54**:171-186.

Houghton B.F., Carey R.J., Cashman K.V., Wilson C.J.N., Hobden B.J. Hammer J.E. 2010. Diverse patterns of ascent, degassing, and eruption of rhyolite magma during the 1.8 ka Taupo eruption, New Zealand: Evidence from clast vesicularity. *Journal of Volcanology and Geothermal Research*, **195**:31-47. DOI: 10.1016/j.jvolgeores.2010.06.002

Janasi V.A., de Freitas V.A., Heaman L.H. 2011. The onset of flood basalt volcanism, Northern Paraná Basin, Brazil: a precise U–Pb baddeleyite/zircon age for a Chapecó type dacite. *Earth and Planet Science Letters*, **302**(1-2):147-153. https://doi.org/10.1016/j.epsl.2010.12.005

Janasi V.A., Montanheiro T.J., Freitas V.A., Reis P.M., Negri F.A., Dantas F.A. 2007. Geology, petrography and geochemistry of the acid volcanism of the Paraná Magmatic Province in the Piraju-Ourinhos region, SE Brazil. *Revista Brasileira de Geociências*, **37**:745-759.

Kirstein L.A., Peate D.W., Hawkesworth C.J., Turner S.P., Harris C., Mantovani M.S.M. 2000. Early Cretaceous basaltic and rhyolitic magmatism in southern Uruguay associated with the opening of the South Atlantic. *Journal of Petrology*, **41**:1413-1438. https://doi.org/10.1093/petrology/41.9.1413

Latin D., White N. 1993. Magmatism in extensional sedimentary basins. *Annali di Geofisica*, **XXXVI**(2):123-138.

Lima E.F., Philipp R.P., Rizzon G. C., Waichel B.L., Rosetti L.M.M. 2012. Sucessões Vulcânicas e Modelo de Alimentação e Geração de Domos de Lava Ácidos da Formação Serra Geral na Região de São Marcos-Antonio Prado (RS). *Geologia USP Série Científica*, **12:**49-64. http://dx.doi.org/10.5327/S1519-874X2012000200004

Lima E.F., Waichel B.L., Rossetti L.M.M., Sommer C.A., Simões M.S. 2017. Feeder systems of acidic lava flows from the Paraná-Etendeka Igneous Province in southern Brazil and their implications for eruption style. *Journal of South American Earth Sciences*. DOI: 10.1016/j.jsames.2017.11.004

Marteleto N.S., Florisbal L.M., Janasi V.A. 2016. Petrologia e geoquímica de diques ácidos do Enxame de Diques de Florianópolis, na Ilha de Santa Catarina. *In:* Congresso Brasileiro de Geologia, 48, Porto Alegre. *Anais*... Porto Alegre.

Massol H., Jaupart C. 1999. The generation of gas overpressure in volcanic eruptions. *Earth and Planetary Science Letters*, **166**:57-70. DOI: 0012-821X/99/$

McKenzie D. 1978. Some remarks on the development of sedimentary basins. *Earth and Planetary Science Letters*, **40**:25-32. https://doi.org/10.1016/0012-821X(78)90071-7

Melfi A.J., Nardy A.J.R., Piccirillo E.M. 1988. Geological and magmatic aspects of the Paraná Basin: An introduction. *In*: Piccirillo E.M. & Melfi A.J. (Eds.). *The Mesozoic flood volcanism of the Paraná Basin:* petrogenetic and geophysical aspects. São Paulo, IAG-USP, p. 1-13.

Milani E.J., Ramos V.A. 1998. Orogenias paleozoicas no domínio sul-ocidental do Gondwana e os ciclos de subsidência da Bacia do Paraná. *Revista Brasileira de Geociências*, **28**(4):473-484.

Milner S.C., Duncan A.R. 1987. Geochemical characterization of quartz latite units in the Etendeka Formation. *Communications of the Geological Survey of Namibia*, **3**:87-95.

Milner S.C., Duncan A.R., Ewart A. 1992. Quartz latite rheoignimbrite flow of the Etendeka Formation, North-Western Namibia. *Bulletin of Volcanology*, **54**:200-219.

Milner S.C., Duncan A.R., Whittingham A.M., Ewart A. 1995. Trans-Atlantic correlation of eruptive sequences and individual silicic volcanic units within Paraná- Etendeka Igneous Province. *Journal of Volcanology and Geothermal Research*, **69**:137-157. https://doi.org/10.1016/0377-0273(95)00040-2

Molina E.C., Ussami N., de Sá N.C., Blitzkow D., Miranda Filho O.F. 1988. Deep crustal structure under the Paraná Basin (Brazil) from gravity study. *In*: Piccirillo E.M., Melfi A.J. (Eds.). *The Mesozoic flood volcanism of the Paraná Basin:* petrogenetic and geophysical aspects. São Paulo, Instituto Astronômico e Geofísico, 600 p.

Muzio R., Morales E., Veroslavsky G., Conti B. 2009. The Arequita Formation (Lower Cretaceous): petrographic features of the volcanics facies in the Laguna Merín Basin, east Uruguay. *Latin American Journal of Sedimentology and Basin Analysis*, **16**(1):19-28.

Nardy A.J.R., Machado F.B., Oliveira M.A.F. 2008. As rochas vulcânicas mesozoicas ácidas da Bacia do Paraná: litoestratigrafia e considerações geoquímicas-estratigráficas. *Revista Brasileira de Geociências*, **38**(1):178-195.

Nummer, A.R., Machado, R., Jacques, P.D. 2014. Tectônica transcorrente mesozoica/cenozoica na porção leste do Planalto do Rio Grande do Sul, Brasil. Pesquisas em Geociências, **41**(2):121-130.

Peate D.W. 1997. The Paraná-Etendeka province. *In*: Mahoney J.J., Coffin M.R. (eds.). Large Igneous Proovinces: Continental, Oceanic and Planetary Flood Volcanism. *Geophysical Monograph*, **100**:217-245.

Peate, D.W., Hawkesworth, C.J., Mantovani, M.S.M. 1992. Chemical stratigraphy of the Paraná lavas (S. America): classification of magma types and their spatial distribution. *Bulletin of Volcanology:* 55, 119-139.

Petit J.P. 1987. Criteria for the sense of movement on fault surfaces in brittle rocks. *Journal of Structural Geology*, **9**(5-6):597-608. https://doi.org/10.1016/0191-8141(87)90145-3

Petrini R., Civetta L., Iacumin P., Longinelli A., Belliene G., Comin-Chiaramonti P., Ernesto N., Marques L.S., Melfi A., Pacca I., Piccirillo E.M. 1989. High temperature flood silicic lavas (?) from the Paraná Basin (Brazil). *New Mexico Bureau of Mines & Mineral Resources Bulletin*, **131**:213.

Piccirillo, E.M., Comin-Chiaramonti, P., Bellieni, G., Civetta, L., Marques, L.S., Melfi, A.J., Petrini, R., Raposo, M.I.B., Stolfa, D. 1988. Petrogenetic aspects of continental flood basalt-rhyolite suites from the Paraná Basin (Brazil). In: Piccirillo, E.M. & Melfi, A.J. The Mesozoic flood volcanism of the Paraná basin: petrogenetic and geophysical aspects, Universidade de São Paulo, 600p.

Polo L.A., Janasi V.A. 2014. Volcanic stratigraphy of intermediate to acidic rocks in Southern Paraná Magmatic Province, Brazil. *Geologia USP Série Científica*, **14**:83-100. http://dx.doi.org/10.5327/Z1519-874X201400020005

Polo L.A., Giordano, D., Janasi, V.A., Guimarães, L.F., 2017. Effusive volcanism in the Paraná Magmatic Province, South Brazil: Physico-chemical conditions of storage and eruption and consideration on the rheological behavior during emplacement. Journal of Volcanology and Geothermal Reserarch (accepted).

Quintas M.C.L., Mantovani M.S.M., Zalán P.V. 1999. Contribuição ao estudo da evolução mecânica da Bacia do Paraná. *Revista Brasileira de Geociências*, **29**(2):217-226.

Raposo M.I.B. 1997. Magnetic fabric and its significance in the Florianópolis dyke swarm, southern Brazil. *Geophysics Journal*, **131**:159-170. DOI: 10.1111/j.1365-246X.1997.tb00602.x

Raposo M.I.B., Ernesto M. 1995. An early Cretaceous paleomagnetic pole from Ponta Grossa dykes (Brazil): implications for the South America Mesozoic APWP. *Journal of Geophysical Research*, **100**(B10):20095-20109. DOI: 10.1029/95JB01681

Raposo M.I.B., Ernesto M., Renne P.R. 1998. Paleomagnetism and dating of the early Cretaceous Florianópolis dike swarm (Santa Catarina Island), Southern Brazil. *Physics of the Earth and Planetary Interiors*, **108**(4):275-290. DOI: 10.1016/S0031-9201(98)00102-2

Richet P., Whittington A., Holtz F., Behrens H., Ohlhorst S., Wilke M. 2000. Water and the density of silicate glasses. *Contributions to Mineralogy and Petrology*, **138**:337-347.

Roisenberg A. 1989. *Petrologia e geoquímica do vulcanismo ácido mesozoico da Província Meridional da Bacia do Paraná*. PhD Thesis, Instituto de Geociências, Universidade Federal do Rio Grande do Sul, Porto Alegre.

Rossetti L., Lima E.F., Waichel B.L, Hole M.J., Simões M.S., Scherer C.M.S. 2017. Lithostratigraphy and volcanology of the Serra Geral Group, Paraná-Etendeka Igneous Province in Southern Brazil: Towards a formal stratigraphical framework. *Journal of Volcanology and Geothermal Research*. https://doi.org/10.1016/j.jvolgeores.2017.05.008

Rossetti L.M.M., Lima E.F., Waichel B.L., Scherer C.M.S., Barreto C.J. 2014. Stratigraphical framework of basaltic lavas in Torres Syncline main valley, Southern Paraná-Etendeka Volcanic Province. *Journal of South American Earth Sciences*, **56**:409-421. DOI: 10.1016/j.jsames.2014.09.025

Sarmento C.C.T., Sommer C.A., Lima E.F. 2017. Mafic subvolcanic intrusions and their petrologic relation with the volcanism in the South hinge Torres Syncline, Paraná-Etendeka Igneous Province, southern Brazil. *Journal of South American Earth Sciences*, **77**:70-91. DOI: 10.1016/j.jsames.2017.04.017

Simões M.S., Lima E.F., Sommer C.A., Rossetti L.M.M. 2015. Reconhecimento de condutos vulcânicos das rochas ácidas da PBC Paraná-Etendeka na porção NE do Rio Grande do Sul. ***In***: Simpósio de Vulcanismo e Ambientes Associados, 6, São Paulo. *Anais*... São Paulo.

Simões M.S., Lima E.F., Sommer C.A., Rossetti L.M.M. 2017. Structures and lithofacies of felsic volcanic feeder conduit systems in the Paraná-Etendeka LIP, southern Brazil. *Journal of Volcanology and Geothermal Research*. https://doi.org/10.1016/j.jvolgeores.2017.12.013

Simões M.S., Rossetti L.M.M., Lima E.F., Ribeiro B.P. 2014. The role of viscosity in the emplacement of high-temperature silicic flows of Serra Geral Formation in Torres Syncline (Rio Grande do Sul State, Brazil). *Brazilian Journal of Geology*, **44**(4):669-679. DOI: 10.5327/Z2317488920140004001O

Sparks R.S.J. 2003. Dynamics of magma degassing. *In*: Oppenheimer C., Pyle D.M., Barclay J. (Eds.). *Volcanic Degassing*, London Special Publications, **213**:5-22.

Thiede D.S. & Vasconcelos P.M. 2010. Parana flood basalts: rapid extrusion hypothesis confirmed by new $^{40}Ar/^{39}Ar$ results. *Geology*, **38**(8):747-750. https://doi.org/10.1130/G30919.1

Thordarson T. & Self S. 1998. The Roza member, Columbia River Basalt Group: a gigantic pahoehoe lava flow field formed by endogenous processes? *Journal of Geophysical Research*, **103**(B11):27411-27445. DOI: 10.1029/98JB01355

Tomazzoli E.R. & Lima E.F. 2006. Magmatismo ácido na Ilha do Arvoredo-SC. *Revista Brasileira de Geociências*, **36**:57-76.

Umann L.V., Lima E.F., Sommer C.A., De Liz J.D. 2001. Vulcanismo ácido da região de Cambará do Sul-RS: litoquímica e discussão sobre a origem dos depósitos. *Revista Brasileira de Geociências*, **31**(3):357-364.

Vieira Jr. N. 1985. *Petrologia e geoquimica do vulcanismo Mesozóico de Jaguarão — RS*. Master Dissertation, Universidade Federal do Rio Grande do Sul, Porto Alegre, 136 p.

Vieira Jr. N. & Roisemberg A. 1985. Formação Jaguarão – nova unidade vulcânica mesozóica no RS. *In*: Simpósio Sul-Brasileiro de Geologia, 2, 1985, Florianópolis. *Anais*... Florianópolis, p. 507.

Waichel B.L., Lima E.F., Viana A.R., Scherer M.S., Bueno G.V., Dutra G.T. 2012. Stratigraphy and volcanic facies architecture of the Torres Syncline, Southern Brazil, and its role in understanding the Paraná-Etendeka Continental Flood Basalt Province. *Journal of Volcanology and Geothermal Research*, **215-216**:74-82. DOI: 10.1016/j.jvolgeores.2011.12.004

Walker G.P.L. 1971. Compound and simple lava flows and flood basalts. *Bulletin of Volcanology*, **35**:579-590. DOI: 10.1007/BF02596829

Walker G.P.L. 1973. Lengths of lava flows. *Philosophical Transactions of the Royal Society of London*, **274**:107-116. DOI: 10.1098/rsta.1973.0030

Witham F. 2011. Conduit convection, magma mixing, and melt inclusion trends at persistently degassing volcanoes. *Earth and Planetary Science Letters*, **301**:345-352. https://doi.org/10.1016/j.epsl.2010.11.017

Assunto	**BUVO-D-18-00026 - BV Acknowledgement of Submission**
Remetente	Bulletin of Volcanology <em@editorialmanager.com>
Para	Matheus Simões <matheus.simoes@ufrgs.br>
Responder para	Bulletin of Volcanology <fran.vanwyk@uca.fr>
Data	2018-03-01 14:51

Dear Mr. Simões,

We acknowledge, with thanks, receipt of the proposed Research Article "Magmatic flow patterns in silicic feeder conduits and lava flows from Paraná-Etendeka LIP, southern Brazil: AMS fabric, magma transport properties and implications for emplacement".

The submission id is: BUVO-D-18-00026
Please refer to this number in any future correspondence.

Andrew Harris, Executive Editor, will assess the suitability of your manuscript for submission to the journal and if his decision is favourable we will then assign an Associate Editor to handle the paper.

You may check on the progress of your paper by logging onto Editorial Manager as an author:

Your username is: matheus.simoes

If you forgot your password, you can click the 'Send Login Details' link on the EM Login page at https://buvo.editorialmanager.com/.

We expect to be able to contact you again shortly.

Sincerely,

Andrew Harris
Editorial Administrator

fran.vanwyk@uca.fr

Now that your article will undergo the editorial and peer review process, it is the right time to think about publishing your article as open access. With open access your article will become freely available to anyone worldwide and you will easily comply with open access mandates. Springer's open access offering for this journal is called Open Choice (find more information on www.springer.com/openchoice). Once your article is accepted, you will be offered the option to publish through open access. So you might want to talk to your institution and funder now to see how payment could be organized; for an overview of available open access funding please go to www.springer.com/oafunding. Although for now you don't have to do anything, we would like to let you know about your upcoming options.

Magmatic flow patterns in silicic feeder conduits and lava flows from Paraná Etendeka LIP, southern Brazil: AMS fabric, magma transport properties and implications for emplacement

Matheus S. Simões[1,2], M. Irene B. Raposo[3], Evandro F. Lima[4], Carlos A. Sommer[4]

[1] Post-graduate Program, Instituto de Geociências, Universidade Federal do Rio Grande do Sul, Av. Bento Gonçalves, 9500, Prédio 43136, Caixa Postal 15001, Agronomia, CEP: 91501-970, Porto Alegre, RS, Brazil (e-mail: matheus.simoes@ufrgs.br), orcid.org/0000-0003-2012-6738

[2] CPRM – Serviço Geológico do Brasil (Geological Survey of Brazil) – Manaus, Av. André Araújo, 2160, CEP 69060-000, AM, Brazil

[3] Instituto de Geociências, Universidade de São Paulo, Rua do Lago, 562, São Paulo, SP 05508-080, Brazil

[4] Instituto de Geociências, Universidade Federal do Rio Grande do Sul, Av. Bento Gonçalves, 9500, Prédio 43136, Caixa Postal 15001, Agronomia, CEP: 91501-970, Porto Alegre, RS, Brazil (e-mail: evandro.lima@ufrgs.br, carlos.sommer@ufrgs.br)

Abstract

The silicic volcanics of the Paraná-Etendeka large igneous province (LIP) occurs extensively in southern Brazil, where feeder conduits and lava flows were recognized with different lithofacies architecture. In this work we compare magmatic flow structures measured in the field to anisotropy of magnetic susceptibility (AMS) data at eleven conduit and lava flow sites. Conduit sites gave mean flat-lying k_{max}, suggesting horizontal flow. High dispersion of the magnetic susceptibility axes in some sites is explained considering obstruction of flow by fragments and complex folding patterns. Silicic lavas show flat-lying k_{max}-k_{int} planes with k_{max} plunging to NE, NW, SE and SW. Viscosity of magma was calculated at 1000°C to for three H_2O content threshold: dry ($10^{6.6}$ Pas), 0.5% ($10^{5.1}$ Pas) and 1.3% ($10^{3.8}$ Pas). Low bubble content in lava flows and central part of conduits is favorable to decrease the capillary number *Ca* and the dynamic capillary number *Cd*, keeping the initial calculated viscosity. These domains have low content of fragments and less than two folding phases, representing potential zones where the magnetic fabric is parallel to the flow. In the boarder of the conduits larger shear rates, high fragment and bubble content inducing the unsteadiness of the flow (high Ca and Cd) favor random distribution of the magnetic fabric. The path of magma to surface through fault zones was in extensional regime. Constant generation and eruption rates explain the large volume of silicic lavas in the southern Paraná-Etendeka LIP, keeping their low viscosity to run long distances and form extensive units.

Keywords: Large Igneous Province, silicic volcanism, AMS, feeder conduits, lava flow

ACKNOWLEDGEMENTS The authors thank *Conselho Nacional de Desenvolvimento Científico e Tecnológico* (CNPq, projects 9784, 441766/2014-5, 303015/2015-2 and 400724/2014-6), FAPESP (project 2012/06082-6) and FAPERGS (project 2311-2551/14-1) for funding. We thank also Roberto J. Noll Filho, Fernando da Luz and Natalia G. Pasqualon for helping in the field work.

1 Introduction

Development of flow patterns in silicic magma creates a series of structures depending, mainly, on strain rates, temperature variation and volatile content. Foliation and banding are noted as penetrative structures in obsidian flows (Manley & Fink, 1987) and several processes were ascribed to generate them, such as magma mixing, stretching and folding, continuous brecciation and welding, microlite variation, vesicularity variation, among others (e.g. Seaman et al. 1995; Castro and Cashmann 1999; Gonnermann and Manga 2005; Perugini and Poli 2012). A wide number of explanations about folding and boudinage of magma in viscous or fragile state can be observed as a result of different flow domains in which compressional, directional or constrictive forces act (e.g. Smith and Houston 1994; Castro and Cashmann 1999; Morrow and McPhie 2000; Morgan et al. 2008) while magma is subjected to progressive deformation (e.g. Smith 1996). Above liquidus temperatures, the rheological response becomes more complex as crystals and bubbles start to grow. In this context, the viscous magma can behave like Bingham fluids (Fink 1983).

In the southern portion of the Paraná-Etendeka Large Igneous Province (LIP), the silicic volcanism prior to the Gondwana break-up is dominantly represented by lava flows (Henry and Wolf 1992; Umann et al. 2001; Polo and Janasi 2014; Guimarães et al. 2017; Polo et al. 2017; Simões et al. 2014, 2017; Lima et al. 2012, 2018; Rossetti et al. 2014, 2017) and inferred shallow portion of conduits for some of these flows are described with steeply inclined banding, folding in several scales (from mm- to m-) and intense brecciation (e.g. Lima et al. 2012; 2018; Simões et al. 2017). Subaerial lavas - some recognized as obsidian flows - are dominated by flat-lying distribution of banding, breccias and vesicles, presenting steeply inclined structures only locally.

Investigation about magma transport properties revealed that high temperature conditions (> 1000°C) may have affected the viscosity and the mode of emplacement of these silicic flows, maybe differing from more common rhyolitic and dacitic magmas (Garland et al. 1995; Lima et al. 2012; Simões et al. 2014; Polo et al. 2017).

The purpose of the present work is to characterize the magmatic flow at occurrences of silicic conduits and lava flows in southern Paraná-Etendeka LIP. For this, we investigate the main structures of these volcanic units in field scale and thin section, and provide an AMS (Anisotropy of Magnetic Susceptibility) study. A brief description of the chemical types, pre-eruptive temperatures and magma viscosity is yielded in order to discuss the magma transport properties and to further describe the conduit magma flow and its behavior during subaerial emplacement of lava.

1.1 Geological setting

The Paraná-Etendeka LIP occupies an area of 917,000±15,000 km² (Frank et al. 2009) of which 90% is located in South America and 10% is in Africa (**Fig. 1a**), above the aeolian sedimentary rocks of Botucatu and Etjo formations. In South America the Paraná-Etendeka LIP comprises a 1700 m-thick association of tholeiitic magmas (Melfi et al. 1988), with basaltic to intermediate lavas, dykes and sills prevalent (97.5% of total volume) over silicic units (2.5%). The volcanic units of Paraná-Etendeka LIP are represented by the Serra Geral Group and in southern Brazil, they have chemically more primitive compound and simple pahoehoe basaltic flows in the base, represented by the Torres Formation (Rossetti et al. 2017). Vertically stacked sheet-like rubbly pahoehoe basaltic flows of the Vale do Sol Formation cover the compound flows and represents the more voluminous basalt lava unit. The silicic volcanics cover these basalt flows and are represented by

the Palmas Formation. The last volcanic manifestations in the area are the compound and simple oxidized basaltic flows of the Esmeralda Formation (Rossetti et al. 2017).

In a regional scale, the distribution of the Paraná-Etendeka LIP volcanic rocks is made by the classification of mafic and silicic types, based in their TiO_2 content (e.g. Bellieni et al. 1984; Peate et al. 1992). In the case of the silicic rocks, the ones presenting high-Ti (TiO_2 > 2 wt.%) are called Chapecó-type magmas (Peate et al. 1992) and are exposed in the northern portion of the basin, between the NW-SE trending Ponta Grossa arch and the Torres structural valley (Fig. 1b). In the southern portion, where the studied areas outcrop, the low-Ti (TiO_2 < 2 wt.%) silicic terms are classified as dacites and rhyolites presenting no more than ~10 vol.% of phenocrysts called Palmas-type magmas.

Further, towards the south of the LIP, a small area (3.2 km^3) of peraluminous dacitic lavas with cordierite, orthopyroxene, plagioclase and ilmenite as liquidus phases (Vieira 1985; Vieira and Roisenberg 1985) occurs in the Jaguarão region. It is located near to major shear zones of Neoproterozoic age that may have been reactivated during Early Cretaceous (Comin-Chiaramonti et al. 2010). In Uruguay, the Cretaceous volcanic rocks occur trending NE-SW (**Fig. 1b**) and the chemical compositions are also bimodal. The basic Santa Lucía type has Ocean Island Basalts (OIB) geochemical signatures and the Treinta Y Trés type is broadly similar to the low-Ti Gramado lavas (Kirstein et al. 2000). Silicic rocks are dacites to rhyolites from Lavalleja Series (high Ti/Zr, low Nb/Y, higher Sr and Nd isotope ratios) and Aigua Series (high Rb/Sr, high Rb/Ba, high Th).

Parts of the plumbing system for basaltic and silicic lavas in southern Brazil are represented by the NW-SE trending Ponta Grossa and the NE-SW trending Santa Catarina and São Paulo dyke swarms (e.g. Raposo 1998, 2017; Florisbal et al. 2014). In Rio Grande do Sul state; postulated conduit systems for silicic lavas were described to the south of a curved NE- trending structure called Antas Lineament (Simões et al. 2017). This structure is parallel to the main regional structures, like NE-SW trending Precambrian Porto Alegre Suture (Fernandes et al. 1995) or younger faults cutting the basin as Leão and Açotea faults (Zalán et al. 1991).

In the present study, the investigation of low-field AMS fabric and rheological characterization were carried out in three key-areas where postulated conduits and related lava flows outcrop near each other (**Fig. 2a, b**). In northeast of Rio Grande do Sul state the conduits outcrop in several elevations, since 400 m to ~ 950 m. Each conduit system and related lava flow units display characteristic lithofacies architecture (Simões et al. 2017), as will be demonstrated in the results section.

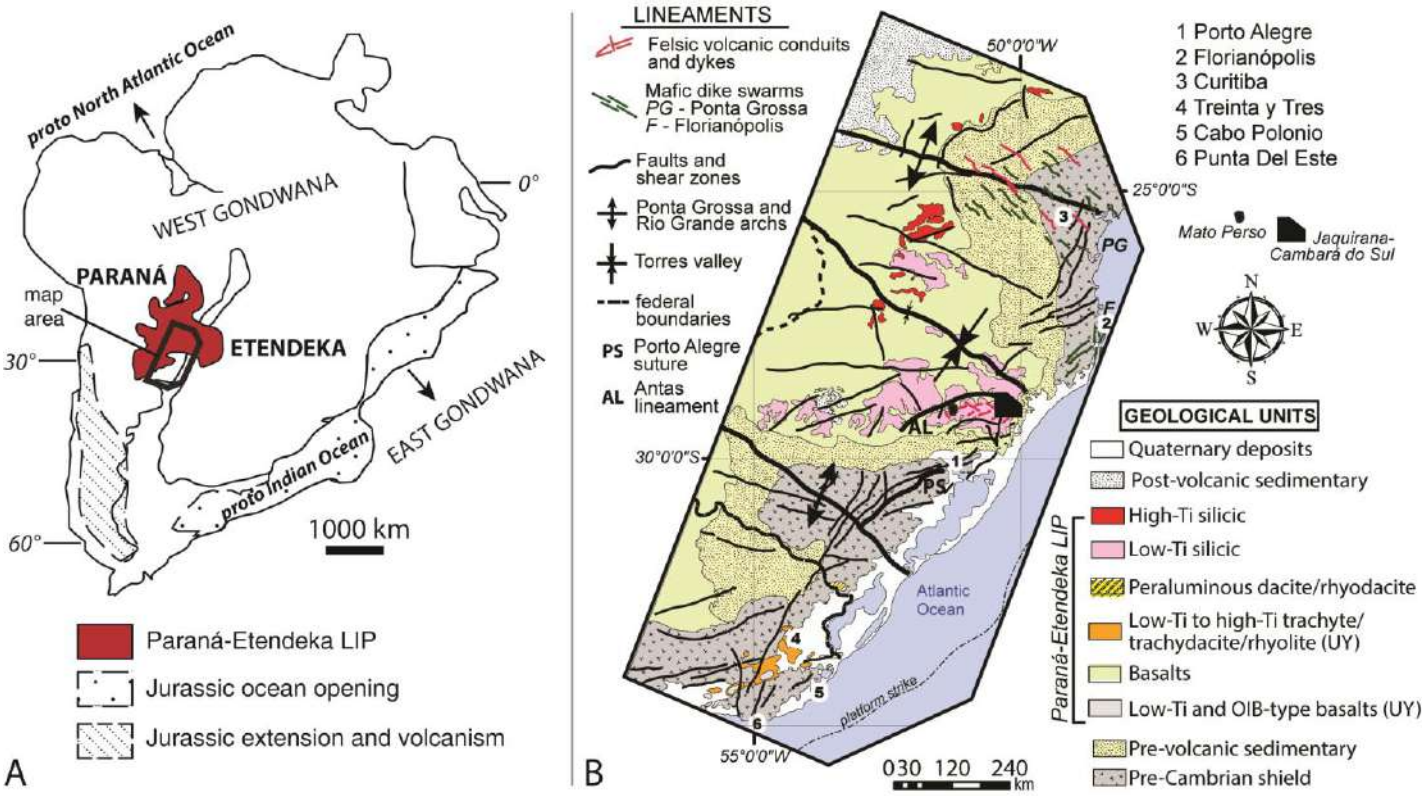

Figure 1 Tectonic setting and location of study areas. (A) Distribution of the Paraná-Etendeka volcanism in Cretaceous (modified from Rapela & Llambias 1999; Mpodozis & Ramos 2008). (B) Regional geological map of the southern Paraná-Etendeka province in Brazil with the main structures. The study areas of Mato Perso and Jaquirana-Cambará do Sul are located and detailed in figure

1.2 Emplacement and correlation of silicic units in Paraná-Etendeka LIP

The silicic volcanics of the Serra Geral Group were firstly described as volatile-poor and high-temperature rheomorphic ignimbrites. Arguments used include their laterally persistent sheet-like nature and the absence of typical ignimbrite textures even near the top and base of each unit, which was attributed to obliteration by intense welding (Bellieni et al. 1986; Melfi et al. 1988; Petrini et al. 1989; Roisenberg 1989; Garland et al. 1995; Milner et al. 1995; Bryan et al. 2010). Milner et al. (1995) proposed the correlation of some subgroups of Palmas magma-type with the Namibian quartz latites. The intrusive, circular Messum Complex, was identified as a potential emission center (Milner and Duncan 1987; Milner et al. 1992; Ewart et al. 1998; Ewart et al. 2002), even though the thickness of the silicic volcanic sequence is inferior in the African counterpart. In these models, the silicic deposits in South America would need to have traveled >300 km from their source and been deposited as extensive pyroclastic density currents (e.g. Milner et al. 1995; Bryan et al. 2010).

Typical pyroclastic deposits in this LIP are found in the Mesozoic (132 – 124 Ma) Arequita Formation (AF), Uruguay, and described by Muzio et al. (2009). The AF contains high SiO_2 (>72 wt.%) lava flows with quartz, K-feldspar and sodic plagioclase phenocrysts. Pyroclastic deposits are confined to the east of the N20°E trending India Muerta Lineament and are consisted of pyroclastic breccias, lappili tuffs and monomitic breccias.

In southern Brazil, the paucity of pyroclastic lithofacies, with recognition of only local pyroclastic textures in extensive petrographic studies (Comin-Chiaramonti et al. 1988), together with the regional description of coherent and autoclastic lithofacies in a variety of lava bodies (lobes, domes and flows) led other authors to suggest that the silicic deposits are predominantly effusive (Henry and Wolf 1992; Umann et al. 2001; Lima et al. 2012; Polo and Janasi 2014; Simões et al. 2014, 2017; Guimarães et al. 2017; Polo et al. 2017a,b). Other features such sand and mud peperites found in both Palmas- and Chapecó-type lava flows favor to the lava flow interpretation also in the center of the LIP (e.g. Lucchetti et al. 2014).

Feeder conduits for silicic lavas were firstly proposed and described in quarries at the city of São Marcos, Rio Grande do Sul (Lima et al. 2012, 2018; De Campos et al. 2016). In this region, the rhyodacites have compound magmatic foliation revealed by the alternation of different crystallinity and oxidation grades (Lima et al. 2012). Fragmentation involving rheomorphic and re-melting events described were assigned by De Campos et al. (2016) to parallel oscillations in a very efficient magma ascent system together with high heat flux for conduit system evolution. Other interpretation of the São Marcos outcrops; based in AMS fabrics, showing dominant flat-lying orientation of K_{max} is of thermal erosion from lavas that developed sort of a peperite of underlying flow fragments (Cañon-Tapia and Raposo 2017).

In other areas at the northeast of Rio Grande do Sul (Mato Perso, Jaquirana and Cambará do Sul) the inferred conduits exhibit lithofacies architecture with banded vitrophyres containing variably vesicular fragments grading laterally into breccias. These structures have dominant sub-vertical orientations trending to NE-SW and NW-SE (Simões et al. 2017). In a regional scale, these conduit outcrops are elongated NW-SE to NE-SW shapes, being covered by flat-lying silicic lava flows (Lima et al. 2012; Simões et al. 2017a,b).

1.3 Conduits and lava flows

In field scale the structural patterns present in the conduits are shared by most expositions. They have near-vertical banding (**Fig. 2 c,d**) in the central and more resistant part, generally composed of grey to black vitrophyre. Toward the boarders of the outcrops it is notable the mixing of this dark rock with a oxidized vitrophyre (Lima et al. 2012; De Campos et al. 2016; Simões et al. 2017a in press). The mixing patterns can be dominantly chaotic (De Campos et al. 2016), where several folding phases are seemingly like the mixing of two fluids in 2D (e.g. Ottino 1989). Despite these mixing features, recognized in outcrop scale, there is a NE-SW to NW-SE trending of the major unfolded sub-vertical banding. In the external parts of the conduits the vitrophyres mix and acquire several colors in the red and grey scales, surrounding red vitrophyre fragments. Fragments are common features in different parts of the conduits, sometimes with meter-size near the center but more abundant in the boarder, with few to dozens of centimeters, where welding of the fragments may be also found. Vesiculation patterns in conduits are not the marker of the banding but they follow the banding and fold axial surfaces orientation (Simões et al. 2017). Where the banding is vertical, the vesicles tend to have the inverse gout shape, i.e., pointing to the paleo-surface.

The lava flows have structures like dominant flat-lying foliation related to an incipient and locally recognized magmatic banding (Fig. 2e). Their vesicles are frequently tube-shaped near the base and spherical-shaped toward the top of the flows. Oxidized lava flows under the conduits also display a vesiculated frothy top (Simões et al. 2018 in press).

The aim of AMS determination in this study is to compare the behavior of the magnetic fabric in those outcrops considered to be feeder conduits and in those interpreted as lava flows. We choose three key-areas for sampling: the exposition of a banded obsidian lava flow in a dimension stone quarry placed at Cambará do Sul city (site CM1), which was an opportunity to collect more robust data (42 drill cores) in horizontal and vertical positions; a vertical succession of obsidian flows (sites CM2, 3, 5) and conduit (site CM4) in Jaquirana city (8 – 11 cores/site); a pair of conduits and associated lava flow in the Itaimbezinho (National Park of Aparados da Serra), where 11 and 12 cores per site (IT1 and IT2) were collected; and in a sequence of conduits and lavas near Caxias do Sul city (Mato Perso district), where 10 to 16 cores/site were obtained (sites MS1, 2, 3 and 4).

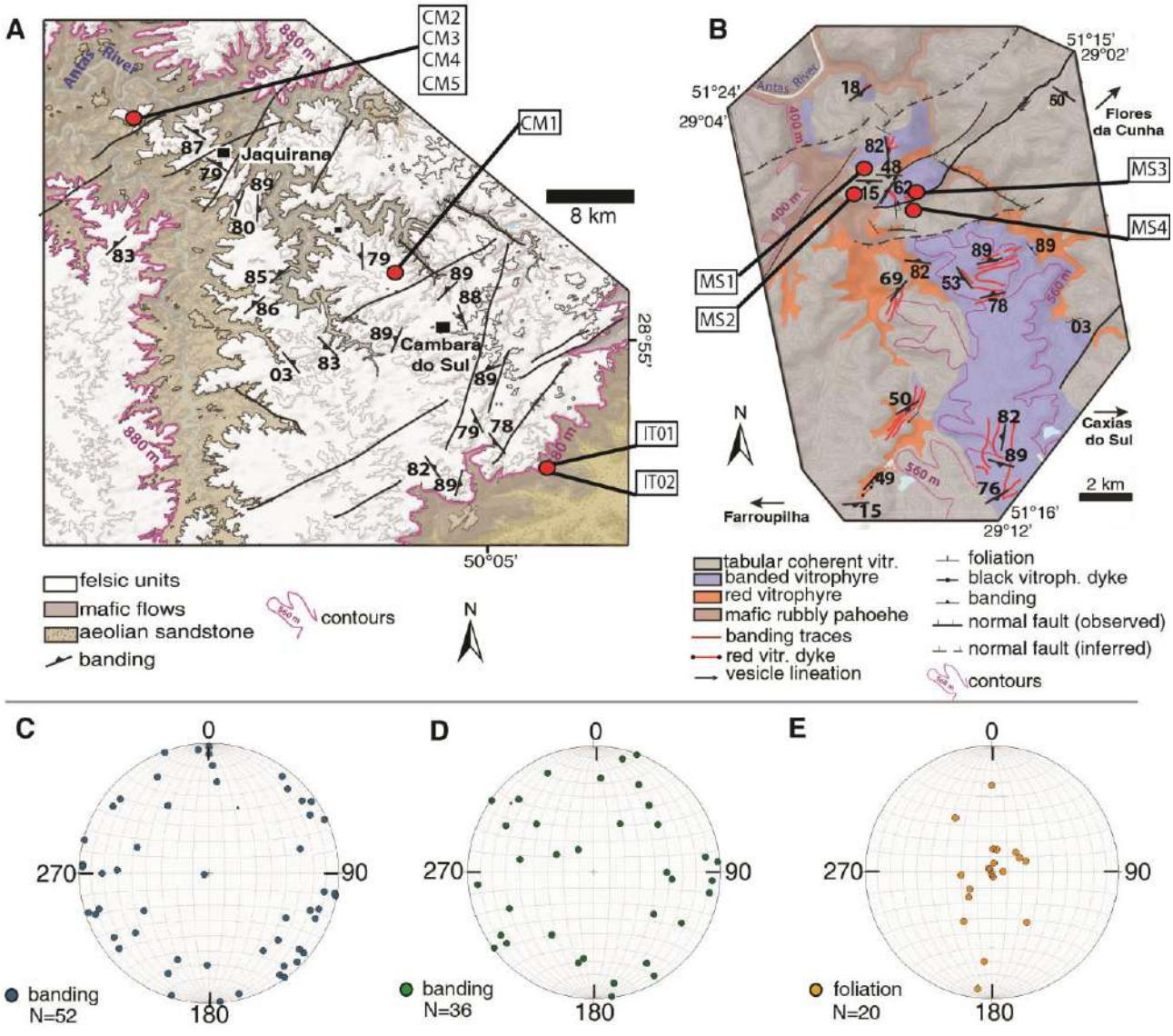

Figure 2 Geological maps and location of sites selected for AMS analyses. (A) Jaquirana-Cambará do Sul area. (B) Mato Perso area. (C, D, E) Stereonets with banding data measured in the field from Jaquirana-Cambará do Sul (N=52), Mato Perso (N=36) and foliation in lava flows at Mato Perso area (N=20)

2 METHODS

2.1 Anisotropy of Magnetic Susceptibility

The measurements involving AMS were obtained in the Laboratory of Magnetic Anisotropies and Rock Magnetism of the Institute of Geosciences – São Paulo University (USP). Each drill core was sliced in approximately 2,2 cm specimens for measurement using an MFK1-FA instrument with 3D rotator of AGICO. The measurement consisted in the application of a low magnetic field (425 A/m) to the sample along its rotation through three orthogonal axes. The AMS orientation of each specimen is represented in the lower hemisphere equal-area stereonets. The average orientations of principal susceptibility axes present in **Table 1** are represented by the mean values (large symbols in the stereonets) and were calculated using the Hext-Jelinek statistics (Hext 1963; Jelinek 1978) in the software ANISOFT 4.2 (Chadima and Jelinek 2009). Calculated variables are divided into magnitude and shape parameters. The mean susceptibility tensor ($k_m = k_{max}+k_{int}+k_{min}/3$) is the average of the total susceptibility of the specimen and the corrected degree of anisotropy (Pj) is assumed as measure of degree of anisotropy. The shape-parameter T defines the eccentricity of the strain ellipsoid where $0 < T \leq 1$ is referred to oblate shapes and $-1 \leq T < 0$ correspond to prolate shapes. This relation can be also observed when plotting the T and Pj parameters (Jelinek 1981; Hrouda 1982).

Thermomagnetic curves in an Ar atmosphere were obtained by a CS-4 apparatus coupled to the MFK1-FA and the specimens were progressively heated up to 700°C and subsequently cooled to room temperature. Hysteresis measurements at room temperature were performed using a vibrating sample magnetometer (VSM—Nuvo, Molspin) in fields up to 1 T.

2.2 Whole-rock geochemical analysis

To calculate estimated temperatures and viscosities a set of whole-rock geochemical analyses was obtained. The analyses were made at Acme Analytical Laboratories LTD., Vancouver, Canada, utilizing analysis routines 4A and 4B. In the first one, the main oxides and several minor elements total abundance were obtained from 0.2 g of analyzed sample by Inductively Coupled Plasma – Emission Spectrometry (ICP-ES) with detection limit of 0.01% for SiO_2, Al_2O_3, Fe_2O_3, CaO, MgO, Na_2O, K_2O, MnO, TiO_2 and P_2O_5. In the second one the rare earth and refractory element results were obtained from 0.2 g of analyzed sample by ICP – MS (Mass Spectrometry).

The apatite saturation model of Harrison & Watson (1984) was used to estimate *liquidus* temperatures. It is based in experimental data of apatite solubility as function of magma temperature and composition. The model used in this work to estimate the viscosity (Giordano et al. 2008) uses whole-rock chemical compositions input and was made out predicting Newtonian non-Arrhenian temperature dependence of silicate melts. It was calibrated from more than 1770 sample experimental analysis in a wide range of temperatures and magma compositions. The effective H_2O content of 1.3 wt.% is an estimated value based in the plagioclase and liquid composition (M.S. Simões, unpublished data).

3 Results

3.1 Magnetic mineralogy

Thermomagnetic curves are present in **figure 3** and display slightly different patterns, but in all cases the intensity of susceptibility (k) decreases at 580°C to 600°C. Irreversible curves are the most common; with exception of sample CM3 which the cooling curve had approximately the same k values of the heating curve. In the other samples, the curves do not coincide and this response is considered as a product of mineralogical alteration or destruction during the heating. The curves and Curie temperatures near ~580 °C are typical of Ti-poor magnetites, which are also verified in thin section in the form of glomeroporphyritic aggregates of microphenocrysts or dispersed as 0.1 – 0.5 mm microlites. In the site IT01 we obtained curves for oxidized (IT01A) and black (IT01) vitrophyres. The oxidized sample had a slightly decrease in k at ~ 350°C and then at ~ 580°C, indicating a probable mixture of Ti-poor magnetite and maghemite, although fine hematite lamellae were observed spread in the groundmass.

The presence of ferromagnetic grains is verified by the use of hysteresis curves (**Fig. 4**). The results of magnetization in VSM yielded Mrs (remanent saturation magnetization), Ms (saturation magnetization), Hc (coercitive force), Hcr (remanent coercivity) values, determined by the application of a decreasing backfield after saturation. Ms and Mrs are from 55.7 to 289.2 A/m and 6.5 to 62.5 A/m, respectively. Hc is between 3.4 and 27.0 A/m, while Hcr values range from 13.4 to 46.9 A/m. In the Day plot (Day et al. 1977; Dunlop 2002), the bulk of samples lie in the pseudo-single domain (PSD) field (**Fig. 5**). The contribution of magnetic minerals is between 97.7% and 99.8%, and the values of Hc are indicative of fine and coarse fully-saturated Ti-poor magnetite as the dominant carrier of magnetic susceptibility.

222 **Table 1** – Shape and directional AMS parameters for conduits and lava flows. CM1 to 5 and IT1-2 are from Jaquirana-Cambará do Sul area. MS1 to 4 are from Mato Perso area.

Site	Coordinates			Type	N	Km [E^{-2}]	Pj	T	k_{max}				k_{int}				k_{min}			
	X	Y	Z (m)						Dec	Inc	α1	α 2	Dec	Inc	α 1	α 2	Dec	Inc	α 1	α 2
CM1	-29.000	-50.174	1034	lava	77	3.51	1.059	-0.009	334.5	2.7	38.2	9.3	244.1	8.2	38.3	23.6	82.4	81.4	23.9	9.7
CM2	-28.832	-50.431	863	lava	8	2.72	1.016	0.118	292.9	19.9	23.1	9.1	28.3	14.6	23.9	9.1	152.2	64.9	12.2	7.8
CM3	-28.832	-50.428	877	lava	9	5.82	1.009	0.224	214.3	4.8	31.9	7.9	304.3	0.3	31.6	16.1	37.5	85.2	16.6	9.5
CM4	-28.833	-50.428	902	conduit	33	7.26 E^{-3}	1.027	-0.077	146.8	23.3	26.9	13.9	38.7	35.8	29.9	22.5	262.4	45	27.6	16.3
CM5	-28.835	-50.429	923	lava	19	3.34	1.022	0.354	241.6	8.1	19	8.7	150.2	9.6	18.2	6.3	11	77.4	10.7	6.4
IT1	-29.178	-50.026	1007	conduit	33	3.76	1.027	-0.036	324.7	85.2	46.6	32.2	46.7	38.1	38.7	31.5	204.2	2.4	38.7	31.5
IT2	-29.179	-50.021	965	lava	32	2.45	1.020	0.466	186	1.5	70	9.4	95.8	6.9	70	9.1	288.1	83	10	9.2
MS1	-29.097	-51.330	646	lava	38	1.67	1.006	-0.4	248.7	0.7	23.3	10.3	158.6	14	23.1	17.2	341.4	76	19	12.2
MS2	-29.099	-51.329	654	conduit	27	3.58	1.044	-0.012	340	0	84	28.2	70.1	38.7	84	42.5	250	51.3	44.8	22.6
MS3	-29.106	-51.327	655	conduit	45	3.39	1.058	0.065	282.5	11.3	37.4	13.7	189.2	16.2	41.2	28.1	46	70	34.9	12.6
MS4	-29.108	-51.327	622	lava	53	2	1.009	-0.005	59.7	3.4	34.1	15.6	151.7	30.6	34	19.1	324	59.2	19.8	14.9

223

224

225

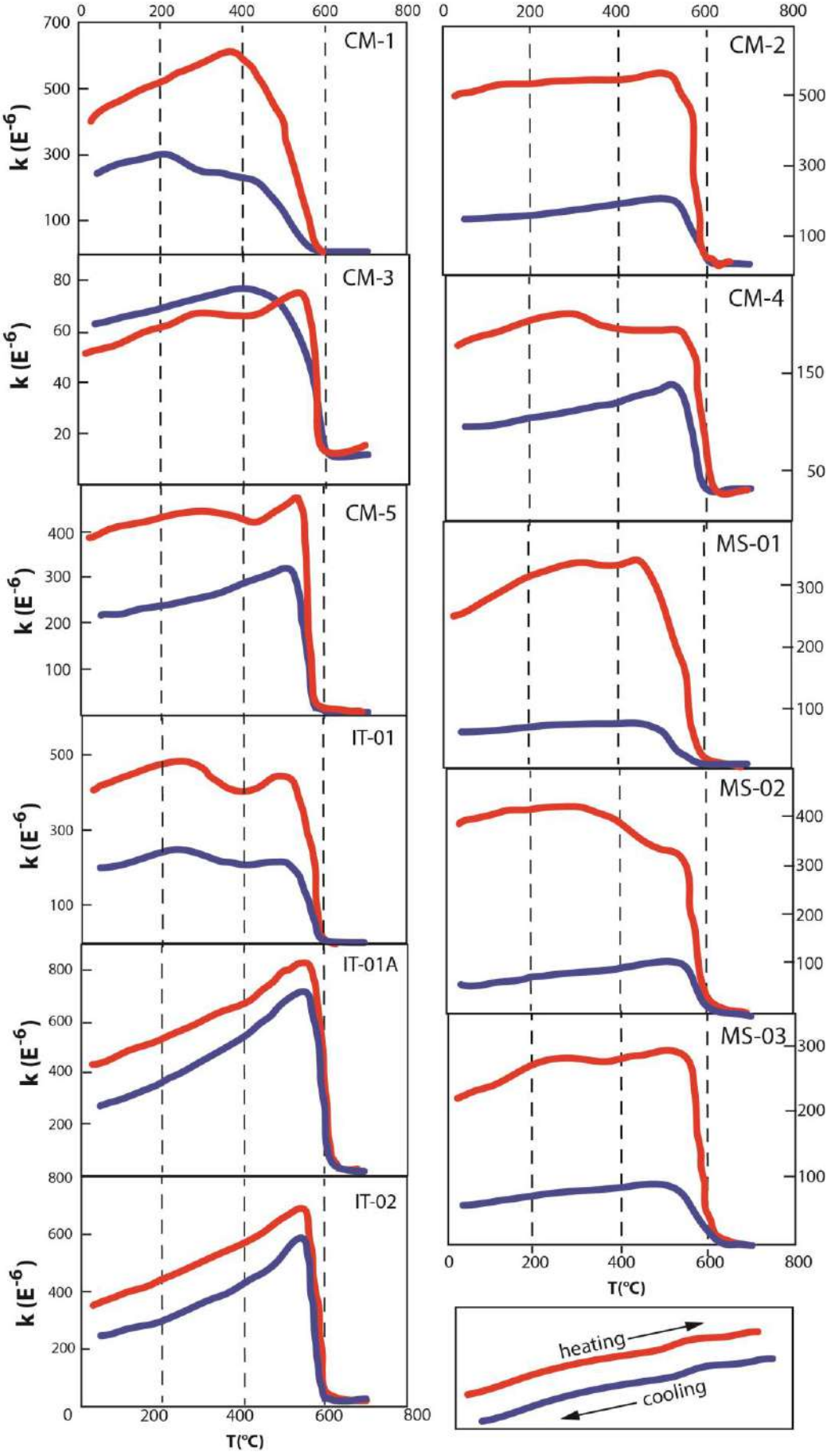

Figure 3 Thermomagnetic curves representative of the analyzed samples

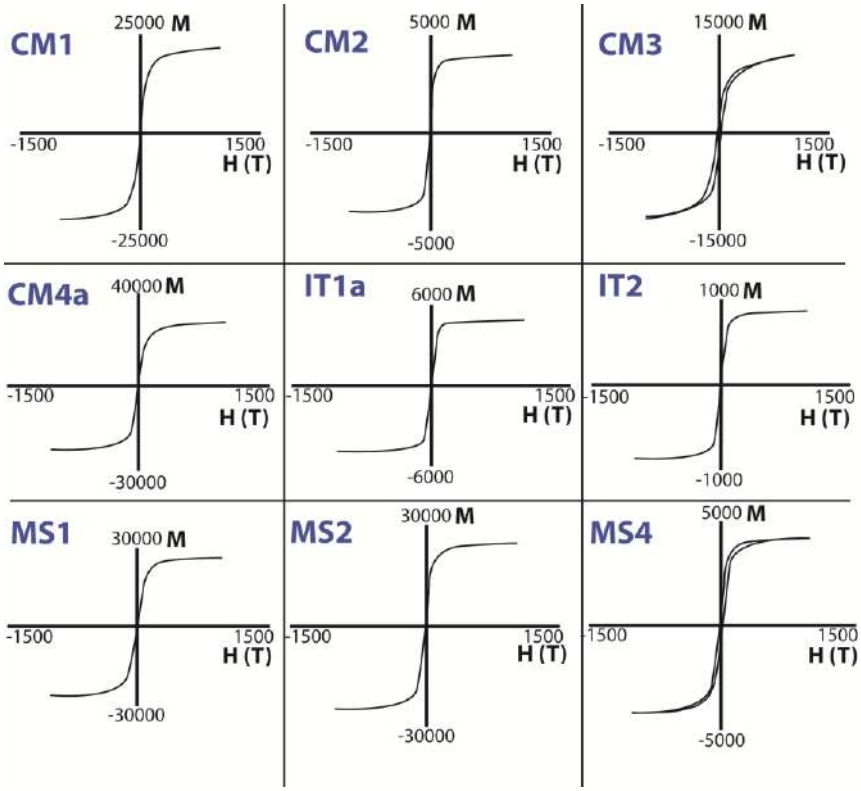

Figure 4 Representative hysteresis curves obtained with increasing of the magnetic field to 500 – 1000 mT

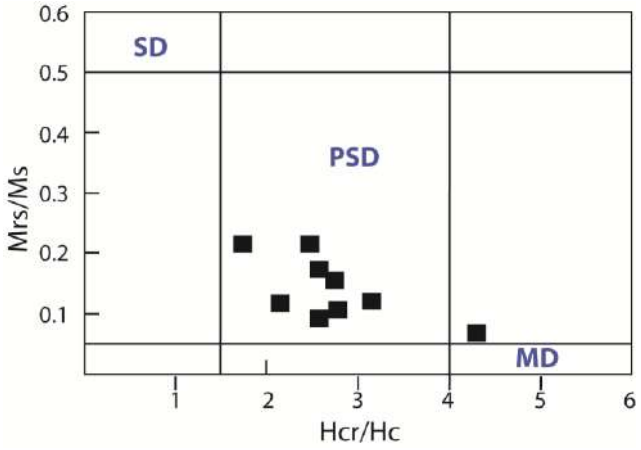

Figure 5 Day plot (Day et al. 1977; Dunlop 2002) with Mrs (magnetization remanence)/Ms (saturation magnetization) versus Hcr (Hcs/coercive force). SD = Single-domain, PSD = Pseudo single-domain, MD = Multi-domain

3.2 Anisotropy of magnetic susceptibility fabric

AMS measurements are compared with macrostructures like banding and folding for each site, considering the field relations when two or more sampled outcrops are adjacent. The strict angles between intrusion margins and the main

magmatic flow is not considered because the contacts of postulated conduits with the surrounding rocks are only observable in site CM4, but these portions were very weathered, thus unsuitable for sampling.

3.2.1 Scalar parameters

The vitrophyres collected in sites correspondent to conduits have mean susceptibility values (k_m) about 10^{-2} SI (**Tab. 1**) with the exception of sample CM4 (7.26 10^{-3} SI). Without this sample, k_m varies between 1.67 10^{-2} SI and 5.82 10^{-2} SI. In a general way, conduit-related samples yielded higher mean susceptibility values when compared to the lava flow samples. This pattern is accompanied by the increase of the mean corrected degree of anisotropy (Pj=exp[root{2[$n_1 - n_m$)2 + ($n_2 - n_m$)2 + ($n_3 - n_m$)2]}]; where $n_1 = \ln k_{max}$, $n_2 = \ln k_{int}$, n3 = $\ln k_{min}$ and $n_m = n_1+n_2+n_3/3$)) from 1.006 to 1.022 in the lavas (MS1,4; CM2,3,5; IT02) and from 1.027 to 1.058 in the conduits (MS2,3; CM4; IT1). The higher value of Pj is at site CM1, a locally banded lava flow.

When the anisotropy degree ($P=K_{max}/K_{min}$) is plotted against the shape-parameter T, [$2\ln(k_{int}/k_{min})/\ln(k_{max}/k_{min})$] -1, there is a range of magnetic susceptibility ellipsoids. Some of the samples representing lava flows display even prolate, oblate an triaxial shapes (**Fig. 6** – CM1-2, MS1), although lavas with dominantly oblate ellipsoids also occur (Fig. 6 – CM5, IT02). An exception, sample MS1 represent a lava flow unit with dominant prolate shapes. For the conduits, the ellipsoid shapes tend to be prolate and oblate with minor triaxial (**Fig. 6** – CM4, IT01, MS2-3).

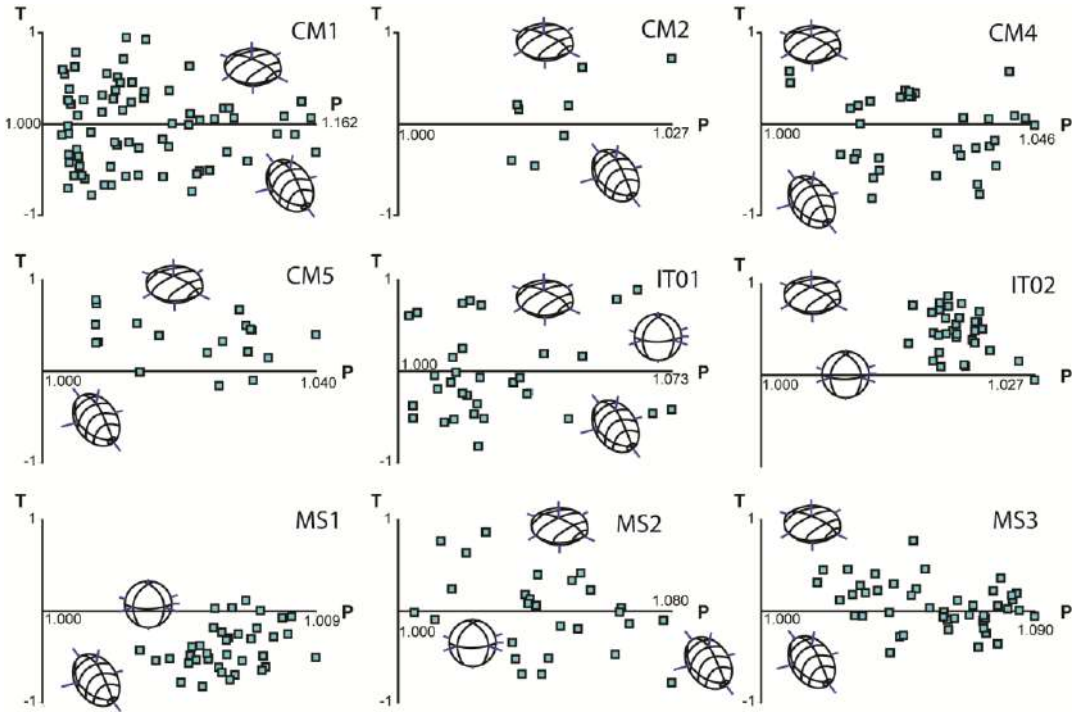

Figure 6 Plots of the shape parameters ($P = K_{max}/K_{min}$) versus T, [$2\ln(k_{int}/k_{min})/\ln(k_{max}/k_{min})$] -1 for the analyzed samples

3.2.2 Site CM1 – Cambará do Sul obsidian flow

Near the road to Capão Penso, Cambará do Sul city rural area, in elevations of 990 - 1020 m above the sea level, there are banded vitrophyres with sub-vertical banding striking to NE-SW and NW-SE. Approximately 60 km to northwest of this city, in elevations from 1030 to 1040 m, obsidian flows with flat-lying flow banding, which is locally steeply inclined and folded, dominate and one of them was picked out for AMS sampling .The wide exposure was used as stone dimension quarry, making possible to better observe the structures and to collect a more significant number of core samples in several positions.

The obsidian flow has a "boomerang" shape with one arm oriented according NW-SE and another oriented along NE-SW direction (**Fig. 7a**). The internal structure of the flow is made of cm-scale obsidian bands (NE-SW oriented) folded in plunging inclined to reclined geometries (**Fig. 7b**). The bands also display interference zones with fan shapes (**Fig. 7b, c**). Complex arrangement of the flow banding is present as several asymmetric folds with autobreccias in the flanks (**Fig. 7d**). Toward the lateral parts of the flow, the obsidian turn into a more homogeneous black-colored lithology and display approximately 10-15% of large flattened amygdales with up to 10 cm, filled by quartz (**Fig. 7e**). Together, the plane formed by the amygdale population is flat with up to 5° dip, suggesting horizontal magma flow to these portions of the outcrop.

AMS data collected along banded, folded and homogeneous obsidian are plotted in an equal-area stereonet (**Fig. 7f**) and show that K_{max} oriented along NW (334.5°, mean), SE and NE with an average plunge of 2.7° (**Tab. 1**). K_{min} have a slightly NE-SW distribution in the diagram, with high inclination angles (81.4°, mean). K_{int} has a preferred direction to SW (244.1°, mean) and display flat plunges of 8.2° in average. The flat K_{max} plunges to NW (mean), NE and SE combined to k_{int} mean values to SW is parallel to the oblate amygdale orientation (**Fig. 7e**) and agree with the major disposal of the lava flow (see **Fig. 7a**).

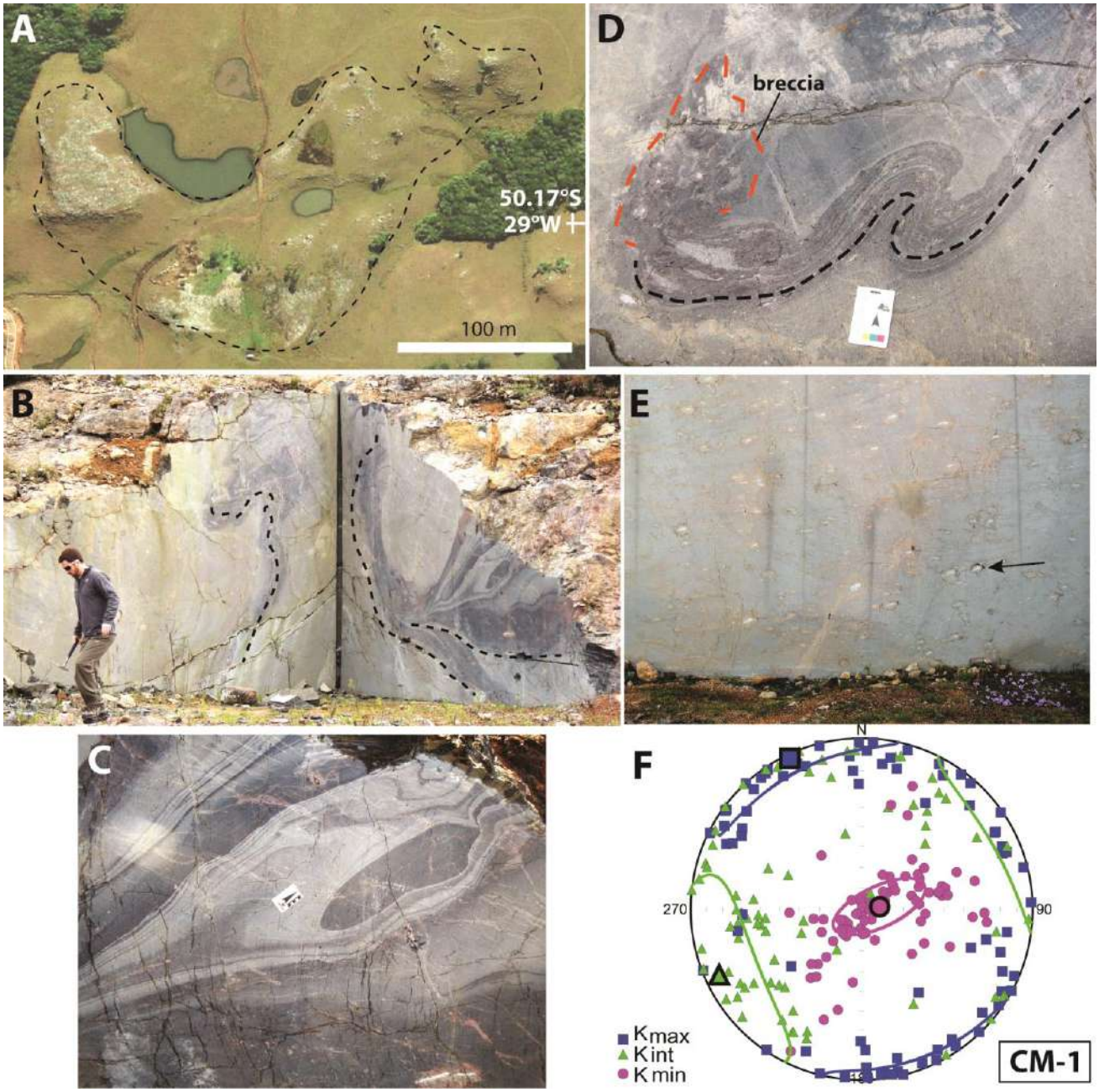

Figure 7 Site CM1, 60 km northwest of the city of Cambará do Sul. (A) Satellite image compiled from Google Earth showing the main orientation of the lava body. (B) Inclined folds and banding in the central part of the lava flow. (C) Interference patterns of the flow banding, dipping 50° to 75°. (D) Asymmetric fold with breccia in the limbs. (E) Flat-lying stretched amygdales with up to 10 cm. (F) Equal-area stereonet showing the AMS orientation of individual specimens and mean K_{max} (horizontal), K_{int} (horizontal) and k_{min} (vertical)

3.2.3 Sites CM2, 3, 4 and 5 – Jaquirana

In the road between Jaquirana and Bom Jesus cities we sampled for AMS in an intercalation exposure of obsidian flows and conduits. The **figure 8a** shows the disposition of the sampled units together with measured structures and the site correspondent AMS stereonet.

In the base of the profile there is an obsidian flow upper portion with massive texture, presenting cm-size amygdales (5 – 10 cm in the longest axis) filled with quartz (site CM2). This site gave K_{max} dipping 19.9° to NW and mean K_{min} dipping 64.9° to SE. This flow has a top breccia with at least 2 m thick covered by a microfractured vitrophyre (site CM3, **fig. 8b**). This vitrophyre have a flat-lying fracture system with sub-millimeter scale aperture and dark halos, developing an apparent banding (**Fig. 8a**, top right sterenonet). It yielded K_{max} mean axes plunging 4.8° to SW and near vertical K_{min} values.

This unit is cross-cut by banded vitrophyres from site CM4, occurring with several magmatic flow domains - i.e. domains in which the flow have different orientation, more or less folding phases or fragment content - but with a tendency to steeply inclined disposal (**Fig. 8c**). The vesicles in this vitrophyre display elongated shapes (**Fig. 8d**) that follow the steep and flat banding orientation, some with inverse drop shapes. Toward the boards of the CM4 outcrop the banding is intensely folded. The folds have several phases with different limb and axial surfaces orientations (**Fig 8e**). Flat-lying sheath folds are also observed. In this site the mean K_{max} has an averaged value of 23.3° in inclination to 146.8° (SE). In the specimens where k_{max} mean axis is steeply inclined, it is parallel to the vertical flow planes measured in the field, according NW-SE (**Fig. 8c**). The k_{int}-k_{min} axes distribution generate a girdle plane (**Fig. 8a**, CM4 stereonet) oriented parallel to one of the outcrop-scale fold flanks, plunging 72° to 350° (NE-SW strike). Given that, we interpret a prevailing flow domain with a near flat-lying K_{max}, dipping to SE controlling the main magma flow in the conduit. Where the banding is steeply dipping and also thicker (**Fig. 8c**) the individual specimens gave sub-vertical K_{max} inclinations (for example, specimen I, 72.7°, see **supplementary material**), suggesting local vertical flow.

This section ends up with another massive obsidian flow with cm-size amygdales (**Fig. 8f**) displaying flat-lying magnetic foliation and mean K_{max} axes plunging to SW, just as site CM2, suggesting that they can be part of the same flow.

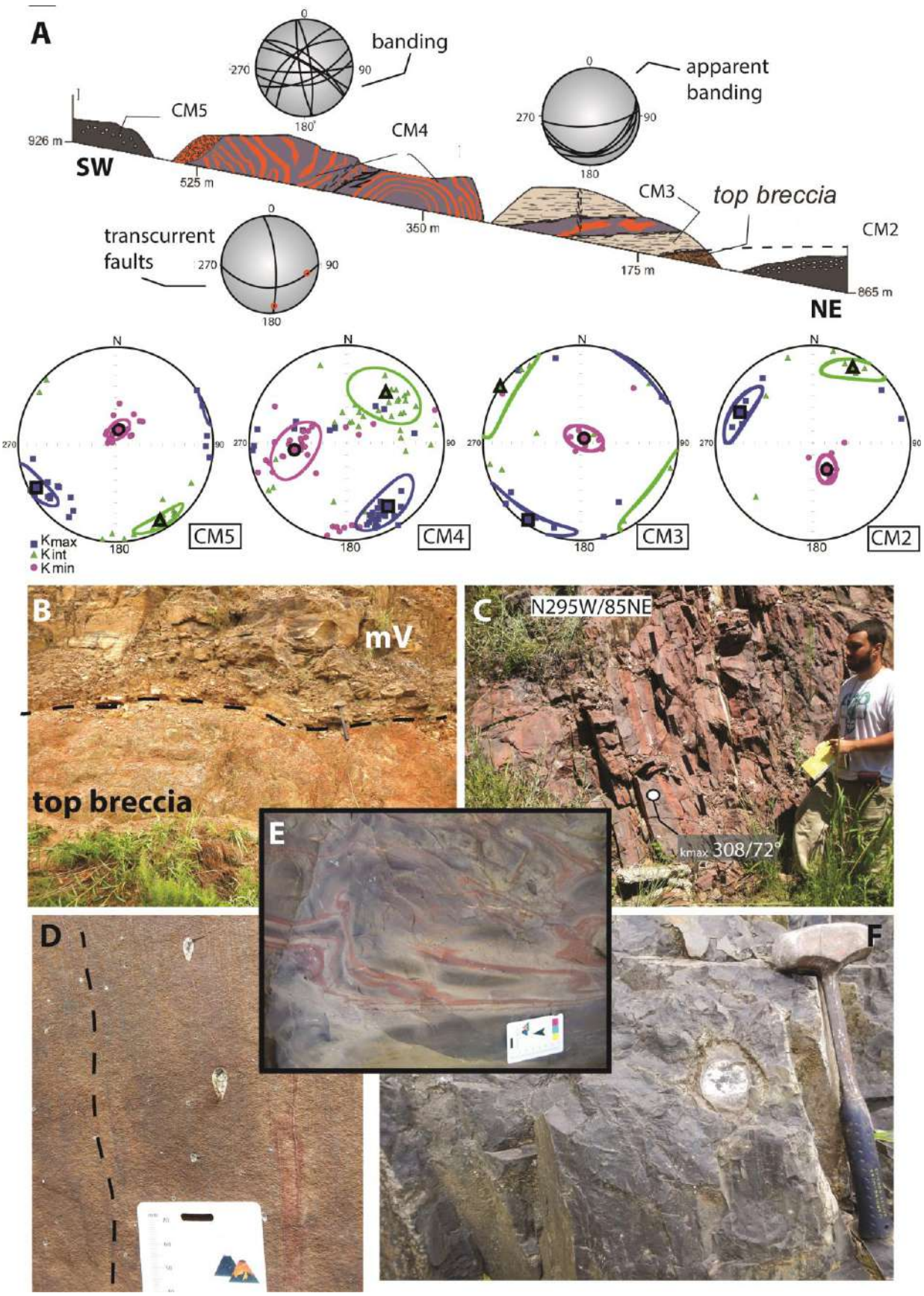

311

312 **Figure 8** Field features of the sites at Jaquirana area. (A) Cross-section with the disposal of the sampled units. In the section
313 the stereonets have semi-circle planes representing structures measured in the field. Below the section there are the
314 correspondent equal-area AMS stereonet for each site. The plane marked in CM4 stereonet is formed by the scatter of k_{int}

315 and k_{min} along NE-SW. (B) Contact between the top breccia of the obsidian flow (site CM2) and the microfractured
316 vitrophyre (mV) of site CM3. (C) Banded vitrophyre with sub-vertical banding disposal (N295W/85NE) in site CM4. This
317 specific location gave steeply inclined (~ 72°) k_{max} values. (D) Vertical-banded vitrophyre showing 0.5 – 1 cm amygdales
318 with inverse gout shape. (E) Contorted banding with several folding phases resembling the mixing of two fluids in site
319 CM4. (D) Black obsidian flow with cm-size spherical amygdales from site CM5

320

321 3.2.4 Sites IT01 an IT02 – Cambará do Sul

322 Sites IT01 and IT02 were collected in the National Park of Aparados da Serra at RS-427 road, connecting Cambará do Sul
323 and Praia Grande cities. In satellite image the site IT01 is located between two large fractures, approximately 300 m spaced
324 (**Fig. 9a**). This outcrop, at 1002 m of elevation display dominant banded vitrophyre with near vertical bands of reddish and
325 greyish vitrophyre (**Fig. 9b**). In spite of a large dispersion of the susceptibility axes, average values for this site gave k_{max}
326 inclination of 85.2° to 324.7° and flat-lying k_{min} (**Fig. 9c**), indicating mean near vertical magnetic foliation combined with
327 steep values of magnetic lineation.

328 Site IT02 is an outcrop of flat-lying vitrophyre at ~ 960 m elevation, interpreted as a lava flow. This exposure is also
329 verified in images as the top of a sequence of stacked basaltic and silicic flows (**Fig. 9a**). The AMS results in this site
330 display well defined flat-lying magnetic foliation characterized by clusters of sub-vertical k_{min} (83° mean inclination) and
331 dispersed flat k_{max} axes distribution (**Fig. 9d**). This pattern is very similar to those found in other lava examples as sites
332 CM1, CM2, CM3 and CM5.

333

334

335

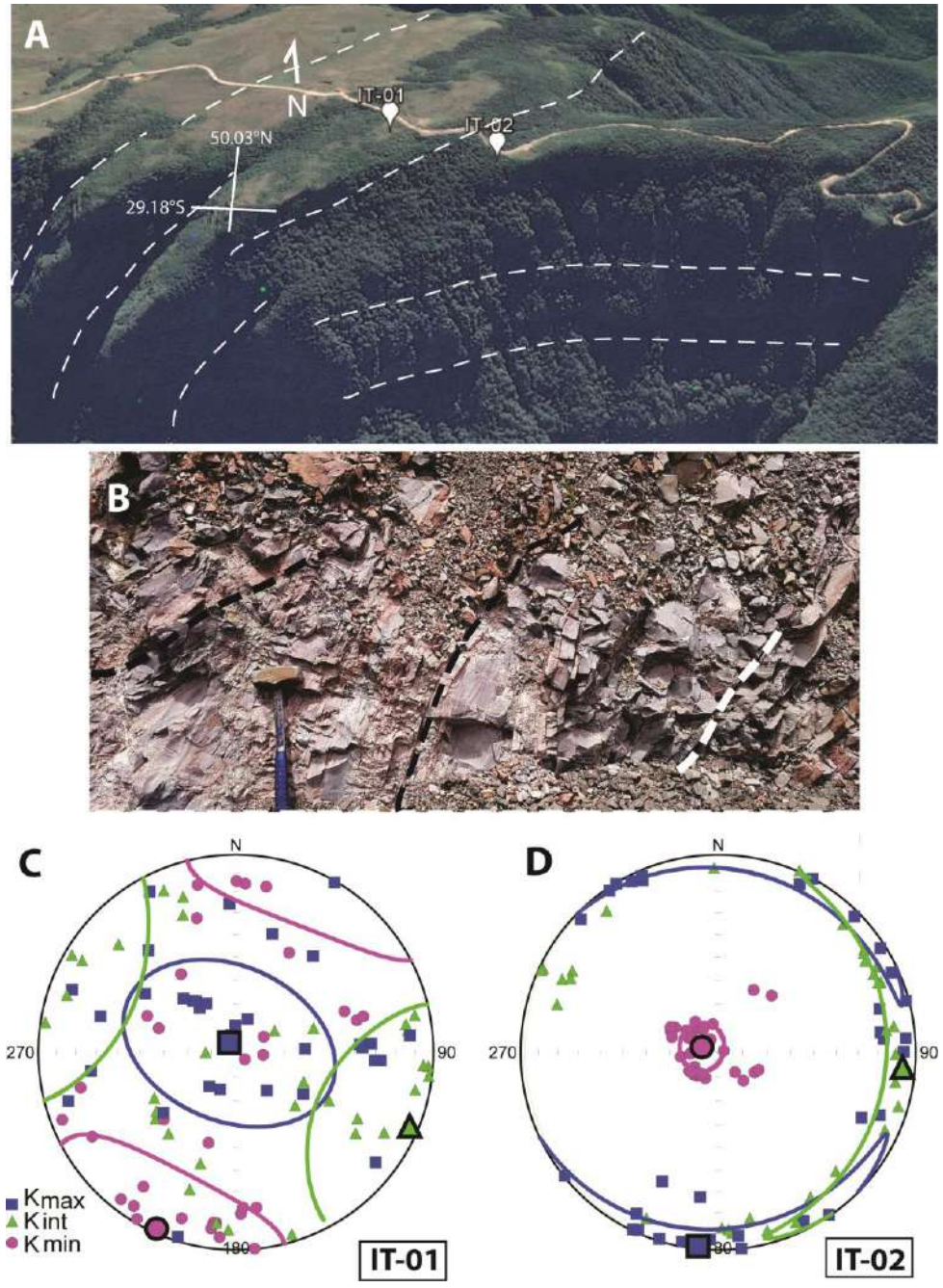

Figure 9 Conduit and lava exposures at Aparados da Serra National Park. (A) Sattelite image from Google Earth showing the location of IT01 between two ~300m spaced vertical structures and IT02 in the top of stacked lava flows; (B) Near vertical banding with cm-scale thickness present in site IT01. (C) Equal-area stereonet showing the orientation of bulk and mean K_{max} (vertical), K_{int} (horizontal) and k_{min} (horizontal) at site IT01. (D) Equal-area stereonet for site IT02 displaying flat-lying magnetic foliation (k_{max}-k_{int}) and flat magnetic lineation (k_{max})

3.2.5 Sites MS-01 to MS-04 – Mato Perso

In Mato Perso area we chose two expositions with paired conduit and lava flow-related lithofacies occurring along the VRS-864 road. The site MS-02 is exposed in the elevation of approximately 665 m (**Fig. 10a**) and is interpreted as a conduit occurrence, displaying 52-20° to 270-275° trends of banding. The lithofacies change from black and grey obsidian to red

vitrophyre towards SSE (**Fig. 10b, c**), where fragments of red vitrophyre are present (**Fig. 10b, d**). In site MS2 there is a large dispersion of the susceptibility axes. The mean axes in site MS-02 gave horizontal K_{max} inclination (0.0°) oriented to NW (340.0°), but at least seven specimens gave sub-vertical angles of k_{max} plunging NE (**Fig. 10e**).

The site MS-01 outcrop at ~647 m elevation (**Fig. 10f**), showing a massive structure and a vesicle population of tube-like vesicles (**Fig. 10g**) pointing vertically and being replaced by spherical vesicles towards the top of the flow. Microscopically, the lava flow is distinguished from conduit-related rocks by a microlite-rich groundmass, where fine plagioclase, clinopyroxene and Fe-Ti oxides developed in the vitreous matrix (**Fig. 10h**). In the lava flow of site MS-01 the axes orientation form the shape of an prolate ellipsoid, with k_{int} and k_{min} forming an girdle and with flat mean k_{max}, dipping 0.7° to 248.7°, (**Fig. 10i**).

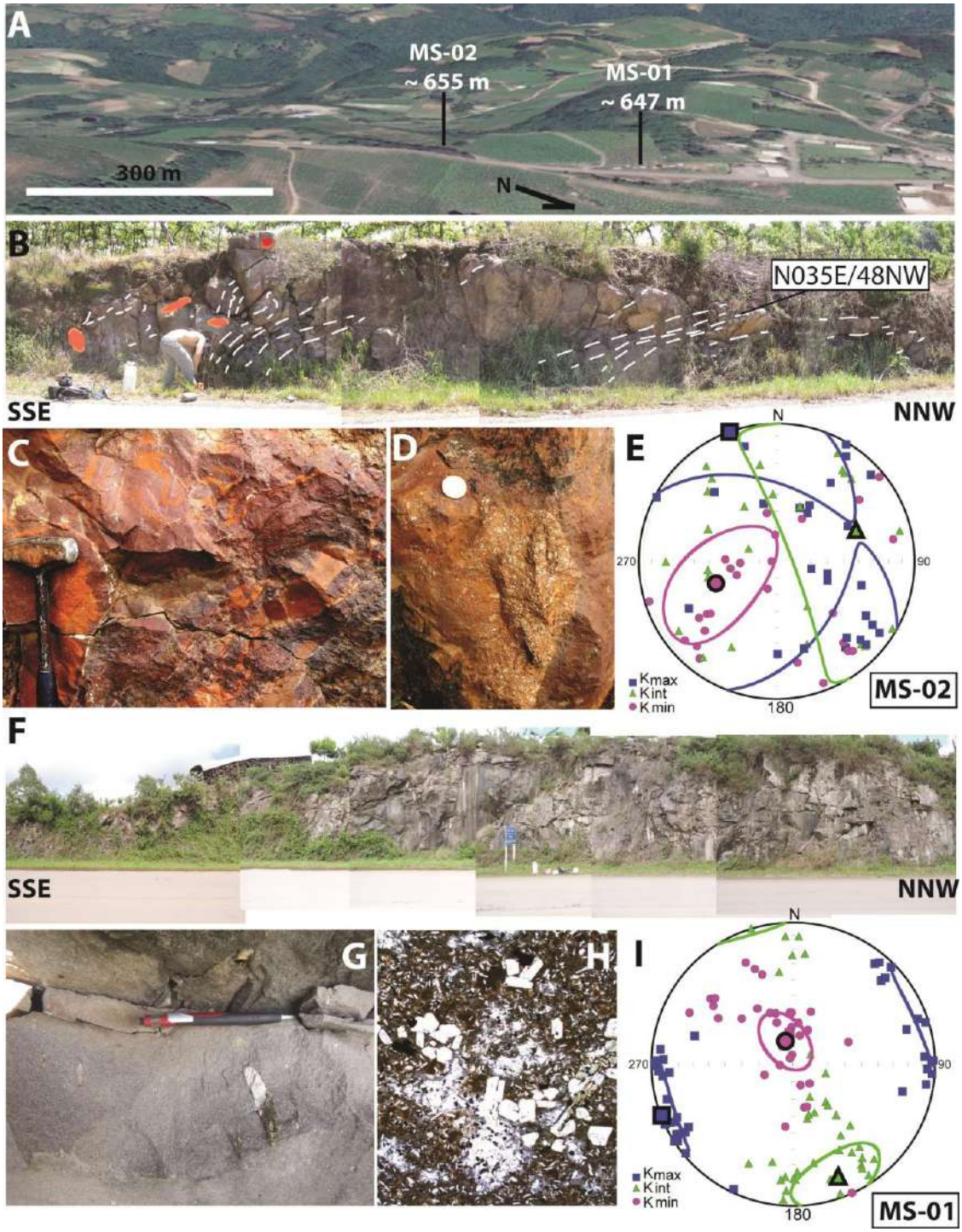

Figure 10 Location, field features and AMS stereonets for sites MS2 and MS1. (A) Google Earth image with the location and correspondent elevations of the two sites. The conduit (MS2) is in a higher elevation than the lava flow (MS1). (B) Banding orientation in site MS2 and position of the largest red vesicular vitrophyre fragments in red polygons. (C) Banded vitrophyre with mixing of black and red vitrophyres, displaying contorted folds. (D) Red vesicular vitrophyre fragment with up to 20 cm into the banded vitrophyre. (E) AMS sterenonet of site MS2 with horizontal k_{max} and tilted k_{min} and k_{int}. (F) Outcrop of massive vitrophyre in site MS1. (G) Tube vesicles in the base of the silicic lava outcrop. (H) Microporphyritic texture in the vitrophyre of site MS1. Note also the presence of plagioclase and opaque microlites in the groundmass (uncrossed polarizers). (I) AMS stereonet of site MS1 with NE-SW horizontal k_{max}. k_{min} and k_{int} are forming a NNW-SSE oriented plane

Site MS-03 is at 654 m elevation (**Fig. 11a**), being composed of breccias and banded vitrophyres. The breccias are positioned in the margins of the outcrop (**Fig. 11b**). To the center, the vitrophyre banding is folded in one major domain (F_1), with limbs parallel to a black vitrophyre tabular band (**Fig. 11b,c**) dipping 62° to 065° (striking NW) and 72° to 134° (striking NE). F_1 contains F_2 parasitic folds with flat-lying (02 – 07°) hinge lines, parallel to the F_1 hinges (**Fig. 11d**) and dipping gently to SE. F_3, F_4 and other phases are restricted to the portions where the folds have cm- to mm- wavelength, with several limb directions, resembling magma mixing structures (e.g. Perugini and Poli 2012). In the southwest margin of site MS-03, a wide number of cm-size vesicular red vitrophyre fragments are dispersed into the banded unit (**Fig. 11e**). The behavior of the magnetic fabric in several portions of this conduit outcrop show near horizontal mean k_{max} (11.3° plunge) plunging to NNW associated to steeply dipping poles of k_{min} (70.0° plunge), indicating and horizontal magma flow. k_{int} and k_{min} form a vertical plane NNW-trending dipping around 80° (**Fig.11f**).

In site MS-04, outcropping at 623 elevation (**Fig. 11a**), there is a flat-lying massive grey vitrophyre displaying mm-size spherical vesicles and a salt-and-pepper like texture (**Fig. 11g, h**). The orientation of the mean axes exposed in **figure 11i** show flat-lying k_{max} (059.7/3.4), and inclined plunges of k_{min} (324.0/59.2) and k_{int} (151.7/30.6). The girdle plane formed by $k_{max\text{-}int}$ dips at low inclination to SE, being its inclination parallel with the NW-SE orientation of k_{max} in the conduit of site MS3. This plane can be also interpreted as parallel to the magnetic foliation, given that k_{max} axes are contained in and k_{min} is orthogonal to it.

A microscopic distinction between the conduit-related and lava flow vitrophyres is made. If we take a look to **figure 11j**, a representative sample of banded vitrophyre, there are two folded parallel bands, but the direction of the magmatic flow (2D) in each dark band, indicated by the traced line, vary depending on the part of the fold. Near the hinges, the traces are sub-vertical, and near the limbs they are near horizontal. Still on this figure, the tabular plagioclase and globular Fe-Ti oxide microphenocrysts are embedded in a fine-grained devitrified groundmass. In figure **10k**, from site MS-04, the microphenocrysts are disposed in a microlite-rich matrix where tabular plagioclase and globular clinopyroxene and Fe-Ti oxides are also well developed and engulfed by a two-phase vitreous matrix (brown and white groundmass with uncrossed polarizers).

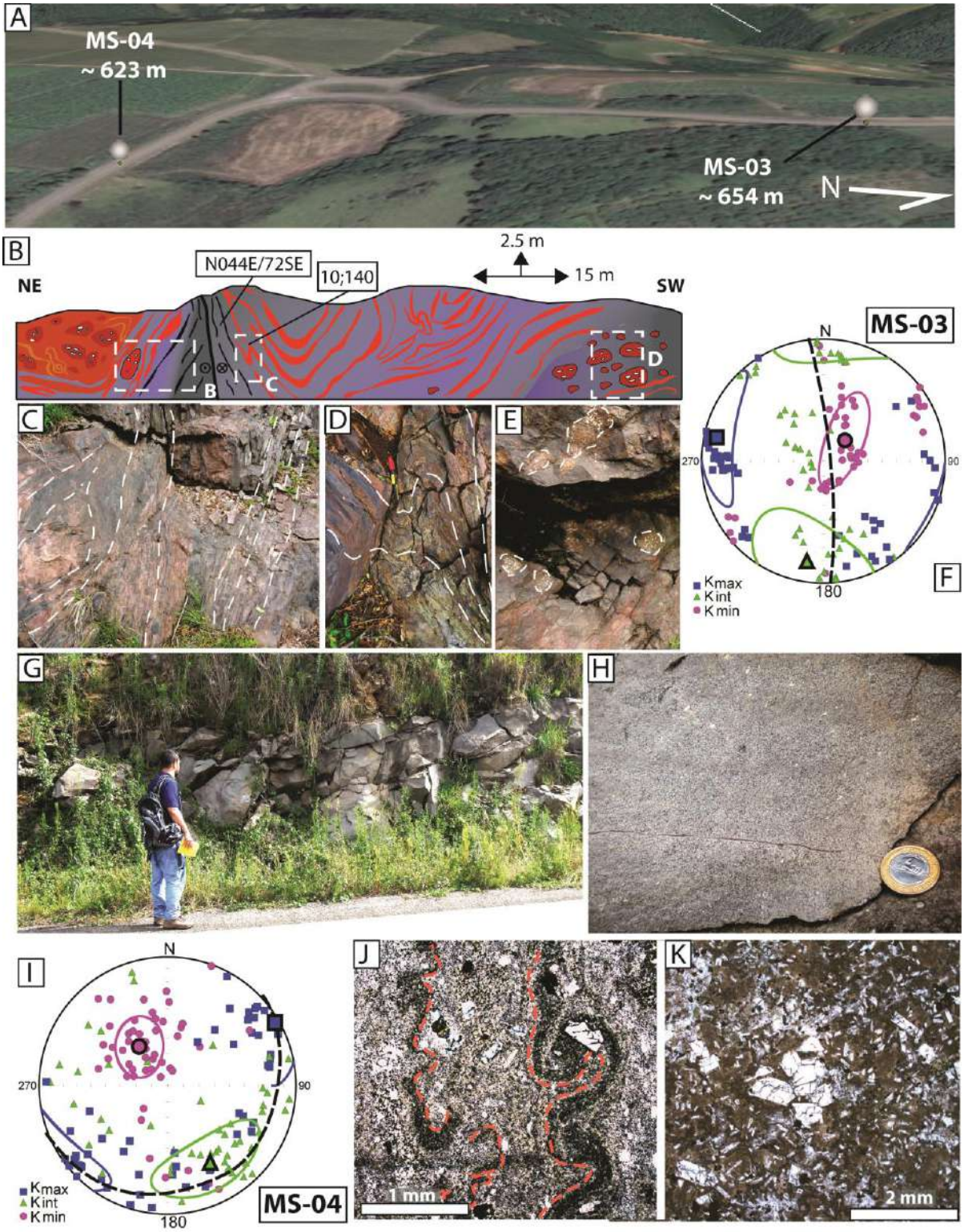

Figure 11 Field features and AMS patterns in sites MS3 e MS4. (A) Location of the sites MS3 and MS4. (B) Cross-section sketch of site MS3. (C) Banded vitrophyre grading to black vitrophyre with tabular sub-vertical banding. (D) F_2 parasitic fold with flat-lying limbs. (E) Red vitrophyre fragments with cm-size embedded in banded vitrophyre. (F) Equal-area stereonet with K_{max}, K_{int} and K_{min} orientations for site MS3, the plane marked is formed by NNW-SSE k_{int}-k_{min} plane. (G) Outcrop of massive grey vitrophyre (lava flow). (H) Salt-and-pepper texture with few spherical mm-size amygdales. (I) Equal-area stereonet with K_{max}, K_{int} and K_{min} orientations for site MS4, $k_{max-int}$ forms a girdle plane (dotted line). (J) Fotomicrography of banded vitrophyre from site MS3 with polyclinal folds (uncrossed polarizers). Note the absence of a

microlite-rich groundmass. (K) Fotomicrography of massive vitrophyre considered to be lava flow (uncrossed polarizers). In this unit there is a separation of the vitric matrix into dark and light halos. The groundmass also has well developed microlites

3.4 RHEOLOGY

The rheology of magma controls its ascent, dynamics of conduit flow and the eruption style (Okomura et al. 2016). In present work, magma rheology is used as a complementary investigation to structural and AMS fabric data, since the behavior of silicic magma strongly variate given a wide range of eruptive temperatures, bubble/crystals content and chemical composition (e.g. Cashman 2004; Manga et al. 1998; Mader et al. 2013).

3.4.1 Temperature and viscosity

In order to characterize the chemical types, temperatures and estimated viscosities we selected one sample from each site, except site CM1, for whole-rock geochemical analysis. For this, we chose two samples of coherent vitrophyre of the lava flows (MS-01 and MS-04), one sample of microfractured vitrophyre of one lava flow (MS-22E, equivalent to site CM3), two samples of banded vitrophyre (MS-03A and MS-05b), one sample of a red band (MS-22E, equivalent to site CM4) and one sample of black band (MS-22D, equivalent to site CM4). The chemical analyses are present in Table 2 and cover a range of representative lithofacies from which we collected the drill cores for AMS studies.

As seen in **Table 2**, The bulk of analyzed samples have SiO_2 content between 64.78 and 68.18 wt.%. Apatite calculated temperatures are considered to depict the liquidus temperatures of the analyzed vitrophyres, since apatite was one of the first phases to crystallize. P_2O_5 contents are very similar, varying from 0.25 to 0.28 wt.%. The calculation of Harrison & Watson (1984) thermometer yielded temperatures of 1005.77 – 1088.70°C. Using the model of Giordano et al. (2008), we obtained respective viscosities of these samples by inserting the chemical composition and to the apatite saturation temperatures. Three H_2O content thresholds were applied for the viscosity estimation model: dry, 0.5%H_2O and 1.3%H_2O, the last is considered a best-fit value for the studied samples of Palmas magma-type rhyodacites. Dry viscosity values range between 5.56 and 6.63 log Pa s and drastically decreases to 4.57-6.63 Pa s using 0.5%H_2O and 3.88 – 4.58 Pa s with the addition of 1.3% of H_2O.

Table 2 – Whole rock geochemical analysis, calculated temperatures and viscosities for studied samples. MS-01-05b are from Mato Perso area, MS-22-24b are from Jaquirana-Cambará

Sample	**MS-01**	**MS-03A**	**MS-04**	**MS-05B**	**MS-22**	**MS-22E**	**MS-22D**	**MS-24A**	**MS-24B**
Lithofacies	coherent	banded vit.	coherent	banded vit.	brown vit.	red vit.	black vit.	black vit.	red vit.
SiO_2	67.32	65.30	67.18	67.23	64.78	65.47	67.80	68.18	67.35
TiO_2	0.92	0.95	0.89	0.93	1.01	0.95	0.92	0.89	0.92
Al_2O_3	12.66	13.11	12.88	12.74	13.75	12.95	12.53	12.05	12.37
$FeO_{(T)}$	6.23	6.30	6.02	6.12	6.83	6.41	6.06	6.05	6.04
MnO	0.11	0.11	0.11	0.10	0.09	0.11	0.11	0.09	0.10
MgO	1.33	1.29	1.27	1.26	0.91	1.52	1.37	1.31	1.32
CaO	3.28	2.96	3.12	3.23	1.02	3.41	2.90	2.83	2.85
Na_2O	2.95	2.90	2.77	2.96	2.09	2.90	2.89	2.89	2.87
K_2O	3.78	3.94	4.00	3.80	4.86	4.00	3.98	3.80	4.13
P_2O_5	0.27	0.28	0.26	0.27	0.25	0.27	0.25	0.26	0.26
Total	98.85	97.14	98.50	98.64	95.59	97.99	98.81	98.35	98.21
T(ap)	1070.29	1015.03	1061.08	1073.04	1005.77	1029.60	1088.70	1093.81	1059.07
Visc (dry)	5.70	6.28	5.87	5.70	6.63	6.01	5.56	5.56	5.87
Visc (0.5 % H2O)	4.60	5.12	4.81	4.68	5.40	4.91	4.57	4.58	4.82
Visc (1.3% H_2O)	3.90	4.35	4.09	3.97	4.58	4.17	3.88	3.89	4.10
Nmix (dry)	7.09	7.81	7.30	7.09	6.69	6.06	5.60	5.61	5.92
Nmix (0.5% H_2O)	5.71	6.37	5.98	5.81	5.45	4.95	4.61	4.62	4.86
Nmix (1.3% H_2O)	4.85	5.40	5.08	4.94	4.62	4.20	3.91	3.92	4.13

3.4.2 Vesiculation, fragments and fragile structures

Vesiculation is an important factor to characterize magma rheology and emplacement conditions (Cashman 2004; Blundy and Cashman 2008; Mader et al. 2013 and other references). In the studied outcrops, the patterns of vesiculation degree and vesicle shapes are notably different when comparing conduits and lava flows. In order to quantify the amount of vesicles in macroscopic scale we processed nine outcrop photographs in the ImageJ (Schneider et al. 2012) software and counted 165 to 850 points per image, depending on the photograph scale.

The coherent vitrophyres from sites MS-01 and MS-04 have 1.9 – 2% of mm-sized spherical vesicles and amygdales. This number must have a little increase near the base of the flow, where pipe vesicles are present (see Fig. 8g). The microfractured vitrophyre of site CM3 gave the lowest value of 0.6% spherical to stretched vesicles with 3-5 mm in size. A red band of site CM-4 has 1.69% of spherical to reverse-drop like mm-sized vesicles, while a grey band presents 4.72 % of dominantly stretched vesicles with few millimeters to 1 – 2 cm in the longest axis. In site CM1 there is a slight variation in the abundance of cm-size oblate amygdales around 4.7%, which seems to be the same case of the top of the flow in site CM-5. Below this top horizon the amount of spherical amygdales is up to 0.96%.

The amount of vesicles in the red vitrophyre fragments carried in the magmatic flow banding was also counted. They share common features as 0.5 – 5 mm sizes and stretched shapes, showing random distributions and preferred elongation planes. In site in site MS-2 the fragments have up to 21% of vesicles (**Fig. 12a**) and in site MS-3 the fragments have 28% CM-4 the fragments vary from 20 to 53% of vesicles. Finally we used a representative count of fragments immersed in the banded vitrophyre and obtained a value of 11.5% in site MS-02 (**Fig. 12b**) and 16.30 fragment% in site CM4 (**Fig. 12c**).

Fragile structures occur parallel to the banding planes with cm-scale spacing. The structures present strong lineations in non-polished surfaces and display oblique-normal and oblique-reverse movements, while into the bands the magmatic flow can be strongly folded, when observing in the X-Z plane (**Fig. 12d**).

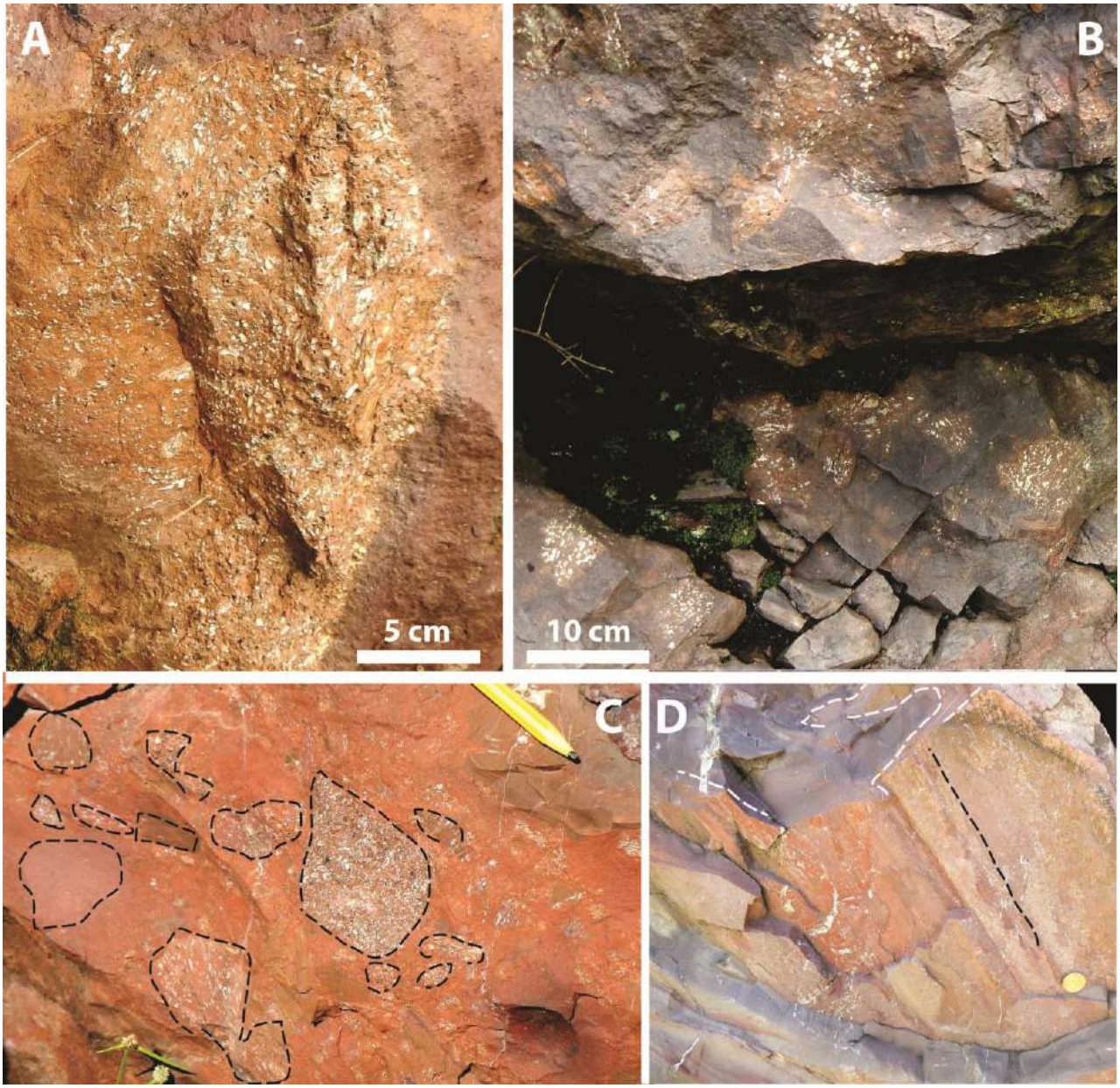

454

455 **Figure 12** Fragments and fragile structures in conduit systems. (A) Fragment of approximately 20 cm composed of red
456 vesicular vitrophyre with up to 21 area% of vesicles (site MS2). (B) Fragments of red vitrophyre with up to 30 area%
457 vesicle content embedded in banded vitrophyre (site MS3). (C) Several cm-size red vitrophyre fragments with different
458 vesicle content, but dominated by vesicle-rich types. The fragments are immersed in a red non-vesicular vitrophyre in site
459 CM4. (D) Fragile oblique structure with marked lineation in a non-polished surface. In the X-Z plane the banding has
460 contorted fold patterns (white dotted lines)

461

462

463

464

4 DISCUSSION

4.1 Interpretation of the AMS data

4.1.1 Conduits

The degree of anisotropy values in the analyzed samples are comparable to those found in sites of high-temperature silicic volcanics (e.g. McPhie et al. 2008; Canón-Tapia and Raposo 2017; Guimarães et al. 2017) and to those obtained in mafic dykes (e.g. Philpotts and Philpotts 2007; Wiegand et al. 2017). In the present work, the sites interpreted as conduit lithofacies display mean degree of anisotropy slightly higher than in the lava flows, contradicting the data presented by Cañón-Tapia and Raposo (2017) at São Marcos city, approximately 60 km west of Mato Perso area. They found smaller degrees of anisotropy in banded vitrophyres than in silicic lava flows. One explanation for this kind of variation is that low degree of anisotropy in evidently deformed magma is experimentally justified in situations where the deformation was taken place at high temperatures or in a complex deformation regime (Cañon-Tapia and Pinkerton 2000).

Sites like IT01 and MS2 yielded high dispersion of the susceptibility axes data, showing similarities with the banded vitrophyres of São Marcos (e.g. Cañón-Tapia and Raposo, 2017). Considering field and petrographic data, this random orientation of the magnetic fabric may be result of very complex magmatic flow patterns, as the intense folding resembling the mixture of two liquids (e.g. Ottino, 1989) or because of severe post-magmatic changes in magnetic minerals (Hrouda 1985; Raposo 2011). Re-arrangement of the magnetic fabric in the conduit margins should be carried by separation of the flow in different domains of fragment and vesicle contents and in parts of constriction or compression of magma. These changes in stress conditions within the moving magma generating several phases of folding are also causes to explain the high dispersion of k_{max}, k_{min} and k_{int}.

In conduit sites where the susceptibility axes have more defined clusters, the orientations of k_{max} are near-horizontal (CM4, MS3), suggesting flat-lying movement of magma along vertical to oblique conduits (**Fig. 13**). In the case of CM4, complex folding perpendicular to the main banding scatter the orientation of the susceptibility axes, but steeply inclined k_{max} parallel to the banding measured in field can be found where thick vitrophyre bands are not folded. This is indicative that the magma flow also had a complex structural control, moving vertically only in some locations. In site MS3 there are no individual specimens with vertical k_{max}, suggesting predominant flat-lying flow.

The obstruction of the main magmatic flow by cm- to meter sized fragments (~ 20 – 50%) should be ascribed to the variation of magma flow during segregation different flow domains. The more often presence of these features near the conduit margins suggests that the flow was not uniform and was probably much more complex than in tabular dykes or sills. The mixing of oxidized and non-oxidized magma towards the boarders of the outcrops reveals a flow domain where magma is stretched, folded and the banding changes the direction vertiginously (**Figs. 8e, 10c and 11j**). Fold patterns observed in the photomicrography of **Figure 11j**, for example, demonstrate how two parallel flow bands may present horizontal, vertical and oblique banding through polyclinal folding during mixing.

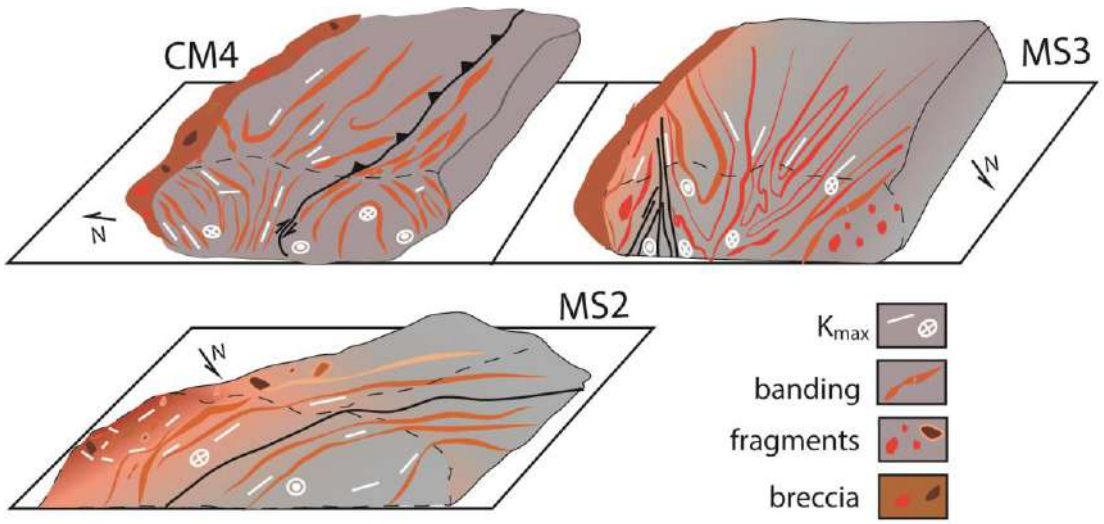

Figure 13 Oriented models of field structures and K_{max} directions in conduit outcrops (CM4, MS3 and MS2)

4.1.2 Lava flows

Silicic lava flows and domes may display near-vertical k_{min} axes (Cañon-Tapia and Castro 2004), steeply inclined k_{max} and k_{max}-k_{int} planes (McPhie et al. 2008), may also exhibit fabric zoning with steep k_{max} near the conduit zone and flat k_{max} in the boarders of the flow (Závada et al. 2009) or tilting of the original structures by collapse (Pueyo Anchuela et al. 2014). The rheological homogeneity of the sampled lava flows permitted us to use the magnetic foliations and k_{max} directions directly to interpret the magmatic flow. The flat-lying disposal of the magnetic foliation in lavas indicate dominant horizontal magmatic flow in sites CM1,2, 3, 5 and IT02 (**Fig. 14**). Where the flow seems to be laminar and the amygdales display flattened shapes, the shape parameters P and T define oblate ellipsoids. Prolate types are also present and in these cases they are explained by zones of more intense stretching, near the core of the flow.

Site CM1 is a good example of how the magnetic fabric behaves in the emplacement of a structurally-controlled lava flow. The magmatic flow represented by the magnetic lineation is parallel to the NW-SE and NE-SW arms of the flow, with ki_{nt} pointing to SW (**Fig. 14**). In sites CM2, 3 and 5 k_{max} is also clustered dipping to NW and SW. The site IT02 has the same kind of distribution of the anisotropy axes, but with k_{max} pointing to the south. Another interesting feature of this site is the prevalence of oblate magnetic fabrics (**Fig. 6**), assigned to a possible laminar lava flow.

In site MS1 the k_{max} is also flat-lying, but the girdle of k_{int} and k_{max} plane forming a prolate shape and the abundance of specimens giving prolate ellipsoids (**Fig. 6**) indicate that the flow could be channelized, flowing according NW-SE. This is reinforced by the fact that cooling joints recognized in the field are in the outer portions of the flow, confining it according to this NW trend. The oblique cluster of k_{min} together with the k_{max} girdle plane in site MS4 indicate that magmatic flow dips ~30° to SE, being parallel to the flat cooling joints observed in the field. Even with a small statistic number of 7 sites, we can estimate that the silicic lavas flowed dominantly trending NW-SE or NE-SW.

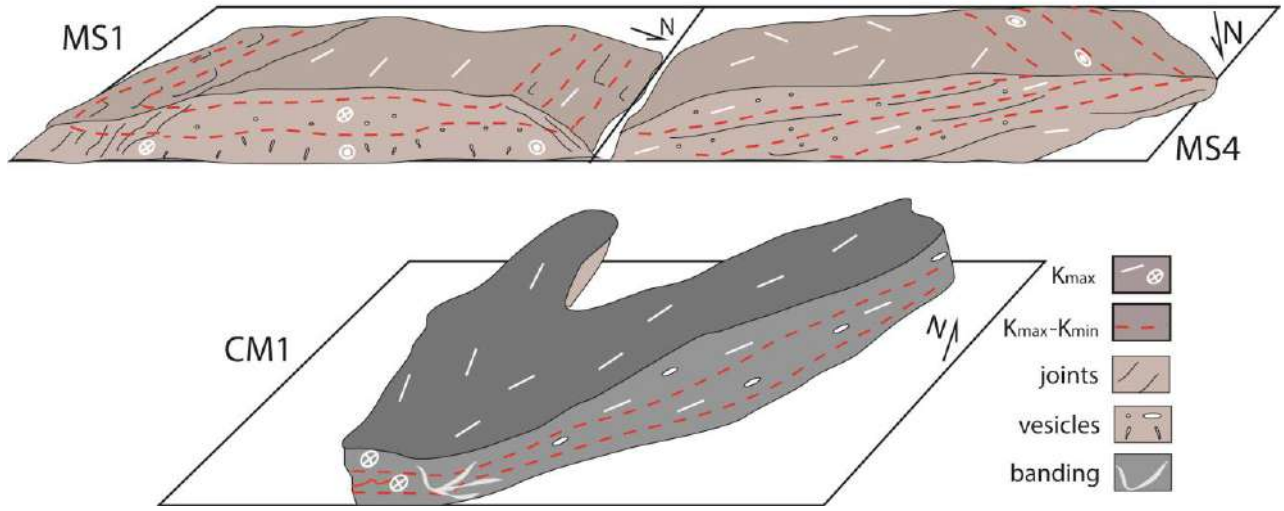

Figure 14 Oriented models of field structures, K_{max}-K_{min} plane and K_{max} directions in lava flow outcrops (CM1, MS1 and MS4)

4.2 Transport properties and implications on magma flow

4.2.1 Initial magmatic viscosity

The rheological properties of magma depend on temperature, bulk composition, pressure, phase assemblage, particle size and shape distribution, spatial arrangement of particles (structure) and shear rate (Lesher & Sphera 2015). To complete the interpretation of structural and magnetic fabric data we must consider the factors influencing the magma flow, so the transport properties need to be constrained. In both conduits and lavas we used magmatic temperatures around 1000°C to calculate viscosity. Values obtained are maximum dry viscosities $\eta_{max(dry)}$ of ~ 6.6 log Pa s and minimum viscosities in more hydrous conditions $\eta_{min(1.3H2O\%)}$ of ~ 3.8 log Pa s.

We confronted our data with the experimental investigation of Whittington et al. (2009), where rhyolitic and andesitic magmas compositions are compared. For hydrous melts, at their respective magmatic temperatures, dacites and andesites have similar viscosities. To quantify the importance of crystallinity effect on viscosity, we used the Einstein-Roscoe equation (Einstein 1906, 1911; Roscoe 1952): $\eta_r = \eta_{mix}/\eta_{melt} = (1 - \phi/\phi_0)^{-2.5}$, where ϕ is crystallinity in volume fraction, ϕ_0 is the maximum packing fraction (assumed as 0.6, value recommended for magmas in Marsh 1981) and η_r is the ratio of the mixture (melt+crystals) viscosity, η_{mix}, to the melt viscosity, η_{melt}. The viscosity increases at ~19% for 5 vol.% of crystals, used for the Mato Perso conduit and lavas. For Jaquirana vitrophyres we used 0.2 vol.%, which increased the viscosity values in <1% (**Fig. 15**). With that we assume that low crystal content of the studied samples influenced irrelevantly for raising up the magma viscosity.

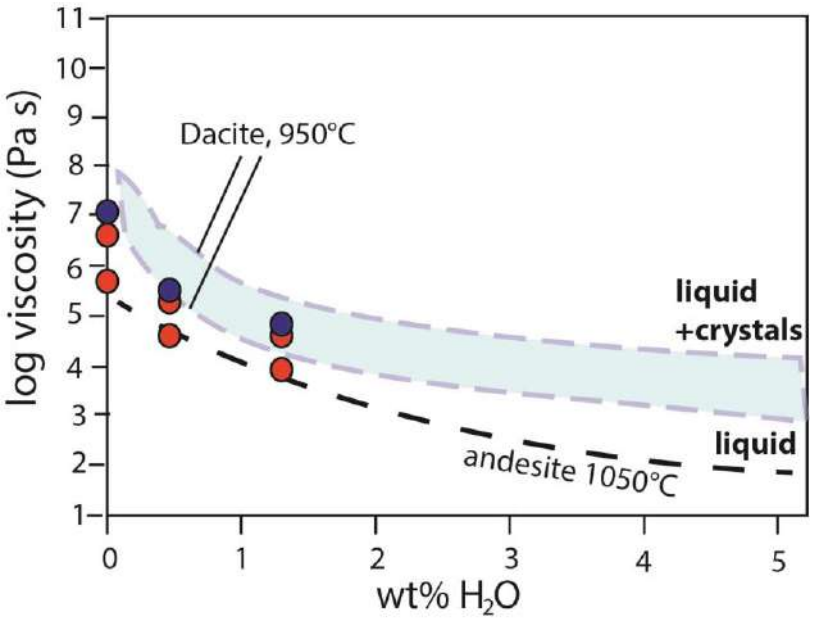

Figure 15 – Water versus viscosity plot with calculated viscosities η_{melt} (red dots) and η_{mix} (blue dots) compared with the viscosity paths of crystallizing hydrous magmas of Whittington et al. (2009). The heavy dashed line represents the andesite at 1050°C differentiating to dacitic liquid plus crystals, delimited by the shaded field, with the upper line representing 40 vol.% of crystals

The water content estimated for rhyodacites in Palmas-type magmas are around 2 wt.% (Garland et al. 1995) or, more precisely, between 0.1 and 2.6 wt.% (Polo et al., 2017) and for the studied areas we are working with a maximum of 1.3 wt.%. This initial dissolved H_2O value give a η_{min} that overlaps the andesite curve at 1050°C, indicating the similar initial viscosities of the rhyodacites and andesitic melts, which is a favorable argument for their sheet-like geometry.

In terms of suspensions contained in the silicic magma, the key parameters controlling the rheological behavior of a bubble suspension are the melt phase viscosity μ_0, the capillary number *Ca*, the dynamic capillary number *Cd* and the relaxation time (Mader et al. 2013). These variables depend on features that could not be experimentally measured, like bubble relaxation time, shear strain rate and tension surface of the bubble-liquid interface. Even though, we observe that most parts of the lava flows resemble monodisperse suspensions, because vesicles and amygdales range little in size and distribution. Limited interaction between bubbles in these portions suggest relative steadiness (low *Cd*) in the flow. Shear strain rates or the radius of spherical undeformed bubble (α) values should be large to contrast with the low μ_0 and give high Ca. So we expect flow regimes with both *Ca* and *Cd* controlled mainly by the initial liquid viscosity.

The central portion of the postulated conduits is similar in bubble content to the lava flows, but display much more stretched vesicles. In the outer portions, where fragments reach more than 50% of vesicles, the viscosity and flow regime were strongly dependent on the response of bubbles to shear rates. In these cases, strain shear rate, bubble relaxation and the bubble content itself had an important control on viscosity, increasing the calculated initial liquid viscosity.

565 4.2.2 Flow domains and viscosity paths

566 In the path from margins to the core of conduits, the magma mixing structures and stretching of unconsolidated oxidized
567 vitrophyre fragments must also increase the viscosity of initial melts, but not as much as in the conduit margins, because the
568 fragments are less frequent. To the center of the flow, where we stablished $\eta_{max(dry)}$ of ~ 6.6 log Pa s and $\eta_{min(1.3H2O\%)}$ of ~ 3.8
569 log Pa s, there is a domain where black obsidian is vertically structured, do not present fragments or mixing features. This
570 portion is where the magma could flow with more freedom at near-magmatic viscosity. The distribution of vesicles,
571 breccias and quartz veinlets in conduit systems is also horizontally profiled: more vesicles and breccias are features of the
572 outermost parts and scarce in the conduit cores. Quartz veinlets constitute discrete stockworks in the margins, while in the
573 center of the conduits the quartz veinlets are near-parallel to the magmatic flow (see **Fig. 8d** in detail).

574 In lavas, the absence of fragments and basal breccias in the sampled sites suggest that low viscosity suppressed the shear in
575 the base, and the high temperature inhibited the transition from ductile to fragile conditions impeding base of the flow to
576 break, such as in the base of some silicic lavas (e.g. Smith 1996; Tuffen et al. 2013) or basaltic/andesitic 'a'a lavas (e.g.
577 Harris et al., 2017). Vesicles are heterogeneously disposed, having tube or spherical morphologies, but remaining at low
578 contents (up to 2%) throughout the main body of the lava flow. Quartz veinlets are almost absent, in exception of some
579 expositions with the development of flat-lying microfractured textures, which can be very late comparing with syn-
580 emplacement structures. An important feature that should increase the melt viscosity in subaerial setting is the
581 crystallization of microlites in the groundmass (as in **Figs. 10h and 11k**). Even so, the crystallization of < 2 vol.% of
582 clinopyroxene, Fe-Ti oxides and calcic plagioclase microlites must increase the relative water content in the magma, as
583 expected in retrograde boiling, thus keeping the viscosity at low values.

584

585 **4.3 Tectonic setting and the emplacement of silicic lava in the southern Paraná-Etendeka LIP**

586 Unraveling the plumbing system of silicic magmas in large igneous provinces is a still evolving matter, principally in the
587 Paraná-Etendeka LIP. Dyke swarms located within the Paraná Basin or intruding Precambrian crust in the Brazilian coast
588 are dominantly composed of mafic magma (basalt, andesi-basalt in composition). Silicic dykes are less common among the
589 intrusive terms. An example is in the Florianópolis dyke swarm, where they are described as ~ 70 - 80 m thick porphyritic
590 vitrophyre dykes trending NNE-SSW and NNW-SSE (Marteleto et al. 2015). Composite dykes with basaltic andesite
591 diabases mingled with rhyodacite also occur (Tomazzoli and Lima 2006). The intrusive silicic magmatism in the south of
592 the basin is represented by one occurrence of ~ 1 m thick rhyodacite dyke in the Praia Grande – Cambará do Sul profile
593 (Piccirillo et al. 1988).

594 The age of the silicic volcanism of ~134 Ma (Pinto et al. 2010; Janasi et al. 2011) and the position of these units in the top
595 of the volcanic pile are evidences that it was the final magmatic manifestations prior to the Gondwana break-up (Renne et
596 al., 1992, 1996; Turner et al., 1994; Bryan et al., 2002). This pre-rift setting (e.g. Stica et al. 2014) was ruled by extensional
597 tectonics (Hawkesworth et al. 1999), thermal influence of anomalously underlying mantle (Quintas et al. 1999;
598 Hawkesworth et al. 2000; Solomon et al. 2017) and reactivation of older Precambrian structures, which forms the shape of
599 the NE-SW coastline in south Brazil (see Figs 1, 2). Glen et al. (1997) obtained AMS data in 31 sites of basalt and diabase
600 in Namibia and 21 basalt flows in Brazil. Both flows and sills yielded magmatic flow directions (=k_{max}) to NE-SW and

minor to NW-SE, suggesting prevolcanic rifting, with magma flowing parallel to the rift. NW-SE and NE-SW trends are also the main directions of mapped conduit occurrences, magmatic banding measured in the field and analyzed magnetic fabric in silicic conduits and lavas (e.g. Canón-Tapia and Raposo 2017; Guimarães et al. 2017; Simões et al. 2017, this study). This scenario of stretched crust with opening and closure of spaces in pre-existent faults is favorable for magmas positioned in the mantle-crust boundaries to ascend and reach the surface.

The Paraná-Etendeka LIP was generated, at least in part, because the continental lithosphere had been thinned in response to regional tectonics (Hawkesworth et al. 1999). High heat flux through the continental crust, generally associated with mantle plumes, is a critical mechanism for voluminous melting (e.g. Condie 2001) maintaining high temperatures in open magmatic reservoirs. In the other hand, mantle plumes may not be necessary for voluminous melting if it takes place in specific extensional regimes (e.g. Foulger 2010; 2017). This type of storage system is way more effective in magma transport than confined ones, where magma is kept stored in the crust for long times and reach high crystallization degrees (Parfitt and Wilson, 2008). In a petrological point of view, the Palmas-type magmas derivate from low pressure fractionation of low-Ti basalt magmas with some crust assimilation, increasing the Sr and Nd isotopic ratios (Peate et al. 1989; Garland et al. 1995) and were ponded at shallow depths, in pressure conditions inferior to 5 kbar (Garland et al. 1995; Polo et al. 2017). The path between shallow crust and surface modelled as an extensional and pulsatory-fed system in which the magma rises more easily through reactivation of fault zones attends well to the observed features, suggesting complex ascending magma flow in the conduits.

The plumbing system, maintained in high temperatures, is the ideal source for these high-temperature silicic lava flows. A constant source of mantle heat can keep fractionating basalt and andesite to form this hot silicic magma, inhibiting crystallization and the association of OH^- radicals to form hydrous minerals. This constant generation and rapid access to the surface can explain the large volume of silicic magma in south Paraná-Etendeka LIP and also why the flows kept their low viscosity and run so long to form extensive lava units (e.g. Hausback 1987; Henry et al. 1990; Henry and Wolff 1992; Pankhurst et al. 2011; Tuffen et al. 2013), as the effect of high temperature also seen in extreme extensive lavas at Mercury (e.g. Vetere et al. 2017), for example.

CONCLUSIONS

In the southern Paraná-Etendeka LIP, a large volume of silicic lava flows are the final stages of the Cretaceous volcanism prior to the Gondwana break-up. We have described vitrophyre units comprised by brecciated, banded and folded lithofacies, mapped as NW-SE to NE-SW trending structures and interpreted them as conduit systems. Measured banding in the field also trends NW-SE and NE-SW, as the inferred magma flow directions obtained by AMS technique for conduits and lavas. The distinction between conduits and lavas is found in both field structures, microscopic textures and in the orientation of the magnetic fabric. Conduits have a greater dispersion of the AMS data and may have flat-lying or locally vertical k_{max}, but the complexity of rheological behavior throughout the conduits have partitioned these systems in different magma flow domains. In the lavas, horizontal k_{max} values coupled with horizontal magnetic foliations are a common pattern. High-temperatures, low viscosity and water contents between 1 – 2 wt.% are explained by a constant high-temperature storage system, linked to a reservoir ponded at the crust-mantle boundary through faults and are the reason why the silicic magma did not explode, depositing as effusive lava flows.

638 **REFERENCES**

639 Auborg C, Giordano G, Mattei M, Speranza F (2002) Magma flow in sub-aqueous rhyolitic dikes inferred from magnetic
640 fabric analysis (Ponza Island, W. Italy). Phys Earth Planet Inter. 27:1263-1272. https://doi.org/10.1016/S1474-
641 7065(02)00113-4.

642 Bellieni G, Brotzu P, Comin-Chiaramonti P, Ernesto M, Melfi AJ, Pacca IG, Piccirillo EM, Stolfa D (1984) Flood basalt to
643 rhyolite suites in the southern Paraná plateau (Brazil): paleomagnetism, petrogenesis and geodynamic implications. Journal
644 of Petrology, 25:579-618. https://doi.org/10.1093/petrology/25.3.579

645 Bellieni G, Comin-Chiaramonti P, Marques LS, Melfi AJ, Nardy AJR, Papatrechas C, Piccirilo EM, Roisenberg A (1986)
646 Petrogenetic aspects of acid and basaltic lavas from Paraná Basin (Brazil): geological, mineralogical and petrochemical
647 relationships. J Petrol, 27:915-944. https://doi.org/ https://doi.org/10.1093/petrology/27.4.915

648 Blundy J, Cashman K (2008) Petrologic Reconstruction of Magmatic System Variables and Processes. Rev Mineral
649 Geochem 69:179-239. https://doi.org/10.2138/rmg.2008.69.6

650 Bryan SE, Peate IU, Peate DW, Self S, Jerram DA, Mawby MR, Marsh JS, Miller JA (2010) The largest volcanic eruptions
651 on Earth. Earth Sci Rev 102(3-4):207-229 (DOI: 10.1016/j.earscirev.2010.07.001). https://doi.org/ DOI
652 10.1016/j.earscirev.2010.07.001

653 Bryan SE, Riley TR, Jerram DA, Stephens CJ, Leat PT (2002) Silicic volcanism: an undervalued component of large
654 igneous provinces and volcanic rifted margins. Special Papers- Geol Soc Am 97-118. https://doi.org/ DOI:
655 https://doi.org/10.1130/0-8137-2362-0.97

656 Cañón-Tapia, E., Castro, J., 2004. AMS measurements on obsidian from the Inyo Domes, CA: a comparison of magnetic
657 and mineral preferred orientation fabrics. J Volcanol Geotherm Res 134:169–182. https://doi.org/
658 10.1016/j.jvolgeores.2004.01.005

659 Cañón-Tapia E, Pinkerton H (2000) The anisotropy of magnetic susceptibility of lava flows: an experimental approach J
660 Volcanol Geotherm Res 98:219–233. https://doi.org/10.106/S0377-0273(99)00155-9

661 Raposo MIB (2017) Anisotropy of magnetic susceptibility of silicic rocks from quarries in the vicinity of São Marcos, Rio
662 Grande do Sul, South Brazil: Implications for emplacement mechanisms. J Volcanol Geotherm Res Accepted.
663 https://doi.org/ 10.1016/j.jvolgeores.2017.07.018

664 Cashman K (2004) Volatile Controls on Magma Ascent and Eruption. Volatile controls on magma ascent and
665 degassing The State of the Planet: Frontiers and Challenges in Geophysics. Am Geophys Union Monog 150:109-124.
666 https://doi.org/ 10.1029/150GM10

667 Castro JM, Cashman KV (1999) Constraints on rheology of obsidian and pumice based on folds in obsidian lavas.
668 J Struct Geol 21:807-819. https://doi.org/ 10.1016/S0191-8141(99)00070-X
669

670 Chadima M, Jelinek V (2009) AniSoft 42 Software, Anisotropy Data Browser for Windows. Brno, Czech Republic.

671 Comin-Chiaramonti P, Bellieni G, Piccirillo EM, Melfi AJ (1988) Classification and petrography of continental stratoid
672 volcanic and related intrusive from the Paraná Basin (Brasil). In: Piccirillo EM, Melfi AJ (eds) The Mesozoic flood
673 volcanism of the Paraná Basin: petrogenetic and geophysical aspects. São Paulo Instituto Astronômico e Geofísico.
674 https://doi.org/

675 Comin-Chiaramonti P, Riccomini C, Slejko F, De Min A, Ruberti E, Gomes CB (2010) Cordierite-bearing lavas from
676 Jaguarão, Southern Brazil: Petrological evidence for crustal melts during early rifting of Gondwana. Gondwana Res 18:514-
677 527 https://doi.org/ 10.1016/j.gr.2009.12.007

678 Condie KC. 2001. Mantle Plumes and Their Record in Earth History. Oxford, UK, Cambridge Univ. Press.

679
680

681 Day R, Fuller M, Schimidt VA (1977) Hysteresis properties of titanomagnetites: Grain size and composition dependence.
682 Phys Earth Planet Inter 13:260-267 https://doi.org/ 10.1016/0031-9201(77)90108-X

683 De Campos CP, Guimarães LF, Lima EF, Janasi VA, Giordano D, Dingwell DB (2016) Chaotic flow and fragmentation
684 patterns in the acidic feeder system from the Paraná-Etendeka Large Igneous Province. Goldschimidt Conference Abstracts
685 2413.

686 Dunlop DJ (2002) Theory and application of the Day plot (Mrs/Ms versus Hcr/Hc) 1. Theoretical curves and tests using
687 titanomagnetite data. J Geophys Res 107:B3 https://doi.org/ 10.1029/2001JB000486.

688 Dunlop DJ, Özdemir Ö (1997) Rock Magnetism, fundamentals and frontiers. Cambridge Studies in Magnetism Series 573
689 pp https://doi.org/ 10.1029/2002EO000275

690 Einstein A. 1906. Eine neue Bestimmung der Moleküldimensionen. Ann. Phys. 19:289–306.
691 http://dx.doi.org/10.1002/andp.19063240204

692 Einstein A. 1911. Berichtigung zu meiner Arbeit: Eine neue Bestimmung der Moleküldimensionen. Ann. Phys. 34:591–592.
693 http://dx.doi.org/10.1002/andp.19113390313

694 Ewart A, Milner SC, Armstrong RA, Duncan AR (1998) Etendeka volcanism of the Goboboseb Mountains and Messum
695 Igneous Complex, Namibia. Part II: voluminous quartz latite volcanism of the Awahab magma system. J Petrol 39:227-253.
696 https://doi.org/10.1093/petroj/39.2.227).

697 Ewart A, Milner SC, Duncan AR, Bailey M (2002) The Cretaceous Messum igneous complex, S.W. Etendeka, Namibia:
698 reinterpretation in terms of a downsag-cauldron subsidence model. J Volcanol Geotherm Res 114: 251-273. https://doi.org/
699 10.1016/S0377-0273(01)00266-9).

700 Fernandes LAD, Menegat R, Costa AFU, Koester E, Porcher CC, Tommasi A, Kraemer G, Ramgrab GE, Camozzato E
701 (1995) Evolução tectônica do Cinturão Dom Feliciano no Escudo Sul-Rio-Grandense: Parte II – uma contribuição a partir
702 das assinaturas geofísicas. Revista Brasileira de Geociências. 25(4):375-384. https://doi.org/

703 Fink JH (1983) Structure and emplacement of a rhyolitic obsidian flow; Little Glass Mountain, Medicine Lake Highland,
704 northern California. Geol Soc Am Bull 94(3):362-380 https://doi.org/ 10.1130/0016-
705 7606(1983)94<362:SAEOAR>2.0.CO;2

706 Florisbal LM, Heaman LM, Janasi VA, Bitencourt MF (2014) Tectonic significance of the Florianópolis Dyke Swarm,
707 Paraná-Etendeka Magmatic Province: A reappraisal based on precise U-Pb dating. J Volcanol Geotherm Res 289:140-150
708 https://doi.org/10.1016/j.jvolgeores.2014.11.007

709 Foulguer GR. 2017. Origin of the South Atlantic igneous province. Journal of Volcanology and Geothermal Research (in
710 press)

711 Foulger GR. 2010. Plates vs Plumes: A Geological Controversy. Wiley-Blackwell, Chichester, United Kingdom.

712 Garland FE, Hawkesworth CJ, Mantovani MSM (1995) Description and petrogenesis of the Paraná rhyolites. J Petrol
713 36:1193–1227. https://doi.org/10.1093/petrology/36.5.1193).

714 Geoffroy L, Callot JP, Auborg C, Moreira M (2002) Divergence between magnetic and plagioclases linear fabrics in dykes:
715 a new approach for defining the flow vector using magnetic foliation. TerraNova; 14:183-190.

716 Giordano D, Russell JK, Dingwell DB (2008) Viscosity of magmatic liquids: A model. Earth Planet Sci Lett 271:123-134.
717 https://doi.org/ 10.1016/j.epsl.2008.03.038

Glenn JMG, Renne PR, Milner SC, Coe RS (1997). Magma flow inferred from anisotropy of magnetic susceptibility in the coastal Paraná-Etendeka igneous province: Evidence for rifting before flood volcanism. Geology. 12:1131-1134. https://doi.org/ 10.1130/0091-7613(1997)025<1131:MFIFAO>2.3.CO;2

Gonnermann HM, Manga M (2005) Flow banding in obsidian: A record of evolving textural heterogeneity during magma deformation. Earth Planet Sci Lett 236:135-147. https://doi.org/ 10.1016/j.epsl.2005.04.031

Guimarães LF, Raposo MIB, Janasi VA, Cañón-Tapia E, Polo LA (2017) An AMS study of different silicic units from the southern Paraná-Etendeka Magmatic Province in Brazil: implications for the identification of flow directions and local feeding. J. Volcanol. Geotherm. Res. (in review). https://doi.org/ 10.1016/j.jvolgeores.2017.11.014

Harris AJLM, Rowland SK, Villeneuve N, Thordarson T (2017) Pahoehoe, 'a'a, and block lava: an illustrated history of the nomenclature. Bull Volcanol 79:7 https://doi.org/10.1007/s00445-016-1075-7

Harrison TM, Watson EB (1984) The behaviour of apatite during crustal anatexis: equilibrium and kinetic considerations. Geochim Cosmochim Acta 48(7):1467-1477. https://doi.org/ 10.1016/0016-7037(84)90403-4

Hastie WW, Watkeys MK, Auborg C (2014) Magma flow in dyke swarms of the Karoo LIP: Implications for the mantle plume hypothesis. Gondwana Res 25:736-755. https://doi.org/ 10.1016/j.gr.2013.08.010

Hausback BP (1987) An extensive, hot, vapor-charged rhyodacite flow, Baja California, Mexico In: Fink JH (ed) The emplacement of silicic domes and lava flows 212 pp https://doi.org/ 10.1130/SPE212-p111

Hawkesworth C, Kelley S, Turner S, Le Roex A, Storey B (1999) Mantle processes during Gondwana break-up and dispersal. J Afr Earth Sci 28:239-261 https://doi.org/10.1016/S0899-5362(99)00026-3

Hawkesworth CJ, Gallagher K, Kirstein L, Mantovani MSM, Peate DW, Turner SP (2000) Tectonic controls on magmatism associated with continental break-up: an example from the Paraná-Etendeka Province. Earth Planet Sci Lett 179:335-349. https://doi.org/ 0.1016/S0012-821X(00)00114-X

Hellwig BM (2006) The viscosity of dacitic liquids measured at conditions relevant to explosive arc volcanism: determining the influence of temperature, silicate composition, and dissolved volatile content. Dissertation, University of Missouri-Columbia

Henry CD, Wolff JA (1992) Distinguishing strongly rheomorphic tuffs from extensive silicic lavas. Bull Volcanol, 54:171-186. https://doi.org/ DOI 10.1007/BF00278387

Henry CD, Price JG, Rubin JN, Laubach SE (1990) Case study of an extensive silicic lava: the Bracks Rhyolite, Trans-Pecos Texas. J Volcanol Geotherm Res 43:113-132. https://doi.org/

Hext GR (1963) The estimation of second-order tensors, with related tests and designs. Biometrika 50:353–373. https://doi.org/10.1016/0377-0273(90)90048-K

Hrouda F (1982) Magnetic anisotropy of rocks and its application in geology and geophysics, Surveys in Geophysics 5: 37–82 https://doi.org/ 10.1007/BF01450244

Hrouda F (1985) The magnetic fabric in the Brno Massif. Sbor Geol Ved, Uz Geol 19:89-112

Janasi VA, Montanheiro TJ, Freitas VA, Reis PM, Negri FA, Dantas FA (2007) Geology, petrography and geochemistry of the acid volcanism of the Paraná Magmatic Province in the Piraju-Ourinhos region, SE Brazil. Rev Bras Geoc 37:745-759 https://doi.org/

Janasi VA, de Freitas VA, Heaman LH (2011) The onset of flood basalt volcanism, Northern Paraná Basin, Brazil: a precise U–Pb baddeleyite/zircon age for a Chapecó type dacite. Earth Planet Sci Lett 302 (1–2):147–153. https://doi.org/ 10.1016/j.epsl.2010.12.005

Jelinek V (1981) Characterization of the magnetic fabric of rocks. Tectonophysics 79:T63– T67 https://doi.org/ 10.1016/0040-1951(81)90110-4

Jelinek V (1978) Statistical processing of anisotropy of magnetic susceptibility measured on groups of specimens and its applications, Stud. Geophys. Geod., 22:50 – 62.

Kirstein LA, Peate DW, Hawkesworth CJ, Turner SP, Harris C, Mantovani MSM (2000). Early Cretaceous basaltic and rhyolitic magmatism in southern Uruguay associated with the opening of the South Atlantic. J Petrol 41:1413-1438 https://doi.org/ 10.1093/petrology/41.9.1413

Lesher CE, Spera FJ (2015). Thermodynamic and Transport Properties of Silicate Melts and Magma. In: Sigurdsson H, Houghton B, McNutt S, Rymer H, Stix J, Encyclopedia of Volcanoes 113-141

Lima EF, Philipp RP, Rizzon GC, Waichel BL, Rossetti LMM (2012) Sucessões Vulcânicas e Modelo de Alimentação e Geração de Domos de Lava Ácidos da Formação Serra Geral na Região de São Marcos-Antonio Prado (RS). Geologia USP Série Científica, 12:49-64. https://doi.org/ 10.5327/Z1519-874X2012000200004

Luchetti ACF, Nardy AJR, Machado FB, Madeira JEO, Arnosio JM (2014) New insights on the occurrence of peperites and sedimentary deposits within the silicic volcanics sequences of the Paraná Magmatic Province, Brazil. Solid Earth. 5:121-130. https://doi.org/ 10.5194/se-5-121-2014

Manley CR, Fink JH (1987) Internal textures of rhyolite flows as revealed by research drilling. Geology: 15(6):549-552. https://doi.org/ 10.1130/0091-7613(1987)15<549:ITORFA>2.0.CO;2

Marteleto NS, Florisbal LM, Janasi VA (2016) Petrologia e geoquímica de diques ácidos do Enxame de Diques de Florianópolis, na Ilha de Santa Catarina. In: Anais do 48° Congresso Brasileiro de Geologia, Porto Alegre

McPhie J, DellaPasqua F, Allen SR, Lackie MA (2008) Extreme effusive eruptions: Paleoflow data on an extensive felsic lava in the Mesoproterozoic Gawler Range Volcanics. J Volcanol Geotherm Res 172:148 – 161. https://doi.org/ 10.1130/B30167.1

Melfi AJ, Nardy AJR, Piccirillo EM (1988) Geological and magmatic aspects of the Paraná Basin: An introduction. In: Piccirillo E. M. & Melfi A. J. (eds.) The Mesozoic flood volcanism of the Paraná Basin: Petrogenetic and geophysical aspects IAG-USP p. 1-13

Milner SC, Duncan AR, Whittingham AM, Ewart A (1995) Trans-Atlantic correlation of eruptive sequences and individual silic volcanic units within Paraná- Etendeka Igneous Province. J Volcanol Geotherm Res 69:137-157. https://doi.org/ 10.1016/0377-0273(95)00040-2

Milner SC, Duncan AR (1987) Geochemical characterization of quartz latite units in the Etendeka Formation. Comm Geol Sur Nam 3:83-90 https://doi.org/10.1007/BF00278389).

Milner SC, Duncan AR, Ewart A (1992) Quartz latite rheoignimbrite flow of the Etendeka Formation, North-Western Namibia. Bull Volcanol 54:200-219.

Morgan S, Stanik A, Horsman E, Tikoff B, Saint Blanquat M, Habert G (2008) Emplacement of multiple magma sheets and wall rock deformation: Trachyte Mesa intrusion, Henry Mountains, Utah. J Struct Geol 30:491-512. https://doi.org/ 10.1016/j.jsg.2008.01.005

Morrow N, McPhie J (2000) Mingled silicic lavas in the Mesoproterozoic Gawler Range Volcanics, South Australia. J Volcanol Geotherm Res 96:1-13.

Mpodozis C, Ramos VA (2008) Tectónica Jurásica en Argentina y Chile: extensión, subducción oblicua, rifting, deriva y colisiones? Revista de la Asociación Geológica Argentina. 63(4):481-497.

Muzio R, Morales E, Veroslavsky G, Conti B (2009) The Arequita Formation (Lower Cretaceous): petrographic features of the volcanics facies in the Laguna Merín Basin, east Uruguay. Lat Am J sedimentol basin anal 16(1):19-28.

Nardy AJR, Machado FB, Oliveira MAF (2008) As rochas vulcânicas mesozoicas ácidas da Bacia do Paraná: litoestratigrafia e considerações geoquímicas-estratigráficas. Revista Brasileira de Geociências, 38(1):178-195. https://doi.org/

Ottino JM (1989) The mixing of fluids. Scientific Am 260:56–67. https://doi.org/10.1038/scientificamerican0189-56

Pankhurst MJ, Schaefer BF, Betts PG, Phillips N, Hand M (2011) A Mesoproterozoic continental flood rhyolite province, the Gawler Ranges, Australia: the end member example of the Large Igneous Province clan. Solid Earth: 2:25-33. https://doi.org/ 10.5194/se-2-25-2011

Peate DW (1997) The Paraná-Etendeka province. In: Mahoney JJ, Coffin MR (Eds) Large Igneous Provinces: Continental, Oceanic and Planetary Flood Volcanism Geophysical Monograph 100:217-245.

Peate DW, Hawkesworth CJ, Mantovani MSM (1992) Chemical stratigraphy of the Paraná lavas (S. America): classification of magma types and their spatial distribution. Bull Volcanol 55:119-139. https://doi.org/ 10.1007/BF00301125

Perugini D, Poli G (2012) The mixing of magmas in plutonic and volcanic environments: Analogies and differences. Lithos 153:261-277. https://doi.org/10.1016/j.lithos.2012.02.002

Petrini R, Civetta L, Iacumin P, Longinelli A, Belliene G, Comin-Chiaramonti P, Ernesto N, Marques LS, Melfi A, Pacca I, Piccirillo EM (1989) High temperature flood silicic lavas (?) from the Paraná Basin (Brasil). New Mexico Bureau of Mines & Mineral Resources Bulletin 131-213.

Philpotts AR, Philpotts DE (2007) Upward and downward flow in a camptonite dike as recorded by deformed vesicles and the anisotropy of magnetic susceptibility (AMS). J Volcanol Geotherm Res 161, 81-94. https://doi.org/ 10.1016/j.jvolgeores.2006.11.006

Pinto VM, Hartmann LA, Santos JOS, McNaughton NJ, Wildner W (2011) Zircon U-Pb geochronolgy from the Paraná bimodal volcanics province support a brief eruptive cycle at ~ 135 Ma. Chem Geol 1-2 (93-102). https://doi.org/ 10.1016/j.chemgeo.2010.11.031

Plenier G, Camps P, Henry B, Ildefonse B (2005) Determination of flow directions by combining AMS and thin-section analyses: Implications for Oligocene volcanism in the Kerguelen Archipelago (southern Indian Ocean). Geophys J Internat 160(1), 63-78. https://doi.org/ 10.1111/j.1365-246X.2004.02488.x

Polo LA, Janasi VA (2014) Volcanic stratigraphy of intermediate to acidic rocks in Southern Paraná Magmatic Province, Brazil. Geologia USP Série Científica 14, 83-100. https://doi.org/ 10.5327/Z1519-874X201400020005

Polo LA, Giordano D, Janasi VA, Guimarães LF (2017) Effusive volcanism in the Paraná Magmatic Province, South Brazil: Physico-chemical conditions of storage and eruption and consideration on the rheological behavior during emplacement. J Volcanol Geotherm Res (accepted) https://doi.org/ 10.1016/j.jvolgeores.2017.05.027

Pueyo Anchuela Ó, Gil Imaz A, Gil-Peña I, Maestro A, Galindo-Zaldivar J, López-Martínez J, Rey J, Soto R, Oliva-Urcia B. Application of MAS for reconstruction of the geological evolution of recente volcanics systems: case of Deception Island (South Shetland Islands, Antartica). Tectonophysics 626:69-85

Quintas MCL, Mantovani MSM, Zalán PV (1999) Contribuição ao estudo da evolução mecânica da Bacia do Paraná. Revista Brasileira de Geociências 29(2):217-226

Rapela CW, Llambías EJ (1999) El magmatismo gondwánico y los ciclos fanerozoicos. In: Caminos R (ed) Geología Argentina, Instituto de Geología y Recursos Minerales, Anales 29:373-376

836 Raposo MIB (2011) Magnetic fabric of the Brazilian dike swarms. A review. In: Petrovský E, Herrero-Bervera E,
837 Harinarayana T, Ivers D (eds) The Earth's Magnetic Interior. IAGA Special Sopron Book Series 1:247–262, Springer
838 Berlin. https://doi.org/ 10.1007/978-94-007-0323-0_17

839 Raposo MIB, Ernesto M, Renne PR (1998) Paleomagnetism and dating of the early Cretaceous Florianópolis dike swarm
840 (Santa Catarina Island), Southern Brazil. Phys Earth Planet. Inter 108 (4), 275–290 https://doi.org/10.1016/S0031-
841 9201(98)00102-2

842 Raposo MIB (2017) Magnetic fabrics of the Cretaceous dike swarms from São Paulo coastline (SE Brazil): Its relationship
843 with South Atlantic Ocean opening. Tectonophysics 721, 395-414 https://doi.org/ 10.1016/j.tecto.2017.10.023

844 Renne PR, Deckart K, Ernesto M, Féraud G, Piccirillo EM (1996) Age of the Ponta Grossa dike swarm (Brazil), and
845 implications to Paraná flood volcanism. Earth Planet Sci Lett 144, 199-212. https://doi.org/ 10.1016/0012-821X(96)00155-0

846 Renne PR, Ernesto M, Pacca IG, Coe RS, Glen J, Prevot M, Perrin M (1992) The age of Parana flood volcanism, rifting of
847 Gondwanaland, and the Jurassic-Cretaceous boundary. Science 258:975-979. https://doi.org/ 10.1126/science.258.5084.975

848 Rochette P, Jenatton L, Dupuy C, Boudier F, Reuber I (1991) Emplacement modes of basaltic dykes in the Oman ophiolite:
849 evidence from magnetic anisotropy with reference to geochemical studies. In: Peters TJ, Nicolas A, Coleman RJ, Dordrecht
850 K (eds) Ophiolite Genesis and the Evolution of the Oceanic Lithosphere 55-82.

851 Roisenberg A (1989) Petrologia e geoquímica do vulcanismo ácido mesozoico da Província Meridional da Bacia do Paraná.
852 Thesis, Universidade Federal do Rio Grande do Sul

853 Roscoe R. 1952. The viscosity of suspensions of rigid spheres. J App. Phys. 2:267–269

854 Rossetti L, Lima EF, Waichel BL Hole MJ, Simões MS, Scherer CMS (2017). Lithostratigraphy and volcanology of the
855 Serra Geral Group, Paraná-Etendeka Igneous Province in Southern Brazil: Towards a formal stratigraphical framework. J
856 Volcanol Geotherm Res in press https://doi.org/ 10.1016/j.jvolgeores.2017.05.008

857 Schneider, C.A., Rasband, W.S., Eliceiri, K.W. 2012. NIH Image to ImageJ: 25 years of image analysis. Nature methods
858 9(7), 671-675

859 Seaman SJ (1995). Multi-stage magma mixing and mingling and the origin of flow banding in the Aliso Lava Dome,
860 Tumacacori Mountains, southern Arizona, J Geophys Res 100, 8381 – 8398. https://doi.org/ 10.1029/94JB03260

861 Shaw HR (1972) Viscosities of magmatic silicate liquids: An empirical method of prediction. AmerJ Sci 272:870–893.
862 https://doi.org/10.2475/ajs.272.9.870

863 Simões MS, Lima EF, Sommer CA, Rossetti LMM (2017) Structures and lithofacies of felsic volcanic feeder conduit
864 systems in the Paraná-Etendeka LIP, southern Brazil. J Volcanol Geotherm Res (in press). https://doi.org/
865 10.1016/j.jvolgeores.2017.12.013

866 Simões MS, Lima EF, Sommer CA, Rossetti LMM (2018) The Mato Perso Conduit System: evidences of silicic magma
867 transport in the southern Paraná-Etendeka LIP. Brazilian J of Geolo (in press).

868 Simões MS, Rossetti LMM, Lima EF, Ribeiro BP (2014) The role of viscosity in the emplacement of high-temperature
869 silicic flows of Serra Geral Formation in Torres Syncline (Rio Grande do Sul State, Brazil). Brazilian J Geol 44(4): 669-
870 679. https://doi.org/10.5327/Z23174889201400040010).

871 Smith JV, Houston EC (1994) Folds produced by gravity spreading of a banded rhyolite lava flow. J Volcanol Geotherm
872 Research: 63, 89-94. https://doi.org/ 10.1016/0377-0273(94)90019-1

873 Tomazzoli ER, Lima EF (2006) Magmatismo ácido na Ilha do Arvoredo-SC. Revista Brasileira de Geociências, 36: 57–76.

874 Tuffen H, James MR, Castro JM, Schipper CI (2013) Exceptional mobility of an advancing rhyolitic obsidian flow at
875 Cordón Caulle volcano in Chile. Nature Comm 4, 1-7. https://doi.org/ 10.1038/ncomms3709

Turner S, Regelous M, Kelley S, Hawkesworth CJ, Mantovani M (1994) Magmatism and continental break-up in the South Atlantic: high precision $^{40}Ar/^{39}Ar$ geochronology. Earth Planet Sci Lett 121, 333-348. https://doi.org/ 10.1016/0012-821X(94)90076-0

Umann LV, Lima EF, Sommer CA, De Liz JD (2001) Vulcanismo ácido da região de Cambará do Sul-RS: litoquímica e discussão sobre a origem dos depósitos. Revista Brasileira de Geociências, 31(3):357-364.

Vetere F, Behrens H, Holtz F, Neuville DR (2006) Viscosity of andesitic melts — New experimental data and a revised calculation model. Chem Geol 228:233–245. https://doi.org/ 10.1016/j.chemgeo.2005.10.009

Vetere F, Rossi S, Namur O, Morgavi D, Misiti V, Mancinelli P, Petrelli M, Pauselli C, Perugini D (2017) Experimental constraints on the rheology, eruption, and emplacement dynamics of analog lavas comparable to Mercury´s northern volcanic plains. J Geophys Res: Planets. 122. https://doi.org/doi:10.1002/2016JE005181.

Vieira Jr N (1985) Petrologia e geoquimica do vulcanismo Mesozóico de Jaguarão — RS Dissertation, Universidade Federal do Rio Grande do Sul

Vieira Jr N, Roisemberg A (1985) Formação Jaguarão — nova unidade vulcânica mesozóica no RS. Anais II Simpósio Sul-Brasileiro de Geologia Florianópolis

Waters LE, Lange RA (2015) An updated calibration of the plagioclase-liquid hygrometer-thermometer applicable to basalts through rhyolites. Amer Miner 100 (10), 2172–2184. https://doi.org/ 10.2138/am-2015-5232

Wiegand M, Trumbull RB, Kontny A, Greiling RO (2017) An AMS study of magma transport and emplacement mechanisms in mafic dykes from the Etendeka Province, Namibia. Tectonophysics, 716, 149-167. https://doi.org/ 10.1016/j.tecto.2016.08.016

Whittington AG, Hellwig BM, Behrens H, Joachim B, Stechern A, Vetere F (2009). The viscosity of hydrous dacitic liquids: Implications for the rheology of evolving silicic magmas, Bull Volcanol 71:185–199. https://doi.org/ 10.1007/s00445-008-0217-y

Závada P, Schulmann K, Lexa O, Hrouda F, Haloda J, Týcová P (2009) The mechanism of flow and fabric development in mechanically anisotropic trachytes lava. J Struct Geol 31: 1295-1307.https://doi.org/ 10.1016/j.jsg.2009.04.002

900 **Supplementary Material** – Individual speciment measures of shape and directional AMS parameters.

	Mean AMS parameters				Mean anisotropy axes		
Specimen	**Km**	**P**	**Pj**	**T**	**K1dec/inc**	**K2dec/inc**	**K3dec/inc**
Site CM1							
CM1A1	33719.25	1.022	1.023	-0.481	107.3/16.1	14.5/9.5	255/71.2
CM1A2	33002.54	1.015	1.016	-0.704	99/15.1	347.5/53.7	198.8/32.1
CM1B1	28813.97	1.025	1.027	-0.601	103.8/26	202.7/17.7	323.2/57.8
CM1B2	28457.1	1.019	1.02	-0.566	109.5/32.7	12.6/10.5	267.1/55.2
CM1C1	36389.29	1.029	1.032	-0.779	124.9/2.5	34/20.2	221.7/69.6
CM1C2	38067.48	1.041	1.044	-0.668	130.7/7.6	37.8/20.5	240/68
CM1D1	28487.1	1.016	1.016	-0.334	295.8/13.1	34.2/32.4	186.8/54.5
CM1D2	27825.35	1.016	1.016	-0.105	297.1/16.2	44.8/46.3	193.3/39.2
CM1E1	31920.33	1.021	1.021	0.097	120.4/5.4	26.8/33.2	218.5/56.2
CM1E2	27647.42	1.016	1.016	-0.421	113.9/10.9	14.8/39.4	216.5/48.5
CM1E3	26163.09	1.02	1.021	-0.278	306.4/2.2	38.2/39.3	213.7/50.6
CM1F1	26297.38	1.021	1.022	-0.355	118.6/0.2	28.6/14.8	209.2/75.2
CM1G1	37829.57	1.093	1.093	0.031	301.2/6.9	209/17.4	52/71.2
CM1G2	39417.71	1.075	1.077	0.368	305.8/1.7	215.2/20.4	40.3/69.6
CM1G3	40061.93	1.087	1.088	0.114	304.1/16.7	208.5/17.7	74.8/65.2
CM1G4	38460.11	1.093	1.093	0.045	301.4/18.8	203.6/21.6	68.7/60.7
CM1H1	38473.54	1.077	1.077	0.007	136.3/0.6	226.7/34.1	45.4/55.9
CM1J1	44722.54	1.023	1.024	-0.565	145.7/40.6	262.6/27.8	15.8/36.8
CM1K1	34820.12	1.06	1.061	0.285	145.4/8	237.9/17.3	31.5/70.8
CM1K2	31936.62	1.075	1.076	-0.247	317.4/0.1	227.4/5.8	48.4/84.2
CM1L1	41719.46	1.049	1.052	-0.572	310.5/12.7	213.6/28.2	62.1/58.6
CM1M1	39735.16	1.093	1.097	-0.515	322.6/3.5	230.4/31.6	58.3/58.2
CM1M2	36576.57	1.099	1.103	-0.507	318.1/6.2	223.7/35.4	56.7/53.9
CM1N1	35195.09	1.143	1.143	0.087	324.8/3.2	234.1/11.4	70.4/78.2
CM1N2	34239.56	1.162	1.164	-0.309	145.5/3.2	235.8/4.7	21.5/84.3
CN1Q1	40256.98	1.102	1.102	0.057	359.1/3	267.3/30.4	94.2/59.4
CN1Q2	37768.21	1.113	1.113	0.068	178.1/1.5	268.8/27.6	85.2/62.4
CN1Q3	30479.43	1.159	1.159	0.067	172.1/3.9	264.6/33.1	76.1/56.6
CM1R1	40143.73	1.057	1.06	-0.561	167.4/2.9	259.8/40.1	74/49.7
CM1R2	41664.85	1.04	1.042	-0.466	173.5/2.6	265.6/39.2	80.3/50.7
CM1S1	35923.68	1.029	1.029	-0.089	178.3/8	274.3/36.7	77.9/52.1
CM1S2	44648.45	1.024	1.025	0.266	166/0.1	256.1/41.8	75.8/48.2
CM1T1	33711.2	1.037	1.039	-0.667	180.4/23.8	292.6/40.5	68.6/40.1
CM1T2	38541.15	1.022	1.023	-0.46	169.6/1.8	261/38.2	77.3/51.7
CM1W1	25650.19	1.057	1.058	-0.262	1.8/7.9	257.1/61.4	96/27.3
CM1AX1	23104.99	1.044	1.045	-0.23	36.5/2.4	306.4/1	194.7/87.4
CM1Y1	26969.51	1.043	1.043	-0.199	356.5/20	255.9/26.7	118.7/55.7
CM1Z1	25017.86	1.087	1.093	0.637	230.9/46	346.8/22.9	94.1/35.1
CM1AA1	20643.25	1.048	1.048	0.151	355.5/11.1	246.8/58.6	91.8/28.9
CM1AB1	44385	1.019	1.02	0.629	267.5/30.9	151.8/36	26.2/38.7
CM1AB2	41292.5	1.017	1.017	0.219	113.6/2.9	210.3/66.6	22.4/23.2
CM1AC1	34028.79	1.149	1.15	-0.113	296.6/0.7	31.8/82.2	206.5/7.8
CM1AD1	26675.24	1.091	1.096	-0.547	178.5/18.8	293.5/51.3	76/32.4

CM1AE1	25250.94	1.088	1.096	-0.739	153.7/1.6	244.1/14.4	57.3/75.5
CM1AE2	31371.7	1.121	1.125	-0.406	338.4/11	239/40.2	80.7/47.8
CM1AF1	28640.67	1.016	1.016	0.385	8.1/15.3	263.5/42.8	113/43.2
CM1AF2	26941.53	1.012	1.012	-0.118	13.9/16.4	275.3/27	131.7/57.7

	Mean AMS parameters				**Mean anisotropy axes**		
Specimen	**Km**	**P**	**Pj**	**T**	**K1dec/inc**	**K2dec/inc**	**k3dec/inc**
CM1AG1	34108.39	1.013	1.014	0.548	260.1/27.3	354.8/9.1	101.5/61
CM1AG2	25121.1	1.015	1.015	0.266	329.5/10.4	234.8/23.9	81.2/63.7
CM1AH1	40628.61	1.071	1.071	-0.165	166.7/11.2	261.6/23.4	53/63.7
CM1AJ1	36135.01	1.071	1.075	-0.576	151.6/7.2	58.7/22.1	258.6/66.6
CM1AK1	44134.28	1.109	1.111	-0.306	326/1.7	235.5/18.2	61.1/71.7
CM1AL1	44570.86	1.05	1.057	0.949	248.7/0.5	338.9/16	157/74
CM1AN1	31163.35	1.012	1.013	0.599	68.4/12.4	336.7/7.4	216.5/75.4
CM1AN2	27444.78	1.016	1.016	0.259	68.5/9.7	338.2/1.8	237.6/80.1
CM1AN3	24727.97	1.015	1.015	-0.021	40.8/3	130.8/0.2	224.7/87
CM1AO1	41324.68	1.043	1.044	0.369	46.1/13.4	316.1/0.2	225.3/76.6
CM1AO2	37606.11	1.044	1.046	0.516	31.2/9.2	121.6/2.1	224.2/80.5
CM1AO3	40147.25	1.053	1.053	0.24	60.1/11.2	150.2/0.5	242.8/78.8
CM1AP1	46359.06	1.06	1.062	0.353	60/10.4	329.1/5	213.8/78.5
CM1AP2	47598.68	1.061	1.062	0.359	65.9/10.9	334.8/6	216.3/77.5
CM1AQ1	33631.68	1.02	1.022	0.787	158.5/3.6	248.6/0.8	351.1/86.3
CM1AR1	42488.86	1.043	1.044	0.37	55.2/1	325.2/2	173/87.8
CM1AT1	40569.31	1.046	1.048	0.454	87.7/0.8	357.6/9	183/80.9
CM1AT2	38770.09	1.061	1.07	0.93	10.7/10.8	279.9/4	169.8/78.5
CM1AT3	39488.02	1.053	1.055	0.459	75.5/2.5	345/11.5	177.4/78.2
CM1AT4	34416.02	1.048	1.052	0.716	31/28.4	122.2/2.3	216.4/61.5
CM1AU1	38481.13	1.035	1.036	0.317	358.7/27.6	100.3/21	222.4/54.1
CM1AU2	40275.76	1.042	1.043	0.277	185.7/1.2	275.7/0.1	12.2/88.8
CM1AV1	37333.54	1.051	1.052	-0.199	214/0.8	123.9/6.3	311/83.6
CM1AV2	33073.41	1.035	1.035	0.132	16.1/3.5	285.8/5.8	136.8/83.2
CM1AW1	34919.86	1.139	1.139	-0.108	336.1/7.5	67.3/8.5	205.5/78.6
CM1AW2	34310.27	1.153	1.155	0.248	3.9/2.5	94/2.3	227.2/86.6
CM1AW3	36913.47	1.038	1.04	0.556	345.5/1.4	255.4/3.7	96.6/86.1
CM1AX1	39387.39	1.107	1.108	0.176	194.3/0.9	284.5/7.3	97.1/82.7
CM1AX2	37709.2	1.11	1.111	0.175	28/4.2	297.7/3.7	166.6/84.4
CM1AX3	39045.26	1.087	1.087	-0.008	201.4/11.5	292.7/6.2	50.6/76.9
Site CM2							
CM2A1	36450.53	1.027	1.029	0.721	52.5/12	314.5/33.1	159.7/54.3
CM2B1	7.275.325	1.018	1.019	0.623	74.7/6.7	343.5/10.7	196/77.3
CM2C1	34790.09	1.017	1.017	0.203	302.1/19.6	35.2/8.5	147.3/68.5
CM2E1	39612.83	1.013	1.014	-0.457	322.2/16.8	226/19.8	89.5/63.6
CM2G1	32069.23	1.012	1.012	0.162	281.1/16.9	12.7/5	118.7/72.3
CM2H1	23738.15	1.011	1.011	-0.399	293.2/25.4	32.1/18.1	153.8/58
CM2I1	21713.62	1.016	1.016	-0.126	285.2/25.8	22.2/14.1	138.1/60.1
CM2J1	22021.05	1.012	1.012	0.213	293.1/26.8	31.5/16.2	149.3/58

Site CM3							
CM3D1	5.289.104	1.006	1.006	0.243	147.2/28.4	281.2/52.1	44/22.9
CM3E1	6.217.712	1.008	1.008	0.376	210.9/11.2	60.2/77.2	302.1/6.1
CM3F1	6.172.902	1.005	1.005	-0.155	166.1/0.8	256.2/4.8	66.8/85.1
CM3G1	6.184.016	1.003	1.004	0.834	319.2/2.5	49.5/7.8	211.5/81.9
CM3H1	5.603.602	1.007	1.008	0.593	343.5/10.2	250.6/15.6	105.4/71.2
CM3I1	4728.48	1.009	1.009	0.168	234.6/13.8	326.2/6.7	81.4/74.6
CM3J1	5.059.994	1.007	1.007	-0.455	197.1/9.7	106.4/4.5	351.8/79.3
CM3K1	7.059.831	1.017	1.017	0.019	230.8/1.4	320.9/4.4	123.3/85.4

	Mean AMS parameters				**Mean anisotropy axes**		
Specimen	**Km**	**P**	**Pj**	**T**	**K1dec/inc**	**K2dec/inc**	**k3dec/inc**
Site CM4							
CM4A1	4.765.285	1.007	1.024	1.025	38.1/50.3	50.3/165.6	165.6/26.8
CM4A2	2.280.576	1.01	1.016	1.016	82/30.5	30.5/341	341/18
CM4A3	10054.05	1.009	1.041	1.044	48/46.9	46.9/192.3	192.3/37.2
CM4B1	1.837.278	1.008	1.026	1.026	285.2/43.5	43.5/77.9	77.9/43.1
CM4B2	1.897.785	1.009	1.025	1.025	286/51.2	51.2/99	99/38.5
CM4B3	1.864.472	1.008	1.025	1.025	292.9/43.1	43.1/85.5	85.5/43.5
CM4C1	4.057.205	1.023	1.038	1.038	152.4/18.7	18.7/50.5	50.5/31.4
CM4C2	4.103.458	1.028	1.039	1.04	147.5/25.2	25.2/43.5	43.5/27.2
CM4C3	13117.14	1.02	1.044	1.044	152.2/16.4	16.4/51	51/33.5
CM4C4	14116.61	1.018	1.038	1.038	155.7/20.2	20.2/54.9	54.9/27.1
CM4D1	13175.06	1.019	1.042	1.042	159.8/9.4	9.4/62.5	62.5/37.6
CM4D2	20692.18	1.022	1.036	1.036	164.2/16.3	16.3/62.7	62.7/34.4
CM4D3	2.511.765	1.032	1.036	1.04	131.5/26	26/30	30/22.2
CM4D4	4.340.832	1.023	1.046	1.046	139.7/15.2	15.2/40.6	40.6/30.1
CM4E1	12229.21	1.021	1.033	1.033	166/14.5	14.5/60.4	60.4/46.1
CM4E2	15800.73	1.016	1.029	1.029	150.2/31.2	31.2/37.2	37.2/32.7
CM4F1	6.833.871	1.023	1.039	1.039	151.8/25.5	25.5/51.3	51.3/20.8
CM4F2	16562.69	1.016	1.034	1.034	154.8/26.7	26.7/51.2	51.2/24.9
CM4F3	4349.26	1.022	1.033	1.034	162.3/23.2	23.2/62.8	62.8/21.1
CM4G1	9.431.038	1.011	1.015	1.016	160.4/10.6	10.6/55.5	55.5/54
CM4G2	8.992.896	1.009	1.013	1.013	157.4/16.1	16.1/45.5	45.5/52.3
CM4G3	11214.2	1.006	1.016	1.016	149.2/24.1	24.1/13.2	13.2/58.1
CM4G4	8.470.593	1.008	1.016	1.016	154.9/19.8	19.8/47	47/40.4
CM4H1	1.785.614	1.015	1.019	1.02	159.4/24.6	24.6/351.7	351.7/64.9
CM4H2	1.822.961	1.017	1.018	1.02	160.9/18.5	18.5/328.1	328.1/71
CM4H3	1.343.997	1.03	1.036	1.039	159.5/15.8	15.8/33.1	33.1/64.5
CM4H4	1.517.891	1.023	1.029	1.031	161.4/21	21/22.8	22.8/62.9
CM4I1	1.324.082	1.015	1.02	1.021	306.8/72.5	72.5/92.1	92.1/14.5
CM4I2	1.179.528	1.013	1.02	1.02	321.3/74.3	74.3/79.3	79.3/7.5
CM4J1	2.301.019	1.008	1.025	1.025	265.4/3.8	3.8/8.5	8.5/73.6
CM4J2	1.641.438	1.007	1.018	1.018	278.7/8	8/37.4	37.4/73.6
CM4J3	1.837.362	1.008	1.023	1.023	268.1/5.2	5.2/15.2	15.2/72.7
CM4K1	16126.16	1.001	1.005	1.005	161.7/8.6	8.6/256	256/26
CM4K2	17768.52	1.001	1.005	1.005	148.1/0.4	0.4/238.1	238.1/12.3
CM4K3	12756.4	1.006	1.015	1.015	146.9/11.4	11.4/238.2	238.2/6.3

	Mean AMS parameters				Mean anisotropy axes		
Specimen	**Km**	**P**	**Pj**	**T**	**K1dec/inc**	**K2dec/inc**	**k3dec/inc**
Site CM5							
CM5A1	34159.17	1.024	1.024	0.205	84.6/6.6	174.8/1.8	280.3/83.2
CM5A2	32539.99	1.017	1.017	0.393	241.9/0.8	151.7/7.5	338.1/82.5
CM5B1	36107.71	1.04	1.041	0.404	232.1/16.1	141/3.7	38.3/73.4
CM5B2	31728.36	1.014	1.014	-0.007	234.3/27.6	139/10	31/60.4
CM5B3	37275.31	1.03	1.03	0.216	232.2/13.1	140.7/6.4	25.3/75.4
CM5C1	37699.38	1.026	1.027	0.329	260.2/14.8	168.8/5.3	59.6/74.2
CM5C2	31471.67	1.031	1.031	-0.098	240.9/21.4	139.9/26	5.3/55.2
CM5D1	39027.05	1.03	1.031	0.503	65.9/3.1	156.2/6.2	309.8/83.1
CM5D2	34263.88	1.033	1.033	0.149	56.3/0.1	146.3/13.2	326/76.8
CM5E1	37282.68	1.031	1.032	0.452	238.1/2.4	147.7/9.1	342.6/80.6
CM5E2	33745.89	1.026	1.026	-0.158	230.7/13.9	139.5/4.8	30.8/75.2
CM5F1	25192.64	1.008	1.008	0.323	212.6/12.3	304/6.3	60.4/76.1
CM5F2	29036.89	1.014	1.014	0.527	212.7/20.1	117.6/13.6	355.7/65.3
CM5G1	27539.58	1.008	1.008	0.314	220.4/29.5	312.6/4	49.6/60.2
CM5G2	29000.15	1.008	1.008	0.514	233/28	141.4/3	45.8/61.8
CM5H1	31773.72	1.008	1.009	0.742	242.4/11.8	150.2/10.5	19.4/74.1
CM5H1	31802.31	1.008	1.009	0.785	240.8/10.4	149/9.8	16.7/75.6
CM5J1	36723.63	1.03	1.031	0.461	97.9/3	187.9/1.2	299.9/86.8
CM5I1	37846.4	1.029	1.031	0.675	91/8.3	182.2/8.1	316/78.3
Site MS01							
MS1A1	14173.01	1.006	1.006	-0.512	239.1/15	141.7/25.4	356.6/59.9
MS1A2	13413.18	1.006	1.006	-0.526	244.6/3.8	152.3/30.9	341/58.9
MS1A3	10871.92	1.006	1.006	-0.476	237.7/11	144.1/18.1	357.5/68.6
MS1B1	14175.63	1.005	1.006	-0.826	236.4/2.5	146.2/4.9	353.3/84.5
MS1B2	11375.51	1.007	1.008	-0.492	238.3/7.4	146.3/14.4	354.9/73.8
MS1B3	11692.83	1.005	1.005	-0.57	239/4.5	146.9/25.3	338.5/64.2
MS1C1	20456.93	1.005	1.005	-0.485	244.9/0.3	154.2/68.1	335/21.9
MS1C2	21904.88	1.005	1.005	-0.781	254.5/8.2	162.3/14.7	12.9/73.1
MS1C3	18852.63	1.005	1.005	-0.535	245.5/10.9	64.5/79.1	155.4/0.2
MS1C4	21510.76	1.003	1.003	-0.428	244/7.6	140.4/60.5	338.1/28.3
MS1C5	20152.78	1.004	1.004	-0.52	72.4/2.3	165.9/56.5	340.9/33.4
MS1D1	13786.08	1.005	1.005	-0.379	104/21.6	203.8/23.2	335.8/57.4
MS1D1	13609.65	1.008	1.008	-0.281	46.4/15.4	163.4/58.7	308.5/26.5
MS1D2	13067.12	1.007	1.008	-0.611	45.2/3.1	137.7/40	311.5/49.9
MS1D3	14488.18	1.009	1.01	-0.507	39/9.5	140.7/50.5	301.5/37.9
MS1D4	13398.64	1.007	1.007	-0.544	46.8/11.9	157/58.6	310.2/28.6
MS1D5	14115.28	1.007	1.008	-0.647	40.2/6.5	140.9/58.2	306.3/30.9
MS1E1	20026.97	1.006	1.006	-0.293	237/0.2	146.9/38.6	327.3/51.4
MS1E2	17887.45	1.007	1.007	-0.251	237.4/1.7	147/11.7	335.6/78.1

	Mean AMS parameters				Mean anisotropy axes		
Specimen	**Km**	**P**	**Pj**	**T**	**K1dec/inc**	**K2dec/inc**	**k3dec/inc**
Site MS02							
MS2A1	34073.79	1.063	1.066	-0.474	33.4/9.5	293.9/44.6	132.7/43.8
MS2A2	34716.22	1.08	1.088	-0.784	30.7/1.5	120.8/2.6	270.5/87
MS2B1	41559.05	1.044	1.046	-0.515	30.3/51.1	134.4/11.1	232.8/36.7
MS2B2	40688.95	1.036	1.039	-0.689	32.7/55.9	268.9/20.7	168.4/25.9
MS2B3	34850.23	1.047	1.048	-0.164	23.4/55.3	135/14.3	233.8/30.9
MS2C1	35784.96	1.037	1.037	0.182	110.9/57.6	314.8/30.1	218.5/10.8
MS2C2	41150.38	1.04	1.04	0.063	102.1/69	323.1/16.2	229.2/13.1
MS2C3	32759.58	1.039	1.039	0.133	103.6/58.9	321.4/25.5	223.2/16.6
MS2D1	37366.37	1.02	1.021	0.64	121.4/25.1	356.7/50.6	226/28.2
MS2D2	39215.18	1.026	1.029	0.867	105.8/36.2	350/30.7	231.7/38.7
MS2E1	43795.63	1.016	1.016	0.244	347.2/54.7	160.1/35.1	252.5/3.3
MS2E2	41497.11	1.005	1.005	-0.014	63.6/42.1	255.5/47.3	159/6
MS2E3	37145.13	1.042	1.045	-0.691	344.4/14.3	76.8/9.1	198.2/72.9
MS2E4	37203.61	1.011	1.011	-0.092	318/32.9	146.7/56.8	50.6/4
MS2F1	29959.9	1.038	1.038	0.085	298.1/1.5	207.3/29.3	30.7/60.7
MS2F2	23187.22	1.033	1.034	-0.343	124.9/9.9	217/12.1	356.7/74.2
MS2G1	29393.32	1.065	1.065	0.037	123.6/17.7	29.7/12	267.4/68.4
MS2G2	32280.84	1.068	1.068	-0.137	132.9/12.3	38/21.4	250.9/65
MS2G3	32529.55	1.077	1.078	-0.101	141.4/21.1	42.8/21.2	272/59.3
MS2H1	37129.7	1.065	1.065	-0.009	133.1/17.9	36.2/20.4	261.1/62.3
MS2I1	36590.51	1.056	1.057	0.232	241.7/28.5	23.5/55.3	141.6/18
MS2I2	39762.18	1.053	1.055	0.418	47.4/8.1	291.3/72.2	139.7/15.8
MS2I3	36946.74	1.051	1.052	0.337	34.6/31.4	261.5/48.2	140.8/24.6
MS2J1	34121.66	1.041	1.042	0.4	179.5/33.2	328.6/52.7	79.3/15.1
MS2J2	33705.18	1.034	1.036	-0.524	162.6/34	294.2/44.6	53.2/26.2
MS2J3	34155.82	1.052	1.053	-0.194	137.5/25.6	233.9/13.1	348.4/60.8
MS-2	35829.57	1.012	1.014	0.769	340/0	70.1/38.7	250/51.3

	Mean AMS parameters				Mean anisotropy axes		
Specimen	**Km**	**P**	**Pj**	**T**	**K1dec/inc**	**K2dec/inc**	**k3dec/inc**
Site IT01							
IT1A1	32427.75	1.005	1.005	0.645	86.3/31.8	182.4/9.7	287.3/56.4
IT1A2	32241.13	1.004	1.004	-0.514	262.7/27	115.2/58.9	0.2/14.3
IT1A3	36059.43	1.004	1.004	-0.378	87.8/36.1	239.5/50.3	347.2/14.1
IT1A4	32932.67	1.003	1.003	0.611	128.2/10.9	229.5/45.7	28.1/42.3
IT1B1	33316.46	1.021	1.022	-0.357	319.9/62.1	124.8/27.1	218/6.2
IT1B2	57150.43	1.017	1.019	0.747	290.9/12.3	63.7/72.2	198.1/12.7
IT1B3	54482.76	1.017	1.017	0.252	87/61.3	312/21.2	214.5/18.5
IT1B4	51344.53	1.022	1.022	-0.068	284.8/29.7	74.3/56.5	186.6/14.1
IT1C1	46249.71	1.015	1.015	-0.011	17.1/37.3	119.1/15.2	227.1/48.7
IT1C2	50015.54	1.015	1.016	-0.526	357.5/25.6	133.2/56.2	257.2/20.5
IT1C3	46887.55	1.01	1.01	-0.045	38.7/37.5	300.2/10.9	196.7/50.4
IT1C4	34371.26	1.011	1.011	-0.193	253.7/12.8	163.1/2.8	60.8/76.9
IT1D1	34386.75	1.031	1.031	-0.122	344.6/82.8	94.8/2.5	185.1/6.8
IT1D2	40321.45	1.035	1.035	-0.228	19.3/75.5	278.2/2.9	187.5/14.2
IT1D3	36409.63	1.034	1.035	-0.246	359/79	97.7/1.7	188/10.9
IT1E1	29395.55	1.064	1.072	0.895	315.8/58.9	119.4/30.1	213.6/7.3
IT1E2	28710.29	1.058	1.064	0.791	302.8/44.6	118.6/45.3	210.7/2.1
IT1F1	41152.26	1.039	1.039	0.195	122/57	338.6/27.5	239.6/16.8
IT1F2	43856.05	1.032	1.033	-0.069	141.3/69.7	341/19.2	248.8/6.3
IT1G1	39173.48	1.012	1.013	-0.56	320.7/66.2	83.5/13.4	178.3/19.2
IT1G2	41569.6	1.014	1.014	-0.119	322/63.1	81.4/14.0	177.3/22.5
Site IT02							
IT2A1	23035.08	1.019	1.02	0.489	114.5/21.4	24.4/0.2	293.9/68.6
IT2A2	32764.08	1.021	1.021	0.389	85.4/17.1	178.8/10.9	299.9/69.6
IT2A3	24586.45	1.021	1.022	0.356	75/16.6	169.3/14.3	298/67.8
IT2A4	24270.48	1.022	1.023	0.697	83/18.3	175.7/8	288.3/69.9
IT2B1	29734.85	1.018	1.018	0.248	203.5/29.6	294.9/2.6	29.5/60.3
IT2B2	23707.96	1.02	1.02	0.098	187.1/27.2	285.8/16.3	43.2/57.6
IT2C2	18989.42	1.018	1.019	0.714	173.2/0	83.2/15.5	263.3/74.5
IT2C3	22111.46	1.017	1.018	0.688	153.1/4.8	62.3/10.4	267.5/78.5
IT2D1	21527.5	1.019	1.02	0.556	65.4/3.8	155.7/4.9	297.4/83.8
IT2D2	23351.97	1.02	1.022	0.786	204.3/1.6	294.4/1.8	72.9/87.6
IT2D3	21652.27	1.017	1.018	0.463	197.5/1.1	107.4/5	299.9/84.8
IT2E1	21541.34	1.019	1.021	0.868	206.8/9.4	115.6/7.1	349.2/78.2
IT2C1	18786.25	1.018	1.019	0.453	145.6/0.6	55.5/11.3	238.7/78.6
IT2E2	23161.03	1.02	1.021	0.629	57.2/2.7	147.9/13.1	315.9/76.6
IT2F1	30643.16	1.018	1.018	0.093	28.5/0.1	298.5/17.1	118.8/72.9
IT2F2	25910.78	1.015	1.016	0.768	231.2/0.3	321.3/10.6	139.9/79.4
IT2F3	25587.12	1.018	1.018	0.44	25.9/6	294.4/14.4	138.1/74.4
IT2F4	26173.02	1.017	1.017	0.157	205.6/0.8	295.9/18.1	113.2/71.8
IT2G1	20669.62	1.015	1.015	0.349	314.1/3.7	44.8/11.2	206.3/78.2
IT2G2	19231.25	1.027	1.027	-0.054	336.3/5.4	67.5/11.7	221.9/77
IT2G3	29876.47	1.018	1.019	0.625	89.8/6.7	358.7/8.7	216.9/79

915

	Mean AMS parameters				Mean anisotropy axes		
Specimen	**Km**	**P**	**Pj**	**T**	**K1dec/inc**	**K2dec/inc**	**K3dec/inc**
Site MS03							
MS3A1	34445.25	1.09	1.09	-0.056	268.7/16.9	169.7/27.1	26.9/57.3
MS3A2	35358.76	1.085	1.085	0.008	270.9/15.6	174.1/23.3	31.9/61.5
MS3A3	31875.65	1.082	1.083	0.126	273.1/13.7	177/23.5	30.8/62.4
MS3B1	27215.02	1.071	1.073	-0.394	229.1/15.6	322/10.4	84.3/71.1
MS3B2	31778.56	1.078	1.079	-0.358	227.1/9.8	318.5/8	87/77.3
MS3B3	30424.51	1.074	1.075	-0.242	224.4/13.4	315.2/3.3	59/76.2
MS3C1	29932.84	1.073	1.073	-0.107	266/23.3	357/2.2	92.2/66.6
MS3C2	29527.59	1.073	1.074	-0.077	265.4/23.9	173.9/3.4	76.2/65.8
MS3C3	29611.79	1.073	1.073	-0.186	266/27.1	174.8/2.3	80.2/62.8
MS3C4	27712.68	1.073	1.073	-0.045	264.7/18.2	174.1/1.9	78.3/71.7
MS3D1	32739.46	1.045	1.046	-0.28	105.9/6.4	200.3/34.4	6.7/54.8
MS3D2	31713.81	1.047	1.047	-0.265	108.7/0.5	199.1/40	18/50
MS3D3	32940.19	1.042	1.044	-0.457	284.3/0.9	193.7/31	15.7/59
MS3E1	42667.19	1.043	1.044	0.299	274.9/11.3	170.8/50.9	13.5/36.8
MS3E2	46383.89	1.034	1.034	0.203	262/29.8	151.5/31.4	25.5/43.9
MS3E3	40085.79	1.037	1.038	0.41	265.7/19.2	159.3/39	15.9/44.8
MS3E4	45342.51	1.032	1.033	0.282	271.9/23.5	165.2/33.4	29.9/47.2
MS3F1	41651.81	1.031	1.031	-0.048	86.1/18.2	293.5/69.7	179/8.7
MS3F2	42296.93	1.042	1.042	-0.014	89.6/13.6	243.6/75	358.1/6.3
Site MS04							
MS4C1	13283.51	1.008	1.008	-0.048	58/23.6	202.1/61.6	321.4/14.8
MS4C2	14426.79	1.012	1.012	-0.666	39/23.9	148.2/36.5	283.7/43.9
MS4C3	12444.35	1.009	1.009	-0.466	50.8/20.4	160.7/42.5	302.3/40.5
MS4D1	23184.76	1.008	1.009	-0.608	79.7/20.3	173/8.9	285.4/67.7
MS4D2	23266.74	1.011	1.012	-0.646	78.6/21.3	342/16.5	217.3/62.5
MS4D3	20926.15	1.014	1.014	-0.544	75.6/18.5	342.3/9.6	226.3/69
MS4D4	22197.52	1.01	1.011	-0.894	73.4/17.3	176.7/36.6	323/48.2
MS4E1	10419.4	1.006	1.007	-0.726	61.1/20.2	174.6/47.3	315.7/35.7
MS4E2	17843.54	1.011	1.012	-0.783	65.1/5.8	318.3/70.7	157/18.3
MS4E3	18149.16	1.011	1.012	-0.563	234.5/2.3	143.7/19	331.2/70.8
MS4E4	7.834.659	1.006	1.006	-0.034	48.8/7.7	144.3/35.5	308.2/53.4
MS4F1	16708.53	1.005	1.005	0.218	173.8/36.8	271/9.4	13.1/51.6
MS4F2	17142.33	1.008	1.008	0.124	229.3/19.2	128.1/29.2	347.9/54
MS4F3	18773.58	1.007	1.007	-0.333	159.4/17.2	258.2/26.4	39.9/57.8
MS4G1	22271.38	1.009	1.009	-0.427	176.8/31.3	74.8/18.9	318.5/52.3
MS4G2	26301	1.005	1.005	-0.094	173.9/46.2	308.7/34	56.2/24.1
MS4G3	20619.76	1.008	1.009	0.885	124.9/34.2	232.4/23.9	349.8/46.1
MS4G4	24099.47	1.005	1.006	0.12	213.7/38.4	102.3/24.7	348.3/41.5
MS4H1	17092.18	1.005	1.005	-0.184	197.9/28	94.8/23	331.4/52.3
MS4H2	15736.57	1.004	1.004	-0.287	214.3/46.7	92.2/26.6	344.5/31.3
MS4I1	22419.76	1.008	1.008	-0.055	111.1/40	288.8/50	20.1/1.1
MS4I2	20142.28	1.006	1.006	0.072	113.3/28.1	231.8/41.7	1.1/35.3
MS4I3	21516.8	1.007	1.007	0.202	112/36.5	242.3/41.2	359.4/27.5
MS4J1	26239.25	1.006	1.006	0.415	231.6/8.3	140.5/7.4	9.1/78.9
MS4J2	24057.37	1.009	1.009	0.193	244.9/17.6	141.6/36	356/48.6

916

International Geology Review - Manuscript ID TIGR-2018-0082 has been submitted online

International Geology Review <onbehalfof@manuscriptcentral.com>

qui 22/03/2018 17:42

Para:mathsimoes@hotmail.com <mathsimoes@hotmail.com>;

Cc:mathsimoes@hotmail.com <mathsimoes@hotmail.com>; evandro.lima@ufrgs.br <evandro.lima@ufrgs.br>; carlos.sommer@ufrgs.br <carlos.sommer@ufrgs.br>;

22-Mar-2018

Dear Dr Simões:

Your manuscript entitled "Storage and emplacement of low-Ti silicic volcanics in the southern Paraná-Etendeka LIP: extensional tectonics controlling the effusive silicic volcanism (~134 Ma) in the early stages of Gondwana break-up" has been successfully submitted online and is presently being given full consideration for publication in the International Geology Review.

Your manuscript ID is TIGR-2018-0082.

Please mention the above manuscript ID in all future correspondence or when calling the office for questions. Please log in to Manuscript Central at https://mc.manuscriptcentral.com/tigr to add your ORCID to this submission and edit your user information as appropriate.

You can also view the status of your manuscript at any time by checking your Author Centre after logging in to https://mc.manuscriptcentral.com/tigr.

Thank you for submitting your manuscript to the International Geology Review.

Sincerely,
International Geology Review Editorial Office

Storage and emplacement of low-Ti silicic volcanics in the southern Paraná-Etendeka LIP: extensional tectonics controlling the effusive silicic volcanism (~134 Ma) in the early stages of Gondwana break-up

Matheus S. Simões[1,2]; Evandro F. Lima[1]; Carlos A. Sommer[1];

[1] Instituto de Geociências, Universidade Federal do Rio Grande do Sul, Av. Bento Gonçalves, 9500, Prédio 43136, Caixa Postal 15001, Agronomia, CEP: 91501-970, Porto Alegre, RS, Brazil (e-mail: matheus.simoes@ufrgs.br)

[2] CPRM – Serviço Geológico do Brasil (Geological Survey of Brazil) – Manaus, Av. André Araújo, 2160, CEP 69060-000, AM, Brazil

Abstract

Low-Ti silicic volcanism of the Paraná-Etendeka large igneous province (LIP) is composed of flat-lying lavas associated to the underlying flood basalts. Conduit-related and lava-related lithofacies architecture was previously recognized in three study areas (from west to east: Mato Perso, MP; São Marcos, SM; and Jaquirana-Cambará do Sul, JC). Silicic rocks are hemi-crystalline, containing <10% of plagioclase+pyroxene+Fe-Ti oxides+apatite±sanidine phenocrysts and microlites. We present geochemical characterization, trace element modelling and estimations of temperature, pressure, H_2O content and viscosity, using mineral chemistry and whole-rock geochemical data. Mineral compositions change from west to east, with calcic plagioclases and less ferric pyroxenes at MP and SM. JC have sodic plagioclases plus sanidine, and more ferric pyroxenes. Whole-rock composition of metaluminous dacites display fractional crystallization trend with the silicic glassy groundmass. Mass balance between basaltic andesite parental magmas and dacites yielded good fits for 40-50% of fractionation using ~50% of plagioclase, 30-40% of clinopyroxene, ~15-20% of titanomagnetite ±7-10% of sanidine. Silicic rocks have trace and rare earth element patterns close to underlying basaltic andesites, being only slightly enriched. Assimilation plus fractional crystallization modelling gave good fits at 20-40% of basalt andesite fractionantion and 20-80% peraluminous granites and orthogneiss assimilation. Difference in trace element geochemical features, like Zr/Nb ratios are ascribed to variation in mantle-derived sources and assimilants. Temperatures around ~950-1100°C dominate in the three areas, in both plagioclase microphenocrysts and microlites, indicating high temperatures at emplacement. Water contents from 0.5-1.3 wt.%, decrease calculated viscosities from ~10^6 to 10^3 Pa s. Paleopressures for clinopyroxene crystallization are compatible to a reservoir at the mantle-crust boundary. The magmatism evolution is explained by extensional tectonics, where the necking of the continental crust decreased the distance between the reservoir and the surface, causing progressively more efficient magma transport. Silicic magmas evolved from basaltic andesites, lost volatile pressure within the conduits and erupted as lava flows. No pyroclastic material was massively ejected to the atmosphere. The effusive character of silicic eruptions helped to avoid great climate changes and mass extinction in Cretaceous.

Keywords: Large Igneous Province; storage; conduit; Paraná-Etendeka; plate tectonics

Introduction

Large igneous provinces (LIPs) are dominated by thick, laterally extensive basaltic flows, sills, dykes and their equivalent plutonic intrusions with some reaching volumes greater than 10^6 km^3 (e.g. Coffin and Eldholm, 1994; Condie, 2001). The rapid and large extrusion of high-temperature magmas is proposed to be triggered in several settings: mantle plumes (e.g. Condie, 2001; Campbell, 2005), crustal delamination and melting of dry eclogite (e.g. Anderson, 2005), meteorite impacts (e.g. Jones, 2005) and distributed crustal extension (e.g. Foulguer, 2010, 2017). Major Phanerozoic LIPs have many differences regarding their eruptive products, stratigraphical framework and even correlation with large mass extinction episodes (e.g. Jones et al., 2016). Almost of them were erupted prior or during the Gondwana break-up, and some were developed during the extensional regimes that led to the formation of the North, Central and South Atlantic Ocean (e.g. Buiter and Torsvik, 2014; Svensen et al., 2017; Will and Frimmel, 2018).

In continental intraplate settings, upwelling mantle and decompression makes melting likely to occur (Wilson, 1989; Condie, 1997; Parfit and Wilson, 2008). The initial phases of volcanism generate picritic lavas in some provinces, as registered in Afar, Deccan and Karoo (e.g. Krishnamurthy, 1977; Natali et al., 2011; Kamenetsky et al., 2016) or may generate more primitive olivine-phyric basalts, as seen in the Paraná-Etendeka Province, where they were emplaced as compound and ponded pahoehoe flows (Jerram et al., 1999; Barreto et al., 2014; Rossetti et al., 2014, 2017). As seen in the Brazilian side of the Paraná-Etendeka LIP, the following products are more evolved lavas as basaltic andesites, forming wide sheet pahoehoe and rubbly pahoehoe lava flow fields (Waichel et al., 2012; Barreto et al., 2014; Rossetti et al., 2014; Rossetti et al., 2017).

Some LIPs display interleaved units of, or are covered by, silicic volcanic rocks (Eldholm et al., 1989; Sheth, 2007; Bryan and Ernst, 2008) which may reach >10^4 km³ in volume (Bryan et al., 2002), being formed mostly of pyroclastic density current deposits and/or lava flows (Bryan et al., 2010). Silicic compositions from Phanerozoic LIPs are similar in mineralogic composition, displaying dacitic to rhyolitic magmas with plagioclase, pyroxene, Ti-magnetite±ilmenite±sanidine±quartz and accessories as apatite±zircon±baddeleyite (Bellieni et al., 1984, 1986; Comin-Chiaramonti, 1988, Garland et al., 1995, Muzio et al., 2009, Kirstein et al., 2000; Janasi et al., 2011; Ellis et al., 2013; Natali et al., 2011; Sheth et al., 2012; Sheth and Pande, 2014).

The southern Paraná-Etendeka LIP comprises a thick sequence with ~1,200 m of exposed volcanic pile with basalt-basaltic andesite lava fields overlain by a 15 x 10³ km² area of dominantly flat-lying silicic lava flows (e.g. Henry and Wolf, 1992; Umann et al., 2001; Lima et al., 2012; 2018, Polo and Janasi, 2014; Simões et al., 2017), locally displaying associated volcaniclastic and sedimentary volcanogenic sediments (Polo and Janasi., 2014; Riccomini et al., 2015). Despite the source of silicic units in the southern Paraná-Etendeka LIP have been proposed to be at the African counterpart of the LIP, travelling more than 300 km as pyroclastic density currents (e.g. Milner et al., 1995; Bryan et al., 2010), studies of magnetic fabric using anisotropy of magnetic susceptibility (AMS) in lava flows (e.g. Cañón-Tapia and Raposo, 2017, Guimarães et al., 2017) and the proposal of inferred silicic feeder conduits for the overlying lava flows in Rio Grande do Sul state(e.g. Lima et al., 2018) re-opened the discussion of the location of magma sources. The feeder conduits are exposed along 15-25 m in width structures and expose processes of fragmentation, deformation and intrusion of oxidized and non-oxidized silicic magma (Lima et al., 2012, 2018). The conduit zones are limited by faults dominantly trending NE- and NW-,

occurring south of the NE- trending Antas lineament, a structure that is parallel to the Precambrian basement older structures.

In the present work we present a study in three areas of outcropping silicic lava flows and related feeder conduits at northeast of Rio Grande do Sul, southern Brazil. In each area we selected samples to obtain a set of mineral and whole-rock chemical analysis for geochemical characterization and geochemical modelling of open-system fractional crystallization and assimilation with fractional crystallization (AFC). A brief discussion about the possible sources of silicic melts is given. Then we calculate transport properties (temperature, pressure, H_2O content and viscosity) and make a tectonic setting review to build a model of low-Ti silicic lava emplacement during the early stages of Gondwana continental break-up.

1.1 *Architecture of the southern Paraná-Etendeka LIP in South America*

The Paraná-Etendeka LIP occupies an area of 917,000±15,000 km² (Frank et al., 2009) of which 90% is located in South America and 10% is in Africa (**Fig. 1a**), being above the aeolian sedimentary rocks of Botucatu and Etjo formations. In South America, the Paraná-Etendeka LIP comprises a 1700 m-thick association of tholeiitic magmas (Melfi et al., 1988), with basaltic to intermediate lavas, dykes and sills prevalent (97.5% of total volume) over silicic units (2.5%).

In a regional scale, the distribution of the Paraná-Etendeka LIP volcanic rocks is made by the classification of mafic and silicic volcanics based in their TiO_2 content (e.g. Bellieni et al. 1984; Peate et al. 1992). In the case of the silicic rocks, the ones presenting high-Ti (TiO_2>2 wt.%) are called Chapecó-type magmas (Peate et al. 1992): porphyritic trachytes with up to ~ 25 vol.% of crystals, exposed in the northern portion of the basin, between the NW-SE trending Ponta Grossa arch and the Torres structural valley (**Fig. 1b**). In the southern portion, where the studied areas outcrop, the low-Ti (TiO_2<2 wt.%) rocks are dacites and rhyolites with less than ~10 vol.% of phenocrysts, called Palmas-type magmas. Parts of the plumbing system for basaltic and silicic low- and high-Ti lavas in southern Brazil are represented by the NW-SE trending Ponta Grossa and the NE-SW trending Santa Catarina and São Paulo dyke swarms (e.g. Raposo 1997; 1998, 2017; Florisbal et al. 2014).

South of the Torres valley, the volcanic units of southern Paraná-Etendeka LIP are represented by the Serra Geral Group and, in southern Brazil, they cover the Aeolian strata of Botucatu Formation (Waichel et al., 2007) and have chemically more primitive compound and simple pahoehoe basaltic flows in the base, represented by the Torres Formation (Rossetti et al., 2017). Vertically stacked sheet-like rubbly pahoehoe basaltic flows of Vale do Sol Formation cover the compound flows and represents the more voluminous basalt lava unit. The silicic volcanics cover these basalt flows and are ascribed to the Palmas Formation. The last volcanic manifestations in the area are the compound and simple oxidized basaltic flows of the Esmeralda Formation (Rossetti et al., 2017).

Silica saturated tholeiite and olivine tholeiite diabase dikes and sills occur striking NE-SE when cutting the sedimentary units of Paraná basin and NW-SE when cutting the lava flows (Sarmento et al., 2017). The postulated conduit systems for silicic lavas were described to the south of a curved NE- trending structure called Antas Lineament. This structure is parallel to the main regional structures, like NE-SW trending Precambrian

Porto Alegre Suture (Fernandes et al., 1995) or younger faults cutting the basin as Leão and Açotea faults (Zalán et al., 1991).

Further, towards the south of the LIP, a small area (3.2 km³) of peraluminous dacitic lavas with cordierite, orthopyroxene, plagioclase and ilmenite as liquidus phases (Vieira 1985; Vieira and Roisenberg 1985) occurs in the Jaguarão region. It contains abundant basement xenoliths and is located near to major shear zones of Neoproterozoic age that may have been reactivated during Early Cretaceous (Comin-Chiaramonti et al., 2010).

In southern Uruguay, Mesozoic volcanics lie in a system of faulted basement blocks trending ~N60°E (Kirstein et al. 2000). The silicic types are distinguished by two main groups of feldspar-phyric and quartz-phyric rocks (Kirstein et al. 2000; 2001). Muzio et al. (2009) described lava flows and pyroclastic deposits of the Arequita Formation, disposed along the N20°E India Muerta Lineament, an important tectonic control of the magmatic evolution in Laguna Merín Basin. The mafic Santa Lucía type has OIB signatures with high Nb/La and Treinta Y Trés is broadly similar to the low-Ti Gramado lavas (Kirstein et al. 2000). Felsic rocks are dacites to rhyolites from Lavalleja Series (high Ti/Zr and Nb/Y, higher Sr and Nd isotope ratios) and Aigüa Series (high Rb/Sr, Rb/Ba, and Th).

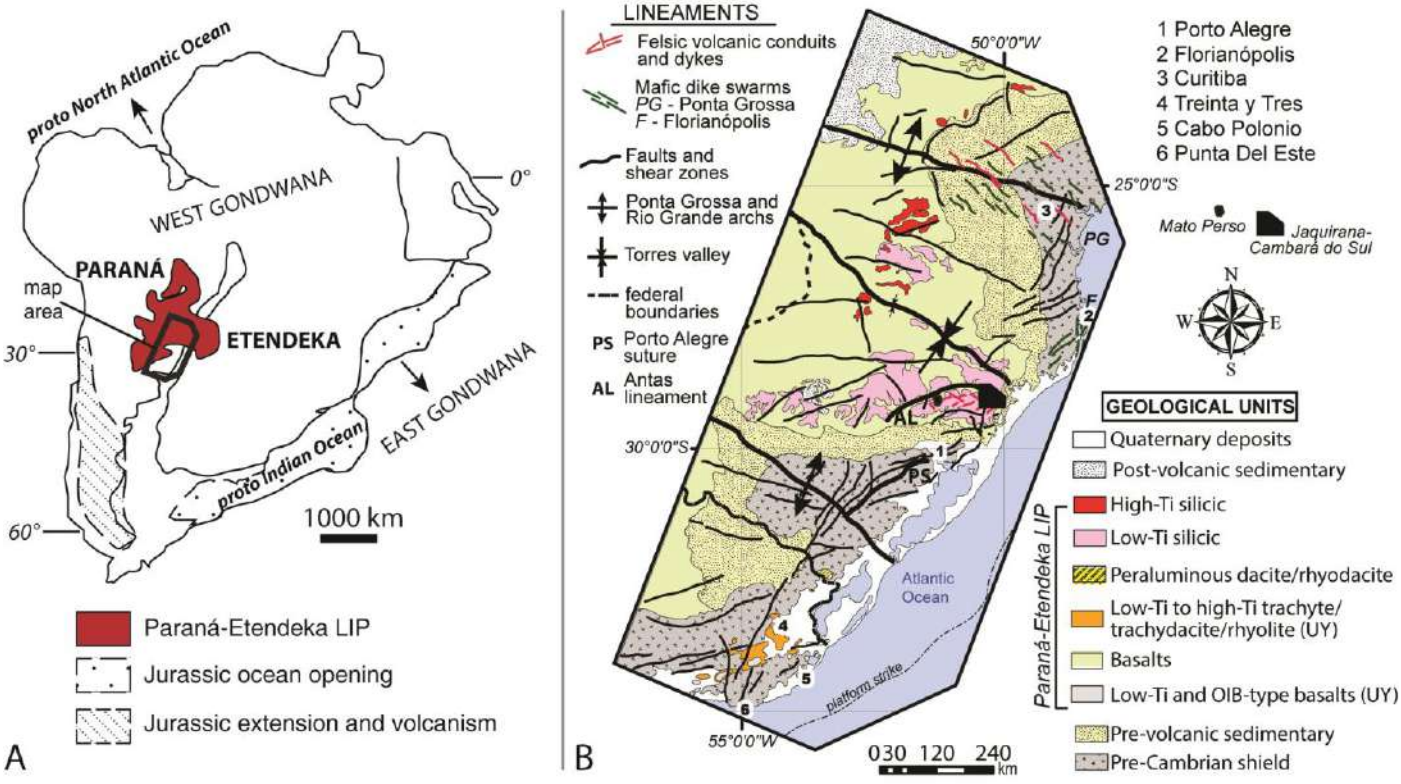

Figure 1 – Tectonic setting and location of study areas. (A) Distribution of the Paraná-Etendeka volcanism in Cretaceous (modified from Rapela & Llambias, 1999; Mpodozis & Ramos, 2008). (B) Regional geological map of the southern Paraná-Etendeka province in Brazil with the main structures. The study areas, Mato Perso and Jaquirana-Cambará do Sul, are located and detailed in figure 3.

1.2 Lava geochemistry and age of silicic volcanics

Low-Ti and high-Ti silicic magma-types also display marked differences in trace element contents. High-Ti volcanics are above high-Ti basalts or directly above the Aeolian sediments of Botucatu Formation (Janasi et al., 2007; 2011; Nardy et al., 2008; Luccheti et al., 2014) and have higher Ba, Nb, La, Ce, Zr (>500 ppm), P, Nd, Y, Yb, Lu and K, being depleted in Rb, Th and U. Their isotopic composition display low $\delta^{18}O$ values and $^{87}Sr/^{86}Sr_{(i)}$ between 0.705 and 0.708 (Peate et al. 1992; Peate 1997; Nardy et al. 2008). Palmas-type volcanics are divided into Caxias do Sul ($0.91\% \leq TiO_2 \leq 1.03\%$, $0.25\% \leq P_2O_5 \leq 0.28\%$), Anita Garibaldi ($1.06\% \leq TiO_2 \leq 1.25\%$, $0.32\% \leq P_2O_5 \leq 0.36\%$) and Jacuí subtypes ($1.05\% \leq TiO_2 \leq 1.16\%$, $0.28\% \leq P_2O_5 \leq 0.31\%$) and the rhyolites are divided into Santa Maria ($P_2O_5 \leq 0.21\%$) and Clevelândia ($0.21\% \leq P_2O_5 \leq 0.23\%$) subtypes (Peate et al., 1992; Nardy et al., 2008), being characterized by low Zr (<400 ppm), high $\delta^{18}O$ values and higher $^{87}Sr/^{86}Sr_{(i)}$ values of 0.714-0.727 (e.g. Garland et al., 1995; Ewart et al., 2004). Crystal chemistry studies indicate dominance of more sodic plagioclase as andesine in the high-Ti types, together with higher Ti contents in Fe-Ti oxides. Low-Ti lavas have more calcic plagioclases (labradorite) and lower Ti in the oxides (Bellieni et al., 1988; Garland et al., 1995). Polo et al. (2017) described plagioclases with An higher than 50 in Caxias do Sul and Barros Cassal dacites and Santa Maria rhyolites.

Geochronological data and discussions presented by Thiede & Vasconcelos (2010) and Janasi et al. (2011) suggest a cluster in ~134 Ma for the the high-Ti magmatism in central and northern Paraná Basin and also for Gramado-type low-Ti basaltic flows and for the Esmeralda basaltic lavas, the uppermost unit of the Serra Geral Group. The emplacement of volcanics of Paraná-Etendeka LIP and neighboring areas in Paraguay and Argentina is consistent with a short duration of ~3 Ma for the building lava pile (Janasi et al. 2011). In the Etendeka Province paleomagnetic studies recently suggested duration of ~4 Ma (Dodd et al., 2015).

1.3 Geomorphology and geological setting

The northeast portion of Rio Grande do Sul is the highest land of the state, reaching ~1,300 m above the sea level (**Fig. 2**). From southwest to northeast, departing from the Jacuí river plain, the relief gradually reach elevations of >1000 m through a horizontal distance of ~150 km. These highlands extend to Santa Catarina state in the northeast direction, reaching ~1,700 m, and then the relief is gradually decreasing towards the Atlantic Ocean. From southeast to northwest, departing from coast at the sea-level, we may reach 1,200 m of elevation following a path of only ~30 km. These highlands gently decrease towards the plains of Paraná and Paraguay rivers at west. The draw of the south Brazilian coast is along NE-trending structures, while more subtle changes in relief are caused by NW-trending faults. **Figure 2** localizes the study areas, namely, Mato Perso, São Marcos and Jaquirana-Cambará do Sul in this context, and we add the information that the contact between basaltic and silicic units in the LIP is at ~ 400m in Mato Perso, ~750 m in São Marcos and ~850 m in Jaquirana and Cambará do Sul.

The geological reconnaissance of individual areas reveal banded vitrophyres and breccias from postulated silicic conduits limited by NW and WNW-trending faults (**Fig. 3a,b**). Banded vitrophyres display steeply dips of banding, grading laterally to more gently dips, and are composed of oxidized and non-oxidized vitrophyre bands of centimeter to meter scale and present fragments with variate vesicle amounts and sizes (e.g. Lima et al.,

2012; 2018; Simões et al., 2017). The Mato Perso area outcrops in high elevations at Farroupilha, Flores da Cunha and Caxias do Sul cities. The highlands (>650 m) of Farroupilha and Caxias do Sul expose the felsic conduit systems which are subtly demoted to ~400-550 m elevations by NE-trending normal faults through the Antas River, where tabular vitrophyres are again in direct contact with basaltic rubbly pahoehoe flows. In Mato Perso it was possible to map flat-lying oxidized lava units and dykes underlying flat-lying non-oxidized grey vitrophyres (**Fig. 3a**). The inferred conduits cut these oxidized vitrophyres, carrying a lot of oxidized dragged out fragments, and appear above the flat-lying grey vitrophyres, which in turn, may present red-grey banding on the base of the flows (Simões et al., 2018, *in press*). In São Marcos and Jaquirana-Cambará do Sul these oxidized lava units were not mapped (**Fig. 3b,c**), but the fragments are present within the inferred conduits.

Overall, the three areas share lithofacies architecture such as red vesicular, red poorly-vesicular, monomictic and welded breccias in the margins and grey poorly vesicular and banded vitrophyres in the central parts (Simões et al., 2017). The bands are dominantly subvertical (>60°) and thick (~10 cm), grading laterally into thin (0,2 – 2 cm) flat-lying (<40°) banding marked by intercalation of 2- to 7- cm thick oxidized red colored bands and grey colored bands. Monomictic breccias occurs in the border of the conduits, are banding-parallel and composed of –mm to –cm scale angular vesicular oxidized red to brown fragments with sharp edges in seriate arrangement cemented by calcite and silica. Spherulitic, microfractured, flay-lying coherent vitrophyres and flat-lying massive obsidian are the subaerial equivalents of the conduits. Flat-lying vitrophyres are ~ 5 - 20 m thick units with at least 10 km² in area and show flat-lying foliation, pipe vesicles in the base, and spheroidal vesicles towards the top of the unit, locally presenting basal breccia.

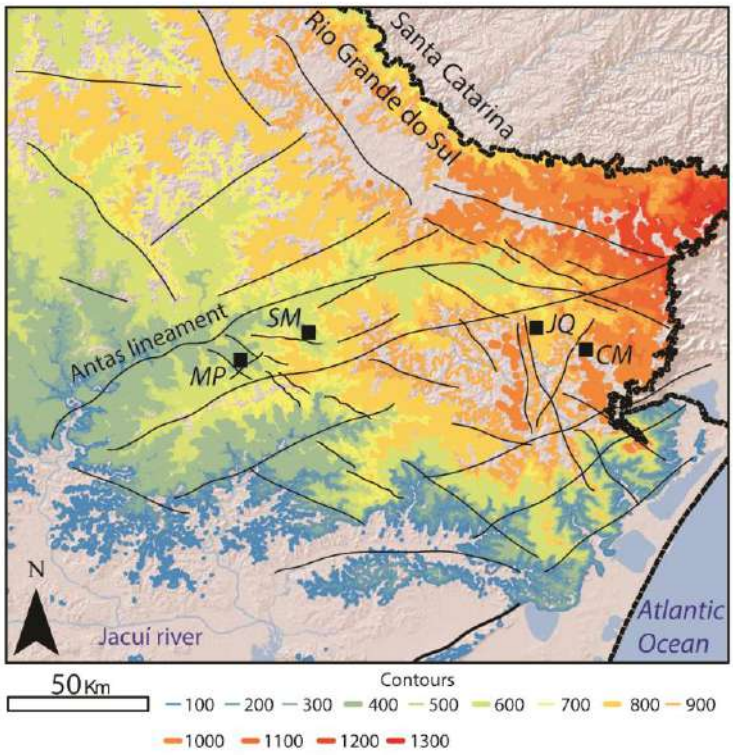

Figure 2 – Structural arrangement of lineaments in the Rio Grande do Sul state. The base of the map is a shaded relief surface terrane topographic model and elevation contours in 1:50.000 scale. Locations/basaltic-silicic contact: MP – Mato Perso/~400 m, SM – São Marcos/~750 m, JQ-Jaquirana/~850 m, CM-Cambará do Sul/~ 850 m.

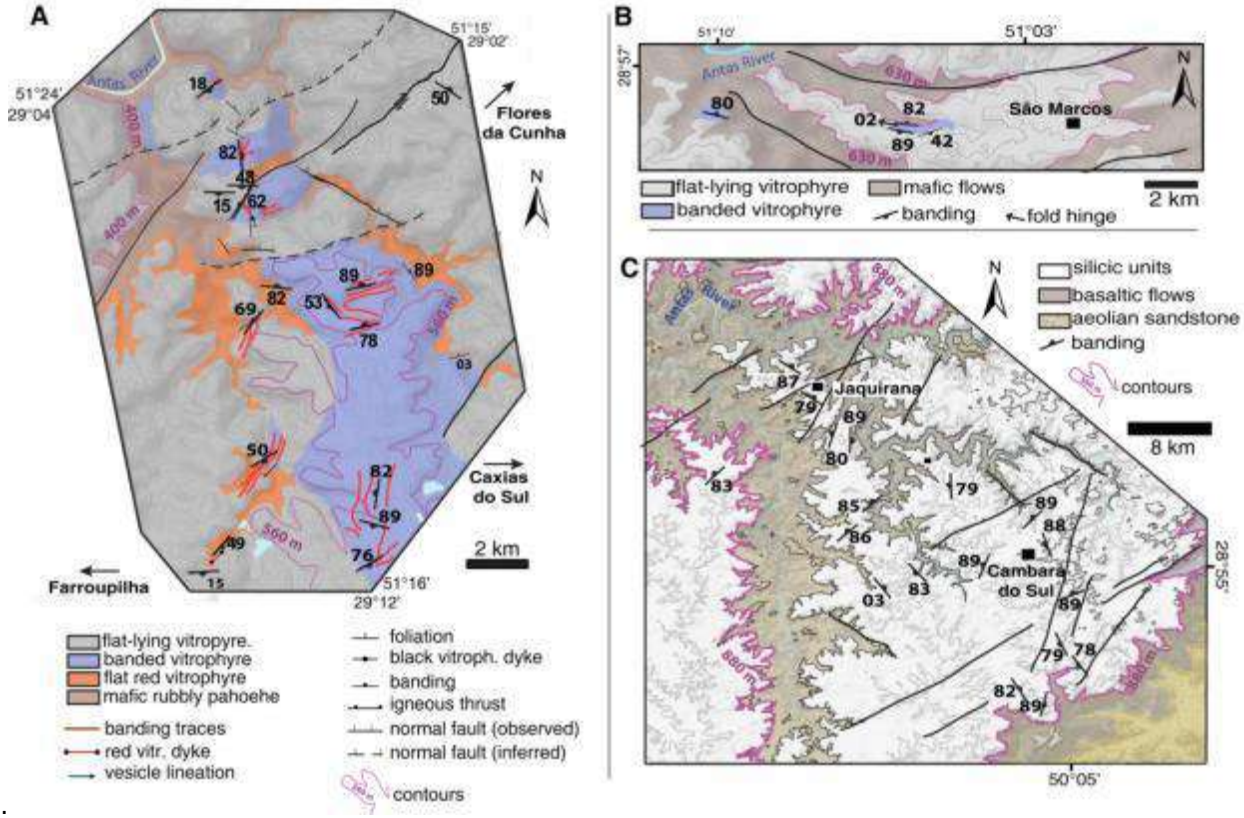

.

Figure 3 Geological maps of the studied areas. (A) Mato Perso. (B) São Marcos. (C) Jaquirana - Cambará do Sul. Banded vitrophyre units in A and B are a simplification of the conduit outcrops, which involve the occurrence of another lithofacies as breccias and other types of vitrophyre.

2 Methods

Detailed description of outcrops and field relations at the investigated areas are presented by Simões et al. (2017, 2018, *in press*). After the field works, 34 samples were selected for petrographic descriptions and 11 thin sections (01 lava flow, 01 conduit-vitrophyre of Mato Perso; 02 microfractured, 02 spherulitic and 02 banded vitrophyres from Jaquirana-Cambará do Sul, 01 banded vitrophyre from São Marcos and 02 lava-flow samples from Cambará do Sul) were polished with diamond paste to use on Scanning Electron Microscope (SEM) coupled with Energy Dispersive Spectrometer (EDS) and obtain high resolution images and chemical element maps. Scanning Electron Microscope (SEM) analyses were made in a LS15 Zeiss microscope in the Geological Survey of Brazil-CPRM laboratory of Belém. A high-vacuum mode (3.0 – 1.5 10^{-5} mPa) and a tungsten filament were used. A 10 μm-thick gold pellicle was utilized to cover the polished sections. Backscattered electron images were obtained with 20 kV, current between 70 and 90 pA, work distance of 8.5 mm and 100 to 500 times magnification. Chemical maps of the sections were obtained by Energy Dispersive Spectrometry in an Oxford Instruments X-Act SSD 10mm^2 detector. Analytical results were obtained with counting rate of 2000 cps and standardized by energy spectrum patterns from the AZTec (Oxford Instruments) program.

The same thin sections were used for major oxides quantification in plagioclase, sanidine, clinopyroxene, Fe-Ti oxides and glassy matrix using Electron Probe Micro Analyzer (EPMA). EPMA analyses were carried out in the University of Brasília (UnB) in a JEOL JXA-8230 microanalyzer model with five WD (wavelength dispersive) and

one ED (electron dispersive) spectrometers. The mineral analyses were made with 15 kV current, 20 nA of acaleration and spot diameter between 5 and 10 micrometers. To avoid the diffusion of elements such Na and K in glass analyses, the currents were reduced to 10 nA and the beam was defocused to 15 to 20 micrometer diameter.

The whole-rock composition of 34 volcanic felsic rock samples was determined for comparison between different sites of conduit systems occurrence and between distinct lithofacies. The whole rock chemical analyses were made at Acme Analytical Laboratories Ltd., in Vancouver, Canada, using analysis routines 4A and 4B. In the former, total abundance of main oxides and several minor elements was obtained from 0.2 g of the analyzed sample by Inductively Coupled Plasma — Emission Spectrometry (ICP-ES) with the detection limit of 0.01% for SiO_2, Al_2O_3, Fe_2O3, CaO, MgO, Na_2O, K_2O, MnO, TiO_2 and P_2O_5. In the second one, the results of rare earth and refractory element were obtained from 0.2 g of analyzed sample by ICP – MS (Mass Spectrometry) with detection limit of 1 ppm for Ba, Be and Sn, 0.1 ppm for Ce, Cs, Hf, La, Nb, Rb, Ta, U, Y and Zr, 0.2 ppm for Co and Th, 0.3 ppm for Nd and 0.01-0.05 ppm for Dy, Er, Eu, Gd, Ho, Lu, Pr, Sm, Tb, Tm and Yb.

3 Results

3.1 Mineral and glassy groundmass chemistry

Vitrophyre mineralogy is composed of plagioclase (minor sanidine), clinopyroxene and Fe-Ti oxides as phenocrysts and microphenocrysts immersed in a microlite-rich hemi-crystalline groundmass made by the same mineral assemblage plus apatite. The totality of samples share general features such plagioclase and pyroxene microphenocrysts altered to clay minerals, more frequently in their core; in lavas the microphenocrysts have no preferred orientation but conduit microphenocrysts can be oriented according to the banding. Lava flow units have far more shape/size developed microlites than banded vitrophyres of inferred conduits. The main textural differences between the three areas are phenocryst and microphenocryst content (plagioclase, clinopyroxene, Fe-Ti oxides±sanidine), decreasing from Mato Perso (<10%) to São Marcos (<2%) and Jaquirana-Cambará do Sul (<1%). Clinopyroxene contents also decrease from Mato Perso and São Marcos to Jaquirana-Cambará do Sul. Microphenocryst size hierarchy is verified in feldspar, pyoxenes and Fe-Ti oxides ranging from larger crystals in Mato Perso to smaller crystals in São Marcos and even smaller crystals in Jaquirana-Cambará area.

Mineral chemistry was carried out in feldspars, pyroxenes and Fe-Ti oxides using representative samples from each studied area. For each mineral group we realized ±90 spots, presented in **appendix A**. The characteristics of each mineral group in the studied areas are present in **table 1**. In Mato Perso area, due to the larger size of the crystals, there was the possibility to compare the chemistry of microlites and microphenocrysts (core, intermediate region and rims, **figure 4**). However, the very fine-grained microlites from São Marcos and Jaquirana-Cambará do Sul could not be analyzed because their size is smaller than the EPMA spot size, so these crystals would not give reliable data, some grains are reported as ‘whole-grain’ because the spot area was near the size of the entire minerals.

254 **Table 1 –** Main features as size, shape and composition of feldspars, pyroxenes and Fe-Ti oxides for the studied
255 areas.

		Feldspars	
Area	*size*	*shape and features*	*composition*
Mato Perso	0.5 - 3 mm	microphenocrysts: tabular, euhedal, subhedral.	An_{52-64}
		resorbed, sieve textures, concentric or parallel zoning.	
	<0.2 mm	microlites*: tabular, subhedral. Locally as empty	An_{50-55}
		laths.	
São Marcos	0.1 - 0.8 mm	microphenocrysts: tabular, subhedral, anhedral.	An_{51-59}
		resorbed,	
	<0.1 mm	microlites: tabular, subhedral, anhedral.	-
		frequently as empty skeleton of disagreggated crysts	
Jaquirana-Cambará	± 0.2 mm	microphenocrysts: tabular, subhedral, anhedral.	An_{34-58} - Ab_{62}
		resorbed, oriented according the banding in conduits.	
	<0.1 mm	microlites: tabular, subhedral, anhedral.	-
		Pyroxene	
Area	*size*	*shape*	*composition*
Mato Perso	0.2 - 2 mm	microphenocrysts: prismatic, subhedral, euhedral	mg#** 11-15
		locally resorbed.	$Wo_{30-31}Ens_{35-37}$-Fer_{31-34}
	<0.2 mm	microlites: prismatic to globular, anhedral.	-
São Marcos	<0.1 - 0.2 mm	microphenocrysts: prismatic, subhedral, anhedral	mg#14 (1 spot)
		locally resorbed and scarce in some bands of conduits.	Wo_{36}-Ens_{30}-Fer_{31}
	<0.1 mm	microlites: very fine (< 0.05 mm) globules.	mg#13-20
			Wo_{22-32}-Ens_{33-46}-Fer_{33-38}
Jaquirana-Cambará	< 0.1 mm	microphenocrysts: prismatic, subhedral, anhedral	mg#11-16
			Wo_{21-31}-Ens_{34-45}-Fer_{32-45}
	<0.1 mm	microlites: very fine (< 0.05 mm) globules.	-
		Fe-Ti oxide	
Area	*size*	*shape*	*composition*
Mato Perso	0.5 - 1 mm	microphenocrysts: rhombohedral, euhedral, subhedral	ulv_{2-51}
	<0.2 mm	microlites: rhombohedral, subhedral, anhedral (globular)	
São Marcos	0.2 - 0.5 mm	microphenocrysts: rhombohedral, subhedral, anhedral	ulv_{2-77}
	<0.1 mm	microlites: globular, anhedral	
Jaquirana-Cambará	0.2 mm	microphenocrysts: rhombohedral, subhedral, anhedral	ulv_{33-58}
	<0.1 mm	microlites: globular, anhedral	ulv_{36-42}

256

257 *3.1.1 Feldspars*

258 The main feldspars in the analyzed samples are plagioclases with minor volume of sanidine, the second only
259 occurring in Jaquirana-Cambará do Sul area. The distinctive features between the study areas are in size, shape
260 and composition of plagioclases. Complete average compositions for feldspars in each area are present in **table**
261 **2**. In Mato Perso area, the microphenocrysts from both lavas (**Fig. 5a**) and conduits (**Fig. 5b**) are subhedral to
262 euhedral. Lavas have subhedral microlites with ~0.2 mm in size, locally with sieve texture or as empty or
263 skeleton crystals (**Fig. 5c**). In São Marcos the microphenocrysts have more subhedral and anhedral shapes,
264 sometimes presenting resorbing textures. A notable feature of lava flow samples near the conduit is the variety
265 of resorbing features, that in advanced stages leave only the external "skeleton" portion of the microlites. In
266 Jaquirana-Cambará do Sul the microphenocrysts are also generally subhedral to euhedral with resorbed faces,
267 and the microlites are tabular and subhedral or anhedral, but do not present much sieving.

268 As seen in **figure 4**, plagioclase microphenocrysts in Mato Perso are labradorites ranging from An_{52} to An_{64}.
269 These values are distributed in individual grains with inverse concentric and sector zoning, where An contents
270 are higher in the crystal rims than in the cores (**Fig. 5d**). The microlites display more restricted An_{50} to An_{55} (**Fig.**
271 **4**). Valuesare similar to those found in São Marcos, from An_{51} to An_{59}, and greater than Jaquirana-Cambará do
272 Sul, where An $_{34\text{-}58}$ andesine dominate. In this area there are also microphenocrysts of sanidine ($Or_{74\text{-}78}$) and
273 oligoclase microlites (Ab_{62}). The K_2O content in plagioclases increases from Mato Perso (0.3-0.4 wt.%) and São
274 Marcos (0.2-0.4 wt.%) to Jaquirana-Cambará do Sul (0.3-1.6 wt,%).

275

276 **Table 2 –** Average feldspar compositions for Mato Perso (n=48), São Marcos (n=16) and Jaquirana-Cambará do Sul
277 (n=25, 23 plagioclases and 03 sanidines).

	plagioclase			sanidine
Local	MP (48)	SM (16)	J-C (22)	JC(03)
SiO_2	53.99	54.01	57.70	58.50
TiO_2	0.09	0.06	0.11	0.48
Al_2O_3	27.29	26.94	24.39	15.48
$Fe_2O_{3(T)}$	1.08	1.06	0.97	0.84
MgO	0.12	0.12	0.07	0.20
CaO	11.69	11.37	8.24	0.57
Na_2O	4.46	4.62	5.59	1.96
K_2O	0.37	0.35	1.56	11.55
Cr_2O_3	0.02	0.03	0.02	0.03
MnO	0.02	0.02	0.44	6.27
NiO	0.01	0.01	0.02	0.02
V_2O_3	0.01	0.01	0.02	0.06
Cl	0.01	0.01	0.01	0.02
Total	99.17	98.61	99.14	95.98
An	57.91	56.42	40.28	3.21
Ab	39.91	41.50	49.79	19.81
Or	2.18	2.08	9.93	76.98
***MP=Mato perso; SM=São Marcos; J-C=Jaquirana-Cambará**				

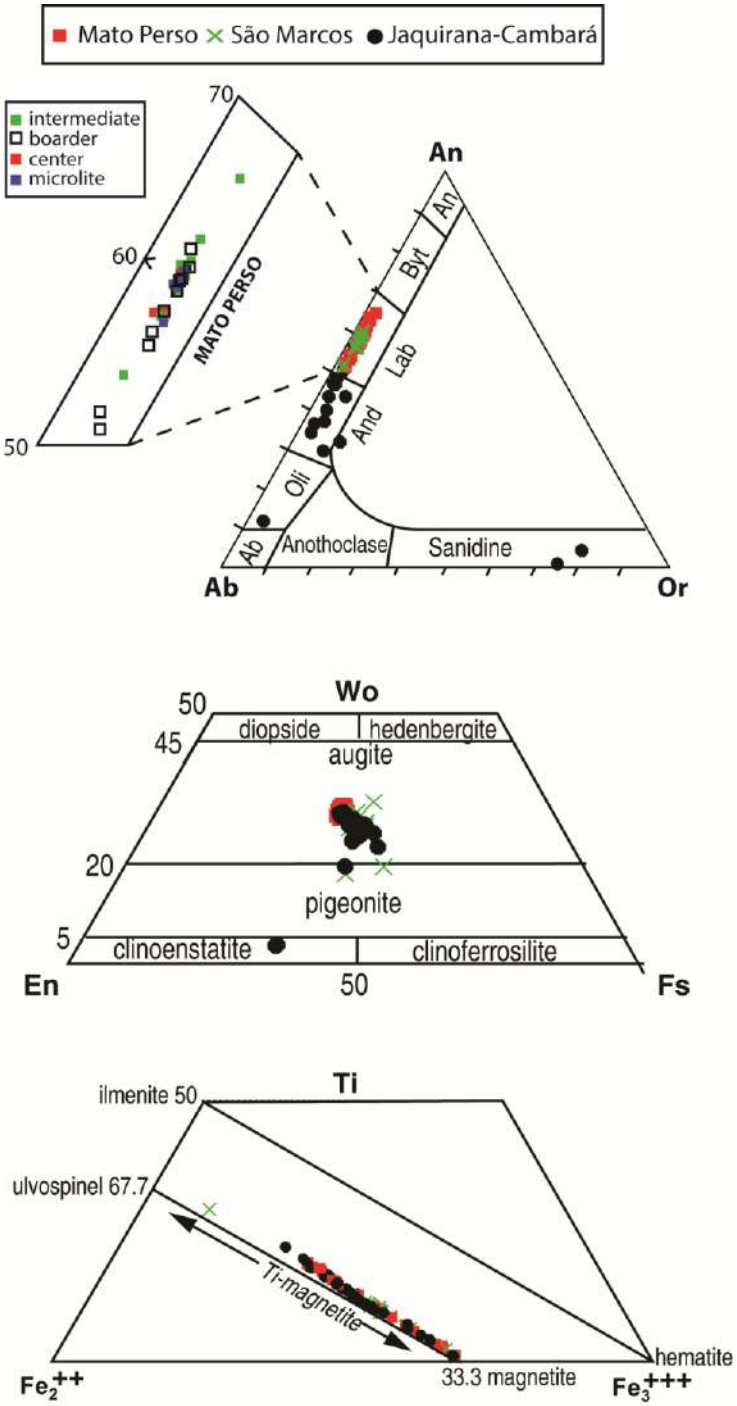

Figure 4 – Mineral compositions obtained by EPMA analyses in the vitrophyre samples from Mato Perso, São Marcos and Jaquirana-Cambará do Sul areas. (A) Plagioclase ternary plot showing decreasing of the anorthite component from Mato Perso to São Marcos and Jaquirana-Cambará do Sul. (B) Diagram for pyroxene composition showing the decrease in Wo from Mato Perso to Jaquirana-Cambará do Sul. (C) Fe-Ti oxides ternary plot showing compositional overlaps between areas.

3.1.2 Pyroxenes

The average of pyroxene composition in the studied areas is present in **table 3**. In Mato Perso area they are subhedral microphenocryst prisms (**Fig. 5a,b**), appearing as anhedral microlites only in lavas. In the other two areas, pyroxene microphenocrysts are also subhedral and may be scarce in some samples from São Marcos. Microphenocrysts display subhedral or anhedral shapes, with swallow-tail or resorbed terminations and microlites are prismatic to globular (**Fig. 5e**). Compositionally, the analyzed pyroxene microphenocrysts from all areas are majorly augites, with minor pigeonite and clinoenstatite in samples from Jaquirana-Cambará do Sul (**Fig. 4**). They vary from $Wo_{28-32}Ens_{35-37}Fer_{31-39}$ with Mg# ($100*Mg^{2+}/Mg^{2+}+Fe^{2+}$) between 7 and 10 at Mato Perso (microphenocrysts and microlites) and from $Wo_{20-33}Ens_{30-46}Fer_{35-50}$ with Mg# between 5 and 8 at São Marcos (microlites) to $Wo_{5-31}Ens_{34-82}Fer_{32-46}$ with Mg# between 5 and 10 at Jaquirana-Cambará do Sul (microlites and microphenocrysts). The FeO_T contents slightly increases from ~ 11-14 wt% in Mato Perso to 12-19 wt.% in São Marcos and Jaquirana-Cambará do Sul areas.

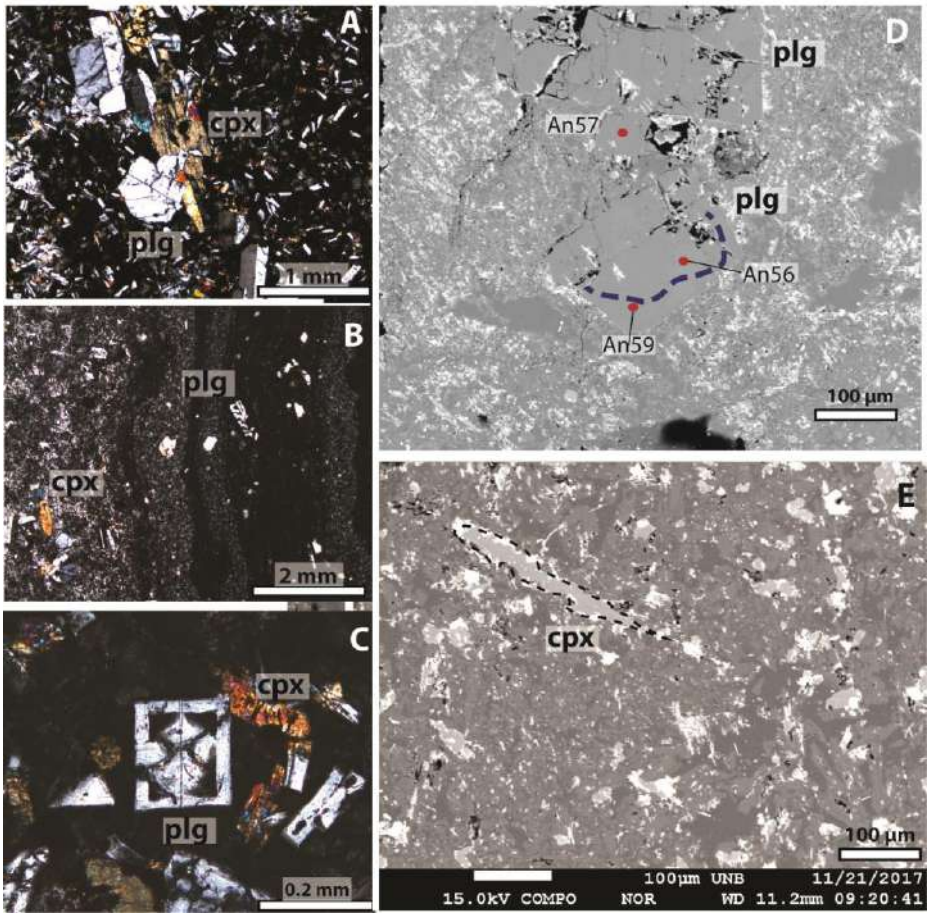

Figure 5 – Microscopic features of the analyzed samples. A,B,C are crossed polarizers photomicrographs. D,E are back-scattered electron (BSE) images. (A) Porphyritic silicic lava unit of Mato Perso area with clinopyroxene and plagioclase microphenocrysts embedded in a microlite-rich hemi-crystalline groundmass. (B) Clinopyroxene and plagioclase microphenocrysts in a banded vitrophyre from inferred conduit at the same area. (C) Resorbed plagioclase and prismatic clinopyroxene microlites in silicic lava. (D) Zonation of plagioclase microphenocrysts in banded vitrophyre showing slightly more calcic rim (An_{59}) than core (An_{56}) and a close crystal with An_{57}. (E) Anhedral elongated clinopyroxene microlite from a banded vitrophyre.

Table 3 – Average pyroxene compositions for Mato Perso (n=50), São Marcos (n=10) and Jaquirana-Cambará do Sul (n=24). *Fe^{2+} as 0.89x$FeO^{(T)}$; **Mg# = Mg^{2+}/Fe^{2+}+Mg^{2+}.

	pyroxenes		
Local	MP (50)	SM (10)	J-C (24)
SiO_2	51.77	50.52	52.25
TiO_2	0.55	0.70	0.54
Al_2O_3	1.66	2.03	1.61
FeO*	10.63	12.94	12.82
$FeO_{(T)}$	11.95	14.54	14.12
MgO	14.70	13.54	15.04
CaO	18.04	16.63	15.79
Na_2O	0.25	0.25	0.30
K_2O	0.01	0.01	0.04
Cr_2O_3	0.03	0.02	0.01
MnO	0.47	0.57	0.50
Total	99.48	98.92	100.40
Mg^{2+}	0.89	0.82	0.91
Fe^{2+} **	8.26	10.06	9.97
Mg# **	9.70	7.60	8.40
Wo	31.41	28.39	27.12
Ens	36.12	37.68	40.88
Fer	33.09	37.69	37.40

3.1.3 Fe-Ti oxides

Fe-Ti oxides are relatively abundant in all analyzed samples and present titanomagnetite composition (**Fig. 4**). In the three areas they occur as single microphenocrysts with euhedral rombohedral shapes or in glomeroporphyritic aggregates and as microlites with globular shape. They show higher values of the ulvospinel component in the cleavage exsolutions (**Fig. 6a**) and increasing values from the core to the rims of the crystals (**Fig. 6b**), although some grains may present more homogeneous compositions (**Fig. 6c**). In general, the analyzed crystals largely overlap, having $ulv_{2\text{-}51}$ in Mato Perso, $ulv_{2\text{-}77}$ in São Marcos and $ulv_{3\text{-}58(microphenocryst)}$, $ulv_{36\text{-}42(microlite)}$ in Jaquirana-Cambará. Al_2O_3 content in titanomagnetites also overlap from 0.3 wt.% to 3.4 wt.%.

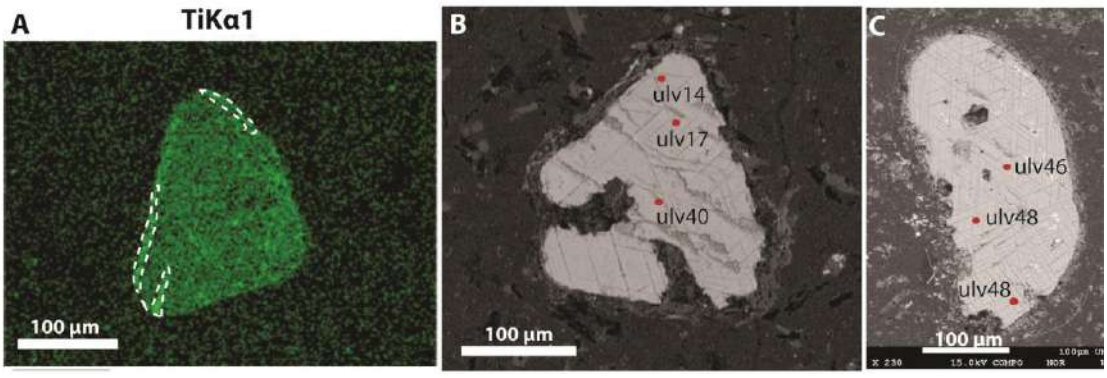

Figure 6 – Chemical composition of Fe-Ti oxides. A is a SEM-EDS compositional map, B and C are BSE images. (A) High titanium contents near crystal rims following cleavage. (B) Titanomagnetite with ulvospinel component decreasing from core (ulv_{40}) to rim ($ulv_{17\text{-}14}$). (C) Titanomagnetite with regular ulvospinel component contents from ulv_{46} to ulv_{48}.

Table 4 - Average Fe-Ti oxide compositions for Mato Perso (n=19), São Marcos (n=25) and Jaquirana-Cambará do Sul (n=51). *Fe^{2+} as 0.89x$FeO_{(T)}$.

	Fe-Ti oxides		
Local	MP (19)	SM (25)	J-C (51)
TiO_2	9.11	9.08	11.59
Al_2O_3	1.24	2.42	2.00
Cr_2O_3	0.05	0.19	0.12
$FeO_{(T)}$	75.89	75.65	72.91
MnO	0.50	0.49	0.46
MgO	0.29	0.47	0.81
Total	87.55	88.97	89.59
Ti^{3+}	9.83	9.75	12.44
Fe^{2+}*	53.96	54.44	51.62
Fe^{3+}	40.83	40.55	41.82

3.1.4 Aggregates

Several types of microphenocryst aggregates occur in both conduits and lavas. The most common types show globular clinopyroxene crystals involving one or two plagioclase laths (**Fig. 7a**), locally with the plagioclase 'c' axis oriented according to the banding, or populations of 4-6 plagioclase crystals involving globular Fe-Ti oxides. A more rare kind of aggregate is similar to those described by Ellis et al. (2012) at the Snake River ignimbrites and is composed of 5-10 subhedral clinopyroxene and plagioclase crystals. One of these aggregates in a banded vitrophyre sample from Mato Perso contains subhedral to anhedral prisms of augite enveloping a silica-rich groundmass. The augites presented very similar composition, with the enstatite component only variying between Ens_{35} and Ens_{36}. A plagioclase crystal, also part of the aggregate display homogeneous composition, with An_{52}, from the core to the rims (**Fig.7b**).

3.1.5 Glassy groundmass

Despite the average of ~ 1-5% for microphenocryst contents in the silicic vitrophyres, there is a slightly difference in microlite/glassy groundmass proportions. However, this difference is accented when comparing conduit and lava flow-related lithofacies. Banded vitrophyres may be almost holohyaline, with few microphenocrysts parallel to the banding. In general the mm-scale bands are marked by hematite-rich and hematite-poor zones, which are cross-cut by *en-echelon* quartz veinlets (**Fig. 8a**). Variation in hematite content is responsible by the different response of the vitrophyres to abrasion, making the hematite-rich zones very difficult to be well-polished (right portion of **figure 8b**), contrasting with hematite-poor zones, characterized to be enriched in microcrystalline quartz, giving well-polished surfaces (left portion of **figure 8b**). In the lava flow units, which are commonly isotropic, the glassy groundmass volume constitutes approximately 50-70% of the vitrophyres and it is separated into hematite-rich and hematite-poor patches. These patches may be silica-rich, white colored in plane-polarized light under the microscope, or hematite-rich, brown colored. This brown colored glass has a plumose texture with several perlitic fractures in larger or thinner lengths (**Fig. 8c, d**). Hematite-rich zones in both conduits and lavas are very difficult to be polished and the EPMA analyses rarely give

considerable results. Thus, we realized most of our analyses in the hematite-poor bands and patches to characterize their chemical composition.

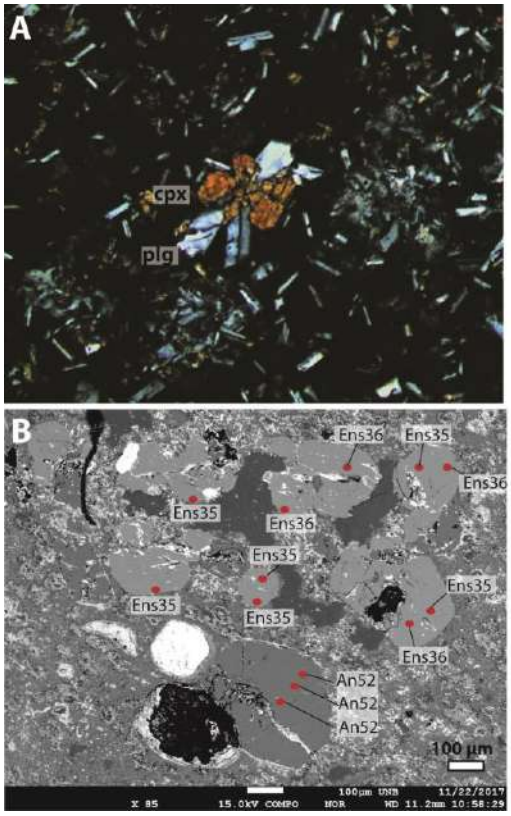

Figure 7 – (A) Glomeroporphyritic aggregate composed of crossed plagioclase laths and globular clinopyroxene within a microlite-rich hemi-crystalline groundmass. (B) BSE image of a clinopyroxene-plagioclase aggregate with very regular compositions, i.e. plagioclase composed of An_{52} and pyroxenes composed of Ens_{35-36}.

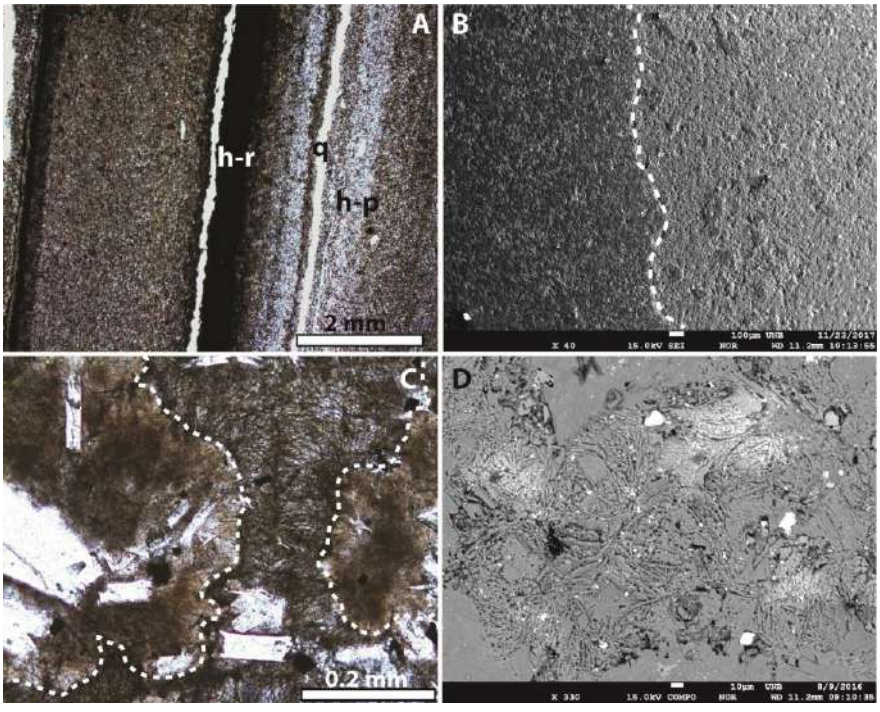

Figure 8 – Textures of glassy matrix in the analyzed vitrophyres. (A) Banded vitrophyre with different hematite distribution along the bands (uncrossed polarizers). (B) Compositional scanning electron image (SEI) showing black vitrophyre layer with well-polished surface at left and oxidized vitrophyre at right with a poorly-polished surface. (C)

Different texture patterns in glassy groundmass of lavas. The boarders contoured by the dashed line have a dirty aspect, suggesting very fine perlitic fracturing, the portion in the center have more spaced perlitic fracturing, noted at the BSE image of (D).

EMPA analyses of the glassy groundmass were carried out, with an average of ~4 spots per sample and are available in **Appendix A** and the average of them in **Table 5**. An exception was São Marcos area, where only 2 analyses used in one sample of banded vitrophyre were reliable. Despite this, in each area we analyzed both conduit and lava flows and considered samples with a minimum of 95% and maximum 102% of total oxides. The results presenting more than 80 wt.% of SiO_2 complemented by low Na_2O and K_2O contents were discarded, considering that the spot have analyzed quartz of devitrified matrix. SiO_2 contents of the glass range between 64.6 and 86.1 wt.%, this is accompanied by a decrease in CaO contents from 5.9 to 0.15 wt.% and Al_2O_3 contents from 18.2 to 5.7 wt.%, being chemically similar to the glasses analyzed by Andrade et al. (2017) using XRD Rietveld-RIR techniques in samples from Barros Cassal, Caxias do Sul and Santa Maria units. $FeO_{(T)}$ values are between 0.2 and 3.9 wt.%. Na_2O+K_2O contents vary from 4.2 to 14.1 wt.% and the samples are classified as dacites, trachydacites (Q_{norm}>20) and rhyolites (**Fig. 9a**) in the TAS diagram (LeBas et al., 1986). In the R1-R2 diagram of De la Roche (1980) they show a wide range from trachyte, quartz latite, dacite, rhyodacite, rhyolite and alkali rhyolite (**Fig. 9b**). This high alkali concentration in some spots is evidenced by the trend from metaluminous field to the peralkaline field (**Fig. 9c**) in the A/NK-A/CNK diagram of Shand (1943).

Table 5 - Average glassy groundmass compositions obtained in samples from the three areas (n=44).

	glassy groundmass
n	44
SiO_2	76.35
TiO_2	0.48
Al_2O_3	11.62
FeO	1.51
MnO	0.05
MgO	0.13
CaO	1.28
Na_2O	2.95
K_2O	5.14
Total	99.51
K_2O/Na_2O	1.96

3.2 Whole-rock chemistry

3.2.1 Major elements

Whole-rock chemistry was performed in 34 samples (10 from Mato Perso, 12 from São Marcos and 12 from Cambará-Jaquirana) and the results are available in **Appendix B**. The bulk of samples gave lost on ignition (LOI) values between 0.8 and 3.2 wt.% with one exception used presenting 4.2 wt.%. The bulk of analyses yielded SiO_2 content of 62.6-69.9 wt.% which is accompanied by the increase of TiO_2 from 0.83 wt.% to 1.06

wt.%. Na_2O+K_2O contents of 6.3-7.9 wt.% plotted against SiO_2 allows the classification of dominantly dacites, with minor trachydacite (sample GA-03v) in the TAS diagram (**Fig. 9d**), while in the R_1-R_2 plot they are rhyodacites with minor rhyolite (**Fig. 9e**). The main trend within the A/NK-A/CNK plot is the metaluminous, with exceptions plotting in the peraluminous field (**Fig. 9e**).

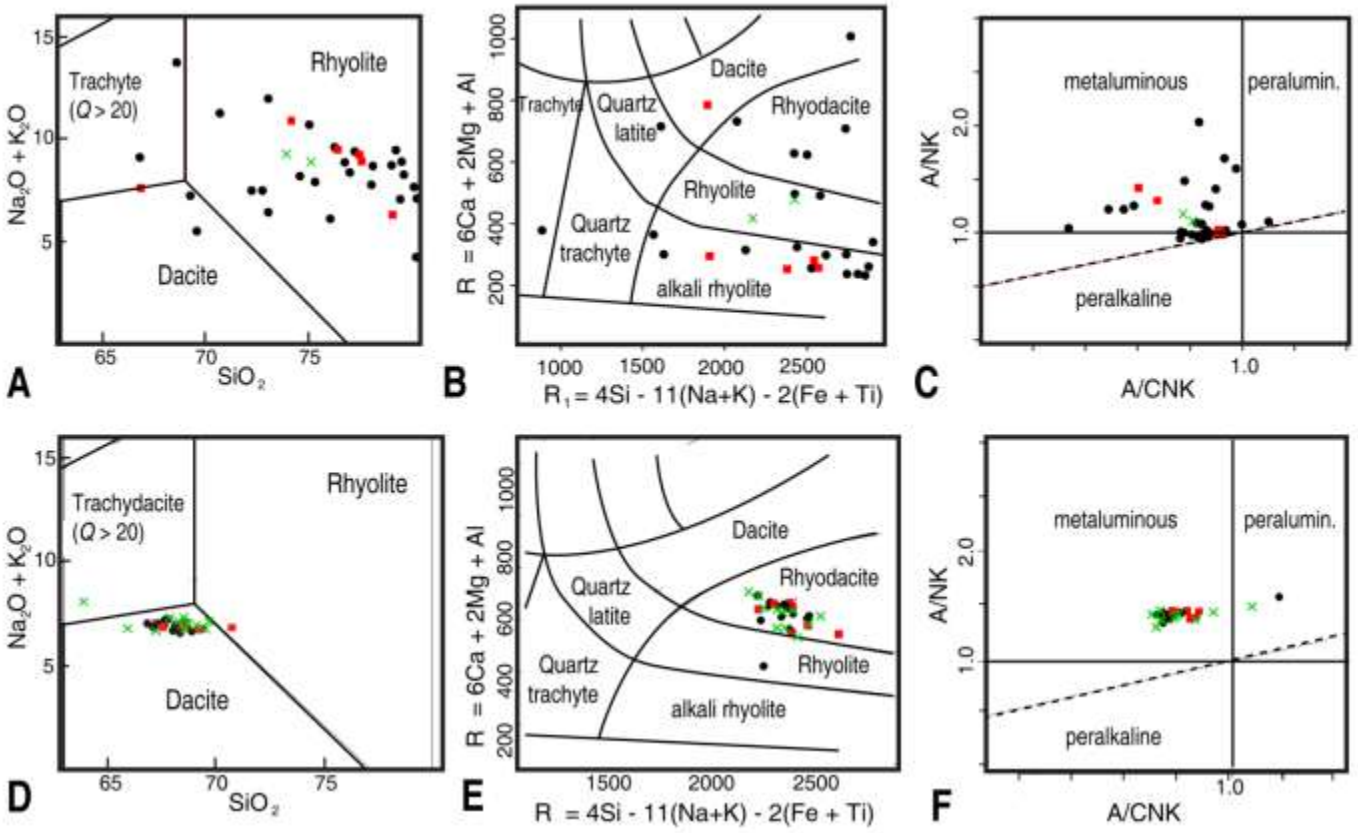

Figure 9 – (A,B, C) – Classification of glassy groundmass chemistry obtained by EPMA A) TAS plot (Le Bas et al., 1986) classification as rhyolites, dacites and trachytes (Q<20); (B) R1-R2 plot (De La Roche, 1980) classification as alkali-rhyolites, rhyolites, rhyodacites, dacites, quartz latites and trachytes.; (C) ANK/ACNK plot of Shand (1940) showing a trend from metaluminous to peralkaline. (D,E,F) – Classification of whole-rock chemistry with the same diagrams: (A) Domination of dacites over trachydacite (Q>20) and rhyolite. (B) Domination of rhyodacites over rhyolite. (F) Metaluminous to slightly peraluminous trend. Symbol legend as in **figure 4**.

SiO_2 contents overlap for oxidized (red, as lava units or within the conduits), banded (within the conduits), black vitrophyre (within the conduits) and grey (lava flow units) vitrophyres. Red vitrophyres have the lowest SiO_2 contents (62.6 wt.% in trachydacite, GA-03v) and also the highest (69.9 wt.% in rhyolite, SV-05), whereas other vitrophyres are dacites and also display more low (~64 wt.%) and high (up to 68 wt.%) values for this oxide (**Fig. 9d**). This overlap is also a common feature for Fe_2O_3, MgO, CaO, Na_2O, K_2O, TiO_2 and P_2O_5. In the plots with major elements against SiO_2 (**Fig. 10**), negative correlations occur for Al_2O_3, MgO, CaO, Na_2O, TiO_2 and $FeO_{(T)}$, agreeing with petrographic features showing the fractionation of plagioclase, clinopyroxene and Fe-Ti oxides.

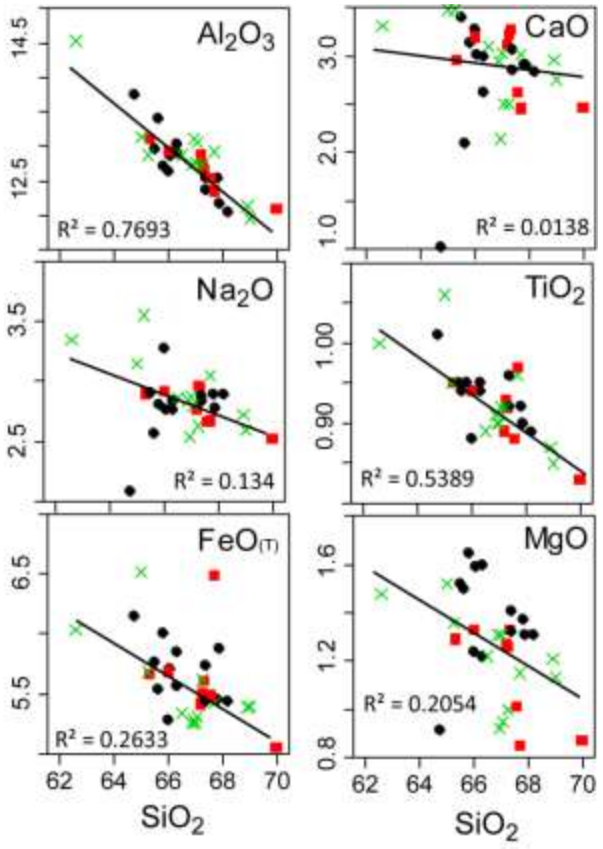

Figure 10 – Harker diagrams of SiO_2 against major elements for silicic rocks displaying strong (linear $r^2>0.5$) negative correlations for Al_2O_3 and TiO_2 and less pronounced negative correlations for CaO, Na_2O, $FeO_{(T)}$ and MgO.

To compare the fractionation trends, we plotted whole rock and glass matrix major elements (Al_2O_3, CaO, MgO and K_2O/Na_2O) against silica as differentiator (**Fig. 11**). Negative correlation is very clear for alumina, mainly because plagioclases occurs as early phenocrysts and microlites as well as pyroxenes, assuming negative correlation of CaO and MgO attributed to their fractionation. MgO has almost a bi-modal distribution ranging from 0.8-1.7 in whole-rock and 0.0-0.9 in the groundmass, suggesting a major role of pyroxene phenocrysts and microlites to Mg^{2+} fractioning, leaving the interstitial liquid depleted in MgO. The K_2O/Na_2O ratio may be very low in the groundmass, but in a general way there is a positive correlation, with an increase from ~ 0.6 in whole-rock to ~3.4 in the glass. Increase of the R1 component and decrease of R2 component (**Fig. 9b**) and increase of peralcalinity shown in **figure 9c** indicate alkali enrichment in the interstitial liquid of the silicic melts.

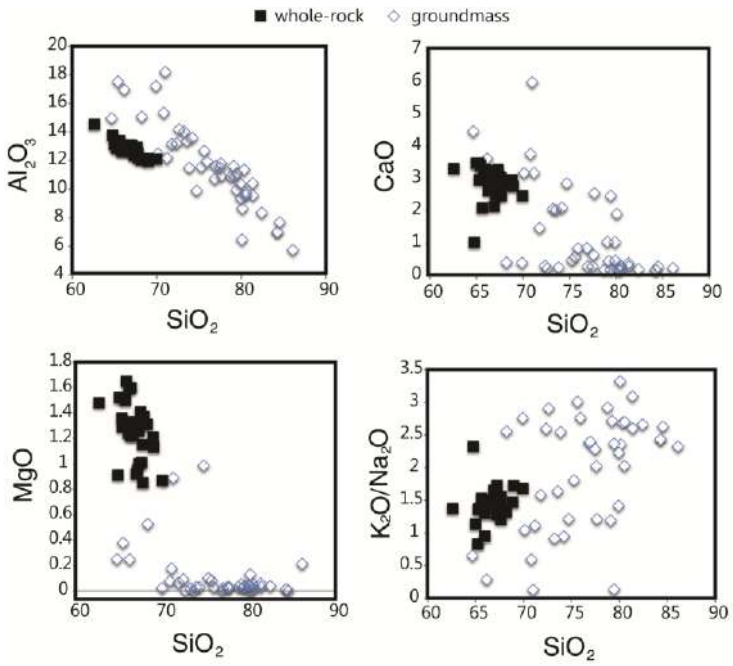

423

424 **Figure 11** – Harker diagrams of SiO_2 against major elements for silicic whole-rock (black squares) and glassy
425 groundmass (empty diamonds). Negative correlation is accented for Al_2O_3 and CaO. MgO display a slight gap
426 between ~0.8 and 0.6 wt.%. K_2O/Na_2O ratios increase with the differentiator.

427

428 3.2.1.1 Mass Balance

429 The mass balance of Stormer and Nichols (1978) present in the Petrograph 2.0 software (Petrelli et al., 2005)
430 was made in order to compare the fit of proposed parental magmas for silicic rocks. Calculations are available in
431 the **Appendix C** and the chemical compositions used as parental magmas are present in **Table 6**.

432 One sample of basalt-andesite from Mato Perso (MP-02; 56.30wt.% of SiO_2 and 3.4wt.% of MgO) was used as
433 parental magma to lava silicic samples MS-01 and MS-04 together with conduit silicic samples MS-03a and MS-
434 05b. The sum of the square of the residuals (Σres^2) varied between 0.26 and 0.58, the lowest being MS-03a,
435 with ~45% of fractionation using assemblage of plagioclase (45%), clinopyroxene (34%) and Ti-magnetite (19%).
436 For São Marcos we used average values of four samples (GA-14b, GA-22, GA-24, GA-30; av.: 53.8wt.% of SiO_2
437 and 4.9wt.% of MgO) of basaltic andesite extracted from Lima et al. (2012). Silicic final melts were samples GA-
438 03v (oxidized band), GA-03p (black obsidian band), GA-04, GA-10 and GA-07 (lavas). Σres^2 values of 0.68-10.2
439 were obtained for a plagioclase/cpx/Ti-magnetite fractioning assemblage with respective proportions of 47%,
440 42% and 10% with 60-70% of fractioned total. To model Jaquirana-Cambará area we compiled a sample (SP-
441 03; 52.2wt.% of SiO_2 and 4.5wt.% of MgO) from Piccirillo et al. (1988) and added sanidine to the mineral
442 assemblage. The modelling with samples MS-22 (banded vitrophyre), MS-19a, MS-24, MS-29 (coherent lavas)
443 and MS-38 (spherulitic lava) assumed a final melts gave Σres^2 = 0.12-0.52, with 0.1% of sanidine, 52% of
444 plagioclase, 37% of clinopyroxene and 9% of Ti-magnetite for ~75% of fractionation.

445 The selected basaltic-andesite samples for rhyodacite parental magmas are in totality from rubbly pahoehoe
446 flows from Vale do Sol Formation. To test parental magmas from underlying volcanic sequences we chose three
447 samples in of compound pahoehoe and five samples of ponded pahoehoe flows from Torres Formation in the

paper of Rossetti et al. (2014). They were tested as parental magmas for samples from Mato Perso, which are geographically closer. Compound lavas (samples LR-15A, LR-12A and LR-48) are in the base of the sequence, have average SiO_2 and MgO contents of 51.4wt.% and 7.9wt.% and gave very poor Σres^2, near a hundred, at 85% of fractionation. Ponded lavas (LR-02A, LR-04A, LBC-1, LBC-12, LBC-19) with 56.6wt.% of SiO_2 and 3.9wt.% of MgO gave variable Σres^2 at ~50% of fractionation, but with the best-fit with $\Sigma res^2 = 1.3$ and fractional assemblage of 51% plagioclase, 34% augite and 13% Ti-magnetite.

3.2.2 Trace and rare earth elements

Some features shared by study areas as Zr<300 ppm, Nb/Y<0.6 and Rb/Zr>0.5 are compatible with Palmas magma-types (e.g. Peate et al., 1992; Garland et al., 1995) and in the TiO_2 vs P_2O_5 plot they lie almost entirely in the Caxias do Sul sub-group field (**Fig. 12a**). A notable distinguishing feature between São Marcos samples from Mato Perso and Jaquirana-Cambará is their Zr/Nb ratios (**Fig.12b**), which are smaller in the former (10.4-11.2) and greater in the other two areas (11.6-13.0). When normalized to Y, another incompatible element, these distinctive ratios are too observed (**Fig. 12c**). Slghtly similar behavior of Th was verified against Zr, with São Marcos samples being relatively enriched in this element (**Fig. 12d**). The Zr/Nb ratio does not correlate with any major element, as Nb display no similar behavior against neither with Ba, Rb (**Fig. 12e**), Sr (**Fig. 12f**), Y, La, Ce, or the Ba/Sr, La/Yb, Ba/La, Zr/Y, Nb/Y, U/Nb, Th/Y ratios.

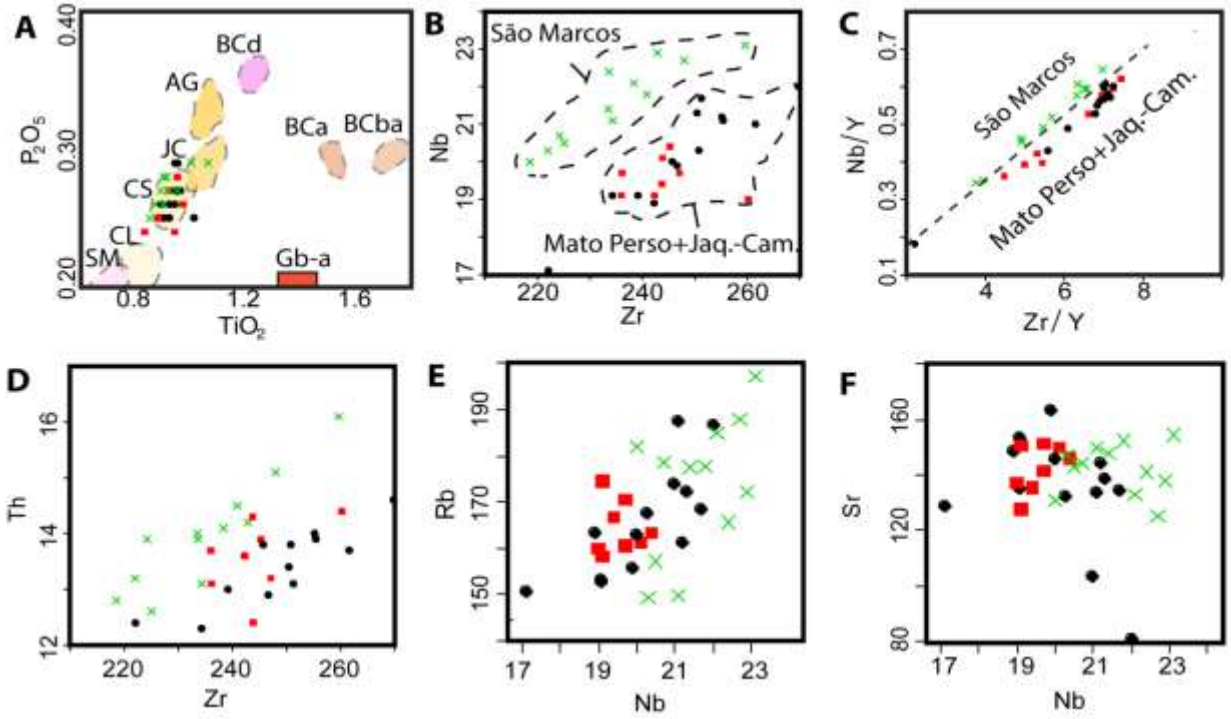

Figure 12 – (A) P_2O_5 against TiO_2 plot with field compiled from Nardy et al. (2008) and Polo and Janasi (2014) indicating the sub-groups of Palmas-type magmas, namely: Santa Maria (SM), Clevelândia (CL), Caxias do Sul (CS), Jacuí (JC), Anita Garibaldi (AG), Barros Cassal dacites (BCd), Barros Cassal andesites (BCa), Barros Cassal basaltic-andesites (BCba) and Gramado basalt-andesites (Gb-a), this last compiled from Barreto et al., (2014) and Rossetti et al. (2014). (B) Nb vs Zr plot showing the composition distinction between São Marcos and Mato

Perso+Jaquirana-Cambará areas. (C) Nb vs Zr normalized by Y plot also displaying a distinct pattern from São Marcos from the other two areas (highlighted by the dashed line). (D) Th against Zr plot showing that São Marcos samples are slightly more enriched in Th. (E) Rb against Nb plot showing slightly positive correlation, but the behavior between the three study areas is not much different. (F) Sr against Nb plot showing no significative correlation.

The spider plot of trace elements, normalized to the upper continental crust of Taylor and McLennan (1995), evidence large ion lithofiles and high-field strenght elements enrichment with Eu negative anomaly, a slight Zr-Hf negative anomaly and gradational Ti negative anomalies (**Fig. 13a**). Against the Primitive Mantle of Sun and McDonough (1989), there is an inclined pattern with well stablished LILE enrichment in relation to HSFE (**Fig. 13b**) accompanied by Ba, Nb, Sr and Ti negative anomalies together with Th-U positive and Pb variable positive to negative anomalies. Anomalies of Ba, Sr and Ti can be easily explained by plagioclase and Fe-Ti oxide fractionation, but Nb, Th-U and Pb anomalies must be related to the parental magma or to crustal contamination. Rare earth elements also exhibit inclined patterns with slight Eu negative anomaly ($Eu_{(N)}/Eu_{(N)}^{*}$ = 0.5.-0.6) and two samples are more enriched in REE (**Fig. 13c**). In both **figures 13a** and **b** it is observable the trace element and REE patterns of silicic samples very similar and only slightly enriched than those of basaltic andesites from Vale do Sol formation (extracted from Rossetti et al., 2014).

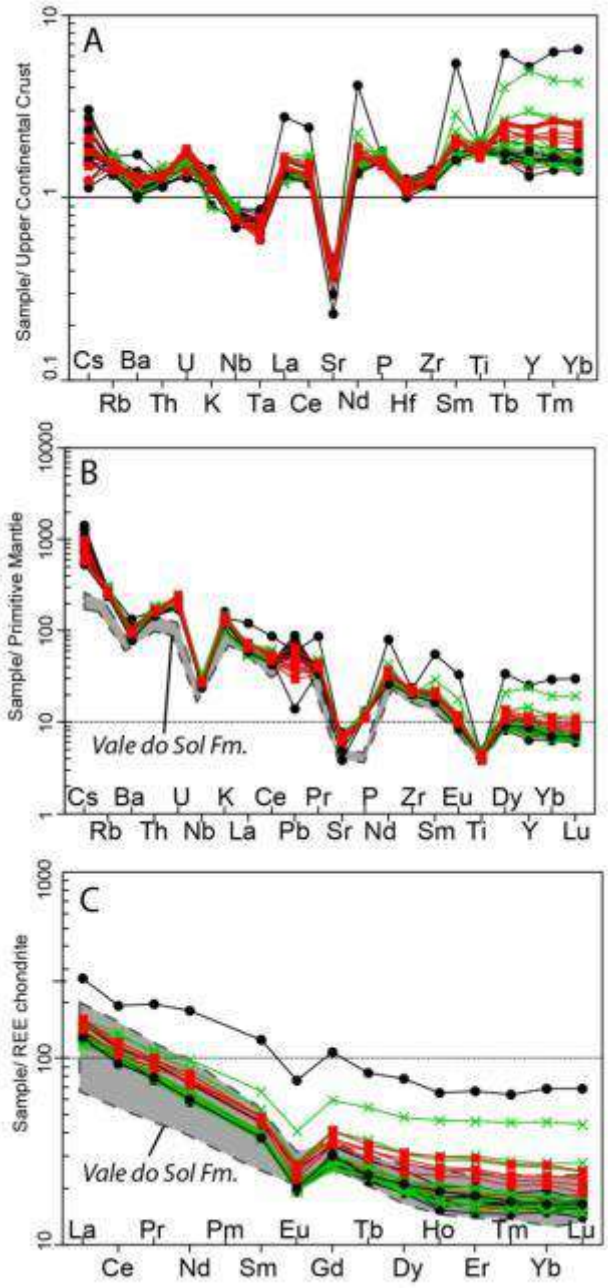

Figure 13 – (A) Trace-element spider diagram normalized to the Upper Continental Crust of Taylor and McLennan (1995). (B) Trace-element spider plot normalized to the Primitive Mantle (PM) of Sun and McDonough (1989). (C) Rare earth element patterns normalized do the REE chondrite of Boynton (1984). Grey shades are the trace element composition of Vale do Sol Formation basaltic andesites normalized to the same PM, extracted from Rossetti et al. (2017).

3.2.2.1 Model of open-system fractional crystallization

Despite that fractional crystallization models have alredy been tested for silicic melts in the Paraná-Etendeka LIP (e.g. Bellieni et al., 1986; Piccirilo et al., 1988; Garland et al., 1995; Ewart et al., 2004), we applied a different approach using an open-magma chamber model from O'Hara (1977) in an excel spreadsheet (**Appendix D**). This model simulates a high-level magma chamber being periodically fed by batches of parental magma. Mixed

magmas undergo continuous fractional crystallization, leaving a mass fraction of a cumulate (X), a mass fraction of the original liquid before fractionation (Y) extracted as a lava flow in each cycle and a mass of parental magma added in each cycle (Z). For this, we selected four samples of Gramado-type andesi-basalts Lima et al. (2012) and used their average (**Table 6**) as parental magma.

The rhyodacites display ~3 to ~5 times more Rb, U and K than the chosen parental magma, with the rest of the elements being 1.5-3 times greater. To run the model we used a solid assemblage with plagioclase (49%), clinopyroxene (35%), K-feldspar (2%), magnetite (10%), ilmenite (3,5%) and apatite (0.5%). Partition coefficients (K_d) were compiled from Schnetzler and Philpotts (1970), Leeman (1979), Leeman and Felps (1981), Nash and Crecraft (1985), Bacon and Druitt (1988), Sisson (1991), Rollinson (1993), Stimac and Hickmott (1994) and Ewart and Griffin (1994). The concentration of the elements in the erupted lava (C_B^S) fits with the composition of our silicic samples in a range of 40-90% of cumulate left (X) for Ba, Sr, Zr, Rb, Nb, Ta, Th, Hf, and Pb. Concentrations of Eu, Yb and Lu were achieved only with >90% of X (**Fig. 14**).

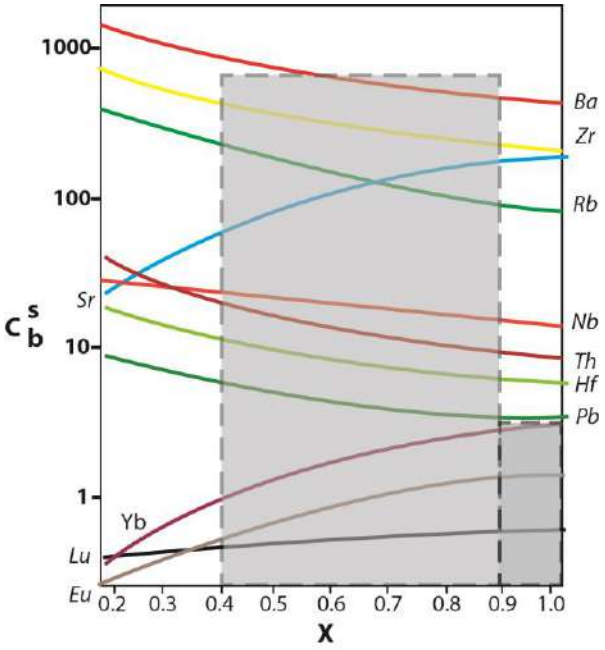

Figure 14 – Open-system fractional crystallization modelling of trace elements. X is the mass fraction of cumulate left in the chamber and C_b^S is the concentration of trace elements in the erupted material. The shaded areas are the range of X needed to satisfactory values which is from 0.4-0.9 for Ba, Sr, Zr, Rb, Nb, Ta, Th, Hf, and Pb and 0.9-1.0 for Eu, Yb and Lu.

3.2.2.1 Model of assimilation and fractional crystallization

To model assimilation and fractional crystallization (AFC) for trace elements we used the AFC curves reproduced by the software Petrograph (version 2.0). Selected parental magmas were sample MP-02a, a basaltic andesite underlying the silicic volcanics at Mato Perso; the average of four basaltic andesites underlying the silicic rocks at São Marcos (extracted from Lima et al., 2012); and the average of ponded pahoehoe basaltic samples from Rossetti et al. (2014) to Jaquirana-Cambará do Sul area. For assimilation, we picked up two chemically contrasting samples (**Table 6**). One is an average of Neoproterozoic peraluminous granites from the

524 Cordilheira Suite extracted from samples in Philipp et al. (2013). These granites have low Ba, Zr and REE. The
525 other assimilant is a Paleoproterozoic orthogneiss from Encantadas Complex (sample 19A from Philipp et al.,
526 2008), with higher contents of trace elements than our volcanic samples.

527 Ba/La, Zr/La, Zr/Ba, Zr/Nb and Zr/Yb ratios were chosen to run the model because they are trustworthy on
528 fractionation models and are the most used in literature. As seen in **figure 15**, the Ba/La, Zr/La, and Zr/Ba ratios
529 were obtained by 20-40% of crystallization and 20-80% of assimilation of both assimilants, in the exception of
530 Jaquirana-Cambará. In samples from this area, the Zr/La ratios were of obtained by 60% of crystallization and
531 20% with assimilation of only peraluminous granites. La/Ba ratios were obtained for only one sample fitting the
532 model at 20% of assimilation. Zr/Nb ratios were reached by AFC in São Marcos samples at ~40% of
533 fractionation assimilating peraluminous granites. Zr/Yb ratios of Mato Perso samples did not fit the AFC trend,
534 while São Marcos and Jaquirana-Cambará yielded similar values of 20% of crystallization plus 20% of
535 Encantadas Complex orthogneiss assimilation.

536 **Table 6** – Whole-rock composition of averages and samples used in mass balance of major elements and in trace
537 element modelling. The composition of 'compound' and 'ponded' are averages of compound and ponded pahoehoe
538 lavas, extracted from Rossetti et al. (2014). MP-av, GA-av and JC-av are the averages of analyzed silicic rocks,
539 present in Appendix B. MP-2A is a sample of rubbly pahoehoe basaltic andesite from Mato Perso. GA* is an average
540 of rubbly pahoehoe basaltic andesites from São Marcos, extracted from Lima et al. (2012) and was used as C_i^0 in the
541 open system modelling of O'Hara (1977) .S3JC is the sample S3 extracted from Piccirilo et al. (1988). The sample
542 enc-19A, an orthogneiss of the Paleoproterozoic Encantadas Complex, and the average av-C, the average of
543 peraluminous granites of Cordilheira Suite (from Philipp et al. 2013), are assimilants.

	compound	**ponded**	**MP-av**	**MP-2A**	**GA-av**	**GA***	**JC-av**	**S3JC**	**enc-19A**	**av-C**
SiO_2	50.12	55.78	66.76	55.3	66.66	52.43	66.43	54.20	67.09	72.54
Al_2O_3	14.44	14.10	12.85	13.35	12.90	13.67	12.79	14.74	14.19	15.01
$FeO_{(T)}$	11.01	10.95	6.17	12.87	6.16	12.53	6.27	11.70	5.47	1.53
MgO	7.73	3.89	1.29	3.36	1.21	4.82	1.40	4.54	1.74	0.45
CaO	9.79	6.76	3.15	6.57	2.94	8.66	2.78	8.77	2.53	1.07
Na_2O	1.85	2.73	2.90	2.43	2.91	2.39	2.78	2.71	3.41	3.62
K_2O	1.02	2.41	3.88	2.23	4.04	1.18	4.00	1.41	3.13	4.46
TiO_2	1.09	1.36	0.92	1.69	0.93	1.33	0.94	1.53	0.789	0.16
P_2O_5	0.15	0.27	0.27	0.25	0.27	0.18	0.27	0.23	0.31	0.14
MnO	0.17	0.15	0.11	0.17	0.11	0.19	0.10	0.17	0.054	0.03
Sum	97.35	98.39	98.28	98.22	98.13	97.39	97.77	100.00	98.71	98.99
LOI	2.33	1.36	1.48	1.5	1.70	2.38	2.02	-	0.79	0.79
Ba	247.25	574.20	603.25	480	649.42	323.50	614.55	417.00	1480	455.81
Hf	-	-	6.64	5.8	7.77	4.13	6.67	-	-	-
Nb	7.50	18.84	19.56	15.5	125.82	12.25	21.58	-	10	11.47
Rb	32.30	85.94	164.35	90.1	53.15	34.80	173.31	47.00	64	277.75
Sr	202.20	267.94	142.58	209.5	63.12	239.30	142.25	240.00	-	178.69
Th	3.65	8.30	13.58	9.1	4.01	5.38	13.96	-	-	-
Zr	103.35	212.96	244.31	211.4	41.20	145.75	235.09	156.00	24	15.07
Y	20.55	30.40	41.61	37.3	41.61	28.58	49.70	30.00	109	16.53
La	15.40	34.80	44.63	34.5	44.63	21.75	41.33	26.00	215	33.39
Nd	16.80	33.62	41.73	35	41.73	23.18	41.26	-	12.1	3.29
Eu	1.14	1.68	1.67	1.72	1.67	1.40	1.69	-	8.9	1.99
Yb	2.14	3.02	4.13	3.54	4.13	2.84	4.34	-	0.26	0.14
Lu	-	-	0.62	0.58	0.62	0.42	0.65	-	-	-

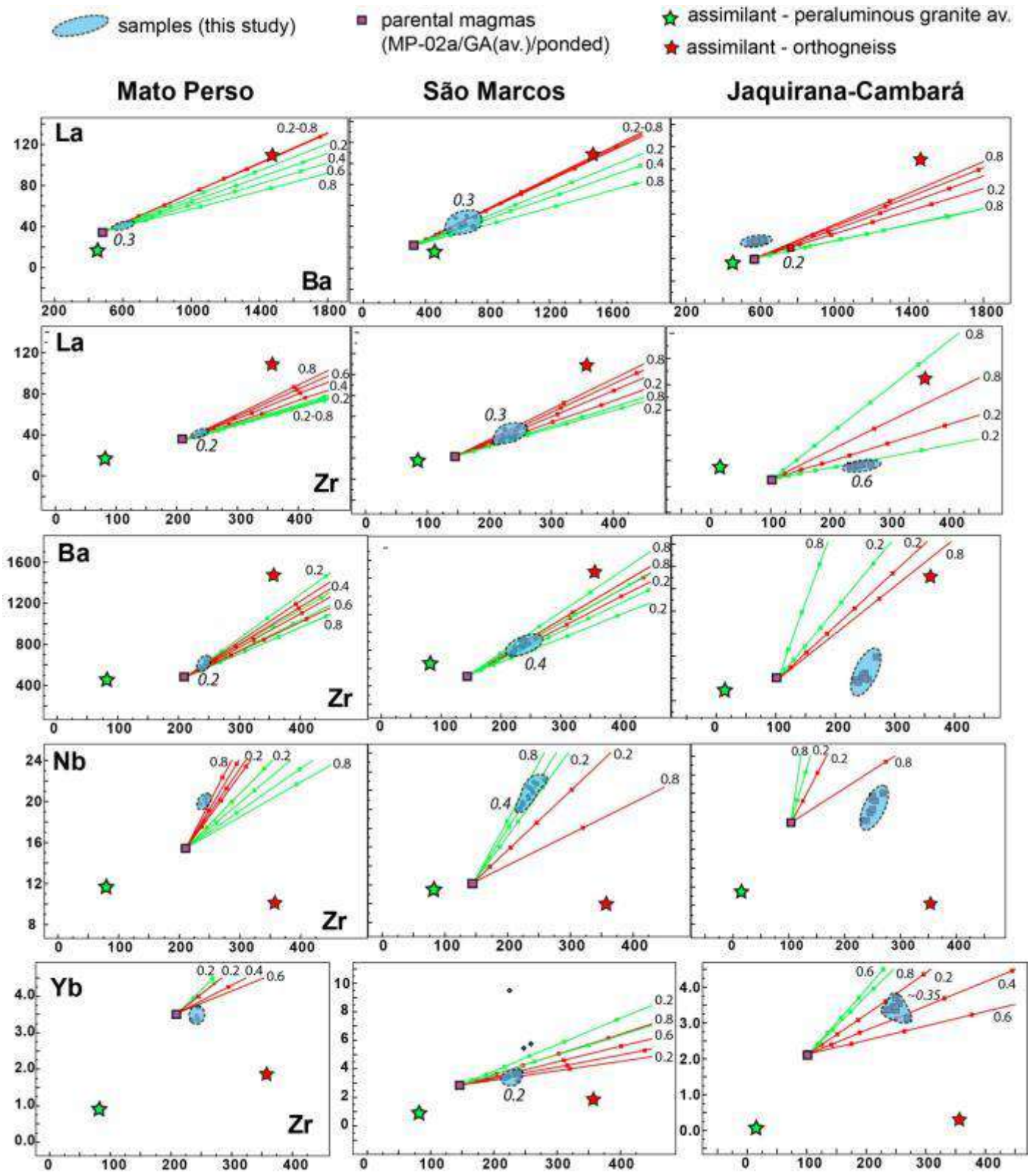

Figure 15 – Assimilation and fractional crystallization (AFC) model curves for trace elements. The parental magma for Mato Perso area is a rubbly pahoehoe basaltic andesite (MP-2A), for São Marcos is an average of four samples of rubbly pahoehoe basaltic andesites (GA-av.) extracted from Lima et al. (2012) and for Jaquirana-Cambará do Sul area is an average of ponded pahoehoe flows extracted from Rossetti et al. (2014). The assimilants are: (1) an average of peraluminous granites with low trace element contents of the Cordilheira Suite, extracted from Philipp et al. (2013); and (2) a trace element enriched orthogneiss of Encantadas Complex, extracted from Philipp et al. (2008). Green lines correspond to the green star of peraluminous granites and red lines correspond to the red star of the

orthogneiss. In the end of the lines are the values of *r* (rate of assimilation/rate of fractionation by crystallization) and the best-fit values of *F* (fractionation degree) are indicated in italic.

3.3 Intensive Parameters

3.3.1 Apatite saturation thermometry

Apatite saturation temperatures were calculated following the model of Harrison & Watson (1984) taking account that the model is limited by diffusion of phosphorous in the melt and apatite is a common accessory mineral in the studied vitrophyres. To calculate the variable $\ln_D$ ($P_2O_{5apatite}/P_2O_{5melt}$), the whole rock P_2O_5 content was used and the phosphorous partition coefficient was considered as 42 (Prowatke & Klemme, 2006). Calculated temperatures range from 1015-1073°C in Mato Perso samples, 1059-1112°C in São Marcos and 1005-1109°C in Jaquirana Cambará. The temperatures should represent the temperature of apatite saturation in the melt. Since apatites are microlites in the groundmass or inclusions in feldspars, those temperatures are good estimates for the magma *liquidus*.

3.3.2 Plagioclase-liquid thermometry

The plagioclase-liquid geothermometry was carried out using the model of Putirka (2005, 2008). This model requires inputs of mineral chemistry data of plagioclase microphenocrysts and microlites achieving equilibrium with a melt, which we chose as whole-rock and glass compositions. As the temperature is pressure-dependent, the constant pressure utilized was 0.1 kbar.

In samples of Mato Perso area (MS-01, 03a, 04, 05b) the plagioclases have $An_{55.35 \pm 1.03}$ and yielded calculated saturation temperature of 1022-1050°C - Kd_{An-Ab}=0.08-0.13, in equilibrium with whole-rock chemical composition (dacites, **see table 7**). Using glass compositions with 74.61±1.7 SiO_2 wt.% (rhyolite), the calculated temperatures decrease to 951-953 °C (Kd_{An-Ab}=0.1 ± 0.01), a difference of ~70°C. The sample MS-11 from São Marcos area gave temperatures of 1006 and 1062°C of plagioclase microphenocrysts with An_{51-59} in equilibruium (Kd_{An-Ab} =0.08-0.1) with dacite (68.8 wt.% SiO_2) and trachydacite (62.6 wt.% SiO_2) and decreases to 913°C when testing equilibrium (Kd_{An-Ab}=0.01) with glass analysis (72-74 wt.% SiO_2). For Cambará-Jaquirana area, a banded vitrophyre (sample PSJ02A) with plagioclase composition of An_{11-47} was used with glass compositions ranging between 65-74 wt.% of SiO_2. The glass with the lower SiO_2 content (red oxidized glass, 65 wt.%) gave a calculated saturation temperature of 1015°C. High silica glassy matrix with 74 wt.% of SiO_2 reached equilibrium with plagioclase under temperatures of 1007°C (Kd_{An-Ab}, median 0.06).

A spherulitic vitrophyre (sample MS-38) from the same region have plagioclase with An_{46-51} and yielded average calculated samples of 931±46 °C for glass composition with SiO_2 content between 68-88 wt.% (Kd_{An-Ab}=0.01-0.02) . Very similar temperatures of 929°C - Kd_{An-Ab}=0.04-0.05 - were obtained for the same plagioclase crystals using the whole-rock chemical composition (dacite, 66.04 wt.% of SiO_2). The sample MS-50, with plagioclase compositions of An_{29-51} together with glass compositions of 69-83 SiO_2 wt.% gave temperatures of 934±72 °C

(921.8°C median) - Kd_{An-Ab} =0.04±0.08 - the same crystals reached equilibrium with the whole rock composition (dacite, 66.30 wt.% SiO_2) in temperatures of 931 °C. Kd_{An-Ab}=0.19 ± 0.3.

3.3.3 Plagioclase-liquid hygrometer

The H_2O content estimates were conducted by the application of the Waters and Lange (2015) model to samples of known whole-rock chemistry, plagioclase chemistry and plagioclase equilibrium temperature (MS-01, 03a, 04, 05b, MS-11b, MS-38, MS-50 and PSJ02A). For Mato Perso samples we obtained values between 0.7 and 0.8 wt.% of H_2O, which are similar to those obtained for São Marcos, of 0.4-1.0 wt.%. In Jaquirana-Cambará, samples MS-38 and MS-50 yielded H_2O contents of 0.2-0.5 wt.%, but the higher Ab component in the sample PSJ02A resulted in water contents between 1.5 and 3.3 wt.%. In general, in the exception of this sample, the average values for H_2O estimated contents are of 1.3±0.3 wt.% for 1 kbar and 931 – 982 °C. When the water content in our samples is estimated for temperatures of 1000°C the values tend decrease to 0.5±0.2 wt.% (**Table 7**). Average values of 1.3 wt.% are very close to those obtained by Polo et al. (2017) of ~1.5 wt.% for their Caxias do Sul dacites at 1000°C. Data obtained by Garland et al. (1995) using the model of Housh & Luhr (1991) yielded higher minimum temperatures of ~ 2% of H_2O in Palmas-type silicic rocks.

3.3.4 Viscosity

Viscosity was calculated with the Giordano et al. (2008) model. This viscometer use calculation based in major oxides, temperature and water content. We chose to use calculated H_2O content values (0.5 and 1.3 wt.%) plus a “dry” composition for comparison. Viscosities were estimated using apatite saturation temperatures as input. Mato Perso samples viscosity ranges from 5.7 to 6.2 log Pa s for dry compositions, decreasing to 4.6-5.1 log Pa s and 3.9-4.3 log Pa s for 0.5 and 1.3 % of H_2O, respectively. In São Marcos they are 5.4-6.0, 4.4-4.9 and 3.8-4.2 log Pa s, while in Jaquirana-Cambará do Sul the values range from 5.2-6.6, 4.5-5.4 and 3.6-4.5 log Pa s (**Appendix B**). These values also agree with previous estimation available in the literature (e.g. Milner et al., 1992, Garland et al., 1995; Simões et al., 2014; Polo et al., 2017).

3.3.5 Pyroxene composition barometer

Geobarometry is an important tool for predicting crustal depth of formation for a mineral phase. We used the equation (32a) of Putirka (2008) for calculation, based only on clinopyroxene EPMA analyses because it does not need a liquid in equilibrium. The calcultated $Kd_{(Fe-Mg)}$ was of 0.269 in all analyses, for an expected value of 0.27±0.03. The input temperature was of 1150°C (1423.15 K) for all samples/spots and the model yielded pressure ranges of 1.4-4.6 kbar for Mato Perso CS, 1.1-8.2 kbar in São Marcos, 2.2-9.9 kbar in Jaquirana-Cambará do Sul. These values are slightly higher than those obtained by semi-quantitative estimates made by Garland et al. (1995), suggesting pressures of 0.5 – 5 kbar to Palmas-type and 5 – 15 kbar for Chapecó-type volcanics and with clinopyroxene-liquid estimate data of Polo et al. (2017) with a range of 2 to 4 kbar (**Table 7**). By presuming a gradient of 3.5 km/kbar, Mato Perso display the most shallow values from 4-16 km, São Marcos

give depths of 3-28 km and Jaquirana-Cambará do Sul the pyroxenes had crystallized from depths up to ~ 7-34 km.

Table 7 – Intensive parameter data for the studied areas. Temperature is given by whole-rock (WR) and glassy groundmass (glass) equilibrium with plagioclase, following the model of Putirka (2008). H_2O estimates were made by using 1000°C and chemical composition of plagioclase as input in the model of Waters and Lange (2015). Geobarometer to calculate pressure of pyroxene formation was the equation 32a from Putirka (2008). *MP=Mato Perso, SM=São Marcos, JC=Jaquirana-Cambará do Sul

Sample(place)*	type	temp. (WR)°C	temp.(glass) °C	H_2O (wt.%)	Pressure (kbar)
MS-01 (MP)	lava (grey)	1022.1	951-953	0.3-0.8	2.4-4.6
MS-03a (MP)	banded	1050	-	0.7-0.8	2.2-3.5
MS-04 (MP)	lava (grey)	1027	-	0.7-0.8	-
MS-05b(MP)	banded	1050	-	0.4-0.8	1.4-4.1
MS-11 (SM)	banded	1006-1062	868	0.4-1.0	1.1-8.2
MS-38(JC)	spher. lava	929.7	931.7	0.4	4.8-9.0
MS-50 (JC)	lava (oxidized)	934.7	931.8	0.2-0.5	4.6-9.9
PSJ02A(JC)	banded	1015.5	1007.5	1.5-3.3	-
MS19B1 (JC)	microfractured	-	-	-	2.2-6.6
MS19B2 (JC)	microfractured	-	-	-	2.3-6.0
MS51A(JC)	lava (banded)	-	-	-	1.4-5.2

4 Discussion

4.1 Textural and compositional variations in the studied areas

Despite very similar in major element composition, the vitrophyres outcropping in the study areas differ in petrographic features, like microphenocryst content from west to east: Mato Perso, ~5-10%; São Marcos, ~<2%; Jaquirana-Cambará do Sul, <1% - and decrease in volume of pyroxene microphenocrysts, also in this direction. Microprobe data presented in this study reveal that the anorthite content of plagioclase decreases in this geographical trend, together with the slightly enrichment of ferrossilite component in augite. Titanium contents in Ti-magnetite and in pyroxenes largely overlap between the three areas, as well as their glassy matrix composition.

Plagioclase composition is controlled by temperature, melt composition and melt H_2O content (e.g. Humphreys et al., 2016). In anhydrous melts, the plagioclase composition in equilibrium shifts systematically toward albite with decreasing temperature (e.g. Bowen, 1913; Kudo and Weill, 1970; Drake, 1976). In hydrous melts, the shape of the albite-anorthite binary loop in T-X space is broadened and shifted to lower temperature relative to anhydrous compositions (Kudo and Weill, 1970; Drake, 1976; Johannes, 1984). In our samples the calculated temperatures using both whole-rock and plagioclase thermometers are very close (**Table 6**), suggesting a major role of the dissolved water content variation in the magma as controller of plagioclase compositions. The prevalence of larger and more calcic plagioclase crystals in Mato Perso suggests lower dissolved H_2O contents in the melt than the other two areas. In São Marcos, plagioclase compositions are also calcic, but the crystals tend to be smaller, probable by variation in undercooling degree. In the whole Paraná-Etendeka LIP the

plagioclase solid-solution has distinguished high-Ti silicic magma-types, with compositions up to An_{50}, from low-Ti magma-types, displaying more calcic compositions up to An_{70} (Bellieni et al., 1984; 1986; Garland et al. 1995; Ewart et al., 2004). Calcic plagioclase composition has also been found in Caxias do Sul dacites of Polo et al. (2017). The results obtained at Jaquirana-Cambará area indicate that Palmas-type/Caxias do Sul sub-type magmas can also have more sodic plagioclase assembly and tend to present associated sanidine microphenocrysts.

Fe-Ti oxide compositions suggest that fO_2 conditions affected only the linear variation of $^{T}Fe^{3+} + {}^{M}Fe^{3+} = {}^{T}Fe^{2+} + {}^{M}Ti^{4+}$ chemical substitution (e.g. Bosi et al., 2008). The variation of Ti and Fe contents is common either in a single sample, varying from cores to rims of the crystals, for example, and since TiO_2 values in whole-rock do not vary too much, these contents appear only to reflect variations in oxygen fugacity during the crystallization. The presence of aggregates with plagioclase and clinopyroxene displaying very close compositions has been reported in Barros Cassal-Santa Maria areas in southern Brazil by Polo et al. (2017) and are interpreted to reflect a magmatic system in which the magma was physically segregated into a number of separate bodies evolving in parallel prior to eruption (Ellis et al., 2012).

In terms of major element whole-rock composition, the analyzed samples do not vary systematically. This is also valid when comparing the investigated areas or the different textural and color types. Despite several textures involving magma mixing patterns, such as polyclinal folds with several folding phases (e.g. Perugini and Poli, 2012) occur in the study areas, this chemical similarity is a favorable argument to postulate there was no mixing of magmas with accented chemical distinction. Although Na loss during devitrification is a common process in Caxias do Sul volcanics (e.g. Andrade et al., 2017), the glass compositions do not variate from one area to another and follow the path of fractional crystallization, increasing the alkalis content of the glass and giving well-fit mass balance at the same mineral proportions as microlite contents observed at thin sections.

In the case of trace element variations, the more pronounced features are the Zr/Nb ratios, which are lower in São Marcos and higher in Mato Perso and Jaquirana-Cambará. The work of Kirstein et al. (2001) in silicic volcanics from Uruguay suggest the Zr and Nb contents being controlled by the presence of halogens as F^- and Cl^-. For them, high Zr/Nb ratios are proportional to high-fluorine content and rocks with high Zr/Nb ratios emplaced effusively. Further, low Zr/Nb ratios in the Palmas and Lavalleja magma-types would be a chemical explanation for their explosive emplacement. We argue firstly that Zr/Nb ratios are not indicative of magma explosivity, and secondly that the majority of Palmas-type volcanic deposits is effusive in origin, not explosive.

Zr and Nb have very different bulk composition coefficients in an upper-mantle melting regime, expressed as $D_{Zr}^{solid/liquid} >> D_{Nb}^{solid/liquid}$ (e.g. Green et al., 1989) and the linearity patterns between these two elements cannot be explained only by fractional crystallization. In OIB magmas the Zr vs Nb concentration arrays must reflect intra-mantle processes like carbonatitic fluid metassomatism or carbonate-silicate immiscibility (Kamber and Collerson, 2000). A sample of basaltic-andesite collected in Mato Perso gave Zr/Nb ratio of 13.6, similar to those found in the rhyodacites. Comparing to the basaltic andesite chemical data of Lima et al. (2012), in São Marcos the Zr/Nb ratios are about 11-12 in samples from pahoehoe and rubbly pahoehoe flows. Chemical data from the Bom Princípio-Caxias do Sul profile (from Rossetti et al., 2014) yielded Zr/Nb ratios of ~13-14 for compound pahoehoe at the base, ~10-13 for simple and pounded pahoehe, and ~11-15 for rubbly pahoehoe flows. In the Santa Cruz do Sul – Herveiras profile, the values lie on 9-18 for pahoehoe (pounded and compound) and 13-15

for rubbly pahoehoe. This marked variation in Zr/Nb ratios between stratigraphic units within the province is thought to be caused by two possible processes acting together: one is the variation in mantle Zr-Nb composition in a large scale (50-150 km) and the other is the assimilation of the underlying basement with various Zr/Nb ratios in a minor scale (5-50 km), for example at different granitic bodies and gneiss complexes. Our model of AFC reached a good fit for Zr-Nb with 40% of assimilation of peraluminous granite and 80% of fractionation, for example, but a lot of sources could be included in a complex process of assimilation because of the horizontal and vertical lithological variation into the continental crust.

4.2 Origin of low-Ti silicic melts and implications for eruption

Far more complete petrogenetic studies for Paraná-Etendeka low-Ti silicic melts were developed, for example, by Mantovani et al. (1985), Garland et al. (1995), Peate (1997) and Ewart et al. (2004). In general, crystal fractionation of low-Ti Gramado magma-types associated to the assimilation of continental crust is a model that efficiently explains the major, trace element and isotopic composition of the silicic rocks. Although melting of mafic basement or underplated low-Ti basalts is too advocated (e.g. Bellieni et al., 1986; Harris et al. 1990; Harris and Milner, 1997). Kilpatrick and Ellis (1992) found the chemical composition of the Paraná-Etendeka silicic volcanics very close to igneous charnockites generated by high-temperature crustal melting, suggesting they are not related to the spatially associated flood basalts. Indeed, trace elements, Sr-Nd isotopic compositions of both silicic and mafic magmas are only explained by vast array of crustal contamination (Garland et al., 1995; Ewart et al., 2004; Barreto et al., 2016). In addition, oxygen isotopic compositions are only explained if the low-Ti silicic magmas are considered approximately pure crustal melts (Harris et al., 1990; Harris and Milner, 1997).

As confirmed in this study by mass balance and AFC modelling, Palmas-type magma compositions deriving from underlying low-Ti basalts and basaltic andesites generally yield at a good fit at 40-60% of fractionation and 20% of basement assimilation (e.g. Garland et al., 1995). The resemblance of trace and rare earth elements behavior of Vale do Sol Formation rubbly pahoehoe basaltic andesites and the low-Ti volcanics is another argument for their conjugate evolution (see **Fig 13**). Similar fractionation-assimilation proportions were also observed for basaltic andesites fractionation from underlying more primitive basalts. Geochemical models supported by Sm-Nd isotopic studies reveal they also need several distinct proportions of Paleoproterozoic to Neoproterozoic mafic and felsic assimilation (e.g. Barreto et al., 2016). Even though, participation of open-system like processes during fractionation is not discarded. Another important geochemical feature to consider in the petrogenesis is that plagioclase, pyroxenes and Fe-Ti oxide compositions overlap their parent basalt and basalt andesite (e.g. Bellieni et al., 1984; Bellieni et al., 1988; Garland et al., 1995).

Based on this and in the fractional crystallization models for underlying compound, ponded and rubbly pahoehoe, we explain the origin of the silicic low-Ti melts from large-scale crystal fractionation of their precursors in the lava pile and assimilation of basement rocks with a wide range of age and chemical/isotopic compositions, as already pointed out by Peate (1997), Garland (1995) and Ewart (1994). Melting of underplated dry eclogite, as proposed by Anderson (2005) for LIP formation, is not discarded to act together with melting of

728 the upper mantle near the base of the crust because of the lower eclogite solidus (~1200°C at 2MPa), compared
729 to lherzolite (~1400°C at 2MPa).

730

731 *4.3 Tectonic setting during lava eruption*

732 According Philipp et al. (2016), the Proterozoic basement exposed in southern Brazil is composed, from east to
733 west, of: (1) a granitic belt with few basement remnants (Pelotas Batolith, Neoproterozoic), (2)
734 Metassedimentary units with minor metagranitoids and orthogneisses (Tijucas Belt, Paleo-Neoproterozoic); (3)
735 tonalite-granite-granodiorite and metaultramafic sequences of arc setting (São Gabriel Terrane, Neoproterozoic)
736 and (4) Mafic and felsic granulites from Taquarembó Terrane (Paleoprotrozoic). The contacts between terranes
737 are dominantly by NE-SW major shear zones as Dorsal de Canguçu and Passo dos Marinheiros besides the
738 NW-trending Ibaré (e.g. Picada, 1971; Fernandes et al., 1995; Chemale Jr, 2000; Philipp et al., 2016). Following
739 the main Neoproterozoic orogenic events, the cratonization of western Gondwana, in the beginning of Cambrian,
740 was marked by crustal displacements at NE-trending transcurrent shear zones, opening spaces for marine,
741 fluviatile and aeolian sediment deposition accompanied by shoshonitic to alkaline magmatism within the
742 Camaquã Basin (Lima & Nardi, 1998; Bitencourt & Nardi, 2000; Chemale Jr., 2000; Hartmann et al., 2007;
743 Philipp et al. 2016).

744 After the post-collisional tectonic stabilization, the intracratonic sedimentation of the Paraná Basin (e.g. Allen and
745 Armitage, 2012) started in the Ordovician. The geodynamic within the active margin of Gondwana influenced the
746 Paleozoic and Mesozoic evolution of the basin. Integrated analysis of the basin subsidence confronted to great
747 orogenic episodes in the continental margin revealed relation between them and the depositional space creation
748 cycles (Milani et al., 2007). Zalán et al. (1990) interpret the thermal contraction succeeding tectonomagmatic
749 events during the Brasiliano Cycle as an important mechanism for the syneclise implantation. The thermo-
750 mechanical model of Quintas et al. (1999) indicate that major tectonic subsidence epidodes occurred during
751 Permian, with a mean value of 50 m/My, growing in time from the deposition of Palermo Formation (30m/My) to
752 the deposition of Rio do Rasto Formation (92m/My). Triassic sequences of southern Paraná Basin were
753 developed during reactivation of NW-SE structures, later again reactivated in the Cretaceous as normal faults by
754 NE-trending extension (Zerfass et al., 2005). During Cretaceous, after a long period of marine followed by
755 continental sedimentation, there was a peak of the Andine chain uplifting (e.g. Karl et al., 2013) in the west
756 board of Gondwana, while continental crust extension accompanied by voluminous basaltic and silicic volcanism
757 dominated within the continent forming the Paraná-Etendeka LIP.

758 Several works regarding the origin of the Paraná-Etendeka LIP enormous hot magma output ascribed its
759 genesis to the action of a mantle plume, generally related to the Tristan da Cunha hot spot (e.g. Hawkesworth et
760 al., 1992; Peate, 1997; Condie, 2001; Campbell, 2005; Gibson et al., 2006; Natali et al., 2018). Usually the
761 authors assume the work of the plume leading to continental stretching and consequent break-up (e.g. Gallagher
762 and Hawkesworth, 1994) with the magma intrusion following reactivation of older faults (e.g. Valente et al.,
763 2007). On the other hand, seismic-tomographic investigations have pointed out to a minor role of mantle plume
764 (e.g. Fromm et al., 2015) and magnetotelluric data interpretation propose the absence of a plume structure
765 under the Tristan da Cunha island (Baba et al., 2016). Geochemical evidence is also recently putting in doubt

766 the role of mantle plumes in the generation of high-Ti melts from the northern portion of the Paraná-Etendeka
767 LIP (Rocha-Júnior et al., 2012, 2013), and for basalts from Central Atlantic and also Ferrar provinces (e.g. Hole,
768 2015), for example.

769 Anisotropy of magnetic susceptibility (AMS) studies developed in dyke swarms (e.g. Raposo, 2017; Wiegand et
770 al., 2011), in silicic lava flows and conduits (Cañón-Tapia and Raposo, 2017; Guimarães et al., 2017) indicate
771 preferred NE-SW and NW-SE trends for magma flow, parallel to the dyke strikes. This is in agreement with the
772 AMS study of Glenn et al. (1997), in dykes and lava flows in the both Brazilian and Namibian sides of the LIP,
773 also presenting dominant NE-SW trending of the magnetic fabric, suggesting lava flow emplacement during a
774 rifting phase. Rifting chronology of interpreted seismic sections positioned parallel to the Torres valley made by
775 Stica et al. (2014) affirm the deposition of the Paraná-Etendeka volcanics only in a pre-rift stage, minimizing the
776 effects of the province being causative of West Gondwana rupture and break-up. Although paleomagnetic data
777 interpretation of Collier et al. (2017) point out the Paraná-Etendeka volcanics as coeval to linear anomalies
778 present in the oceanic crust at South Altantic off-shore.

779 McKenzie and Bickle (1988) demonstrated that, the amount of melt generated in basins with associated
780 volcanism depends on the potential temperature of the asthenosphere and the amount of extension. It is given
781 that normal asthenosphere temperatures are ~1280°C, and the additional temperature of 100°C would be
782 needed to generated 2 km of melt in a 100 km-thick lithosphere stretched by a factor of 2 (Allen and Allen,
783 2009). The reconstruction model of Foulguer (2017) for the province at 134 Ma requires ~150 km of dextral slip
784 and ~70 km of extension between Santos and Rio de La Plata blocks, and proposing the magmatism would be
785 formed by rifting spread as in the North Atlantic Province. These recent models of Foulguer (2010, 2017) explain
786 elegantly how tectonic stretching, as response for an orogenic event in the craton margin, can be responsible for
787 mantle upwelling confined to the upper mantle, thus not restricting heat anomalies to the lower mantle.

788

789 *4.4 Storage, magma transport and emplacement conditions*

790 Mineral chemistry of pyroxene crystals in this study and equilibrium tests between pyroxenes and liquid present
791 in Polo et al. (2017) suggest pressures of formation (~1.5-9 kbar) equivalent to depths of ~10-30 km for this
792 phase in low-Ti silicic rocks. As postulated by Bellieni et al. (1988), the Mg content of pyroxenes from silicic
793 volcanics is relatively high and the pyroxene compositions plot essentially in the same fields corresponding to
794 pyroxenes from the andesi-basalts and andesite, so the same depth of formation can be inferred to mafic melts.
795 This depth represents, like demonstrated in the model of Molina et al. (1988), for example, the position of a
796 reservoir ponded in the mantle-crust boundary.

797 **Figure 16a** presents a sketch with the model of transport from this source. The magma crosses the crust
798 facilitated by tectonic movements during crustal necking and migrates through the opening of spaces into the
799 transcrustal basement faults, and then through major basin faults. Progressive stretching of continental crust
800 started with accommodation of the major blocks and reactivation of the Neoproterozoic and basin faults (**Fig.**
801 **16a-i**). Primitive olivine-phyric basalts from Torres Formation are generated by mantle melting driven by
802 decompression and increasing mantle temperatures (**Fig. 16a-ii**). The reservoir is kept in high temperature, then
803 higher melting degrees, fractional crystallization plus constant assimilation of the base of continental crust

generated thick basaltic-andesite units from Vale do Sol Formation in few thousands, or at maximum ~1-2 Ma (**Fig. 16a-iii**). After a period of huge Fe-Ti oxide crystallization in mafic magmas, silicic melts become more stable (e.g. Melfi et al., 1988; Peate, 1997) and the magma continue erupting from faults trending NE-/NW- (**Fig. 16a-iv**), fractionating and assimilating country-rocks (**Fig. 16a-v, b**). This high-temperature silicic magma ascended through paths, from the reservoir to the surface, which became shorter and shorter due to progressive stretching. The following scenario is the continental break-up and generation of oceanic crust, with rift phase dominated by magma-rich passive margin basins. **Figure 16a-v** is a compilation of recent seismic data interpretation made by Stica et al. (2014) in the coast of Rio Grande do Sul (Brazil) and Bauer et al. (2000) in the Cape Cross transect (Namibia), with oceanic crust minimized in the cartoon, showing that actual margins have possible zones of underplating.

Considering the fine textures in mafic and silicic volcanics, it is evident that there was a very short time for crystals to grow. In addition to that, another latent fact is the short time for the emplacement of the entire Paraná-Etendeka LIP magmatism. In southeast and southern Brazil, it have been estimated to be in ~ 3 Ma (e.g. Janasi et al., 2011), and in Namibia it is estimated to last ~4 Ma (e.g. Dodd et al., 2015). These arguments imply that a plumbing system remained connected and constantly draining the subaerial eruptions, until the final silicic manifestation.

Besides high eruptive temperatures >1000°C, another consensus in literature is the low dissolved water contents (<2 wt.%) for silicic volcanics in the LIP (e.g. Garland et al., 1995; Polo et al., 2017; this study). This is in agreement with the absence of magmatic hydrous phases such as amphibole. The ascending magma with low dissolved water contents taken place in a progressive extensional regime makes the existent gas to scape very efficiently (e.g. Cashman, 2004, **Fig. 16c**). In subsurface, shallow conduits of magma were tectonically controlled, and the paths of volatile loss described in inferred conduits such as brecciation, welding and fracturing (**Fig. 16d1**) prevented explosive eruptions (Lima et al., 2012; Simões et al., 2017; Lima et al., 2018).

The lavas present closed-system vesicle architecture paths (Simões et al., 2018, *in press*), since there was no development of an upper breccia carapace (**Fig. 16d2**). Field and AMS data obtained in sites at São Marcos and Gramado Xavier regions have pointed out to the presence of channelized flows (e.g. Canõn-Tapia and Raposo, 2017; Guimarães et al., 2017). Plagioclase-liquid temperatures estimated from the chemistry of microlites, present only in lava flows, yielded temperatures of ~ 950°C, suggesting that the lava body kept the high temperature conditions during emplacement.

In our samples, the water dissolved in the magma, with contents up to ~ 0.5-1.3 wt.%, is favorable to decrease viscosity to values of ~ $10^{3.5}$ Pa s, being a key factor to keep the flow running to long distances. Considering closed-system lavas with well-insulated carapaces (c.f. Harris and Rowland, 2009), for example, these silicic flows may attain even greater distances than expected for these viscosities. The crystallization of anhydrous microlite assemblage should increase the relative water content of the lavas during emplacement, thus decreasing viscosity even more. As anorther example of low viscosity lavas, values near $10^{3.5}$ Pa s were also suggested to the emplacement of >100 km in length silicic lobate flows of the Gawler Range Silicic LIP, making these silicic sequences geometrically similar to the basaltic provinces. In their specific case, the A-type geochemical affinity of the lavas and consequent high fluorine content was the more relevant geochemical feature to decrease the lava viscosity (Agangi et al., 2011; Pankhurst et al., 2011).

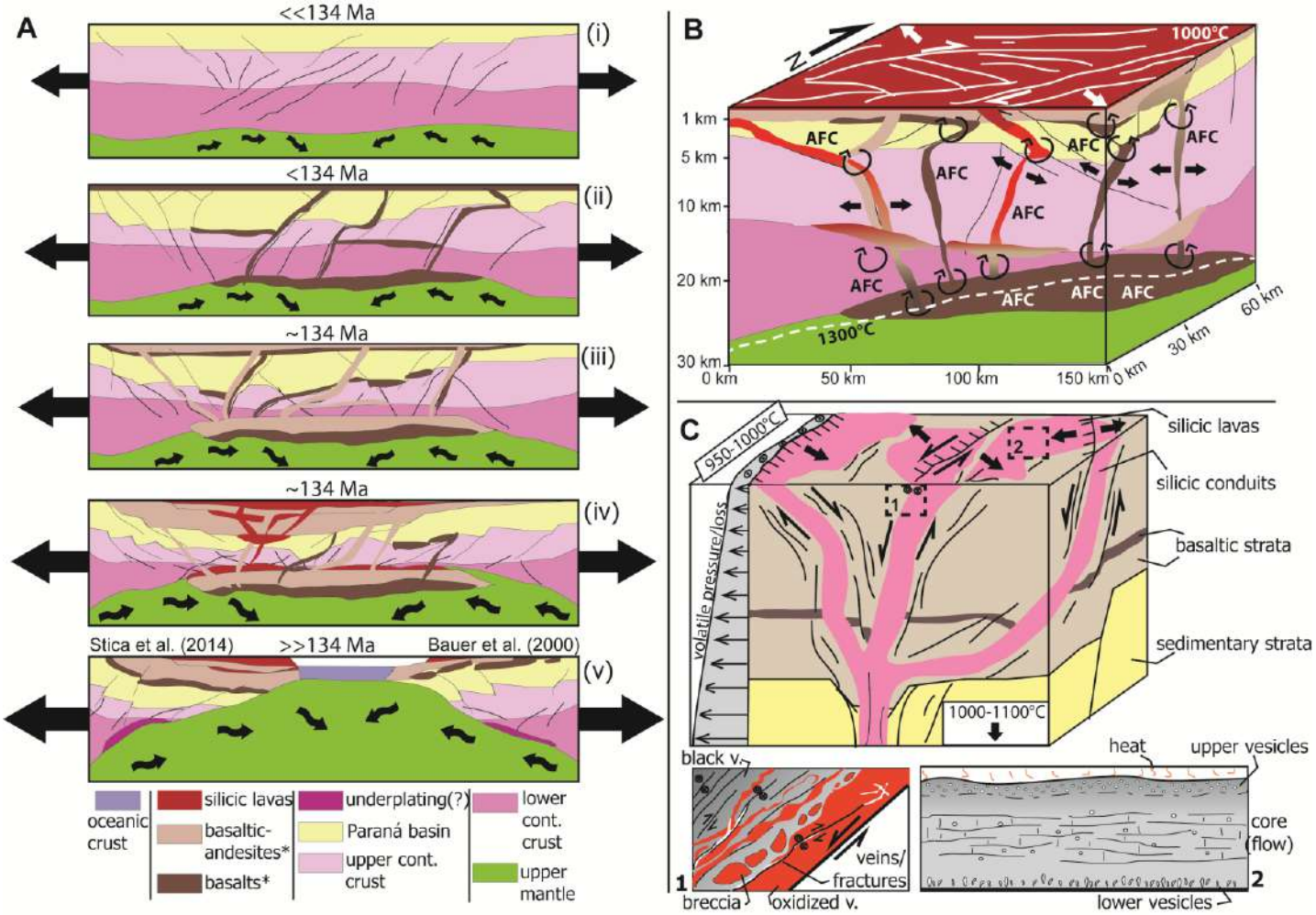

Figure 16 – Tectonic and emplacement models for low-Ti silicic volcanics from the Paraná-Etendeka LIP. (A) Continental break-up evolution before and after ~134 Ma, the age assumed for silicic volcanics. From (i) to (v) the increasing rates of extension from (i) to (v) are represented by the sizes of the lateral arrows. Anomalous heat of the rising mantle, as response of extension, is represented by curved arrows into the sketch. The final cartoon is a compilation of actual seismic data interpretation at the Brazilian side (extracted from Stica et al., 2014) and in the Namibian side (extracted from Bauer et al., 2000). (B) Slightly approximation of figure A-iv showing the 1,300°C mantle adiabat under extension in the mantle-crust boundary. Arrows indicate sites where AFC processes may have occurred. (C) Proximal model simulating the spread of a conduit though normal and oblique faults during extension and the decrease of volatile pressure. (D) 1-model of the magma flow within the shallow portion of conduits; 2-Schematic draw of the main parts of silicic lava flows and representation of heat loss.

The most known cases of large-volume silicic volcanism, is ascribed to plinian eruptions and large amounts of ignimbrite succeeded by emplacement of small-volume coulées or domes (Branney et al., 2008), being capable of regional obliteration and climatic perturbation (e.g. Sparks et al., 2005). In the case of LIPs, global environment may be impacted by eruptive release of gas and aerosols like SO_2, CO_2 and halogens (Saunders, 2005; Self, 2005). The role of silicic volcanism in this theme has been brought to explain the end-Guadalupian mass extinction in the Emeishan LIP, where silicic pyroclastic beds are thought to participate in the climate changes (e.g. Xu et al., 2016). On contrary of Emeishan, Central Atlantic, and Deccan provinces, the Brazilian side of Paraná-Etendeka LIP does not correlate with great mass extinctions. Although investigation of SO_2, CO_2, CH_4, F and Cl mass fluxes for mafic and silicic volcanics are not available yet, we argue the effusive behavior of

the silicic eruptions can minimize climate impact, if compared with dominant explosive eruptions, avoiding large amount of particles rise up in an eruptive column, reach the stratosphere and disperse.

Conclusions

Large-volume lavas were the prevalent deposit of silicic volcanism in southern Brazil. Our study in three key areas of low-Ti Caxias do Sul magma sub-types revealed mineralogic composion varies from west, where calcic plagioclase and less ferric pyroxenes are more common to east, where sodic plagioclases and ferric pyroxenes are present. Differences in trace element geochemical features are ascribed to variation in mantle-derived sources and crustal assimilant compositions. Low-Ti silicic volcanics are derived from fractional crystallization of underlying basaltic andesite and assimilation of various lithologies, different in chemical and isotopic composition. Values near 40-50% of fractionation and 40-80% of assimilation, generating the same proportions of mineral assemblages observed in thin sections, agree with previous models for silicic and mafic lavas.

The magmatism of Paraná-Etendeka LIP has taken place during early extensional movements of the Gondwana Supercontinent, probably in response to subduction at its margins. Since that, constriction processes responding to a dominant NE-SW extension caused the necking of the continental crust and allowed large amounts of basaltic and silicic magma to achieve the surface. The source of melted mantle could be achieved by decompression melting, reaching the 1,300°C adiabat. The emplacement of silicic low-Ti units in the southern part of the LIP was the last volcanic episode within the southern Paraná basin, culminating in the separation of the continent, believed to have begun at <134 Ma. Absence of important pyroclastic units within the volcanic pile was a fundamental feature for reducing the climate impact of silicic eruptions.

Acknowledgements

The authors thank *Conselho Nacional de Desenvolvimento Científico e Tecnológico* (CNPq, projects 9784, 441766/2014-5, 303015/2015-2 and 400724/2014-6), FAPESP (project 2012/06082-6) and FAPERGS (project 2311-2551/14-1) for funding.

REFERENCES

Agangi, A., Kamenetsky, V.S., McPhie, J. 2012. Evolution and emplacement of high fluorine rhyolites in the Mesoproterozoic Gawler silicic large igneous province, South Australia. Precambrian Research, 208-211, 124-144.

Allen, P. A., Armitage, J.J. 2012 Cratonic basins. In: Tectonics of Sedimentary Basins: Recent Advances. Eds.: Busby, C., Azor, A. Blackwell Publishing Ltd.

Allen, P.A., Allen, J.R. 2009. Basin analysis: principles and applications, Blackwell.

Anderson, D. L. 2005. Large Igneous Provinces, Delamination and Fertile Mantle. Elements, 1, 271-275.

Andrade, F.R.D., Polo, L.A., Janasi, V.A., Carvalho ,F.M.S.C. 2017. Volcanic glass in Cretaceous dacites and rhyolites of the Paraná Magmatic Province, Southern Brazil: Characterization and quantification by XRD-Rietveld. Journal of Volcanology and Geothermal Research, in press.

Baba, K., J. Chen, Ma. Sommer, H. Utada, W. H. Geissler, W. Jokat, M. Jegen. (2016), Marine magnetotellurics imaged no distinct plume beneath the Tristan da Cunha hotspot in the southern Atlantic Ocean, Tectonophysics,

903 Bacon, C.R., Druitt, T.H. 1988. Compositional Evolution of the Zoned Calcalkaline Magma Chamber of Mount-
904 Mazama, Crater Lake, Oregon. Contributions to Mineralogy and Petrology 98(2), 224-256.

905 Barreto, C.J.S., Lafon, J.M., Lima, E.F., Sommer, C.A. 2016. Geochemical and Sr-Nd-Pb isotopic insight into the low-
906 Ti basalts from Southern Paraná Igneous Province, Brazil: the role of crustal contamination. International Geology
907 Review, 58, 1324-1349.

908 Barreto, C.J.S., Lima, E.F., Scherer, C.M.S., Rossetti, L.M.M. 2014 Lithofacies analysis of basic lava flows of the
909 Paraná igneous province in the south hinge of Torres Syncline, Southern Brazil. J. Volcanol. Geoth. Res. 285, 81-99
910 (DOI: 10.1016/j.jvolgeores.2014.08.008).

911 Bauer, K., Neben, S., Schreckenberger, B., Emmermann, R., Hinz, K., Fechner, N., Gohl, K., Schulze, A., Trumbull, R.
912 B. & Weber, K. 2000. Deep structure of the Namibia continental margin as derived from integrated geophysical
913 studies. Journal of Geophysical Research, vol. 105, B11, 25829-25853.

914 Bellieni G., Brotzu, P., Comin-Chiaramonti, P., Ernesto, M., Melfi, A.J., Pacca, I.G., Piccirillo, E.M., Stolfa, D. 1984.
915 Flood basalt to rhyolite suites in the southern Paraná plateau (Brazil): paleomagnetism, petrogenesis and geodynamic
916 implications. J. Petrol. 25, 579-618 (DOI: 10.1093/petrology/25.3.579).

917 Bellieni, G., Brotzu, P., Comin-Chiaramonti, P., Ernesto, M., Melfi, A.J., Pacca, I.G., Piccirillo, E.M., Stolfa, D. 1983.
918 Petrological and paleomagnetic data on the plateau basalt to rhyolite sequences of the Southern Paraná Basin
919 (Brazil). An. Acad. Bras. Cienc. 55, 355-383.

920 Bellieni, G., Comin-Chiaramonti, P., Marques, L.S., Melfi, A.J., Nardy, A.J.R., Papatrechas, C., Piccirilo, E.M.,
921 Roisenberg, A. 1986. Petrogenetic aspects of acid and basaltic lavas from Paraná Basin (Brazil): geological,
922 mineralogical and petrochemical relationships. J. Petrol. 27, 915-944 (DOI: 10.1093/petrology/27.4.915).

923 Bellieni, G., Piccirillo, E.M., Comin-Chiaramonti, P., Melfi, A.J., Da Roit, P. 1988. Mineral chemistry of continental
924 stratoid volcanics and related intrusives from the Paraná Basin (Brasil). In: Piccirillo, E.M., Melfi, A.J. (Eds.) The
925 Mesozoic flood volcanism of the Paraná Basin: petrogenetic and geophysical aspects. São Paulo, Instituto
926 Astronômico e Geofísico.

927 Bitencourt, M.F. & Nardi, L.V.S. 2000. Tectonic setting and sources of magmatism related to the Southern Brazilian
928 Shear Belt. Revista Brasileira de Geociências, 30:184-187.

929 Bosi, F., Halenius, U., Skogby, H. 2009. Crystal chemistry of the magnetite-ulvöspinel series. American Mineralogist,
930 94, 181-189.

931 Bowen, N.L. (1913) The melting phenomena of the plagioclase feldspar. American Journal of Science, 35, 577–599.

932 Boynton, W.V., 1984, Geochemistry of the rare earth elements: Meteorite studies, in Henderson, P., ed., Rare earth
933 element geochemistry, Volume 63: Amsterdam, Elsevier, p. 114.

934 Branney M.J., Bonnichsen B., Andrews G.D.M., Ellis B., Barry T.L., McCurry M. 2008. “Snake River (SR)-type”
935 volcanism at the Yellowstone hotspot track: distinctive products from unusual, high-temperature silicic super-
936 eruptions. Bulletin of Volcanology: 70(3), 293-314.

937 Bryan, S.E., Ernst, R.E. 2008 Revised definition of Large Igneous Provinces (LIPs). Earth Sci. Rev. 86, 175–202.

938 Bryan, S.E., Peate, I.U., Peate, D.W., Self, S., Jerram, D.A., Mawby, M.R., Marsh, J.S., Miller, J.A. 2010. The largest
939 volcanic eruptions on Earth. Earth Sci. Rev. 102(3-4), 207-229.

940 Bryan, S.E., Riley, T.R., Jerram, D.A., Stephens, C.J., Leat, P.T. 2002. Silicic volcanism: an undervalued component
941 of large igneous provinces and volcanic rifted margins. Special Papers-Geological Society of America: 97-118.

942 Buiter, S.J.H., Torsvik, T.H., 2014. A review of Wilson Cycle plate margins: a role for mantle plumes in continental
943 break-up along sutures? Gondwana Research 26, 627–653.

944 Campbell, I.H. 2005. Large Igneous Provinces and the Mantle Plume Hypothesis. Elements, 1, 265-269.

945 Cañón-Tapia, E., Raposo, M.I.B. 2017. Anisotropy of magnetic susceptibility of silicic rocks from quarries in the vicinity
946 of São Marcos, Rio Grande do Sul, South Brazil: Implications for emplacement mechanisms. J. Volcanol. Geoth. Res.
947 In press.

948 Cashman, K.V., 2004. Volatile controls on magma ascent and eruption. Geophysical Monograph,150 (19),109–124.

949 Channell, J.E.T., Cecca, F., and Erba, E., 1995b, Correlations of Hauterivian and Barremian (Early Cretaceous) stage
950 boundaries to polarity chrons: Earth and Planetary Science Letters, v. 134, p. 237–252.

951 Chemale Jr. F. 2000. Evolução Geológica do Escudo Sul-Rio-Grandense. : Holz M., De Ros L.F. (eds.) Geologia do
952 Rio Grande do Sul . Editora UFRGS, Porto Alegre, p. 13-52.

953 Coffin, M.F., Eldholm, O. 1994. Large Igneous Provinces: crustal structure, dimensions and external consequences.
954 Reviews of Geophysics 32,1-36.

955 Collier, J.S., McDermott, C., Warner, G., Gyori, N., Schnabel, M., McDermott, K., Horn, B.W., 2017. New constraints
956 on the age and style of continental breakup in the South Atlantic from magnetic anomaly data. Earth Planet. Sci. Lett.
957 477, 27–40.

958 Comin-Chiaramonti, P., Bellieni, G., Piccirillo, E.M., Melfi, A.J. 1988. Classification and petrography of continental
959 stratoid volcanic and related intrusive from the Paraná Basin (Brasil). In: Piccirillo, E.M., Melfi, A.J. (Eds.) The
960 Mesozoic flood volcanism of the Paraná Basin: petrogenetic and geophysical aspects. São Paulo, Instituto
961 Astronômico e Geofísico.

962 Comin-Chiaramonti, P., Riccomini, C., Slejko, F., De Min, A., Ruberti, E., Gomes, C.B. 2010. Cordierite-bearing lavas
963 from Jaguarão, Southern Brazil: Petrological evidence for crustal melts during early rifting of Gondwana. Gondwana
964 Research, 18: 514-527.

965 Condie, K.C. 2001. Mantle Plumes and Their Record in Earth History. Oxford, UK: Cambridge Univ. Press. 306 pp.

966 Condie, K. C. 1997. Plate Tectonics and Crustal Evolution, 282 pp. Oxford: Butterworth/Heinemann.

967 De La Roche, H., Leterrier, J., Grandclaude, P., Marchal, M. 1980. A classification of volcanic and plutonic rocks using
968 R1R2-diagram and major element analyses – its relationships with current nomenclature. Chem. Geol. 29, 183–210.
969 (DOI: 10.1016/0009-2541(80)90020-0).

970 Dodd, S.C., Niocaill, C.M., Muxworthy, A.R. 2015. Long duration (>4 Ma) and steady-state volcanic activity in the early
971 Cretaceous Paraná-Etendeka Large Igneous Province: New paleomagnetic data from Namibia. Earth and Planetary
972 Science Letters, 414, 16-29.

973 Drake, M.J. (1976) Plagioclase-melt equilibria. Geochimica et Cosmochimica Acta, 40, 457–465.

974 Eldholm, O., Thiede, J., and Taylor, E., 1989. Evolution of the Vøring volcanic margin. In Eldholm, O., Thiede, J.,
975 Taylor, E., et al. (Eds.), Proc. ODP, Sci. Res., 104. College Station, Texas (Ocean Drilling Program), 1033–1065.

976 Ellis, B.S., Wolff, J.A. 2012. Complex storage of rhyolite in the central Snake River Plain. Journal of Volcanology and
977 Geothermal Research, 211-212, 1-11.

978 Ellis, B.S., Wolff, J.A., Boroughs, S. Mark, D.F., Starkel, W.A., Bonnichsen, B. 2013. Rhyolitic volcanism of the central
979 Snake River Plain: a review. Bulletin of Volcanology, 75, 745.

980 Ewart, A., Griffin, W.L. 1994. Application of Proton-Microprobe Data to Trace-Element Partioning in Volcanic-Rocks.
981 Chemical Geology, 117(1-4), 251-284.

982 Ewart, A., Marsh, J.S., Milner, S.C., Duncan, A.R., Kamber, B.S., Armstrong, R.A. 2004. Petrology and Geochemistry
983 of Early Cretaceous Bimodal Continental Flood Volanism of the NW Etendeka, Namibia. Part 2: Characteristics and
984 Petrogenesis of the High-Ti Latite and High-Ti and Low-Ti Voluminous Quartz Latite Eruptives. Journal of Petrology,
985 45(1), 107-138.

986 Fernandes, L.A.D., Menegat, R., Costa, A.F.U., Koester, E., Porcher, C.C., Tommasi, A., Kraemer, G., Ramgrab,
987 G.E., Camozzato, E. 1995. Evolução tectônica do Cinturão Dom Feliciano no Escudo Sul-Rio-Grandense: Parte II –
988 uma contribuição a partir das assinaturas geofísicas. Rev. Bras. Geosci. 25(4), 375-384.

989 Florisbal, L.M., Heaman, L.M., Janasi, V.A., Bitencourt, M.F. 2014. Tectonic significance of the Florianópolis Dyke
990 Swarm, Paraná-Etendeka Magmatic Province: A reappraisal based on precise U-Pb dating. J. Volc. Geoth. Res. 289,
991 140-150. (DOI: 10.1016/j.jvolgeores.2014.11.007).

992 Florisbal, L.M., Janasi, V.A., Bitencourt, M.F., Nardi, L.V.S., Marteleto, N.S. 2017. Geological, geochemical and
993 isotope diversity of ~134 Ma dykes from the Florianópolis Dyke Swarm, Paraná Magmatic Province: Geodynamic
994 controls on petrogenesis. Journal of Volcanology and Geothermal Research, in press.

995 Foulger, G.R.. 2010. Plates vs Plumes: A Geological Controversy.Wiley-Blackwell, Chichester,U.K.

996 Foulguer, G.R. 2017. Origin of the South Atlantic igneous province. Journal of Volcanology and Geothermal Research,
997 in press.

998 Fromm, T., Planert, L., Jokat, W., Ryberg, T., Behrmann, J.H., Weber, M.H., Haberland, C.,2015. South Atlantic
999 opening: a plume-induced breakup? Geology 43, 931–934.

000 Gallagher, K., Hawkesworth, C.J. 1994. Mantle plumes, continental magmatism and asymmetry in the South Atlantic.
001 Earth and Planetary Science Letters, 123, 105-117.

002 Garland, F.E., Hawkesworth, C.J., Mantovani, M.S.M. 1995. Description and petrogenesis of the Paraná rhyolites. J.
003 Petrol. 36, 1193–1227.(DOI: 10.1093/petrology/36.5.1193).

004 Gibson, S.A., Thompson, R.N., Day, J.A., 2006. Timescales and mechanisms of plume–lithosphere interactions:
005 40Ar/39Ar geochronology and geochemistry of alkaline igneous rocks from the Paraná–Etendeka large igneous
006 province. Earth Planet. Sci. Lett. 251, 1–17.

007 Giordano, D., Russell. J.K., Dingwell, D.B. 2008. Viscosity of magmatic liquids: A model.Earth and Planetary Science
008 Letters, 271:123-134.

009 Glenn, J.M.G., Renne, P.R., Milner, S.C., Coe, R.S. 1997. Magma flow inferred from anisotropy of magnetic
010 susceptibility in the coastal Paraná-Etendeka igneous province: Evidence for rifting before flood volcanism. Geology,
011 12, 1131-1134.

012 Green, T.H., Die, S.H., Ryan, C.G., Cousens, D.R. 1989. Proton microprobe-determined portioning of Nb, Ta, Zr and
013 Y between garnet, clinopyroxene and basaltic magma at high pressure and temperature. Chemical Geology, 74, 201-
014 216.

015 Guimarães, L.F., Raposo, M.I.B., Janasi, V.A., Cañón-Tapia, E., Polo, L.A. 2017. An AMS study of different silicic
016 units from the southern Paraná-Etendeka Magmatic Province in Brazil: implications for the identification of flow
017 directions and local feeding. J. Volcanol. Geoth. Res. this issue.

018 Harris, A., Rowland, S. 2009. Effusion rate controls on lava flowlength and the role of heat loss: a review. In:
019 Thordarson, T., Self, S., Larsen, G., Rowland, S.K., Hoskuldsson, A. (eds.), Studies in Volcanology: The Legacy of
020 George Walker. Special Publications of IAVCEI, p. 33–51.

021 Harris, C., Milner, S. 1997. Crustal Origin for the Paraná Rhyolites: Discussion of 'Description and Petrogenesis of the
022 Paraná Rhyolites, Southern Brazil' by Garland et al. (1995). Journal of Petrology, 38(2), 299-302.

023 Harris, C., Whittingham, A.M., Milner, S.C., Armstrong, R.A. 1990. Oxygen isotope geochemistry of the silicic volcanic
024 rocks of the Etendeka/Paraná Province: source constraints. Geology 18, 1119-1121.

025 Harrison, T. M., Watson, E. B. 1984. The behaviour of apatite during crustal anatexis: equilibrium and kinetic
026 considerations. Geochimica et Cosmochimica Acta, 48(7):1467-1477.

027 Hartmann, L.A., Chemale Jr., F., Philipp, R.P., 2007. Evolução geotectônica do Rio Grande do Sul no Precambriano.
028 In: Ianuzzi, R., Frantz, J.C. (Eds.), 50 Anos de Geologia. Instituto de Geociências. Contribuições. Edit. Comunicação
029 e Identidade- CIGO-IG-UFRGS, Porto Alegre, pp. 97e123.

030 Hawkesworth, C.J., Gallagher, K., Kelley, S., Mantovani, M., Peate, D.W., Regelous, M., Rogers, N.W. 1992. Parana
031 magmatism and the opening of the South Atlantic. Geological Society of London, Spec. Publ. 68(1): 221–240.

032 Henry, C.D., Wolff, J.A. 1992. Distinguishing strongly rheomorphic tuffs from extensive silicic lavas. Bull. Volcanol. 54,
033 171-186.

034 Hole, M. J. 2015. The generation of continental flood basalts by decompression melting of internally heated
035 mantle. Geology, 43 (4): 311-314.

Housh, T.B., and Luhr, J.F. 1991. Plagioclase-melt equilibria in hydrous systems. American Mineralogist, 76, 477–492.

Humphreys, M.C.S. 2016. The validity of plagioclase-melt geothermometry for degassing-driven magma crystallization. American Mineralogist, 101, 769-779.

Janasi, V.A., de Freitas, V.A., Heaman, L.H., 2011. The onset of flood basalt volcanism, Northern Paraná Basin, Brazil: a precise U–Pb baddeleyite/zircon age for a Chapecó type dacite. Earth and Planet Science Letters. 302 (1–2): 147–153.

Janasi, V.A., Montanheiro, T.J., Freitas, V.A., Reis, P.M., Negri, F.A., Dantas, F.A. 2007. Geology, petrography and geochemistry of the acid volcanism of the Paraná Magmatic Province in the Piraju-Ourinhos region, SE Brazil. Rev. Bras. Geosci. 37, 745-759.

Jerram, D., Mountney, N., Holzforster, F., Stollhofen, H., 1999. Internal stratigraphic relationships in the Etendeka group in the Huab Basin, NW Namibia: understanding the onset of flood volcanism. J. Geodyn. 28 (4–5), 393–418.

Johannes, W. 1984. Beginning of melting in the granite system Qz-Or-Ab-An-H2O. Contributions to Mineralogy and Petrology, 86, 264–273.

Johannes, W. 1984. Beginning of melting in the granite system Qz-Or-Ab-An-H_2O. Contributions to Mineralogy and Petrology, 86, 264–273.

Jones, A.P. 2005. Meteorite Impacts as Triggers to Large Igneous Provinces. Elements, 1, 277-281.

Jones, M.T., Jerram, D.A., Svensen, H.H., Grove, C. 2016. The effects of large igneous provinces on the global carbon and Sulphur cycles. Palaeo, 441 4-21.

Kamber, B.S., Collerson, K.D. 2000. Zr/Nb Systematics of Ocean Island Basalts Reassessed – the Case for Binary Mixing. Journal of Petrology, 41(7), 1007-1021.

Kamenetsky, V.S., Maas, R., Kamenetsky, M.B., Yaxley, G.M., Ehrig, K., Zellmer, G.F., Bindeman, I.N., Sobolev, A.V., Kuzmin, D.V., Ivanov, A.V., Woodhead, J., Schilling, J. 2017. Multiple mantle sources of continental magmatism: Insights from “high-Ti” picrites of Karoo and other large igneous provinces. Chemical Geology, 455, 22-31.

Karl, M., Glasmacher, U.A., Kollenz, S., Franco-Magalhaes, A.O.B., Stockli, D.F., Hackspacher, P.C. 2013. Evolution of the South Atlantic passive continental margin in southern Brazil derived from zircon and apatite (U-Th-Sm)/He and fission-track data. Tectonophysics, 604, 224-244.

Kilpatrick, J. A. & Ellis, D. J., 1992. C-type magmas: igneous charnockites and their extrusive equivalents. Transactions of the Royal Society of Edinburgh: Earth Sciences 83, 155–164.

Kirstein, L.A., Hawkesworth, C.J., Garland, F.G. 2001. Felsic lavas or rheomorphic ignimbrites: is there a chemical distinction? Contrib. Mineral. Petrol. 142, 309-322.

Kirstein, L.A., Peate, D., Hawkesworth, C., Turner, S., Harris, C., Mantovani, M. 2000. Early Cretaceous basaltic and rhyolitic magmatism in southern Uruguay associated with the opening of the South Atlantic. J. Petrol. 41, 1413-1438.

Krishnamurthy, P., Cox, K.G. 1977. Picrite basalts and related lavas from the Deccan Traps of Western India. Contributions to Mineralogy and Petrology, 1, 53-75.

Kudo, A.M., and Weill, D.F. (1970) An igneous plagioclase thermometer. Contributions to Mineralogy and Petrology, 25, 52–65.

Le Bas, M.J., Le Maitre, R.W., Zanettin, B., 1986. A chemical classification of volcanic rocks based on the total alkali e silica diagram. J. Pet. 27, 745e750.

Leeman, W.P. 1979. Partioning of Pb between volcanic glass and coexisting sanidine and plagioclase feldspars. Geochimica et Cosmochimica Acta, 43, 171-175.

Leeman, W.P., Phelps, D.W. 1981. Partioning of rare earths and other trace elements between sanidine and coexisting volcanic glass. Journal of Geophysical Research, 86.

Lima E.F. & Nardi L.V.S. 1998. The Lavras do Sul Shoshonitic Association: implications for the origin and evolution of Neoproterozoic shoshonitic magmatism in the southernmost Brazil. Journal of South American Earth Sciences, 11:67-77.

Lima, E.F., Philipp, R.P., Rizzon, G.C., Waichel, B.L., Rossetti, L.M.M. 2012 Sucessões Vulcânicas e Modelo de Alimentação e Geração de Domos de Lava Ácidos da Formação Serra Geral na Região de São Marcos-Antonio Prado (RS). Geologia USP Série Científica 12, 49-64.

Lima, E.F., Waichel, B.L., Rossetti, L.M.M., Sommer, C.A., Simões, M.S. 2018. Feeder systems of acidic lava flows from the Paraná-Etendeka Igneous Province in Southern Brazil and their implications for eruption style. J. South Am. Earth Sci. 81, 1-9.

Luchetti, A.C.F., Nardy, A.J.R., Machado, F.B., Madeira, J.E.O., Arnosio, J.M. 2014. New insights on the occurrence of peperites and sedimentary deposits within the silicic volcanic sequences of the Paraná Magmatic Province, Brazil. Solid Earth, 5:121-130.

Mantovani, M.S.M., Cordani, U.G., Roisenberg, A. 1985. Geoquímica isotópica em vulcânicas ácidas da Bacia do Paraná e implicações genéticas associadas. Revista Brasileira de Geociências, 15 (1), 61-65.

McKenzie, D. 1978. Some remarks on the development of sedimentary basins. Earth and Planetary Science Letters, 40: 25-32.

Melfi, A.J., Nardy, A.J.R., Piccirillo, E.M. 1988. Geological and magmatic aspects of the Paraná Basin: An introduction. In: Piccirillo, E.M., Melfi, A.J. (Eds.) The Mesozoic flood volcanism of the Paraná Basin: petrogenetic and geophysical aspects. São Paulo, Instituto Astronômico e Geofísico.

Milani, E.J., Melo, J.H.G., Souza, P.A., Fernandes, L.A., França, A.B. 2007. Bacia do Paraná. In: Boletim de Geociências da PETROBRAS: 15(2), 265-287.

Milner, S.C., Duncan, A.R., Whittingham, A.M., Ewart, A. 1995. Trans-Atlantic correlation of eruptive sequences and individual silicic volcanic units within Paraná- Etendeka Igneous Province. J. Volcanol. Geoth. Res. 69,137-157.

Molina, E.C., Ussami, N., de Sá, N.C., Blitzkow, D., Miranda Filho, O.F. Deep crustal structure under the Paraná Basin (Brazil) from gravity study. In: Piccirillo E. M., Melfi A. J. (eds). The Mesozoic flood volcanism of the Paraná Basin: petrogenetic and geophysical aspects. São Paulo, Instituto Astronômico e Geofísico, 600 p.

Mpodozis, C., Ramos, V.A., 2008. Tectónica Jurásica en Argentina y Chile: extensión, subducción oblicua, rifting, deriva y colisiones? Revista de la Asociación Geológica Argentina. 63(4), 481-497.

Muzio, R. Morales, E., Veroslavsky, G., Conti, B. 2009. The Arequita Formation (Lower Cretaceous): petrographic features of the volcanics facies in the Laguna Merín Basin, east Uruguay. Latin American Journal of Sedimentology and Basin Analysis, 16(1): 19-28.

Nardy, A.J.R., Machado, F.B., Oliveira, M.A.F. 2008. As rochas vulcânicas mesozoicas ácidas da Bacia do Paraná: litoestratigrafia e considerações geoquímicas-estratigráficas. Rev. Bras. Geosci. 38(1), 178-195.

Nash, W.P., Crecraft, H.R. 1985. Partition coefficients for trace elements in silicic magmas. Geochimica et Cosmochimica Acta, 49, 2309-2322.

Natali, C., Beccaluva, L., Bianchini, G., Siena, F. 2011. Rhyolites associated to Ethiopian CFB: Clues for initial rifting at the Afar plume axis. Earth and Planetary Science Letters, 312, 59-68.

Natali, C., Beccaluva, L., Bianchini, G., Siena, F. 2018. Coexistence of alcaline-carbonatite complexes and high-MgO CFB in the Paraná-Etendeka province: Insights on plume-lithosphere interactions in the Gondwana realm. Lithos, 296-299, 54-66.

O'Hara, M.J. 1977. Geochemical evolution during fractional crystallization of a periodically refilled magma chamber. Nature, 266.

Pankhurst, M.J., Schaefer, B.F., Betts, P.G., Phillips, N., Hand, M. 2011. A Mesoproterozoic continental flood rhyolite province, the Gawler Ranges, Australia: the end member example of the Large Igneous Province clan. Solid Earth. 2, 25-33.

124 Parfitt, E.A., Wilson, L. 2008. Fundamentals of Physical Volcanology. Blackwell Publishing.

125 Peate, D.W. 1997. The Paraná-Etendeka province. In: Mahoney, J.J., Coffin, M.R. (Eds.) Large Igneous Proovinces:
126 Continental, Oceanic and Planetary Flood Volcanism Geoph. Monog. 100, 217-245.

127 Peate, D.W., Hawkesworth, C.J., Mantovani, M.S.M. 1992. Chemical stratigraphy of the Paraná lavas (S. America):
128 classification of magma types and their spatial distribution. Bull. Volcanol. 55,119-139.

129 Petrelli, M., Poli, G., Perugini, D., Peccerillo, A. 2005. PetroGraph: A new software to visualiza, model, and
130 presente geochemical data in igneous petrology. Geochemistry, Geophysics, Geosystems, 6(7), 1-15.

131 Philipp, R.P., Lusa, M., Nardi, L.V.S., 2008. Geochemistry and petrology of dioritic, tonalitic and trondhjemitic gneisses
132 from Encantadas Complex, Santana da Boa Vista, southernmost Brazil: a Paleoproterozoic continental-arc
133 magmatism. Anais da Academia Brasileira de Ciências 80, 1e14.

134 Philipp, R.P., Massone, H., Campos, R.S. 2013. Peraluminous leucogranites of the Cordilheira Suite: A record of
135 Neoproterozoic collision and the generation of the Pelotas Batholith, Dom Feliciano Belt, Southern Brazil. Journal
136 of South American Earth Sciences, 43, 8-24.

137 Philipp, R.P., Pimentel, M.M., Chemale Jr., F. Tectonic evolution of the Dom Feliciano Belt in Southern Brazil:
138 Geological relationships and U-Pb geochronology. Brazilian Journal of Geology, 46(suppl 1), 83-104.

139 Picada, R.S. 1971. Ensaio sobre a tectônica do Escudo Sul-riograndense. Anais, 25° Congresso Brasileiro de
140 Geologia, São Paulo.

141 Piccirillo, E.M., Comin-Chiaramonti, P., Bellieni, G., Civetta, L., Marques, L.S., Melfi, A.J., Petrini, R., Raposo, M.I.B.,
142 Stolfa, D. 1988. Petrogenetic aspects of continental flood basalt-rhyolite suites from the Paraná Basin (Brazil). In:
143 Piccirillo, E.M., Melfi, A.J. (Eds.) The Mesozoic flood volcanism of the Paraná Basin: petrogenetic and geophysical
144 aspects. São Paulo, Instituto Astronômico e Geofísico.

145 Pinto, V.M., Hartmann, L.A., Santos, J.O.S., McNaughton, N.J., Wildner, W., 2011. Zircon U-Pb geochronolgy from
146 the Paraná bimodal volcanics province support a brief eruptive cycle at ~ 135 Ma. Chemical Geology. 1-2 (93-102).

147 Polo, L.A., Giordano, D., Janasi, V.A., Guimarães, L.F. 2017. Effusive silicic volcanism in the Paraná Magmatic
148 Province, South Brazil: Physico-chemical conditions of storage and eruption and considerations on the rheological
149 behaviour during emplacement. J. Volcanol. Geoth. Res., in press.

150 Polo, L.A., Janasi, V.A. 2014. Volcanic stratigraphy of intermediate to silicic rocks in Southern Paraná Magmatic
151 Province, Brazil. Geologia USP Série Científica 14, 83-100.

152 Prowatke S. & Klemme S. 2006. Trace element partitioning between apatite and silicate melts. Geochimica et
153 Cosmochimica Acta, 70:4513-4527.

154 Putirka, K.D. 2008. Thermometers and barometers for volcanic systems. Reviews in Mineralogy and Geochemistry,
155 69, 61–120.

156 Putirka, K.D. 2005. Igneous thermometers and barometers based on plagioclase + liquid equilibria: Tests of some
157 existing models and new calibrations. American Mineralogist, 90, 336–346.

158 Quintas, M.C.L., Mantovani, M.S.M., Zalán, P.V. 1999. Contribuição ao estudo da evolução mecânica da Bacia do
159 Paraná. Revista Brasileira de Geociências, 29(2):217-226.

160 Rapela, C.W., Llambías, E.J. 1999. El magmatismo gondwánico y los ciclos fanerozoicos. Em Caminos, R. (ed.)
161 Geología Argentina, Instituto de Geología y Recursos Minerales, Anales 29: 373-376, Buenos Aires.

162 Raposo, M.I.B. 1997. Magnetic fabric and its significance in the Florianópolis dyke swarm, southern Brazil. Geophys.
163 J. Int. 131, 159-170.

164 Raposo, M.I.B. 2017. Magnetic fabrics of the Cretaceous dike swarms from São Paulo coastline (SE Brazil): Its
165 relationship with South Atlantic Ocean opening. Tectonophysics, 721, 395-414.

166 Raposo, M.I.B., Ernesto, M., Renne, P.R., 1998. Paleomagnetism and dating of the early Cretaceous Florianópolis
167 dike swarm (Santa Catarina Island), Southern Brazil. Phys. Earth Planet. Inter. 108 (4), 275–290.

168 Riccomini, C., Sant'Anna, L.G., Fambrini, G.L. 2016. The Early Cretaceous Jacuí Group, a newly discovered
169 volcaniclastic-epiclastic accumulation at the top of the Paraná Basin, southern Brazil. Cretaceous Research, 59, 111-
170 128.

171 Rocha-Júnior, E.R.V., Marques, L.S., Babinski, M., Nardy, A.J.R., Figueiredo, A.M.G., Machado, F.B., 2013. Sr-Nd-Pb
172 isotopic constraints on the nature of the mantle sources involved in the genesis of the high-Ti tholeiites from northern
173 Paraná continental flood basalts (Brazil). J. S. Am. Earth Sci. 46, 9–25.

174 Rocha-Júnior, E.R.V., Puchtel, I.S., Marques, L.S., Walker, R.J., Machado, F.B., Nardy, A.J.R., Babinski, M.,
175 Figueiredo, A.M.G., 2012. Re–Os isotope and highly siderophile element systematics of the Paraná continental flood
176 basalts (Brazil). Earth Planet. Sci. Lett. 337, 164–173.

177 Rollinson, H.R. (1993) Using Geochemical Data: Evaluation, Presentation and Interpretation. Longman, Harlow, 352
178 p.

179 Rossetti, L., Lima, E.F., Waichel, B.L, Hole, M.J., Simões, M.S., Scherer, C.M.S. 2017. Lithostratigraphy and
180 volcanology of the Serra Geral Group, Paraná-Etendeka Igneous Province in Southern Brazil: Towards a formal
181 stratigraphical framework. J. Volcanol. Geoth. Res., in press.

182 Rossetti, L.M.M., Lima, E.F., Waichel, B.L., Scherer, C.M.S., Barreto, C.J. 2014 Stratigraphical framework of basaltic
183 lavas in Torres Syncline main valley, Southern Paraná-Etendeka Volcanic Province. J. S. Am. Earth Sci. 56, 409-421.
184 (DOI: 10.1016/j.jsames.2014.09.025).

185 Sarmento, C.C.T., Sommer, C.A., Lima, E.F. 2017. Mafic subvolcanic intrusions and their petrologic relation with the
186 volcanism in the South hinge Torres Syncline, Paraná-Etendeka Igneous Province, southern Brazil. Journal of South
187 American Earth Sciences, 77: 70-91.

188 Schnetzler, C.C., Philpotts, J.A. 1970. Partition coefficients of rare-earth elements between igneous matrix material
189 and rock-forming mineral phenocrysts. Geochimica et Cosmochimica Acta, 34(3), 331-340.

190 Shand S. J. 1943. Eruptive Rocks. Their Genesis, Composition, Classification, and their Relation to Ore Deposits, with
191 a chapter on Meteorites (revised second edition): Hafner Publishing Co., New York, 444 p.

192 Sheth H. 2007. Large Igneous Provinces (LIPs): definition, recommended terminology, and a hierarchical
193 classification. Earth Science Reviews, 85:117-124.

194 Sheth, H.C., Choudhary, A.K., Cucciniello, C., Bhattacharyya, S., Laishram, R., Gurav, T., 2012. Geology,
195 petrochemistry, and genesis of the bimodal lavas of Osham Hill, Saurashtra, northwestern Deccan Traps. Journal of
196 Asian Earth Sciences 43, 176–192.

197 Sheth, H.C., Pande, K. 2014. Geological and $^{40}Ar/^{39}Ar$ age constraints on late-stage Deccan rhyolitic volcanism, inter-
198 volcanic sedimentation, and the Panvel flexure from Dongri area, Mumbai. Journal of Asian Earth Sciences, 84, 167-
199 175.

200 Simões, M.S., Lima, E.F., Sommer, C.A., Rossetti, L.M.M. 2017. Structures and lithofacies of inferred silicic conduits
201 in the Paraná-Etendeka LIP, southernmost Brazil. Journal of Volcanology and Geothermal Research, in press.

202 Simões, M.S., Lima, E.F., Sommer, C.A., Rossetti, L.M.M. 2018. The Mato Perso Conduit System: evidence of silicic
203 magma transport in the Paraná-Etendeka LIP. Braz. J. Geol., accepted manuscript.

204 Simões, M.S., Rossetti, L.M.M., Lima, E.F., Ribeiro, B.P. 2014. The role of viscosity in the emplacement of high-
205 temperature silicic flows of Serra Geral Formation in Torres Syncline (Rio Grande do Sul State, Brazil). Brazilian
206 Journal of Geology 44(4), 669-679.

207 Sisson, T.W. 1991. Pyroxene-High Silica Rholite trace-element partition coefficients measured by ion microprobe.
208 Geochimica et Cosmochimica Acta 55(6), 1575-1585.

209 Sparks, R.S.J., Self, S., et al. 2005. Super-eruptions: global effects and future threats. Rep Geological Society of
210 London Working Group.

211 Stica, J.M., Zalán, P.V., Ferrari, A.L. 2014. The evolution of rifting on the volcanic margin of the Pelotas Basin and the
212 contextualization of the Paraná-Etendeka LIP in the separation of Gondwana in the South Atlantic. Marine and
213 Petroleum Geology, 50: 1-21.

Stimac, J. and Hickmott, D. (1994). Trace-Element Partition-Coefficients for Ilmenite, Ortho-Pyroxene and Pyrrhotite in Rhyolite Determined by Micro-Pixe Analysis. Chemical Geology 117(1-4): 313-330. doi: 10.1016/0009-2541(94)90134-1.

Stormer, J.C., and Nicholls, J., 1978, XLFRAC: A program for the interactive testing of magmatic differentiation models: Computers & Geosciences, v. 4. p. 143–159. doi:10.1016/0098-3004(78)90083-3.

Sun, S.S., McDonough, W.F., 1989. Chemical and isotopic systematics of oceanic basalts; implications for mantle composition and processes. In: Saunders, A.D., Norry, M.J. (Eds.), Magmatism in the Ocean Basins, vol. 42. J Geol Soc London, pp. 313-345.

Svensen, H.H., Torsvik, T.H., Callegaro, S., Augland, L., Heimdal, T.H., Jerram, D.A., Planke, S., Pereira, E. 2017. Gondwana Large Igneous Provinces: plate reconstructions, volcanic basins and sill volumes. In: Sensarma, S. & Storey, B. C. (eds) Large Igneous Provinces from Gondwana and Adjacent Regions. Geological Society, London, Special Publications, 463.

Taylor, S.R., McLennan, S.M. 1985. The Continental Crust: Its composition and evolution, an examination of the geochemical record preserved in sedimentary rocks. Blackwell, Oxford.

Thiede, D.S., Vasconcelos, P.M., 2010. Parana flood basalts: rapid extrusion hypothesis confirmed by new $^{40}Ar/^{39}Ar$ results. Geology, 38 (8): 747–750.

Umann, L.V., Lima, E.F., Sommer, C.A., De Liz, J.D. 2001. Vulcanismo ácido da região de Cambará do Sul-RS: litoquímica e discussão sobre a origem dos depósitos. Rev. Bras. Geosci. 31(3), 357-364.

Valente, S.d.C., Corval, A., Duarte, B.P., Ellam, R.M., Fallick, A.E., Meighan, I.G., Dutra, T. 2007. Tectonic boundaries, crustal weakness zones and plume-subcontinental lithospheric mantle interactions in the Serra do Mar dyke swarm, SE Brazil. Rev. Bras. Geosci. 37 (1), 194–201.

Vieira Jr., N. 1985. Petrologia e geoquimica do vulcanismo Mesozóico de Jaguarão — RS. Ms dissertation, Universidade Federal do Rio Grande do Sul, Porto Alegre, RS, Brazil,136 pp.

Vieira Jr., N., Roisemberg, A. 1985. Formação Jaguarão — nova unidade vulcânica mesozóica no RS. Anais II Simpósio Sul-Brasileiro de Geologia, 1985, Florianópolis, p. 507.

Waichel, B.L., Lima, E.F., Sommer, C.A., Lubachesky, R. 2007. Peperite formed by lava flows over sediments: an example from the central Paraná Continental Flood Basalts, Brazil. Journal of Volcanology and Geothermal Research 159(4), 343-354.

Waichel, B.L., Lima, E.F., Viana, A.R., Scherer, C.M.S., Bueno, G.V., Dutra, G.T. 2012. Stratigraphy and volcanic facies architecture of the Torres Syncline, Southern Brazil, and its role in understanding the Paraná-Etendeka Continental Flood Basalt Province. Journal of Volcanology and Geothermal Research, 215, 74–82.

Waters, L.E., and Lange, R.A. 2015. An updated calibration of the plagioclase-liquid hygrometer-thermometer applicable to basalts through rhyolites. American Mineralogist, 10, 2172–2184.

Wiegand. M., Trumbull, R.B., Kontny, A., Greiling, R.O. 2017. An AMS study of magma transport and emplacement mechanisms in mafic dykes from the Etendeka Province, Namibia. Tectonophysics, 716, 149-167.

Will, T.M., Frimmel, H.E. 2018. Where does a continent prefer to break up? Some lessons from the South Atlantic margins. Gondwana Research, 53, 9-19.

Wilson, M., 1989, Igneous Petrogenesis: A global tectonic approach: Ed. Dordrecht, Springer, 466 p.

Zalán, P.V., Wolff, S., Astolfi, M.A., Vieira, I.S., Conceicao, J.C., Appi, V.T., Neto, E.V.S., Cerqueira, J.R., Marques, A. 1990, The Parana Basin, Brazil, in Leighton, M.W., Kolata, D.R., Oltz, D.F., and Eidel, J.J.,eds., Interior cratonic basins: American Association of Petroleum Geologists, Memoir 51, pp. 681-708.

Zalán, P.V., Wolff, S., Conceição, J.C.J., Astolfi, M.A.M., Vieira, I.S., Appi, V.T., Zanotto, A.O., Marques, A. 1991. Tectonics and sedimentation of the Paraná Basin. Gondwana Symposium, 7: São Paulo, Brazil.

257 Zerfass, H., Chemale Jr., F., Lavina, E., 2005. Tectonic Control of the Triassic Santa Maria Supersequence of the
258 Paraná Basin, Southernmost Brazil, and its Correlation to the Waterberg Basin, Namibia. Gondwana Reseach, 8, 163-
259 176.

260 Xu, Y., Chung, S., Shao, H., He, B. 2010. Silicic magmas from the Emeishan large igneous province, Southwest
261 China: Petrogenesis and their link with the end-Guadalupian biological crisis. Lithos, 119, 47-60.

APPENDIX A – Feldspar major oxide compositions analyzed by EPMA and structural formulae. m/p=microlite/phenocryst; An=anorthite, Ab=albite, Or=orthoclase; Struc. Form.=structural formula; 4 Ca=04 cation based structural formula; c=core; b=boarder; c-b=core-boarder intermediate region; x=whole grain.

Plagioclase analyses, structural formulas based on 32 oxygens – one page

Sample	MS01	MS01	MS01	MS01	MS01	MS01	MS01	MS01	MS01	MS01	MS01	MS01
m/p	p	p	p	p	p	p	p	p	p	m	m	p
Position	c	c	c-b	c-b	b	b	b	b	b	x	x	x
Local Phase	Mato Perso plagioclase	Mato Perso plagioclase	Mato Perso plagioclase	Mato Perso plagioclase	Mato Perso plagioclase	Mato Perso plagioclase	Mato Perso plagioclase	Mato Perso plagioclase	Mato Perso plagioclase	Mato Perso plagioclase	Mato Perso plagioclase	Mato Perso plagioclase
SiO_2	53.94	54.22	55.42	54.80	55.83	54.45	55.37	55.33	53.05	57.26	56.94	52.92
TiO_2	0.00	0.17	0.17	0.14	0.00	0.00	0.24	0.17	0.14	0.00	0.09	0.00
Al_2O_3	26.90	26.88	26.94	27.19	27.09	27.81	27.06	26.51	26.89	26.69	26.85	27.61
$Fe_2O_{3(T)}$	1.10	1.15	1.11	1.04	1.09	1.08	1.20	1.15	1.04	0.94	1.01	0.95
MgO	0.12	0.16	0.16	0.15	0.11	0.13	0.15	0.15	0.15	0.05	0.05	0.17
CaO	11.65	12.10	11.52	11.99	11.54	12.29	11.98	11.19	11.72	10.30	10.44	12.15
Na_2O	4.36	4.30	4.72	4.37	4.51	4.22	4.44	4.72	4.29	5.25	5.17	4.39
K_2O	0.38	0.38	0.40	0.40	0.40	0.33	0.36	0.43	0.36	0.42	0.33	0.35
Cr_2O_3	0.00	0.07	0.08	0.05	0.02	0.00	0.00	0.03	0.00	0.00	0.00	0.03
MnO	0.00	0.00	0.06	0.00	0.06	0.00	0.00	0.00	0.08	0.05	0.00	0.03
NiO	0.00	0.00	0.02	0.03	0.00	0.00	0.00	0.00	0.03	0.02	0.00	0.00
V_2O_3	0.00	0.04	0.00	0.05	0.04	0.01	0.02	0.08	0.00	0.00	0.00	0.00
Total	98.46	99.49	100.58	100.21	100.70	100.32	100.83	99.77	97.74	100.99	100.87	98.59
An	58.26	59.50	56.08	58.84	57.20	60.51	58.59	55.30	58.87	50.75	51.72	59.23
Ab	39.47	38.28	41.63	38.82	40.43	37.59	39.33	42.20	39.00	46.78	46.33	38.75
Or	2.27	2.22	2.29	2.33	2.38	1.91	2.08	2.50	2.13	2.47	1.95	2.01
Struct. Form.												
Si	5.26	5.26	8.38	5.27	9.15	5.17	5.32	5.39	5.20	5.51	5.47	5.10
Al	13.13	13.07	8.23	13.09	7.12	13.24	13.01	12.93	13.19	12.86	12.91	13.32
Fe3	0.08	0.08	0.13	0.07	0.13	0.08	0.09	0.08	0.08	0.07	0.07	0.07
T	18.47	18.41	16.74	18.43	16.40	18.49	18.41	18.40	18.47	18.44	18.45	18.49
Ca	1.22	1.26	1.87	1.23	2.03	1.25	1.23	1.17	1.23	1.06	1.07	1.25
K	0.05	0.05	0.08	0.05	0.08	0.04	0.04	0.05	0.04	0.05	0.04	0.04
Na	0.82	0.81	1.39	0.81	1.43	0.78	0.83	0.89	0.82	0.98	0.96	0.82
T	2.09	2.12	3.33	2.10	3.54	2.07	2.10	2.11	2.09	2.09	2.08	2.12

Sample	MS01	MS03a	MS03a	MS03a	MS03a	MS03a	MS03a	MS03a	MS03a	MS03a	MS03a	MS03a
m/p	p	p	p	p	p	p	p	p	p	p	p	p
Position	x	c-b	c-b	c-b	c-b	b	b	b	x	x	x	x
Local	Mato Perso	Mato Perso	Mato Perso	Mato Perso	Mato Perso	Mato Perso	Mato Perso	Mato Perso	Mato Perso	Mato Perso	Mato Perso	Mato Perso
Phase	plagioclase	plagioclase	plagioclase	plagioclase	plagioclase	plagioclase	plagioclase	plagioclase	plagioclase	plagioclase	plagioclase	plagioclase
SiO_2	53.01	52.79	54.61	52.73	54.12	55.18	54.11	53.06	53.26	54.33	53.84	54.40
TiO_2	0.00	0.22	0.12	0.09	0.25	0.18	0.00	0.00	0.00	0.11	0.09	0.00
Al_2O_3	26.93	27.31	28.64	27.28	27.64	27.95	27.56	27.77	27.65	27.45	27.84	27.54
$Fe_2O_{3(T)}$	0.81	1.10	1.07	1.08	1.35	1.08	0.99	1.12	1.09	1.14	1.13	1.16
MgO	0.11	0.09	0.12	0.18	0.15	0.18	0.20	0.16	0.17	0.11	0.11	0.11
CaO	11.91	12.16	12.28	11.77	11.89	11.22	11.60	12.16	11.96	11.70	11.97	11.89
Na_2O	4.31	4.06	4.37	4.12	4.41	5.10	4.59	3.49	4.75	4.59	4.32	4.43
K_2O	0.36	0.34	0.32	0.36	0.34	0.37	0.43	0.36	0.33	0.40	0.40	0.43
Cr_2O_3	0.01	0.00	0.00	0.00	0.00	0.00	0.00	0.01	0.00	0.00	0.06	0.00
MnO	0.00	0.00	0.00	0.00	0.00	0.00	0.00	0.10	0.00	0.07	0.00	0.00
NiO	0.02	0.02	0.06	0.00	0.00	0.00	0.00	0.00	0.00	0.04	0.02	0.00
V_2O_3	0.00	0.03	0.00	0.00	0.00	0.01	0.00	0.01	0.01	0.02	0.00	0.01
Total	97.45	98.14	101.58	97.59	100.15	101.27	99.47	98.26	99.23	99.98	99.81	99.95
An	59.17	61.05	59.69	59.91	58.63	53.72	56.82	64.30	57.09	57.13	59.08	58.21
Ab	38.71	36.91	38.46	37.91	39.37	44.16	40.70	33.42	41.02	40.56	38.59	39.29
Or	2.12	2.04	1.84	2.18	2.00	2.12	2.48	2.28	1.88	2.31	2.32	2.50
Struct. Form.												
Si	5.19	5.13	5.09	5.13	5.17	5.21	5.19	5.10	5.11	5.21	5.13	5.21
Al	13.21	13.28	13.36	13.30	13.22	13.21	13.23	13.36	13.29	13.18	13.29	13.20
Fe3	0.06	0.08	0.07	0.08	0.10	0.08	0.07	0.08	0.08	0.08	0.08	0.08
Total	18.47	18.49	18.52	18.51	18.49	18.49	18.49	18.54	18.48	18.47	18.50	18.48
Ca	1.25	1.26	1.23	1.23	1.22	1.13	1.19	1.25	1.23	1.20	1.22	1.22
K	0.04	0.04	0.04	0.04	0.04	0.04	0.05	0.04	0.04	0.05	0.05	0.05
Na	0.82	0.76	0.79	0.78	0.82	0.93	0.85	0.65	0.88	0.85	0.80	0.82
Total	2.11	2.07	2.05	2.05	2.08	2.11	2.10	1.95	2.15	2.10	2.07	2.09

Sample	MS03a	MS03a	MS03a	MS03a	MS03a	MS03a	MS03a	MS05b	MS05b	MS05b	MS05b	MS05b
m/p	p	p	p	p	p	p	p	p	p	p	p	p
Position	x	x	x	x	x	x	x	c	c	c-b	c-b	c-b
Local	Mato Perso	Mato Perso	Mato Perso	Mato Perso	Mato Perso	Mato Perso	Mato Perso	Mato Perso	Mato Perso	Mato Perso	Mato Perso	Mato Perso
Phase	plagioclase	plagioclase	plagioclase	plagioclase	plagioclase	plagioclase	plagioclase	plagioclase	plagioclase	plagioclase	plagioclase	plagioclase
SiO_2	53.86	52.53	54.33	53.83	54.18	53.88	54.14	53.71	52.52	53.05	53.75	52.86
TiO_2	0.19	0.01	0.06	0.00	0.04	0.12	0.12	0.10	0.00	0.00	0.19	0.03
Al_2O_3	27.57	27.18	27.25	27.68	27.63	27.61	27.57	27.12	27.33	27.56	27.65	26.81
$Fe_2O_{3(T)}$	1.16	0.95	0.96	1.24	1.16	1.22	1.02	0.90	1.05	1.09	0.99	1.09
MgO	0.15	0.14	0.12	0.13	0.08	0.17	0.14	0.11	0.16	0.08	0.15	0.18
CaO	11.78	12.19	11.56	11.97	12.08	11.75	12.09	11.63	12.29	12.12	11.89	11.74
Na_2O	4.67	4.38	4.62	4.44	4.40	4.36	4.31	4.38	3.85	4.30	4.39	4.12
K_2O	0.39	0.37	0.44	0.39	0.39	0.39	0.40	0.33	0.32	0.31	0.38	0.36
Cr_2O_3	0.01	0.00	0.03	0.00	0.00	0.00	0.11	0.02	0.05	0.00	0.08	0.07
MnO	0.00	0.03	0.01	0.01	0.07	0.02	0.00	0.04	0.00	0.05	0.12	0.04
NiO	0.00	0.03	0.00	0.05	0.00	0.00	0.08	0.00	0.05	0.00	0.00	0.09
V_2O_3	0.00	0.00	0.00	0.00	0.00	0.00	0.00	0.00	0.02	0.05	0.01	0.03
Total	99.78	97.80	99.37	99.76	100.04	99.52	99.98	98.35	97.65	98.60	99.61	97.43
An	56.92	59.30	56.56	58.46	58.89	58.45	59.40	58.33	62.57	59.78	58.61	59.80
Ab	40.82	38.55	40.88	39.25	38.85	39.23	38.29	39.72	35.48	38.41	39.18	38.01
Or	2.26	2.14	2.56	2.29	2.26	2.32	2.31	1.95	1.95	1.82	2.22	2.19
Struct. Form.												
Si	5.16	5.12	5.24	5.15	5.18	5.16	5.18	5.22	5.11	5.11	5.15	5.19
Al	13.23	13.28	13.16	13.26	13.22	13.25	13.21	13.19	13.31	13.31	13.26	13.19
Fe3	0.08	0.07	0.07	0.09	0.08	0.09	0.07	0.07	0.08	0.08	0.07	0.08
Total	18.48	18.47	18.47	18.49	18.48	18.50	18.46	18.48	18.50	18.50	18.48	18.47
Ca	1.21	1.27	1.19	1.23	1.24	1.21	1.24	1.21	1.28	1.25	1.22	1.24
K	0.05	0.05	0.05	0.05	0.05	0.05	0.05	0.04	0.04	0.04	0.05	0.05
Na	0.87	0.83	0.86	0.82	0.82	0.81	0.80	0.82	0.73	0.80	0.82	0.79
Total	2.12	2.15	2.11	2.10	2.10	2.06	2.09	2.08	2.05	2.09	2.08	2.07

Sample	MS05b	MS05b	MS05b	MS05b	MS05b	MS05b	MS05b	MS04	MS04	MS04	MS04	MS04
m/p	p	p	p	p	p	p	p	m	m	m	p	p
Position	b	b	b	x	x	x	x	m	m	m	m	m
Local	Mato Perso	Mato Perso	Mato Perso	Mato Perso	Mato Perso	Mato Perso	Mato Perso	Mato Perso	Mato Perso	Mato Perso	Mato Perso	Mato Perso
Phase	plagioclase	plagioclase	plagioclase	plagioclase	plagioclase	plagioclase	plagioclase	plagioclase	plagioclase	plagioclase	plagioclase	plagioclase
SiO_2	53.36	53.73	52.78	53.24	53.98	52.62	52.62	54.10	54.22	53.94	54.97	54.61
TiO_2	0.11	0.02	0.00	0.11	0.03	0.15	0.15	0.18	0.12	0.04	0.23	0.07
Al_2O_3	27.48	26.59	26.93	27.35	26.23	27.65	27.65	27.25	27.30	27.06	26.86	26.86
$Fe_2O_{3(T)}$	1.18	1.12	0.93	1.13	1.33	1.10	1.10	1.12	1.02	0.89	1.15	1.22
MgO	0.10	0.12	0.15	0.08	0.11	0.09	0.09	0.11	0.11	0.07	0.06	0.07
CaO	11.91	11.15	12.14	11.68	11.07	11.84	11.84	11.48	11.40	10.72	10.69	10.85
Na_2O	4.24	4.59	4.21	4.21	4.44	4.05	4.05	4.80	4.80	4.98	5.07	4.97
K_2O	0.31	0.44	0.37	0.33	0.45	0.30	0.30	0.36	0.38	0.31	0.40	0.38
Cr_2O_3	0.01	0.07	0.00	0.00	0.00	0.00	0.00	0.00	0.06	0.00	0.00	0.00
MnO	0.00	0.03	0.00	0.00	0.02	0.00	0.00	0.00	0.02	0.07	0.00	0.00
NiO	0.03	0.00	0.00	0.00	0.00	0.00	0.00	0.00	0.00	0.00	0.03	0.00
V_2O_3	0.01	0.00	0.00	0.01	0.00	0.03	0.03	0.01	0.01	0.04	0.00	0.00
Total	98.73	97.86	97.52	98.13	97.64	97.83	97.83	99.41	99.43	98.12	99.46	99.02
An	59.73	55.82	60.06	59.30	56.38	60.64	60.64	55.73	55.53	53.34	52.55	53.47
Ab	38.44	41.57	37.74	38.69	40.91	37.55	37.55	42.19	42.27	44.80	45.10	44.32
Or	1.83	2.60	2.20	2.02	2.71	1.82	1.82	2.07	2.21	1.86	2.35	2.21
Struct. Form.												
Si	5.15	5.28	5.17	5.16	5.35	5.08	5.08	5.22	5.22	5.25	5.33	5.31
Al	13.27	13.09	13.22	13.27	13.01	13.38	13.38	13.17	13.17	13.18	13.05	13.08
Fe3	0.09	0.08	0.07	0.08	0.10	0.08	0.08	0.08	0.07	0.06	0.08	0.09
T	18.50	18.46	18.46	18.51	18.45	18.54	18.54	18.47	18.47	18.50	18.46	18.47
Ca	1.23	1.17	1.27	1.21	1.17	1.23	1.23	1.19	1.18	1.12	1.11	1.13
K	0.04	0.05	0.05	0.04	0.06	0.04	0.04	0.04	0.05	0.04	0.05	0.05
Na	0.79	0.87	0.80	0.79	0.85	0.76	0.76	0.90	0.90	0.94	0.95	0.94
T	2.06	2.10	2.12	2.04	2.08	2.02	2.02	2.13	2.12	2.10	2.11	2.11

Sample	MS11B	MS11B	MS11B	MS11B	MS11b	MS11b	MS11b	MS11b	MS11b	MS11b	MS11b	MS11b
m/p	p	p	p	p	p	p	p	p	p	p	p	p
Position	x	x	x	x	x	x	x	x	x	x	x	x
Local	São Marcos	São Marcos	São Marcos	São Marcos	São Marcos	São Marcos	São Marcos	São Marcos	São Marcos	São Marcos	São Marcos	São Marcos
Phase	plagioclase	plagioclase	plagioclase	plagioclase	plagioclase	plagioclase	plagioclase	plagioclase	plagioclase	plagioclase	plagioclase	plagioclase
SiO_2	55.05	53.13	55.63	55.50	53.35	53.78	53.50	53.43	53.23	53.06	53.15	55.26
TiO_2	0.02	0.19	0.01	0.00	0.12	0.02	0.05	0.00	0.18	0.00	0.04	0.10
Al_2O_3	27.23	26.20	27.71	27.79	26.78	27.46	26.83	27.33	26.52	26.86	26.87	26.32
$Fe_2O_{3(T)}$	1.15	1.15	1.15	1.10	0.93	1.33	0.89	1.10	1.17	0.95	0.99	0.95
MgO	0.07	0.07	0.16	0.14	0.13	0.13	0.17	0.10	0.13	0.10	0.17	0.12
CaO	11.32	11.26	11.50	11.29	11.38	12.04	11.36	11.97	11.18	11.67	11.71	10.31
Na_2O	4.74	4.42	4.83	4.68	4.72	4.58	4.53	4.25	4.62	4.48	4.24	5.23
K_2O	0.38	0.36	0.41	0.36	0.33	0.34	0.39	0.30	0.44	0.40	0.34	0.27
Cr_2O_3	0.00	0.00	0.07	0.00	0.01	0.01	0.00	0.00	0.03	0.07	0.09	0.00
MnO	0.00	0.10	0.05	0.01	0.04	0.05	0.02	0.00	0.00	0.00	0.10	0.00
NiO	0.00	0.00	0.00	0.00	0.00	0.00	0.00	0.01	0.00	0.00	0.00	0.03
V_2O_3	0.00	0.03	0.00	0.01	0.00	0.00	0.00	0.00	0.00	0.01	0.00	0.00
Total	99.98	96.93	101.52	100.86	97.79	99.76	97.73	98.50	97.50	97.62	97.71	98.58
An	55.61	57.19	55.48	55.93	56.02	58.09	56.77	59.79	55.71	57.61	59.16	51.32
Ab	42.15	40.64	42.17	41.97	42.02	39.97	40.93	38.46	41.66	40.03	38.77	47.11
Or	2.24	2.17	2.35	2.11	1.96	1.94	2.30	1.75	2.63	2.36	2.07	1.57
Struct. Form.												
Si	5.29	5.29	5.26	5.25	5.23	5.17	5.24	5.17	5.26	5.20	5.21	5.43
Al	13.10	13.06	13.12	13.17	13.16	13.21	13.16	13.24	13.11	13.19	13.18	12.94
Fe3	0.08	0.09	0.08	0.08	0.07	0.10	0.07	0.08	0.09	0.07	0.07	0.07
Total	18.47	18.44	18.47	18.50	18.46	18.47	18.47	18.49	18.45	18.46	18.46	18.44
Ca	1.17	1.20	1.16	1.14	1.20	1.24	1.19	1.24	1.18	1.23	1.23	1.08
K	0.05	0.05	0.05	0.04	0.04	0.04	0.05	0.04	0.06	0.05	0.04	0.03
Na	0.88	0.85	0.89	0.86	0.90	0.85	0.86	0.80	0.88	0.85	0.81	1.00
Total	2.10	2.10	2.10	2.05	2.14	2.13	2.10	2.07	2.12	2.13	2.08	2.11

Sample	MS11b	MS11b	MS11b	MS11b	MS19B1	MS38	PSJ02A	PSJ02A	PSJ02A	PSJ04	PSJ04	PSJ04
m/p	p	p	p	p	m	m	m	m	m	p	p	p
Position	x	x	x	x	x	x	x	x	x	x	x	x
Local	São Marcos	São Marcos	São Marcos	São Marcos	Jaquirana	Jaquirana	Jaquirana	Jaquirana	Jaquirana	Jaquirana	Jaquirana	Jaquirana
Phase	plagioclase	plagioclase	plagioclase	plagioclase	sanidine	plagioclase	plagioclase	plagioclase	plagioclase	plagioclase	plagioclase	plagioclase
SiO_2	55.17	54.05	53.52	53.35	56.25	57.68	64.09	55.17	55.58	53.38	56.65	53.33
TiO_2	0.12	0.00	0.14	0.00	0.67	0.37	0.10	0.09	0.03	0.00	0.00	0.11
Al_2O_3	25.88	26.85	27.14	27.35	14.80	26.67	21.74	25.75	26.19	27.19	25.29	26.73
$Fe_2O_{3(T)}$	0.85	1.24	1.04	1.05	0.89	0.87	0.53	1.14	1.34	1.13	1.35	1.31
MgO	0.10	0.11	0.11	0.09	0.24	0.03	0.04	0.07	0.08	0.09	0.12	0.09
CaO	10.19	11.39	11.53	11.78	0.76	9.69	2.34	10.25	10.02	11.75	8.68	11.29
Na_2O	5.30	4.53	4.39	4.39	1.69	5.98	9.24	5.44	5.87	4.50	6.06	4.63
K_2O	0.31	0.33	0.35	0.32	11.56	0.30	0.56	0.39	0.31	0.33	0.38	0.32
Cr_2O_3	0.00	0.00	0.08	0.04	0.03	0.00	0.00	0.05	0.02	0.07	0.06	0.00
MnO	0.00	0.01	0.00	0.00	9.38	0.02	0.04	0.00	0.00	0.02	0.00	0.00
NiO	0.00	0.00	0.07	0.00	0.03	0.00	0.00	0.02	0.00	0.00	0.03	0.00
V_2O_3	0.00	0.06	0.03	0.00	0.07	0.01	0.03	0.02	0.03	0.01	0.00	0.01
Cl	0.00	0.01	0.01	0.02	0.01	0.02	0.00	0.01	0.00	0.00	0.00	0.01
Total	97.94	98.57	98.41	98.38	96.39	101.63	98.70	98.39	99.48	98.48	98.62	97.83
An	50.58	56.99	57.98	58.56	4.33	46.42	11.87	49.84	47.68	57.89	43.17	56.29
Ab	47.59	41.02	39.91	39.52	17.40	51.86	84.75	47.91	50.58	40.16	54.55	41.79
Or	1.83	1.99	2.11	1.92	78.26	1.72	3.38	2.25	1.74	1.95	2.27	1.92
Struct. Form.												
Si	5.48	5.27	5.20	5.16	10.91	5.53	6.74	5.49	5.45	5.18	5.66	5.24
Al	12.87	13.11	13.20	13.26	4.17	12.81	11.46	12.82	12.86	13.22	12.65	13.14
Fe3	0.06	0.09	0.08	0.08	0.13	0.06	0.04	0.08	0.10	0.08	0.10	0.10
Total	18.41	18.47	18.48	18.50	15.21	18.40	18.24	18.39	18.41	18.48	18.40	18.47
Ca	1.08	1.19	1.20	1.22	0.16	1.00	0.26	1.09	1.05	1.22	0.93	1.19
K	0.04	0.04	0.04	0.04	2.86	0.04	0.08	0.05	0.04	0.04	0.05	0.04
Na	1.02	0.86	0.83	0.82	0.64	1.11	1.88	1.05	1.12	0.85	1.17	0.88
Total	2.14	2.09	2.07	2.09	3.65	2.14	2.22	2.19	2.21	2.11	2.15	2.11

Sample	PSJ04	PSJ04	PSJ04	MS19B1	MS50	MS50	MS50	MS50	MS50	MS50	MS50	MS50
m/p	p	p	p	m	m	m	p	p	p	m	m	m
Position	x	x	x	x	x	x	x	x	x	x	x	x
Local	Jaquirana	Jaquirana	Jaquirana	Cambará	Cambará	Cambará	Cambará	Cambará	Cambará	Cambará	Cambará	Cambará
Phase	plagioclase	plagioclase	plagioclase	sanidine	sanidine	plagioclase	plagioclase	plagioclase	plagioclase	plagioclase	plagioclase	plagioclase
SiO_2	52.83	53.50	53.22	56.25	62.99	60.72	59.88	67.57	60.46	56.92	59.55	59.42
TiO_2	0.06	0.00	0.00	0.67	0.12	0.31	0.00	0.00	0.14	0.19	0.05	0.00
Al_2O_3	27.38	26.75	27.25	14.80	16.83	23.14	25.31	21.13	24.80	26.51	24.99	23.60
$Fe_2O_{3(T)}$	1.13	0.94	1.16	0.89	0.74	0.79	0.94	0.58	0.85	1.08	0.86	0.66
MgO	0.09	0.06	0.06	0.24	0.10	0.07	0.04	0.03	0.00	0.03	0.06	0.03
CaO	11.82	10.77	11.31	0.76	0.18	5.95	8.88	6.07	7.67	10.65	7.77	7.07
Na_2O	4.43	5.07	4.74	1.69	2.51	6.98	5.76	6.10	6.71	5.34	7.25	7.19
K_2O	0.30	0.41	0.30	11.56	11.53	1.36	1.03	1.68	0.80	0.37	0.45	0.50
Cr_2O_3	0.00	0.02	0.06	0.03	0.03	0.00	0.00	0.00	0.00	0.00	0.00	0.02
MnO	0.05	0.00	0.00	9.38	0.05	0.00	0.00	0.00	0.00	0.01	0.00	0.00
NiO	0.00	0.00	0.03	0.03	0.00	0.00	0.12	0.01	0.00	0.02	0.01	0.00
V_2O_3	0.00	0.00	0.00	0.07	0.04	0.05	0.00	0.04	0.00	0.06	0.03	0.00
Total	98.08	97.53	98.13	96.39	95.16	99.36	101.95	103.23	101.43	101.18	101.00	98.47
An	58.55	52.70	55.89	4.33	0.98	29.44	43.23	31.78	36.94	51.33	36.28	34.20
Ab	39.69	44.93	42.35	17.40	24.61	62.55	50.78	57.77	58.46	46.58	61.24	62.93
Or	1.75	2.37	1.76	78.26	74.41	8.01	5.99	10.44	4.60	2.09	2.47	2.87
Struct. Form.												
Si	5.12	5.25	5.17	10.91	11.50	10.27	8.29	10.36	8.32	8.75	9.76	10.09
Al	13.30	13.16	13.25	4.17	4.62	5.89	8.72	6.07	8.73	7.77	6.48	6.10
Fe3	0.08	0.07	0.08	0.13	0.10	0.10	0.10	0.07	0.09	0.12	0.11	0.08
Total	18.50	18.48	18.50	15.21	16.23	16.26	17.10	16.49	17.14	16.65	16.35	16.28
Ca	1.23	1.13	1.18	0.16	0.04	1.08	1.32	1.00	1.13	1.76	1.37	1.29
K	0.04	0.05	0.04	2.86	2.69	0.29	0.18	0.33	0.14	0.07	0.09	0.11
Na	0.83	0.97	0.89	0.64	0.89	2.29	1.55	1.81	1.79	1.59	2.30	2.37
Total	2.10	2.15	2.11	3.65	3.61	3.66	3.04	3.14	3.06	3.42	3.76	3.76

Sample	MS50	MS51A	MS51A
m/p	m	m	m
Position	x	x	x
Local	Cambará	Cambará	Cambará
Phase	plagioclase	plagioclase	plagioclase
SiO_2	56.92	58.36	55.04
TiO_2	0.19	0.05	0.00
Al_2O_3	26.51	23.34	24.79
$Fe_2O_{3(T)}$	1.08	0.93	1.02
MgO	0.03	0.09	0.06
CaO	10.65	7.95	9.70
Na_2O	5.34	6.26	5.94
K_2O	0.37	0.61	0.43
Cr_2O_3	0.00	0.08	0.01
MnO	0.01	0.04	0.00
NiO	0.02	0.08	0.06
V_2O_3	0.06	0.02	0.00
Total	101.18	97.81	97.05
An	51.33	39.74	46.29
Ab	46.58	56.62	51.30
Or	2.09	3.64	2.42
Struct. Form.			
Si	5.50	6.05	5.61
Al	12.82	12.12	12.65
Fe3	0.08	0.07	0.08
Total	18.39	18.25	18.34
Ca	1.10	0.88	1.06
K	0.04	0.08	0.06
Na	1.00	1.26	1.17
Total	2.15	2.22	2.29

Pyroxene analyses, structural formula based in 6 oxygens and 4 cations – two pages

Sample	MS01	MS01	MS01	MS01	MS01	MS01	MS01	MS01	MS01	MS01	MS01	MS_01
m/f	f	f	f	f	f	f	f	f	f	f	m	m
Position	c	c	c-b	c-b	b	b	b	b	x	x	x	x
Local	Mato Perso	Mato Perso	Mato Perso	Mato Perso	Mato Perso	Mato Perso	Mato Perso	Mato Perso	Mato Perso	Mato Perso	Mato Perso	Mato Perso
SiO_2	53.20	52.31	52.83	53.27	52.21	53.30	53.00	52.75	52.52	53.16	52.58	51.29
TiO_2	0.40	0.53	0.49	0.43	0.45	0.68	0.48	0.41	0.71	0.50	0.44	0.56
Al_2O_3	1.87	1.78	1.74	1.65	1.58	1.45	1.79	1.57	1.84	1.84	1.61	1.20
FeO*	10.57	10.65	10.34	11.31	10.71	10.61	10.91	10.41	10.96	10.78	10.64	13.32
$Fe_2O_{3(T)}$	11.88	11.96	11.62	12.71	12.03	11.93	12.26	11.70	12.31	12.11	11.95	14.97
MgO	14.99	15.15	15.17	15.19	15.38	15.54	15.26	15.07	15.50	15.53	15.33	13.56
CaO	18.14	18.00	18.08	17.98	17.81	17.69	17.58	18.28	17.69	18.26	18.33	17.15
Na_2O	0.21	0.29	0.23	0.23	0.30	0.33	0.21	0.22	0.22	0.25	0.27	0.20
K_2O	0.00	0.00	0.01	0.01	0.10	0.04	0.02	0.05	0.00	0.00	0.01	0.04
Cr_2O_3	0.04	0.00	0.04	0.00	0.07	0.00	0.06	0.00	0.05	0.00	0.01	0.03
MnO	0.44	0.45	0.40	0.44	0.52	0.50	0.63	0.47	0.47	0.45	0.49	0.59
NiO	0.02	0.07	0.00	0.01	0.03	0.00	0.00	0.00	0.01	0.00	0.00	0.05
V_2O_3	0.06	0.00	0.00	0.04	0.05	0.02	0.00	0.07	0.07	0.04	0.02	0.01
Cl	0.00	0.01	0.01	0.01	0.02	0.00	0.02	0.02	0.01	0.00	0.00	0.00
Total	101.23	100.55	100.62	101.96	100.55	101.47	101.30	100.60	101.41	102.13	101.03	99.63
Mg2+**	90433.28	91380.26	91476.76	91591.36	92761.51	93738.65	92013.58	90921.85	93515.48	93678.33	92471.99	81789.85
Fe2+**	821588.69	827676.58	804016.82	879008.58	832311.68	824978.54	848292.39	809343.72	851889.79	837638.58	826915.59	1035287.53
Mg#***	9.92	9.94	10.22	9.44	10.03	10.20	9.79	10.10	9.89	10.06	10.06	7.32
Wo	31.52	31.17	31.54	30.51	30.72	30.54	30.34	31.78	30.25	31.07	31.43	28.88
Ens	36.51	36.93	36.85	37.01	37.53	37.94	37.64	36.46	37.88	37.18	36.79	35.49
Fer	32.22	32.34	31.65	33.65	32.38	32.13	33.03	31.75	32.87	32.16	31.99	39.34
4 Ca												
Si	1.82	1.80	1.82	1.80	1.79	1.81	1.81	1.81	1.79	1.80	1.80	1.76
Ti	0.01	0.01	0.01	0.01	0.01	0.02	0.01	0.01	0.02	0.01	0.01	0.01
Al	0.03	0.03	0.03	0.02	0.02	0.02	0.03	0.02	0.03	0.03	0.02	0.02
Fe2	0.68	0.69	0.67	0.72	0.69	0.68	0.70	0.67	0.70	0.69	0.68	0.86
Mg	0.77	0.78	0.78	0.77	0.79	0.79	0.78	0.77	0.79	0.78	0.78	0.69
Ca	0.67	0.66	0.67	0.65	0.65	0.64	0.64	0.67	0.65	0.66	0.67	0.63

Na	0.01	0.02	0.02	0.02	0.02	0.02	0.01	0.01	0.01	0.02	0.02	0.01
K	0.00	0.00	0.00	0.00	0.00	0.00	0.00	0.00	0.00	0.00	0.00	0.00
Cr	0.00	0.00	0.00	0.00	0.00	0.00	0.00	0.00	0.00	0.00	0.00	0.00
Mn	0.01	0.01	0.01	0.01	0.01	0.01	0.02	0.01	0.01	0.01	0.01	0.02
Ni	0.00	0.00	0.00	0.00	0.00	0.00	0.00	0.00	0.00	0.00	0.00	0.00
V	0.00	0.00	0.00	0.00	0.00	0.00	0.00	0.00	0.00	0.00	0.00	0.00
Cl	0.00	0.00	0.00	0.00	0.00	0.00	0.00	0.00	0.00	0.00	0.00	0.00
Total	4.00	4.00	4.00	4.00	4.00	4.00	4.00	4.00	4.00	4.00	4.00	4.00
Struc. Form.												
Site T												
Si T	1.82	1.80	1.82	1.80	1.79	1.81	1.81	1.81	1.79	1.80	1.80	1.76
Al (n)	0.18	0.20	0.18	0.20	0.21	0.19	0.19	0.19	0.21	0.20	0.20	0.24
Al	0.03	0.03	0.03	0.02	0.02	0.02	0.03	0.02	0.03	0.03	0.02	0.02
Al T	0.03	0.03	0.03	0.02	0.02	0.02	0.03	0.02	0.03	0.03	0.02	0.02
Fe3 (n)	0.15	0.18	0.16	0.18	0.19	0.17	0.17	0.16	0.18	0.17	0.18	0.23
Fe3	0.68	0.69	0.67	0.72	0.69	0.68	0.70	0.67	0.70	0.69	0.68	0.86
Fe3 T	0.15	0.18	0.16	0.18	0.19	0.17	0.17	0.16	0.18	0.17	0.18	0.23
Fe (rest)	0.53	0.51	0.51	0.54	0.50	0.51	0.53	0.51	0.52	0.51	0.50	0.63
Total	2.00	2.00	2.00	2.00	2.00	2.00	2.00	2.00	2.00	2.00	2.00	2.00
Site M1												
Fe 3 (M1)	0.53	0.51	0.51	0.54	0.50	0.51	0.53	0.51	0.52	0.51	0.50	0.63
Ti (M1)	0.01	0.01	0.01	0.01	0.01	0.02	0.01	0.01	0.02	0.01	0.01	0.01
Cr (M1)	0.00	0.00	0.00	0.00	0.00	0.00	0.00	0.00	0.00	0.00	0.00	0.00
V (M1)	0.00	0.00	0.00	0.00	0.00	0.00	0.00	0.00	0.00	0.00	0.00	0.00
Mn (M1)	0.01	0.01	0.01	0.01	0.01	0.01	0.02	0.01	0.01	0.01	0.01	0.02
Mg	0.77	0.78	0.78	0.77	0.79	0.79	0.78	0.77	0.79	0.78	0.78	0.69
Mg (n)	0.45	0.46	0.46	0.43	0.47	0.46	0.43	0.46	0.45	0.46	0.47	0.34
Mg (M1)	0.45	0.46	0.46	0.43	0.47	0.46	0.43	0.46	0.45	0.46	0.47	0.34
Mg (rest)	0.32	0.32	0.32	0.33	0.32	0.33	0.34	0.31	0.34	0.32	0.31	0.36
Total	1.00	1.00	1.00	1.00	1.00	1.00	1.00	1.00	1.00	1.00	1.00	1.00
Site M2												
Mg (M2)	0.32	0.32	0.32	0.33	0.32	0.33	0.34	0.31	0.34	0.32	0.31	0.36
Ca (M2)	0.67	0.66	0.67	0.65	0.65	0.64	0.64	0.67	0.65	0.66	0.67	0.63
Na (M2)	0.01	0.02	0.02	0.02	0.02	0.02	0.01	0.01	0.01	0.02	0.02	0.01

Sample	MS_01	MS_01	MS_01	MS_01	MS_03a	MS_03a	MS_03a	MS_03a	MS_03a	MS_03a	MS_03a	MS_03a
m/f	f	f	f	f	f	f	f	f	f	f	f	f
Position	x	x	x	x	b	b	b	x	x	x	x	x
Local	Mato Perso	Mato Perso	Mato Perso	Mato Perso	Mato Perso	Mato Perso	Mato Perso	Mato Perso	Mato Perso	Mato Perso	Mato Perso	Mato Perso
SiO_2	51.22	50.92	51.22	50.92	52.20	51.73	52.16	51.46	51.69	52.21	51.95	52.16
TiO_2	0.44	0.82	0.44	0.82	0.82	0.67	0.90	0.40	0.40	0.50	0.68	0.75
Al_2O_3	1.73	1.69	1.73	1.69	1.63	1.70	1.69	1.79	1.77	1.59	1.61	1.62
FeO*	10.42	10.95	10.42	10.95	10.48	10.72	10.33	10.40	10.46	10.46	10.77	11.21
$Fe_2O_{3(T)}$	11.70	12.31	11.70	12.31	11.77	12.05	11.61	11.69	11.75	11.75	12.10	12.59
MgO	14.83	15.12	14.83	15.12	14.50	14.38	14.58	14.45	14.58	14.50	14.64	14.74
CaO	18.48	18.25	18.48	18.25	18.22	18.08	17.81	18.14	18.11	18.50	18.14	18.02
Na_2O	0.28	0.24	0.28	0.24	0.24	0.25	0.21	0.24	0.23	0.19	0.21	0.25
K_2O	0.00	0.00	0.00	0.00	0.01	0.00	0.00	0.00	0.00	0.00	0.02	0.01
Cr_2O_3	0.00	0.04	0.00	0.04	0.00	0.01	0.00	0.16	0.02	0.01	0.05	0.03
MnO	0.39	0.55	0.39	0.55	0.53	0.55	0.56	0.48	0.39	0.49	0.43	0.47
NiO	0.03	0.00	0.03	0.00	0.00	0.03	0.00	0.03	0.04	0.00	0.01	0.00
V_2O_3	0.03	0.02	0.03	0.02	0.01	0.06	0.08	0.05	0.05	0.04	0.05	0.03
Cl	0.01	0.01	0.01	0.01	0.00	0.00	0.01	0.00	0.00	0.00	0.01	0.00
Total	99.13	99.95	99.13	99.95	99.92	99.50	99.61	98.88	99.02	99.80	99.88	100.67
Mg2+**	89450.11	91175.18	89450.11	91175.18	87483.78	86711.72	87948.22	87127.91	87924.09	87465.68	88316.15	88877.10
Fe2+**	809620.44	851405.52	809620.44	851405.52	814324.72	833349.39	803048.29	808651.92	812871.93	813079.47	836808.42	871052.81
Mg#***	9.95	9.67	9.95	9.67	9.70	9.42	9.87	9.73	9.76	9.71	9.55	9.26
Wo	32.20	31.20	32.20	31.20	32.09	31.78	31.68	32.12	31.92	32.45	31.61	30.98
Ens	35.83	36.56	35.83	36.56	35.65	35.61	36.28	35.65	35.90	35.28	35.96	36.26
Fer	31.84	32.84	31.84	32.84	32.36	33.05	32.23	32.30	32.33	32.17	32.90	33.78
4 Ca												
Si	1.79	1.76	1.79	1.76	1.81	1.80	1.82	1.80	1.81	1.81	1.80	1.79
Ti	0.01	0.02	0.01	0.02	0.02	0.02	0.02	0.01	0.01	0.01	0.02	0.02
Al	0.03	0.02	0.03	0.02	0.02	0.02	0.02	0.03	0.03	0.02	0.02	0.02
Fe2	0.68	0.71	0.68	0.71	0.68	0.70	0.68	0.69	0.69	0.68	0.70	0.72
Mg	0.77	0.78	0.77	0.78	0.75	0.75	0.76	0.75	0.76	0.75	0.76	0.75
Ca	0.69	0.67	0.69	0.67	0.68	0.67	0.67	0.68	0.68	0.69	0.67	0.66
Na	0.02	0.02	0.02	0.02	0.02	0.02	0.01	0.02	0.02	0.01	0.01	0.02
K	0.00	0.00	0.00	0.00	0.00	0.00	0.00	0.00	0.00	0.00	0.00	0.00

Cr	0.00	0.00	0.00	0.00	0.00	0.00	0.00	0.00	0.00	0.00	0.00	0.00
Mn	0.01	0.02	0.01	0.02	0.02	0.02	0.02	0.01	0.01	0.01	0.01	0.01
Ni	0.00	0.00	0.00	0.00	0.00	0.00	0.00	0.00	0.00	0.00	0.00	0.00
V	0.00	0.00	0.00	0.00	0.00	0.00	0.00	0.00	0.00	0.00	0.00	0.00
Cl	0.00	0.00	0.00	0.00	0.00	0.00	0.00	0.00	0.00	0.00	0.00	0.00
Total	4.00	4.00	4.00	4.00	4.00	4.00	4.00	4.00	4.00	4.00	4.00	4.00
Struc. Form.												
Site T												
Si T	1.79	1.76	1.79	1.76	1.81	1.80	1.82	1.80	1.81	1.81	1.80	1.79
Al (n)	0.21	0.24	0.21	0.24	0.19	0.20	0.18	0.20	0.19	0.19	0.20	0.21
Al	0.03	0.02	0.03	0.02	0.02	0.02	0.02	0.03	0.03	0.02	0.02	0.02
Al T	0.03	0.02	0.03	0.02	0.02	0.02	0.02	0.03	0.03	0.02	0.02	0.02
Fe3 (n)	0.19	0.22	0.19	0.22	0.16	0.17	0.16	0.17	0.17	0.16	0.18	0.19
Fe3	0.68	0.71	0.68	0.71	0.68	0.70	0.68	0.69	0.69	0.68	0.70	0.72
Fe3 T	0.19	0.22	0.19	0.22	0.16	0.17	0.16	0.17	0.17	0.16	0.18	0.19
Fe (rest)	0.49	0.49	0.49	0.49	0.52	0.53	0.52	0.52	0.52	0.52	0.52	0.53
Total	2.00	2.00	2.00	2.00	2.00	2.00	2.00	2.00	2.00	2.00	2.00	2.00
Site M1												
Fe 3 (M1)	0.49	0.49	0.49	0.49	0.52	0.53	0.52	0.52	0.52	0.52	0.52	0.53
Ti (M1)	0.01	0.02	0.01	0.02	0.02	0.02	0.02	0.01	0.01	0.01	0.02	0.02
Cr (M1)	0.00	0.00	0.00	0.00	0.00	0.00	0.00	0.00	0.00	0.00	0.00	0.00
V (M1)	0.00	0.00	0.00	0.00	0.00	0.00	0.00	0.00	0.00	0.00	0.00	0.00
Mn (M1)	0.01	0.02	0.01	0.02	0.02	0.02	0.02	0.01	0.01	0.01	0.01	0.01
Mg	0.77	0.78	0.77	0.78	0.75	0.75	0.76	0.75	0.76	0.75	0.76	0.75
Mg (n)	0.48	0.47	0.48	0.47	0.44	0.44	0.44	0.45	0.46	0.45	0.44	0.43
Mg (M1)	0.48	0.47	0.48	0.47	0.44	0.44	0.44	0.45	0.46	0.45	0.44	0.43
Mg (rest)	0.29	0.31	0.29	0.31	0.31	0.31	0.32	0.30	0.30	0.30	0.31	0.32
Total	1.00	1.00	1.00	1.00	1.00	1.00	1.00	1.00	1.00	1.00	1.00	1.00
Site M2												
Mg (M2)	0.29	0.31	0.29	0.31	0.31	0.31	0.32	0.30	0.30	0.30	0.31	0.32
Ca (M2)	0.69	0.67	0.69	0.67	0.68	0.67	0.67	0.68	0.68	0.69	0.67	0.66
Na (M2)	0.02	0.02	0.02	0.02	0.02	0.02	0.01	0.02	0.02	0.01	0.01	0.02

Sample	MS_03a	MS_05b	MS_05b	MS_05b	MS_05b	MS_05b	MS_05b	MS_05b	MS_05b	MS_05b	MS_05b	MS_05b
m/f	f	f	f	f	f	f	f	f	f	f	f	f
Position	x	c	c	b	x	x	x	x	x	x	x	x
Local	Mato Perso	Mato Perso	Mato Perso	Mato Perso	Mato Perso	Mato Perso	Mato Perso	Mato Perso	Mato Perso	Mato Perso	Mato Perso	Mato Perso
SiO_2	52.10	51.80	50.98	51.92	51.37	51.13	51.94	50.74	51.10	51.91	51.92	52.23
TiO_2	0.49	0.73	0.45	0.43	0.49	0.77	0.49	0.41	0.60	0.59	0.31	0.45
Al_2O_3	1.71	1.76	1.66	1.72	1.71	1.68	1.68	1.57	1.61	1.64	1.81	1.57
FeO*	10.72	10.57	10.35	10.68	10.35	10.27	10.62	10.14	10.15	10.66	10.47	10.28
$Fe_2O_{3(T)}$	12.05	11.87	11.63	12.00	11.63	11.54	11.93	11.40	11.40	11.97	11.76	11.55
MgO	14.66	14.34	14.64	14.54	14.23	14.45	14.45	14.86	14.57	14.94	14.33	14.60
CaO	18.69	18.22	17.98	18.29	17.68	17.74	17.96	18.07	18.15	18.13	18.25	18.42
Na_2O	0.28	0.27	0.26	0.25	0.20	0.21	0.26	0.27	0.23	0.29	0.28	0.18
K_2O	0.03	0.00	0.00	0.00	0.00	0.00	0.00	0.03	0.02	0.05	0.02	0.00
Cr_2O_3	0.05	0.02	0.00	0.01	0.05	0.03	0.00	0.07	0.00	0.06	0.07	0.06
MnO	0.50	0.44	0.54	0.34	0.40	0.36	0.38	0.47	0.53	0.53	0.37	0.41
NiO	0.02	0.06	0.01	0.09	0.01	0.03	0.04	0.04	0.04	0.02	0.05	0.06
V_2O_3	0.07	0.01	0.05	0.08	0.02	0.00	0.00	0.00	0.04	0.02	0.03	0.01
Cl	0.00	0.01	0.00	0.00	0.02	0.03	0.01	0.01	0.01	0.00	0.00	0.01
Total	100.64	99.52	98.20	99.66	97.82	98.01	99.14	97.92	98.29	100.15	99.20	99.53
Mg2+**	88430.75	86482.51	88298.06	87719.01	85855.22	87127.91	87146.00	89637.09	87887.90	90137.72	86428.23	88038.69
Fe2+**	833626.11	821381.15	804501.08	830236.26	804846.98	797998.11	825531.98	788382.00	788866.27	828299.20	813632.92	799105.00
Mg#***	9.59	9.53	9.89	9.56	9.64	9.84	9.55	10.21	10.02	9.81	9.60	9.92
Wo	32.28	32.13	31.83	31.95	31.77	31.96	32.29	31.47	32.28	32.45	32.40	31.70
Ens	35.31	35.38	36.16	35.61	35.90	36.40	35.83	36.45	35.32	35.54	35.41	36.01
Fer	32.49	32.68	32.13	32.71	32.63	31.47	31.66	32.44	32.46	31.77	32.08	32.63
4 Ca												
Si	1.79	1.80	1.80	1.80	1.82	1.79	1.80	1.79	1.81	1.82	1.81	1.79
Ti	0.01	0.02	0.01	0.01	0.01	0.01	0.02	0.02	0.01	0.01	0.02	0.02
Al	0.02	0.03	0.02	0.02	0.03	0.02	0.02	0.02	0.03	0.02	0.02	0.02
Fe2	0.69	0.69	0.68	0.70	0.69	0.67	0.67	0.69	0.69	0.67	0.68	0.70
Mg	0.75	0.74	0.77	0.75	0.75	0.78	0.77	0.77	0.75	0.76	0.75	0.76
Ca	0.69	0.68	0.68	0.68	0.67	0.68	0.69	0.67	0.68	0.69	0.69	0.68
Na	0.02	0.02	0.02	0.02	0.01	0.02	0.02	0.02	0.02	0.01	0.02	0.02

K	0.00	0.00	0.00	0.00	0.00	0.00	0.00	0.00	0.00	0.00	0.00	0.00
Cr	0.00	0.00	0.00	0.00	0.00	0.00	0.00	0.00	0.00	0.00	0.00	0.00
Mn	0.01	0.01	0.02	0.01	0.01	0.01	0.02	0.02	0.01	0.01	0.01	0.02
Ni	0.00	0.00	0.00	0.00	0.00	0.00	0.00	0.00	0.00	0.00	0.00	0.00
V	0.00	0.00	0.00	0.00	0.00	0.00	0.00	0.00	0.00	0.00	0.00	0.00
Cl	0.00	0.00	0.00	0.00	0.00	0.00	0.00	0.00	0.00	0.00	0.00	0.00
Total	4.00	4.00	4.00	4.00	4.00	4.00	4.00	4.00	4.00	4.00	4.00	4.00
Struc. Form.												
Site T												
Si T	1.79	1.80	1.80	1.80	1.82	1.79	1.80	1.79	1.81	1.82	1.81	1.79
Al (n)	0.21	0.20	0.20	0.20	0.18	0.21	0.20	0.21	0.19	0.18	0.19	0.21
Al	0.02	0.03	0.02	0.02	0.03	0.02	0.02	0.02	0.03	0.02	0.02	0.02
Al T	0.02	0.03	0.02	0.02	0.03	0.02	0.02	0.02	0.03	0.02	0.02	0.02
Fe3 (n)	0.18	0.17	0.18	0.17	0.15	0.19	0.17	0.19	0.16	0.16	0.17	0.18
Fe3	0.69	0.69	0.68	0.70	0.69	0.67	0.67	0.69	0.69	0.67	0.68	0.70
Fe3 T	0.18	0.17	0.18	0.17	0.15	0.19	0.17	0.19	0.16	0.16	0.17	0.18
Fe (rest)	0.51	0.52	0.51	0.52	0.54	0.49	0.50	0.51	0.53	0.51	0.51	0.51
Total	2.00	2.00	2.00	2.00	2.00	2.00	2.00	2.00	2.00	2.00	2.00	2.00
Site M1												
Fe 3 (M1)	0.51	0.52	0.51	0.52	0.54	0.49	0.50	0.51	0.53	0.51	0.51	0.51
Ti (M1)	0.01	0.02	0.01	0.01	0.01	0.01	0.02	0.02	0.01	0.01	0.02	0.02
Cr (M1)	0.00	0.00	0.00	0.00	0.00	0.00	0.00	0.00	0.00	0.00	0.00	0.00
V (M1)	0.00	0.00	0.00	0.00	0.00	0.00	0.00	0.00	0.00	0.00	0.00	0.00
Mn (M1)	0.01	0.01	0.02	0.01	0.01	0.01	0.02	0.02	0.01	0.01	0.01	0.02
Mg	0.75	0.74	0.77	0.75	0.75	0.78	0.77	0.77	0.75	0.76	0.75	0.76
Mg (n)	0.46	0.45	0.47	0.45	0.44	0.49	0.47	0.46	0.45	0.46	0.46	0.46
Mg (M1)	0.46	0.45	0.47	0.45	0.44	0.49	0.47	0.46	0.45	0.46	0.46	0.46
Mg (sobra)	0.29	0.30	0.30	0.30	0.31	0.29	0.30	0.31	0.30	0.30	0.29	0.30
Total	1.00	1.00	1.00	1.00	1.00	1.00	1.00	1.00	1.00	1.00	1.00	1.00
Site M2												
Mg (M2)	0.29	0.30	0.30	0.30	0.31	0.29	0.30	0.31	0.30	0.30	0.29	0.30
Ca (M2)	0.69	0.68	0.68	0.68	0.67	0.68	0.69	0.67	0.68	0.69	0.69	0.68
Na (M2)	0.02	0.02	0.02	0.02	0.01	0.02	0.02	0.02	0.02	0.01	0.02	0.02

Sample	MS_05b	MS_05b	MS_05b	MS_05b	MS_05b	MS_05b	MS_05b	MS_05b	MS_05b	MS_05b	MS_05b	MS_05b
m/f	f	f	f	f	f	f	f	f	f	f	f	f
Position	x	x	x	x	x	x	x	x	x	x	x	x
Local	Mato Perso	Mato Perso	Mato Perso	Mato Perso	Mato Perso	Mato Perso	Mato Perso	Mato Perso	Mato Perso	Mato Perso	Mato Perso	Mato Perso
SiO_2	52.18	52.20	51.57	51.27	50.98	51.34	51.02	50.61	50.69	50.90	50.99	51.00
TiO_2	0.58	0.68	0.53	0.44	0.79	0.33	0.49	0.47	0.44	0.47	0.61	0.60
Al_2O_3	1.69	1.62	1.75	1.70	1.76	1.51	1.62	1.61	1.64	1.69	1.64	1.63
FeO*	10.41	10.78	10.47	10.23	10.52	10.52	10.60	10.60	10.64	10.37	10.86	10.67
$Fe_2O_{3(T)}$	11.70	12.11	11.77	11.50	11.82	11.82	11.91	11.91	11.96	11.65	12.21	11.99
MgO	14.53	14.85	14.37	14.52	14.36	14.22	14.62	14.59	14.25	14.26	14.35	14.61
CaO	18.44	18.36	18.18	18.02	17.90	17.84	17.87	17.59	17.30	17.93	17.92	17.81
Na_2O	0.30	0.29	0.29	0.27	0.30	0.25	0.24	0.33	0.25	0.23	0.16	0.21
K_2O	0.00	0.01	0.01	0.03	0.03	0.00	0.00	0.01	0.01	0.01	0.02	0.00
Cr_2O_3	0.00	0.00	0.02	0.03	0.01	0.00	0.06	0.01	0.02	0.05	0.03	0.00
MnO	0.46	0.53	0.41	0.32	0.48	0.50	0.39	0.56	0.56	0.41	0.48	0.57
NiO	0.00	0.00	0.01	0.00	0.00	0.00	0.01	0.01	0.00	0.00	0.00	0.00
V_2O_3	0.03	0.01	0.05	0.06	0.05	0.04	0.02	0.02	0.00	0.03	0.07	0.01
Cl	0.02	0.00	0.00	0.01	0.00	0.00	0.00	0.01	0.00	0.01	0.00	0.00
Total	99.93	100.66	98.95	98.15	98.47	97.86	98.24	97.72	97.12	97.64	98.50	98.47
Mg2+**	87664.73	89558.68	86663.47	87550.13	86597.12	85782.84	88207.58	88026.63	85939.66	86030.14	86524.74	88111.07
Fe2+**	809274.54	837776.94	814117.18	795300.06	817507.03	817922.12	823594.92	823594.92	827261.50	806230.60	844418.28	829613.64
Mg#***	9.77	9.66	9.62	9.92	9.58	9.49	9.67	9.66	9.41	9.64	9.29	9.60
Wo	32.16	31.78	31.81	31.47	31.47	31.14	31.01	32.04	31.48	31.33	31.65	31.90
Ens	35.47	35.82	35.67	36.27	36.27	36.60	36.42	35.62	35.77	36.33	36.12	35.89
Fer	32.49	32.75	32.90	32.71	32.71	32.90	33.46	32.50	33.47	32.92	32.54	32.38
4 Ca												
Si	1.81	1.79	1.81	1.79	1.79	1.79	1.80	1.80	1.79	1.79	1.80	1.79
Ti	0.01	0.02	0.01	0.01	0.01	0.01	0.01	0.01	0.02	0.02	0.02	0.02
Al	0.03	0.03	0.02	0.02	0.02	0.02	0.02	0.02	0.02	0.02	0.02	0.02
Fe2	0.69	0.70	0.70	0.70	0.70	0.70	0.71	0.69	0.72	0.70	0.69	0.69
Mg	0.75	0.75	0.75	0.77	0.77	0.77	0.76	0.75	0.75	0.76	0.76	0.76
Ca	0.68	0.67	0.68	0.67	0.67	0.67	0.66	0.68	0.67	0.67	0.67	0.68
Na	0.02	0.02	0.02	0.02	0.02	0.02	0.02	0.02	0.01	0.01	0.01	0.02

K	0.00	0.00	0.00	0.00	0.00	0.00	0.00	0.00	0.00	0.00	0.00	0.00
Cr	0.00	0.00	0.00	0.00	0.00	0.00	0.00	0.00	0.00	0.00	0.00	0.00
Mn	0.01	0.01	0.01	0.01	0.01	0.02	0.02	0.01	0.01	0.02	0.01	0.01
Ni	0.00	0.00	0.00	0.00	0.00	0.00	0.00	0.00	0.00	0.00	0.00	0.00
V	0.00	0.00	0.00	0.00	0.00	0.00	0.00	0.00	0.00	0.00	0.00	0.00
Cl	0.00	0.00	0.00	0.00	0.00	0.00	0.00	0.00	0.00	0.00	0.00	0.00
Total	4.00	4.00	4.00	4.00	4.00	4.00	4.00	4.00	4.00	4.00	4.00	4.00
Struc. Form.												
Site T												
Si T	1.81	1.79	1.81	1.79	1.79	1.79	1.80	1.80	1.79	1.79	1.80	1.79
Al (n)	0.19	0.21	0.19	0.21	0.21	0.21	0.20	0.20	0.21	0.21	0.20	0.21
Al	0.03	0.03	0.02	0.02	0.02	0.02	0.02	0.02	0.02	0.02	0.02	0.02
Al T	0.03	0.03	0.02	0.02	0.02	0.02	0.02	0.02	0.02	0.02	0.02	0.02
Fe3 (n)	0.17	0.18	0.16	0.18	0.18	0.19	0.17	0.17	0.19	0.19	0.17	0.18
Fe3	0.69	0.70	0.70	0.70	0.70	0.70	0.71	0.69	0.72	0.70	0.69	0.69
Fe3 T	0.17	0.18	0.16	0.18	0.18	0.19	0.17	0.17	0.19	0.19	0.17	0.18
Fe (rest)	0.52	0.51	0.53	0.52	0.52	0.51	0.54	0.52	0.53	0.52	0.52	0.51
Total	2.00	2.00	2.00	2.00	2.00	2.00	2.00	2.00	2.00	2.00	2.00	2.00
Site M1												
Fe 3 (M1)	0.52	0.51	0.53	0.52	0.52	0.51	0.54	0.52	0.53	0.52	0.52	0.51
Ti (M1)	0.01	0.02	0.01	0.01	0.01	0.01	0.01	0.01	0.02	0.02	0.02	0.02
Cr (M1)	0.00	0.00	0.00	0.00	0.00	0.00	0.00	0.00	0.00	0.00	0.00	0.00
V (M1)	0.00	0.00	0.00	0.00	0.00	0.00	0.00	0.00	0.00	0.00	0.00	0.00
Mn (M1)	0.01	0.01	0.01	0.01	0.01	0.02	0.02	0.01	0.01	0.02	0.01	0.01
Mg	0.75	0.75	0.75	0.77	0.77	0.77	0.76	0.75	0.75	0.76	0.76	0.76
Mg (n)	0.45	0.45	0.44	0.46	0.46	0.46	0.43	0.45	0.44	0.45	0.45	0.46
Mg (M1)	0.45	0.45	0.44	0.46	0.46	0.46	0.43	0.45	0.44	0.45	0.45	0.46
Mg (sobra)	0.30	0.30	0.31	0.31	0.31	0.31	0.32	0.30	0.31	0.32	0.31	0.30
Total	1.00	1.00	1.00	1.00	1.00	1.00	1.00	1.00	1.00	1.00	1.00	1.00
Site M2												
Mg (M2)	0.30	0.30	0.31	0.31	0.31	0.31	0.32	0.30	0.31	0.32	0.31	0.30
Ca (M2)	0.68	0.67	0.68	0.67	0.67	0.67	0.66	0.68	0.67	0.67	0.67	0.68
Na (M2)	0.02	0.02	0.02	0.02	0.02	0.02	0.02	0.02	0.01	0.01	0.01	0.02

Sample	MS_05b	MS_05b	MS_11c	MS_11b	MS_11b	MS_11b	MS_11b	MS_11b	MS_11b	MS_11b	MS_11b	MS_11b
m/f	f	f	f	m	m	m	m	m	m	m	m	m
Position	x	x	x	x	x	x	x	x	x	x	x	x
Local	Mato Perso	Mato Perso	São Marcos	São Marcos	São Marcos	São Marcos	São Marcos	São Marcos	São Marcos	São Marcos	São Marcos	São Marcos
SiO_2	51.16	51.05	48.15	48.45	51.61	50.44	51.75	51.26	50.99	50.47	51.32	50.80
TiO_2	0.63	0.58	1.14	0.94	0.38	0.60	0.39	0.71	0.67	0.87	0.78	0.51
Al_2O_3	1.66	1.48	5.45	2.47	1.65	1.45	1.46	1.47	1.79	1.55	1.44	1.52
FeO*	10.47	10.47	11.85	17.15	14.49	12.96	11.78	12.25	12.13	11.55	12.13	13.15
$Fe_2O_{3(T)}$	11.77	11.76	13.32	19.27	16.28	14.56	13.23	13.76	13.63	12.97	13.63	14.78
MgO	14.52	14.55	11.60	11.85	14.99	12.97	14.38	14.71	14.26	13.63	13.76	13.20
CaO	17.87	18.09	18.71	13.16	11.86	16.81	17.88	16.89	17.24	18.15	17.80	17.84
Na_2O	0.18	0.23	0.33	0.26	0.27	0.35	0.20	0.21	0.25	0.20	0.25	0.22
K_2O	0.02	0.00	0.04	0.04	0.00	0.00	0.01	0.01	0.00	0.01	0.00	0.00
Cr_2O_3	0.00	0.07	0.00	0.00	0.00	0.00	0.07	0.00	0.00	0.00	0.00	0.09
MnO	0.37	0.46	0.50	0.74	0.58	0.48	0.47	0.70	0.59	0.50	0.53	0.65
NiO	0.00	0.01	0.00	0.00	0.00	0.03	0.00	0.03	0.04	0.03	0.05	0.00
V_2O_3	0.01	0.02	0.06	0.07	0.00	0.04	0.01	0.02	0.00	0.06	0.02	0.04
Cl	0.01	0.01	0.01	0.01	0.01	0.01	0.00	0.01	0.00	0.00	0.01	0.00
Total	98.19	98.31	99.30	97.28	97.62	98.16	99.84	99.77	99.45	98.47	99.61	99.65
Mg2+**	87586.32	87779.33	69937.56	71475.65	90433.28	78243.21	86711.72	88726.31	86006.01	82230.17	83020.32	79630.50
Fe2+**	814048.00	813632.92	921485.46	1333248.33	1125983.28	1007269.39	915535.93	951855.74	943000.62	897410.61	943138.98	1022212.40
Mg#***	9.71	9.74	7.05	5.09	7.43	7.21	8.65	8.53	8.36	8.39	8.09	7.23
Wo	33.63	22.03	20.40	29.18	30.55	28.71	29.54	31.63	30.57	30.10	31.33	21.88
Ens	30.13	38.51	46.80	34.94	35.87	37.73	36.53	34.33	34.97	33.99	36.30	45.35
Fer	37.37	50.36	43.71	39.47	35.28	36.50	36.46	35.30	36.54	38.91	32.95	41.81
4 Ca												
Si	1.72	1.68	1.78	1.76	1.78	1.76	1.76	1.77	1.77	1.75	1.80	1.79
Ti	0.03	0.02	0.01	0.02	0.01	0.02	0.02	0.02	0.02	0.01	0.01	0.01
Al	0.08	0.04	0.02	0.02	0.02	0.02	0.03	0.02	0.02	0.02	0.02	0.02
Fe2	0.80	1.12	0.94	0.85	0.76	0.79	0.79	0.76	0.79	0.85	0.70	0.90
Mg	0.62	0.61	0.77	0.68	0.74	0.75	0.73	0.71	0.71	0.68	0.76	0.78
Ca	0.72	0.49	0.44	0.63	0.66	0.62	0.64	0.68	0.66	0.66	0.66	0.47
Na	0.02	0.02	0.02	0.02	0.01	0.01	0.02	0.01	0.02	0.01	0.02	0.01

K	0.00	0.00	0.00	0.00	0.00	0.00	0.00	0.00	0.00	0.00	0.00	0.00
Cr	0.00	0.00	0.00	0.00	0.00	0.00	0.00	0.00	0.00	0.00	0.00	0.00
Mn	0.01	0.02	0.02	0.01	0.01	0.02	0.02	0.01	0.02	0.02	0.02	0.02
Ni	0.00	0.00	0.00	0.00	0.00	0.00	0.00	0.00	0.00	0.00	0.00	0.00
V	0.00	0.00	0.00	0.00	0.00	0.00	0.00	0.00	0.00	0.00	0.00	0.00
Cl	0.00	0.00	0.00	0.00	0.00	0.00	0.00	0.00	0.00	0.00	0.00	0.00
Total	4.00	4.00	4.00	4.00	4.00	4.00	4.00	4.00	4.00	4.00	4.00	4.00
Struc. Form.												
Site T												
Si T	1.72	1.68	1.78	1.76	1.78	1.76	1.76	1.77	1.77	1.75	1.80	1.79
Al (n)	0.28	0.32	0.22	0.24	0.22	0.24	0.24	0.23	0.23	0.25	0.20	0.21
Al	0.08	0.04	0.02	0.02	0.02	0.02	0.03	0.02	0.02	0.02	0.02	0.02
Al T	0.08	0.04	0.02	0.02	0.02	0.02	0.03	0.02	0.02	0.02	0.02	0.02
Fe3 (n)	0.20	0.29	0.19	0.21	0.20	0.22	0.21	0.21	0.21	0.23	0.17	0.20
Fe3	0.80	1.12	0.94	0.85	0.76	0.79	0.79	0.76	0.79	0.85	0.70	0.90
Fe3 T	0.20	0.29	0.19	0.21	0.20	0.22	0.21	0.21	0.21	0.23	0.17	0.20
Fe (rest)	0.60	0.83	0.74	0.64	0.56	0.57	0.58	0.55	0.58	0.62	0.53	0.71
Total	2.00	2.00	2.00	2.00	2.00	2.00	2.00	2.00	2.00	2.00	2.00	2.00
Site M1												
Fe 3 (M1)	0.60	0.83	0.74	0.64	0.56	0.57	0.58	0.55	0.58	0.62	0.53	0.71
Ti (M1)	0.03	0.02	0.01	0.02	0.01	0.02	0.02	0.02	0.02	0.01	0.01	0.01
Cr (M1)	0.00	0.00	0.00	0.00	0.00	0.00	0.00	0.00	0.00	0.00	0.00	0.00
V (M1)	0.00	0.00	0.00	0.00	0.00	0.00	0.00	0.00	0.00	0.00	0.00	0.00
Mn (M1)	0.01	0.02	0.02	0.01	0.01	0.02	0.02	0.01	0.02	0.02	0.02	0.02
Mg	0.62	0.61	0.77	0.68	0.74	0.75	0.73	0.71	0.71	0.68	0.76	0.78
Mg (n)	0.36	0.12	0.23	0.33	0.41	0.39	0.39	0.41	0.39	0.35	0.44	0.27
Mg (M1)	0.36	0.12	0.23	0.33	0.41	0.39	0.39	0.41	0.39	0.35	0.44	0.27
Mg (rest)	0.26	0.49	0.54	0.35	0.33	0.36	0.34	0.30	0.32	0.33	0.31	0.52
Total	1.00	1.00	1.00	1.00	1.00	1.00	1.00	1.00	1.00	1.00	1.00	1.00
Site M2												
Mg (M2)	0.26	0.49	0.54	0.35	0.33	0.36	0.34	0.30	0.32	0.33	0.31	0.52
Ca (M2)	0.72	0.49	0.44	0.63	0.66	0.62	0.64	0.68	0.66	0.66	0.66	0.47
Na (M2)	0.02	0.02	0.02	0.02	0.01	0.01	0.02	0.01	0.02	0.01	0.02	0.01

Sample	MS19B1	MS19B1	MS19B1	MS19B1	MS19B2	MS19B2	MS19B2	MS19B2	MS19B2	MS19B2	MS_30	MS38
m/f	f	f	f	f	m	m	m	m	m	m	f	m
Position	x	x	x	x	x	x	x	x	x	x	x	x
Local	Jaquirana	Jaquirana	Jaquirana	Jaquirana	Jaquirana	Jaquirana	Jaquirana	Jaquirana	Jaquirana	Jaquirana	Jaquirana	Jaquirana
SiO_2	53.00	53.05	53.14	52.73	51.93	51.86	52.46	52.96	52.89	51.93	51.41	52.39
TiO_2	0.51	0.36	0.48	0.72	0.55	0.83	0.46	0.27	0.58	0.55	0.70	0.45
Al_2O_3	1.74	1.21	1.83	1.52	1.83	1.39	1.80	1.64	1.39	1.83	1.43	1.55
FeO*	10.94	14.27	10.90	11.73	12.90	13.10	10.93	10.70	10.78	12.90	14.56	12.04
$Fe_2O_{3(T)}$	12.29	16.04	12.25	13.18	14.50	14.71	12.29	12.03	12.12	14.50	11.83	13.53
MgO	14.95	15.62	15.23	14.59	13.67	13.42	15.42	15.21	15.65	13.67	13.29	14.68
CaO	18.25	13.10	17.80	17.17	15.85	17.46	18.05	17.95	18.41	15.85	16.99	17.05
Na_2O	0.30	0.14	0.23	0.27	0.19	0.18	0.22	0.45	0.26	0.19	0.17	0.31
K_2O	0.04	0.01	0.06	0.07	0.04	0.05	0.01	0.02	0.04	0.04	0.02	0.04
Cr_2O_3	0.01	0.01	0.02	0.00	0.00	0.04	0.00	0.03	0.03	0.00	0.07	0.01
MnO	0.56	0.54	0.51	0.57	0.43	0.56	0.37	0.28	0.41	0.43	0.60	0.58
NiO	0.00	0.00	0.00	0.00	0.00	0.01	0.02	0.00	0.00	0.00	0.03	0.01
V_2O_3	0.03	0.04	0.00	0.04	0.00	0.05	0.01	0.03	0.04	0.00	0.00	0.04
Cl	0.02	0.00	0.00	0.00	0.00	0.00	0.00	0.00	0.00	0.00	0.00	0.00
Total	101.68	100.12	101.53	100.86	98.98	100.56	101.09	100.86	101.83	98.98	99.27	100.63
Mg2+**	90149.79	94227.22	91862.79	88014.57	82465.40	80927.32	92978.66	91760.25	94378.01	82465.40	80185.42	88551.39
Fe2+**	850506.17	1109310.76	847185.51	911869.36	1002841.83	1017923.20	849883.55	831896.59	838122.85	1002841.83	1131452.44	935944.20
Mg#***	9.58	7.83	9.78	8.80	7.60	7.36	9.86	9.93	10.12	7.60	6.62	8.64
Wo	31.33	21.88	30.63	29.58	27.56	29.54	30.77	31.01	31.16	27.56	31.49	29.09
Ens	36.30	45.35	37.32	37.15	37.51	34.84	37.27	37.09	37.15	37.51	35.24	37.47
Fer	32.95	41.81	32.90	35.44	39.35	38.87	32.68	32.42	32.00	39.35	34.23	36.04
4 Ca												
Si	1.80	1.79	1.81	1.80	1.80	1.77	1.79	1.81	1.79	1.80	1.85	1.79
Ti	0.01	0.01	0.01	0.02	0.01	0.02	0.01	0.01	0.01	0.01	0.02	0.01
Al	0.02	0.02	0.03	0.02	0.03	0.02	0.03	0.02	0.02	0.03	0.02	0.02
Fe2	0.70	0.90	0.70	0.75	0.84	0.84	0.70	0.69	0.69	0.84	0.71	0.77
Mg	0.76	0.78	0.77	0.74	0.71	0.68	0.78	0.78	0.79	0.71	0.71	0.75
Ca	0.66	0.47	0.65	0.63	0.59	0.64	0.66	0.66	0.67	0.59	0.65	0.62
Na	0.02	0.01	0.02	0.02	0.01	0.01	0.01	0.03	0.02	0.01	0.01	0.02
K	0.00	0.00	0.00	0.00	0.00	0.00	0.00	0.00	0.00	0.00	0.00	0.00

Cr	0.00	0.00	0.00	0.00	0.00	0.00	0.00	0.00	0.00	0.00	0.00	0.00
Mn	0.02	0.02	0.01	0.02	0.01	0.02	0.01	0.01	0.01	0.01	0.02	0.02
Ni	0.00	0.00	0.00	0.00	0.00	0.00	0.00	0.00	0.00	0.00	0.00	0.00
V	0.00	0.00	0.00	0.00	0.00	0.00	0.00	0.00	0.00	0.00	0.00	0.00
Cl	0.00	0.00	0.00	0.00	0.00	0.00	0.00	0.00	0.00	0.00	0.00	0.00
Total	4.00	4.00	4.00	4.00	4.00	4.00	4.00	4.00	4.00	4.00	4.00	4.00
Struc. Form.												
Site T												
Si T	1.80	1.79	1.81	1.80	1.80	1.77	1.79	1.81	1.79	1.80	1.85	1.79
Al (n)	0.20	0.21	0.19	0.20	0.20	0.23	0.21	0.19	0.21	0.20	0.15	0.21
Al	0.02	0.02	0.03	0.02	0.03	0.02	0.03	0.02	0.02	0.03	0.02	0.02
Al T	0.02	0.02	0.03	0.02	0.03	0.02	0.03	0.02	0.02	0.03	0.02	0.02
Fe3 (n)	0.17	0.20	0.16	0.18	0.17	0.21	0.18	0.17	0.19	0.17	0.13	0.19
Fe3	0.70	0.90	0.70	0.75	0.84	0.84	0.70	0.69	0.69	0.84	0.71	0.77
Fe3 T	0.17	0.20	0.16	0.18	0.17	0.21	0.18	0.17	0.19	0.17	0.13	0.19
Fe (rest)	0.53	0.71	0.53	0.57	0.66	0.63	0.52	0.52	0.50	0.66	0.58	0.58
Total	2.00	2.00	2.00	2.00	2.00	2.00	2.00	2.00	2.00	2.00	2.00	2.00
Site M1												
Fe 3 (M1)	0.53	0.71	0.53	0.57	0.66	0.63	0.52	0.52	0.50	0.66	0.58	0.58
Ti (M1)	0.01	0.01	0.01	0.02	0.01	0.02	0.01	0.01	0.01	0.01	0.02	0.01
Cr (M1)	0.00	0.00	0.00	0.00	0.00	0.00	0.00	0.00	0.00	0.00	0.00	0.00
V (M1)	0.00	0.00	0.00	0.00	0.00	0.00	0.00	0.00	0.00	0.00	0.00	0.00
Mn (M1)	0.02	0.02	0.01	0.02	0.01	0.02	0.01	0.01	0.01	0.01	0.02	0.02
Mg	0.76	0.78	0.77	0.74	0.71	0.68	0.78	0.78	0.79	0.71	0.71	0.75
Mg (n)	0.44	0.27	0.44	0.39	0.31	0.33	0.46	0.46	0.48	0.31	0.38	0.39
Mg (M1)	0.44	0.27	0.44	0.39	0.31	0.33	0.46	0.46	0.48	0.31	0.38	0.39
Mg (rest)	0.31	0.52	0.33	0.35	0.40	0.35	0.32	0.31	0.31	0.40	0.33	0.36
Total	1.00	1.00	1.00	1.00	1.00	1.00	1.00	1.00	1.00	1.00	1.00	1.00
Site M2												
Mg (M2)	0.31	0.52	0.33	0.35	0.40	0.35	0.32	0.31	0.31	0.40	0.33	0.36
Ca (M2)	0.66	0.47	0.65	0.63	0.59	0.64	0.66	0.66	0.67	0.59	0.65	0.62
Na (M2)	0.02	0.01	0.02	0.02	0.01	0.01	0.01	0.03	0.02	0.01	0.01	0.02

Sample	MS38	MS38	MS38	MS50	MS50	MS50	MS50	MS_50	MS51A	MS51A	MS51A	MS51A
m/f	m	m	m	f	f	f	f	f	f	f	m	m
Position	x	x	x	x	x	x	x	x	x	x	x	x
Local	Jaquirana	Jaquirana	Jaquirana	Cambará	Cambará	Cambará	Cambará	Cambará	Cambará	Cambará	Cambará	Cambará
SiO_2	52.11	52.92	52.05	52.58	51.10	53.84	52.24	50.76	52.73	52.49	50.19	51.13
TiO_2	0.63	0.34	0.58	0.42	1.11	0.61	0.41	0.56	0.34	0.21	0.57	0.82
Al_2O_3	1.58	1.71	1.67	1.69	3.97	1.39	1.38	1.70	0.86	0.75	1.33	1.40
FeO*	12.47	11.16	11.58	12.29	12.12	12.98	15.73	12.78	17.22	17.02	14.30	12.30
$Fe_2O_{3(T)}$	14.01	12.54	13.01	13.81	13.61	14.59	17.67	12.14	19.35	19.13	16.06	13.82
MgO	14.42	14.87	13.93	14.10	14.07	14.54	12.75	13.64	22.78	22.78	12.81	14.78
CaO	16.62	17.61	17.08	17.36	17.12	15.53	15.71	16.97	3.33	3.53	16.87	17.39
Na_2O	0.40	0.20	0.92	0.24	0.27	0.94	0.34	0.24	0.02	0.07	0.35	0.26
K_2O	0.03	0.03	0.00	0.04	0.07	0.06	0.09	0.05	0.02	0.01	0.03	0.02
Cr_2O_3	0.03	0.00	0.00	0.02	0.01	0.00	0.00	0.00	0.05	0.00	0.02	0.00
MnO	0.55	0.46	0.34	0.57	0.58	0.42	0.66	0.55	0.62	0.61	0.60	0.34
NiO	0.03	0.06	0.01	0.03	0.00	0.01	0.00	0.03	0.02	0.04	0.01	0.05
V_2O_3	0.04	0.08	0.06	0.03	0.09	0.03	0.06	0.05	0.07	0.05	0.01	0.07
Cl	0.00	0.02	0.00	0.01	0.01	0.02	0.00	0.00	0.01	0.00	0.02	0.00
Total	100.48	100.82	99.65	100.92	102.01	101.98	101.31	97.33	100.20	99.66	98.86	100.07
Mg2+**	86971.08	89685.35	84015.55	85059.03	84853.96	87712.98	76916.24	82278.42	137414.19	137390.06	77254.01	89148.53
Fe2+**	969496.79	867524.60	900316.20	955453.13	941755.37	1009137.27	1222559.39	993246.72	1338644.42	1323286.33	1111247.82	956006.57
Mg#***	8.23	9.37	8.54	8.17	8.27	8.00	5.92	7.65	9.31	9.41	6.50	8.53
Wo	28.39	30.43	30.09	29.65	29.55	26.54	25.74	30.91	5.11	5.42	28.23	29.21
Ens	37.63	37.01	36.19	36.11	36.37	39.44	36.09	35.87	82.62	81.80	34.56	37.16
Fer	37.35	33.82	35.78	36.83	36.67	38.90	45.19	34.52	46.30	45.88	41.95	36.24
4 Ca												
Si	1.78	1.81	1.79	1.79	1.75	1.80	1.74	1.82	1.70	1.70	1.72	1.75
Ti	0.02	0.01	0.02	0.01	0.03	0.02	0.01	0.02	0.01	0.01	0.01	0.02
Al	0.02	0.02	0.02	0.02	0.06	0.02	0.02	0.03	0.01	0.01	0.02	0.02
Fe2	0.80	0.72	0.75	0.79	0.78	0.81	0.99	0.73	1.04	1.04	0.92	0.79
Mg	0.73	0.76	0.72	0.72	0.72	0.72	0.63	0.73	1.10	1.10	0.66	0.75
Ca	0.61	0.65	0.63	0.63	0.63	0.56	0.56	0.65	0.12	0.12	0.62	0.64
Na	0.03	0.01	0.06	0.02	0.02	0.06	0.02	0.02	0.00	0.00	0.02	0.02
K	0.00	0.00	0.00	0.00	0.00	0.00	0.00	0.00	0.00	0.00	0.00	0.00

Cr	0.00	0.00	0.00	0.00	0.00	0.00	0.00	0.00	0.00	0.00	0.00	0.00
Mn	0.02	0.01	0.01	0.02	0.02	0.01	0.02	0.02	0.02	0.02	0.02	0.01
Ni	0.00	0.00	0.00	0.00	0.00	0.00	0.00	0.00	0.00	0.00	0.00	0.00
V	0.00	0.00	0.00	0.00	0.00	0.00	0.00	0.00	0.00	0.00	0.00	0.00
Cl	0.00	0.00	0.00	0.00	0.00	0.00	0.00	0.00	0.00	0.00	0.00	0.00
Total	4.00	4.00	4.00	4.00	4.00	4.00	4.00	4.00	4.00	4.00	4.00	4.00
Struc. Form.												
Site T												
Si T	1.78	1.81	1.79	1.79	1.75	1.80	1.74	1.82	1.70	1.70	1.72	1.75
Al (n)	0.22	0.19	0.21	0.21	0.25	0.20	0.26	0.18	0.30	0.30	0.28	0.25
Al	0.02	0.02	0.02	0.02	0.06	0.02	0.02	0.03	0.01	0.01	0.02	0.02
Al T	0.02	0.02	0.02	0.02	0.06	0.02	0.02	0.03	0.01	0.01	0.02	0.02
Fe3 (n)	0.20	0.16	0.18	0.18	0.19	0.18	0.24	0.16	0.29	0.29	0.26	0.23
Fe3	0.80	0.72	0.75	0.79	0.78	0.81	0.99	0.73	1.04	1.04	0.92	0.79
Fe3 T	0.20	0.16	0.18	0.18	0.19	0.18	0.24	0.16	0.29	0.29	0.26	0.23
Fe (rest)	0.60	0.55	0.57	0.60	0.58	0.63	0.75	0.57	0.76	0.75	0.66	0.56
Total	2.00	2.00	2.00	2.00	2.00	2.00	2.00	2.00	2.00	2.00	2.00	2.00
Site M1												
Fe 3 (M1)	0.60	0.55	0.57	0.60	0.58	0.63	0.75	0.57	0.76	0.75	0.66	0.56
Ti (M1)	0.02	0.01	0.02	0.01	0.03	0.02	0.01	0.02	0.01	0.01	0.01	0.02
Cr (M1)	0.00	0.00	0.00	0.00	0.00	0.00	0.00	0.00	0.00	0.00	0.00	0.00
V (M1)	0.00	0.00	0.00	0.00	0.00	0.00	0.00	0.00	0.00	0.00	0.00	0.00
Mn (M1)	0.02	0.01	0.01	0.02	0.02	0.01	0.02	0.02	0.02	0.02	0.02	0.01
Mg	0.73	0.76	0.72	0.72	0.72	0.72	0.63	0.73	1.10	1.10	0.66	0.75
Mg (n)	0.37	0.42	0.41	0.37	0.37	0.34	0.22	0.40	0.21	0.23	0.30	0.41
Mg (M1)	0.37	0.42	0.41	0.37	0.37	0.34	0.22	0.40	0.21	0.23	0.30	0.41
Mg (rest)	0.36	0.34	0.31	0.35	0.35	0.38	0.41	0.33	0.88	0.87	0.35	0.34
Total	1.00	1.00	1.00	1.00	1.00	1.00	1.00	1.00	1.00	1.00	1.00	1.00
Site M2												
Mg (M2)	0.36	0.34	0.31	0.35	0.35	0.38	0.41	0.33	0.88	0.87	0.35	0.34
Ca (M2)	0.61	0.65	0.63	0.63	0.63	0.56	0.56	0.65	0.12	0.12	0.62	0.64
Na (M2)	0.03	0.01	0.06	0.02	0.02	0.06	0.02	0.02	0.00	0.00	0.02	0.02

Fe-Ti oxide analyses, structural formula based on 4 oxygens – one page

Sample	MS01	MS01	MS01	MS01	MS02A	MS02A	MS02A	MS02A	MS02A	MS02A	MS02A	MS02A
Local	Mato Perso	Mato Perso	Mato Perso	Mato Perso	Mato Perso	Mato Perso	Mato Perso	Mato Perso	Mato Perso	Mato Perso	Mato Perso	Mato Perso
m/f	f	f	f	f	f	f	f	f	f	f	f	f
Position	x	x	x	x	c	c	c-b	c-b	b	b	b	b
TiO_2	14.73	15.67	15.94	15.54	2.99	6.40	2.67	13.36	0.84	1.27	2.21	2.88
Al_2O_3	2.04	2.07	1.48	1.82	0.48	0.35	0.41	0.56	1.63	0.34	1.04	0.49
Cr_2O_3	0.13	0.00	0.00	0.05	0.09	0.01	0.04	0.03	0.00	0.15	0.06	0.05
$Fe_2O_{3(T)}$	63.05	71.19	65.48	64.60	81.58	78.49	82.56	70.82	83.17	83.30	80.23	84.50
MnO	0.50	0.71	0.75	0.34	0.09	0.28	0.19	0.28	0.24	0.12	0.22	0.28
NiO	0.03	0.00	0.02	0.00	0.01	0.00	0.05	0.07	0.00	0.09	0.03	0.11
MgO	0.97	0.99	0.57	0.66	0.00	0.04	0.07	0.12	0.08	0.03	0.08	0.13
Total	81.46	90.64	84.25	83.00	85.23	85.57	85.98	85.23	85.96	85.30	83.87	88.43
Ti	17.37	16.53	17.96	17.79	3.19	6.83	2.83	14.51	0.90	1.36	2.42	2.97
Fe^{2+}	56.65	56.08	57.00	57.46	51.48	52.60	51.04	55.96	51.02	50.54	51.27	50.92
Fe^{3+}	33.30	34.61	32.42	32.07	47.23	44.40	47.82	36.25	48.64	48.93	47.77	47.90
4 O												
Ti	0.49	0.47	0.51	0.51	0.09	0.20	0.08	0.43	0.03	0.04	0.07	0.09
Al	0.11	0.10	0.07	0.09	0.02	0.02	0.02	0.03	0.08	0.02	0.05	0.02
Cr	0.00	0.00	0.00	0.00	0.00	0.00	0.00	0.00	0.00	0.00	0.00	0.00
Fe^{3+}	0.92	0.97	0.90	0.89	1.78	1.58	1.81	1.11	1.87	1.90	1.80	1.80
Fe^{2+}	1.40	1.38	1.45	1.45	1.09	1.19	1.07	1.41	1.01	1.03	1.06	1.07
Mn	0.02	0.02	0.03	0.01	0.00	0.01	0.01	0.01	0.01	0.00	0.01	0.01
Ni	0.00	0.00	0.00	0.00	0.00	0.00	0.00	0.00	0.00	0.00	0.00	0.00
Mg	0.06	0.06	0.04	0.04	0.00	0.00	0.00	0.01	0.01	0.00	0.01	0.01
Zn	0.00	0.00	0.00	0.00	0.00	0.00	0.00	0.00	0.00	0.00	0.00	0.00
Total	3.00	3.00	3.00	3.00	3.00	3.00	3.00	3.00	3.00	3.00	3.00	3.00
$Mg/(Mg+Fe^{2+})$	0.04	0.04	0.02	0.03	0.00	0.00	0.00	0.01	0.01	0.00	0.00	0.01
$Fe2/(Fe2++Fe^{3+})$	0.61	0.59	0.62	0.62	0.38	0.43	0.37	0.56	0.35	0.35	0.37	0.37
$Al/(Al+Fe^{3+}+Cr)$	0.10	0.09	0.08	0.09	0.01	0.01	0.01	0.02	0.04	0.01	0.03	0.01

Sample	MS03a	MS03a	MS03a	MS03a	MS03a	MS04	MS04	MS11b São Marcos	MS11b São Marcos	MS11b São Marcos	MS11b São Marcos	MS11b São Marcos
Local	Mato Perso	Mato Perso	Mato Perso	Mato Perso	Mato Perso	Mato Perso	Mato Perso					
m/f	f	f	f	f	f	m	m		f	f	f	f
Position	x	x	x	x	x	x	x	c	c	c	c-b	c-b
TiO_2	5.52	14.03	11.76	7.83	9.61	13.59	16.26	8.46	9.23	6.38	9.08	9.20
Al_2O_3	1.59	1.93	1.35	2.29	1.66	1.12	0.87	3.12	2.78	1.81	2.71	2.95
Cr_2O_3	0.05	0.12	0.00	0.03	0.05	0.00	0.02	0.10	0.14	0.20	0.12	0.06
$Fe_2O_{3(T)}$	83.24	72.28	75.79	78.62	76.80	74.68	71.56	75.87	77.34	83.12	77.79	76.27
MnO	0.35	0.61	0.71	0.99	0.42	0.44	1.89	0.51	0.52	0.28	0.51	0.50
NiO	0.00	0.00	0.04	0.01	0.03	0.02	0.00	0.00	0.12	0.03	0.00	0.00
MgO	0.20	0.52	0.35	0.25	0.33	0.00	0.07	0.66	0.62	0.15	0.56	0.64
Total	92.25	90.63	91.43	91.28	90.01	91.03	91.93	88.72	90.74	91.98	90.77	89.62
Ti	5.63	14.86	12.25	8.22	10.11	14.07	16.97	9.11	9.69	6.46	9.50	9.79
Fe^{2+}	52.59	56.15	54.65	53.45	54.25	56.20	55.93	54.19	54.18	53.22	54.26	54.40
Fe^{3+}	44.99	35.79	39.18	42.80	40.90	36.30	34.42	41.54	41.22	43.94	41.25	40.94
4 O												
Ti	0.16	0.42	0.35	0.23	0.29	0.41	0.49	0.25	0.27	0.19	0.27	0.27
Al	0.07	0.09	0.06	0.11	0.08	0.05	0.04	0.15	0.13	0.08	0.13	0.14
Cr	0.00	0.00	0.00	0.00	0.00	0.00	0.00	0.00	0.00	0.01	0.00	0.00
Fe^{3+}	1.60	1.06	1.23	1.42	1.34	1.12	0.98	1.34	1.32	1.54	1.33	1.31
Fe^{2+}	1.14	1.37	1.31	1.19	1.26	1.40	1.42	1.20	1.22	1.17	1.22	1.22
Mn	0.01	0.02	0.02	0.03	0.01	0.01	0.06	0.02	0.02	0.01	0.02	0.02
Ni	0.00	0.00	0.00	0.00	0.00	0.00	0.00	0.00	0.00	0.00	0.00	0.00
Mg	0.01	0.03	0.02	0.01	0.02	0.00	0.00	0.04	0.04	0.01	0.03	0.04
Zn	0.00	0.00	0.00	0.00	0.00	0.00	0.00	0.00	0.00	0.00	0.00	0.00
Total	3.00	3.00	3.00	3.00	3.00	3.00	3.00	3.00	3.00	3.00	3.00	3.00
$Mg/(Mg+Fe^{2+})$	0.01	0.02	0.02	0.01	0.02	0.00	0.00	0.03	0.03	0.01	0.03	0.03
$Fe2/(Fe^{2+}+Fe^{3+})$	0.42	0.56	0.52	0.45	0.48	0.55	0.59	0.47	0.48	0.43	0.48	0.48
$Al/(Al+Fe^{3+}+Cr)$	0.04	0.08	0.05	0.07	0.06	0.05	0.04	0.10	0.09	0.05	0.09	0.10

Sample	MS11b	MS11b	MS11b	MS11b	MS11b	MS11b	MS11b	MS11b	MS11b	MS11b	MS11b	MS11b
Local	São Marcos	São Marcos	São Marcos	São Marcos	São Marcos	São Marcos	São Marcos	São Marcos	São Marcos	São Marcos	São Marcos	São Marcos
m/f	f	f	f	f	f	f	f	f	f	f	f	f
Position	b	b	b	b	b	b	x	x	x	x	x	x
TiO_2	9.74	8.98	8.67	9.33	25.56	5.82	0.88	8.42	8.91	10.02	11.96	11.32
Al_2O_3	2.90	2.91	2.62	2.75	2.69	1.55	2.01	0.84	2.72	2.82	2.67	3.06
Cr_2O_3	0.05	0.13	0.11	0.13	0.24	0.08	0.20	0.10	0.21	0.18	0.00	0.00
$Fe_2O_{3(T)}$	77.45	74.11	74.05	77.07	60.78	80.71	84.76	68.50	77.87	73.59	75.69	73.25
MnO	0.48	0.56	1.24	0.37	0.16	0.52	0.42	0.35	0.33	0.56	0.32	0.51
NiO	0.00	0.00	0.06	0.00	0.04	0.03	0.05	0.11	0.03	0.06	0.00	0.00
MgO	0.74	0.62	0.36	0.50	0.33	0.23	0.19	0.33	0.60	0.99	0.64	0.67
Total	91.35	87.31	87.12	90.15	89.79	88.94	88.51	78.64	90.65	88.23	92.09	89.69
Ti	10.16	9.83	9.53	9.82	27.44	6.09	0.92	9.95	9.33	10.91	12.45	12.21
Fe^{2+}	54.37	54.41	53.80	54.65	64.19	52.55	50.95	53.61	54.30	54.15	55.53	55.46
Fe^{3+}	40.74	40.90	41.71	40.65	13.62	44.81	48.70	41.67	41.29	40.53	38.11	38.35
4 O												
Ti	0.29	0.28	0.27	0.28	0.78	0.18	0.03	0.29	0.26	0.30	0.35	0.34
Al	0.13	0.14	0.13	0.13	0.13	0.07	0.09	0.05	0.13	0.13	0.12	0.14
Cr	0.00	0.00	0.00	0.00	0.01	0.00	0.01	0.00	0.01	0.01	0.00	0.00
Fe^{3+}	1.29	1.31	1.34	1.31	0.31	1.57	1.85	1.37	1.34	1.25	1.17	1.17
Fe^{2+}	1.23	1.22	1.20	1.24	1.75	1.14	1.00	1.25	1.22	1.22	1.30	1.28
Mn	0.02	0.02	0.04	0.01	0.01	0.02	0.01	0.01	0.01	0.02	0.01	0.02
Ni	0.00	0.00	0.00	0.00	0.00	0.00	0.00	0.00	0.00	0.00	0.00	0.00
Mg	0.04	0.04	0.02	0.03	0.02	0.01	0.01	0.02	0.03	0.06	0.04	0.04
Zn	0.00	0.00	0.00	0.00	0.00	0.00	0.00	0.00	0.00	0.00	0.00	0.00
Total	3.00	3.00	3.00	3.00	3.00	3.00	3.00	3.00	3.00	3.00	3.00	3.00
$Mg/(Mg+Fe^{2+})$	0.03	0.03	0.02	0.02	0.01	0.01	0.01	0.02	0.03	0.05	0.03	0.03
$Fe2/(Fe^{2+}+Fe^{3+})$	0.49	0.48	0.47	0.48	0.85	0.42	0.35	0.48	0.48	0.49	0.53	0.52
$Al/(Al+Fe^{3+}+Cr)$	0.09	0.10	0.09	0.09	0.29	0.04	0.05	0.03	0.09	0.10	0.10	0.11

Sample	MS11b	MS11b	MS11b	MS11b	MS11b	MS11b	MS11c	MS11c	MS19B1	MS19B1	MS_19B1	MS19b1
Local	São Marcos	São Marcos	São Marcos	São Marcos	São Marcos	São Marcos	São Marcos	São Marcos	Jaquirana	Jaquirana	Jaquirana	Jaquirana
m/f	f	f	f	f	f	f	m	m	m	m	f	f
Position	x	x	x	x	x	x	x	x	x	x	x	x
TiO_2	10.70	7.86	9.33	8.60	9.05	2.19	8.21	9.05	13.44	12.49	16.56	11.21
Al_2O_3	2.64	0.36	2.31	2.84	2.36	0.45	3.23	3.46	1.05	1.17	0.94	2.27
Cr_2O_3	0.10	0.13	0.12	0.07	0.08	0.06	1.09	1.01	0.00	0.00	0.01	0.27
$Fe_2O_{3(T)}$	77.94	77.05	72.10	76.34	70.83	80.05	75.06	73.59	71.24	72.81	71.56	73.25
MnO	0.36	0.50	0.46	0.61	0.65	0.59	0.57	0.33	0.61	0.53	0.62	0.45
NiO	0.00	0.02	0.00	0.02	0.04	0.00	0.00	0.09	0.00	0.04	0.00	0.00
MgO	0.67	0.01	0.50	0.38	0.41	0.00	0.39	0.48	0.16	0.17	0.08	0.48
Total	93.21	90.06	85.73	89.71	84.57	88.70	89.30	88.77	86.50	87.21	90.56	88.71
Ti	10.99	8.40	10.43	9.20	10.31	2.40	8.96	9.96	14.51	13.37	17.23	12.10
Fe^{2+}	54.81	53.14	54.56	54.38	54.47	50.68	55.03	55.59	55.93	55.52	57.33	55.39
Fe^{3+}	39.79	43.02	40.40	41.29	40.56	48.37	40.75	39.58	36.28	37.52	32.67	38.49
4 O												
Ti	0.31	0.25	0.30	0.26	0.29	0.07	0.25	0.27	0.42	0.39	0.50	0.34
Al	0.12	0.02	0.11	0.13	0.12	0.02	0.15	0.16	0.05	0.06	0.05	0.11
Cr	0.00	0.00	0.00	0.00	0.00	0.00	0.03	0.03	0.00	0.00	0.00	0.01
Fe^{3+}	1.26	1.48	1.29	1.34	1.30	1.83	1.32	1.25	1.10	1.16	0.95	1.20
Fe^{2+}	1.26	1.23	1.25	1.22	1.24	1.05	1.21	1.23	1.39	1.36	1.48	1.30
Mn	0.01	0.02	0.02	0.02	0.02	0.02	0.02	0.01	0.02	0.02	0.02	0.02
Ni	0.00	0.00	0.00	0.00	0.00	0.00	0.00	0.00	0.00	0.00	0.00	0.00
Mg	0.04	0.00	0.03	0.02	0.03	0.00	0.02	0.03	0.01	0.01	0.00	0.03
Zn	0.00	0.00	0.00	0.00	0.00	0.00	0.00	0.00	0.00	0.00	0.00	0.00
Total	3.00	3.00	3.00	3.00	3.00	3.00	3.00	3.00	3.00	3.00	3.00	3.00
$Mg/(Mg+Fe^{2+})$	0.03	0.00	0.02	0.02	0.02	0.00	0.02	0.02	0.01	0.01	0.00	0.02
$Fe2/(Fe^{2+}+Fe^{3+})$	0.50	0.45	0.49	0.47	0.49	0.36	0.48	0.50	0.56	0.54	0.61	0.52
$Al/(Al+Fe^{3+}+Cr)$	0.09	0.01	0.08	0.09	0.08	0.01	0.10	0.11	0.04	0.05	0.05	0.08

Sample	MS19b1	MS19b1	MS19B2	MS19b2	MS24b	MS24b	MS24b	MS24b	MS24b	MS24b	MS24b	MS24b
Local	Jaquirana	Jaquirana	Jaquirana	Jaquirana	Jaquirana	Jaquirana	Jaquirana	Jaquirana	Jaquirana	Jaquirana	Jaquirana	Jaquirana
m/f	f	f	m	f	f	f	f	f	f	f	f	f
Position	x	x	x	x	x	x	x	x	x	x	x	x
TiO_2	11.78	13.59	10.54	11.99	11.65	9.42	11.08	10.10	8.95	9.86	11.78	9.96
Al_2O_3	2.32	1.07	2.28	2.72	2.58	1.92	2.63	2.78	1.44	1.70	2.46	2.09
Cr_2O_3	0.43	0.02	0.00	0.34	0.07	0.21	0.14	0.07	0.11	0.13	0.14	0.12
$Fe_2O_{3(T)}$	72.15	72.32	71.78	72.82	76.71	79.78	77.02	76.18	80.13	77.32	76.44	78.96
MnO	0.47	0.82	0.22	0.55	0.28	0.12	0.13	0.25	0.31	0.36	0.30	0.28
NiO	0.00	0.00	0.07	0.00	0.03	0.06	0.00	0.03	0.07	0.00	0.02	0.11
MgO	0.48	0.17	0.14	0.58	0.09	0.04	0.13	0.33	0.21	0.23	0.34	0.24
Total	88.40	88.93	85.03	89.90	92.23	92.32	92.02	90.70	91.93	90.86	92.43	92.65
Ti	12.80	14.46	11.67	12.90	12.02	9.60	11.46	10.65	9.13	10.29	12.17	10.19
Fe^{2+}	55.79	55.74	55.84	55.82	56.21	54.94	56.10	55.38	53.95	54.63	55.82	54.78
Fe^{3+}	37.60	36.52	38.28	37.51	37.67	40.48	38.14	39.40	41.78	40.40	37.98	40.31
4 O												
Ti	0.36	0.42	0.33	0.36	0.34	0.28	0.33	0.30	0.27	0.30	0.35	0.29
Al	0.11	0.05	0.11	0.13	0.12	0.09	0.12	0.13	0.07	0.08	0.11	0.10
Cr	0.01	0.00	0.00	0.01	0.00	0.01	0.00	0.00	0.00	0.00	0.00	0.00
Fe^{3+}	1.15	1.11	1.22	1.14	1.19	1.35	1.22	1.26	1.40	1.32	1.19	1.31
Fe^{2+}	1.32	1.38	1.32	1.31	1.33	1.27	1.32	1.27	1.24	1.27	1.32	1.27
Mn	0.02	0.03	0.01	0.02	0.01	0.00	0.00	0.01	0.01	0.01	0.01	0.01
Ni	0.00	0.00	0.00	0.00	0.00	0.00	0.00	0.00	0.00	0.00	0.00	0.00
Mg	0.03	0.01	0.01	0.03	0.01	0.00	0.01	0.02	0.01	0.01	0.02	0.01
Zn	0.00	0.00	0.00	0.00	0.00	0.00	0.00	0.00	0.00	0.00	0.00	0.00
Total	3.00	3.00	3.00	3.00	3.00	3.00	3.00	3.00	3.00	3.00	3.00	3.00
$Mg/(Mg+Fe^{2+})$	0.02	0.01	0.01	0.03	0.00	0.00	0.01	0.01	0.01	0.01	0.01	0.01
$Fe2/(Fe^{2+}+Fe^{3+})$	0.53	0.56	0.52	0.54	0.53	0.48	0.52	0.50	0.47	0.49	0.53	0.49
$Al/(Al+Fe^{3+}+Cr)$	0.09	0.04	0.09	0.10	0.09	0.06	0.09	0.09	0.05	0.06	0.09	0.07

Sample	MS24b	MS24b	MS24b	MS24b	MS24b	MS38	MS38	MS38	MS38	MS38	MS38	MS38
Local	Jaquirana	Jaquirana	Jaquirana	Jaquirana	Jaquirana	Jaquirana	Jaquirana	Jaquirana	Jaquirana	Jaquirana	Jaquirana	Jaquirana
m/f	f	f	f	f	f	f	f	f	f	f	f	f
Position	x	x	x	x	x	b	c-b	c	c-b	b	b	c
TiO_2	9.94	10.99	13.75	5.95	4.79	13.85	15.34	14.07	14.70	12.33	14.28	15.07
Al_2O_3	2.15	2.26	1.84	2.22	0.89	2.51	2.38	2.43	2.47	2.39	1.88	2.22
Cr_2O_3	0.08	0.10	0.11	0.16	0.07	0.00	0.09	0.08	0.18	0.07	0.13	0.03
$Fe_2O_{3(T)}$	78.06	76.93	75.34	84.12	81.32	71.72	70.78	69.10	68.75	66.04	68.55	67.98
MnO	0.27	0.10	0.36	0.28	0.49	0.46	0.35	0.50	0.60	0.41	0.38	0.63
NiO	0.01	0.00	0.00	0.00	0.09	0.12	0.00	0.01	0.04	0.00	0.00	0.00
MgO	0.20	0.25	0.05	0.00	0.01	1.03	1.09	1.10	1.12	0.81	1.12	1.02
Total	91.59	91.86	92.46	93.50	88.66	89.69	90.02	87.28	87.85	82.04	86.34	86.94
Ti	10.28	11.39	14.10	5.98	5.03	14.80	16.31	15.48	16.13	14.37	15.78	16.62
Fe^{2+}	55.01	55.67	56.73	53.51	52.02	55.62	56.42	55.83	56.07	55.89	55.71	56.25
Fe^{3+}	40.01	38.64	35.71	43.88	45.86	36.41	34.40	35.68	34.92	36.42	35.59	34.34
4 O												
Ti	0.30	0.33	0.41	0.17	0.15	0.41	0.46	0.43	0.45	0.40	0.45	0.47
Al	0.10	0.11	0.09	0.10	0.04	0.12	0.11	0.12	0.12	0.12	0.09	0.11
Cr	0.00	0.00	0.00	0.00	0.00	0.00	0.00	0.00	0.01	0.00	0.00	0.00
Fe^{3+}	1.31	1.24	1.09	1.55	1.66	1.05	0.97	1.02	0.98	1.07	1.01	0.96
Fe^{2+}	1.27	1.31	1.39	1.16	1.13	1.33	1.38	1.35	1.36	1.34	1.36	1.38
Mn	0.01	0.00	0.01	0.01	0.02	0.02	0.01	0.02	0.02	0.01	0.01	0.02
Ni	0.00	0.00	0.00	0.00	0.00	0.00	0.00	0.00	0.00	0.00	0.00	0.00
Mg	0.01	0.01	0.00	0.00	0.00	0.06	0.06	0.07	0.07	0.05	0.07	0.06
Zn	0.00	0.00	0.00	0.00	0.00	0.00	0.00	0.00	0.00	0.00	0.00	0.00
Total	3.00	3.00	3.00	3.00	3.00	3.00	3.00	3.00	3.00	3.00	3.00	3.00
$Mg/(Mg+Fe^{2+})$	0.01	0.01	0.00	0.00	0.00	0.04	0.04	0.05	0.05	0.04	0.05	0.04
$Fe2/(Fe^{2+}+Fe^{3+})$	0.49	0.51	0.56	0.43	0.40	0.56	0.59	0.57	0.58	0.56	0.57	0.59
$Al/(Al+Fe^{3+}+Cr)$	0.07	0.08	0.07	0.06	0.03	0.10	0.10	0.10	0.11	0.10	0.08	0.10

Sample	MS38	MS38	MS38	MS38	MS38	MS38	MS50	MS50	MS50	MS50	MS50	MS50
Local	Jaquirana	Jaquirana	Jaquirana	Jaquirana	Jaquirana	Jaquirana	Cambará	Cambará	Cambará	Cambará	Cambará	Cambará
m/f	f	f	f	f	f	f	f	f	f	f	m	m
Position	b	b	c-b	c	c-b	b	x	x	x	x	x	x
TiO_2	16.85	18.46	14.98	15.28	14.70	14.73	15.83	15.86	15.99	14.75	3.87	11.42
Al_2O_3	2.13	1.77	1.97	2.34	2.13	2.21	1.90	1.89	1.85	2.23	0.77	3.15
Cr_2O_3	0.15	0.22	0.02	0.04	0.14	0.10	0.07	0.14	0.05	0.19	0.17	0.27
$Fe_2O_{3(T)}$	65.63	63.18	67.29	71.89	72.14	69.45	67.85	68.98	67.88	71.49	78.99	74.65
MnO	0.98	1.08	0.49	0.41	0.58	0.49	0.70	0.66	0.75	0.57	0.83	0.36
NiO	0.04	0.00	0.00	0.00	0.07	0.06	0.00	0.00	0.06	0.00	0.00	0.02
MgO	1.03	0.95	1.15	1.03	0.96	1.01	0.32	0.33	0.30	0.48	0.05	0.92
Total	86.81	85.65	85.89	90.99	90.71	88.05	86.66	87.86	86.88	91.02	87.02	91.66
Ti	18.76	20.81	16.68	16.05	15.49	16.02	17.34	17.14	17.49	15.65	4.22	12.10
Fe^{2+}	56.84	57.72	55.98	56.28	55.82	56.09	57.58	57.51	57.51	56.87	51.35	55.30
Fe^{3+}	31.91	29.01	34.59	34.75	35.68	34.99	32.31	32.56	32.26	34.42	46.91	38.59
4 O												
Ti	0.52	0.58	0.47	0.45	0.44	0.45	0.50	0.49	0.50	0.44	0.12	0.34
Al	0.10	0.09	0.10	0.11	0.10	0.11	0.09	0.09	0.09	0.11	0.04	0.15
Cr	0.00	0.01	0.00	0.00	0.00	0.00	0.00	0.00	0.00	0.01	0.01	0.01
Fe^{3+}	0.84	0.74	0.96	0.99	1.02	0.99	0.91	0.92	0.91	1.00	1.71	1.17
Fe^{2+}	1.42	1.49	1.38	1.38	1.36	1.37	1.45	1.45	1.45	1.40	1.09	1.27
Mn	0.03	0.04	0.02	0.01	0.02	0.02	0.02	0.02	0.03	0.02	0.03	0.01
Ni	0.00	0.00	0.00	0.00	0.00	0.00	0.00	0.00	0.00	0.00	0.00	0.00
Mg	0.06	0.06	0.07	0.06	0.06	0.06	0.02	0.02	0.02	0.03	0.00	0.05
Zn	0.00	0.00	0.00	0.00	0.00	0.00	0.00	0.00	0.00	0.00	0.00	0.00
Total	3.00	3.00	3.00	3.00	3.00	3.00	3.00	3.00	3.00	3.00	3.00	3.00
$Mg/(Mg+Fe^{2+})$	0.04	0.04	0.05	0.04	0.04	0.04	0.01	0.01	0.01	0.02	0.00	0.04
$Fe2/(Fe^{2+}+Fe^{3+})$	0.63	0.67	0.59	0.58	0.57	0.58	0.61	0.61	0.62	0.58	0.39	0.52
$Al/(Al+Fe^{3+}+Cr)$	0.11	0.11	0.09	0.10	0.09	0.10	0.09	0.09	0.09	0.09	0.02	0.11

Sample	MS50	PSJ02a	PSJ02a	PSJ02a	PSJ02a	PSJ02a	PSJ04	PSJ04	PSJ06	PSJ06	PSJ06
Local	Cambará	Jaquirana	Jaquirana	Jaquirana	Jaquirana	Jaquirana	Jaquirana	Jaquirana	Jaquirana	Jaquirana	Jaquirana
m/f	m	f	f	f	f	f	f	f	f	f	f
Position	x	x	x	x	x	x	x	x	x	x	x
TiO_2	17.07	12.76	11.49	6.31	11.80	11.29	11.34	0.46	3.95	1.28	1.04
Al_2O_3	2.36	2.59	2.64	0.89	2.67	2.10	2.92	1.01	0.50	0.60	2.16
Cr_2O_3	0.17	0.18	0.17	0.10	0.12	0.09	0.13	0.00	0.00	0.13	0.15
$Fe_2O_{3(T)}$	69.36	73.89	74.90	77.22	73.67	72.16	72.36	25.11	86.40	87.31	87.66
MnO	0.57	0.31	0.42	0.34	0.40	0.74	0.42	0.85	0.07	0.14	0.11
NiO	0.05	0.00	0.05	0.00	0.07	0.04	0.02	0.02	0.00	0.01	0.03
MgO	1.11	0.48	0.52	0.51	0.53	0.52	1.36	15.62	0.02	0.07	0.18
Total	91.76	90.99	91.14	86.95	90.14	88.53	89.68	96.97	91.92	90.73	92.26
Ti	18.12	13.45	12.12	6.85	12.59	12.33	12.36	1.63	3.95	1.30	1.05
Fe^{2+}	57.02	56.30	55.51	52.15	55.70	54.90	54.38	-135.98	51.73	50.68	51.36
Fe^{3+}	32.27	36.62	38.34	44.85	37.84	38.86	39.40	239.88	46.64	48.82	48.23
4 O											
Ti	0.51	0.38	0.34	0.20	0.36	0.35	0.34	0.02	0.12	0.04	0.03
Al	0.11	0.12	0.12	0.04	0.13	0.10	0.14	0.08	0.02	0.03	0.10
Cr	0.01	0.01	0.01	0.00	0.00	0.00	0.00	0.00	0.00	0.00	0.00
Fe^{3+}	0.87	1.11	1.19	1.55	1.16	1.20	1.18	1.88	1.74	1.89	1.84
Fe^{2+}	1.42	1.34	1.30	1.15	1.31	1.29	1.25	-0.53	1.11	1.03	1.02
Mn	0.02	0.01	0.01	0.01	0.01	0.03	0.01	0.05	0.00	0.00	0.00
Ni	0.00	0.00	0.00	0.00	0.00	0.00	0.00	0.00	0.00	0.00	0.00
Mg	0.07	0.03	0.03	0.03	0.03	0.03	0.08	1.50	0.00	0.00	0.01
Zn	0.00	0.00	0.00	0.00	0.00	0.00	0.00	0.00	0.00	0.00	0.00
Total	3.00	3.00	3.00	3.00	3.00	3.00	3.00	3.00	3.00	3.00	3.00
$Mg/(Mg+Fe^{2+})$	0.04	0.02	0.02	0.03	0.02	0.02	0.06	1.54	0.00	0.00	0.01
$Fe2/(Fe^{2+}+Fe^{3+})$	0.62	0.55	0.52	0.43	0.53	0.52	0.51	-0.39	0.39	0.35	0.36
$Al/(Al+Fe^{3+}+Cr)$	0.11	0.10	0.09	0.03	0.10	0.08	0.10	0.04	0.01	0.01	0.05

Glassy groundmass analyses – 1/2 page

Sample	MS01	MS01	MS01	MS01	MS_03a	MS_03a	MS11b São	MS11b São	MS19B1	MS19B1	MS19B1	MS19B1
Local	Mato Perso	Mato Perso	Mato Perso	Mato Perso	Mato Perso	Mato Perso	Marcos	Marcos	Jaquirana	Jaquirana	Jaquirana	Jaquirana
SiO_2	72.36	75.28	76.96	73.85	77.68	64.67	73.57	71.79	80.09	76.87	71.00	81.35
TiO_2	0.34	0.38	0.39	1.01	0.15	0.89	0.15	0.40	1.78	0.97	0.10	0.37
Al_2O_3	13.20	11.55	11.63	11.49	10.92	14.97	13.37	13.16	6.47	10.71	18.20	10.41
$Fe_2O_{3(T)}$	0.85	0.95	1.23	1.01	1.15	3.97	0.38	1.43	3.32	2.45	0.77	1.57
MnO	0.00	0.00	0.03	0.14	0.04	0.03	0.00	0.00	0.05	0.00	0.27	0.08
MgO	0.09	0.10	0.02	0.03	0.03	0.25	0.00	0.07	0.04	0.00	0.18	0.06
CaO	0.30	0.47	0.27	0.25	2.55	4.47	2.03	1.47	1.91	0.85	5.99	0.37
Na_2O	3.00	3.13	2.74	2.62	2.84	4.49	3.33	3.53	1.19	2.51	5.02	2.09
K_2O	7.77	5.65	6.57	6.65	3.44	2.93	5.46	5.59	3.94	5.97	0.65	6.45
Total	97.90	97.51	99.84	97.05	98.87	96.78	98.30	97.43	98.78	100.33	102.17	102.75
K_2O/Na_2O	2.59	1.81	2.40	2.54	1.21	0.65	1.64	1.58	3.32	2.38	0.13	3.09

Sample	MS19B1	MS19B1	MS19B2	MS19B2	MS19B2	MS19B2	MS19B2	MS38	MS38	MS38	MS38	MS38
Local	Jaquirana	Jaquirana	Jaquirana	Jaquirana	Jaquirana	Jaquirana	Jaquirana	Jaquirana	Jaquirana	Jaquirana	Jaquirana	Jaquirana
SiO_2	80.34	75.64	79.09	77.60	66.16	79.91	75.93	80.13	78.77	68.23	79.45	80.53
TiO_2	0.09	0.10	0.84	0.94	0.16	0.98	0.53	0.31	0.35	0.88	1.25	0.65
Al_2O_3	11.36	12.69	11.61	11.80	16.97	10.38	11.94	8.65	10.88	15.07	11.12	9.57
$Fe_2O_{3(T)}$	0.26	1.10	1.25	1.47	1.45	1.56	1.07	3.84	0.47	0.60	1.25	1.09
MnO	0.00	0.10	0.02	0.04	0.04	0.06	0.00	0.02	0.03	0.00	0.03	0.04
MgO	0.00	0.08	0.05	0.02	0.25	0.04	0.03	0.13	0.03	0.53	0.04	0.05
CaO	0.16	0.59	1.04	0.64	3.62	1.03	0.84	0.22	0.18	0.40	0.18	0.30
Na_2O	2.64	2.72	3.64	3.00	5.42	2.98	2.57	2.14	2.28	3.09	2.66	2.43
K_2O	7.10	8.19	4.34	6.07	1.55	4.23	7.10	5.04	6.66	7.89	6.29	4.93
Total	101.94	101.20	101.87	101.58	95.60	101.17	100.01	100.47	99.64	96.67	102.25	99.59
K_2O/Na_2O	2.69	3.01	1.19	2.02	0.29	1.42	2.76	2.35	2.92	2.56	2.37	2.03

Sample	MS38	PSJ4	PSJ4	PSJ4	PSJ4	PSJ4	PSJ4	PSJ06	PSJ06	PSJ06	PSJ06	PSJ02A
Local	Jaquirana	Jaquirana	Jaquirana	Jaquirana	Jaquirana	Jaquirana	Jaquirana	Jaquirana	Jaquirana	Jaquirana	Jaquirana	Jaquirana
SiO_2	77.49	84.55	82.44	79.24	72.62	80.56	70.83	70.13	71.20	74.72	79.43	84.29
TiO_2	0.79	0.29	0.00	0.60	0.24	0.32	0.02	0.35	0.11	0.17	0.85	0.51
Al_2O_3	11.51	7.69	8.35	10.88	14.19	9.73	15.35	12.49	12.18	9.90	9.95	7.00
$Fe_2O_{3(T)}$	1.04	0.46	0.25	0.69	0.39	0.47	0.89	2.89	2.96	3.89	2.49	2.55
MnO	0.12	0.03	0.00	0.08	0.01	0.00	0.00	0.05	0.18	0.11	0.16	0.00
MgO	0.03	0.00	0.04	0.02	0.00	0.02	0.08	0.87	0.89	0.99	0.03	0.01
CaO	0.28	0.27	0.19	0.44	0.22	0.19	3.77	3.18	3.18	2.85	2.47	0.17
Na_2O	2.91	1.73	1.94	2.39	3.09	2.14	3.96	3.60	3.50	2.74	3.74	1.70
K_2O	6.64	4.55	5.16	6.49	8.97	5.77	2.35	3.76	3.90	3.33	0.51	4.14
Total	100.80	99.58	98.36	100.83	99.71	99.21	97.23	97.31	98.10	98.69	99.64	100.37
K_2O/Na_2O	2.28	2.63	2.66	2.71	2.91	2.70	0.59	1.04	1.11	1.21	0.14	2.43

Sample	PSJ02A	PSJ02A	PSJ02A	PSJ02A	MS_19B1	MS50	MS50	MS50
Local	Jaquirana	Jaquirana	Jaquirana	Jaquirana	Jaquirana	Cambará	Cambará	Cambará
SiO_2	65.39	73.24	74.21	84.29	79.94	81.39	86.13	69.91
TiO_2	0.47	0.43	0.41	0.51	0.10	0.60	0.27	0.00
Al_2O_3	17.52	14.03	13.60	7.00	9.38	9.57	5.74	17.21
$Fe_2O_{3(T)}$	1.69	0.61	0.69	2.55	0.92	2.37	3.98	0.25
MnO	0.08	0.04	0.00	0.00	0.00	0.05	0.05	0.04
MgO	0.38	0.02	0.03	0.01	0.00	0.03	0.21	0.02
CaO	3.31	2.06	2.10	0.17	0.46	0.28	0.23	0.39
Na_2O	4.83	4.26	4.05	1.70	2.35	2.20	1.28	3.76
K_2O	4.16	3.89	3.83	4.14	5.25	5.72	2.97	10.38
Total	97.82	98.57	98.91	100.37	98.42	102.19	100.86	101.96
K_2O/Na_2O	0.86	0.91	0.95	2.43	2.23	2.60	2.32	2.76

APPENDIX B – Whole-rock geochemical analyses results obtained by ICP-ES and LA-ICP-MS for major, trace and rare earth elements.

Area	Mato Perso							
Sample	MS-01	MS-03A	MS-04	MS-05B	MP-01	NR-01	CR-3	SV-5
lat (S)*	6781199.7	6780192.8	6779911.2	6778913.3	6781552.33	6785954.9	6775685.1	6781130.5
long (E)	467814.1	468152.7	468150.4	469494.5	470341.51	458020.62	474984.79	470250.7
elevation	653.0	679.0	639.0	661.0	354.0	602.0	564.0	598.0
SiO_2	67.32	65.30	67.18	67.23	67.68	66.01	67.56	69.95
Al_2O_3	12.66	13.11	12.88	12.74	12.35	12.93	12.53	12.1
Fe_2O_3	6.23	6.30	6.02	6.12	7.21	6.32	6.1	5.62
MgO	1.33	1.29	1.27	1.26	0.85	1.33	1.01	0.87
CaO	3.28	2.96	3.12	3.23	2.46	3.2	2.63	2.47
Na_2O	2.95	2.90	2.77	2.96	2.67	2.92	2.66	2.52
K_2O	3.78	3.94	4.00	3.80	4.16	3.78	3.94	4.24
TiO_2	0.92	0.95	0.89	0.93	0.97	0.94	0.88	0.83
P_2O_5	0.27	0.28	0.26	0.27	0.26	0.24	0.25	0.24
MnO	0.11	0.11	0.11	0.10	0.13	0.11	0.1	0.1
Cr_2O_3	<0.002	<0.002	<0.002	<0.002	<0.002	<0.002	<0.002	<0.002
Sum	99.84	99.82	99.84	99.84	99.86	99.85	99.86	99.86
LOI	0.9	2.6	1.3	1.1	1	2	2.1	0.8
Ba	575	647	613	578	720	683	651	696
Ni	<20	<20	<20	<20	<20	<20	<20	<20
Co	12.6	12.4	10.1	10.9	11.9	12.6	10.9	13.1
Cs	6.5	9.2	6.5	7.2	5.5	7.8	4.6	6.6
Ga	16.8	18.8	16.3	18.1	15.4	15.5	15.1	15.1
Hf	6.5	6.9	6.4	6.7	7.1	6.4	6.9	6.2
Nb	20.1	19.7	20.4	19.7	19	19.1	19.4	19.1
Rb	161.1	170.4	163.3	160.5	159.9	158.3	166.8	174.5
Sr	150.2	151.6	146.0	141.4	137.3	150.9	135.5	127.7
Ta	1.7	1.6	1.5	1.6	1.3	1.5	1.7	1.4
Th	12.4	13.2	13.9	13.1	14.4	13.6	14.3	13.7
U	4.6	4.3	5.1	5.0	3.9	4.8	4.9	5.2
Zr	243.8	247.1	245.3	236.1	260.2	242.3	243.7	236
Y	33.7	37.3	35.3	31.7	47.8	48.5	45.9	52.7
La	40.6	41.7	42.6	38.7	50.3	49.4	49.6	44.1
Ce	80.1	82.4	87.2	78.9	98.7	94.5	92.2	85
Pr	9.46	9.93	9.92	9.32	12.14	11.29	11.98	10.8
Nd	35.8	39.2	37.9	36.5	46.8	43.2	49.4	45
Sm	7.52	7.94	7.96	7.59	9.37	8.73	9.42	9.42
Eu	1.57	1.55	1.48	1.42	1.75	1.65	1.93	1.97
Gd	7.11	7.72	7.36	6.72	9.17	8.84	9.6	10.55
Tb	1.06	1.19	1.10	1.04	1.5	1.37	1.52	1.63
Dy	6.63	7.15	6.74	6.41	9.22	7.78	8.77	9.95
Ho	1.31	1.39	1.25	1.23	1.85	1.67	1.81	2.12
Er	3.72	3.90	3.34	3.39	5.32	4.77	5.23	6.09
Tm	0.53	0.59	0.49	0.50	0.76	0.67	0.72	0.87
Yb	3.44	3.68	3.32	3.32	4.88	4.34	4.52	5.56
Lu	0.51	0.60	0.51	0.50	0.72	0.61	0.67	0.8
SumREE	199.36	208.94	211.17	195.54	252.48	238.82	247.37	233.86
Zr/Nb	12.1	12.5	12.0	12.0	13.69	12.69	12.56	12.36
Zr/Th	19.66	18.72	17.65	18.02	18.07	17.82	17.04	17.23
Nb/Y	0.60	0.53	0.58	0.62	0.40	0.39	0.42	0.36
Zr/Y	7.23	6.62	6.95	7.45	5.44	5.00	5.31	4.48
D (ap)*	16238.46	16238.46	16888.00	15637.04	16238.46	17591.67	16888.00	17591.67
T°C (ap)	1070.29	1015.03	1061.08	1073.04	1080.13	1023.79	1071.44	1130.69
η (dry)**	5.7	6.28	5.87	5.7	5.68	6.19	5.89	5.47
η (0.5)	4.68	5.12	4.81	4.68	4.67	5.06	4.83	4.52
η (1.3)	3.98	4.35	4.09	3.97	3.97	4.30	4.11	3.84

Area	Jaquirana-Cambará do Sul												
Sample	MS-19A	MS-22	MS-22E	MS-22D	MS-24A	MS-24B	MS-29A	MS-32C	MS-38	MS-50	MS-67	PSJ-003	PSJ-006
lat (S)*	6798957.4	6810422.1	6810422.1	6810422.1	6809398.1	6809398.1	6804625.9	6805796.2	6805226.8	6790890.7	6783937.7	6810422.1	6810422.1
long (E)	553601.8	555766.8	555766.8	555766.8	556465.6	556465.6	562439.1	560526.6	562014.1	581524.9	594908.2	555766.8	555766.8
elevation	923.0	882.0	882.0	882.0	932.0	932.0	940.0	901.0	934.0	1054.0	1002.0	943.0	950.0
SiO_2	65.80	64.78	65.47	67.80	68.18	67.35	66.32	67.38	66.04	66.30	65.64	67.87	66.00
Al_2O_3	12.72	13.75	12.95	12.53	12.05	12.37	12.90	12.55	12.85	13.04	13.40	12.17	12.63
Fe_2O_3	6.68	6.83	6.41	6.06	6.05	6.04	6.18	6.37	6.35	6.50	6.16	6.53	5.87
MgO	1.65	0.91	1.52	1.37	1.31	1.32	1.60	1.41	1.59	1.22	1.50	1.31	1.24
CaO	3.14	1.02	3.41	2.90	2.83	2.85	2.99	3.07	3.02	2.63	2.09	2.90	3.28
Na_2O	2.80	2.09	2.90	2.89	2.89	2.87	2.76	2.83	2.77	2.84	2.56	2.78	3.27
K_2O	3.95	4.86	4.00	3.98	3.80	4.13	4.06	4.04	4.14	4.26	3.91	3.78	3.10
TiO_2	0.95	1.01	0.95	0.92	0.89	0.92	0.95	0.96	0.94	0.94	0.94	0.90	0.88
P_2O_5	0.29	0.25	0.27	0.25	0.26	0.26	0.27	0.27	0.29	0.27	0.26	0.25	0.25
MnO	0.12	0.09	0.11	0.11	0.09	0.10	0.10	0.11	0.11	0.09	0.10	0.10	0.11
Cr_2O_3	<0.002	<0.002	<0.002	<0.002	<0.002	<0.002	<0.002	<0.002	0.002	<0.002	<0.002	0.006	0.003
Sum	99.84	99.84	99.83	99.84	99.85	99.84	99.84	99.83	99.84	99.79	99.84	99.82	99.82
LOI	1.7	4.2	1.8	1.0	1.4	1.6	1.6	0.8	1.7	1.6	3.2	1.2	3.2
Ba	621	767	584	562	546	613	583	568	576	948	748	563	592
Ni	<20	<20	<20	<20	<20	<20	<20	<20	<20	<20	<20	<20	2.4
Co	11.7	11.2	12.2	11.4	10.6	11.6	11.9	11.9	12.7	19.4	12.1	11.1	10.9
Cs	8.5	4.6	5.9	5.6	5.6	4.2	7.1	7.6	6.3	10.2	11.3	5.9	8.7
Ga	16.7	17.7	17.6	15.5	15.8	15.1	15.5	17.2	16.8	16.1	16.4	16.7	17.0
Hf	6.6	7.4	6.6	6.8	6.3	6.7	7.1	6.8	7.0	7.1	7.2	5.8	6.6
Nb	21.3	22.0	20.0	19.1	19.1	19.9	20.3	21.2	21.7	21.1	21.0	17.1	18.9
Rb	172.1	186.5	163.0	152.7	153.2	155.8	167.7	161.4	168.4	187.7	173.9	150.6	163.5
Sr	139.0	80.8	145.9	153.8	135.0	163.4	132.2	144.1	134.2	133.9	103.5	128.8	148.8
Ta	1.7	1.9	1.4	1.3	1.5	1.6	1.6	1.6	1.8	1.6	1.6	1.5	1.6
Th	13.4	14.6	13.8	12.3	13.0	12.9	13.8	14.0	13.1	13.9	13.7	12.4	13.6
U	4.6	4.9	4.6	3.9	3.6	4.1	4.5	4.6	4.3	4.3	4.9	3.7	4.9
Zr	250.4	269.7	245.7	234.3	239.2	246.6	250.8	255.1	251.2	255.4	261.6	222.1	242.2
Y	35.7	29.0	34.5	34.0	33.4	36.1	35.8	35.2	35.7	116.0	42.9	39.8	35.7
La	41.0	42.9	40.2	39.1	38.7	40.7	40.6	41.9	41.4	83.6	47.6	40.3	40.6
Ce	81.7	80.6	83.8	79.0	78.5	82.3	80.4	83.5	84.7	155.6	90.7	75.6	83.9
Pr	9.50	9.86	9.83	9.25	9.25	9.48	9.76	9.67	9.82	23.88	11.48	9.60	9.90
Nd	37.9	37.1	38.0	35.0	36.2	37.4	36.8	37.5	38.0	108.0	44.1	35.9	37.9
Sm	7.65	7.63	7.63	7.45	7.29	7.45	7.65	7.86	7.77	24.57	8.88	7.28	7.41
Eu	1.57	1.41	1.54	1.41	1.44	1.43	1.56	1.49	1.52	5.60	1.88	1.47	1.46

Gd	7.53	7.06	7.56	7.15	6.99	7.34	7.50	7.99	7.53	27.85	8.76	7.77	7.47
Tb	1.14	1.03	1.08	1.05	1.05	1.11	1.08	1.11	1.11	3.94	1.32	1.12	1.09
Dy	6.65	6.09	6.80	6.41	6.42	6.44	6.93	6.84	6.60	25.00	8.11	6.76	6.64
Ho	1.29	1.10	1.25	1.22	1.14	1.28	1.24	1.28	1.27	4.69	1.47	1.38	1.27
Er	3.59	3.10	3.67	3.41	3.45	3.75	3.70	3.75	3.86	14.04	4.28	3.84	3.64
Tm	0.53	0.47	0.51	0.52	0.53	0.50	0.57	0.54	0.55	2.08	0.61	0.55	0.55
Yb	3.70	3.11	3.40	3.34	3.37	3.44	3.35	3.54	3.45	14.39	4.05	3.46	3.12
Lu	0.53	0.45	0.55	0.48	0.50	0.51	0.50	0.55	0.52	2.20	0.56	0.53	0.51
SumREE	204.28	201.91	205.82	194.79	194.83	203.13	201.64	207.52	208.10	495.44	233.80	195.56	205.46
Zr/Nb	11.76	12.26	12.29	12.27	12.52	12.39	12.35	12.03	11.58	12.10	12.46	12.99	12.81
Zr/Th	18.69	18.47	17.80	19.05	18.40	19.12	18.17	18.22	19.18	18.37	19.09	17.91	17.81
Nb/Y	0.60	0.76	0.58	0.56	0.57	0.55	0.57	0.60	0.61	0.18	0.49	0.43	0.53
Zr/Y	7.01	9.30	7.12	6.89	7.16	6.83	7.01	7.25	7.04	2.20	6.10	5.58	6.78
D (ap)*	15078.57	15637.04	15078.57	15637.04	16238.46	16238.46	16888.00	15637.04	15078.57	15637.04	15078.57	16888.00	16888.00
T°C (ap)	1038.70	1005.77	1029.60	1088.70	1093.81	1059.07	1109.58	1053.27	1068.47	1068.65	1072.05	1079.88	1028.93
η (dry)**	5.90	6.63	6.01	5.56	5.56	5.87	5.23	5.88	5.62	5.69	5.73	5.67	6.18
η (0.5)	4.82	5.40	4.91	4.57	4.58	4.82	4.29	4.83	4.60	4.66	4.68	4.64	5.05
η (1.3)	4.09	4.58	4.17	3.88	3.89	4.10	3.63	4.11	3.90	3.95	3.97	3.93	4.29

***UTM 22J; **viscosities for dry, 0.5 and 1.3 H_2O wt.%**

Area	São Marcos											
Sample	GA-03V	GA-03P	GA-04	GA-07	GA-10	GA-11	GA-12	GA-13	GA-16	GA-34	GA-35	GA-37
lat (S)*	6795474.0	6795474.0	6795526.0	6795476.0	6795360.0	6795721.0	6795245.0	6794956.0	6795622.0	6796246.0	6796310.0	6795204.0
long (E)	489079.0	489079.0	487754.0	488839.0	491862.0	488531.0	492231.0	492287.0	488643.0	494773.0	494631.0	494494.0
elevation	658.0	658.0	710.0	665.0	732.0	747.0	753.0	768.0	624.0	896.0	851.0	767.0
SiO_2	62.6	68.88	66.91	68.96	66.51	66.88	67.07	67.01	67.24	64.99	67.66	65.25
Al_2O_3	14.53	12.13	13.1	11.95	12.87	12.74	13.05	12.76	12.74	13.14	12.92	12.87
Fe_2O_3	6.71	5.99	5.87	6	5.93	5.84	5.9	5.84	6.24	7.24	6.03	6.32
MgO	1.48	1.21	0.92	1.13	1.22	1.31	0.95	1.31	1	1.52	1.15	1.36
CaO	3.31	2.96	2.14	2.76	3.1	2.94	2.5	3.03	2.5	3.48	3.02	3.48
Na_2O	3.34	2.72	2.54	2.59	2.86	2.84	2.8	2.87	2.63	3.15	3.05	3.55
K_2O	4.58	3.99	4.19	4.46	4.3	4.02	4.09	4.14	4.54	3.57	3.68	2.94
TiO_2	1	0.87	0.9	0.85	0.89	0.91	0.92	0.9	0.92	1.06	0.96	0.95
P_2O_5	0.29	0.26	0.26	0.25	0.27	0.28	0.27	0.28	0.27	0.29	0.26	0.27
MnO	0.13	0.1	0.07	0.1	0.11	0.09	0.11	0.09	0.11	0.15	0.09	0.11
Cr_2O_3	0.002	0.002	0.002	0.003	0.002	0.002	0.002	0.002	0.002	0.002	0.002	0.002
Sum	99.79	99.84	99.82	99.85	99.83	99.83	99.83	99.82	99.83	99.81	99.81	99.83
LOI	1.8	0.70	2.90	0.80	1.80	2.00	2.20	1.60	1.70	1.20	1.00	2.70
Ba	721	631	669	565	702	634	718	661	628	715	596	553
Ni	4.8	3	2.2	3.2	2.3	2.3	2	2	3.2	2.8	2.1	1.4
Co	13.8	11.3	10.2	11.5	11.3	10.4	10.2	10.9	11.8	15.2	13.3	12.2
Cs	7.8	7.9	6.6	6.8	6.3	6.2	7.3	7.5	7.8	6.4	7.2	8.3
Ga	19.2	16.8	17.6	15.6	17.3	16.7	17.5	17.3	17.1	18.1	16.3	16.6
Hf	7.2	6.4	6.9	5.9	7	6.9	6.8	7	6.9	6.5	6.3	6.2
Nb	23.1	20.7	22.7	20	21.4	22.4	22.9	21.8	22.1	21.1	20.5	20.3
Rb	197.2	178.5	187.9	181.9	177.5	165.6	172.3	177.6	185	149.7	157.2	149.3
Sr	154.5	144.2	125.1	130.9	147.7	141.2	137.8	152.5	133	150	143.1	147
Ta	1.8	1.7	1.7	1.5	1.6	1.7	1.5	1.6	1.6	1.4	1.5	1.5
Th	16.1	13.9	15.1	12.8	14	13.9	14.2	14.5	14.1	13.1	12.6	13.2
U	4.6	4.6	4.7	4.6	4.5	5	4.9	4.6	4.6	4.2	4.4	4.5
Zr	259.6	224.2	248	218.6	233.5	233.6	242.9	240.9	238.4	234.3	225.1	222
Y	65.6	45.5	65.9	34.6	41.1	36.9	49.5	36.6	34.2	42.9	109.5	34.1
La	48.1	39.9	49.9	36.6	39.8	39.5	39.3	41.1	38.1	39.9	47.6	36.2
Ce	94.1	84.2	110.6	81	85.7	85	82.9	89.9	85.1	86.9	106.3	80.6
Pr	11.91	9.65	12.95	9.15	9.8	9.75	9.75	10.24	9.63	9.67	13.49	9.09
Nd	46.8	37.7	52	35.5	40.2	38.2	37.2	39.4	37.4	36.8	58.9	35
Sm	9.56	7.51	10.34	7.08	7.75	7.6	7.59	7.86	7.28	7.76	12.93	7.2
Eu	1.88	1.44	2.03	1.42	1.54	1.47	1.54	1.5	1.43	1.61	2.98	1.41

Gd	10.43	7.3	10.57	6.52	7.35	7.05	7.81	7.12	6.61	7.59	15.4	6.69
Tb	1.72	1.17	1.72	1.08	1.18	1.15	1.25	1.17	1.09	1.26	2.58	1.11
Dy	10.01	6.39	9.84	6.08	6.59	6.41	6.9	6.7	6.22	7.16	15.45	6.33
Ho	2.13	1.38	2.04	1.2	1.36	1.29	1.52	1.28	1.2	1.45	3.32	1.21
Er	6.29	3.79	5.9	3.41	3.88	3.65	4.24	3.6	3.2	4.05	9.65	3.41
Tm	0.91	0.54	0.86	0.51	0.57	0.55	0.61	0.55	0.5	0.6	1.46	0.51
Yb	5.71	3.42	5.42	3.3	3.6	3.58	3.76	3.48	3.15	3.76	9.48	3.36
Lu	0.88	0.51	0.79	0.48	0.54	0.51	0.58	0.53	0.47	0.57	1.42	0.51
SumREE	250.43	204.90	274.96	193.33	209.86	205.71	204.95	214.43	201.38	209.08	300.96	192.63
Zr/Nb	11.24	10.83	10.93	10.93	10.91	10.43	10.61	11.05	10.79	11.10	10.98	10.94
Zr/Th	16.12	16.13	16.42	17.08	16.68	16.81	17.11	16.61	16.91	17.89	17.87	16.82
Nb/Y	0.35	0.45	0.34	0.58	0.52	0.61	0.46	0.60	0.65	0.49	0.19	0.60
Zr/Y	3.96	4.93	3.76	6.32	5.68	6.33	4.91	6.58	6.97	5.46	2.06	6.51
D (ap)*	14558.62	16238.46	16238.46	16888.00	15637.04	15078.57	15637.04	15078.57	15637.04	14558.62	16238.46	15637.04
T°C (ap)	1021.07	1079.59	1059.07	1109.58	1053.27	1068.47	1068.65	1072.05	1073.32	1021.07	1079.59	1018.67
η (dry)**	5.81	5.43	6.09	5.80	5.90	5.79	5.89	5.73	5.79	5.97	5.69	6.12
η (0.5)	4.71	4.48	4.99	4.78	4.84	4.74	4.83	4.70	4.75	4.86	4.67	4.99
η (1.3)	3.97	3.81	4.23	4.07	4.11	4.03	4.10	3.99	4.04	4.00	3.97	4.23

***UTM 22J; **viscosities for dry, 0.5 and 1.3 H_2O wt.%**

APPENDIX C – Mass balance (Stomer and Nichols, 1978) results obtained in the software Petrograph.

Mato Perso

Test 1	Lo (MP-02)	Lf (MS-01)	Plag	Cpx	Ti-mag	XL-frac	Δ0	Δf	residual (Δ0-Δf)
SiO_2	56.30	68.10	54.49	52.06	0	43.137	11.801	11.614	0.187
TiO_2	1.72	0.93	0.09	0.55	10.47	2.252	-0.79	-0.615	-0.175
Al_2O_3	13.59	12.80	27.52	1.67	1.42	14.23	-0.785	-0.662	-0.123
FeO_{tot}	13.10	6.30	1.09	12.04	87.21	21.295	-6.801	-6.974	0.173
MnO	0.17	0.11	0.02	0.47	0.57	0.27	-0.062	-0.074	0.012
MgO	3.42	1.34	0.13	14.79	0.33	4.83	-2.075	-1.621	-0.455
CaO	6.68	3.31	11.79	18.15	0	11.524	-3.371	-3.817	0.446
Na_2O	2.47	2.98	4.5	0.25	0	2.275	0.51	0.33	0.18
K_2O	2.27	3.82	0.37	0.01	0	0.186	1.554	1.692	-0.139
P_2O_5	0.25	0.27	0	0	0	0	0.019	0.127	-0.108
								$\sum res^2$	**0.5803**
subtracted phases (100%)			48.77	31.81	19.42				
fractionated total (%)									46.52

Plag= plagioclase; cpx= clinopyroxene; Ti-mag= titanomagnetite
Lo= initial liquid; Lf= final liquid; F= crystallized fraction in the parental magma;
Δ0= observed difference between the magmas ; Δ0= calculated difference between the magmas
∑res2= sum of the squares of residuals.

Test 2	Lo (MP-02)	Lf (MS-03a)	Plag	Cpx	Ti-mag	XL-frac	Δ0	Δf	residual (Δ0-Δf)
SiO_2	56.30	67.22	54.49	52.06	0	43.221	10.92	10.823	0.097
TiO_2	1.72	0.98	0.09	0.55	10.47	2.236	-0.743	-0.567	-0.175
Al_2O_3	13.59	13.49	27.52	1.67	1.42	13.496	-0.096	0	-0.096
FeO_{tot}	13.10	6.48	1.09	12.04	87.21	21.385	-6.618	-6.719	0.101
MnO	0.17	0.11	0.02	0.47	0.57	0.283	-0.06	-0.076	0.017
MgO	3.42	1.32	0.13	14.79	0.33	5.289	-2.093	-1.786	-0.307
CaO	6.68	3.04	11.79	18.15	0	11.759	-3.642	-3.928	0.286
Na_2O	2.47	2.98	4.5	0.25	0	2.155	0.511	0.375	0.137
K_2O	2.27	4.05	0.37	0.01	0	0.176	1.786	1.75	0.036
P_2O_5	0.25	0.29	0	0	0	0	0.034	0.13	-0.096
								$\sum res^2$	**0.2651**
subtracted phases (100%)			45.93	34.95	19.12				
fractionated total (%)									45.09

Test 3	Lo (MP-02)	Lf (MS-04)	Plag	Cpx	Ti-mag	XL-frac	Δ0	Δf	residual (Δ0-Δf)
SiO_2	56.30	68.20	54.49	52.06	0	43.109	11.901	11.734	0.167
TiO_2	1.72	0.90	0.09	0.55	10.47	2.258	-0.817	-0.633	-0.184
Al_2O_3	13.59	13.07	27.52	1.67	1.42	13.982	-0.516	-0.423	-0.092
FeO_{tot}	13.10	6.11	1.09	12.04	87.21	21.407	-6.992	-7.152	0.161
MnO	0.17	0.11	0.02	0.47	0.57	0.274	-0.061	-0.076	0.015
MgO	3.42	1.28	0.13	14.79	0.33	4.97	-2.132	-1.721	-0.41
CaO	6.68	3.16	11.79	18.15	0	11.584	-3.522	-3.936	0.414
Na_2O	2.47	2.81	4.5	0.25	0	2.234	0.338	0.27	0.068
K_2O	2.27	4.06	0.37	0.01	0	0.183	1.791	1.813	-0.023
P_2O_5	0.25	0.26	0	0	0	0	0.009	0.123	-0.114
								ξres^2	**0.4542**
subtracted phases (100%)			47.81	32.76	19.42				
fractionated total (%)									46.76

Test 4	Lo (MP-02)	Lf (MS-05b)	Plag	Cpx	Ti-mag	XL-frac	Δ0	Δf	residual (Δ0-Δf)
SiO_2	56.30	68.15	54.49	52.06	0	43.113	11.855	11.672	0.183
TiO_2	1.72	0.94	0.09	0.55	10.47	2.257	-0.778	-0.612	-0.165
Al_2O_3	13.59	12.91	27.52	1.67	1.42	14.099	-0.676	-0.551	-0.125
FeO_{tot}	13.10	6.20	1.09	12.04	87.21	21.368	-6.899	-7.067	0.168
MnO	0.17	0.10	0.02	0.47	0.57	0.272	-0.072	-0.08	0.008
MgO	3.42	1.27	0.13	14.79	0.33	4.901	-2.144	-1.689	-0.454
CaO	6.68	3.27	11.79	18.15	0	11.553	-3.415	-3.858	0.444
Na_2O	2.47	3.00	4.5	0.25	0	2.253	0.527	0.349	0.178
K_2O	2.27	3.85	0.37	0.01	0	0.185	1.582	1.709	-0.127
P_2O_5	0.25	0.27	0	0	0	0	0.019	0.128	-0.108
								ξres^2	**0.5677**
subtracted phases (100%)			48.27	32.3	19.44				
fractionated total (%)									46.61

São Marcos

Test 1	Lo (Av.*)	Lf (GA-03v)	Plag	Cpx	Ti-mag	XL-frac	Δ0	Δf	residual (Δ0-Δf)
SiO_2	53.83	63.89	54.87	51.14	0	47.344	10.062	10.273	-0.211
TiO_2	1.36	1.02	0	0.71	10.3	1.416	-0.345	-0.246	-0.099
Al_2O_3	14.03	14.83	27.32	2.05	2.75	13.148	0.792	1.044	-0.252
FeO_{tot}	12.86	6.84	1.08	14.72	85.86	16.315	-6.019	-5.875	-0.144
MnO	0.19	0.13	0.03	0.58	0.55	0.336	-0.057	-0.126	0.069
MgO	4.94	15.10	0.12	13.7	0.53	6.381	-3.439	-3.023	-0.416
CaO	8.89	3.37	11.51	16.84	0	12.728	-5.516	-5.802	0.286
Na_2O	2.45	3.40	4.71	0.26	0	2.17	0.953	0.769	0.183
K_2O	1.21	4.67	0.36	0.01	0	0.162	3.461	2.801	0.66
P_2O_5	0.19	0.29	0	0	0	0	0.109	0.184	-0.075
								$\sum res^2$	0.8732
subtracted phases (100%)			43.62	45.78	10.6				
fractionated total (%)									62.06

*average of samples from Lima et al. (2012)

Test 2	Lo (Av.*)	Lf (GA-03p)	Plag	Cpx	Ti-mag	XL-frac	Δ0	Δf	residual (Δ0-Δf)
SiO_2	53.83	69.49	54.87	51.14	0	47.234	15.663	15.53	0.134
TiO_2	1.36	0.88	0	0.71	10.3	1.437	-0.488	-0.39	-0.098
Al_2O_3	14.03	12.23	27.32	2.05	2.75	14.52	-1.8	-1.591	-0.209
FeO_{tot}	12.86	6.04	1.08	14.72	85.86	16.011	-6.825	-6.952	0.128
MnO	0.19	0.10	0.03	0.58	0.55	0.305	-0.089	-0.143	0.054
MgO	4.94	1.22	0.12	13.7	0.53	5.566	-3.728	-3.031	-0.697
CaO	8.89	2.98	11.51	16.84	0	12.337	-5.908	-6.522	0.614
Na_2O	2.45	2.74	4.71	0.26	0	2.409	0.288	0.234	0.054
K_2O	1.21	4.02	0.36	0.01	0	0.181	2.812	2.682	0.13
P_2O_5	0.19	0.26	0	0	0	0	0.075	0.183	-0.108
								$\sum res^2$	0.9848
subtracted phases (100%)			49.03	39.76	11.21				
fractionated total (%)									69.75

Test 3	Lo (Av.*)	Lf (GA-04)	Plag	Cpx	Ti-mag	XL-frac	Δ0	Δf	residual (Δ0-Δf)
SiO_2	53.83	69.05	54.87	51.14	0	47.372	15.215	15.109	0.107
TiO_2	1.36	0.93	0	0.71	10.3	1.411	-0.437	-0.336	-0.101
Al_2O_3	14.03	13.51	27.32	2.05	2.75	14.039	-0.52	-0.362	-0.158
FeO_{tot}	12.86	6.05	1.08	14.72	85.86	15.978	-6.811	-6.914	0.103
MnO	0.19	0.72	0.03	0.58	0.55	0.316	-0.118	-0.17	0.052
MgO	4.94	0.95	0.12	13.7	0.53	5.877	-4	-3.434	-0.565
CaO	8.89	2.20	11.51	16.84	0	12.507	-6.686	-7.177	0.491
Na_2O	2.45	2.62	4.71	0.26	0	2.326	0.165	0.206	-0.041
K_2O	1.21	4.32	0.36	0.01	0	0.174	3.11	2.892	0.218
P_2O_5	0.19	0.27	0	0	0	0	0.081	0.187	-0.106
								$\sum res^2$	0.681
subtracted phases (100%)			47.13	42.06	10.8				
fractionated total (%)									69.69

Test 4	Lo (Av.*)	Lf (GA-07)	Plag	Cpx	Ti-mag	XL-frac	Δ0	Δf	residual (Δ0-Δf)
SiO_2	53.83	69.62	54.87	51.14	0	47.31	15.786	15.689	0.097
TiO_2	1.36	0.86	0	0.71	10.3	1.422	-0.507	-0.397	-0.111
Al_2O_3	14.03	12.06	27.32	2.05	2.75	14.567	-1.974	-1.76	-0.215
FeO_{tot}	12.86	6.05	1.08	14.72	85.86	15.889	-6.811	-6.914	0.103
MnO	0.19	0.10	0.03	0.58	0.55	0.304	-0.089	-0.143	0.054
MgO	4.94	1.14	0.12	13.7	0.53	5.558	-3.808	-3.106	-0.702
CaO	8.89	2.78	11.51	16.84	0	12.35	-6.108	-6.725	0.617
Na_2O	2.45	2.61	4.71	0.26	0	2.418	0.158	0.139	0.019
K_2O	1.21	4.50	0.36	0.01	0	0.181	3.289	3.039	0.25
P_2O_5	0.19	0.25	0	0	0	0	0.065	0.177	-0.112
								$\sum res^2$	10.296
subtracted phases (100%)			49.22	39.71	11.08				
fractionated total (%)									70.32

Test 5	Lo (Av.*)	Lf (GA-10)	Plag	Cpx	Ti-mag	XL-frac	Δ0	Δf	residual (Δ0-Δf)
SiO_2	53.83	67.82	54.87	51.14	0	47.183	13.991	13.953	0.038
TiO_2	1.36	0.91	0	0.71	10.3	1.446	-0.458	-0.364	-0.094
Al_2O_3	14.03	13.12	27.32	2.05	2.75	14.134	-0.914	-0.682	-0.232
FeO_{tot}	12.86	6.04	1.08	14.72	85.86	16.21	-6.821	-6.869	0.048
MnO	0.19	0.11	0.03	0.58	0.55	0.314	-0.078	-0.136	0.059
MgO	4.94	1.24	0.12	13.7	0.53	5.776	-3.705	-3.063	-0.642
CaO	8.89	3.16	11.51	16.84	0	12.421	-5.733	-6.259	0.525
Na_2O	2.45	2.91	4.71	0.26	0	2.341	0.46	0.389	0.071
K_2O	1.21	4.38	0.36	0.01	0	0.175	3.171	2.845	0.325
P_2O_5	0.19	0.28	0	0	0	0	0.088	0.186	-0.098
								$\sum res^2$	0.8788
subtracted phases (100%)			47.5	41.3	11.2				
fractionated total (%)									67.59

Jaquirana-Cambará

Test 1	Lo (SP-03*)	Lf (MS-19A)	San.**	Plag	Cpx	Ti-mag	XL-frac	Δ0	Δf	residual (Δ0-Δf)
SiO_2	54.2	67.07	61.03	56.54	52.33	0	49.488	12.874	12.871	0.003
TiO_2	1.53	0.97	0.5	0.09	0.53	14.07	1.657	-0.562	-0.504	-0.058
Al_2O_3	14.74	12.96	16.15	26.31	1.6	2.31	15.091	-1.774	-1.555	-0.219
FeO_{tot}	11.7	6.80	0.88	1.1	13.22	82.53	13.492	-4.891	-4.891	0
MnO	0.17	0.12	6.54	0.01	0.48	0.5	0.369	-0.048	-0.181	0.133
MgO	4.54	1.68	0.21	0.07	14.54	0.59	5.15	-2.858	-2.538	-0.32
CaO	8.77	3.20	0.59	9.75	16.97	0	11.073	-5.569	-5.761	0.192
Na_2O	2.71	2.85	2.05	5.77	0.29	0	3.204	0.144	-0.256	0.4
K_2O	1.41	4.02	12.05	0.37	0.03	0	0.476	2.617	2.599	0.018
P_2O_5	0.23	0.29	0	0	0	0	0	0.066	0.216	-0.151
									$\sum res^2$	0.3914
subtracted phases (100%)			2.22	53	34.71	10.06				
fractionated total (%)										73.19

*sample from Piccirilo et al. (1988)
**sanidine

Test 2	Lo (SP-03*)	Lf (MS-22)	San.**	Plag	Cpx	Ti-mag	XL-frac	Δ0	Δf	residual (Δ0-Δf)
SiO_2	54.2	67.76	61.03	56.54	52.33	0	49.647	13.569	13.53	0.039
TiO_2	1.53	1.05	0.5	0.09	0.53	14.07	1.569	-0.473	-0.382	-0.091
Al_2O_3	14.74	14.38	16.15	26.31	1.6	2.31	14.747	-0.356	-0.271	-0.085
FeO_{tot}	11.7	7.14	0.88	1.1	13.22	82.53	13.308	-4.555	-4.601	0.046
MnO	0.17	0.94	6.54	0.01	0.48	0.5	0.245	-0.076	-0.113	0.037
MgO	4.54	0.95	0.21	0.07	14.54	0.59	5.56	-3.588	-3.441	-0.147
CaO	8.77	1.06	0.59	9.75	16.97	0	11.533	-7.703	-7.814	0.111
Na_2O	2.71	2.18	2.05	5.77	0.29	0	3.161	-0.524	-0.728	0.204
K_2O	1.41	5.08	12.05	0.37	0.03	0	0.229	3.674	3.625	0.049
P_2O_5	0.23	0.26	0	0	0	0	0	0.032	0.195	-0.164
									$\sum res^2$	0.1255
subtracted phases (100%)			0.17	52.84	37.59	9.4				
fractionated total (%)										74.66

Test 3	Lo (SP-03*)	Lf (MS-24)	San.**	Plag	Cpx	Ti-mag	XL-frac	Δ0	Δf	residual (Δ0-Δf)
SiO_2	54.2	69.32	61.03	56.54	52.33	0	49.598	15.124	15.13	-0.006
TiO_2	1.53	0.90	0.5	0.09	0.53	14.07	1.658	-0.625	-0.578	-0.047
Al_2O_3	14.74	12.25	16.15	26.31	1.6	2.31	15.169	-2.488	-2.237	-0.251
FeO_{tot}	11.7	6.15	0.88	1.1	13.22	82.53	13.371	-5.549	-5.538	-0.011
MnO	0.17	0.91	6.54	0.01	0.48	0.5	0.465	-0.078	-0.286	0.208
MgO	4.54	1.33	0.21	0.07	14.54	0.59	5.017	-3.208	-2.826	-0.382
CaO	8.77	2.87	0.59	9.75	16.97	0	10.866	-5.893	-6.127	0.235
Na_2O	2.71	2.93	2.05	5.77	0.29	0	3.199	0.228	-0.2	0.428
K_2O	1.41	3.86	12.05	0.37	0.03	0	0.657	2.454	2.459	-0.006
P_2O_5	0.23	0.26	0	0	0	0	0	0.034	0.203	-0.168
									$\sum res^2$	0.5212

subtracted phases (100%)	3.75	52.42	33.77	10.06	
fractionated total (%)					76.7

Test 4	Lo (SP-03*)	Lf (MS-29)	San.**	Plag	Cpx	Ti-mag	XL-frac	Δ0	Δf	residual (Δ0-Δf)
SiO_2	54.2	67.58	61.03	56.54	52.33	0	49.376	13.384	13.377	0.007
TiO_2	1.53	0.96	0.5	0.09	0.53	14.07	1.681	-0.562	-0.523	-0.039
Al_2O_3	14.74	13.14	16.15	26.31	1.6	2.31	15.03	-1.594	-1.384	-0.21
FeO_{tot}	11.7	6.29	0.88	1.1	13.22	82.53	13.651	-5.402	-5.402	0
MnO	0.17	0.10	6.54	0.01	0.48	0.5	0.357	-0.068	-0.188	0.12
MgO	4.54	1.63	0.21	0.07	14.54	0.59	5.175	-2.91	-2.604	-0.306
CaO	8.77	3.04	0.59	9.75	16.97	0	11.087	-5.723	-5.907	0.184
Na_2O	2.71	2.81	2.05	5.77	0.29	0	3.193	0.103	-0.28	0.382
K_2O	1.41	4.13	12.05	0.37	0.03	0	0.451	2.727	2.709	0.019
P_2O_5	0.23	0.28	0	0	0	0	0	0.045	0.202	-0.157
									$\sum res^2$	0.3581
subtracted phases (100%)			2.02	52.88	34.88	10.23				
fractionated total (%)										73.47

Test 5	Lo (SP-03*)	Lf (MS-38)	San.**	Plag	Cpx	Ti-mag	XL-frac	Δ0	Δf	residual (Δ0-Δf)
SiO_2	54.2	67.31	61.03	56.54	52.33	0	49.389	13.119	13.115	0.004
TiO_2	1.53	0.95	0.5	0.09	0.53	14.07	1.673	-0.572	-0.523	-0.049
Al_2O_3	14.74	13.09	16.15	26.31	1.6	2.31	15.051	-1.641	-1.428	-0.213
FeO_{tot}	11.7	6.47	0.88	1.1	13.22	82.53	13.619	-5.227	-5.227	0
MnO	0.17	0.11	6.54	0.01	0.48	0.5	0.341	-0.058	-0.167	0.109
MgO	4.54	1.62	0.21	0.07	14.54	0.59	5.184	-2.919	-2.607	-0.313
CaO	8.77	3.07	0.59	9.75	16.97	0	11.121	-5.692	-5.882	0.191
Na_2O	2.71	2.82	2.05	5.77	0.29	0	3.202	0.114	-0.277	0.39
K_2O	1.41	4.22	12.05	0.37	0.03	0	0.421	2.81	2.779	0.031
P_2O_5	0.23	0.30	0	0	0	0	0	0.066	0.216	-0.151
									$\sum res^2$	0.37
subtracted phases (100%)			1.76	53.11	34.95	10.18				
fractionated total (%)										73.15

Compound pahoehoe - Torres Formation

Test 1	Lo (av.*)	Lf (MS-01)	Plag	Cpx	Ti-mag	XL-frac	Δ0	Δf	residual (Δ0-Δf)
SiO_2	51.48	68.10	54.49	52.06	0	49.072	16.62	16.07	0.551
TiO_2	1.11	0.93	0.09	0.55	10.47	1.122	-0.189	-0.161	-0.028
Al_2O_3	14.83	12.80	27.52	1.67	1.42	14.291	-2.024	-1.253	-0.771
FeO_{tot}	1.13	6.30	1.09	12.04	87.21	12.716	-5.002	-5.416	0.413
MnO	0.17	0.11	0.02	0.47	0.57	0.258	-0.063	-0.124	0.061
MgO	7.93	1.34	0.13	14.79	0.33	6.459	-6.593	-4.318	-2.274
CaO	10.05	3.31	11.79	18.15	0	13.585	-6.736	-8.669	1.933
Na_2O	1.89	2.98	4.5	0.25	0	2.308	1.086	0.571	0.516
K_2O	1.04	3.82	0.37	0.01	0	0.188	2.776	3.07	-0.294
P_2O_5	0.15	0.27	0	0	0	0	0.124	0.231	-0.106
								$\sum res^2$	103.467
subtracted phases (100%)			48.9	43.08	8.02				
fractionated total (%)									84.44

*average of samples from Rossetti et al. (2014)

Test 2	Lo (av.*)	Lf (MS-03a)	Plag	Cpx	Ti-mag	XL-frac	Δ0	Δf	residual (Δ0-Δf)
SiO_2	51.48	67.22	54.49	52.06	0	49.085	15.739	15.169	0.571
TiO_2	1.11	0.97	0.09	0.55	10.47	1.12	-0.142	-0.118	-0.023
Al_2O_3	14.83	13.49	27.52	1.67	1.42	14.157	-1.335	-0.553	-0.782
FeO_{tot}	1.13	6.48	1.09	12.04	87.21	12.737	-4.819	-5.228	0.409
MnO	0.17	0.11	0.02	0.47	0.57	0.26	-0.061	-0.123	0.062
MgO	7.93	1.32	0.13	14.79	0.33	6.542	-6.61	-4.361	-2.25
CaO	10.05	3.04	11.79	18.15	0	13.626	-7.007	-8.848	1.841
Na_2O	1.89	2.98	4.5	0.25	0	2.286	1.088	0.585	0.503
K_2O	1.04	4.05	0.37	0.01	0	0.186	3.008	3.236	-0.228
P_2O_5	0.15	0.28	0	0	0	0	0.139	0.241	-0.102
								$\sum res^2$	98.717
subtracted phases (100%)			48.38	43.65	7.97				
fractionated total (%)									83.63

Ponded pahoehoe - Torres Formation

Test 1	Lo (av.*)	Lf (GA-04)	Plag	Cpx	Ti-mag	XL-frac	Δ0	Δf	residual (Δ0-Δf)
SiO_2	56.69	69.05	54.87	51.14	0	47.036	12.36	11.919	0.441
TiO_2	1.38	0.92	0	0.71	10.3	1.474	-0.451	-0.295	-0.156
Al_2O_3	14.33	13.51	27.32	2.05	2.75	14.973	-0.811	-0.787	-0.024
FeO_{tot}	11.12	6.05	1.08	14.72	85.86	16.136	-5.071	-5.456	0.385
MnO	0.15	0.72	0.03	0.58	0.55	0.295	-0.082	-0.121	0.039
MgO	3.95	0.94	0.12	13.7	0.53	5.257	-3.004	-2.332	-0.672
CaO	6.86	2.20	11.51	16.84	0	12.156	-4.658	-5.386	0.728
Na_2O	2.77	2.62	4.71	0.26	0	2.486	-0.149	0.073	-0.222
K_2O	2.45	4.32	0.36	0.01	0	0.187	1.873	2.24	-0.367
P_2O_5	0.27	0.27	0	0	0	0	-0.006	0.145	-0.151
								ξres^2	15.578
subtracted phases (100%)			50.8	37.47	11.73				
fractionated total (%)									54.14

*average of samples from Rossetti et al. (2014)

Test 2	Lo (MP-02)	Lf (MS-01)	Plag	Cpx	Ti-mag	XL-frac	Δ0	Δf	residual (Δ0-Δf)
SiO_2	56.69	68.10	54.49	52.06	0	46.064	11.413	10.983	0.429
TiO_2	1.38	0.93	0.09	0.55	10.47	1.695	-0.449	-0.381	-0.069
Al_2O_3	14.33	12.80	27.52	1.67	1.42	15.556	-1.523	-1.37	-0.153
FeO_{tot}	11.12	6.30	1.09	12.04	87.21	16.691	-4.826	-5.177	0.351
MnO	0.15	0.11	0.02	0.47	0.57	0.242	-0.043	-0.065	0.022
MgO	3.95	1.34	0.13	14.79	0.33	4.864	-2.608	-1.754	-0.854
CaO	6.86	3.31	11.79	18.15	0	12.179	-3.548	-4.416	0.868
Na_2O	2.77	2.98	4.5	0.25	0	2.504	0.214	0.239	-0.026
K_2O	2.45	3.82	0.37	0.01	0	0.205	1.373	1.803	-0.431
P_2O_5	0.27	0.27	0	0	0	0	-0.001	0.136	-0.137
								ξres^2	20.239
subtracted phases (100%)			53.85	32.12	14.03				
fractionated total (%)									49.83

Test 2	Lo (MP-02)	Lf (MS-03a)	Plag	Cpx	Ti-mag	XL-frac	Δ0	Δf	residual (Δ0-Δf)
SiO_2	56.69	67.22	54.49	52.06	0	46.196	10.532	10.174	0.358
TiO_2	1.38	0.97	0.09	0.55	10.47	1.669	-0.402	-0.335	-0.068
Al_2O_3	14.33	13.49	27.52	1.67	1.42	14.944	-0.834	-0.701	-0.133
FeO_{tot}	11.12	6.48	1.09	12.04	87.21	16.676	-4.643	-4.931	0.288
MnO	0.15	0.11	0.02	0.47	0.57	0.252	-0.041	-0.067	0.026
MgO	3.95	1.32	0.13	14.79	0.33	5.264	-2.626	-1.905	-0.721
CaO	6.86	3.04	11.79	18.15	0	12.396	-3.819	-4.523	0.704
Na_2O	2.77	2.98	4.5	0.25	0	2.404	0.215	0.281	-0.066
K_2O	2.45	4.05	0.37	0.01	0	0.197	1.605	1.867	-0.263
P_2O_5	0.27	0.28	0	0	0	0	0.014	0.139	-0.126
								Σres^2	1.339
subtracted phases (100%)			51.48	34.85	13.67				
fractionated total (%)									48.39

APPENDIX D – Open-system fractional crystallization modelling (O'Hara, 1977) results. D_{ij}=total partition coefficient for any element x contained into i-j mineral phases; C_s^B/C_0=concentration of element in the residual liquido f the fractionation cycle, in steady state/concentration of element in the parental magma ; C_i^0=initial concentration of element in the parental liquid ; *1-0.1*=concentration of element in each degree of fractionation

	D^x_{ij}	C_s^B/C_0	C_i^0	*1*	*0.9*	*0.8*	*0.7*	*0.6*	*0.5*	*0.4*	*0.3*	*0.2*	*0.1*
Rb	0.07	4.69	90.1	90.10	99.38	110.89	125.55	144.91	171.70	211.31	276.15	402.68	767.37
Sr	2.33	0.11	209.5	209.50	182.07	155.63	130.27	106.09	83.22	61.82	42.14	24.56	9.75
Ba	0.30	3.21	480	480.00	516.90	561.52	616.79	687.39	781.39	914.10	1118.99	1488.05	2422.37
Pb	0.38	2.79	3.2	3.20	3.42	3.67	3.99	4.39	4.91	5.64	6.73	8.65	13.27
Zr	0.22	3.63	211.4	211.40	229.40	251.35	278.78	314.19	361.92	430.31	537.90	736.71	1261.25
Hf	0.25	3.48	5.8	5.80	6.28	6.86	7.58	8.51	9.76	11.54	14.33	19.43	32.70
Nb	0.56	2.08	15.5	15.50	16.24	17.10	18.13	19.41	21.03	23.20	26.33	31.47	42.70
Ta	0.31	3.15	0.9	0.90	0.97	1.05	1.15	1.28	1.45	1.69	2.07	2.73	4.41
Th	0.06	4.79	9.1	9.10	10.05	11.23	12.74	14.73	17.49	21.59	28.32	41.50	79.79
La	0.76	1.50	34.5	34.50	35.40	36.43	37.64	39.08	40.86	43.14	46.28	51.09	60.51
Eu	2.11	0.16	1.72	1.72	1.53	1.34	1.16	0.98	0.80	0.62	0.45	0.29	0.13
Yb	2.45	0.09	3.54	3.54	3.04	2.56	2.11	1.69	1.30	0.94	0.62	0.34	0.13
Lu	1.24	0.67	0.58	0.58	0.57	0.55	0.53	0.51	0.49	0.47	0.43	0.39	0.33

CONSIDERAÇÕES FINAIS

A presente tese caracterizou três áreas relevantes no contexto do vulcanismo ácido do Grupo Serra Geral no Rio Grande do Sul. O reconhecimento de lavas e condutos associados já havia sido proposto para a área de São Marcos, no entanto foram agregados o distrito de Flores da Cunha, Mato Perso, e a vasta área dos municípios de Jaquirana e Cambará do Sul.

No primeiro artigo, "*Structures and lithofacies of inferred silicic conduits in the Paraná-Etendeka LIP, southernmost Brazil*", foram reconhecidas litofácies que caracterizam condutos alimentadores, como brechas nas porções externas e vitrófiros bandados e dobrados nas porções internas. Nas lavas foram reconhecidas texturas coerentes, padrões de vesiculação em sistema fechado e foliação horizontal. As estruturas regionais de direção NE-, como o lineamento formado pelo leito do rio das Antas, limitam estruturas de menor porte, de direção NW-, onde ocorrem os afloramentos de condutos. Os afloramentos de condutos, com 15-25 m, juntamente com os bandamentos subverticais, estão dispostos majoritariamente de acordo com as direções NE- e NW-.

O mapeamento geológico na região de Mato Perso, contido no artigo "*The Mato Perso Conduit System: evidence of silicic magma transport in the southern Paraná-Etendeka LIP*", revelou que: (1) as rochas bandadas e brechadas dos condutos ocorrem dominantemente entre duas estruturas de direção NW-; (2) Derrames de lavas oxidadas, de cor vermelha, estão sotopostos aos derrames de lavas não-oxidadas, de cor cinza; (3) Estruturas similares a diques, com ~4 m de espessura e diques de ~1,5 m de espessura compõem o sistema de alimentação.

A caracterização do fluxo magmático, presente no artigo "*Magmatic flow patterns in silicic feeder conduits and lava flows from Paraná-Etendeka LIP, Southern Brazil: AMS fabric, magma transport properties and implications for emplacement*", sugere que as partes internas dos condutos e das lavas são os locais onde a fábrica magnética tem o maior potencial de estar paralela ao fluxo magmático, pois a menor quantidade de vesículas e de fragmentos possibilitou a manutenção fluxo original do magma, sob baixas viscosidades. Já nas porções externas dos condutos, o dobramento complexo e a obstrução do fluxo por fragmentos altamente vesiculares deve ser a causa do espalhamento das direções dos eixos de susceptibilidade. O fluxo nos condutos foi sub-horizontal, mas com algumas das bandas verticais mostrando fluxo vertical. Nas

lavas o fluxo foi dominantemente horizontal. A direção do fluxo tanto para porções de alimentação quanto para fluxos de lavas é prevalente nas direções NE-SW e NW-SE.

No último artigo, "*Storage and emplacement of low-Ti silicic volcanics in the southern Paraná-Etendeka LIP: extensional tectonics controlling the ~134 Ma silicic volcanism in the early stages of Gondwana break-up*", a caracterização da química mineral em cada área indicou que em Mato Perso e São Marcos os plagioclásios são cálcicos (An>50) e os piroxênios levemente menos férricos que em Jaquirana-Cambará do Sul, onde os plagioclásios são sódicos (An<50) e ocorrem com microfenocristais de sanidina. A matriz vítrea mostra composições similares em todas as áreas, além de *trends* de cristalização fracionada quando comparada com as análises de rocha-total. A razão Zr/Nb é menor nas amostras de São Marcos, sendo sua variação atribuída à heterogeneidade composicional das fontes derivadas do manto e das rochas assimiladas. Cálculos de balanço de massa e curvas de assimilação e cristalização são modelados pelo fracionamento de 40-50% de andesitos basálticos e cristalização de uma assembleia mineral com proporções similares às observadas em lâmina. O modelamento de razões de elementos-traço sugere a assimilação de 20-80% de granitos peraluminosos e ortognaisses com 40-80% de fracionamento. Temperaturas da ordem de 1000°C, conteúdos de H_2O entre 0,5 e 1,3% e viscosidades entre 10^6 e 10^3 Pa s foram calculadas como parâmetros pré- e sin-eruptivos.

Ao final deste artigo, é montado um modelo para a ascensão do magma ácido de alta temperatura, baixa viscosidade e baixo conteúdo de voláteis. Um cenário tectônico evidente para a época (~134 Ma) é o de extensão crustal e desmembramento continental, portanto, sustentando que a reativação de falhas pretéritas por sistemas transtrativos de larga escala, com movimentação nas direções NW-SE e NE-SW tenham controlado a ascensão do magma. O modelo final proposto sugere que os movimentos constritivos da crosta continental em resposta à tectônica Andina e às consequentes anomalias do manto superior geraram ampla fusão no limite manto-crosta. A fusão envolveu fontes mantélicas, mas a assimilação de crosta continental foi inevitável, devido às altas temperaturas mantidas. A eficiência de transporte deste reservatório foi ampliada devido à extensão progressiva da crosta, fazendo com que o caminho até a superfície tenha se tornado cada vez mais curto e as taxas de efusão mais altas. Assim, o transporte de lava até a superfície tornou-se proporcionalmente mais eficiente.